DISSERTATION

submitted to the
Combined Faculties for the Natural Sciences and Mathematics
of the Ruperto-Carola-University of Heidelberg, Germany
for the degree of

Doctor of Natural Sciences

put forward by

Sascha Stahl

born in Bad Kreuznach, Germany.

Oral examination: 23.07.2014

Measurement of CP asymmetry in muon-tagged $D^0 \to K^-K^+$ and $D^0 \to \pi^-\pi^+$ decays at LHCb

Referees: Prof. Dr. Stephanie Hansmann-Menzemer

Prof. Dr. Hans-Christian Schultz-Coulon

Abstract: This thesis presents the measurement of the time-integrated *CP* asymmetries in $D^0 \rightarrow K^-K^+$ and $D^0 \rightarrow \pi^-\pi^+$ decays. The analysis uses data corresponding to an integrated luminosity of $3\,\mathrm{fb}^{-1}$ collected at the LHCb experiment in proton–proton collisions at centre-of-mass energies of 7 TeV and 8 TeV. The D^0 mesons are produced in semileptonic *b*-hadron decays, where the charge of the accompanying muon determines the initial flavour of the D^0 meson. By taking the difference of the observed asymmetries in the selected $D^0 \rightarrow K^-K^+$ and $D^0 \rightarrow \pi^-\pi^+$ samples, production and detection asymmetries cancel. The difference in *CP* asymmetries between the two final states is measured to be

$$\Delta A_{CP} = A_{CP}(K^-K^+) - A_{CP}(\pi^-\pi^+) = (+0.14 \pm 0.16\,(\mathrm{stat}) \pm 0.08\,(\mathrm{syst}))\,\% \,.$$

In order to obtain a measurement of $A_{CP}(K^-K^+)$, large samples of Cabibbo-favoured *D* meson decays are used to determine production and detection asymmetries to a high precision. The *CP* asymmetry is found to be

$$A_{CP}(K^-K^+) = (-0.06 \pm 0.15\,(\mathrm{stat}) \pm 0.10\,(\mathrm{syst}))\,\% \,,$$

where the correlation coefficient between ΔA_{CP} and $A_{CP}(K^-K^+)$ is $\rho = 0.28$. By combining these results, the *CP* asymmetry in $D^0 \rightarrow \pi^-\pi^+$ decays is derived to be $A_{CP}(\pi^-\pi^+) = (-0.20 \pm 0.19\,(\mathrm{stat}) \pm 0.10\,(\mathrm{syst}))\,\%$. The results of this thesis show that there is no significant *CP* violation in $D^0 \rightarrow K^-K^+$ and $D^0 \rightarrow \pi^-\pi^+$ decays at the level of 10^{-3}.

Kurzfassung: In der vorliegenden Arbeit werden die Messungen der zeitintegrierten *CP*-Asymmetrien in den Zerfällen $D^0 \rightarrow K^-K^+$ und $D^0 \rightarrow \pi^-\pi^+$ vorgestellt. Die benutzten Daten wurden in Proton–Proton Kollisionen mit den Schwerpunktsenergien 7 TeV und 8 TeV mit dem LHCb-Experiment aufgenommen. Sie entsprechen einer integrierten Luminosität von $3\,\mathrm{fb}^{-1}$. Die D^0 Mesonen stammen aus semileptonischen *b*-Hadron-Zerfällen, wobei die Ladung des einhergehenden Myons den anfänglichen Flavour des D^0-Mesons bestimmt. Produktions- und Detektionsasymmetrien kürzen sich in der Differenz der beobachteten Asymmetrien in den selektierten $D^0 \rightarrow K^-K^+$ und $D^0 \rightarrow \pi^-\pi^+$ Datensätzen. Die Differenz der *CP* Asymmetrien zwischen den beiden Endzuständen wird gemessen zu

$$\Delta A_{CP} = A_{CP}(K^-K^+) - A_{CP}(\pi^-\pi^+) = (+0.14 \pm 0.16\,(\mathrm{stat}) \pm 0.08\,(\mathrm{syst}))\,\% \,.$$

Große Mengen von Cabibbo-bevorzugten *D*-Meson-Zerfällen werden benutzt, um Produktions- und Detektionsasymmetrien mit hoher Präzision zu bestimmen. Diese Resulate ergeben eine Messung der *CP*-Asymmetrie $A_{CP}(K^-K^+)$ von

$$A_{CP}(K^-K^+) = (-0.06 \pm 0.15\,(\mathrm{stat}) \pm 0.10\,(\mathrm{syst}))\,\% \,.$$

Die Korrelation der Messungen von ΔA_{CP} und $A_{CP}(K^-K^+)$ beträgt $\rho = 0.28$. Beide Resultate kombiniert ergeben eine *CP*-Asymmetrie in $D^0 \rightarrow \pi^-\pi^+$ Zerfällen von $A_{CP}(\pi^-\pi^+) = (-0.20 \pm 0.19\,(\mathrm{stat}) \pm 0.10\,(\mathrm{syst}))\,\%$. Die vorgestellen Resultate zeigen, dass es keine signifikante *CP* Verletzung in den Zerfällen $D^0 \rightarrow K^-K^+$ and $D^0 \rightarrow \pi^-\pi^+$ bis zu einer Größenordnung $\mathcal{O}(10^{-3})$ gibt.

Contents

Chapter 1

Introduction

The study of fundamental interactions between elementary particles has a long tradition in physics which was started by ancient Greek and Indian philosophers more than two thousand years ago. Along the way, the definition of fundamental interactions and elementary particles has changed while probing higher energies and smaller structures. The current understanding is summarised in the Standard Model of particle physics. It has been developed from the 1960's onwards by many theoretical physicists with its fundamentals dating back to the development of quantum mechanics and quantum field theories in the 1920's. The Standard Model predictions have been challenged by many experiments until today, no significant discrepancy has been observed.

However, there are phenomena in nature which are not described by the Standard Model. The most obvious is that it cannot explain why apples fall from trees into the direction of the earth, as the theory does not include gravity. More subtle is the observation that the matter described by the Standard Model accounts only for about 5 % of the energy content in the universe. Due to their unknown origin, the remaining parts are called dark matter and dark energy. In general, the Standard Model alone has no explanation for the evolution of the universe from the Big Bang to its current state. In particular, it cannot explain the inflationary epoch.

To be able to answer some of these questions, the Large Hadron Collider (LHC), the biggest (and most expensive) particle accelerator, was built. It collides protons with the highest rate and energy ever produced in a laboratory. This enables us to probe the physics of fundamental particles with high precision. The discovery of the Higgs boson by the ATLAS and CMS experiments was one of the biggest milestones in particle physics as it was the last missing particle of the Standard Model.

The general purpose experiments CMS and ATLAS were built to directly observe up-to-now undiscovered particles by searching for their decays. In contrast, the LHCb experiment is designed to measure processes affected by quantum corrections in the decays of c and b hadrons. These high-precision measurements are sensitive to contributions from unknown particles. One of the main goals of the LHCb experiment is to study *CP*-violating effects in the decay of c and b hadrons. *CP* violation refers to differences between particle and antiparticle decays and is very sensitive to quantum corrections. It was first discovered in the decay of neutral kaons in 1964. Decades after, it was also established in the decay of neutral and charged b hadrons.

The picture for c hadrons, however, is not yet clear. Their decays provide an attractive testing ground of the Standard Model as it predicts very small *CP*-violating effects. *CP* violation can occur in the singly Cabibbo-suppressed $D^0 \to K^-K^+$ and

$D^0 \to \pi^-\pi^+$ decays, where significant contributions from loop processes are expected. In 2012 the LHCb experiment reported a first evidence of *CP* violation in the difference of the time-integrated asymmetries in $D^0 \to K^-K^+$ and $D^0 \to \pi^-\pi^+$ decays [1]:

$$\Delta A_{CP} = A_{CP}(K^-K^+) - A_{CP}(\pi^-\pi^+) = (-0.82 \pm 0.21\,(\text{stat}) \pm 0.11\,(\text{syst}))\,\% \quad .$$

This result sparked a theoretical discussion on whether the size of the measured *CP* violation can be accommodated within the Standard Model or not, and also renewed the interest in charm physics from the experimental side. The work presented in this thesis measures ΔA_{CP} on an independent data set recorded by the LHCb experiment. Furthermore, the experimental more challenging measurement of the individual *CP* asymmetries is performed for the first time at the LHCb experiment.

In order to determine the time-integrated *CP* asymmetries in D^0 decays to the *CP* eigenstates K^-K^+ and $\pi^-\pi^+$, the initial flavour, D^0 or $\overline{D}{}^0$, has to be identified. There are two main production channels of neutral charm mesons in proton–proton collisions: a D meson can be produced directly in the hadronization process, then it is often accompanied by a charged pion as both are originating from the same $D^{*\pm}$ resonance. The charge of the pion determines whether the hadron was initially a D^0 or a $\overline{D}{}^0$ meson. The aforementioned analysis selects D^0 mesons from this production mechanism. In the analysis presented here an alternative approach is used. D^0 mesons are selected by reconstructing semileptonic b-hadron decays where the b quark decayed weakly to a c quark, a muon and a neutrino. Thus, the charge of the accompanying muon determines the initial flavour of the charm meson. These events have a distinct signature. Charm and b hadrons produced in the LHCb experiment fly in average a few millimetre. This makes it is easier to discriminate these decays from the light hadron background. Furthermore, in contrast to hadrons, muons are clean to detect as they traverse the whole apparatus without being stopped. The disadvantage is that the production rate of b hadrons is a factor of 20 smaller than the rate of directly produced c hadrons. Nevertheless, the latter measurement reaches a sensitivity comparable to the former due to the higher trigger and reconstruction efficiency of semileptonic b-hadron decays. Both analyses measure the time-integrated *CP* asymmetries in $D^0 \to K^-K^+$ and $D^0 \to \pi^-\pi^+$ decays with a precision at the level of 10^{-3}.

In addition, there are several effects which have to be controlled when performing these measurements at the LHCb experiment. The two main effects are production and detection asymmetries. First, the LHC collides protons. Hence, there is an excess of baryons in the initial state which translates to a different production rate of D^0 and $\overline{D}{}^0$ mesons. Second, the determination of the flavour requires the reconstruction of at least one additional charged particle. Charged particles are prone to have different detection efficiencies depending on their charge. One reason is that the detector is not completely symmetric and the other is that particles and their corresponding antiparticles can have different material interaction rates. Both asymmetries, detection and production, are expected to be at the per-mille to per-cent level. This is larger or of the same order as the expected *CP* asymmetry. As the final sensitivity to *CP* asymmetries is at the low per-mille level, the main challenge of this analysis is to control and measure these spurious asymmetries and discriminate them from the *CP* asymmetries. This also shows the importance to have two independent analyses. As the selection of muons is very different to the selection of charged pions, this analysis has complementary systematic errors compared to the measurement with directly produced D^0 mesons.

In the following three chapters the underlying theory of the measurement, the LHCb experiment and the reconstruction of proton–proton collisions are introduced. After that the analysis strategy is presented. There the course of the document is detailed.

The author of this thesis was one of the main proponents of the two publications [2,3] which cover the same analysis as presented in this document. Both publications are based on LHCb internal analysis notes [4, 5].

The author also significantly contributed to publications which are not described in this work. They are in chronological order: The measurement of the K^0_S production cross-section in proton–proton collisions at $\sqrt{s} = 450\,\mathrm{GeV}$ [6]; the measurement of the B^0 and B^0_s oscillation frequencies Δm_d and Δm_s with the data set recorded in 2010 [7]; the measurement of the $\mathit{\Lambda}_c$ production cross-section in proton–proton collisions at $\sqrt{s} = 7\,\mathrm{TeV}$ [8]; and the measurement of the *CP*-violating phase ϕ_s in the decay $B^0_s \to J/\psi\phi$ [9]. Furthermore, he worked on the track reconstruction in the LHCb software trigger [10].

CHAPTER 2

Theory of particle–antiparticle asymmetries

This chapter introduces the theoretical understanding of *CP* violation in charm decays. First, a brief introduction to the Standard Model of particle physics is given, followed by a discussion of the charged currents of the weak interaction. The discussion includes a summary of B and D decays.[1] Afterwards, the concepts of meson mixing and *CP* violation are introduced. The focus is put on the charm sector but the analysis also requires an understanding of kaons and B mesons. Asymmetries in particle and antiparticle creation in pp collisions are briefly discussed before the chapter concludes with a small discourse on material interaction asymmetries.

2.1 Brief introduction to the Standard Model of particle physics

The Standard Model of particle physics (SM) is the widely accepted and best-tested theory to describe particles and their interactions.[2] It contains the fundamental particles, quarks and leptons, that build all visible matter. The electromagnetic interaction holds atoms, molecules and solid state bodies together. The strong interaction binds the constituents of nucleons and forms a nucleus out of them. And finally, the weak interaction describes decays of quarks and leptons, which leads, for example, to radioactivity.

The Standard Model of particle physics is a renormalizable quantum field theory. Its Lagrangian, see Figure 2.1, is gauge invariant under local transformations of the

$$SU(3)_C \otimes SU(2)_L \otimes U(1)_Y$$

symmetry group.

The **matter fields** of spin 1/2 (fermions) are the quarks and leptons. Quarks and leptons appear in three generations each of them consisting of a doublet. The up-type quarks are the up, the charm and the top quark. The down-type quarks are the down, the strange and the bottom quark:

$$\begin{pmatrix} u \\ d \end{pmatrix}, \begin{pmatrix} c \\ s \end{pmatrix}, \begin{pmatrix} t \\ b \end{pmatrix} \quad .$$

---

[1] Throughout the document B stands for B^0 and B^+ mesons and D for D^0 and D^+ mesons. The inclusion of charge-conjugate processes is implied throughout the work, unless explicitly stated otherwise.

[2] The introduction to the Standard Model is based on Refs. [11–13].

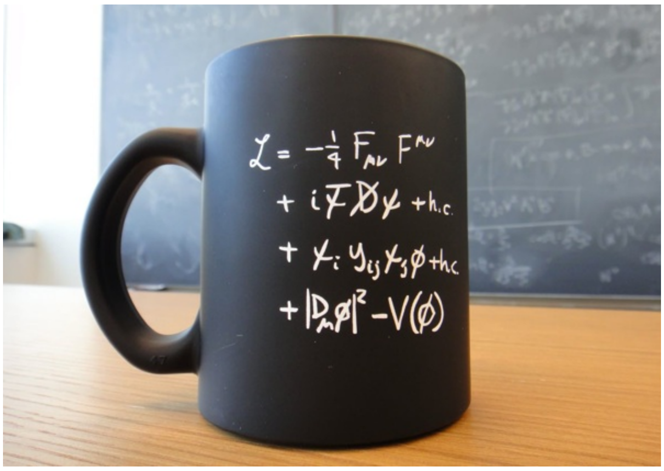

Figure 2.1: A concise description of the SM Lagrangian. Credits: Cern Gift Shop.

The three doublets of leptons consist of the electron, the muon, the tau and the related neutrinos:

$$\begin{pmatrix} \nu_e \\ e^- \end{pmatrix}, \begin{pmatrix} \nu_\mu \\ \mu^- \end{pmatrix}, \begin{pmatrix} \nu_\tau \\ \tau^- \end{pmatrix} \quad .$$

Each fermion has a corresponding antiparticle with opposite quantum numbers but the same mass.

The force carriers of spin 1 are the generators of the symmetry groups. The generators of **quantum chromodynamics (QCD)**, the $SU(3)_c$ symmetry group, are the eight massless gluons, g. Gluons couple only to quarks and to themselves via their colour charges. The two main features of the strong interaction are confinement and asymptotic freedom. Confinement means that only colour-neutral objects exist, which have to be made from multiple quarks. Hence, free quarks cannot be observed. Asymptotic freedom of quarks appears due to the running of the strong coupling constant that is very large at low energies but very small at high energies. Thus, quarks are are quasi-free at small distances. The strong interaction is discussed in more detail in Section 2.6 in the context of particle production at the Larger Hadron Collider (LHC).

The **electroweak** symmetry group, $SU(2)_L \times U(1)_Y$, is generated by the photon, γ, and the gauge bosons, W^+, W^- and Z^0. Their masses are generated by **spontaneous symmetry breaking** of this symmetry group. Spontaneous symmetry breaking is implemented in the Standard Model through the so-called Higgs mechanism, which leads to a massive spin 0 particle, the Higgs boson. Fermion masses are generated by Yukawa interactions between the Higgs and fermion fields. The generated masses range from $511\,\text{keV}/c^2$ for the electron to more than $170\,\text{GeV}/c^2$ for the top quark. The masses of each fermion and boson are given in Table 2.1. The Higgs boson was the last missing particle of the Standard Model. The discovery was announced in July 2012 by the ATLAS [14] and CMS [15] experiments. After breaking the electroweak symmetry group to the **electromagnetic** and **weak interaction**, one generator, the photon, remains massless. The photon couples to the electric charge of quarks and leptons; neutrinos are electrically neutral and do not take part in electromagnetic interactions. While Z^0 bosons couple with different strengths to the left- and right-handed (chiral)

Table 2.1: The particle content of the Standard Model including measured masses [16].

Fermions

Spin 1/2	**Quarks**		**Leptons**	
Generation	Type	Mass	Type	Mass
1	u	$2.3\,\mathrm{MeV}/c^2$	ν_e	$< 2\,\mathrm{eV}/c^2$
	d	$4.8\,\mathrm{MeV}/c^2$	e^-	$511.0\,\mathrm{keV}/c^2$
2	c	$1.28\,\mathrm{GeV}/c^2$	ν_μ	$< 2\,\mathrm{eV}/c^2$
	s	$95\,\mathrm{MeV}/c^2$	μ^-	$105.7\,\mathrm{MeV}/c^2$
3	t	$173.5\,\mathrm{GeV}/c^2$	ν_τ	$< 2\,\mathrm{eV}/c^2$
	b	$4.18\,\mathrm{GeV}/c^2$	τ^-	$1.78\,\mathrm{GeV}/c^2$

Bosons

Spin 1		**Spin 0**	
Type	Mass	Type	Mass
γ	0	H^0	$125\,\mathrm{GeV}/c^2$
g (8)	0		
Z^0	$91.2\,\mathrm{GeV}/c^2$		
$W^\pm$	$80.4\,\mathrm{GeV}/c^2$		

components of particles, the charged gauge bosons of the weak interaction, W^+ and W^-, couple only to left-handed particles. The weak interaction is short-ranged due to the high masses of $W^\pm$ and Z^0 bosons, $80\,\mathrm{GeV}/c^2$ and $91\,\mathrm{GeV}/c^2$, respectively. Charged currents allow transitions between up- and down-type quarks as well as transitions between charged and neutral leptons. This is discussed in more detail in Chapter 2.2 as it is a requisite for mixing of neutral mesons and CP violation.

2.2 Charged weak currents

The following section introduces charged weak currents. Furthermore bottom and charm decays are discussed, including higher order corrections.

2.2.1 Charged currents and CKM matrix

The $W^\pm$ bosons mediate the charged currents of the weak interaction. They change the flavour of particles, e.g., a charged lepton radiating a W^- boson turns into a neutrino or a down-type quark turns into an up-type quark. The interaction Lagrangian of $W^\pm$ bosons with fermions is given by

$$\mathcal{L} = -\frac{g_2}{2\sqrt{2}} \left(J^\mu_W W^-_\mu + J^{\mu\dagger}_W W^+_\mu \right) \quad , \tag{2.1}$$

where g_2 is the $SU(2)_L$ coupling constant and $J_W^{\mu\dagger}$ the weak charge-raising current. It can be written as

$$J_W^{\mu\dagger} = \begin{pmatrix}\overline{\nu}_e & \overline{\nu}_\mu & \overline{\nu}_\tau\end{pmatrix} \gamma^\mu(1-\gamma^5) \begin{pmatrix} e^- \\ \mu^- \\ \tau^- \end{pmatrix} + \begin{pmatrix}\overline{u} & \overline{c} & \overline{t}\end{pmatrix} \gamma^\mu(1-\gamma^5) V_q \begin{pmatrix} d \\ s \\ b \end{pmatrix} \quad , \tag{2.2}$$

where V_q is a unitary matrix, the quark fields are given in their mass eigenstates and the leptons in their flavour eigenstates.[3] The matrix V_q is discussed after a short discourse on the structure of charged currents.

The matrices γ^μ and γ^5 are also known as the Dirac matrices. The operator $\frac{1}{2}\left(1 \mp \gamma^5\right)$ projects onto the left(right)-handed component of a Dirac-spinor. An interaction of the form $\overline{\psi}\gamma^\mu\psi$ is called vectorial as it transforms like a vector under parity transformation, P,

$$P\vec{x} = -\vec{x} \quad . \tag{2.3}$$

Terms like $\overline{\psi}\gamma^\mu\gamma^5\psi$ transform as an axial-vector, $\vec{L}$ with $P\vec{L} = \vec{L}$. Thus, the weak interaction Lagrangian has a $V-A$ structure which maximally violates parity.

A similar argument holds for the charge conjugation operator, C, which reverses all charge quantum numbers, e.g.

$$C\left|e^-\right\rangle = \left|e^+\right\rangle \quad . \tag{2.4}$$

The transformation C of Dirac-spinors is given by

$$C\psi = i\gamma^2\psi \quad . \tag{2.5}$$

As γ^5 and γ^μ anti-commute ($\{\gamma^5, \gamma^\mu\} = \gamma^5\gamma^\mu + \gamma^\mu\gamma^5 = 0$), the C transformation of $\overline{\psi}\gamma^\mu\gamma^5\psi$ accumulates an additional minus sign. Therefore, the weak interaction also violates C maximally. A more concrete consequence is that charged currents only couple to left-handed particles and right-handed antiparticles. The relevant particle–antiparticle transformation in the context of the weak interaction is the combined transformation CP.

As already mentioned, the fermion fields are given in their mass eigenstates in Equation 2.2. Mass eigenstates diagonalise the Yukawa interaction terms which generate quark masses in the SM Lagrangian:

$$m_q(\overline{q}_L q_R + \overline{q}_R q_L) \quad , \tag{2.6}$$

where m_q is the quark mass, q_L and q_R are the left- and right-handed components of a spinor, respectively. The mass eigenstates q defined by this equation and the weak eigenstates q' do not have to be the same. The matrix V_q is a unitary transformation matrix between the two bases:

$$\begin{pmatrix} d' \\ s' \\ b' \end{pmatrix} = V_q \begin{pmatrix} d \\ s \\ b \end{pmatrix} \quad . \tag{2.7}$$

---

[3] The effect of non-vanishing neutrino masses is negligible in all processes relevant for this analysis.

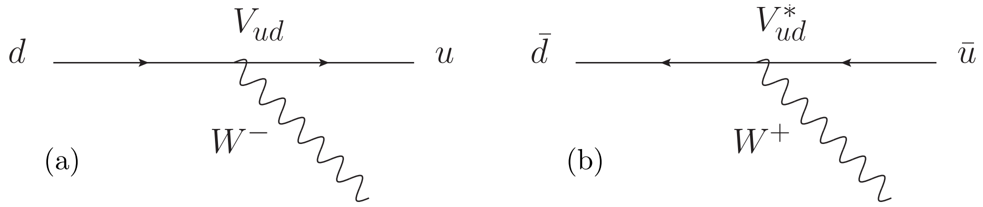

Figure 2.2: The Feynman diagrams for (a) d-to-u and (b) $\overline{d}$-to-$\overline{u}$ transitions.

In the basis of the states q' the charged current has only transitions within the doublet of each generation

$$\begin{pmatrix} u \\ d' \end{pmatrix}, \begin{pmatrix} c \\ s' \end{pmatrix}, \begin{pmatrix} t \\ b' \end{pmatrix} .$$

A non-diagonal matrix V_q allows transitions between different generations of quarks. The matrix V_q is also known as the Cabibbo-Kobayashi-Maskawa (CKM) matrix

$$V_{\text{CKM}} \equiv V_q = \begin{pmatrix} V_{ud} & V_{us} & V_{ub} \\ V_{cd} & V_{cs} & V_{cb} \\ V_{td} & V_{ts} & V_{tb} \end{pmatrix} . \tag{2.8}$$

As an example, the Feynman diagram for a d-to-u transition is shown in Figure 2.2. Feynman diagrams are pictorial representations of the calculation rules to obtain the transition matrix element of fundamental processes. The transition matrix element of a d-to-u transition is proportional to V_{ud}, while the matrix element of a $\overline{d}$-to-$\overline{u}$ quark transition is proportional to the complex conjugate, V^*_{ud}.

The CKM matrix has four free parameters, three real amplitudes and one phase. A common parameterisation which emphasises the hierarchy of the CKM matrix is the Wolfenstein parameterisation [17]

$$V_{\text{CKM}} = \begin{pmatrix} 1 - {}^1\!/_2\,\lambda^2 & \lambda & A\lambda^3(\rho - i\eta) \\ -\lambda & 1 - {}^1\!/_2\,\lambda^2 & A\lambda^2 \\ A\lambda^3(1 - \rho - i\eta) & -A\lambda^2 & 1 \end{pmatrix} + \mathcal{O}(\lambda^4) . \tag{2.9}$$

The expansion parameter λ is roughly 0.22. The parameterisation shows that transitions from one to the next generation are suppressed by λ and λ^2, whereas the elements on the diagonal are close to one. Transitions between the first and the third generation are suppressed by three orders of λ. Suppression by orders of λ are referred as *Cabibbo-suppressed* in the following. The other parameters of the Wolfenstein parameterisation are between 0.1 and 1, they do not change the order of magnitude. Up to λ^3 terms, the only elements with complex components are V_{ub} and V_{td}.

2.2.2 Charmed beauty decays

As the top quark has a mass of about $170\,\text{GeV}/c^2$, B mesons with a mass of about $5.3\,\text{GeV}/c^2$ cannot decay into hadrons containing a top quark. The transition with the largest amplitude is $b \to cW^-$, which is already suppressed by two orders of λ, see Equation 2.9. This gives b hadrons a substantial lifetime. For example, the lifetime

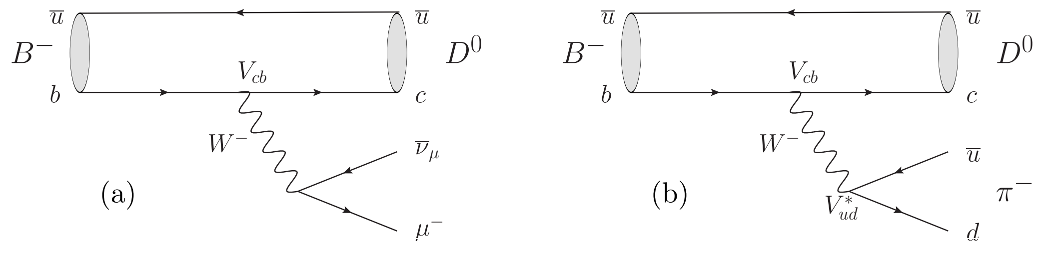

Figure 2.3: The tree-level diagrams for (a) $B^- \to D^0\mu^-\overline{\nu}_\mu$ and (b) $B^- \to D^0\pi^-$. The branching fractions are $(2.26 \pm 0.11)\,\%$ and $(0.481 \pm 0.015)\,\%$, respectively [16].

of a B^0 meson is $(1.519 \pm 0.007)\,\text{ps}$ [16]. Transitions between the third and the first generation are suppressed by an additional factor of λ. Therefore, the majority of the decays has a c hadron[4] in the final state. In this thesis the decays of interest are decays with a D^0 meson in the final state. B^- mesons are more likely to decay into a D^0 meson as the spectator quark, a u quark, can be used to form a D^0 state. The decay of $\overline{B}^0$ mesons to D^0 mesons proceeds predominantly via the D^{*+} resonance which has a branching fraction of $(67.7 \pm 0.5)\,\%$ [16] to the final state $D^{*+} \to D^0\pi^+$. The measured inclusive branching fractions of $B^- \to D^0X$ is $(79 \pm 4)\,\%$, the one of $\overline{B}^0 \to D^0X$ is $(47.4 \pm 2.8)\,\%$ [16].

The W^- boson then decays further into two fermions. All quark and lepton doublets except the third quark generation are accessible. Decays containing a $b \to c\,\ell^-\,\overline{\nu}_\ell$ transition are called semileptonic decays, whereas $b \to c\,q\,\overline{q}'$ transitions are called hadronic decays. The Feynman diagrams for one specific semileptonic and one specific hadronic decay are shown in Figure 2.3. These types of Feynman diagrams are called tree-level diagrams as they figuratively have a trunk and branches. They are the diagrams of lowest order.

As the mass of B mesons is substantially larger than the D^0 meson mass, $1.86\,\text{GeV}/c^2$, additional particles can be produced in the hadronization process. Most decays do not appear as clean as Figure 2.3. Very often higher D resonances are created in the B decay, which then decay further to D^0, D^+ or D_s^+ mesons. Final states, excluding the D^0 decay products, with seven and more particles have been observed. In fact the particle data group (PDG) lists much more than 100 observed final states with a D meson [16]. In order to identify the flavour of a neutral charm meson, D^0 or $\overline{D}^0$, the charge of the $W^\mp$ boson from the $b \to cW^-$ or $\overline{b} \to \overline{c}W^+$ transition, respectively, has to be determined. In a semileptonic decay the lepton in the final state originates from the $b \to c\,\ell^-\,\overline{\nu}_\ell$ transition. It is sufficient to reconstruct the lepton and its charge to *tag* the flavour of the D^0 meson. Roughly 20 % of the B decays are semileptonic. The remainder are hadronic final states. The full hadronic decay has to be reconstructed to determine the flavour, for example in a decay like $B^- \to D^0\pi^-\pi^+\pi^-$ the pion from the $b \to cq\overline{q}'$ transition is hard to identify. The branching fraction to the simplest hadronic final state, $D^0\pi^-$, is significantly smaller than the semileptonic branching fraction, see Figure 2.3. Hence, semileptonic B decays are a rich and clean source of D^0 mesons.

---

[4] Due to convention, B^0 and B^+ mesons contain a $\overline{b}$ quark, while D^0 and D^+ mesons contain a c quark.

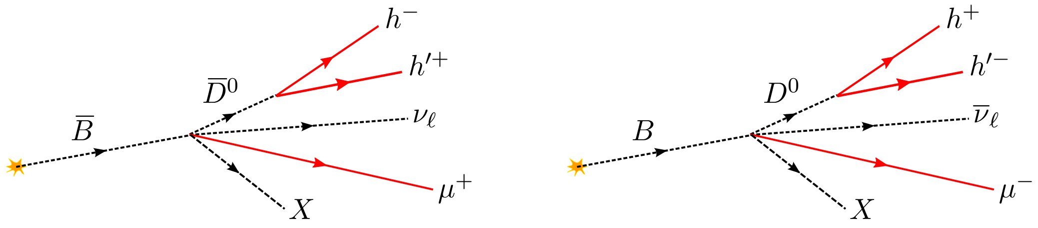

(a) negatively-tagged (b) positively-tagged

Figure 2.4: The topology of semileptonic (a) $\overline{B}$ and (b) B decays. The reconstructed final states are D^0 and μ^- or $\overline{D}^0$ and μ^+. The neutrino and further particles X are not reconstructed.

Semileptonic B decays with taus and electrons are experimentally more challenging than decays with muons in the final state. Taus have a short lifetime. If produced at the LHC, they decay in average after a few millimetre and the tau final state always contains at least one neutrino. Therefore, the reconstruction efficiency is small. Electrons are also harder to reconstruct than muons as they undergo much more electromagnetic interactions than muons when passing through matter. The interaction of particles with detector material is discussed later in Chapter 2.5.1. In contrast, the lifetime of muons is long enough to traverse the whole detector and their interaction rate with the detector material is low. Particles which are produced in the acceptance of the LHCb detector have a large boost. Chapter 2.6 is dedicated to particle production at the LHC. Due to the large boost, the muon and the D^0 meson form a vertex which is displaced from the pp collision as B mesons have a long lifetime. Therefore, semileptonic B decays with a muon in the final state have clean detection signature.

The decays considered in this analysis are $B^- \to D^0\mu^-\overline{\nu}_\mu X$ and $\overline{B}^0 \to D^0\mu^-\overline{\nu}_\mu X$ where X are any other possible particles. As mentioned before, the decay of B^0 mesons to D^0 mesons proceeds via a charged D^{*+} resonance, $\overline{B}^0 \to D^{*+}(\to D^0\pi^+)\mu^-\overline{\nu}_\mu X$. Thus, in B^0 decays there is at least one additional charged meson. However, only the D^0 meson and the muon, for the flavour tag, need to be reconstructed. Both decays are collectively referred to as $\overline{B} \to D^0\mu^- X$ where X are not reconstructed particles. Due to the different branching fractions to D^0 mesons [16] and assuming the same reconstruction efficiency, the fraction of B^0 mesons in this sample, $f(B^0) \equiv N(B^0)/(N(B^0) + N(B^+))$, is $(37.5 \pm 2.9)\,\%$.

A D^0 meson is tagged by the charge of the muon in the reconstructed decay $\overline{B} \to D^0\mu^- X$ and a $\overline{D}^0$ meson by $B \to \overline{D}^0\mu^+ X$. The selected sample of semileptonic B decays is also referred to as *muon-tagged* D^0 decays. The topology of positively- and negatively-tagged events is depicted in Figure 2.4. The final states of the D^0 decays are discussed in the following section.

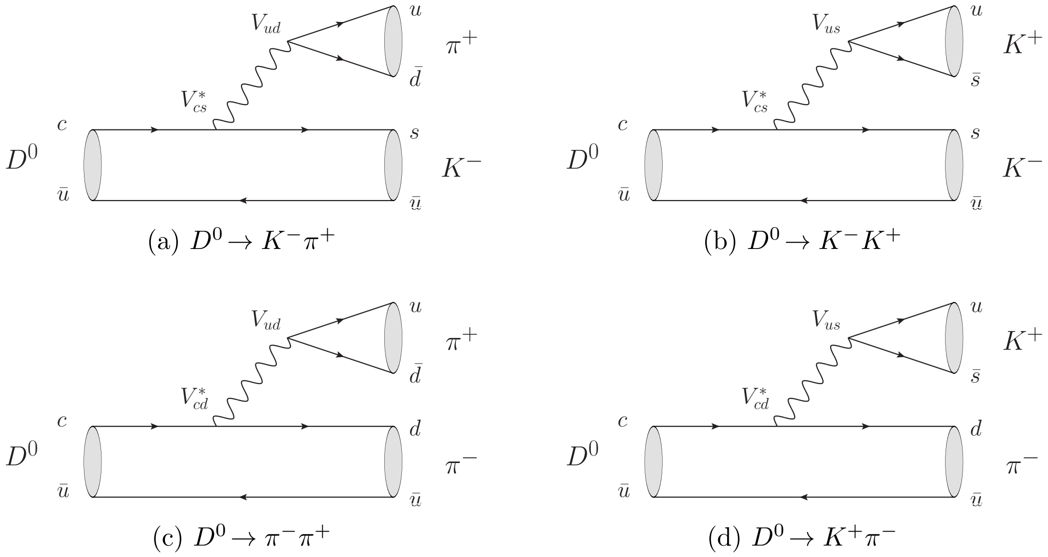

(a) $D^0 \to K^-\pi^+$ (b) $D^0 \to K^-K^+$ (c) $D^0 \to \pi^-\pi^+$ (d) $D^0 \to K^+\pi^-$

Figure 2.5: The tree-level diagrams of two-body D^0 decays.

2.2.3 Tree-level charm decays

A D^0 meson decays into lighter mesons via the weak interaction. The simplest system are two-body decays. Only final states with charged kaons and pions are considered as they are experimentally less challenging to reconstruct. This leaves four possible decays: $D^0 \to K^-\pi^+$, $D^0 \to K^-K^+$, $D^0 \to \pi^-\pi^+$ and $D^0 \to K^+\pi^-$. They can be divided into three categories:

Cabibbo-favoured (CF): The decay $D^0 \to K^-\pi^+$ is called Cabibbo-favoured. Both transitions are within one quark generation. The decay rate is proportional to $|V_{cs}^* V_{ud}|^2 \approx 1$, see Figure 2.5a. The measured branching fraction is $(3.88 \pm 0.05) \times 10^{-2}$ [16].

Singly Cabibbo-suppressed (SCS): The decays $D^0 \to K^-K^+$ and $D^0 \to \pi^-\pi^+$ are singly Cabibbo-suppressed as in both decays one transition from the second to the first quark generation appears. The matrix elements are of order λ as they are proportional to $V_{cs}^* V_{us}$ and $V_{cd}^* V_{ud}$, respectively, see Figure 2.5b and 2.5c. Both decay rates are proportional to λ^2. The measured branching fraction of $D^0 \to K^-K^+$ is $(3.96 \pm 0.08) \times 10^{-3}$ and of $D^0 \to \pi^-\pi^+$ is $(1.402 \pm 0.026) \times 10^{-3}$ [16].

Doubly Cabibbo-suppressed (DCS): The decay $D^0 \to K^+\pi^-$ is a so-called *wrong-sign* decay as the final state particles have opposite charges compared to the Cabibbo-favoured decays, see Figure 2.5d. The decay rate is proportional to $|V_{cd}^* V_{us}|^2 \propto \lambda^4$. The measured branching fraction is $(1.37 \pm 0.06) \times 10^{-4}$ [16].

The analysis uses $D^+ \to \overline{K}^0\pi^+$ and $D^+ \to K^-\pi^+\pi^+$ decays for calibration purposes. Both involve a $c \to s u \bar{d}$ transition and are therefore Cabibbo-favoured. The $D^+ \to K^-\pi^+\pi^+$ branching fraction is about six times higher than the $D^+ \to \overline{K}^0\pi^+$ branching fraction, $(9.13 \pm 0.19)\,\%$ and $(1.47 \pm 0.07)\,\%$ [16], respectively.

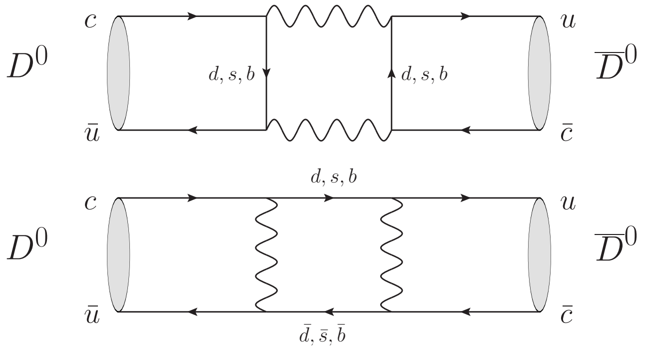

Figure 2.6: Two box diagrams describing D^0–$\overline{D}^0$ mixing.

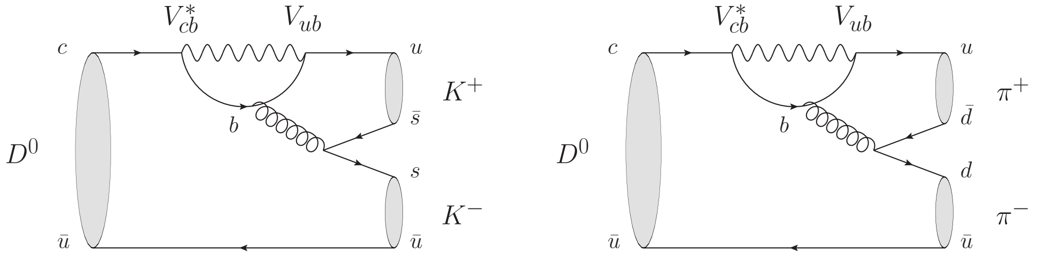

Figure 2.7: Two penguin diagrams for (left) $D^0 \to K^-K^+$ and (right) $D^0 \to \pi^-\pi^+$ decays. The contribution of d and s quarks in the loop is GIM suppressed.

2.2.4 Higher order processes: Box and penguin contributions

The Standard Model does not allow for flavour-changing neutral currents (FCNC) at tree-level. Consequently, in order to change the flavour of one up(down)-type to another up(down)-type quark, two subsequent charged currents are necessary. Two so-called *box diagrams* are shown in Figure 2.6. The flavour is changed twice by virtual particles in the loop. In both diagrams the flavour of the charm quark changes from c to $\overline{c}$ and the D^0 meson oscillates into a $\overline{D}^0$ meson. All generations of quarks contribute as the particles in the loop are virtual. The contribution of each individual box diagram scales with m_q^2/M_W^2 and the involved CKM matrix elements. In the limit of equal or vanishing quark masses, the different box diagrams would cancel due to the unitarity of the CKM matrix (GIM-mechanism). Here, the contribution of b quarks in the loop to the matrix element is highly CKM suppressed, as $|V_{cb}||V_{ub}| \propto \lambda^5$. The dominating diagrams with internal d and s quarks effectively cancel each other as d and s masses are similar compared to the c mass. This leads to a very small the D^0 mixing frequency.

Another type of FCNC diagrams are so-called *penguin diagrams*. The penguin contribution to $D^0 \to K^-K^+$ and $D^0 \to \pi^-\pi^+$ decays is shown in Figure 2.7. Penguin diagrams are characterised by the topology that a quark changes flavour via an internal loop with a charged current. The virtual quark in the loop then participates in a strong or electromagnetic interaction. The gluon or photon from the interaction creates a quark–antiquark pair which hadronizes together with the other quarks to the final states mesons. The size of the penguin contribution depends on the particles in the loop. Here, the b quark contribution is Cabibbo-suppressed with respect to the matrix element of the tree diagram by the factor $|V_{cb}^{*}V_{ub}/V_{cd}^{*}V_{ud}| \propto \lambda^{4}$ for $D^{0} \to \pi^{-}\pi^{+}$ and $|V_{cb}^{*}V_{ub}/V_{cs}^{*}V_{us}| \propto \lambda^{4}$ for $D^{0} \to K^{-}K^{+}$ decays. The contribution of d and s quarks in the loop is suppressed by the already discussed GIM mechanism.

It should be pointed out that in both mentioned processes CKM matrix elements with a non-zero phase are involved. When looking at the *CP* mirrored process, the complex conjugated of the matrix element is used. The implications are discussed in the next section as it leads to *CP* violation in the Standard Model.

2.3 Neutral meson phenomenology

The weak interaction discussed in Chapter 2.2 leads to neutral meson mixing and *CP* violation in the Standard Model. Here, the phenomenology of mixing and *CP* violation is discussed with the focus on neutral charm mesons. [5]

2.3.1 Neutral meson mixing

The charged currents couple a meson, D^{0}, and its anti-meson, $\overline{D}^{0}$, to a two-state system.[6] The effective Schroedinger equation with the Hamiltonian $\boldsymbol{H} = \left(\boldsymbol{M} - \frac{i}{2}\boldsymbol{\Gamma}\right)$ is[7]

$$\begin{aligned} i\frac{\mathrm{d}}{\mathrm{d}t}\begin{pmatrix} |D^{0}(t)\rangle \\ |\overline{D}^{0}(t)\rangle \end{pmatrix} &= \left(\boldsymbol{M} - \frac{i}{2}\boldsymbol{\Gamma}\right)\begin{pmatrix} |D^{0}(t)\rangle \\ |\overline{D}^{0}(t)\rangle \end{pmatrix} \\ &= \left(\begin{pmatrix} M_{11} & M_{12} \\ M_{12}^{*} & M_{22} \end{pmatrix} - i\begin{pmatrix} \Gamma_{11} & \Gamma_{12} \\ \Gamma_{12}^{*} & \Gamma_{22} \end{pmatrix}\right)\begin{pmatrix} |D^{0}(t)\rangle \\ |\overline{D}^{0}(t)\rangle \end{pmatrix} \end{aligned} \tag{2.10}$$

where $\boldsymbol{M} = \boldsymbol{M}^{\dagger}$ and $\boldsymbol{\Gamma} = \boldsymbol{\Gamma}^{\dagger}$. $\boldsymbol{M}$ is the mass matrix and $\boldsymbol{\Gamma}$ the decay matrix. *CPT* symmetry requires that $m = M_{11} = M_{22}$ and $\Gamma = \Gamma_{11} = \Gamma_{22}$. Off-diagonal elements of the mass matrix $\boldsymbol{M}$ are related to the box diagrams shown in Figure 2.6. The off-diagonal elements of the decay matrix $\boldsymbol{\Gamma}$ originate from weak decays common to the states D^{0} and $\overline{D}^{0}$.

The mass eigenstates, $D_{H/L}$, of $\boldsymbol{H}$ obey an exponential decay,

$$|D_{H/L}(t)\rangle = e^{-iM_{H/L}\,t}\,e^{-\Gamma_{H/L}\,t/2}\,|D_{H/L}\rangle \ , \tag{2.11}$$

where the masses and lifetimes are given by:

$$\begin{aligned} m &= \frac{M_H + M_L}{2}\,, & \Gamma &= \frac{\Gamma_L + \Gamma_H}{2} = \frac{1}{\tau}\,, \\ \Delta m &= M_H - M_L\,, & \Delta\Gamma &= \Gamma_L - \Gamma_H\,. \end{aligned} \tag{2.12}$$

Δm is always chosen to be positive, $\Delta\Gamma$ can have both signs. The combinations $x \equiv \Delta m/\Gamma$ and $y \equiv \Delta\Gamma/(2\Gamma)$ are commonly used to describe the mixing parameters. The mass eigenstates, D_H and D_L, can be written in terms of the strong interaction eigenstates, D and $\overline{D}$, as

$$\begin{aligned} |D_H\rangle &\propto p\,|D^{0}\rangle + q\,|\overline{D}^{0}\rangle \ , \\ |D_L\rangle &\propto p\,|D^{0}\rangle - q\,|\overline{D}^{0}\rangle \ , \end{aligned} \tag{2.13}$$

---

[5] The presented summary is based on References [16,18,19].

[6] The discussion is equivalent for all neutral meson systems.

[7] The convention $\hbar = c = 1$ is used here to simplify the formulas.

Table 2.2: The mixing parameters of K^0, D^0, B^0 and B_s^0 mesons [16]. Approximate numbers are calculated from the measured values in the table.

Meson	**Mass**	**Lifetime**
K^0 K^0_{S} K^0_{L}	$m = (497.614 \pm 0.024)\,\mathrm{MeV}/c^2$ $\Delta m = (0.5293 \pm 0.0009) \times 10^{10} \hbar\,\mathrm{s}^{-1}$ $x \approx 0.9$	$\tau_S = (0.8954 \pm 0.0004) \times 10^{-10}\,\mathrm{s}$ $\tau_L = (5.116 \pm 0.021) \times 10^{-8}\,\mathrm{s}$ $y \approx 1$
D^0	$m = (1864.86 \pm 0.13)\,\mathrm{MeV}/c^2$ $\Delta m = (1.44^{+0.48}_{-0.5}) \times 10^{10} \hbar\,\mathrm{s}^{-1}$ $x \approx 0.006$	$\tau = (410.1 \pm 1.5) \times 10^{-15}\,\mathrm{s}$ $2y = (1.60^{+0.25}_{-0.26}) \times 10^{-2}$ $y \approx 0.008$
B^0	$m = (5279.58 \pm 0.17)\,\mathrm{MeV}/c^2$ $\Delta m = (0.507 \pm 0.004) \times 10^{12} \hbar\,\mathrm{s}^{-1}$ $x \approx 0.77$	$\tau = (1.519 \pm 0.007) \times 10^{-12}\,\mathrm{s}$ $\Delta\Gamma \approx 0$ $y \approx 0$
B_s^0	$m = (5366.77 \pm 0.24)\,\mathrm{MeV}/c^2$ $\Delta m = (17.69 \pm 0.08) \times 10^{12} \hbar\,\mathrm{s}^{-1}$ $x \approx 27$	$\tau = (1.497 \pm 0.015) \times 10^{-12}\,\mathrm{s}$ $\Delta\Gamma = (0.100 \pm 0.013) \times 10^{12}\,\mathrm{s}^{-1}$ $y \approx 0.07$

where p and q are complex parameters with the normalisation requirement $|p|^2 + |q|^2 = 1$. The ratio is given by

$$\left(\frac{q}{p}\right)^2 = \frac{2M_{12}^* - i\Gamma_{12}^*}{2M_{12} - i\Gamma_{12}} \,. \tag{2.14}$$

The time evolution of the states D^0 and $\overline{D}^0$ can be obtained by combining Equations 2.11 and 2.13:

$$\left|D^0(t)\right\rangle = \quad g_+(t)\,\left|D^0\right\rangle + \frac{q}{p}\,g_-(t)\,\left|\overline{D}^0\right\rangle \,, \tag{2.15}$$

$$\left|\overline{D}^0(t)\right\rangle = \frac{p}{q}\,g_-(t)\,\left|D^0\right\rangle + \quad g_+(t)\,\left|\overline{D}^0\right\rangle \,, \tag{2.16}$$

where the functions $g_+(t)$ and $g_-(t)$ are given by

$$g_+(t) = e^{-imt}\,e^{-\Gamma t/2}\left[\quad\cosh\frac{\Delta\Gamma\,t}{4}\,\cos\frac{\Delta m\,t}{2} - i\sinh\frac{\Delta\Gamma\,t}{4}\,\sin\frac{\Delta m\,t}{2}\right] \,, \tag{2.17}$$

$$g_-(t) = e^{-imt}\,e^{-\Gamma t/2}\left[-\sinh\frac{\Delta\Gamma\,t}{4}\,\cos\frac{\Delta m\,t}{2} + i\cosh\frac{\Delta\Gamma\,t}{4}\,\sin\frac{\Delta m\,t}{2}\right] . \tag{2.18}$$

Equations 2.15 and 2.16 are not symmetric under *CP* transformation if $\left|\frac{q}{p}\right|$ is different from 1. This defines *CP* violation in mixing. Different types of *CP* violation are discussed in Section 2.3.2.

Table 2.2 summarises the mixing parameters of K^0, D^0, B^0 and B_s^0 mesons. Neutral kaons have a very large lifetime splitting. The lifetime of the long-lived state, K^0_{L}, is about 500 times larger than the one of the short-lived state, K^0_{S}. The mixing frequency is small compared to the average lifetime. The mixing frequency of B^0 mesons is comparable to their lifetime, $x \approx 0.77$, while B_s^0 mesons mix many times before they decay, $x \approx 27$. Both b-quark meson systems have only a small lifetime splitting. Neutral charm mesons neither oscillate fast nor have a substantial lifetime splitting as the parameters x and y are of the order of 10^{-2}.

2.3.2 *CP* violation

The decay amplitude of a state D^0 to a multi-particle final state, f, is given by

$$A_f = \langle f|\,\mathcal{H}\,|D^0\rangle \ ,$$

where $\mathcal{H}$ is the Hamiltonian describing the weak interaction. The amplitude of the *CP*-conjugate decay is

$$\overline{A}_{\overline{f}} = \langle \overline{f}|\,\mathcal{H}\,|\overline{D}^0\rangle \ . \tag{2.19}$$

If $|A_f|$ is different from $|\overline{A}_{\overline{f}}|$, the decay is *CP*-violating. This is called **direct *CP* violation**. Direct *CP* violation occurs in neutral and charged meson decays. The main subject of this thesis is direct *CP* violation in D^0 decays.

For neutral mesons, final states $\overline{f}$ with non-vanishing decay amplitudes

$$\overline{A}_f = \langle f|\,\mathcal{H}\,|\overline{D}^0\rangle \quad \text{and} \quad A_{\overline{f}} = \langle \overline{f}|\,\mathcal{H}\,|D^0\rangle \tag{2.20}$$

exist. The doubly Cabibbo-suppressed $D^0 \to K^+\pi^-$ and $\overline{D}^0 \to K^-\pi^+$ decays, discussed in Chapter 2.2.3, are examples. ***CP* violation in mixing** appears if

$$\left|\frac{q}{p}\right| \neq 1 \ , \tag{2.21}$$

cf. Chapter 2.3.1. *CP* violation in mixing does not depend on the final state. If there is a final state common to D^0 and $\overline{D}^0$ the direct decay interferes with mixing followed by the decay. The quantity

$$\lambda_f = \frac{q}{p}\frac{\overline{A}_f}{A_f} \tag{2.22}$$

encodes the two related types of *CP* violation. ***CP* violation in the interference of mixing and decay** is characterised by

$$\operatorname{Im}\lambda_f \neq 0 \ . \tag{2.23}$$

The requirement that the final state is common to D^0 and $\overline{D}^0$ is automatically fulfilled if the final state is a *CP* eigenstate. A *CP* eigenstate is defined by

$$CP\,|f_{CP}\rangle = \eta_f^{CP}\,|f_{CP}\rangle \ \text{with}\ \eta_{CP} = \pm 1 \ . \tag{2.24}$$

The final states of $D^0 \to \pi^-\pi^+$ and $D^0 \to K^-K^+$ decays are *CP* eigenstates with $\eta_{CP} = 1$ (*CP*-even). The final state $K^-\pi^+$ is not a *CP* eigenstate. *CP* violation in mixing and in the interference of mixing and decay are commonly called **indirect *CP* violation** as both are induced by mixing in contrast to direct *CP* violation which appears only in the decay.

2.4 Neutral charm meson phenomenology

This section transfers the concepts from the previous discussion to the sector of neutral charm mesons with the focus on $D^0 \to K^-K^+$ and $D^0 \to \pi^-\pi^+$ decays.

2.4.1 *CP* violation in charm decays

The decay amplitude of D^0 and $\overline{D}^0$ meson decays to a common *CP*-even eigenstate ($\eta_f^{CP} = 1$) can be written as [19]:

$$\begin{aligned} A_f &= A_f^T \left(1 + r_f e^{i(\delta_f + \phi_f)}\right) \quad , \\ \overline{A}_f &= A_f^T \left(1 + r_f e^{i(\delta_f - \phi_f)}\right) \quad . \end{aligned} \tag{2.25}$$

The individual components are discussed in the context of the Standard Model for $D^0 \to K^-K^+$ and $D^0 \to \pi^-\pi^+$ decays. A_f^T is the tree-level contribution, see also Figure 2.5 and is real by convention. Phases of other contributions are relative to the tree-level contribution as an overall phase in the decay amplitude cancels in the transition probability. The real number r_f is the ratio of tree and penguin contributions. Naively, the value of r_f is of order $\lambda^4 \sim 0.002$ for $D^0 \to \pi^-\pi^+$ and $D^0 \to K^-K^+$ decays with a b quark in the loop, see Figure 2.7, as the ratio of CKM matrix elements is $|V_{cb}^* V_{ub}/V_{cd}^* V_{ud}|$ and $|V_{cb}^* V_{ub}/V_{cs}^* V_{us}|$, respectively. Therefore, the second term can be treated as a small correction. The phase ϕ_f is the relative weak phase of the penguin to the tree-level contribution . It is a so-called *weak phase* as it changes sign under *CP* transformation. In the Standard Model the only source of weak phases are the CKM matrix elements that are involved in the weak interaction. At order λ^4, the CKM matrix element V_{ub} has a complex component, see Equation 2.9. The phase δ_f is a so-called *strong phase*. A strong phase is defined as a phase which does not change sign under *CP* transformation. Here, a relative strong phases of the penguin to the tree-level contribution is induced by the hadronization to the final state. The latter is invariant under *CP* transformation as the strong interaction is *CP* conserving. The presented decomposition is generally valid and not restricted to the Standard Model.

The time-integrated *CP* asymmetry of D^0 mesons decaying into a *CP* eigenstate f is defined as

$$A_{CP}(f) = \frac{\Gamma(D^0 \to f) - \Gamma(\overline{D}^0 \to f)}{\Gamma(D^0 \to f) + \Gamma(\overline{D}^0 \to f)} \quad , \tag{2.26}$$

where $\Gamma(D^0 \to f)$ and $\Gamma(\overline{D}^0 \to f)$ are the decay rates of $D^0 \to f$ and $\overline{D}^0 \to f$ decays, respectively. The *CP* asymmetry has contributions from direct *CP* violation but also from *CP* violation in mixing and the interference of mixing and decay. All three contributions are small given the current experimental constraints and Standard Model predictions. Therefore, they can be separated:

$$A_{CP}(f) = a_{CP}^{\text{dir}}(f) + a_{CP}^{\text{int}}(f) + a_{CP}^{\text{mix}} \quad , \tag{2.27}$$

where $a_{CP}^{\text{dir}}(f)$ is the direct *CP* asymmetry, $a_{CP}^{\text{int}}(f)$ the contribution from interference of mixing and decay and a_{CP}^{mix} the contribution from *CP* violation in mixing. In principle, direct and indirect *CP* asymmetries depend on the final state. However, inserting Equation 2.25 into Equation 2.22 yields

$$\lambda_f = \frac{q}{p}\frac{\overline{A}_f}{A_f} = \frac{q}{p}\frac{1 + r_f e^{i(\delta_f + \phi_f)}}{1 + r_f e^{i(\delta_f - \phi_f)}} \approx \frac{q}{p} \equiv -R_m e^{i\phi} \quad , \tag{2.28}$$

where terms of order r_f have been neglected in the ratio. At this order, λ_f is universal for every *CP* eigenstate. R_m is defined as $|q/p|$ and ϕ is the relative weak phase between the mixing and the decay amplitude. The time integrated *CP* asymmetry is then

$$A_{CP}(f) = a_{CP}^{\text{dir}}(f) + a_{CP}^{\text{int}} + a_{CP}^{\text{mix}} \quad , \tag{2.29}$$

where the direct part depends on the final state and the indirect part is independent of the final state.

The direct *CP* asymmetry can be written as follows:

$$a_{CP}^{\text{dir}}(f) = \frac{|A_f|^2 - |\overline{A}_f|^2}{|A_f|^2 + |\overline{A}_f|^2} = 2\, r_f \,\sin\phi_f \,\sin\delta_f \quad , \tag{2.30}$$

which shows that a non-vanishing relative weak phase and a non-vanishing relative strong phase of two contributions to the decay amplitude are necessary conditions to establish direct *CP* violation. Following Reference [19], the components of the indirect *CP* violation can be written as

$$\begin{aligned} a_{CP}^{\text{int}} &= \frac{x}{2}(R_m + R_m^{-1})\sin\phi \quad , \\ a_{CP}^{\text{mix}} &= \frac{y}{2}(R_m - R_m^{-1})\cos\phi \quad . \end{aligned} \tag{2.31}$$

As x and y are small in the D^0 system, see Table 2.2, indirect *CP* violation is expected to be small.

2.4.2 Predictions and theoretical uncertainties of direct *CP* violation

Naively, the penguin contribution of $D^0 \to K^-K^+$ and $D^0 \to \pi^-\pi^+$ is Cabibbo-suppressed by $\lambda^4 \sim 10^{-3}$ and a QCD loop factor which is usually estimated to be smaller than 1, thus,

$$a_{CP}^{\text{dir}}(f) < 0.1\,\% \quad . \tag{2.32}$$

In the limit of vanishing quark masses and neglecting strong interaction dynamics, $\sin\delta_{K^-K^+} = \sin\delta_{\pi^-\pi^+}$, the direct *CP* asymmetry $|a_{CP}^{\text{dir}}(\pi^-\pi^+)|$ would be equal to the direct *CP* asymmetry $|a_{CP}^{\text{dir}}(K^-K^+)|$ and both would have opposite sign as $\frac{V_{cb}^* V_{ub}}{V_{cd}^* V_{ud}}\left(\frac{V_{cb}^* V_{ub}}{V_{cs}^* V_{us}}\right)^{-1} \sim -1$, cf. Chapter 2.2.4.

The LHCb experiment measured the experimentally robust[8] difference of *CP* asymmetries, $\Delta A_{CP} = A_{CP}(K^-K^+) - A_{CP}(\pi^-\pi^+)$, in 2012 [1] to be

$$\Delta A_{CP} = (-0.82 \pm 0.21\,(\text{stat}) \pm 0.11\,(\text{syst}))\,\% \quad . \tag{2.33}$$

---

[8] It will become clear in the course of the document that it is experimentally less challenging to measure the difference of *CP* asymmetries at a proton–proton collider, rather than a single asymmetry.

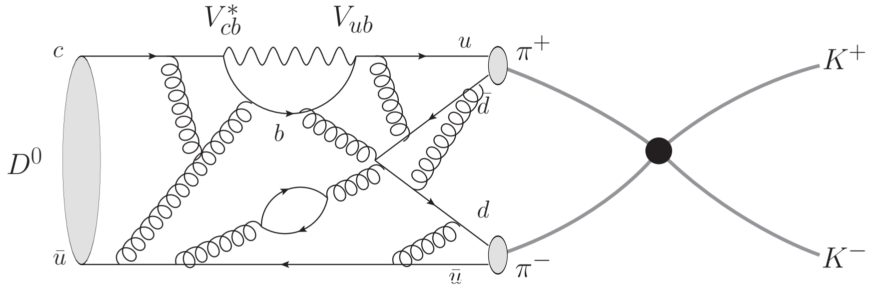

Figure 2.8: A sketch of the long-distance effects contributing to the Penguin amplitude in $D^0 \to K^-K^+$. First, the matrix element of the penguin contribution is modified by hadronic interactions between the colour-charged constituents. Second, the final state $\pi^-\pi^+$ can rescatter via long-range dynamics to the final state K^-K^+ and, thus, contribute to $D^0 \to K^-K^+$ decays.

Although the value is small compared to *CP* asymmetries in other meson systems, the measured value was larger than previously expected.

However, theoretical predictions in the charm system are difficult, see e.g. References [20, 21] for detailed studies. Hadrons are not systems of free quarks. Only colour-neutral multi-quark states exist. Therefore, the initial and final state are always in a confined hadronic state. The scale of QCD, Λ_{QCD}, is around $300\,\text{MeV}/c^2$ which is roughly the binding energy of a valence quark in a proton. The coupling constant, α_S, increases at small energies or *long distances* but decreases for high energies or *short distances* (asymptotic freedom). In a weak decay of a hadron the short distance is mainly determined by the weak interaction and the long distance is dominated by non-perturbative QCD dynamics. In b-hadron decays, this allows to separate the calculation of decay amplitudes into two distinct parts, see also Reference [22]. The b mass ($4.18\,\text{GeV}/c^2$) is sufficiently larger than Λ_{QCD}. Kaon decays are at the other end of the spectrum at low energies as $m_s \approx 95\,\text{MeV}/c^2$. In both systems it is possible to separate the two scales and to make precise predictions. Nevertheless, the main theoretical uncertainties are still coming from non-tractable long-distance effects. The charm quark mass of $1.28\,\text{GeV}/c^2$ is somewhere between both regimes. It is larger than Λ_{QCD} but only by a factor of four. Thus, it is difficult to separate the short- and long-distance effects. This makes reliable predictions difficult. A sketch of the non-perturbative QCD dynamics is shown in Figure 2.8.

A common approach in physics to simplify calculations or to categorise processes is to exploit symmetries even if they are not perfect. The decays $D^0 \to K^-\pi^+$, $D^0 \to K^+\pi^-$, $D^0 \to K^-K^+$, $D^0 \to \pi^-\pi^+$ and other two-body D decays can be all treated alike if u, d and s quark masses are assumed to be equal. Then the flavour, u, d or s, is simply another degree of freedom similar to the colour charge. Equivalent to QCD, the symmetry group is $SU(3)_F$. In the $SU(3)_F$ limit the measured ratios of branching fractions are simply given by the ratios of CKM matrix elements after correcting for phase-space effects [20], e.g.:

$$\begin{aligned} R_1 &= \frac{\Gamma(D^0 \to K^+\pi^-)}{\Gamma(D^0 \to K^-\pi^+)} = \frac{|V_{cd}^* V_{us}|^2}{|V_{cs}^* V_{ud}|^2} \approx \lambda^4 \ , \\ R_2 &= \frac{\Gamma(D^0 \to K^-K^+)/|\vec{p}_K|}{\Gamma(D^0 \to \pi^-\pi^+)/|\vec{p}_\pi|} = \frac{|V_{cs}^* V_{us}|^2}{|V_{cd}^* V_{ud}|^2} \approx 1 \ . \end{aligned}$$

The experimental results yield that R_1/λ^4 is approximately 1.28 ± 0.03 and R_2 about 3.22 ± 0.09 [16, 23]. Both deviate significantly from unity and the $SU(3)_F$ symmetry is obviously broken. There are several possible reasons for this breaking. First, the approach that m_s is equal to $m_{u/d}$ holds only approximately at the scale of m_c. Second, the penguin diagrams shown in Figure 2.7 could be enhanced by long-distance effects. Third, there could be unknown effects beyond the Standard Model.

The breaking of the symmetry has been studied, among others, in References [20, 21] by performing global fits to several observables, including branching ratios and *CP* asymmetries in two-body decays of D mesons. The conclusion of the studies is that $SU(3)_F$ is broken by at least 30 %. The difference in branching ratios can be due to the non-vanishing s quark mass. The *CP* asymmetries of $\mathcal{O}(1\,\%)$ require an enhancement of the naive penguin contribution of $\mathcal{O}(2-5)$. This enhancement might be attributed to non-perturbative hadronic effects and is not necessarily a sign of physics beyond the Standard Model. However, contributions from models with an extended flavour sector cannot be excluded. An important consequence of the $SU(3)_F$ breaking is that the direct *CP* asymmetries in $D^0 \to K^-K^+$ and $D^0 \to \pi^-\pi^+$ decays are not inevitably equal in magnitude and of opposite sign.

2.4.3 Motivation of the analysis

In the decays of B^+, K^0, B^0 and recently B_s^0 mesons *CP* violation has been well established. The neutral mesons have in common that they are exclusively built out of down-type quarks. The only mesons consisting of up-type quarks and where *CP* violation has not yet been discovered are D^0 mesons. The main reason for the lack of discovery are the small *CP*-violating effects in the charm sector predicted by the Standard Model. The world average of direct *CP* violation in September 2012 was

$$\Delta a_{CP}^{\text{dir}} = a_{CP}^{\text{dir}}(D^0 \to K^-K^+) - a_{CP}^{\text{dir}}(D^0 \to \pi^-\pi^+) = (-0.678 \pm 0.147)\,\% \ \ [23]\ , \tag{2.34}$$

which was a first evidence for *CP* violation. A comparison of all the measurements is shown in Figure 2.9. It shows the results for the difference of $A_{CP}(K^-K^+)$ and $A_{CP}(\pi^-\pi^+)$, ΔA_{CP}. As this is experimentally less challenging, most analyses determine this quantity. A better theoretical interpretation of long-distance effects is possible if both *CP* asymmetries are measured individually. The best measurements of the individual asymmetries are from the CDF collaboration [24]

$$\begin{aligned} A_{CP}(K^-K^+) &= (-0.32 \pm 0.21)\,\% \ \ , \\ A_{CP}(\pi^-\pi^+) &= (+0.31 \pm 0.22)\,\% \ \ . \end{aligned} \tag{2.35}$$

Both measurements are consistent with small *CP*-violating effects.

Especially, the ΔA_{CP} results sparked a huge interest in the theory community as the size of the measured *CP* violation was larger than previously expected. In several publications the results were analysed. The publication "*Evidence for CP violation in time-integrated* $D \to h^-h^+$ *decay rates*" [1] is one of the most cited analyses from the LHCb experiment. Most theoretical studies concluded that the Standard Model can accommodate *CP*-violating effects of this magnitude due to non-perturbative contributions. However, most also state that it is difficult to explain the QCD dynamics and might also be due to physics beyond the Standard Model [20, 21].

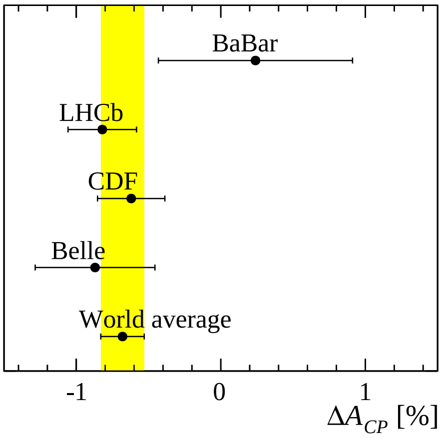

Figure 2.9: An overview of relevant ΔA_{CP} measurements in September 2012 from BaBar [25], LHCb [1], CDF [24] and Belle [26].

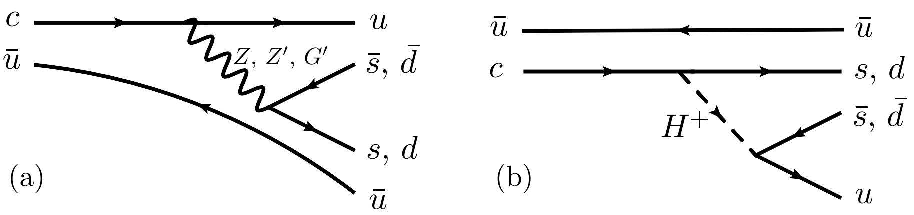

Figure 2.10: Possible contributions by (a) heavy gauge bosons and (b) charged scalars to $D^0 \to \pi^-\pi^+$ and $D^0 \to K^-K^+$ decays. Figure taken from Ref. [27].

There are several models with an extended flavour sector which can explain larger values of direct *CP* violation in the charm sector. A comprehensive list can be found in Reference [27]. Physics beyond the Standard Model could introduce extra flavour-changing neutral currents with additional heavy gauge bosons or additional charged currents with an extended Higgs sector. Both would introduce extra tree-level and box diagrams. Exemplary Feynman diagrams are shown in Figure 2.10. As mentioned before, a particularity of D^0 mesons is that they consist of up-type quarks. Due to its high mass the top quark is more sensitive to physics at large energy scales. This could then effect processes involving charm quarks through additional flavour-changing neutral currents, either at the tree-level or in loop diagrams.

In summary, it is important to pursue measurements of *CP* asymmetries in the charm sector and to make more precise measurements until *CP* violation in the charm sector is as well established as for kaons and B mesons. Nevertheless, it might be more difficult to interpret the results compared to B mesons.

One of the main achievements of this work is to develop the necessary tools which enable measurements of the difference and the individual asymmetries at the low per-mille level. This makes these measurements a good test of the Standard Model and beyond but also an important benchmark of the performance of the LHCb experiment. The experimental challenges are detailed in the course of this document.

2.5 Material interaction asymmetries

In an experiment, *CP* asymmetries are not the only source of particle–antiparticle asymmetries. To detect decay products of D or B mesons, the particles have to traverse at least parts of a detector. Here, in particular, it is the LHCb detector which is discussed in in Chapter 3.2. Detectors consist out of matter, while decay products are particles and antiparticles. The interaction with the detector material gives rise to detection asymmetries as discussed in the following.

2.5.1 Particle passage through matter

While traversing the detector, different types of particles experience different types of interactions [16]:

Bremsstrahlung: A charged particle loses kinetic energy when it is deflected by another charged particle. The energy is released in the form of photons. The amount of so-called bremsstrahlung depends on the rest mass and the velocity of the deflected particle. The geometry of the detector requires that charged particles have a momentum of more than 2 GeV/c, otherwise they are bent out by the magnet. Therefore, all electrons of interest are ultra-relativistic and bremsstrahlung is the dominant contribution of energy loss. For heavier particles with mass M bremsstrahlung is not relevant as it is suppressed by the factor $\left(\frac{m_e}{M}\right)^2$. The amount of energy loss is quantified by the *radiation length* of a specific material, X_0. The energy of an electron particle after traversing a distance, x, in that material is given by

$$E_e(x) = E_0 \; e^{-\frac{x}{X_0}} \quad , \tag{2.36}$$

where E_0 is the initial energy. As an example, the radiation length of aluminium is about 65 cm. The contribution of each component of the LHCb detector is given later in Table 3.1. An electron loses about 35 % of its initial energy when traversing the tracking system.

Ionisation: Heavy charged particles lose energy due to single collisions with electrons in the material. Atoms are either ionised or excited by the interactions. The mean rate of energy loss, $-\langle \mathrm{d}E/\mathrm{d}x \rangle$, is described by the Bethe-Bloch formula. In the momentum range of 2 to 100 GeV/c this effect is minimal. The energy loss in a specific material, ΔE, after a distance, x, can be approximated by

$$\Delta E = -\left.\frac{\mathrm{d}E}{\mathrm{d}X}\right|_{\mathrm{min}} x \quad . \tag{2.37}$$

Typical values for detector material are a few MeV energy loss per cm. Thus, heavy charged particles have to traverse large amounts of material to lose significant energy. As muons only interact electromagnetically, they can traverse the whole detector.

Multiple scattering: Charged particles can also be deflected by the electromagnetic field of nuclei. A sequence of Coulomb scatterings is called multiple scattering. The angular dispersion can be modelled as a Gaussian. Multiple scattering does not change the charged particle's energy but changes the initial flight direction and, thus, affects the momentum resolution of the tracking system. Multiple scattering limits the relative momentum resolution of the LHCb tracking system to 0.4 %.

Hadronic interactions: Charged and neutral hadrons can also interact strongly with nuclei. The *nuclear collision length*, λ_T, is the typical length before hadrons scatter elastically or inelastically with nuclei in the material. The rate of collisions, $\mathrm{d}N/\mathrm{d}x$, per travelled length, x, is given by

$$\frac{\mathrm{d}N}{\mathrm{d}x} = -\frac{x}{\lambda_T} = -\sigma_T\, n\, x \quad . \tag{2.38}$$

It can also be expressed by the cross section, σ_T, multiplied with the number density, n, of the scattering material. The *nuclear interaction length*, λ_I, is larger as it excludes elastic and quasi-elastic from its definition. For example, aluminium has a nuclear collision length of 188 cm and a nuclear interaction length of 290 cm. In many cases, the relevant number is λ_T as elastic scattering angles are large. About 20 % of all hadrons undergo hadronic interactions before they reach the last tracking station of the LHCb detector. The tracking system is discussed later in Chapter 3.3.

2.5.2 Hadronic interaction asymmetries

This analysis requires to reconstruct $D^0 \to K^-K^+$ and $D^0 \to \pi^-\pi^+$ decays to measure the *CP* asymmetries $A_{CP}(K^-K^+)$, $A_{CP}(\pi^-\pi^+)$ and ΔA_{CP}. For calibration purposes also the asymmetries in $D^0 \to K^-\pi^+$, $D^+ \to K^-\pi^+\pi^+$ and $D^+ \to \overline{K}^0\pi^+$ decays need to be reconstructed. Their final states are not symmetric under *CP* transformation. Therefore, different nuclear collision lengths for particles and antiparticles induce different detection efficiencies as explained in the following.

For example, the $D^0 \to K^-\pi^+$ decay has a K^- meson and the $\overline{D}^0 \to K^+\pi^-$ decay has a K^+ meson in the final state. A K^- meson has the quark content ($\overline{u}s$) and a K^+ meson is composed of ($u\overline{s}$). The detector consists to a good approximation out of the same number of protons and neutrons (isoscalar) [28]. The valence quarks of protons and neutrons are (uud) and (udd), respectively. Sea quarks appear as $q\overline{q}$-pairs. The $\overline{u}$ quark in a K^- meson can annihilate with valence and sea quarks, whereas the s quark can only interact strongly with sea quarks. The u and $\overline{s}$ quark of a K^+ meson annihilate only with sea quarks. Thus, a different cross section of positively- and negatively-charged kaons with protons and neutrons is expected. The parton density function of sea quarks increases at low Bjorken x, see later Figure 2.13. Hence, the relative fraction of valence quarks which take part in the scattering process decreases with a higher kaon momentum. This diminishes the interaction asymmetry. In the case of pions the situation is symmetric for isoscalar targets as the antiquark can in both cases annihilate with a valence quark.

The measured kaon and pion cross sections on deuterium and proton targets are shown as a function of momentum in Figure 2.11. Deuterium is an isoscalar target and a good proxy of the detector material. As expected, the cross section is clearly higher for negative kaons in both cases. The difference is larger at low momentum and

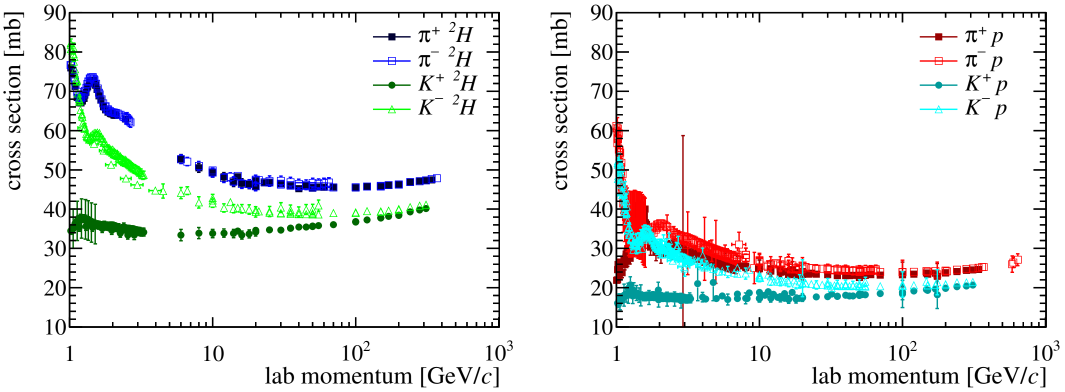

Figure 2.11: Measured kaon and pion cross sections on (left) deuterium and (right) proton targets, as a function of momentum. The data are taken from the COMPAS group [16].

decreases for high momenta. The cross sections of positive and negative pions are equal for deuterium. For protons, a difference at low momentum can be seen as a proton has two u and one d quark. However, only charged particles with a momentum larger than 2 GeV/c are of interest for the analysis.

A similar argumentation is valid for K^0 and $\overline{K}^0$ mesons. This is discussed in detail in Chapter 9 as it requires additional treatment due to mixing and CP violation of neutral kaons.

2.5.3 Detection asymmetries of charged hadrons

The efficiencies, $\varepsilon(h^+)$ and $\varepsilon(h^-)$, to reconstruct a positively- or negatively-charged particle, $h^\pm$, with momentum $\vec{p}$ are given by

$$\varepsilon(h^\pm, \vec{p}) = \frac{N_{\text{rec}}(h^\pm, \vec{p})}{N_{\text{created}}(h^\pm, \vec{p})} \quad , \tag{2.39}$$

where it is assumed that the particles are produced in the acceptance of the detector. As discussed, one source of inefficiency are interactions with the material. Other sources of inefficiency which are related to the reconstruction of events or which are specific to the LHCb detector are discussed in Chapter 4. In the case discussed here, the reconstruction efficiency is reduced by the material interaction as

$$\varepsilon(h^\pm, \vec{p}) = \frac{N_{\text{created}}(h^\pm, \vec{p})\; e^{-\frac{d}{\lambda_T(h^\pm, \vec{p})}}}{N_{\text{created}}(h^\pm, \vec{p})} = e^{-\frac{d}{\lambda_T(h^\pm, \vec{p})}} \quad , \tag{2.40}$$

where $\lambda_T(h^\pm, \vec{p})$ is the nuclear collision length of particle h with momentum $\vec{p}$ and d is the flight length in the material. Here, it is assumed that the trajectory of a particle cannot be reconstructed by the tracking system[9] if a particles scatters elastically and inelastically. Thus, the nuclear collision length is the interesting quantity. The average $d/\lambda_T(h^\pm, \vec{p})$ is typically around 20 % for kaons and pions with a momentum of 20 GeV/c

---

[9] The tracking system and the track reconstruction are discussed in Chapter 3.3 and 4.

when traversing the full tracking system of the LHCb detector. Therefore, roughly 20 % of the charged hadrons are already lost because they are absorbed by the detector material.

The difference in the reconstruction efficiencies of positive and negative particles to detect a charged particle $h^{\pm}$ with momentum $\vec{p}$ is the detection asymmetry. It is defined as

$$a_D(h^-)(\vec{p}) \equiv \frac{\varepsilon(h^-,\vec{p}) - \varepsilon(h^+,\vec{p})}{\varepsilon(h^-,\vec{p}) + \varepsilon(h^+,\vec{p})} \quad . \tag{2.41}$$

Integrated asymmetries are denoted with capital A:

$$A_D(h^-) \equiv \frac{\varepsilon(h^-) - \varepsilon(h^+)}{\varepsilon(h^-) + \varepsilon(h^+)} \quad . \tag{2.42}$$

The charged kaon cross section is about 14 % different for K^+ and K^- mesons at 20 GeV/c, see Figure 2.11. This creates a detection asymmetry of about (−1 %) for charged kaons. It should be pointed out that the actual detection asymmetry depends on the kinematics of a particle. The measured asymmetry of a multi-body final state contains the effects of several particles. This is discussed later in Chapter 5.

2.6 Particle production and hadronization

In this section the production of heavy quarks[10] and their hadronization are discussed. First, particle production in proton–proton collisions is addressed. Afterwards, differences in the production rate of mesons and the corresponding anti-mesons are treated as this leads to production asymmetries.

2.6.1 Particle production at the LHC

The LHC collides two beams of protons to create particles. The centre-of-mass energies in 2011 and 2012 were 7 TeV and 8 TeV, respectively. A proton is a complicated object built out of three valence quarks, sea quarks and gluons. All constituents interact via the strong interaction. As the strong interaction conserves flavour, heavy quarks are produced as $q\overline{q}$ pairs in inelastic proton–proton collisions at the LHC. Either two gluons or a quark and antiquark collide and subsequently form a heavy quark pair.

Higher orders diagrams play an important role in QCD processes. Therefore, multiple partons can be emitted. According to Reference [30], parton showers can be divided into three topologies, based on how many heavy quarks are part of the hard process. The hard process is the s- or t-channel exchange in the three diagrams shown in Figure 2.12. If two quarks participate in the hard process, it is called pair creation. A $q\overline{q}$ pair is created, followed by one or more gluon emissions. The topology is shown in Figure 2.12a. In Figure 2.12b the final state of the hard process is gb. If only one of the quarks participates in the hard interaction, it is called flavour excitation. When none of the quarks is part of the interaction, the topology is called gluon splitting, see Figure 2.12c. The $b\overline{b}$ pair emerges from a gluon which participates in the t-channel process. The dominant processes at LHC energies are pair creation and flavour excitation [30].

---

[10] Heavy quark refers to c and b quarks. Top quarks are not of interest here.

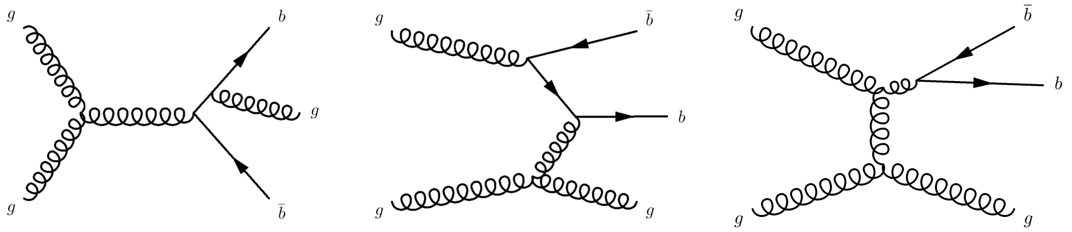

(a) Pair creation (b) Flavour excitation (c) Gluon splitting

Figure 2.12: Topologies of heavy $q\bar{q}$ production. The hard process in (a) is the gluon s-channel exchange, in (b) the gluon t-channel exchange and in (c) the gluon t-channel exchange. Diagrams taken from Ref. [29].

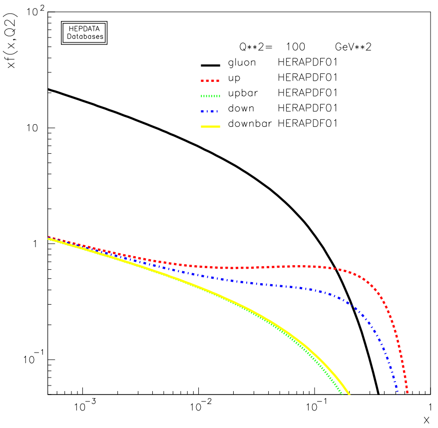

Figure 2.13: The proton parton density functions for gluons, u and d quarks at $Q = 100\,\mathrm{GeV}^2$. Data taken from HERAPDF [31].

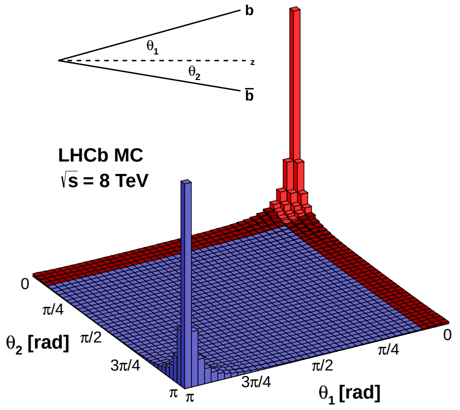

Figure 2.14: Polar angle distribution of b and $\bar{b}$ quarks in pp collisions at $\sqrt{s} = 8\,\mathrm{TeV}$. The beam line is the z-axis, red the LHCb acceptance. Figure taken from Ref. [32].

A $b\bar{b}$ pair has an invariant mass of about $10\,\mathrm{GeV}/c^2$ which is small compared to the centre-of-mass energy of the colliding protons. The parton distribution function at the corresponding scale of $Q = 100\,\mathrm{GeV}^2$ is shown in Figure 2.13. Gluons clearly dominate at low Bjorken x. Partons with low and very different Bjorken x enter the above described processes to produce a $b\bar{b}$ pair. Thus, it is likely that the $b\bar{b}$ pair is not produced at rest but boosted into the direction of one of the protons. As quark and antiquark are produced in the same interaction, the kinematic correlation between the two is high. The polar angle distribution of b and $\bar{b}$ quarks is shown in Figure 2.14. The large production rate in the so-called *forward* region drives the design of the LHCb detector, cf. Chapter 3.2. The same arguments also hold for the production of $c\bar{c}$ pairs.

The heavy quarks then hadronize to form a confined state. During the hadronization the heavy quark combines with one or two lighter quarks to create a meson or a baryon, respectively. The lighter quarks come from the proton remnants or the fragmentation process of the initial interaction. The measured fractions of hadronizations to B^+,

Table 2.3: The measured production fraction ratios. Combination done by HFAG [33].

Quantity		**value**
B^+ or B^0 fraction	$f_u = f_d$	0.401 ± 0.007
B_s^0 fraction	f_s	0.107 ± 0.005
b-baryon fraction	f_{baryon}	0.091 ± 0.015

B^0, B_s^0 mesons and b-baryons are shown in Table 2.3. It is usually assumed that the same amount of B^+ and B^0 mesons is produced (isospin symmetry). Differences in the production rate of B^+ and B^- mesons or B^0 and $\overline{B}^0$ mesons are discussed in the next section.

The production cross section of B hadrons at $\sqrt{s} = 7\,\text{TeV}$ in the pseudorapidity[11] interval $2 < \eta < 6$ has been measured by the LHCb collaboration to be

$$\sigma(pp \to H_b X) = (75.3 \pm 5.4\,(\text{stat}) \pm 13.0\,(\text{syst}))\,\mu\text{b} \ . \tag{2.43}$$

The pseudorapidity interval corresponds to the acceptance of the LHCb detector, cf. Chapter 3.2.

The production cross section of c hadrons at $\sqrt{s} = 7\,\text{TeV}$ has been measured in a rapidity[12] interval of $2.0 < y < 4.5$ and a transverse momentum, p_{T}, smaller than $8\,\text{GeV}/c$ to be [34]

$$\sigma(c\overline{c})_{p_{\text{T}}<8\,\text{GeV}/c,\,2.0<y<4.5} = (1419 \pm 12\,(\text{stat}) \pm 116\,(\text{syst}) \pm 65(\text{frag}))\,\mu\text{b} \ . \tag{2.44}$$

The given rapidity range roughly corresponds to the pseudorapidity range of the aforementioned measurement. The last uncertainty is due to uncertainties on fragmentation functions of c hadrons. The charm cross section is about a factor 20 higher than the bottom cross section. However, the difference reduces to about a factor of 4 when counting the number of recorded and selected events. The selection of c and b hadrons at the LHCb experiment is discussed in Chapters 4 and 6.

2.6.2 Production asymmetries

On the one hand, heavy quarks are predominantly produced in quark-antiquark pairs. On the other hand, the LHC is colliding two beams of protons. This prevalence of particles in the initial state has to be transported to the hadronized final states as QCD is *CP*-conserving. However, it is not straightforward to translate these two effects into a production asymmetry of heavy mesons.

B meson production asymmetry

In the following the production asymmetry of B mesons is defined as

$$A_P(\overline{B}) \equiv \frac{\mathcal{P}(\overline{B}) - \mathcal{P}(B)}{\mathcal{P}(\overline{B}) + \mathcal{P}(B)} \ , \tag{2.45}$$

---

[11] The pseudorapidity is defined as $\eta = -\ln\left(\tan\frac{\theta}{2}\right)$ where θ is the polar angle with respect to the beam-axis.

[12] The rapidity is defined as $y = \frac{1}{2}\ln\frac{E+p_z c}{E-p_z c}$ where the z-axis is along the beam line.

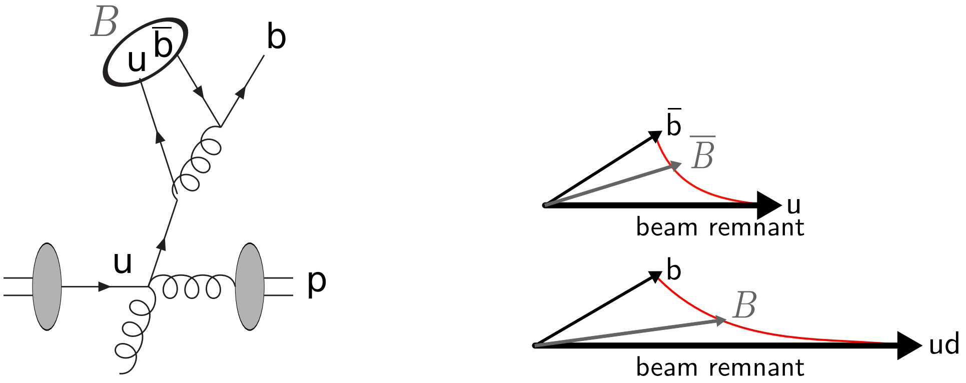

(a) (b)

Figure 2.15: (a) The collapse to a B meson is depicted at high p_{T}, from [30]. (b) The beam drag effect is illustrated, from [37]. The red line represents a colour string, pulling on either the b or $\bar{b}$ quark.

where $\mathcal{P}(\overline{B})$ and $\mathcal{P}(B)$ are the probabilities to produce a $\overline{B}$ and B meson[13], respectively. A simple argument why more B mesons (with a $\bar{b}$ quark) are produced is that the structure of the Standard Model is baryon number conserving. Therefore, it is more likely that the proton remnants combine with a b quark to form a heavy baryon. The $\bar{b}$ quark hadronizes preferentially to a meson with a quark from the fragmentation. Thus, more B than $\overline{B}$ mesons originate from the hadronization process and the asymmetry defined in Equation 2.45 is negative.

While the argument explains the sign of the asymmetry, it does not explain the dynamics of production asymmetries in multiple parton showers. The *Lund string model* [35] is a phenomenological approach to describe the hadronization process. Within the model, the colour flow is described by strings which are formed by self-interacting gluons. The Lund string model is also the basis of the widely-used event generator PYTHIA [36]. Two different sources of asymmetries are shown in Figure 2.15.

The first effect, see Figure 2.15a, is more important at high transverse momenta. A valence quark is scattered to high transverse momentum in the primary interaction. When a $b\bar{b}$ pair is created close in phase space by one of the mechanisms discussed in the previous section, the b quark and the scattered valence quark can collapse to a B meson. This effect favours heavy mesons with a light quark in common with the proton.

The second effect, Figure 2.15b, is the so-called beam drag effect. The quark and the two beam remnants can be in a colour-neutral state, while the antiquark can only be in a colour-neutral state with one beam remnant as the beam remnants have different colour charges. Therefore, the heavy quark is "dragged" by two partons to higher rapidities, whereas only one parton is pulling on the heavy antiquark. The resulting asymmetry at high rapidity is opposite to the first effect.

The predicted production asymmetries are shown[14] in Figure 2.16. The production asymmetry depends on the momentum and the rapidity. It is very small in the central

---

[13] As a reminder, B ($\overline{B}$) refers to B^0 and B^- ($\overline{B}^0$ and B^+).

[14] Note the different sign conventions.

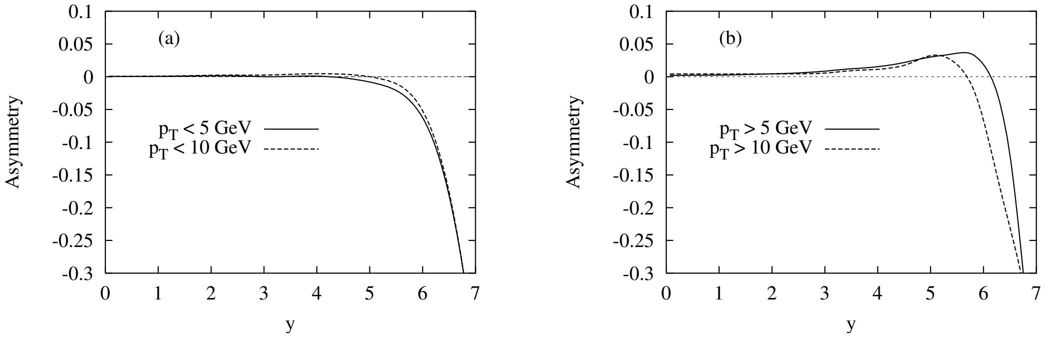

(a) $p_{\mathrm{T}} < 5, 10\,\mathrm{GeV}/c$

(b) $p_{\mathrm{T}} > 5, 10\,\mathrm{GeV}/c$

Figure 2.16: The predicted production asymmetry, $A_P(B^0) = \frac{\mathcal{P}(B^0)-\mathcal{P}(\overline{B}^0)}{\mathcal{P}(B^0)+\mathcal{P}(\overline{B}^0)}$, as a function of rapidity for different p_{T} cuts at the LHC. Figure taken from Ref. [30].

region but gets larger for higher rapidities. Very close to the beam, the drag effect becomes stronger and the asymmetry even changes sign. Production asymmetries with an absolute value of the order $\mathcal{O}(0.1\,\% - 1\,\%)$ are expected within the LHCb acceptance which corresponds to approximately $2.0 < y < 4.5$. It is expected that more mesons with a $\overline{b}$ quark are produced than mesons with a b quark in the given rapidity range.

The only measurement at the LHCb experiment is based on a small data set from 2010 and, thus, has a large uncertainty. The measured value is $A_P(B^+) = (-0.3 \pm 0.9)\,\%$ [38].

D meson production asymmetry

The same arguments hold for production asymmetries of D^0 or D^+ mesons that are directly produced in *pp* collisions. However, the size and the dependency on the kinematic variables are different due to the smaller charm quark mass. The production asymmetry is equivalently given as

$$A_P(D) \equiv \frac{\mathcal{P}(D) - \mathcal{P}(\overline{D})}{\mathcal{P}(D) + \mathcal{P}(\overline{D})} \ , \tag{2.46}$$

where $\mathcal{P}(D)$ and $\mathcal{P}(\overline{D})$ are the probabilities to produce a D and $\overline{D}$ meson, respectively, D can be either D^0 or D^+. In this work the production asymmetry of D^+ mesons is of interest later. It has been measured by the LHCb experiment to be $(-0.96 \pm 0.26\,(\mathrm{stat}) \pm 0.18\,(\mathrm{syst}))\,\%$ at a centre-of-mass energy of 7 TeV [39].

Effective D^0 production asymmetry in semileptonic B decays

The analysis uses muon-tagged D^0 decays to measure *CP* asymmetries. Therefore, the *effective D^0 production asymmetry* in semileptonic B decays is of interest. This slightly differs from the B production asymmetry due to two reasons.

First, possible *CP* violation in the decay of charged and neutral B mesons leads to different amounts of produced D^0 and $\overline{D}^0$ mesons. Direct *CP* violation can be neglected, as semileptonic B decays are Cabibbo-favoured. Also *CP* violation in B^0 mixing is expected to be small. The theoretical prediction of the charge asymmetry, a^d_{sl}, is

$(-4.1 \pm 0.6) \times 10^{-4}$ [40], and the world average of all measurements, as of September 2012, is $a_{sl}^{d} = (-0.03 \pm 0.21)\,\%$ [23].

Second, the production asymmetry is diluted by neutral meson mixing as an initial B^0 meson can decay to a D^0 meson after is has oscillated to a $\overline{B}^0$ meson. Assuming no decay-time acceptance and $\Delta\Gamma = 0$, the oscillation probability, $\mathcal{P}_{\text{osc}}$ (also known as χ_d), is given by

$$\mathcal{P}_{\text{osc}} = \frac{\Gamma_d}{2} \int_0^\infty e^{-\Gamma_d t}\,(1 - \cos \Delta m_d t)\,\mathrm{d}t \tag{2.47}$$

$$= \frac{1}{2}\left(1 - \frac{1}{1+x^2}\right) \ , \tag{2.48}$$

with $x = \Delta m_d / \Gamma_t = 0.770$, see Table 2.2, $\mathcal{P}_{\text{osc}}$ is calculated to 0.186. Hence, the production asymmetry of B^0 mesons is diluted by a factor $D = (1-2)\mathcal{P}_{\text{osc}} = 0.628$. Assuming no *CP* violation in Cabibbo-favoured B decays and in B^0 mixing, the effective D^0 production asymmetry in semileptonic B decays is given as

$$A_P(D^0 \text{ from } \overline{B}) = f(B^0)\,D\,A_P(\overline{B}^0) + (1 - f(B^0))\,A_P(B^+) \ , \tag{2.49}$$

where $f(B^0)$ is the fraction of B^0 mesons in the sample, $A_P(\overline{B}^0)$ and $A_P(B^+)$ are the production asymmetries of B^0 and B^+ mesons, respectively. As the B production asymmetry is expected to be at the per cent level or below, the absolute change of the B^0 production asymmetry is small. The effect is further reduced as the fraction of B^0 mesons in the semileptonic B sample is smaller than the B^+ fraction, $f(B^0) \approx 37.5\,\%$, cf. Chapter 2.2.2.

2.7 Summary

The main messages of this chapter are:

- The flavour-changing currents of the weak interaction induce *CP* violation and neutral meson mixing.
- The singly Cabibbo-suppressed D^0 decay modes, $D^0 \to K^-K^+$ and $D^0 \to \pi^-\pi^+$, are a good system to challenge the Standard Model due to small expected *CP*-violating effects. More experimental results are needed to improve our the theoretical understanding.
- The production cross sections of $b\bar{b}$ and $c\bar{c}$ pairs are high in pp collision at LHC energies, particularly in the forward region. Direct production and semileptonic B decays, with a branching fraction of around 10 %, are an abundant source of D^0 mesons.
- Particles and antiparticles have different interaction rates in the detector material depending on their momentum.
- The hadronization leads to small differences in the number of produced mesons and anti-mesons depending on the kinematic region.

Chapter 3

The LHCb experiment

In this chapter the LHCb experiment at the LHC is discussed briefly. The focus is put on the detector components that are important for this analysis. A comprehensive description of the LHCb detector is found in Reference [28].

3.1 CERN and the LHC

The European Council for Nuclear Research or CERN[1] was founded in 1952 by twelve European countries to create a laboratory for nuclear research. Today, more than 3, 000 employees and more than 10, 000 scientists from all over the world collaborate to study the frontiers of particle physics. CERN and its experiments are located near Geneva.

The first particle accelerator at CERN was built in 1957, the Synchrocyclotron. It was followed by many accelerators and detectors. Often the size had to increase to reach higher energies and smaller scales. The largest accelerator, to date, is the Large Hadron Collider (LHC). It is accommodated in the former LEP tunnel which has a circumference of 26.7 km. The location of the LHC is depicted in Figure 3.1. The LHC has been designed to collide two beams of protons at a centre-of-mass energy of 14 TeV. At a design luminosity of $10^{34}\,\mathrm{cm}^{-2}\,\mathrm{s}^{-1}$ the protons are packed into 2808 bunches with 1.1×10^{11} particles each. The spacing between two bunches is 25 ns in that case. The

---

[1] CERN is derived from the acronym for the French “Conseil Européen pour la Recherche Nucléaire”.

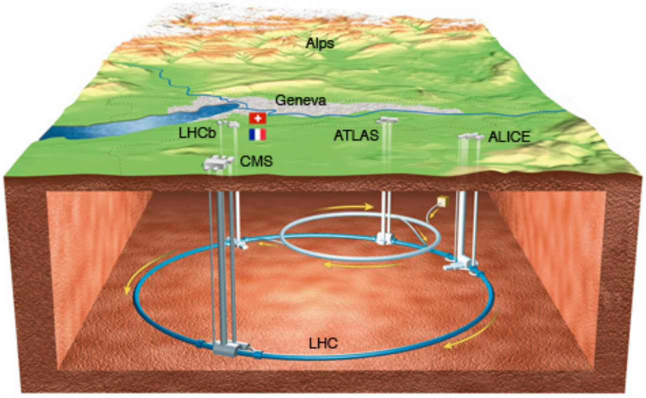

Figure 3.1: Location of the LHC and the four main experiments. Figure taken from Ref. [32].

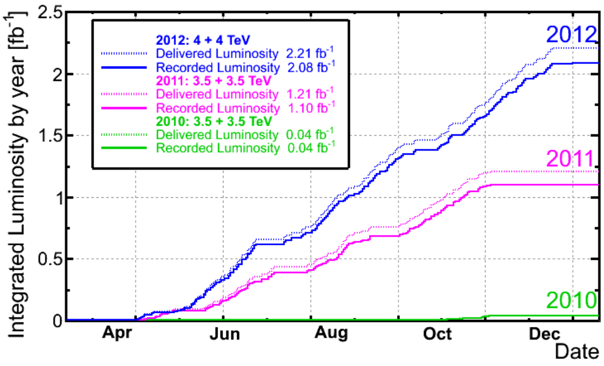

Figure 3.2: The integrated luminosity at the LHCb experiment in 2010, 2011 and 2012. Figure taken from Ref. [32].

proton beams are kept on a circular orbit by superconducting magnets with a peak field strength of 8.33 T, for a detailed description of the machine see Reference [41].

The LHC has four collision points around the ring where the four big and a few smaller experiments are located in order to analyse the proton–proton collisions, see Figure 3.1. ATLAS and CMS are general purpose detectors which cover the full spectrum of high-energy physics. The ALICE experiment is specialised in studying the properties of QCD in heavy ion collisions. The LHCb experiment is dedicated to measure the properties of c- and b-hadron decays.

After some delays the LHC started colliding protons at the end of 2009. In 2010 and 2011 the machine ran at a centre-of-mass energy of $\sqrt{s} = 7\,\text{TeV}$, in 2012 at $\sqrt{s} = 8\,\text{TeV}$. The number of bunches steadily increased in 2010 and 2011, up to about 1300 colliding bunches and a bunch spacing of 50 ns. In 2012 the running conditions were more stable such that the delivered luminosity was about twice the one of 2011. ALICE and LHCb are operated at an average lower number of collisions per bunch crossing than CMS and ATLAS. The delivered and recorded luminosity of the LHCb experiment is shown in Figure 3.2. The analysis presented here uses the full data set taken in 2011 and 2012.

3.2 The LHCb detector

Two properties of heavy quark production[2] have driven the design of the LHCb detector. As it is shown in Section 2.6.1, heavy quark pairs are predominantly produced in the forward or backward direction. Therefore, a detector with a small solid angle coverage in the forward region can cover a large fraction of the produced $q\bar{q}$ pairs. Additionally, the heavy quarks in the forward region have a large boost as they originate from very asymmetric parton collisions. Thus, their flight distance is on average longer than the one of centrally produced particles. This has a large impact on the decay time resolution and makes it easier to distinguish the decay products of long lived particles (secondary particles) from particles produced in the initial collision.

The LHCb detector, as a forward spectrometer, exploits both features. A schematic

---

[2] and funding agencies

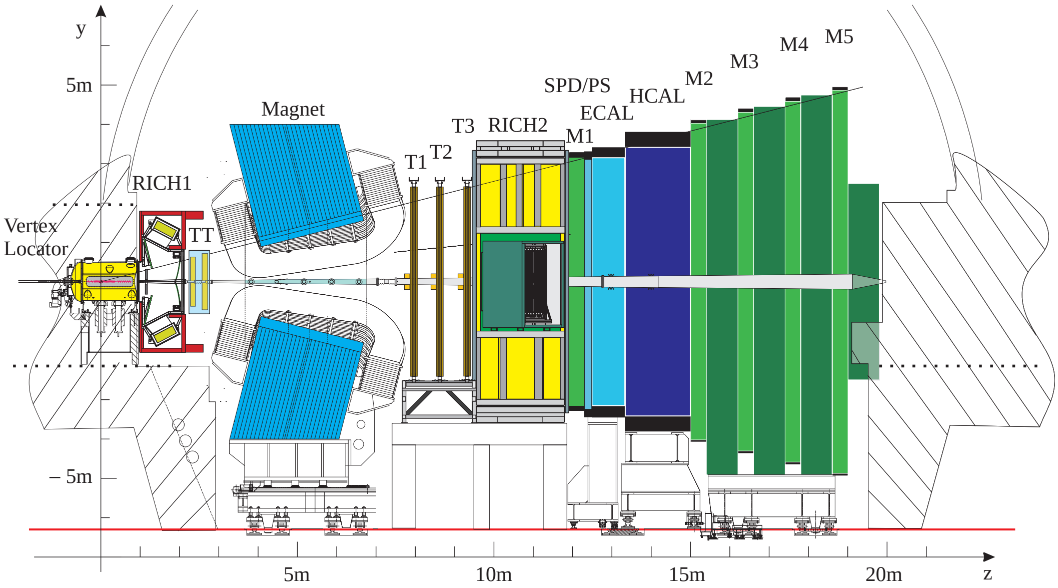

Figure 3.3: Schematic view of the LHCb detector (y-z plane). The detector components are described in the text. Figure taken from Ref. [32].

view is shown in Figure 3.3. The z-axis is aligned with the beam line and the y-axis is in vertical direction. The subsystems are placed along the beam line and enclose the beam pipe. Charged particles are bent in the x-z plane by the dipole field of the magnet. The pp interaction region is surrounded by the Vertex Locator. The geometrical acceptance of the spectrometer is 10–300 mrad in the bending plane (x-z) and 10–250 mrad in the non-bending plane (y-z).

The target instantaneous luminosity of the experiment is about $2 \times 10^{32}\,\mathrm{cm}^{-2}\,\mathrm{s}^{-1}$ with an integrated luminosity of $2\,\mathrm{fb}^{-1}$ per year data taking. This corresponds to a $b\bar{b}$ and $c\bar{c}$ production rate in the detector acceptance of roughly 15 kHz and 300 kHz, respectively[3]. In order to reach the luminosity goal, the LHCb detector is designed for an average number of inelastic proton–proton collisions of 0.4 per bunch crossing at LHC design conditions. The lower number of collisions compared to the general purpose experiments has the advantage that the particle flux in the forward region is reduced. First, this lowers the radiation damage in the detectors. Second, the occupancy of the detector parts is reduced which simplifies the event reconstruction as less particles create detector signals. As the maximum number of bunches in the LHC was 1380 in 2011 and 2012, the average number of interactions per crossing was increased to about 1.5. The average number of interactions per crossing can be changed by shifting the two beams towards each other. Therefore, the experiment is able to keep the instantaneous luminosity constant during a fill although the intensity of a proton beam decreases over time while particles collide. The LHCb experiment has been able to record a data sample corresponding to its design luminosity in the second full year of data taking, see Figure 3.2.

---

[3] The measured production cross-sections at $\sqrt{s} = 7\,\mathrm{TeV}$ are given in Chapter 2.6.1.

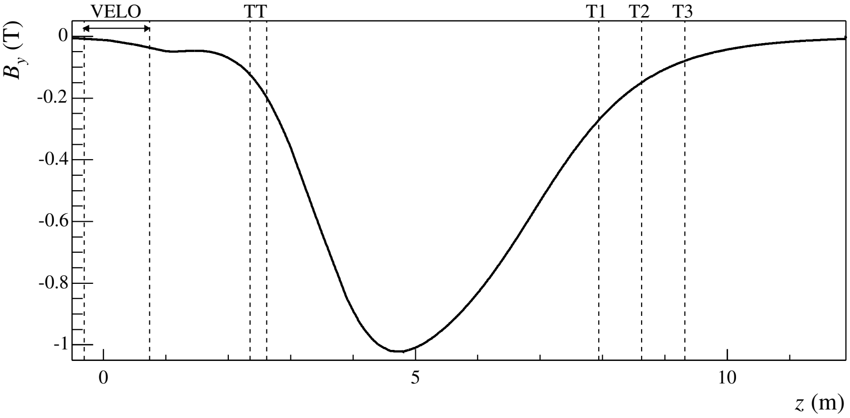

Figure 3.4: The main component B_y of the magnetic field as function of z. The position of tracking detectors is indicated with dashed lines. Figure taken from Ref. [28].

The detector components can be divided into two categories. The tracking system reconstructs the trajectories of charged particles to determine their origin vertex and their momentum. It consists of the Vertex Locator (VELO) and the Trigger Tracker[4] (TT) in front of and the T stations (T1-T3) behind the magnet. The following detector components are dedicated to particle identification, the two ring-imagining Cherenkov detectors before and after the magnet (RICH1 and RICH2); then, follows the calorimetry system consisting of the Scintillating Pad Detector (SPD), the Pre-Shower detector (PS), the Electromagnetic (ECAL) and the Hadronic (HCAL) calorimeter; one muon station (M1) is located in front of the calorimetry system, the other four (M2 to M5) behind. All detector components except of the VELO and the RICH detectors are divided into two halves that can be moved away from the beam pipe. The individual detector components are explained in more detail in the following.

3.3 Tracking system

Precisely reconstructed vertices and a high momentum resolution are vital parts of the detector's performance. The tracking system is designed to accomplish both goals by reconstructing the trajectories of charged particles, so-called *tracks*. The tracking system consists of a dipole magnet, the VELO and the TT in front of the magnet and the T stations behind.

Magnet

The LHCb dipole magnet is located about 5 m *downstream* of the interaction region. The main component, B_y, of the magnetic field is pointing in y direction. Charged particles are predominantly bent in the horizontal plane (x-z). The field strength B_y along the z-axis is shown in Figure 3.4. The integrated magnetic field, $\int B \mathrm{d}l$, for particles traversing the whole tracking system is about 4 Tm. All tracking detectors are

---

[4] Also known as Tracker Turicensis as it was not used in the trigger until mid 2012.

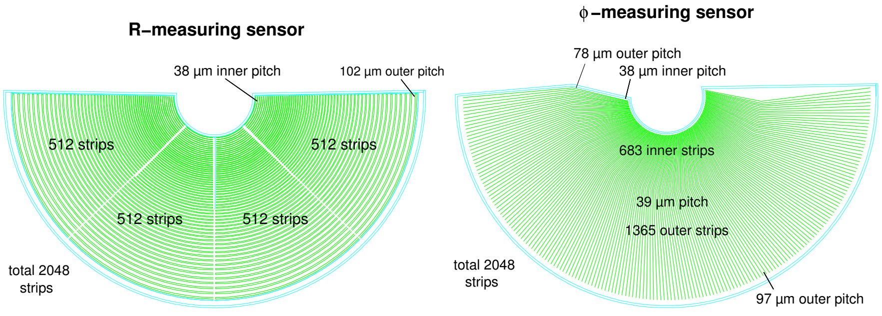

(a) (b)

Figure 3.5: A sketch of the layout of (a) r- and (b) ϕ-sensors. Figure taken from Ref. [28].

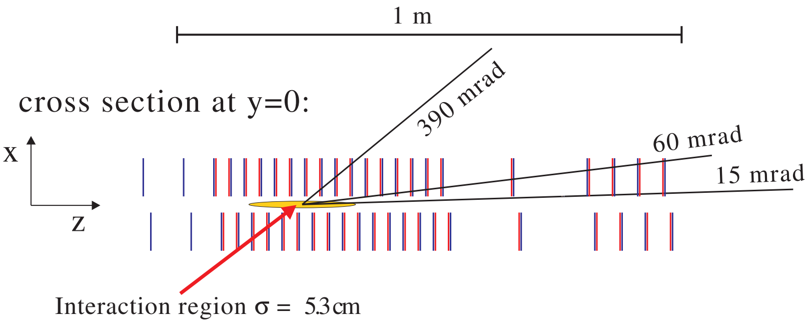

Figure 3.6: The placement of VELO modules, top view. Figure taken from Ref. [28].

located outside or in the fringe field of the magnet. The momentum resolution, $\Delta p/p$, for these particles is 0.4 % at 2 GeV/c and 0.6 % at 100 GeV/c.

Due to the detector geometry and the dipole field, particles with a given charge are bent preferentially to one side of the detector. An important feature to control detector related systematics, here in particular detection asymmetries, is the possibility to change the direction of the magnetic field. The magnet polarity is reversed frequently during data taking as shown later in Figure 12.3.

Vertex Locator

The Vertex Locator (VELO) measures the track coordinates close to the interaction region. Its main task is to reconstruct the position of a primary pp interaction, the so-called primary vertex (PV), and the determination of displaced vertices of b- and c-hadron decays. The VELO consists of 21 modules with two different types of silicon microstrip sensors, mounted back to back. One type measures the radial coordinate, r, with circular-shaped strips. The other type has strips in approximately radial direction to determine the azimuthal angle[5], ϕ. The strip pitch varies from 38 to 102 µm with a finer granularity close to the beam. The layout of both types is shown in Figure 3.5.

---

[5] The azimuthal angle, ϕ, is defined as the angle between the x-axis and a direction vector in the x-y plane. The coordinate system is right-handed and the y-axis is pointing vertically and the z-axis along the beamline into the direction of the muon stations.

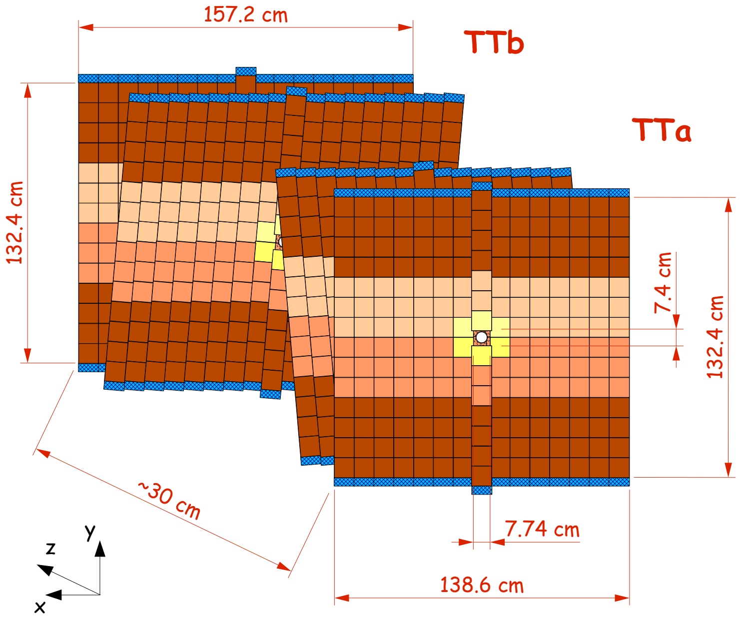

Figure 3.7: Schematic view of the Trigger Tracker. The readout electronics is indicated in blue. The other colours correspond to different readout sectors. Figure taken from Ref. [28].

The half-disc shaped modules are positioned around the z-axis at a minimum distance of 8 mm to the beam line, see Figure 3.6. Both sides are staggered such that there is a small overlap of the sensors to avoid holes in the acceptance. Inside the VELO the beam pipe has been removed, between the beam line and the sensors is the so-called RF foil which separates the beam and the VELO vacuum. The RF foil is made out of an aluminium alloy to shield the sensors from beam induced electromagnetic effects. It accounts for about 40 % of the VELO material budget and, thus, significantly degrades the resolution due to multiple scattering. While new proton beams are setup in the LHC, both halves are moved out into a safe position. As soon as protons are colliding, the VELO closes fully automated.

Trigger Tracker

The Trigger Tracker (TT) is located behind RICH1 in front of the dipole magnet. The detector technology is based on silicon strips with a pitch of 183 µm which results in a single hit resolution of about 50 µm. The detector layout is shown in Figure 3.7. The TT has four layers in a 2 × 2 configuration where the first pair is 27 cm apart from the second pair. Each layer is covering the full acceptance of the LHCb detector. The last two layers have a height of 157.2 cm and a width of 132.4 cm. The layers consist of several readout zones with a finer granularity close to the beam where the particle flux is higher. The silicon strips have a length of up to 38 cm. The first and the fourth layer have vertical aligned strips, whereas the strips of the second and the third layer are tilted by $(-5°)$ and $(+5°)$, respectively ((x, u, v, x)-configuration). This configuration

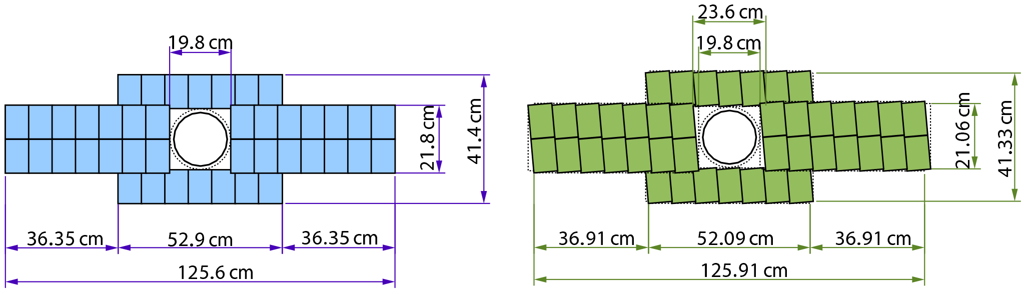

(a) (b)

Figure 3.8: The geometrical layout of (a) x layers and (b) stereo layers of the Inner Tracker. The circle in the middle is the beam pipe. Figure taken from Ref. [28].

allows to reconstruct track parameters with a high resolution in the bending plane (x-z) but also adds information in y direction to reduce combinatorics. Layers with a tilted geometry are referred to as stereo layers. In total, the TT has an active area of $8.4\,\text{m}^2$ with $143,360$ readout channels.

The TT allows the reconstruction of particles which are bent out of the spectrometer because their momentum is smaller than about $2\,\text{GeV}/c$ and it can detect particles which left no signal in the VELO. Its measurements improve the momentum resolution of tracks reconstructed in the VELO and the T stations. Furthermore, the information from the TT can be used to reject fake tracks from random combinations of measurements. Since mid 2012 the TT has been used to verify the authenticity of VELO tracks in the trigger.

T stations – Inner and Outer Tracker

The largest tracking system of the LHCb detector consists of the so-called T Stations that are located behind the dipole magnet to provide a precise momentum measurement. The twelve detector layers are grouped into three stations of four layers in a (x, u, v, x)-configuration, where each layer covers an active area of $6\times5\,\text{m}^2$. The higher particle flux in the forward region requires two different technologies, one technology with a fine granularity in the region with the largest particle flux and a technology covering a large area at reasonable costs and material budget. The part of the T stations close to the beam line consists of a silicon strip detector, the Inner Tracker (IT), and the outer part of a straw-tube detector, the Outer Tracker (OT).

Each IT station is built out of four boxes which are arranged in a cross-shape around the beam pipe, see Figure 3.8, with a maximum width of 126 cm and a maximum height of 41.4 cm. Each box contains four detection layers, (x, u, v, x)-configuration, built out of seven modules. The IT uses a similar silicon strip technology as the TT with a single hit resolution of $50\,\mu\text{m}$. The active area is about $4.0\,\text{m}^2$. The length of each silicon strip is 11 cm. In the modules left and right of the beam pipe two strips are combined to one readout channel. The IT has in total $129,024$ readout strips. The detector occupancy closest to the beam is around $2.5\,\%$ and drops to about $0.5\,\%$ in the outer regions of the IT.

The largest part of the T stations is covered by the OT, a gas detector. The outer

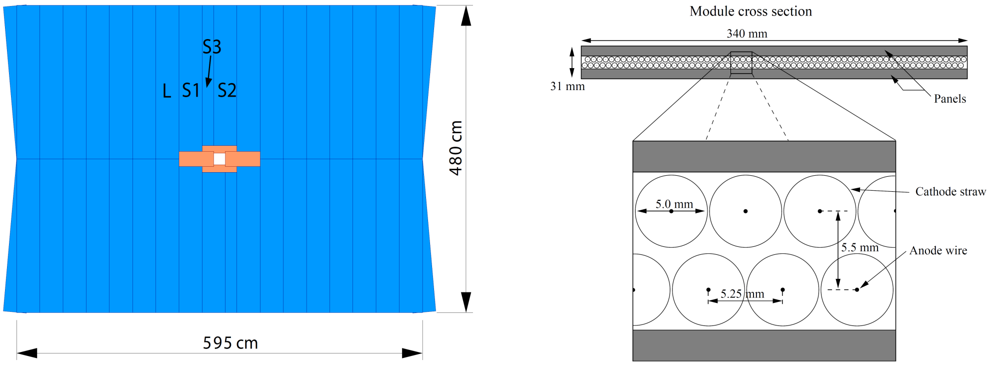

(a) (b)

Figure 3.9: The (a) top and (b) front view of an OT module. (b) The orange part is the IT. Figure taken from Ref. [28].

dimensions of each of the twelve detection layers are $595 \times 480\,\mathrm{cm}^2$, see Figure 3.9a. Each layer consists of several individual straw-tube modules where a single module is built out of two staggered layers of drift-tubes. Each drift-tube has a diameter of 4.9 mm, see Figure 3.9b, a length of 2.4 m and is filled with a gas mixture of $\mathrm{Ar/CO_2/O_2}$ (70/28.5/1.5 %). The drift time is below 50 ns which is important as the design bunch spacing of the LHC is 25 ns. The twelve layers are placed correspondingly to the IT in three stations of four layers in an (x, u, v, x)-configuration. In total the detector has roughly 53, 760 straw-tube channels. The occupancy of the detector does not exceed 10 %. The single hit efficiency is 99.8 % near the centre of a straw and the single hit resolution is about 210 µm.

Material budget

The material thickness in front of the last tracking station determines the momentum resolution due to multiple scattering and the reconstruction efficiency of charged particles due to absorption. The contribution of each detector to the material thickness in terms of the total radiation length and the total nuclear interaction length is given in Table 3.1. The different types of material interactions of particles are explained in Chapter 2.5.1.

3.4 Particle identification system

Pions are the most abundant particles produced in pp collisions at the LHC. Many interesting decays of c and b hadrons contain a number of kaons, pions, protons and leptons. Therefore, the task of the particle identification system is to identify which type of particles passed through the detector to suppress combinatorial background. For example, in this analysis the Cabibbo-favoured $D^0 \to K^-\pi^+$ decay mode has a very similar decay topology to the Cabibbo-suppressed $D^0 \to K^-K^+$ decay mode. It is difficult to discriminate the two decay modes without information from the particle identification systems. Another important role of the particle identification systems is to identify muons to distinguish between hadronic decays and decays with one or more

Table 3.1: The material thickness, d, in terms of radiation lengths X_0 and nuclear interaction lengths λ_I for the different detectors. Table taken from Ref. [42].

Detector	$\boldsymbol{d/X_0}$ [%]	$\boldsymbol{d/\lambda_I}$ [%]
VELO	15.8	3.8
RICH1	7.6	3.1
TT	3.5	1.1
Air in magnet	1.6	0.7
IT/OT	13.2	3.3
Total before RICH2	41.7	12.0
RICH2	12.4	4
SPD/PS	200	10
ECAL	2500	110
HCAL	–	560
Muon stations	–	2000

muons in the final state. The particle identification consists of three systems the RICH detectors, the calorimetry system and the muon stations.

RICH1 and RICH2

Ring-Imaging Cherenkov (RICH) detectors utilise the Cherenkov effect to discriminate between pions, kaons and protons. If a charged particle traverses a dielectric medium with a velocity that is larger than the phase velocity of light in that medium, electromagnetic radiation occurs. The medium is called radiator. So-called Cherenkov photons are emitted in a light cone around the flight direction of the charged particle. The opening angle, θ_C, is given by

$$\cos\theta_C = \frac{1}{n\beta} = \frac{1}{n}\frac{\sqrt{p^2c^2 + m^2c^4}}{pc} \quad , \tag{3.1}$$

where p is the particle's momentum, m its rest mass and n the refractive index of the radiator. A RICH detector measures the Cherenkov angle θ_C by detecting the Cherenkov photons. The momentum measurement is provided by the tracking system. The opening angle θ_C is given as a function of the particle's momentum for different media in Figure 3.10. It shows that the choice of the radiator depends on the momentum spectrum of the particles.

The LHCb detector features two Ring-Imaging Cherenkov detectors with different radiators to cover the momentum range from 2 to 100 GeV/c. RICH1 is located directly behind the VELO exit window and RICH2 is situated behind T3. The layout of both detectors is very similar, see Figure 3.11. Cherenkov photons are produced in the radiators. They are focused by a mirror system into ring images on the photon detector planes which are located outside of the LHCb acceptance. Photons are detected by so-called hybrid photon detectors (HPD). Each HPD has a silicon detector with 1024 pixels to detect the photo-electrons.

RICH1 covers the full angular acceptance of the LHCb tracking system of $25-300$ mrad. It contains two radiators to provide kaon, pion and proton separation in a momentum range of $2-40$ GeV/c: aerogel with a refractive index of $n = 1.03$ for particles

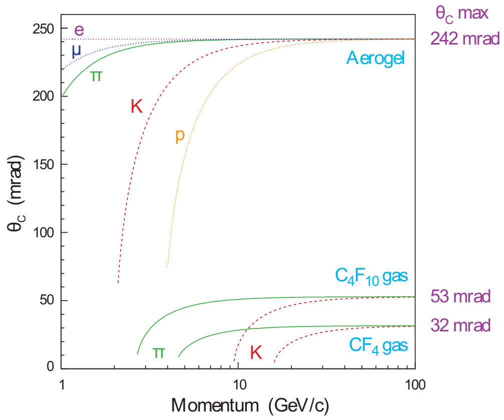

Figure 3.10: Cherenkov angle versus particle momentum for the RICH radiators. Figure taken from Ref. [28].

with a momentum below 9.3 GeV/c and the fluorocarbon gas C_4F_{10} for a momentum up to 40 GeV/c. As RICH1 is placed in front of the TT and the T stations it contributes $0.076X_0$ to the total absorption length of $0.417X_0$ in front of RICH2, see Table 3.1.

RICH2 uses the fluorocarbon gas CF_4 as radiator and provides particle discrimination from 15 to 100 GeV/c. Its angular acceptance is limited to $15 - 120$ mrad as high-momentum particles are preferentially produced in the forward region.

Calorimeters – SPD, PS, ECAL and HCAL

The calorimetry system of the LHCb detector consists of four detector components, the Scintillting Pad Detector (SPD), the Pre-Shower detector (PS), the Electromagnetic (ECAL) and the Hadronic (HCAL) calorimeter. All four detectors are built of alternating plates of absorbing material, lead or iron, and scintillating plates, see Figure 3.12a. When a particle deposits parts of its energy or is stopped in the absorber material, energy is released in the form of charged particles and photons. The released energy is converted to photons in the scintillating material. The photons can be detected by photomultipliers. The number of detected photons is proportional to the original particle's energy. The basic layout of SPD, PS, ECAL and HCAL is similar. They are segmented in the plane perpendicular to the beam axis into square cells. The layout of the HCAL is shown in Figure 3.12b. The large particle density close to the beam pipe demands a finer segmentation there, while a coarser segmentation is used in the outer part. The HCAL has two different cell sizes, the other three detectors have three different cell sizes.

The number of hits in the SPD is a measure of the particle multiplicity in an event. It can be used to veto or accept events with low or high particle multiplicities. The PS and the ECAL measure the energy of photons and electrons. The HCAL measures the energy of hadronic showers. ECAL and HCAL together provide a discrimination of electromagnetic and hadronic showers and are important to identify electrons and photons.

The main application of the calorimetry system in the context of this analysis is the energy measurement of hadrons. As this can be done quickly in contrast to the

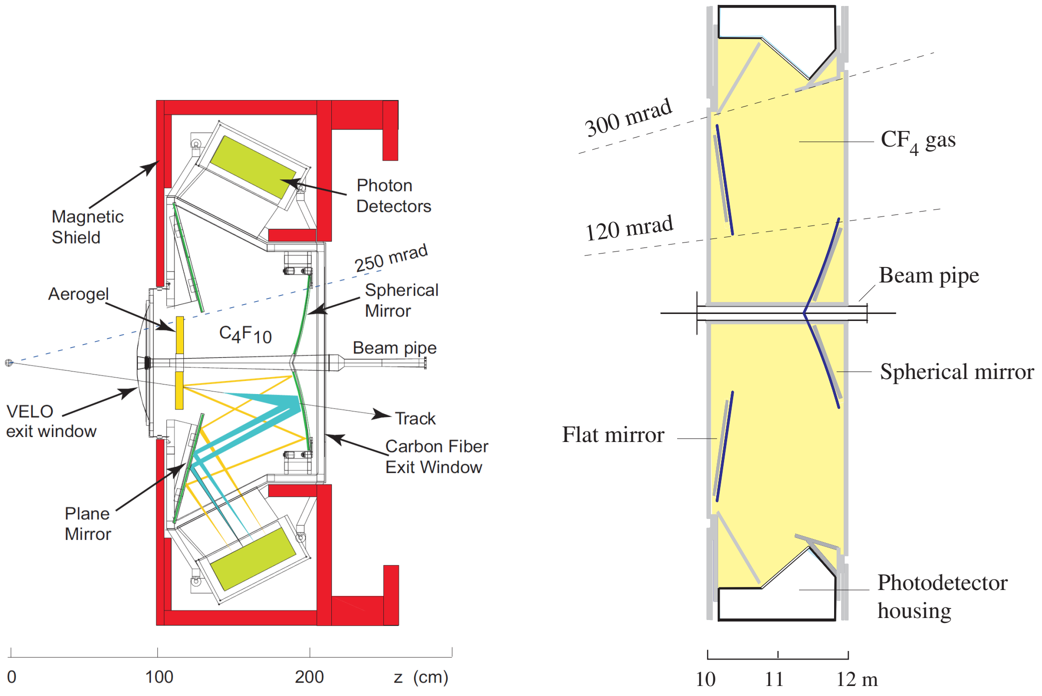

(a)

(b)

Figure 3.11: The layout of (a) RICH1 and (b) RICH2. The light path of Cherenkov photons is sketched in (a). The shown z-axes correspond to the LHCb coordinate system. Figure taken from Ref. [28].

more complicated momentum measurement by the tracking system, it is used in the first stage of the trigger system. This is discussed in detail in Chapter 4.1.

Muon stations

The identification of muons is an essential requirement to select semileptonic B decays. As muons are long-lived and minimum ionising particles, the muon stations are the last detector along the beam line.

The muon detector consists of five stations, M1–M5, which are placed along the beam axis, see Figure 3.13a. Four stations are located behind the calorimeters with 80 cm thick iron absorbers between them. A muon has to have initially more than 6 GeV/c to reach the last muon station since the total absorber thickness in front is approximately 20 nuclear interaction length. The first station, M1, is placed before the calorimeters. It is only used in the first trigger stage to provide an additional measurement of a muon track improving the transverse momentum resolution. The use of the muon detector in the trigger system is discussed in detail in Chapter 4.1.

Each muon station, except M1, has 276 multi-wire proportional chambers (MWPC) which cover a total area of 435 m^2. The inner region of M1 is equipped with 12 Gas Electron Multipliers (GEM) detectors as this type of detector has a larger radiation tolerance. Adjacent chambers are staggered to avoid gaps in the detector acceptance.

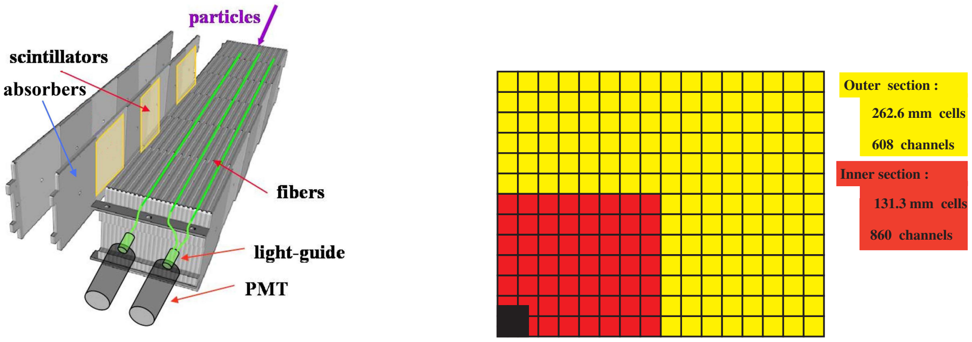

(a) (b)

Figure 3.12: (a) Schematic view of an HCAL cell. (b) Lateral segmentation of the HCAL. One quarter of the detector front face is shown. Figures taken from Ref. [28].

Each station is divided into four regions with increasing chamber size when going away from the beam line. Each chamber is divided into rectangular so-called logical pads that define a point in the plane perpendicular to the beam axis. Henceforth, each station provides space point measurements which can be used in the muon track reconstruction. As charged particles are bent in the horizontal plane, the segmentation is finer in the horizontal direction. The size of each station and its chambers increases from one to the next station, see Figure 3.13a. The transverse dimensions scale with the distance from the interaction point. This so-called projective geometry has the advantage that a muon with an almost straight trajectory (high momentum) from the interaction region is passing through the logical pad with the same logical number in each station. This allows to implement a fast track finding algorithm with logical units.

3.5 Trigger system

The information from various detectors is combined in the trigger system to select events with c and b hadrons. The trigger strategy is depicted in Figure 3.14. The first stage of the trigger system, L0, is implemented in hardware. The decision is mainly based on information from the muon and the calorimetry system. The hardware trigger is discussed in Chapter 4.1. If an event is selected, the detectors are fully read out at a rate of about 1 MHz. The second stage, the so-called High Level Trigger (HLT), is implemented fully in software. It runs on a large computer farm and performs an almost full event reconstruction. The selection of events is explained in detail in Chapter 6.2 when the selection of semileptonic B decays and D^+ mesons is discussed. The software trigger writes events at a rate of about 5 kHz to a storage system and, thus, these events are available for physics analyses.

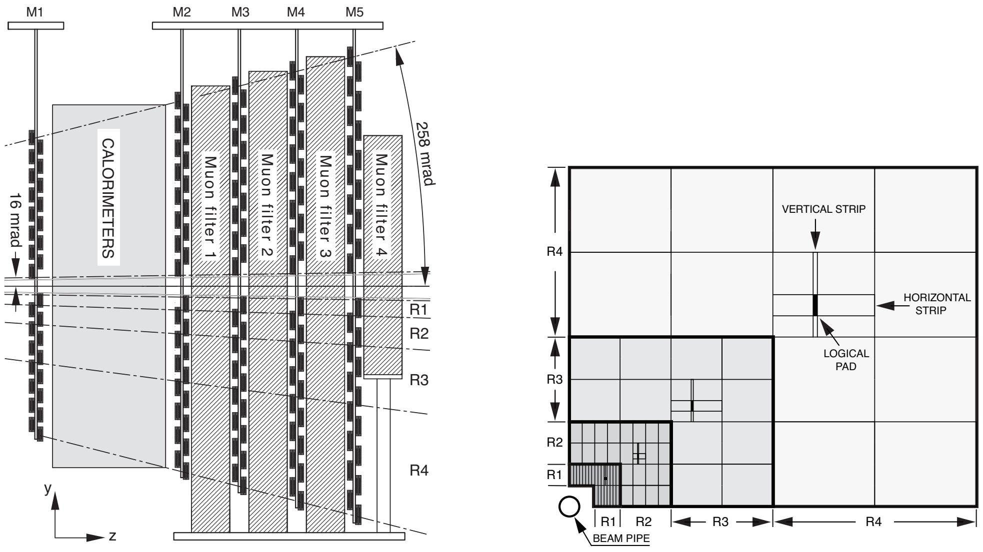

(a) (b)

Figure 3.13: (a) Side view of the muon stations. The geometry of the five stations is projective to the interaction point. (b) Segmentation of a quarter of a muon station in regions and logical pads. Each quadrant represents one chamber. The linear dimensions of each region scale in the ratio 1 : 2 : 4 : 8. Figures taken from Ref. [28].

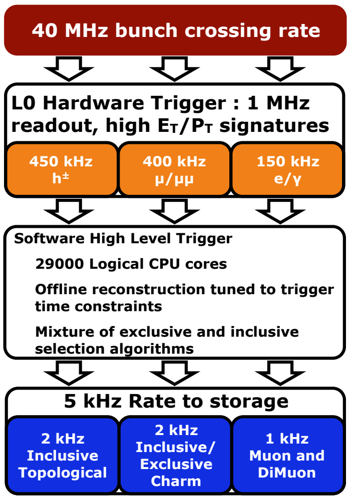

Figure 3.14: The trigger scheme of the 2012 data taking. In 2012 data were written to storage with a rate of 5 kHz, in 2011 the rate was 3 kHz. Figure taken from Ref. [32].

Chapter 4

Event reconstruction

The electronic signals of the various detector components have to be combined to reconstruct the particles that originated from the primary collision and subsequent decays. Here, this process is summarised under the term event reconstruction.

First, it is discussed how basic objects from the calorimetry system and the muon stations are used in the hardware trigger to decide if the event potentially contains a c or b hadron. Second, the measurements in the tracking system can be combined to reconstruct the trajectories of particles, once the detector has been readout. Therefore, the basic principles of the track reconstruction at the LHCb experiment are explained. Third, it is detailed how reconstructed tracks are linked to information from the particle identification systems to determine the particle species.

At each step it is pointed out that the reconstruction and detection efficiencies can be different for positively- and negatively-charged particles. This leads to spurious detection asymmetries that affect the *CP* asymmetry measurements discussed later in Chapter 5. The selection of c- and b-hadron decays used in this analysis is discussed in Chapter 6.

4.1 First level trigger

The hardware trigger, L0, selects inelastic pp interaction at a rate of 1.1 MHz at which all detector components can be read out. Two independent systems are used to select heavy quark events, the L0-calorimeter trigger and the L0-muon trigger.

4.1.1 L0-calorimeter trigger

The energy deposit in SPD, PS, ECAL and HCAL is used in the L0-calorimeter system to trigger events. All detector components are segmented transverse to the beam axis into cells of different size. The decision to trigger an event is based on the transverse energy deposit in a cluster of 2×2 cells. The transverse energy of a cluster is defined as

$$E_{\mathrm{T}} = \sum_{i=1}^{4} E_i \sin\theta_i \quad , \tag{4.1}$$

where E_i is the energy deposited in cell i and θ_i the angle between the z-axis and a line from the cell centre to the average pp interaction point. The L0-calorimeter trigger distinguishes between hadron, photon and electron candidates based on the calorimetry

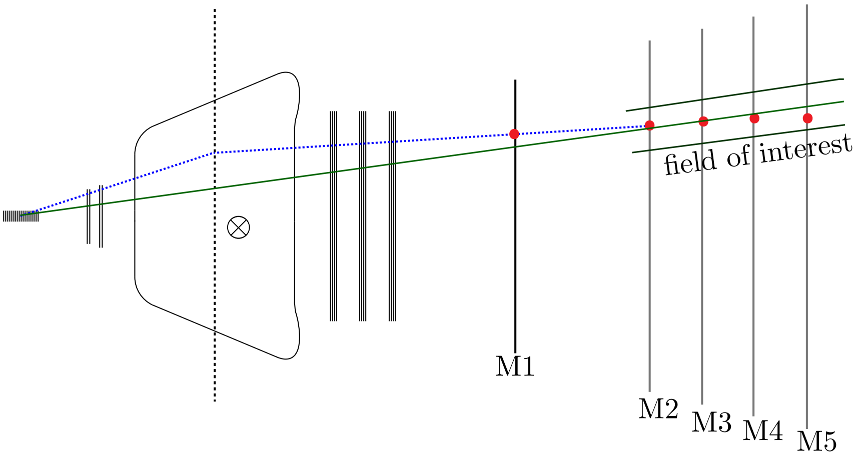

Figure 4.1: The track finding of the muon trigger. The hits (red dots) in the logical-pads are from a negative muon. The field of interest around the line projecting from M3 to the interaction region is depicted. The size of the field of interest is given by the requirement $p_{\mathrm{T}} \gtrsim 0.5\,\mathrm{GeV}/c$. The dashed lines indicate the single p_{T}-kick to estimate the transverse momentum of the muon candidate.

systems.[1] Hadron candidates are triggered if the transverse energy E_{T} is larger than 3.5 GeV.

The trigger efficiency of hadronic c and b decays depends on the transverse momentum, p_{T}, of the c or b hadron. It ranges from 10 % at $p_{\mathrm{T}} \approx 5\,\mathrm{GeV}/c$ to 90 % at $p_{\mathrm{T}} \approx 15\,\mathrm{GeV}/c$, for more details see Reference [43].

4.1.2 L0-muon trigger

The L0-muon trigger searches for straight line tracks in the five muon stations. Each muon station is sub-divided into logical pads in the x-y plane. The pad size scales with the distance to the interaction region. The track finding algorithm is implemented in four dedicated L0-muon processors. Each processor is only connected to one of the four quadrants[2] around the beam pipe. Thus, muons crossing two quadrants cannot be reconstructed in the L0 trigger.

The track finding algorithm is depicted in Figure 4.1. Starting with a hit in M3, the L0-muon processors search for an alignment of hits in stations M2 to M5 inside a field of interest around a line projecting to the interaction region. If this alignment is found, the hits in M2 and M3 are used to predict the position of a hit in M1. The nearest hit in M1, in a suitable field of interest, and the hit in M2 are used to determine the slope of the trajectory behind the magnetic field. The track direction indicated by the hits in M1 and M2 is used to estimate the transverse momentum p_{T} of a muon candidate, assuming a particle from the interaction point and a single kick from the magnetic field. The transverse momentum resolution of the L0-muon trigger is about 25 %.

Each of the four L0-muon processors identifies the two muon candidates

---

[1] The different trigger decisions are called `L0Hadron`, `L0Photon` and `L0Electron`.

[2] The four quadrants are $(x > 0, y > 0)$, $(x > 0, y < 0)$, $(x < 0, y > 0)$ and $(x < 0, y < 0)$.

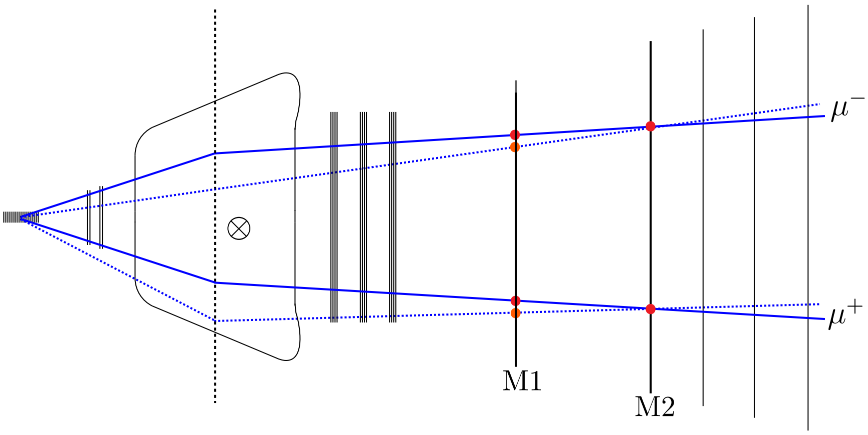

Figure 4.2: The effect of a relative misalignment of M1 and M2 on the momentum measurement. The solid line is the real trajectory of a particle. The dashed line is the measured trajectory if M1 is misaligned relative to M2. The transverse momentum is estimated from a single kick by the magnetic field.

with the largest p_{T}. The trigger decision is based on these maximally eight candidates, either the largest ${p_{\mathrm{T}}}^{\mathrm{largest}}$ is above a certain threshold (`L0Muon`) or the multiplication of the largest and second largest transverse momentum, ${p_{\mathrm{T}}}^{\mathrm{largest}} \times {p_{\mathrm{T}}}^{\mathrm{2nd\,largest}}$, is larger than a certain value (`L0DiMuon`). Most of the available data from 2011 have been selected with the requirements ${p_{\mathrm{T}}}^{\mathrm{largest}} > 1.48\,\mathrm{GeV}/c$ and $\sqrt{{p_{\mathrm{T}}}^{\mathrm{largest}} \times {p_{\mathrm{T}}}^{\mathrm{2nd\,largest}}} > 1.296\,\mathrm{GeV}/c$. In 2012 the thresholds were increased to ${p_{\mathrm{T}}}^{\mathrm{largest}} > 1.76\,\mathrm{GeV}/c$ and $\sqrt{{p_{\mathrm{T}}}^{\mathrm{largest}} \times {p_{\mathrm{T}}}^{\mathrm{2nd\,largest}}} > 1.6\,\mathrm{GeV}/c$.

The `L0Muon` efficiency[3] of $B \to J/\psi X$ decays where the J/ψ meson decays into two muons is around 70 % for $p_{\mathrm{T}}(J/\psi) \approx 1\,\mathrm{GeV}/c$ and more than 95 % at $p_{\mathrm{T}}(J/\psi) \gtrsim 4\,\mathrm{GeV}/c$ [43]. The trigger efficiency of semileptonic B decays with one muon in the final state is around 60 %, for more details see Reference [44].

4.1.3 `L0Muon` asymmetry

In order to understand one source of detection asymmetries, some technical details of the `L0Muon` trigger are necessary. The `L0Muon` trigger selects an event if ${p_{\mathrm{T}}}^{\mathrm{largest}}$ is larger than a defined threshold. The transverse momentum estimate is obtained from lookup tables in the L0-muon processors which use the coordinates of the hits in M1 and M2.

If the coordinates in the lookup table and the real coordinates differ, the momentum is wrongly determined. The effect of wrong coordinates on the transverse momentum measurement is depicted in Figure 4.2. A relative misalignment between M1 and M2 leads to an under- or overestimation of the transverse momentum depending on the muon charge. The effect is reversed when changing the field polarity. A misalignment of the muon stations is one source of these differences. Another source is a simply wrong lookup table. In the 2011 data taking both issues were present. The lookup table did

---

[3] If not stated otherwise, trigger efficiencies are quoted relative to off-line selected events. The off-line reconstruction of relevant decay modes is discussed in Chapter 6.

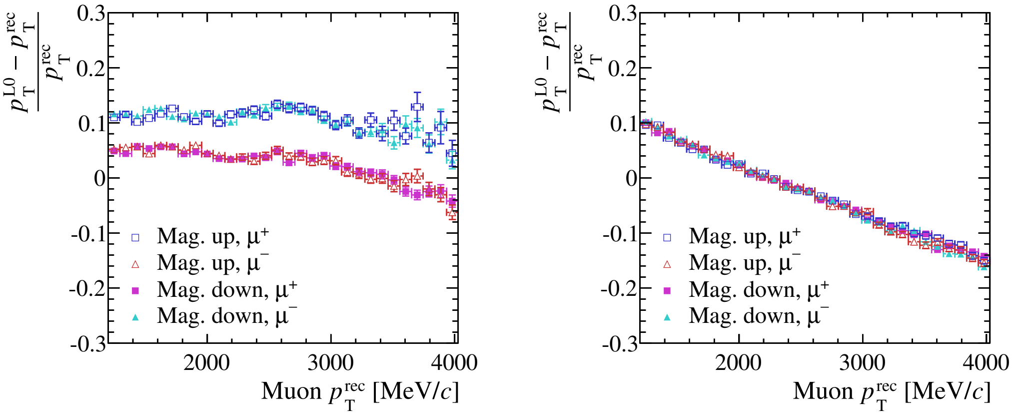

(a) Before calibration (b) After calibration

Figure 4.3: The relative error of the L0-muon trigger transverse momentum as a function of the reconstructed momentum (a) before and (b) after calibration in 2011 data.

not use the real centre of each pad[4] as coordinates but used coordinates corresponding to the average position of two staggered[5] chambers in the muon stations. Furthermore, no proper alignment has been performed during the data taking in 2011.

The result can be seen in Figure 4.3a where the momentum of the L0-decision unit is compared with the momentum obtained from the tracking system. Depending on the charge and the magnet polarity, different biases are present. Thus, a cut on ${p_T}^{\text{largest}}$ introduces different efficiencies for positive and negative muons at low transverse momenta. The measured asymmetry of $\overline{B} \to D^0\mu^- X$ decays where the D^0 decays into a $K^-\pi^+$ pair is shown in Figure 4.4a. It will be discussed later in Chapter 7.3 how asymmetries are determined. Only the change as function of p_T is of interest here, the offset is induced by the kaon detection asymmetry. The measurement of the kaon detection asymmetry is an integral part of the analysis, which is discussed later in Chapter 5. Variations of up to 5 % of the raw asymmetry are observed over the total p_T range. However, the effect exactly flips when changing the polarity of the magnetic field. This shows that it is very important that the dipole field can be reversed. First, detection asymmetries like this can be identified. Second, they cancel in the arithmetic mean of the asymmetry in the magnet up and the asymmetry in the magnet down sample.

If the source of a particular detection asymmetry is known and if it is large compared to other asymmetries, it is preferable to correct this detection asymmetry. Therefore, the `L0Muon` p_T of recorded events is emulated with a corrected lookup table. The result of the p_T calibration is shown in Figure 4.3b. However, events which are not triggered during data taking cannot be recovered. Hence, the cut on the calibrated `L0Muon` p_T is tightened to 1.64 GeV/c (from 1.48 GeV/c) to compensate the inefficiencies which resulted from a wrong momentum calculation in the L0-muon trigger. After the calibration the bias is the same for each charge and magnet polarity. The measured raw

---

[4] The problem was also visible in simulation. The use of correct coordinates solved the problem.

[5] The staggered chambers are shown in Figure 3.13a.

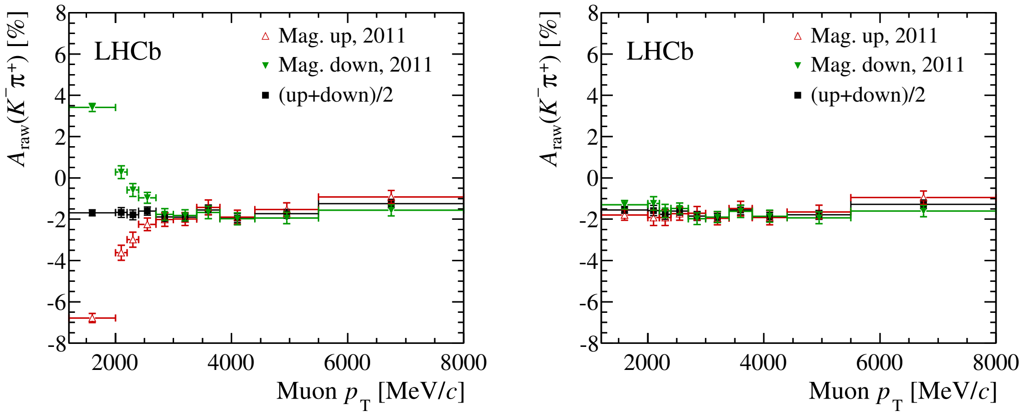

(a) Before calibration

(b) After calibration

Figure 4.4: The measured raw asymmetry as a function of reconstructed muon p_{T} in the $D^0 \to K^- \pi^+$ channel (a) before and (b) after calibration in 2011 data. The offset from zero is induced by the kaon interaction asymmetry.

asymmetry after calibration and with a raised threshold is shown in Figure 4.4b, no up–down difference is seen.

As this problem had been known before the restart of the data taking in 2012, the first data of 2012 were used to align the muon stations after they had been moved in the shutdown between 2011 and 2012. The effect is highly reduced as can be seen in Figure 4.5 and no further calibration is needed for this data taking period.

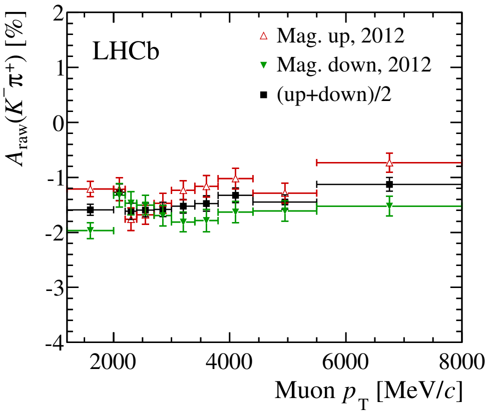

Figure 4.5: The measured raw asymmetry as a function of reconstructed muon p_{T} in the $D^0 \to K^- \pi^+$ channel in 2012 data. The y-scale is changed relative to Figure 4.4. The data used for the alignment of the muon stations are excluded.

4.2 The LHCb software framework

Several software packages are used to reconstruct and select the events which are triggered by the hardware stage and written subsequently to a mass storage system. The LHCb software is based on the GAUDI framework [45]. The following applications are used to reconstruct events out of the detector response:

- **Brunel:** The so-called *off-line reconstruction* of a stored event is performed by the BRUNEL software package [46]. It implements the algorithms to reconstruct the trajectories of charged particles and neutral particles from the measurements of the tracking and calorimetry system. The reconstructed tracks are combined with measurements from the particle identification system to form basic objects (particle candidates). These particle candidates are then available for further analysis. The off-line reconstruction needs a lot of processing time. Therefore, the execution of the event reconstruction software is performed centrally by the LHCb computing team.
- **DaVinci:** The DAVINCI project [47] is designed to reconstruct and select the decays of interest based on the output of the BRUNEL off-line reconstruction. It provides a framework to apply selection requirements to particle candidates and to fit common vertices in order to reconstruct the decay vertices of c and b hadrons. As this is a computing intensive task, it is run centrally to reduce the number of events the analyst has to deal with. Further selections can then be applied to decrease contributions from background events. In many cases this first central selection has already produced samples with very low background.
- **Moore:** The software trigger stage is implemented in the MOORE project [48]. It has to be fast but should not differ too much from the off-line reconstruction to minimise reconstruction artefacts. Thus, it shares most of the reconstruction and selection algorithms with the BRUNEL and DAVINCI projects. However, it uses in many cases speed optimised tunings.

Some aspects of an analysis are studied with simulated events. The reconstruction of the simulated events is performed by the aforementioned trigger and reconstruction software packages. The simulation of the pp collision, particle decays and detector response is performed by the following software packages:

- **Gauss:** Simulated events are generated by the GAUSS software package [49]. The pp collision, including soft and hard processes, is simulated by the event generator PYTHIA [36] based on the Lund string model discussed in Chapter 2.6. Version 6 and 8 of PYTHIA are available in the GAUSS software project. The decays of c and b hadrons are simulated with the EVTGEN package [50] taking mixing and interference effects into account. The electromagnetic and hadronic interactions of particles with the detector material are described by the GEANT4 package [51].
- **Boole:** The detector response to the simulated interactions is generated by the BOOLE software package [52]. The output of BOOLE can be processed with BRUNEL and MOORE to get simulated events with the same trigger and off-line reconstruction as in data.

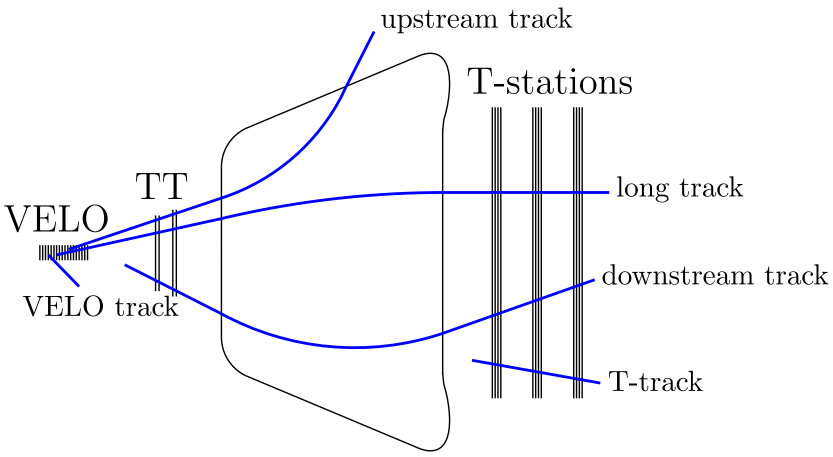

Figure 4.6: Sketch of the different types of tracks. Figure taken from Ref. [53].

4.3 Track reconstruction

The track reconstruction is performed in three different stages. First, the *pattern recognition* tries to identify measurements in the tracking detectors which one charged particle initiates. All tracking detectors are either located outside of the magnetic field (VELO) or inside the fringe field (TT and T -stations). Thus, the trajectories of charged particles are to a good approximation straight lines in the tracking systems of the LHCb detector. This and that they originate from the primary interaction region is exploited by the pattern recognition algorithms. The momentum of a charged particle is determined by measuring the slopes of its trajectory before and after the magnet. The reconstructed tracks can be categorised into five distinct types, see Figure 4.6:

Long tracks are associated to particles which traverse the whole tracking system. They contain measurements from the VELO, the T stations and optionally from the TT. They have the best possible momentum and impact parameter[6] resolution and are the basis of most reconstructed decays. The momentum resolution varies from 0.4 % at 2 GeV/c to 0.6 % at 100 GeV/c. The impact parameter resolution is about 20 µm for particles with $p_{\mathrm{T}} > 2\,\mathrm{GeV}/c$.

Downstream tracks are built out of measurements from the TT and the T stations. Their momentum resolution is comparable to long tracks for low momentum particles but gets worse for high momentum particles. The impact parameter resolution is significantly worse as the trajectory has to be propagated through a part of the magnetic field. They are important to reconstruct the decays of K^0_{S} mesons and Λ baryons as these often decay outside of the VELO due to their relatively long lifetime.

Upstream tracks contain measurements from the VELO and the TT and belong to charged particles that are bent out of the detector due to their relatively small

---

[6] The impact parameter is defined as the distance of closest approach between a particle trajectory and the primary vertex. In the case of multiple primary vertices, usually the nearest is taken.

momentum ($p \lesssim 2\,\mathrm{GeV}/c$). As the integrated field strength in front of the TT is small, their momentum resolution is about 15 %.

VELO tracks are built exclusively of measurements in the VELO. VELO tracks serve as input to long and upstream tracks. Tracks which are not extended with measurements in the TT or the T stations are still useful for the primary vertex reconstruction.

T tracks are reconstructed in the T stations only. They are used as input to the pattern recognition of long and downstream tracks.

There are two almost redundant pattern recognition algorithms to reconstruct long tracks. The so-called *forward tracking* [54] starts with VELO tracks and tries to extend them with measurements in the T stations. The search window in the T stations is defined by a minimum momentum requirement. The larger the momentum threshold the smaller is the search window. The possibility to change the search window size is important as it reduces the processing time of an event. However, the reconstruction efficiency of low momentum particles is highly reduced. The so-called *track matching* uses VELO and T tracks and combines them to long tracks. Its efficiency is lower as the selection of standalone T tracks is more difficult as no information from the VELO is used. The pattern recognition efficiency of long tracks has been determined with a data-driven method to be above 95 % [55]. The pattern recognition efficiency is defined relative to charged particles which traversed the whole tracking system. Inefficiencies due to absorption by material interactions are not included.

In a subsequent step the trajectory of a particle is reconstructed from the collected measurements. A *Kalman filter* [56, 57] is used to fit the tracks. A Kalman filter is based on minimising the χ^2 of the measurements on the tracks. It takes multiple scattering and energy loss into account. The track fit provides an estimate of all track parameters at any point along the trajectory. The exact procedure is described in detail in References [42, 58]. An important output of the track fit, besides the track parameters, is a measure of the quality of the fit, the χ^2 per degrees of freedom or $\chi^2_{\mathrm{track}}/\mathrm{ndf}$. It can be used to discriminate tracks which are associated to one charged particle from tracks which contain measurements from several particles or detector noise. The latter type are called *ghost* tracks in the following.

The last step of the track reconstruction identifies tracks that are associated to the same particles, so-called *clones*. Clones originate either from redundant algorithms – e.g. a particle can be reconstructed as a long and a downstream track, then the measurements of the latter are a subset of the former – or one pattern recognition algorithms finds two similar sets of measurements. Tracks with more measurements are favoured if their $\chi^2_{\mathrm{track}}/\mathrm{ndf}$ is smaller than some fixed value[7].

Reconstructed tracks which have measurements in the VELO are used to reconstruct the collision point (primary vertex). A primary vertex is accepted when at least five tracks form a common vertex which is close to the beam line. The spatial resolution increases with the number of tracks which are fitted to a common vertex. The average number of tracks used in the primary vertex reconstruction is about 30 for events containing a *b*- or *c*-hadron decay. For primary vertices reconstructed with more than

---

[7] In the reconstruction, Reco 14, used for this work the requirement is $\chi^2_{\mathrm{track}}/\mathrm{ndf} < 3$.

25 tracks the spatial resolution is found to be 13 μm in y and x direction and 71 μm in z direction [59].

The impact parameter resolution of a track which is not contained in the primary vertex is 20 μm in x and y direction for particles with large transverse momentum. It degrades for low momenta as multiple scattering increases. The decay time resolution of multi-body B decays is typically around 45 fs [60].

4.3.1 Detection asymmetries of charged particles

Charged particles have to traverse the whole tracking system and leave enough hits in the tracking detectors such that the pattern recognition algorithms and the track fit can reconstruct their trajectories. Hence, there are two sources of relative inefficiencies between positive and negative particles.

First, particles can be absorbed by the detector material before they left enough hits in the VELO and the T stations. The dominating material interactions of various particle species are discussed in Chapter 2.5. Importantly for this analysis, the different material interaction rates of positive and negative kaons introduce a detection asymmetry in their reconstruction. This effect is expected to be negligible for pions and muons in the relevant momentum range.

Second, a different reconstruction efficiency can be introduced by asymmetries of the LHCb tracking system. The LHCb dipole magnet bends particles with a given charge preferentially to one side of the detector. Thus, some non-functioning modules or misalignments of the tracking detectors introduce different reconstruction efficiencies of positively- and negatively-charged particles. These asymmetries change sign when reversing the magnet polarity in contrast to the asymmetries induced by different material interaction rates of positively- and negatively-charged particles.

The reconstruction efficiency depends on several parameters. It depends on the momentum p, the rapidity η and the azimuthal angle ϕ around the beam line of a given particle. Hence, detection asymmetries are a function of the these quantities. According to Equation 2.41, a detection asymmetry is defined as

$$a_D(h^-,\vec{p}) \equiv \frac{\varepsilon(h^-,\vec{p}) - \varepsilon(h^+,\vec{p})}{\varepsilon(h^-,\vec{p}) + \varepsilon(h^+,\vec{p})} \ , \tag{4.2}$$

where $\varepsilon(h^{\pm},\vec{p})$ is the reconstruction efficiency of a particle $h^{\pm}$ with momentum vector $\vec{p}$. As explained, the efficiency can include effects from the track reconstruction and material interactions, for this analysis only the combination of both is relevant. It depends on the particle species which part is dominating. If the asymmetry is written with a capital A, an integration over the momentum spectrum is implied.

The detection asymmetry of charged pion candidates, including material interactions and track reconstruction effects, has been measured in an independent study with a tag-and-probe method in data [61]. It is measured consistent with zero when arithmetically averaging the efficiencies obtained from a sample with magnet up and magnet down data. The uncertainty of the measurement is 0.18 %.

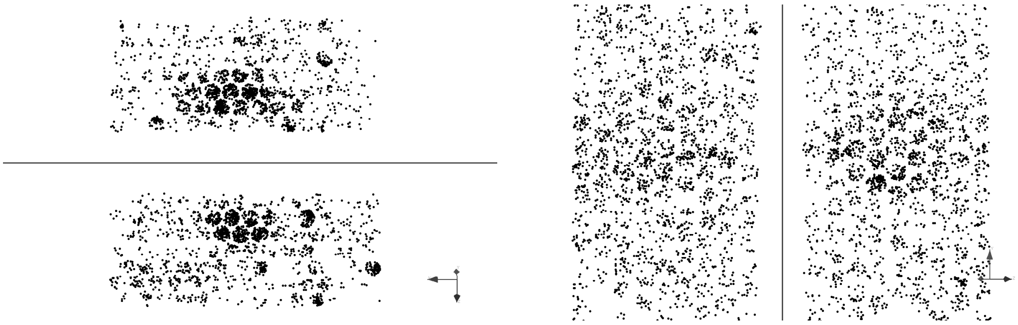

(a) RICH1 (b) RICH2

Figure 4.7: An example of a typical LHCb event as seen by the RICH detectors. Each black point corresponds to a measurement in an HPD. Due to the high occupancy, several Cherenkov cones overlap and, thus, individual light cones are difficult to distinguish. Figure taken from Ref. [63].

4.4 RICH particle identification

Cherenkov light is emitted in a light cone around the flight direction of a charged particle if the particle's velocity is above the Cherenkov threshold. The light cone is visible as a ring in the photon detectors of RICH1 and RICH2. As many charged particles are created in the LHCb acceptance in *pp* collisions at the LHC [62], it is likely that light cones overlap. The detected Cherenkov photons of an example event are shown in Figure 4.7.

The RICH reconstruction considers simultaneously all reconstructed tracks and all signals in RICH1 and RICH2 in one event. The reconstruction algorithm computes an overall *event log-likelihood*, $\ln\mathcal{L}$, as explained in the following. First, each track is projected into the photon detection plane. Second, photon measurements are associated to a track according to the measured momentum and a mass hypothesis. Since most particles are pions, the algorithm starts with the pion hypothesis for each track. Then, for each track the mass hypothesis is changed to e, μ, π, K and proton while all other hypotheses are unchanged. The change in mass hypothesis that gives the largest increase of the event log-likelihood is fixed. This procedure is repeated until all tracks have the optimal mass hypothesis and the event log-likelihood is maximised.

The final result for each track is the difference of the overall event log-likelihood when changing from the pion hypothesis to the e, μ, K or proton hypothesis. For example, kaons and pions are discriminated by the variable $\mathrm{DLL}_{K\pi} \equiv \ln\mathcal{L}_K - \ln\mathcal{L}_\pi$. The larger the value the more likely it is that the reconstructed track belongs to a kaon instead of a pion. Pions can be selected when requiring a small or negative value.

The efficiency and misidentification rate has been measured with a tag-and-probe method in data [63]. The result is shown in Figure 4.8. For particles with a momentum below 40 GeV/c the kaon identification efficiency is larger than 90 % while retaining a misidentification probability of less than a few per cent. For larger momenta the efficiency decreases, whereas the misidentification probability increases. The selections presented in Chapter 6.3 employ a $\mathrm{DLL}_{K\pi}$ requirement of larger than 7 to select kaon candidates. In Figure 4.9 it is shown that the kaon identification efficiency decreases

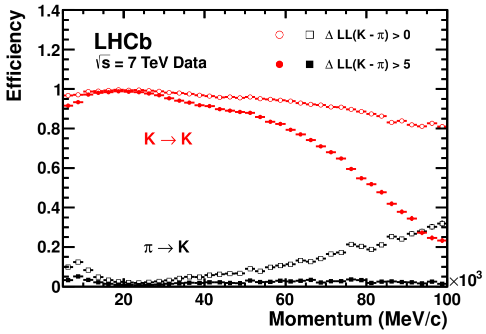

Figure 4.8: Kaon identification efficiency and pion misidentification rate measured in data as a function of track momentum. Two different $\mathrm{DLL}_{K\pi}$ requirements have been imposed on the samples. Figure taken from Ref. [63].

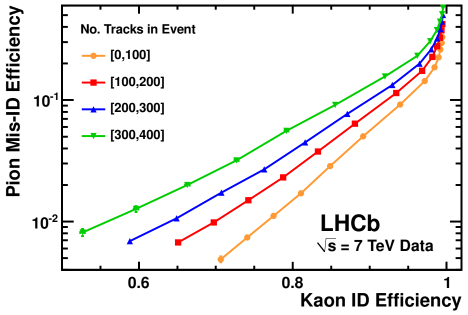

Figure 4.9: Pion misidentification fraction versus kaon identification efficiency as a function of the number of tracks in an event. Figure taken from Ref. [63].

with the number of charged particles for a given pion misidentification probability as it becomes more complicated to discriminate the individual light cones.

Similarly to detection asymmetries which are induced by the track reconstruction, the particle identification can induce detection asymmetries as well. The particle identification asymmetry is defined as

$$A_{\mathrm{PID}}(\mathrm{DLL}_{K\pi} > x) \equiv \frac{\epsilon^{-}(\mathrm{DLL}_{K\pi} > x) - \epsilon^{+}(\mathrm{DLL}_{K\pi} > x)}{\epsilon^{-}(\mathrm{DLL}_{K\pi} > x) + \epsilon^{+}(\mathrm{DLL}_{K\pi} > x)} \quad , \tag{4.3}$$

where $\epsilon^{\pm}(\mathrm{DLL}_{K\pi} > x)$ are the particle identification efficiencies with a selection value of x. In Figure 4.10 A_{PID} is shown as a function of the momentum for kaon and pion candidates. The asymmetry is determined with the same tag-and-probe method as used for the kaon and pion identification efficiencies. It is split up into the data taking periods of 2011 and 2012 and samples with different magnet polarities. The measured asymmetry of the 2011 and 2012 data sample show the same behaviour. The asymmetries for pion and kaon candidates are of opposite sign. The asymmetries obtained in a data sample with magnet up and magnet down are averaged arithmetically[8]. Only for very high momenta a residual asymmetry can be seen after the arithmetic averaging.

4.5 Off-line muon identification

The muon identification starts with reconstructed tracks from the tracking algorithms. Measurements in M2 to M5 are searched for in a momentum-dependent field of interest around the track extrapolation. As muons with a momentum smaller than 6 GeV/c are likely absorbed before they reach the last station, the number of required measurements depends on the momentum assigned to the track. The requirements are given in Table 4.1. If the given requirements are fulfilled, the binary flag, `ISMUON`, is assigned to the muon candidate.

---

[8] In Chapter 5.3 it is described how different data sets are combined.

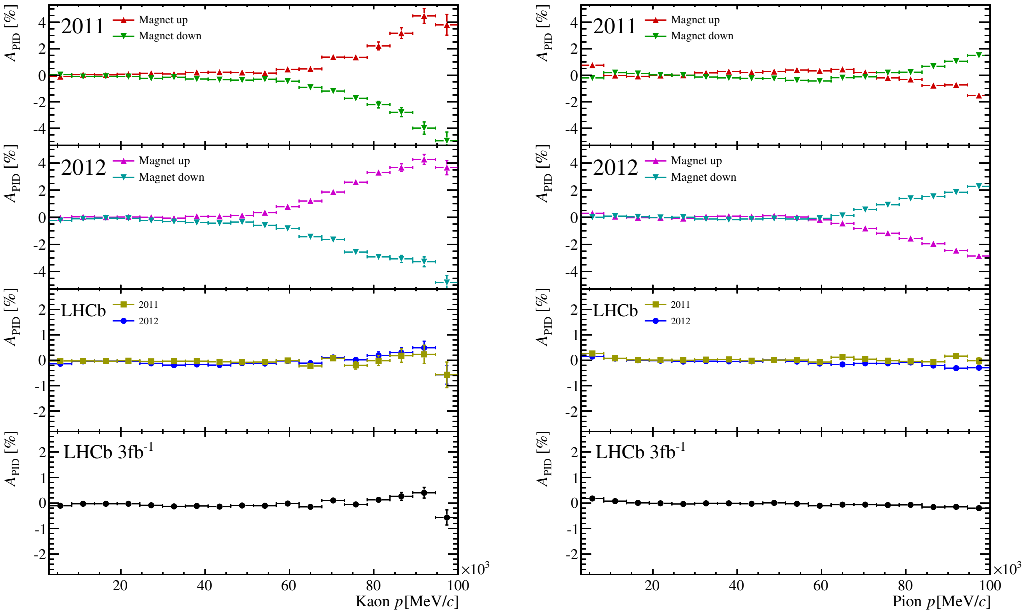

(a) Kaon candidates (b) Pion candidates

Figure 4.10: The asymmetry of the particle identification is shown for (a) kaon candidates with a requirement of $\mathrm{DLL}_{K\pi} > 7$ and (b) pion candidates with a requirement of $\mathrm{DLL}_{K\pi} < 0$ for each magnet polarity and each year of data taking. The plotted combined asymmetry of the magnet up and the magnet down samples are their arithmetic mean, see Chapter 5.3 for a description how different data sets are combined.

The muon identification efficiency and the misidentification probabilities are given in Table 4.2. Generally the efficiency is larger than 97 % for muons with a transverse momentum larger than 1 GeV/c. The misidentification probabilities of below 2 % are mainly due to decays in flight.

The muon identification algorithm provides a second discriminating variable which is based on the distance of the measurements in the muon stations and the track extrapolation. The sum of the squared distances should be small for a muon which traverses the muon stations, while it is large for random combinations of measurements. Similarly to the RICH identification algorithms, a likelihood for the muon hypothesis is calculated. This likelihood can be combined with the information from the RICH detectors and the calorimetry system to form a combined log-likelihood to discriminate

***p* range** [GeV/c]	**Muon stations**
$3 < p < 6$	M2 and M3
$6 < p < 10$	M2 and M3 and (M4 or M5)
$p > 10$	M2 and M3 and M4 and M5

Table 4.1: Muon stations required to trigger the `ISMUON` decision as a function of momentum range. Table taken from Ref. [64].

p_T **range** [GeV/c]	**Muon**	**Proton**	**Pion**	**Kaon**
$0.8 < p_\mathrm{T} < 1.7$	96.94 ± 0.07	0.737 ± 0.003	2.19 ± 0.01	1.93 ± 0.1
$1.7 < p_\mathrm{T} < 3.0$	98.53 ± 0.05	0.149 ± 0.004	0.61 ± 0.01	0.93 ± 0.01
$3.0 < p_\mathrm{T} < 5.0$	98.51 ± 0.06	0.12 ± 0.02	0.40 ± 0.01	0.72 ± 0.01
$p_\mathrm{T} > 5.0$	98.51 ± 0.07		0.33 ± 0.02	0.69 ± 0.01

Table 4.2: Average `ISMUON` efficiency (second column) and misidentification probabilities (third to fifth column) in different transverse momentum intervals (in per cent). Uncertainties are statistical.

muons from other particle species. This is especially helpful to reject muon candidates where a pion or kaon decays into a muon and neutrino before M2. In the case of muon–pion discrimination the variable is called $\mathrm{DLL}_{\mu\pi}$. The misidentification of muons as kaons or pions is further reduced when using this quantity in the selection of muon candidates. At a loss of in average 5 % real muons the misidentification rates of kaons and pions reduce in average to 0.65 % and 0.38 %, respectively, for muon candidates with a momentum larger than 3 GeV/c.

The off-line muon identification can introduce a detection asymmetry similar to the RICH particle identification or the `L0Muon` asymmetry. The combined detection asymmetry of `L0Muon` and muon identification has been measured in an independent study to be (0.04 ± 0.25) % after averaging the magnet up and magnet down data samples of 2011 [65]. It should be noted that the value depends on the kinematics of the studied decay channel.

4.6 Summary

The trigger and off-line event reconstruction has a high efficiency and precision. However, imperfections in the various detector components and material interactions lead to different reconstructions efficiencies of positively- and negatively-charged particles. These detection asymmetries are at the per-mille and per-cent level. Some detection asymmetries change sign when the polarity of the magnetic field is reversed. In the next chapter the method to extract small *CP* asymmetries is presented. The strength of this method is that detection asymmetries do not need to be measured individually. It is exploited that detection asymmetries are the same for decays of c and b hadrons with similar topology.

Chapter 5

Analysis strategy

In this chapter the strategy to measure *CP* asymmetries in muon-tagged $D^0 \to K^-K^+$ and $D^0 \to \pi^-\pi^+$ decays is discussed. The analysis includes the measurements of the difference of *CP* asymmetries and the individual *CP* asymmetries. The latter uses samples of Cabibbo-favoured D^0 and D^+ decays to correct for detection and production asymmetries.

5.1 Observed asymmetries in muon-tagged D^0 decays

The quantities of interest of this analysis are *CP* asymmetries in $D^0 \to K^-K^+$ and $D^0 \to \pi^-\pi^+$ decays, cf. Chapter 2.4. *CP* violation manifests itself in different decay rates of a D^0 meson to a final state, f, and a $\overline{D}^0$ meson decaying into the final state, $\overline{f}$. Both final states, $\pi^-\pi^+$ and K^-K^+, are *CP* eigenstates, thus $f = \overline{f}$. The time-integrated *CP* asymmetry of a D^0 meson decaying into a *CP* eigenstate, f, is defined as

$$A_{CP}(f) = \frac{\Gamma(D^0 \to f) - \Gamma(\overline{D}^0 \to f)}{\Gamma(D^0 \to f) + \Gamma(\overline{D}^0 \to f)} \quad , \tag{5.1}$$

where $\Gamma(D^0 \to f)$ and $\Gamma(\overline{D}^0 \to f)$ are the decay rates for D^0 and $\overline{D}^0$ mesons, respectively, in this case $f = \pi^-\pi^+$ or $f = K^-K^+$. Useful expressions of the branching fractions in terms of the *CP* asymmetries are

$$\begin{aligned} \Gamma(D^0 \to f) &= \frac{1}{2}\left(\Gamma(D^0 \to f) + \Gamma(\overline{D}^0 \to f)\right)\,(1 + A_{CP}(f)) \quad , \\ \Gamma(\overline{D}^0 \to f) &= \frac{1}{2}\left(\Gamma(D^0 \to f) + \Gamma(\overline{D}^0 \to f)\right)\,(1 - A_{CP}(f)) \quad . \end{aligned} \tag{5.2}$$

Both final states contain no information on the initial flavour of the D meson. The flavour can be determined by reconstructing the origin of the D meson. Here, the semileptonic B decays, $\overline{B} \to D^0\mu^-X$ and $B \to \overline{D}^0\mu^+X$, are used to tag the initial flavour. A negatively-charged muon tags the flavour as D^0 and a positively-charged muon as $\overline{D}^0$. The observed *raw asymmetry* for a D meson decay into a final state f is defined as

$$A_{\mathrm{raw}}(f) \equiv \frac{N(f,\mu^-) - N(f,\mu^+)}{N(f,\mu^-) + N(f,\mu^+)} \quad , \tag{5.3}$$

where $N(f,\mu^\pm)$ denotes the observed yield for a given decay and tag. The numbers of reconstructed $\overline{B} \to D^0\mu^-X$ and $B \to \overline{D}^0\mu^+X$ decays are affected by two additional asymmetries.

First, B and $\overline{B}$ mesons have different productions rates which leads to an effective production asymmetry of D mesons in semileptonic B decays, cf. Chapter 2.6.2. The production asymmetry is defined as

$$A_P(\overline{B}) \equiv \frac{\mathcal{P}(\overline{B}) - \mathcal{P}(B)}{\mathcal{P}(\overline{B}) + \mathcal{P}(B)} \quad , \tag{5.4}$$

where $\mathcal{P}(\overline{B})$ and $\mathcal{P}(B)$ are the probabilities to produce semileptonic $\overline{B}$ and B decays. This includes the semileptonic branching fraction as well as B^0 mixing and possible CP asymmetries in semileptonic B decays. It is referred to as B production asymmetry to keep a clear distinction to the production asymmetry of prompt D mesons. The production rates can be written as

$$\begin{aligned} \mathcal{P}(\overline{B}) &= \frac{1}{2}\left(\mathcal{P}(\overline{B}) + \mathcal{P}(B)\right)\left(1 + A_P(\overline{B})\right) \quad , \\ \mathcal{P}(B) &= \frac{1}{2}\left(\mathcal{P}(\overline{B}) + \mathcal{P}(B)\right)\left(1 - A_P(\overline{B})\right) \quad . \end{aligned} \tag{5.5}$$

Second, negative and positive muons have different detection efficiencies, see Chapter 4. The muon detection asymmetry is defined as

$$A_D(\mu^-) \equiv \frac{\varepsilon(\mu^-) - \varepsilon(\mu^+)}{\varepsilon(\mu^+) + \varepsilon(\mu^-)} \quad , \tag{5.6}$$

where $\varepsilon(\mu^+)$ and $\varepsilon(\mu^-)$ are the efficiencies to detect a positive or negative muon, which can be expressed as

$$\varepsilon(\mu^\mp) = \frac{1}{2}(\varepsilon(\mu^+) + \varepsilon(\mu^-))\ (1 \pm A_D(\mu^-)) \quad . \tag{5.7}$$

The efficiency includes effects from the detection, the trigger reconstruction and the off-line track finding.

Summarising, the observed yields, $N(f, \mu^\pm)$, can be expressed in terms of branching fractions, production rates and detection efficiencies:

$$\begin{aligned} N(f, \mu^-) &= \alpha\ \Gamma(D^0 \to f)\ \mathcal{P}(\overline{B})\ \varepsilon(\mu^-) \quad , \\ N(f, \mu^+) &= \alpha\ \Gamma(\overline{D}^0 \to f)\ \mathcal{P}(B)\ \varepsilon(\mu^+) \quad , \end{aligned} \tag{5.8}$$

where α contains everything which is common to both decays, e.g., the reconstruction efficiencies of $\pi^-\pi^+$ or K^-K^+ pairs or the efficiency to form a vertex out of muon and D candidates. As this proportionality cancels, it is not important for the discussion concerning asymmetries. Inserting Equations 5.2, 5.5 and 5.7 into Equation 5.8 yields

$$\begin{aligned} & N(f, \mu^-) \propto (1 + A_{CP}(f))\ (1 + A_P(\overline{B}))\ (1 + A_D(\mu^-)) \\ & \quad = 1 + A_{CP}(f) + A_P(\overline{B}) + A_D(\mu^-) + A_P(\overline{B})A_{CP}(f) + A_P(\overline{B})A_D(\mu^-) + A_{CP}(f)A_D(\mu^-) + A_P(\overline{B})A_{CP}(f)A_D(\mu^-)\ , \\ & N(f, \mu^+) \propto (1 - A_{CP}(f))\ (1 - A_P(\overline{B}))\ (1 - A_D(\mu^-)) \\ & \quad = 1 - A_{CP}(f) - A_P(\overline{B}) - A_D(\mu^-) + A_P(\overline{B})A_{CP}(f) + A_P(\overline{B})A_D(\mu^-) + A_{CP}(f)A_D(\mu^-) - A_P(\overline{B})A_{CP}(f)A_D(\mu^-)\ , \end{aligned} \tag{5.9}$$

The raw asymmetry from Equation 5.3 is then given by

$$A_{\text{raw}}(f) = \frac{A_{CP}(f) + A_P(\overline{B}) + A_D(\mu^-) + A_{CP}(f)A_P(\overline{B})A_D(\mu^-)}{1 + A_P(\overline{B})\,A_{CP}(f) + A_P(\overline{B})\,A_D(\mu^-) + A_{CP}(f)\,A_D(\mu^-)} \quad . \tag{5.10}$$

The numerator contains the odd combinations of the individual asymmetries, whereas the denominator contains the even combinations. All *CP*, production and detection asymmetries do not exceed the per cent level, as it is explained in Chapters 2 and 4. Therefore, neglecting third-order terms in the asymmetries, the raw asymmetry can be written as

$$A_{\text{raw}}(f) = A_{CP}(f) + A_P(\overline{B}) + A_D(\mu^-) \quad . \tag{5.11}$$

Corrections are of the order $\mathcal{O}(10^{-6})$. This is an important result as it means that the individual components of the raw asymmetry are independent of each other.

5.2 Determination of *CP* asymmetries

The method to extract ΔA_{CP}, $A_{CP}(K^-K^+)$ and $A_{CP}(\pi^-\pi^+)$ is presented. The strategy is based on the assumption derived in the previous section that a raw asymmetry can be written as the sum of its components if all contributing asymmetries are small.

5.2.1 Determination of ΔA_{CP}

The previous discussion shows that the observed asymmetry contains not only *CP* asymmetries but also spurious asymmetries induced by production and detection effects. The raw asymmetries of muon-tagged $D^0 \to K^-K^+$ and $D^0 \to \pi^-\pi^+$ decays are given by

$$A_{\text{raw}}(K^-K^+) = A_{CP}(K^-K^+) + A_P(\overline{B}) + A_D(\mu^-) \tag{5.12}$$

and

$$A_{\text{raw}}(\pi^-\pi^+) = A_{CP}(\pi^-\pi^+) + A_P(\overline{B}) + A_D(\mu^-) \quad , \tag{5.13}$$

respectively. Therefore, an experimentally very robust observable is the difference of the two raw asymmetries

$$\Delta A_{CP} = A_{\text{raw}}(K^-K^+) - A_{\text{raw}}(\pi^-\pi^+) = A_{CP}(K^-K^+) - A_{CP}(\pi^-\pi^+) \quad , \tag{5.14}$$

where production and detection asymmetries cancel. The strength of the method is that the individual components of the raw asymmetry do not need to be known. This makes ΔA_{CP} very robust and sensitive to *CP* asymmetries.

It is shown, among others, in Chapter 2.6 and 4 that detection and production asymmetries depend on the kinematic distributions of the involved particles. The kinematic distributions of both reconstructed decays have to be equal such that no residual effects of the spurious asymmetries remain in ΔA_{CP}. The procedure to equalise the slightly different momentum distributions of muon-tagged $D^0 \to K^-K^+$ and $D^0 \to \pi^-\pi^+$ decays is an essential part of the analysis and is discussed in detail in Chapter 8.

Both $A_{CP}(K^-K^+)$ and $A_{CP}(\pi^-\pi^+)$ contain effects from direct and indirect *CP* violation through D^0 mixing, see Equation 2.29. Indirect *CP* violation is expected to be negligible at the current level of experimental precision [19] and measured to be consistent with zero [23]. Furthermore, it is considered to be largely independent of the final state. Hence, indirect *CP* violation cancels to first order in the difference and ΔA_{CP} is predominantly sensitive to direct *CP* violation.[1]

5.2.2 Determination of $A_D(K^-\pi^+)$, $A_{CP}(K^-K^+)$ and $A_{CP}(\pi^-\pi^+)$

The sum of muon detection and B production asymmetry can be determined by using the Cabibbo-favoured $D^0 \to K^-\pi^+$ mode. *CP* violation in this decay can be neglected at the level of the experimental precision as it is very much suppressed compared to the *CP* asymmetry in the decays $D^0 \to K^-K^+$ and $D^0 \to \pi^-\pi^+$. The final state $K^-\pi^+$, however, is not a *CP* eigenstate. The detection asymmetry in this final state has its origin in the different material interaction rates of positively and negatively charged kaons, cf. Chapter 2.5. Additionally, kaons and pions do not have the same momentum distributions. Therefore, the final states, $K^-\pi^+$ or $K^+\pi^-$, are also sensitive to selection- or detection-induced asymmetries. The $K^-\pi^+$ detection asymmetry, $A_D(K^-\pi^+)$, is defined as

$$A_D(K^-\pi^+) \equiv \frac{\varepsilon(K^-\pi^+) - \varepsilon(K^+\pi^-)}{\varepsilon(K^-\pi^+) + \varepsilon(K^+\pi^-)} \quad , \tag{5.15}$$

where $\varepsilon(K^-\pi^+)$ and $\varepsilon(K^+\pi^-)$ are the efficiencies to detect and reconstruct a $K^-\pi^+$ and $K^+\pi^-$ pair. The largest part of the asymmetry is expected to come from the kaon detection asymmetry, cf. Chapter 2.5.2.

The previous discussion about raw asymmetries in $D^0 \to K^-K^+$ and $D^0 \to \pi^-\pi^+$ decays is equally valid for decay channels where the D final state itself has a small detection asymmetry at the per-cent level. The expression of the raw asymmetry of muon-tagged $D^0 \to K^-\pi^+$ decays, $A_{\text{raw}}(K^-\pi^+)$, is obtained when replacing $A_{CP}(f)$ in Equation 5.10 with $A_D(K^-\pi^+)$. Neglecting third-order terms in the asymmetries, the raw asymmetry of the $D^0 \to K^-\pi^+$ mode is

$$A_{\text{raw}}(K^-\pi^+) = A_D(\mu^-) + A_P(\overline{B}) + A_D(K^-\pi^+) \quad . \tag{5.16}$$

Hence, by determining $A_{\text{raw}}(K^-\pi^+)$ one gets a handle on $A_D(\mu^-) + A_P(\overline{B})$ in muon-tagged $D^0 \to K^-K^+$ and $D^0 \to \pi^-\pi^+$ decays if $A_D(K^-\pi^+)$ is known. The measurement of $A_D(K^-\pi^+)$ is described in the following.

Determination of $A_D(K^-\pi^+)$

The detection asymmetry $A_D(K^-\pi^+)$ can be determined with two calibration modes: $D^+ \to K^-\pi^+\pi^+$ and $D^+ \to \overline{K}^0\pi^+$. Charm mesons are directly produced at large rates in proton–proton collisions at the LHC. Directly produced charm mesons are referred to as *prompt* D mesons. The $c\bar{c}$ cross section is about a factor 20 higher than the $b\bar{b}$ cross section, cf. Chapter 2.6.1 and both decay channels are Cabibbo-favoured due to the common $c \to su\bar{d}$ transition. Consequently, large data samples are available.

---

[1] If the decay-time acceptance of reconstructed $D^0 \to K^-K^+$ and $D^0 \to \pi^-\pi^+$ decays is different, the time-integrated measurement of ΔA_{CP} can be sensitive to indirect *CP* violation. The effect has been studied in Refs. [2,3] and is found to be negligibly small for muon-tagged D^0 decays.

The flavour tag is unambiguous because of the charged initial and final states. The raw asymmetry of prompt D^+ decays is defined as

$$A_{\text{raw}}(f) \equiv \frac{N(D^+ \to f) - N(D^- \to \overline{f})}{N(D^+ \to f) + N(D^- \to \overline{f})} \quad , \tag{5.17}$$

where f can be $K^-\pi^+\pi^+$ or $\overline{K}^0\pi^+$ and $\overline{f}$ is the corresponding *CP*-conjugate state. This convention is chosen such that the $K^-\pi^+$ pair has the same signs in $D^0 \to K^-\pi^+$ and $D^+ \to K^-\pi^+\pi^+$ decays.

The detection asymmetry of charged pions is defined as

$$A_D(\pi^+) \equiv \frac{\varepsilon(\pi^+) - \varepsilon(\pi^-)}{\varepsilon(\pi^+) + \varepsilon(\pi^-)} \quad , \tag{5.18}$$

where $\varepsilon(\pi^\pm)$ is the detection and reconstruction efficiency of $\pi^\pm$ mesons. Pions do not have a significant material interaction asymmetry, cf. Chapter 2.5.2. Any non-vanishing $A_D(\pi^+)$ is dominated by an asymmetry in the track reconstruction. Using the definition of $A_P(D^+)$, see Equation 2.45, and that the reconstruction efficiency of $D^\pm$ mesons is proportional to the product $\varepsilon(K^\mp\pi^\pm)\varepsilon(\pi^\pm)$, the raw asymmetry of $D^+ \to K^-\pi^+\pi^+$ decays can be expressed as

$$A_{\text{raw}}(K^-\pi^+\pi^+) = A_P(D^+) + A_D(K^-\pi^+) + A_D(\pi^+) \quad , \tag{5.19}$$

where terms of third order in the asymmetries are neglected.

Similarly, the raw asymmetry of $D^+ \to \overline{K}^0\pi^+$ decays is written as

$$A_{\text{raw}}(\overline{K}^0\pi^+) = A_P(D^+) + A_D(\pi^+) + A_D(\overline{K}^0) \quad , \tag{5.20}$$

where $A_D(\overline{K}^0)$ is the neutral kaon asymmetry. The convention here is that K^- and $\overline{K}^0$ states contain an s quark. Therefore, $A_D(\overline{K}^0)$ is defined as

$$A_D(\overline{K}^0) \equiv \frac{\varepsilon(\overline{K}^0) - \varepsilon(K^0)}{\varepsilon(\overline{K}^0) + \varepsilon(K^0)} \quad . \tag{5.21}$$

K^0 and $\overline{K}^0$ mesons are reconstructed in the *CP* eigenstate $\pi^+\pi^-$. Henceforth, the detection efficiencies $\varepsilon(K^0)$ and $\varepsilon(\overline{K}^0)$ include effects from *CP* violation in the decay $K^0 \to \pi^+\pi^-$ and from different interaction rates of K^0 and $\overline{K}^0$ in the detector material. Compared to the charged kaon detection asymmetry, it is a small but still non-negligible correction. The neutral kaon asymmetry is discussed and determined later in Chapter 9.

Using Equations 5.19 and 5.20 , $A_D(K^-\pi^+)$ can be obtained as

$$A_D(K^-\pi^+) = A_{\text{raw}}(K^-\pi^+\pi^+) - A_{\text{raw}}(\overline{K}^0\pi^+) + A_D(\overline{K}^0) \quad . \tag{5.22}$$

It should be stressed that the presented method assumes that direct *CP* violation can be neglected in Cabibbo-favoured D^+ decay modes.

Determination of $A_{CP}(K^-K^+)$

The *CP* asymmetry in singly Cabibbo-suppressed $D^0 \to K^-K^+$ decays where the flavour is determined by reconstructing semileptonic B decays is then determined by combining Equations 5.12 and 5.16

$$A_{CP}(K^-K^+) = A_{\text{raw}}(K^-K^+) - A_{\text{raw}}(K^-\pi^+) + A_D(K^-\pi^+) \ , \tag{5.23}$$

where $A_D(K^-\pi^+)$ is obtained from Equation 5.22. The measurements of $A_{CP}(K^-K^+)$ and ΔA_{CP} are correlated as both use the same muon-tagged $D^0 \to K^-K^+$ events. Equation 5.23 is only valid in the case that production and detection asymmetries cancel. The cancellation, however, depends on the agreement of the kinematic distributions. Without going into detail, the agreement of the kinematic distributions is not as good as in the ΔA_{CP} determination as kinematically very different decay channels are used. First of all, the kinematics of prompt produced D^+ mesons and their decay products are compared with secondary D^0 mesons and their decay products. Furthermore, the kinematic distributions of two-body decays are compared with those of three-body decays. The implications are discussed in Chapter 8.

Determination of $A_{CP}(\pi^-\pi^+)$

The measurements of $A_{CP}(K^-K^+)$ and ΔA_{CP} determine the *CP* asymmetry in the $D^0 \to \pi^-\pi^+$ decay mode:

$$A_{CP}(\pi^-\pi^+) = A_{CP}(K^-K^+) - \Delta A_{CP} \ . \tag{5.24}$$

The individual asymmetry $A_{CP}(K^-K^+)$ is determined as the $D^0 \to K^-K^+$ decay channel has a higher signal yield than the $D^0 \to \pi^-\pi^+$ decay mode.

5.2.3 Wrong flavour tags

The previous discussion omitted another correction for the sake of convenience. The flavour tag, given by the muon charge, may be wrong if a non-genuine semileptonic B decay is selected. Possible sources are prompt D^0 mesons or muons from the other b hadron in the event. The probability that such an event occurs is given by the *mistag probability*, ω, which dilutes the measured *CP* asymmetries. A detailed discussion follows later in Chapter 10. A mistag probability around 1 % is found and the formula to determine ΔA_{CP}, including a small mistag probability, is modified as

$$\Delta A_{CP} = (1 + 2\omega) \left[A_{\text{raw}}(K^-K^+) - A_{\text{raw}}(\pi^-\pi^+)\right] \ . \tag{5.25}$$

Also in the $D^0 \to K^-\pi^+$ decay mode the flavour tag is exclusively given by the muon; thus, doubly Cabibbo-suppressed $D^0 \to K^+\pi^-$ decays are included in the selection, as well as the Cabibbo-favoured $D^0 \to K^-\pi^+$ decays, cf. Chapter 2.2.3. The reasons for the inclusion are discussed later in Chapter 10. Similarly to the mistag probability, the kaon detection asymmetry is damped by the wrong-sign decays. The formula to determine $A_{CP}(K^-K^+)$ is modified as

$$A_{CP}(K^-K^+) = (1{+}2\omega) \left[A_{\text{raw}}(K^-K^+) - A_{\text{raw}}(K^-\pi^+)\right] {+} (1{-}2R)\, A_D(K^-\pi^+) \, , \tag{5.26}$$

where R is the ratio of branching fractions of wrong-sign $D^0 \to K^-\pi^+$ over right-sign $D^0 \to K^+\pi^-$ decays.

5.3 Combining different data sets

The data set used can be divided into four disjoint samples according to the magnet polarity, *up* and *down*, and the year of data taking, *2011* and *2012*. Detection asymmetries are treated as different in each data set as the state of the LHCb detector changes. The production asymmetry is expected to be slightly different in 2011 and 2012 due to the changed centre-of-mass energy.

The LHCb dipole magnet is breaking the left-right symmetry of the detector for charged particles. Depending on the polarity, particles of one charge are more often bent into one half of the detector as the other. Detection asymmetries originating from a left-right asymmetric detector change sign when reversing the magnet polarity:

$$A_D^{\uparrow} = -A_D^{\downarrow} \ . \tag{5.27}$$

The methods described in this chapter are designed to work for each polarity individually as detection asymmetries cancel in the difference of raw asymmetries. This assumption of cancellation is tested by performing all measurements independently for the two polarities. This is important as magnet up and down data are not taken at the same time. Thus, there might be small variations as detection asymmetries can change over time. Nevertheless, the arithmetic mean of the two magnet polarities is taken as an additional precaution against unaccounted asymmetries:

$$A_{\text{raw}}(\text{year}) = \frac{A_{\text{raw}}^{\uparrow}(\text{year}) + A_{\text{raw}}^{\downarrow}(\text{year})}{2} \ , \tag{5.28}$$

where charge dependent left-right asymmetries (mostly) cancel independently of the size of the magnet up and down data samples. This is at the expense of sensitivity as the statistical uncertainty is then given by the smaller data sample. The loss is small as in 2011 the split is about 40 % magnet up data and 60% magnet down data. In 2012 nearly equal amounts of data were taken with each polarity.

Likewise, the analysis is performed independently for the two data taking periods, 2011 and 2012. The centre-of-mass energy of the *pp* collisions was increased from 7 TeV to 8 TeV and detectors were repaired or moved. Hence, production and detection asymmetries changed. The final result is the weighted average of the two measurements obtained in the 2011 and 2012 data samples:

$$A_{\text{raw}} = \frac{1}{\frac{1}{\sigma_{2011}^2} + \frac{1}{\sigma_{2012}^2}} \left(\frac{1}{\sigma_{2011}^2} A_{\text{raw}}(2011) + \frac{1}{\sigma_{2012}^2} A_{\text{raw}}(2012) \right) \ , \tag{5.29}$$

where σ_{2011} and σ_{2012} are the statistical uncertainties of the 2011 and 2012 measurements.

The measurements of ΔA_{CP} and $A_{CP}(K^-K^+)$ are determined from the final combinations of the raw asymmetries. The *CP* asymmetry measurements are also performed individually for each of the four samples to test their stability in different data taking periods. Additionally, results are quoted separately for the magnet up and magnet down samples, averaged over both data taking periods.

5.4 Structure of the following chapters

The remaining part of this thesis is structured as follows:

- In Chapter 6 the trigger and off-line selection of the various channels is described.
- In Chapter 7 the procedure to extract raw asymmetries from data is introduced. The raw asymmetries of all channels are measured to give the scale of the asymmetries and their dependence on various kinematic variables.
- In Chapter 8 it is explained how kinematic distributions are adjusted such that the cancellations of spurious asymmetries work in the differences.
- In Chapter 9 the neutral kaon detection asymmetry is discussed and determined.
- In Chapter 10 the measurement of the mistag probability is performed.
- In Chapter 11 all components of the measurements are combined to present the results of the *CP* asymmetries.
- In Chapter 12 the stability of the presented method is tested extensively on data.
- In Chapter 13 systematic uncertainties are evaluated.
- In Chapter 14 the results are summarised.

The last section of each chapter summarises its important results.

Chapter 6

Trigger and off-line selection

The trigger and off-line selection is based on the output of the event reconstruction discussed in Chapter 4. Particle candidates formed out of tracks and particle identification information are combined to reconstruct decays of c and b hadrons. This chapter discusses the trigger and off-line selections of muon-tagged $D^0 \to K^-K^+$, $D^0 \to \pi^-\pi^+$ and $D^0 \to K^-\pi^+$ decays originating from semileptonic B decays and the selections of prompt $D^+ \to K^-\pi^+\pi^+$ and $D^+ \to \overline{K}^0\pi^+$ decays. Even the samples of the singly Cabibbo-suppressed D^0 decays have signal yields of several hundred thousands as semileptonic B decays have a branching fraction of 10 %. The signal yields of the Cabibbo-favoured D^0 and D^+ decays considered in the analysis are several millions, especially for the prompt $D^+ \to K^-\pi^+\pi^+$ decay mode. As shown in previous chapters, the selection and reconstruction of events leads to detection asymmetries of positively- and negatively-charged particles. Therefore, the focus of the selections is to be clearly defined, particularly in the trigger, such that detection asymmetries are controllable.

First, the general topology of of semileptonic B and prompt D^+ decays is introduced. Second, the selections applied in the trigger are discussed in detail. Third, the off-line selection of all decay modes is explained. Fourth, the signal yields of all decay channels, after trigger and off-line selection, are given in the last section of this chapter.

6.1 Topologies of semileptonic B and prompt D^+ decays

The distinct signatures of B and D decays are exploited to select events at the trigger stage and in the off-line event reconstruction. Therefore, the topologies of all decay channels used in the analysis are shortly introduced.

Semileptonic B decays

The reconstructed particles of a semileptonic B decay and their topology are depicted in Figure 6.1. The lifetime of B and D^0 meson is large enough that they fly several millimetre, if they are produced in the acceptance of the LHCb detector. The lifetime of a D^0 meson is about three times shorter than the lifetime of B^0 and B^+ mesons.

The two-body $D^0 \to K^-\pi^+$, $D^0 \to K^-K^+$ and $D^0 \to \pi^-\pi^+$ decay channels are used in the measurement. The $D^0 \to K^-\pi^+$ decay channel includes the Cabibbo-favoured $D^0 \to K^-\pi^+$ mode and the doubly Cabibbo-suppressed $D^0 \to K^+\pi^-$ mode. The flavour of the D^0 meson is determined by the charge of the muon which originates from the B decay vertex. The neutrino and other charged or neutral particles are not used

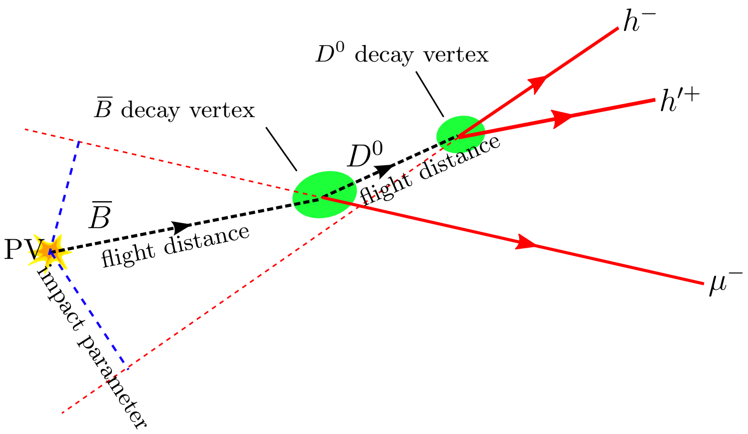

Figure 6.1: The reconstructed particles and vertices of a semileptonic $\overline{B}$ decay followed by a two-body D^0 decay. The sketch indicates the following selection variables: The flight distances of $\overline{B}$ and D^0 candidates, the so-called impact parameter of one of the decay products and the primary vertex position. Note: At least the neutrino is not reconstructed.

in the selection of the decays. Therefore, the invariant mass of the B meson is not fully reconstructed and the reconstructed B momentum does not point directly to the primary vertex due to the missing momentum.

The main handles on the authenticity of the reconstructed decays are large impact parameters of the reconstructed tracks, see Figure 6.1 for the definition of the impact parameter, two displaced secondary vertices with a good quality and a track which is associated to a muon candidate in the muon stations. The types of hadrons, kaon or pion, are identified with the particle identification systems of the LHCb detector. Furthermore, the final state particles have in general a harder transverse momentum spectrum than the light quark background from the primary interaction.

If not explicitly stated otherwise, it is implied that $D^0 \to K^-\pi^+$, $D^0 \to K^-K^+$ and $D^0 \to \pi^-\pi^+$ decays originate from semileptonic B decays. They are referred to as *muon-tagged* D^0 *decays*.

Prompt D^+ decays

The two decay channels $D^+ \to K^-\pi^+\pi^+$ and $D^+ \to \overline{K}^0\pi^+$ are used to measure the detection asymmetry $A_D(K^-\pi^+)$. In both cases D^+ mesons originating from the primary interaction are selected. The $D^+ \to K^-\pi^+\pi^+$ branching fraction, $(9.13 \pm 0.19)\%$, is about six times higher than the $D^+ \to \overline{K}^0\pi^+$ branching fraction, $(1.47 \pm 0.07\,\%)$ [16]. Additionally, the reconstruction efficiency of $D^+ \to \overline{K}^0\pi^+$ is much lower as explained in the following.

The topologies of both decays are shown in Figure 6.2. The lifetime of D^+ mesons is shorter than that of B mesons. Therefore, the final state particles are less displaced than those originating from B decays. Furthermore, the final states are purely hadronic which is harder to separate from the light hadron background than a muon in the final state. Nevertheless, the production rate of prompt D mesons is so large, cf. Chapter 2.6.1, that tight selection cuts on the transverse momenta and the impact parameters of

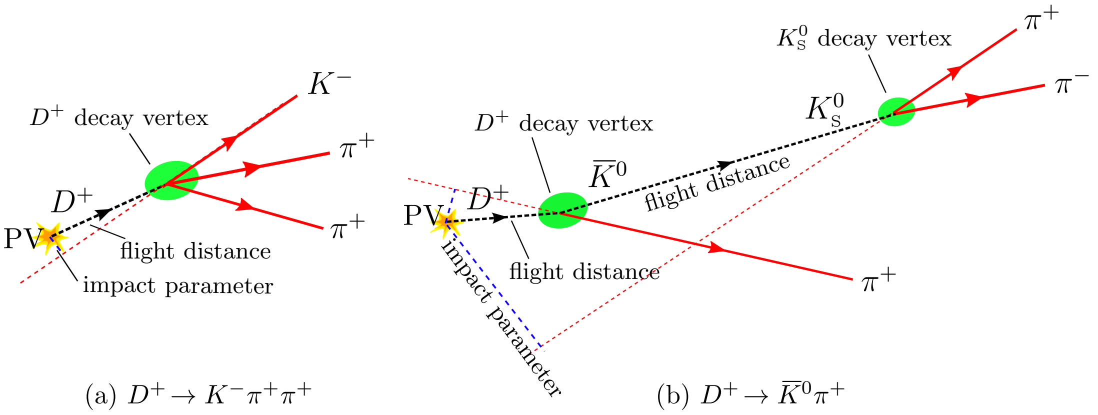

(a) $D^+ \to K^-\pi^+\pi^+$ (b) $D^+ \to \overline{K}{}^0\pi^+$

Figure 6.2: The reconstructed particles of prompt (a) $D^+ \to K^-\pi^+\pi^+$ and (b) $D^+ \to \overline{K}{}^0\pi^+$ decays. The sketch indicates the following selection variables: The flight distances of D^+ and K^0_S candidates, the impact parameters of decay products and the primary vertex positions. The $\overline{K}{}^0$ state is produced in the decay $D^+ \to \overline{K}{}^0\pi^+$, the reconstructed final state is the K^0_S state.

the decay products can be applied to suppress light hadrons from the primary vertex. Combinatorial background can be further reduced by requiring that the D^+ candidate is pointing to the primary vertex and that it has a significant flight distance and decay time.

In the decay $D^+ \to \overline{K}{}^0\pi^+$ the flavour of the neutral kaon is fixed at creation to K^0. Then, the state evolves as a superposition of the K^0_S and K^0_L states. In this analysis, only the decay to the *CP* eigenstate $\pi^+\pi^-$ is reconstructed which is an almost pure K^0_S state. Therefore, in the selection of the decay it also referred to as a K^0_S meson. The K^0_S meson's lifetime is rather long; hence, only a quarter of the K^0_S mesons of $D^+ \to \overline{K}{}^0\pi^+$ decays in the LHCb acceptance occur inside the VELO. In this case the pions are reconstructed as long tracks[1]. If required, this type of events is labelled as *long-reconstructed* or short *LL*. Half of the K^0_S mesons decay between VELO and TT and are reconstructed with two downstream tracks, labelled as *downstream-reconstructed* or short *DD*. K^0_S decays behind the TT are not reconstructed. The lifetime of K^0_L mesons is about a factor of 50 larger than the K^0_S lifetime. They rarely decay inside the LHCb detector.

As explained, many reconstructed K^0 and $\overline{K}{}^0$ mesons traverse large amounts of detector material, the downstream-reconstructed candidates more than the long-reconstructed candidates. Analogously to charged kaons, K^0 and $\overline{K}{}^0$ mesons have different material interaction rates. Additionally, the decay into the final state $\pi^+\pi^-$ is *CP*-violating and both effects interfere as it is explained later in Chapter 9. In order to properly describe the measured asymmetry, all effects have to be taken into account. The effect on downstream-reconstructed K^0_S mesons is large enough that they are not considered in the *CP* asymmetry measurement. However, they are essential to be able to extract a systematic uncertainty on the neutral kaon asymmetry $A_D(\overline{K}{}^0)$.

If not explicitly stated otherwise, it is implied that $D^+ \to K^-\pi^+\pi^+$ and $D^+ \to \overline{K}{}^0\pi^+$ decays originate from the primary interaction and are referred to as *prompt D^+ decays*.

---

[1] The different types of tracks are defined in Chapter 4.3.

6.2 Trigger selection

The task of the trigger system is to rapidly select “interesting” events during data taking as detector readout and off-line resources are limited. The LHCb trigger system is divided into two stages. The first stage is a system implemented in hardware. It is described in Chapter 4.1. The second stage is implemented in software and runs on a large computer farm. The trigger algorithms and selections relevant for this analysis are explained in the following.

6.2.1 First level trigger (L0)

The hardware trigger L0 selects events at a rate of about 1 MHz. Two independent systems are used to select heavy quark events, the L0-calorimeter trigger and the L0-muon trigger. Both systems are described in Chapter 4.1. The L0-calorimeter trigger effectively selects hadronic final states of prompt D^+ decay modes. The trigger selection of semileptonic B decays uses the `L0Muon` decision as input.

6.2.2 High Level Trigger (HLT)

Events selected by L0 are transferred to a large computer farm where the software stage, the High Level Trigger (HLT), is executed. The HLT reduces the L0 rate of about 1 MHz in two stages. The first stage (HLT1) performs a partial event reconstruction to reduce the rate to $40-80$ kHz. The second stage (HLT2) uses almost fully reconstructed events to decide which events are written to storage and, hence, are available for physics analyses. The HLT uses reconstruction algorithms close to the off-line reconstruction but simplified in some places to meet the timing requirements. The HLT2 output rate was about 3 kHz in 2011 and about 5 kHz in 2012.

A sequence of reconstruction and selection algorithms to trigger an event is called *trigger line*. As the HLT is fully implemented in software, it is very adaptable to changing running conditions. The principles of the trigger lines to select signal and calibration channels have not significantly changed during 2011 and 2012. They are explained in the following.

HLT1

The first stage of the software trigger exploits that decay products of c and b hadrons have a larger transverse momentum than light quark background and are displaced from the primary interaction. Therefore, the first stage searches for one charged particle meeting these criteria.

The first step in HLT1 is to reconstruct tracks in the VELO to measure the position of the primary vertex (PV) and to determine the impact parameter (IP) of all tracks. VELO tracks with an impact parameter to any PV larger than 0.1 mm are processed further. To identify signal candidates, the VELO track is extended with hits in the tracking stations behind the magnet. Two different routes are possible.

The so-called `Hlt1TrackAllL0` line runs independently of the type of L0 decision. Corresponding hits in the T-stations are searched for in a small window around a straight line extrapolation by the forward tracking. The requirement $p_{\mathrm{T}} \gtrsim 1.6\,\mathrm{GeV}/c$ implies a

Table 6.1: Settings of the HLT1 track trigger lines. If thresholds changed, they are given as 2011/first half 2012/second half 2012. The definition of $\chi^2_{\text{track}}/\text{ndf}$ changed between 2011 and 2012. The requirement $\chi^2_{\text{track}}/\text{ndf} < 2.0$ in 2012 is looser than $\chi^2_{\text{track}}/\text{ndf} < 2.0$ in 2011. If between hits in two different VELO layers one layer is omitted, it is counted as a missed hit.

	`Hlt1TrackAllL0`	`Hlt1TrackMuon`
IP	$> 0.1\,\text{mm}$	$> 0.1\,\text{mm}$
$\chi^2(\text{IP})$	> 16	> 16
p	$> 10/10/3\,\text{GeV}/c$	$> 8/8/3\,\text{GeV}/c$
p_{T}	$> 1.7/1.7/1.6\,\text{GeV}/c$	$> 1.0\,\text{GeV}/c$
$\chi^2_{\text{track}}/\text{ndf}$	$< 2.0/1.5/2.0$	$< 2.0/2.5/2.5$
# VELO hits	> 9	> 6
# Missed VELO hits	< 3	-
#OT+#IT×2 hits	> 16	> 12
TT confirmation	no/no/yes	no/no/no
Muon confirmation	no	no

search window size of maximally 50 cm. Afterwards a Kalman filter [56] is applied to determine the $\chi^2_{\text{track}}/\text{ndf}$ and the covariance matrix of each track. This allows for a cut on the significance of the impact parameter ($\chi^2(\text{IP}) > 16$) to further suppress prompt particles. Ghost tracks are rejected by requirements on the track quality, like $\chi^2_{\text{track}}/\text{ndf}$ or numbers of observed hits in each tracking detector. In order to further reduce ghost tracks at an early stage, VELO tracks are required to be additionally confirmed by TT hits. The latter requirement had not been introduced before the middle of 2012.

The so-called `Hlt1TrackMuon` line is executed exclusively if the event is triggered by the L0-muon trigger. First, muon candidates are identified by matching VELO tracks to hits in the muon stations [66]. Second, selected VELO tracks are extended to long tracks. As the rate of muons is considerably lower than those of hadrons, looser requirements on p_{T} and track quality are possible. The requirement on the significance of the impact parameter is the same. The cuts are summarised in Table 6.1.

This analysis is restricted to semileptonic B decays triggered by `Hlt1TrackMuon` and `Hlt1TrackAllL0`, while the prompt D^+ decay modes are solely selected by `Hlt1TrackAllL0`.

HLT2

The second stage of the software trigger, HLT2, performs an event reconstruction similar to the off-line reconstruction at a rate of $40 - 80\,\text{kHz}$. The forward tracking is run for all VELO tracks with wider search windows. The momentum requirements are $p \gtrsim 5\,\text{GeV}/c$ and $p_{\text{T}} \gtrsim 0.5\,\text{GeV}/c$ in 2011 and $p \gtrsim 3\,\text{GeV}/c$ and $p_{\text{T}} \gtrsim 0.3\,\text{GeV}/c$ in 2012. For comparison, the off-line reconstruction searches for all particles in an event with a p_{T} larger than $50\,\text{MeV}/c$. Particles with a momentum below $2\,\text{GeV}/c$ are bent out of the detector acceptance.

Due to a larger computer farm and improvements in the trigger software, more processing time was available in 2012. The additional computing time was used to run a

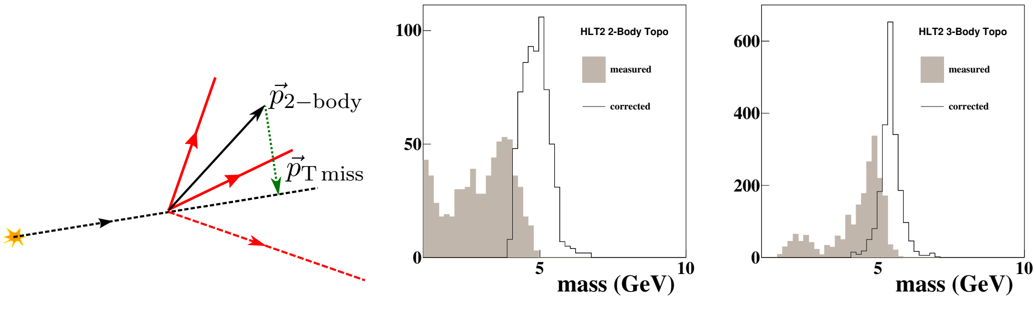

(a) (b) 2-body m_{corr} (c) 3-body m_{corr}

Figure 6.3: (a) The definition of $p_{\mathrm{T\,miss}}$. The dashed black line is the direction of flight of the B meson. The black momentum vector is the momentum of the 2-body combination. The dashed red line belongs to a not-reconstructed particle. The distribution of m_{corr} for (b) 2-body and (b) 3-body combinations of a genuine 4-body B decay. Figure from Ref. [67].

tracking algorithm (on unused hits) which starts searching for tracks in the T-Stations. The T-tracks can be combined with VELO tracks to increase the long track efficiency by 1–2 %. Additionally, this allowed to run the downstream tracking to reconstruct tracks without hits in the VELO. This is important to trigger on decays involving K^0_{S} mesons. The muon identification is performed on all tracks with the same algorithm as used in the off-line reconstruction, cf. Chapter 4.5.

The reconstructed tracks are used as input for 100–200 trigger lines in HLT2 to select events for physics analyses. Two approaches are used: *Inclusive lines* search for a variety of partially reconstructed b-hadron decays and *exclusive lines* fully reconstruct mainly prompt c-hadron production.

The so-called *topological* trigger lines are based on n-body combinations of 2,3, or 4 tracks to partially reconstruct b-hadron decays. They exploit the topology of B decays, previously shown in Figure 6.1. The principle is the following: First, a set of reconstructed tracks is selected by cuts on the track quality and the impact parameter to reject prompt particles. Second, two tracks are combined to a 2-body object by requiring that their distance of closest approach (DOCA) is less than 0.2 mm. Subsequently, up to two additional tracks are added with the same DOCA requirement to form 3- and 4-body objects. The D mesons of $B \to D\mu X$ decays have a finite lifetime and, therefore, not all decay products of b hadrons originate from a common vertex. Although the DOCA requirement is chosen loose, the tracks of decay products might be rejected by this requirement. Therefore, the topological trigger is designed to make a decision on partially reconstructed decays. The neutrino of a semileptonic B decay is not reconstructed in any case. One important variable is a corrected mass, m_{corr}, which is defined as

$$m_{\mathrm{corr}} = \sqrt{m^2 + |p_{\mathrm{T\,miss}}|^2} + |p_{\mathrm{T\,miss}}| \quad ,$$

where $p_{\mathrm{T\,miss}}$ is the missing momentum transverse to the direction of flight, as defined by the PV and the n-body vertex [43], see Figure 6.3a, and m the invariant mass of the n-body object. The distribution of m_{corr} for a genuine 4-body B decay is shown in Figure 6.3b and 6.3c for 2- and 3-body combinations. It can be seen that it is closer to the real B mass if more decay products are added. Prompt charm hadrons are discarded by requiring that m_{corr} is above $2\,\text{GeV}/c$ and each $(n-1)$-body object of an n-body trigger must have an invariant mass greater than $2.5\,\text{GeV}/c$. A multivariate selection is used to make a decision if a candidate is accepted or not. The topological lines with at least one track identified as a muon are called `Hlt2TopoMuNBodyBBDT`.

A special line to select muons from secondary vertices is the so-called `Hlt2SingleMuon` line which searches for one highly displaced track identified as a muon. As its rate is very high, it is executed only in 50 % of all events (randomly selected).

The rate of prompt c-hadron events is a factor of 20 higher than the $b\bar{b}$ rate. About 10 % of all pp collisions at the LHC contain a c hadron. In order to control the rate, prompt charm mesons are selected by exclusive lines which select certain decays interesting for physics analyses. These lines fully reconstruct the final state. First, tight requirements on the impact parameters and the transverse momenta of final state candidates are applied to suppress combinatorics from the light hadron background. Second, c-hadron candidates are accepted if the reconstructed invariant mass, the flight distance and the pointing to the primary vertex are consistent with a prompt produced c hadron.

As the particle identification of hadrons is a time consuming task, cf. Chapter 4.4, it cannot be executed for trigger lines which have a high rate. Thus, the HLT2 reconstruction does not distinguish between three-body D^+ or D_s^+ decays with different combinations of charged kaons and pions in the final state, e.g. $D^+ \to K^-\pi^+\pi^+$, $D^+ \to K^-K^+\pi^+$ or $D^+ \to \pi^-\pi^+\pi^+$. Therefore, the algorithm to select these class of decays tests all possible combination and accepts a trigger candidate if the three-body invariant mass is in the range $[1800, 2040]\,\text{MeV}/c^2$. The decay $D^+ \to K^-\pi^+\pi^+$ is triggered by the so-called `Hlt2CharmHadD2HHH` line.

The decay $D^+ \to \overline{K}^0\pi^+$ is selected by combining $K_S^0 \to \pi^+\pi^-$ candidates with an additional charged pion. The $K_S^0 \to \pi^+\pi^-$ candidates have to have a reconstructed invariant mass consistent with the mass of neutral kaons and a significant displacement between decay and primary vertex is required. As mentioned before, the downstream tracking which reconstructs the decay products of long-lived particles was not used in the trigger in the 2011 data taking. Thus, there was no trigger line in 2011 to select $D^+ \to \overline{K}^0\pi^+$ decays where the K_S^0 meson had a flight distance larger than the VELO acceptance. The trigger line based on long-reconstructed K_S^0 candidates is called `Hlt2CharmHadD2KS0H_D2KS0Pi` and the trigger line based on downstream-reconstructed K_S^0 candidates is called `Hlt2CharmHadD2KS0H_D2KS0DDPi`.

6.2.3 Trigger categories

In order to fully control reconstruction effects, it is important to know if a signal candidate which is used in the analysis has been used in the trigger decision. Therefore, the trigger line which selected an event and all detector hits which were used to form the given trigger candidate are saved when writing an event to storage. This allows to check if the off-line reconstructed signal candidate was used in the decision process of a specific trigger line. Three categories are defined [68]:

Triggered On Signal (TOS): The off-line signal candidate was sufficient to trigger the event.

Triggered Independent of Signal (TIS): Something else which has a disjoint set of detector hits was sufficient to trigger the event.

Triggered On Both (TOB): Neither the signal nor the rest of the event was sufficient to generate a positive trigger decision.

It is important to note that an off-line candidate can be *triggered independent of signal* (TIS) and *triggered on signal* (TOS).

In the case of a single reconstructed off-line track the definition of TOS is: A trigger track is matched to an off-line track when more than 70 % of the hits of the trigger track are contained in the off-line track. The definition for composite particles is: The off-line reconstructed tracks of the candidate's final state particles contain the tracks of the trigger candidate.

As an example the reconstructed decay $\overline{B} \rightarrow D^0(\rightarrow K^-K^+)\mu^-$ is considered. The reconstructed final state is composed of three tracks. The two kaons and the muon can trigger the `Hlt1TrackAllL0` line. Hence, each of the kaon and muon candidates can be `Hlt1TrackAllL0` TOS. If at least one of the reconstructed decay products fulfilled the `Hlt1TrackAllL0` criteria, the composite $\overline{B}$ candidate is `Hlt1TrackAllL0` TOS.

A $\overline{B} \rightarrow D^0(\rightarrow K^-K^+)\mu^-$ candidate can be `Hlt2TopoMu2BodyBBDT` TOS and `Hlt2TopoMu3BodyBBDT` TOS. Then, two or three of the off-line reconstructed tracks are matched to trigger tracks which were used in the `Hlt2TopoMu2BodyBBDT` or `Hlt2TopoMu3BodyBBDT` line, respectively. The $\overline{B}$ candidate cannot be `Hlt2TopoMu4BodyBBDT` TOS as this requires a four-body off-line candidate.

6.2.4 Trigger requirements of muon-tagged D^0 and prompt D^+ decays

The trigger lines are selected such that potential detection asymmetries introduced by the hardware and software trigger cancel in the difference of raw asymmetries of two decay channels. Therefore, a clear and simple trigger path is chosen for each decay mode. Additionally, specific TIS and TOS requirements are applied at each trigger stage to be certain that the signal decay either has or has not triggered the event.

Semileptonic modes

The trigger requirements of the ΔA_{CP} measurement have been chosen in such a way that muon detection and B production asymmetries cancel in the difference of the raw asymmetries of muon-tagged $D^0 \rightarrow K^-K^+$ and $D^0 \rightarrow \pi^-\pi^+$ decays, see Equation 5.11.

First in L0, the off-line muon candidate is required to have triggered the `L0Muon` line. The efficiency with respect to off-line selected events, obtained from simulation [44],[2] is around 60 %. In an analysis of exclusively $D^0 \rightarrow K^-K^+$ and $D^0 \rightarrow \pi^-\pi^+$ decays the hadronic trigger could be used as the symmetric final states cannot introduce a detection asymmetries. However, its efficiency is around 10 % for semileptonic B decays. It does not add significant statistics after the final selection and is omitted for simplicity.

---

[2] Trigger efficiencies from simulated data are quoted with respect to off-line reconstructed signal decays. The efficiencies of HLT1 and HLT2 lines are given with respect to off-line selected events passing L0 and HLT1, respectively. The off-line reconstruction and trigger efficiencies were determined by a summer student on simulated events. The work is documented in Reference [44].

Table 6.2: Contributions of different trigger lines to the sample of off-line selected events in data. The numbers shown give the fraction of events in the selected data sample that pass a given trigger requirement (note that this is not the trigger efficiency). The numbers for the HLT1 (HLT2) are defined with respect to the number of candidates passing the combined L0 (HLT1) lines. The fractions are given for 2011 and 2012 data in parenthesis.

Trigger line	$D^0 \to \pi^-\pi^+$	$D^0 \to K^-K^+$	$D^0 \to K^-\pi^+$
`L0Muon` TOS on muon	0.974 (0.855)	0.974 (0.860)	0.973 (0.855)
`Hlt1TrackAllL0` TOS on B	0.910 (0.875)	0.899 (0.865)	0.903 (0.869)
`Hlt1TrackMuon` TOS on muon	0.806 (0.866)	0.813 (0.872)	0.809 (0.870)
combined HLT1	0.981 (0.986)	0.977 (0.985)	0.978 (0.986)
`Hlt2SingleMuon` TOS on muon	0.175 (0.182)	0.184 (0.192)	0.180 (0.189)
`Hlt2TopoMu2BodyBBDT` TOS on B	0.696 (0.707)	0.688 (0.698)	0.691 (0.704)
`Hlt2TopoMu3BodyBBDT` TOS on B	0.618 (0.664)	0.590 (0.648)	0.596 (0.651)
`Hlt2TopoMuNBodyBBDT` TOS on B	0.847 (0.865)	0.822 (0.841)	0.831 (0.853)
combined HLT2	0.889 (0.901)	0.875 (0.885)	0.880 (0.894)
combined trigger	0.849 (0.759)	0.832 (0.750)	0.838 (0.753)

Second in HLT1, $D^0 \to K^-K^+$ and $D^0 \to \pi^-\pi^+$ candidates are selected if either the muon candidate triggered `Hlt1TrackMuon` or one of the decay products triggered `Hlt1TrackAllL0`. The latter cannot introduce an additional asymmetry as both final states are *CP* eigenstates. Any asymmetry introduced due to the muon is cancelled in the difference of the two raw asymmetries. The efficiency relative to L0 and off-line selection, obtained from simulation [44], of the `Hlt1TrackMuon` line is around 65 %. The efficiency of the `Hlt1TrackAllL0` line is higher with 75 % as three particles can fulfil the criteria. The combined efficiency is about 85 %.

Third in HLT2, semileptonic B decays are triggered by the `Hlt2TopoMuNBodyBBDT` and the `Hlt2SingleMuon` lines. The 2- and 3-body combinations contribute in roughly equal amounts. The combined efficiency of the topological lines is around 70 % [44], The `Hlt2SingleMuon` line adds about 5 % signal candidates. The fractions[3] in data of selected signal decays after the final off-line selections are shown for each trigger line and decay mode in Table 6.2. It is seen that the tight requirements at all trigger stages select about 85 % of the signal candidates of the 2011 data sample and roughly 75 % of the 2012 data sample. The trigger requirements in 2012 were in general looser compared to 2011. Thus, more candidates have been triggered independent of the signal. However, these candidates are not considered in this analysis. It is also important to point out that the individual fractions of the three decay channels are similar. If that was not the case, trigger induced contributions to the raw asymmetries might be different between the different decay channels.

The $A_{CP}(K^-K^+)$ measurement requires tighter trigger requirements as the muon detection and the B production asymmetry are determined with muon-tagged $D^0 \to K^-\pi^+$

---

[3] The given fractions should not be confused with trigger efficiencies. They show which trigger line selected which fraction of off-line reconstructed decays.

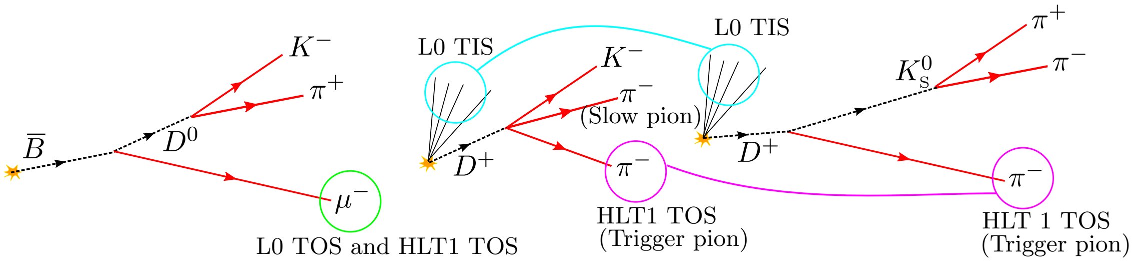

Figure 6.4: Illustration of the L0 and HLT1 strategy for correcting $A_D(K^-\pi^+)$ in the raw asymmetry of muon-tagged $D^0 \to K^-\pi^+$ decays. Circles indicate the particle which is used in the trigger decision. The Trigger pion is defined as the pion which has triggered the `Hlt1TrackAllL0` line. If both pions of $D^+ \to K^-\pi^+\pi^+$ have triggered, it is randomly assigned. The other pion is called Slow pion.

decays. This channel is affected by the charged kaon detection asymmetry, see Equation 5.16. In order to avoid any additional asymmetry induced by the HLT1 reconstruction, only events where the muon candidate triggered the `Hlt1TrackMuon` line are accepted. The HLT2 selection is also simplified by omitting events triggered exclusively by the `Hlt2SingleMuon` line. This additionally ensures that the selection of the $K^-\pi^+$ pair is closer to the exclusive selection of prompt $D^+ \to K^-\pi^+\pi^+$ candidates in HLT2. For consistency, the same trigger requirements are applied to muon-tagged $D^0 \to K^-K^+$ candidates which are used in the $A_{CP}(K^-K^+)$ measurement. Consequently, the $D^0 \to K^-K^+$ sample of the $A_{CP}(K^-K^+)$ measurement is a subset of the sample used in the ΔA_{CP} measurement.

Prompt modes

Prompt $D^+ \to K^-\pi^+\pi^+$ and $D^+ \to \overline{K}^0\pi^+$ decays are used to determine the detection asymmetry $A_D(K^-\pi^+)$, see Equation 5.15. The $K^-\pi^+$ pair of muon-tagged $D^0 \to K^-\pi^+$ decays is not used in the trigger decision of L0 and HLT1. This has to be reflected in the trigger selection of $D^+ \to K^-\pi^+\pi^+$ and candidates to ensure the same trigger detection asymmetries in $D^+ \to K^-\pi^+\pi^+$ and $D^0 \to K^-\pi^+$ decays. The strategy is depicted in Figure 6.4 and explained in words in the following.

First in L0, the spatial resolution of the hadronic calorimeter is not enough to trigger on a single particle. As the decays $D^+ \to K^-\pi^+\pi^+$ and $D^+ \to \overline{K}^0\pi^+$ have different hadrons in the final state, potential detection asymmetries do not cancel in the difference of both raw asymmetries. Thus, it is required that events are triggered independently of the signal candidate in L0. Any asymmetry coming from the rest of the event, e.g., the other c hadron, is the same for both decay modes. About 70 % of the off-line selected $D^+ \to K^-\pi^+\pi^+$ and $D^+ \to \overline{K}^0\pi^+$ samples are triggered independently of the reconstructed D^+ decay in the hardware trigger (`L0Global` TIS). The trigger line selection of both prompt decay modes is summarised in Table 6.3.

Second in HLT1, only candidates where a pion of the D^+ decay triggered the `Hlt1TrackAllL0` line are selected. This pion is defined as the *Trigger pion*. The other pion is called *Slow pion*. For $D^+ \to \overline{K}^0\pi^+$ decays the Trigger pion is unambiguous as the decay products of K^0_S mesons are not considered. Both pions of $D^+ \to K^-\pi^+\pi^+$

Table 6.3: The trigger lines used to select prompt charm events. The TIS and TOS requirements are given.

Trigger line	**Decay channel**
`L0Global` TIS on D^+	$D^+ \to K^-\pi^+\pi^+$ and $D^+ \to \overline{K}^0\pi^+$
`Hlt1TrackAllL0` TOS on one (Trigger) pion	$D^+ \to K^-\pi^+\pi^+$ and $D^+ \to \overline{K}^0\pi^+$
`Hlt2CharmHadD2HHH` TOS on D^+	$D^+ \to K^-\pi^+\pi^+$
`Hlt2CharmHadD2KS0H_D2KS0Pi` TOS on D^+	$D^+ \to \overline{K}^0\pi^+$ (LL)
`Hlt2CharmHadD2KS0H_D2KS0DDPi` TOS on D^+	$D^+ \to \overline{K}^0\pi^+$ (DD)

decays can have triggered the event then the Trigger pion is chosen randomly. The other pion is defined as Slow pion. This trigger line selection ensures that the $K^-\pi^+$ pair of prompt $D^+ \to K^-\pi^+\pi^+$ decays is not used to generate a positive trigger decision in L0 and HLT1 as it is the case for muon-tagged $D^0 \to K^-\pi^+$ decays. For the prompt $D^+ \to K^-\pi^+\pi^+$ and $D^+ \to \overline{K}^0\pi^+$ decay modes the selection guarantees that a potential detection asymmetry of charged pions induced by L0 and HLT1 is the same.

The `Hlt1TrackAllL0` efficiency with respect to off-line reconstructed $D^+ \to K^-\pi^+\pi^+$ candidates varies from 50 to 70 % depending on the momentum of the D mesons [43]. In the off-line selected data sample at least one of the pion candidates fulfils the `Hlt1TrackAllL0` line criteria in 78 % of all events where the `Hlt1TrackAllL0` line has triggered the D^+ candidate. In the other events the kaon candidate has generated the positive trigger decision of the `Hlt1TrackAllL0` line. For `Hlt1TrackAllL0` selected $D^+ \to \overline{K}^0\pi^+$ decays the (Trigger) pion has been used in about 75 % of all events to trigger the event. In the other cases the decay products of the K^0_S candidate have been used in HLT1.

Third in HLT2, exclusive lines which fully reconstruct the final states of $D^+ \to K^-\pi^+\pi^+$ and $D^+ \to \overline{K}^0\pi^+$ decays are used. As the track reconstruction in HLT2 is very similar to the off-line reconstruction, it does not significantly add detection asymmetries with respect to the off-line reconstruction. The `Hlt2CharmHadD2HHH` is used to select $D^+ \to K^-\pi^+\pi^+$ candidates. The decay $D^+ \to \overline{K}^0\pi^+$ is triggered by the lines `Hlt2CharmHadD2KS0H_D2KS0Pi` and `Hlt2CharmHadD2KS0H_D2KS0DDPi` where the latter combines downstream tracks to construct a K^0_S candidate. This line was only present during 2012 data taking. The exclusive `Hlt2CharmHadD2HHH` line has an efficiency of about 50 % relative to HLT1 and off-line selected events.

6.2.5 Selection of trigger configurations

The trigger configuration had be to adapted to changing running conditions throughout the years. The philosophy of the analysis is to control detection asymmetries. As different trigger configuration could have different detection asymmetries, short periods with different trigger settings are excluded from the analysis. If a large fraction of data has been taken with the same trigger configuration, potential problems are visible when looking at only this period. A large part of later chapters is dedicated to studying the measured raw and *CP* asymmetries in different data taking periods defined among others by changing trigger conditions.

In 2011 the majority of the data was taken with stable conditions. The `L0Muon` p_T threshold was 1.48 GeV/c for most of the data. In a few trigger configurations the threshold was lowered to 0.8 GeV/c or raised to 1.6 GeV/c. This induces a different `L0Muon` asymmetry; thus, these data are not considered in the analysis. This requirement rejects about 1.8 % of the 2011 sample.

In 2012 the first recorded data[4] were used to calibrate the transverse momentum estimate of the `L0Muon` trigger. The integrated luminosity of this sample is about 80 pb^{-1} which corresponds to 8 % of the magnet down data of 2012. These data are not used to measure detection and *CP* asymmetries. Furthermore, negligible amounts (0.1 %) of data are rejected due to different HLT1 thresholds. There were significant changes in the momentum and track quality thresholds in `Hlt1TrackAllL0` and `Hlt1TrackMuon` in the middle of 2012, see Table 6.1. The first part of the data sample corresponding to an integrated luminosity of 0.7 fb^{-1} has a tighter selection than the second part corresponding to an integrated luminosity of 1.3 fb^{-1}.

For reference, the full list of used and not used trigger configurations is given in Appendix A.

6.3 Off-line selection

The off-line selection of semileptonic B and prompt D^+ decays follows the same principles as the selection in the trigger. However, as more processing time is available, a more detailed event reconstruction can be performed.[5] Most significantly, particle identification of hadrons is performed by using information from the RICH detectors and the calorimeters. The track reconstruction is performed with looser momentum requirements and redundant algorithms are used to increase the efficiency. The off-line track fit uses the full available detector geometry to transport trajectories through the detector, whereas the trigger reconstruction uses a simplified detector geometry.

The selection of all channels is explained in the following. A dedicated cut to reject $B \to J/\psi X$ decays is discussed in more detail.

6.3.1 Off-line decay reconstruction

The off-line reconstruction combines reconstructed tracks, particle identification observables and a mass hypothesis to form $K^\pm$, $\pi^\pm$, $\mu^\pm$, $e^\pm$, p and $\overline{p}$ candidates. These particles are considered as stable as their lifetime is large enough that the majority of particles produced in the forward region can traverse the whole LHCb detector before decaying. Among these particles the charged kaon has the shortest lifetime with $\tau \approx 1.2\times10^{-8}\,\mathrm{s} \approx 3.7\,\mathrm{m}/c$. Combinations of stable particles form composite particles with a finite decay time.

Two different vertex fitters[6] are used to reconstruct decays and their corresponding vertices, the `OfflineVertexFitter` and the `DecayTreeFitter`. The main difference is

---

[4] The so-called run number of these data is smaller than 114000.

[5] The data of both years are reconstructed off-line with the same software versions of BRUNEL and DAVINCI. The analysis uses data reconstructed and selected by the campaigns Stripping 20 for 2012 and 20r1 for 2011. Both are based on the Reco 14 reconstruction.

[6] In fact the trigger uses a third one, the so-called `LokiVertexFitter`

how decays involving multiple decay vertices are treated.

The `OfflineVertexFitter` follows a bottom-up approach. For example, when reconstructing the decay $\overline{B} \to D^0(\to K^-K^+)\mu^-$, first a vertex out of a K^- and a K^+ candidate is fitted, then the D^0 and muon candidate are combined to a B candidate.

The `DecayTreeFitter` (DTF) fits simultaneously the full decay chain with a Kalman filter [69]. The advantage of this approach is that the knowledge of a common D^0 and muon vertex can influence the D^0 vertex fit. This is especially important for extracting the D^0 decay time. Another advantage is that a particle can be constrained to originate from the primary vertex which adds more information and improves the mass resolution. The disadvantage is that the approach takes more processing time. The off-line and the trigger reconstruction use first the bottom-up approach to reduce the number of events. The DTF is applied after an event is selected to improve mass and decay time resolution. Its use is explicitly stated in the following.

6.3.2 Momentum scale correction

The momentum measurement depends on the alignment of the tracking detectors and the knowledge of the magnetic field. As there are variations over time, the momentum scale changes. The momentum scale has been calibrated to make precise measurements of D meson masses [70,71]. The calibration has been adapted for this analysis. By applying the correction the mean of the mass is shifted closer to the PDG value. Additionally, the fitted mean mass is more stable in different data taking periods. The mass resolution improves by about 1 % for the considered decays and tails in the mass distribution are reduced.

6.3.3 Semileptonic *B* decay modes

The off-line reconstruction partially reconstructs semileptonic B decays as one or more particles of the final state are missing. This means that D^0 candidates are combined with muon candidates to form b-hadron candidates. The partially reconstructed decays are written as $\overline{B} \to D^0\mu^-$ and the CP conjugate $B \to \overline{D}^0\mu^+$ in the following. The D^0 and $\overline{D}^0$ candidates are either reconstructed from K^-K^+, $\pi^-\pi^+$ or $K^\mp\pi^\pm$ pairs. The latter includes Cabibbo-favoured $D^0 \to K^-\pi^+$ and doubly Cabibbo-suppressed $D^0 \to K^+\pi^-$ decays. The flavour of the D^0 candidate is given solely by the charge of the muon candidate.

The off-line selection cuts are summarised in Table 6.4. In order to minimise differences in the selection and, thus, different detection asymmetries, the selection is the same for all three decay modes. The only necessary difference are cuts to select different types of hadrons. The reconstruction of $\overline{B} \to D^0\mu^-$ and $B \to \overline{D}^0\mu^+$ candidates is performed in three steps.

First, kaon, pion and muon candidates are chosen. Ghost tracks are rejected by a cut on the track fit quality, $\chi^2_{\text{track}}/\text{ndf}$, and the so-called ghost probability, $P_{\text{track}}(\text{ghost})$. The ghost probability is a multivariate classifier, using kinematic variables and track reconstruction parameters as inputs, to identify reconstructed tracks which are not associated to a real particle [72]. An additional track reconstruction artefact is when a charged particle is reconstructed by two or more similar tracks. These

Table 6.4: The selection requirements of muon-tagged $D^0 \to K^-K^+$, $D^0 \to \pi^-\pi^+$ and $D^0 \to K^-\pi^+$ decays. The selection cuts are explained in the text. The selection of the three decay channels only differs in the particle identification cuts. The $D^0 \to K^-\pi^+$ selection runs randomly on 50 % of all events.

Kaons		**Pions**		**Muon**	
KL distance	< 5000	KL distance	< 5000	KL distance	< 5000
χ^2_{track}/ndf	< 3	χ^2_{track}/ndf	< 3	χ^2_{track}/ndf	< 3
P_{track}(ghost)	< 0.5	P_{track}(ghost)	< 0.5	P_{track}(ghost)	< 0.5
χ^2(IP)	> 9	χ^2(IP)	> 9	χ^2(IP)	> 9
p	$> 2\,\text{GeV}/c$	p	$> 2\,\text{GeV}/c$	p	$> 3\,\text{GeV}/c$
p_{T}	$> 0.3\,\text{GeV}/c$	p_{T}	$> 0.3\,\text{GeV}/c$	p_{T}	$> 1.2\,\text{GeV}/c$
$\text{DLL}_{K\pi}(KK)$	> 7	$\text{DLL}_{K\pi}(KK)$	–	`ISMUON`	yes
$\text{DLL}_{K\pi}(\pi\pi)$	–	$\text{DLL}_{K\pi}(\pi\pi)$	< -2	$\text{DLL}_{\mu\pi}$	> 0
$\text{DLL}_{K\pi}(K\pi)$	> 7	$\text{DLL}_{K\pi}(K\pi)$	< 0		

D^0 candidate	
$M(D^0)$	$\in [1780, 1950]\,\text{MeV}/c^2$
DTF $M(D^0)$	$\in [1795, 1940]\,\text{MeV}/c^2$
χ^2(DOCA tracks)	< 20
Sum p_{T} D^0 decay products	$> 1.4\,\text{GeV}/c$
p_{T}	$> 0.5\,\text{GeV}/c$
χ^2-distance D^0 vertex–PV	> 100
χ^2_{vertex}/ndf	< 6
DTF χ^2_{vertex}/ndf	< 6
$\cos\alpha$	> 0.99

B candidate	
Mass from four-vector sum	$< 6.2\,\text{GeV}$
$M(B)$	$\in [2.5, 6.0]\,\text{GeV}/c^2$
DTF $M(B)$	$\in [2.5, 5.0]\,\text{GeV}/c^2$
χ^2_{vertex}/ndf	< 6
DTF χ^2_{vertex}/ndf	< 6
$\cos\alpha$	> 0.999
DTF $\tau(D^0)$	$> 0.0\,\text{ps}$
J/ψ veto (see text)	yes

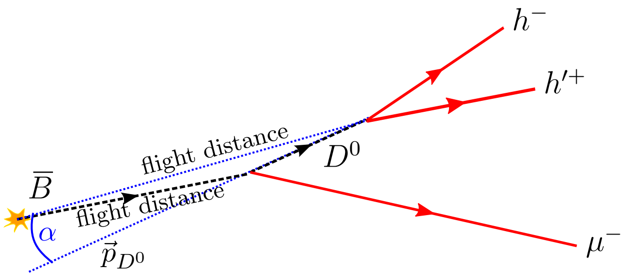

Figure 6.5: The reconstructed $\overline{B} \to D^0\mu^-$ decay. The pointing angle α, B and D^0 flight distance, and the reconstructed D^0 momentum are sketched.

duplicated tracks are suppressed by a cut on the Kullback-Leibler (KL) distance [73]. The KL distance is a measure of the shared information of two tracks, based on the determined track parameters. The larger the KL distance is the less likely is that two tracks are duplicates of each other. Background from light prompt hadrons or prompt muons is further rejected by a cut on the impact parameter significance, $\chi^2(\text{IP})$, and minimum momentum and transverse momentum requirements. A reconstructed track is identified as a muon candidate by reconstructing a matching track in the muon stations. These tracks get assigned the flag `ISMUON`, cf. Chapter 4.5. A better estimate for the authenticity of a hadron or lepton can be done by combining information of all particle identification systems. The information is combined in the differences between the logarithms of the particle identification likelihoods under different mass hypotheses, DLL. Muon candidates are required to have $\text{DLL}_{\mu\pi} \equiv ln\mathcal{L}_\mu - \ln\mathcal{L}_\pi$ larger than zero. The kaon or pion identification requirements, $\text{DLL}_{K\pi} \equiv ln\mathcal{L}_K - \ln\mathcal{L}_\pi$, differ for the different decay modes. Kaon and pion separation is mostly given by the information from the RICH detectors, cf. Chapter 4.4.

The kaon and pion candidates are then combined to form a D^0 candidate. Before a common vertex is fitted, the two tracks are required to have χ^2-distance of closest approach, $\chi^2(\text{DOCA tracks})$, smaller than 20 and the sum of their transverse momenta has to be larger than $1.4\,\text{GeV}/c$. The χ^2 per degrees of freedom of the D^0 vertex fit, $\chi^2_{\text{vertex}}/\text{ndf}$, is required to be smaller than 6 for the `OfflineVertexFitter` and the `DecayTreeFitter`. The reconstructed invariant mass of the D^0 candidate has to be between $1780\,\text{MeV}/c^2$ and $1950\,\text{MeV}/c^2$. The reconstructed mass of the DTF is used later in the analysis when fits to the invariant mass distributions are performed. As B and D mesons have a finite lifetime, the χ^2-distance between primary and D^0 vertex[7] should be larger than 100. The p_T of the D^0 candidate has to be larger than $0.5\,\text{GeV}/c$. Although the D^0 meson does not originate from the primary vertex, its momentum still roughly points to the primary interaction due to the large boost in the forward direction, see Figure 6.5. Therefore, the cosine of the angle, α, between the D^0 momentum and the direction from the primary vertex to the D^0 decay vertex has to be larger than 0.99. The invariant mass distribution of selected $D^0 \to K^-K^+$, $D^0 \to \pi^-\pi^+$ and $D^0 \to K^-\pi^+$ candidates is shown in Figure 6.6. The peaking structures in the $D^0 \to K^-K^+$ and $D^0 \to \pi^-\pi^+$ invariant mass distributions are misreconstructed decays. The structure

---

[7] In DaVinci this quantity is called `BPVVDCHI2`.

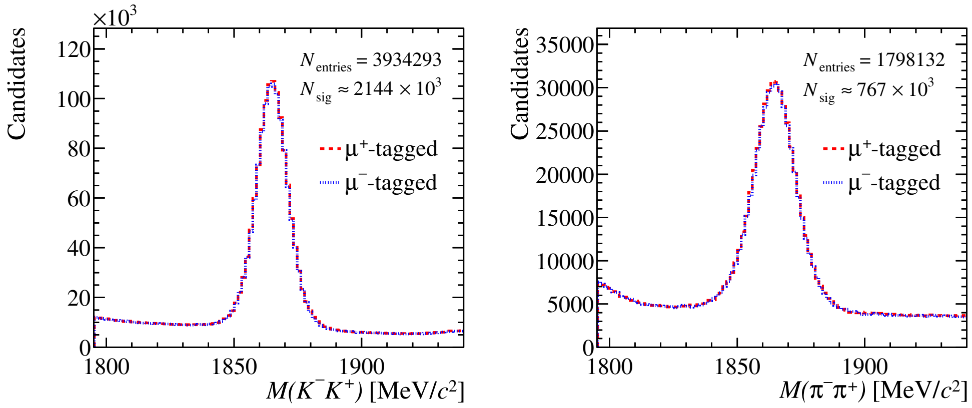

(a) $D^0 \to K^-K^+$ (b) $D^0 \to \pi^-\pi^+$

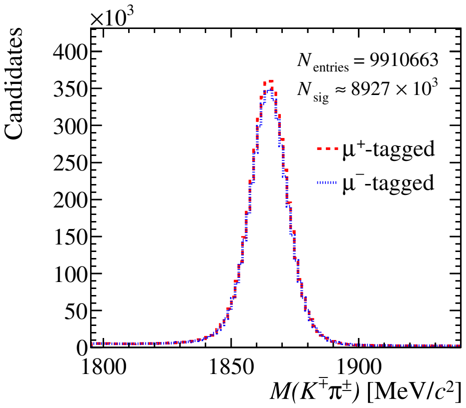

(c) $D^0 \to K^-\pi^+$

Figure 6.6: The invariant mass distribution of reconstructed muon-tagged D^0 candidates separately for μ^-- and μ^+-tags for the full data set. The signal yield is obtained from a simple fit to the invariant mass distribution with a Gaussian to describe the signal peak and a linear background model.

left of the $D^0 \to \pi^-\pi^+$ and right of the $D^0 \to K^-K^+$ signal peak are falsely identified $D^0 \to K^-\pi^+$ decays. The distribution at the lower edge of the $D^0 \to K^-K^+$ mass range has contributions from $D^0 \to K^-K^+\pi^0$ or $D^+ \to K^-K^+\pi^+$ decays where the pion is not reconstructed. These and other background sources are discussed in more detail in Chapter 7.1 where fit models for the D^0 and D^+ mass distributions are developed.

Finally, a D^0 and a muon candidate are combined to a B candidate. As the neutrino is not reconstructed, the invariant mass of the B mesons cannot be fully reconstructed. Only loose cuts on the invariant B mass[8] are possible. In a first step the invariant mass is obtained from the simple four-vector sum of muon and D^0 candidate, a loose cut $M(D^0\mu) < 6.2\,\text{GeV}/c^2$ is applied. Then, a common vertex of the D^0 and the muon candidate is fitted, only candidates with a $\chi^2_{\text{vertex}}/\text{ndf}$ smaller than 6 are accepted. The invariant mass has to be larger than $2.5\,\text{GeV}/c^2$ to suppress prompt charm

---

[8] The B^0 mass in MeV/c^2 and a mile in feet have the same number, 5276.

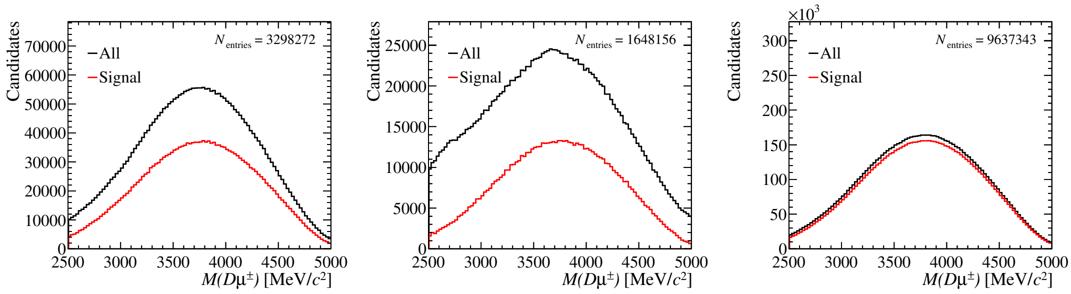

(a) $D^0 \rightarrow K^-K^+$ (b) $D^0 \rightarrow \pi^-\pi^+$ (c) $D^0 \rightarrow K^-\pi^+$

Figure 6.7: The $D^0\mu$ invariant mass distribution of reconstructed muon-tagged D^0 decays for the full data set and each D^0 final state. In the red distribution the non-D^0 background is statistically subtracted by fitting the D^0 invariant mass distribution. The so-called *sPlot* technique is used [74], see also Appendix E.

background. In order to reject fully-reconstructed hadronic B decays, the reconstructed invariant mass is required to be smaller than 5 GeV/c^2. The invariant mass distribution of selected $\overline{B} \rightarrow D^0\mu^-$ candidates is shown in Figure 6.7. Qualitatively, the same distribution is obtained for each decay mode after combinatorial D^0 background is subtracted statistically.

Although the B momentum is not fully reconstructed, it still points close to the primary vertex due to the large boost in the forward direction. Thus, $\cos\alpha$ of the B candidate is required to be larger than 0.999. Figure 6.8 sketches the topologies of combinatorial background from prompt D mesons where the D^0 decay vertex is closer to the primary vertex than the B decay vertex and background from multi-body B decays like $B \rightarrow J/\psi X$ where all decay products form a common vertex. These types of background can be rejected by requiring that the D^0 decay vertex is in downstream direction of the B decay vertex. Instead of a cut on the z-coordinates of the vertices the D^0 decay time reconstructed by the DTF is required to be larger than zero.[9] Negative decay times are reconstructed when the flight distance and momentum vector point into opposite directions. It is found that a tighter cut on the D^0 decay time rejects as much signal as background. Multi-body B decays are generally a source of background as this type of background forms a common vertex and has the same topology as semileptonic B decays. The case depicted in Figure 6.8c, where one muon from the J/ψ decay and a hadron are combined to a D^0 candidate can be effectively suppressed by a dedicated J/ψ *veto* which is discussed in the next section. Further background contributions are discussed in Chapter 7.1.

6.3.4 J/ψ veto

One muon from a secondary J/ψ decay and an oppositely charged hadron from the rest of a $B \rightarrow J/\psi X$ decay can be combined to form a D^0 candidate as shown in Figure 6.8c. The tag is then given by the charge of the other muon, the *tagging muon*. The decay

---

[9] The advantage of decay time cuts in contrast to flight distance cuts are that they do not introduce biases in the decay time distribution. This is not important for this analysis as it is a time-integrated measurement. However, there are time-dependent analyses ongoing using the same data set.

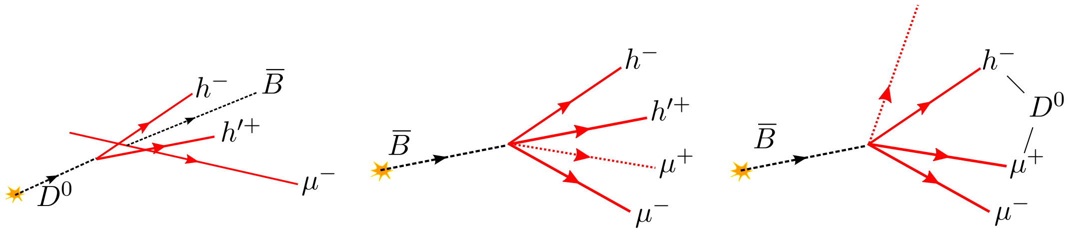

(a) (b) (c)

Figure 6.8: Different types of background sources are sketched. The dashed red lines correspond to not-reconstructed particles. (a) A prompt D^0 meson combined with a random muon to a $\overline{B} \to D^0\mu^-$ candidate. (b) and (c) $B \to J/\psi X$ decays reconstructed as $\overline{B} \to D^0\mu^-$.

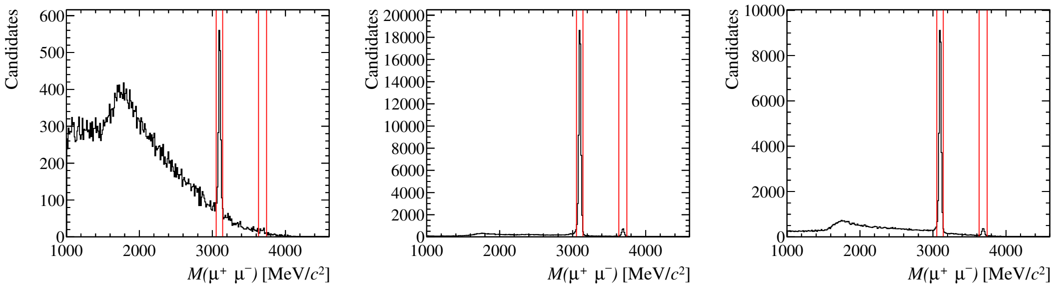

(a) $D^0 \to K^-K^+$ (b) $D^0 \to \pi^-\pi^+$ (c) $D^0 \to K^-\pi^+$

Figure 6.9: The invariant mass distribution of J/ψ candidates. The hadron candidate with opposite charge as the tagging muon is identified as `ISMUON`. The mass ranges of the J/ψ and $\psi(2S)$ vetos are shown with red vertical lines. Only a part of the data was used to make these plots. Note the different y-scales. The structure around $1.8 - 1.9\,\text{GeV}/c^2$ are genuine D^0 decays where a hadron was misidentified as a muon, likely because the light hadron decayed semileptonically to a muon in front of the muon stations.

$B^0 \to J/\psi K^{*0}$, where the K^{*0} meson decays to a charged kaon and pion, is an obvious source of this type of background. Its contribution can be reduced by reconstructing the J/ψ meson. In case the D^0 candidate decay product with the opposite charge of the tagging muon is identified as a muon with the `ISMUON` flag, it is combined with the tagging muon to form a J/ψ candidate. The mass hypothesis of the hadron candidate is adjusted accordingly to the muon mass hypothesis. The χ^2/ndf of the fitted J/ψ vertex has to be smaller than 9 to only select candidates which form a common vertex. The invariant mass distribution of these J/ψ candidates is shown in Figure 6.9 for all three decay modes.

The measured J/ψ and $\psi(2S)$ masses are $(3096.916 \pm 0.011)\,\text{MeV}/c^2$ and $(3686.109 \pm 0.014)\,\text{MeV}/c^2$ [16], respectively. Clear peaks at these positions are seen in all three distributions. In order to suppress this type of background and to keep all signal decays, the $\overline{B} \to D^0\mu^-$ candidate is rejected if the reconstructed invariant mass of the J/ψ candidate is in a window of 45 MeV or 55 MeV of the J/ψ or $\psi(2S)$, respectively. The misidentification of muons as pions is higher as the misidentification of muons as kaons because the pion mass is close to the muon mass. Thus, mainly the $D^0 \to \pi^-\pi^+$

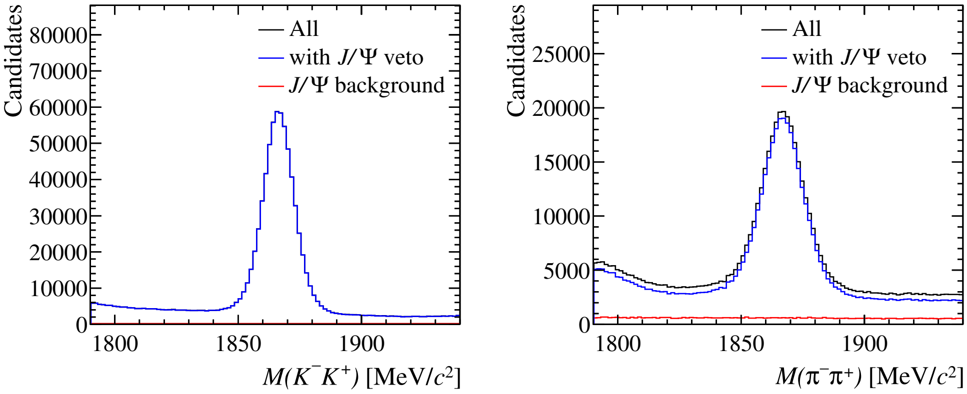

(a) $D^0 \to K^-K^+$

(b) $D^0 \to \pi^-\pi^+$

Figure 6.10: The invariant mass distribution of D^0 candidates with and without J/ψ veto. Only a part of the data was used to make these plots.

decay channel is affected by this background. A significant fraction of the combinatorial background of $D^0 \to \pi^-\pi^+$ candidates is of this type, as can be seen in Figure 6.10. An important observation is that the rejected events are evenly distributed in the D^0 mass range. Consequently, the J/ψ veto cannot affect the asymmetry determination.

The J/ψ veto has already been applied in all plots and tables except in Figure 6.9 and 6.10.

6.3.5 Prompt D^+ decay modes

The off-line reconstruction of the prompt $D^+ \to K^-\pi^+\pi^+$ and $D^+ \to \overline{K}^0\pi^+$ decays follows the principles which are discussed for the trigger selection of prompt charm mesons and the off-line selection of B decays. However, D mesons have a shorter lifetime than B mesons and are much lighter. Thus, the cuts on impact parameters, flight distances and momenta are tighter to reject more light hadron background. The selection requirements are summarised for $D^+ \to K^-\pi^+\pi^+$ candidates in Table 6.5 and for $D^+ \to \overline{K}^0\pi^+$ candidates in Table 6.6.

Nevertheless, a few things are pointed out. The particle identification, the ghost probability and the $\chi^2_{\text{track}}/\text{ndf}$ selections of K^- and π^+ candidates of reconstructed $D^+ \to K^-\pi^+\pi^+$ decays are aligned to the selection cuts of muon-tagged $D^0 \to K^-\pi^+$ candidates, in order to have the same detection asymmetries. Differences in the kinematic distributions are treated separately in Chapter 8.

In the selection, K^0 or $\overline{K}^0$ candidates are referred to as a K^0_S candidate to indicate that the final state $\pi^+\pi^-$ is reconstructed. The invariant mass distribution for long- and downstream-reconstructed K^0_S candidates is shown in Figure 6.11. The mass resolution of downstream-reconstructed candidates is significantly better than for downstream-reconstructed candidates.

The decay trees of $D^+ \to K^-\pi^+\pi^+$ and $D^+ \to \overline{K}^0\pi^+$ candidates are fitted with the DTF. For both modes, the D^+ candidate is constrained to the PV to improve the mass resolution. In the decay $D^+ \to \overline{K}^0\pi^+$ the mass of K^0_S candidates is constrained to the

Table 6.5: Selection requirements of $D^+ \to K^-\pi^+\pi^+$ candidates. The selection cuts are explained in Chapter 6.3.3.

$\boldsymbol{D^+}$ **decay products**	
$\chi^2_{\text{track}}/\text{ndf}$	< 3
$P_{\text{track}}(\text{ghost})$	< 0.5
p_{T}	$> 250\,\text{MeV}/c$
p	$> 2.0\,\text{GeV}/c$
$\chi^2(\text{IP})$	> 4
$\chi^2(\text{IP})$ of > 1 track	> 10
$\sum p_{\text{T}}$	$> 2.8\,\text{GeV}/c$
DOCA tracks	$< 0.5\,\text{mm}$
$\text{DLL}_{K\pi}$ of K^-	> 7
$\text{DLL}_{K\pi}$ of π^+	< 0

$\boldsymbol{D^+}$ **candidate**	
p_{T}	$> 1\,\text{GeV}/c$
$\chi^2_{\text{vertex}}/\text{ndf}$	< 10
DTF $\chi^2_{\text{vertex}}/\text{ndf}$	< 15
$\cos\alpha$	> 0.98
$\chi^2(\text{IP})$	< 12
χ^2-distance D^0 vertex–PV	> 36
$\chi^2(\text{FD})$	> 125
$M(D^+)$	$\in [1800, 1940]\,\text{MeV}/c^2$
Prescale	0.2

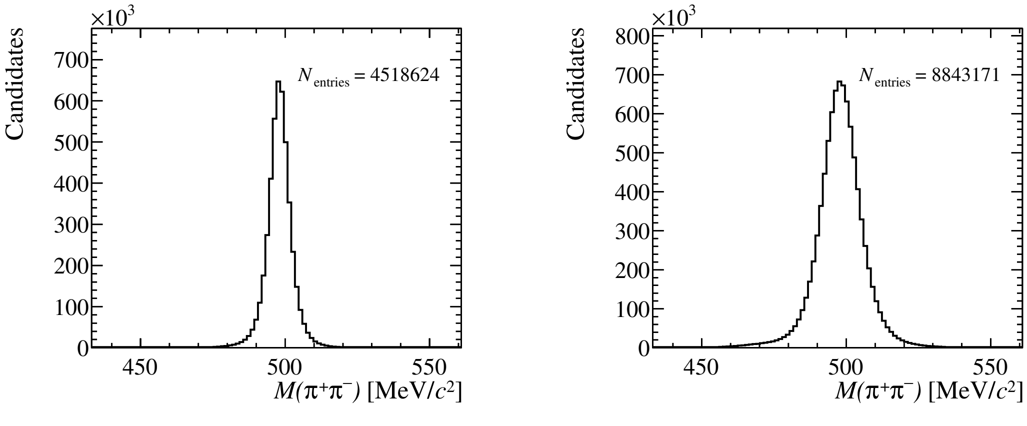

(a) long-reconstructed (b) downstream-reconstructed

Figure 6.11: The invariant mass distribution of (a) long-reconstructed and (b) downstream-candidates K^0_{S} candidates.

Table 6.6: Selection requirements of $D^+ \to \overline{K}^0\pi^+$ candidates. The selection cuts are explained in Chapter 6.3.3.

K^0_S decay products

	LL combinations	DD combinations
$\chi^2_\mathrm{track}/\mathrm{ndf}$	< 3	< 3
p_T	$> 250\,\mathrm{MeV}/c$	–
p	$> 2.0\,\mathrm{GeV}/c$	$> 2.0\,\mathrm{GeV}/c$
$\chi^2(\mathrm{IP})$	> 40	> 40
$\chi^2(\mathrm{DOCA\ tracks})$	< 25	< 25

K^0_S candidate

	LL combinations	DD combinations
p_T	$> 1\,\mathrm{GeV}/c$	$> 1\,\mathrm{GeV}/c$
$\chi^2(\mathrm{IP})$	> 7	–
$\chi^2_\mathrm{vertex}/\mathrm{ndf}$	< 10	< 10
χ^2-distance D^0 vertex–PV	-	> 200
$M(\overline{K}^0)$	$\in [462, 532]\,\mathrm{MeV}/c^2$	$\in [433, 561]\,\mathrm{MeV}/c^2$

Trigger pion

p_T	$> 250\,\mathrm{MeV}/c$
p	$> 2\,\mathrm{GeV}/c$
$\chi^2_\mathrm{track}/\mathrm{ndf}$	< 3
$P_\mathrm{track}(\mathrm{ghost})$	< 0.5
$\chi^2(\mathrm{IP})$	> 15
$\mathrm{DLL}_{K\pi}$	< 0

D^+ candidate

$\sum p_\mathrm{T}(K^0_\mathrm{S}, \pi^+)$	$> 1\,\mathrm{GeV}/c$
$\chi^2(\mathrm{DOCA\ of\ }\overline{K}^0\mathrm{\ and\ }\pi^+)$	< 11
p_T	$> 1\,\mathrm{GeV}/c$
$\chi^2_\mathrm{vertex}/\mathrm{ndf}$	< 10
DTF $\chi^2_\mathrm{vertex}/\mathrm{ndf}$	< 15
$\chi^2(\mathrm{IP})$	< 15
χ^2-distance D^0 vertex–PV	> 5
$z(D^+) - z(PV)$	> 10
$M(D^+)$	$\in [1770, 2080]\,\mathrm{MeV}/c^2$

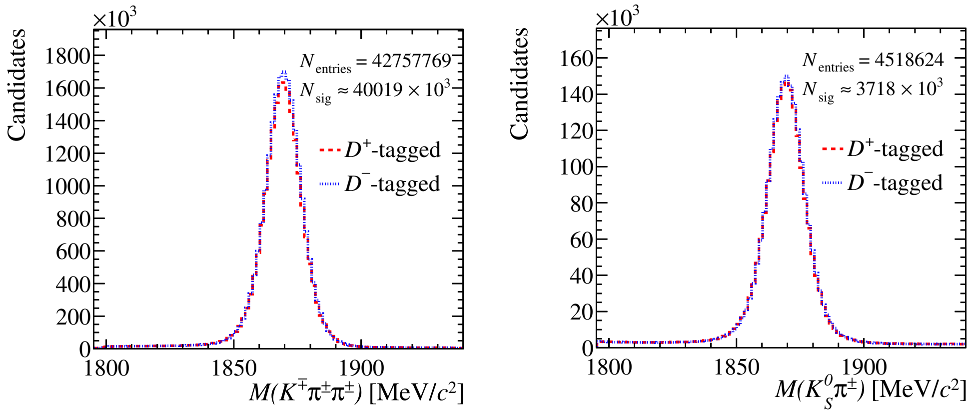

(a) $D^+ \to K^-\pi^+\pi^+$ (b) long-reconstructed $D^+ \to \overline{K}^0\pi^+$

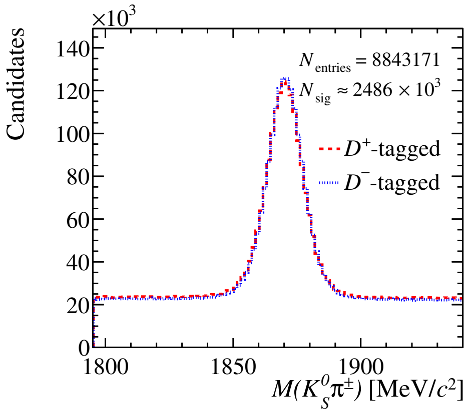

(c) downstream-reconstructed $D^+ \to \overline{K}^0\pi^+$

Figure 6.12: The invariant mass distributions of reconstructed D^+ candidates for the full data set and all decay modes considered. The signal yield is obtained from a simple fit to the invariant mass distribution with a Gaussian to described the signal peak and a linear background model.

PDG mass to improve the mass resolution of the D^+ candidates. This also reduces the effect of a worse momentum resolution of downstream-reconstructed K^0_S candidates compared to long-reconstructed K^0_S candidates. Failing fits are rejected by a loose cut on DTF $\chi^2_\text{vertex}/\text{ndf}$. The invariant mass distributions are shown in Figure 6.12. There is hardly any background contribution in $D^+ \to K^-\pi^+\pi^+$ and long-reconstructed $D^+ \to \overline{K}^0\pi^+$ mass distributions. The downstream-reconstructed $D^+ \to \overline{K}^0\pi^+$ decays are less clean compared to the long-reconstructed.

Table 6.7: Approximate signal yields of the various decay channels after all selection cuts. A simple fit is performed to obtain these yields.

	2011		**2012**			
Sample	**Up**	**Down**	**Up**	**Down**	**Total**	
$D^0 \to \pi^-\pi^+$ from B	90 k	124 k	283 k	269 k	0.77 M	
$D^0 \to K^-K^+$ from B	263 k	360 k	786 k	736 k	2.2 M	ΔA_{CP}
$D^0 \to K^-K^+$ from B	210 k	295 k	675 k	629 k	1.8 M	$A_{CP}(K^-K^+)$
$D^0 \to K^-\pi^+$ from B	1.02 M	1.43 M	3.36 M	3.14 M	8.9 M	
Prompt $D^+ \to K^-\pi^+\pi^+$	3.94 M	5.63 M	15.7 M	14.9 M	40.2 M	
Prompt $D^+ \to \overline{K}^0\pi^+$	373 k	539 k	1.46 M	1.36 M	3.7 M	LL K^0_S
Prompt $D^+ \to \overline{K}^0\pi^+$	0	0	1.28 M	1.21 M	2.5 M	DD K^0_S

6.4 Summary: Event yields

The analysis uses the full data set taken by LHCb in 2011 and 2012. This corresponds to a total integrated luminosity of $3\,\mathrm{fb}^{-1}$. An integrated luminosity of $1\,\mathrm{fb}^{-1}$ was recorded in 2011 at a centre-of-mass energy of 7 TeV, an integrated luminosity of $2\,\mathrm{fb}^{-1}$ was recorded in 2012 at a centre-of-mass energy of 8 TeV. The trigger and off-line selections discussed previously are applied to select semileptonic B decays where the D^0 meson decays into K^-K^+, $\pi^-\pi^+$ and $K^-\pi^+$ pairs and prompt $D^+ \to K^-\pi^+\pi^+$ and $D^+ \to \overline{K}^0\pi^+$ decays. Selection cuts in the trigger and off-line are aligned between different decay channels such that possible detection asymmetries are the same and, hence, cancel in the difference of raw asymmetries.

The approximate signal yields divided into year and magnet polarity are given in Table 6.7. The number of signal candidates used in the analysis ranges from 0.767×10^6 $D^0 \to \pi^-\pi^+$ decays to 40.1×10^6 $D^+ \to K^-\pi^+\pi^+$ decays. The $D^0 \to K^-\pi^+$ selection is only run on 50 % of all recorded events due to limited computing resources of the LHCb experiment. The $D^+ \to K^-\pi^+\pi^+$ sample is reduced to 20 % at analysis level[10] to make the analysis faster. In both cases it is randomly but reproducible decided if an event is kept or not. Two different yields are quoted for the $D^0 \to K^-K^+$ sample as the $A_{CP}(K^-K^+)$ measurement uses a tighter trigger line selection than the ΔA_{CP} measurement.

The yields of 2012 are more than a factor two higher as the production cross section increases with the centre-of-mass energy and the trigger selection is more efficient in 2012, especially for the prompt D^+ decays. The relative yields of $D^0 \to K^-K^+$, $D^0 \to \pi^-\pi^+$ and $D^0 \to K^-\pi^+$ are roughly consistent with the relative branching fractions, cf. Chapter 2.2.3. The $D^+ \to \overline{K}^0\pi^+$ yield compared to the $D^+ \to K^-\pi^+\pi^+$ yield is significantly lower than what is expected from the ratio of branching fractions. This is due to the low reconstruction efficiency of K^0 and $\overline{K}^0$ mesons.

The uncertainty on the measured raw asymmetries is, neglecting background contributions, proportional to $1/\sqrt{N_\mathrm{sig}}$. The statistically limiting factor of the ΔA_{CP} analysis are the number of $D^0 \to \pi^-\pi^+$ candidates. The limiting factor of the $A_{CP}(K^-K^+)$ measurement are the number of $D^0 \to K^-K^+$ candidates and as shown later in Chapter 8 the number long-reconstructed $D^+ \to \overline{K}^0\pi^+$ candidates.

---

[10] due to limited patience of the author.

Chapter 7

Measurement of raw asymmetries

The raw asymmetries of muon-tagged D^0 and prompt D^+ decays are obtained from fits to the invariant mass distributions of reconstructed D^0 and D^+ candidates. The invariant mass distributions are shown in Figures 6.6 and 6.12, respectively. The shapes of signal and background contributions have to be modelled to extract the corresponding signal yields. The fits are performed simultaneously in the samples of negatively- and positively-tagged events to determine the raw asymmetries.

This chapter is structured as follows: First, possible background contributions are systematically studied. Second, the raw asymmetries of each decay channel in bins of the reconstructed D masses are discussed. Third, the fit models of the invariant mass distributions are introduced. Fourth, the raw asymmetries of muon-tagged D^0 and prompt D^+ decays are measured separately for each magnet polarity and year. The last part of the chapter additionally illustrates that raw asymmetries depend on the kinematics of the particles involved in the decays of c and b hadrons.

7.1 Background contributions to semileptonic *B* decays

The observed asymmetry of a class of events depends on its physics context. Background events typically have different sources of detection and production asymmetries than the signal decays. In order to develop a fit model to extract raw asymmetries from the invariant mass distributions, possible background contributions are studied.

The contributions from combinatorial background are generally small in the decay channels considered in this analysis, especially in the muon-tagged $D^0 \to K^-\pi^+$ and prompt D^+ samples, see Figures 6.6 and 6.12. As these decay modes are Cabibbo-favoured, any physical background is relatively suppressed and background contributions below the signal peak have a small impact on the asymmetry determination. Consequently, the following discussion focuses on physical background contributions to the muon-tagged $D^0 \to K^-K^+$ and $D^0 \to \pi^-\pi^+$ samples.

The expected rate of different background sources can be estimated by looking at observed branching fractions of b- and c-hadron decays in the PDG [16]. If a background category is expected to contribute significantly, the reconstructed mass distribution is studied with fully simulated events.[1] The background contributions are divided into two categories: *The first category* are background events from correctly reconstructed two-body D^0 decays where the D^0 mesons do not originate from semileptonic B decays.

---

[1] Unfortunately, not for all decays a simulated sample was available at the time of this work.

An example are prompt D^0 decays combined with a random muon candidate in the event. A further possibility is the case that the other b hadron decay involves a muon. These peaking backgrounds are hard to distinguish from signal decays as the numbers of signal decays is determined from the D^0 mass distribution. However, the muon charge might give wrong flavour tags in these cases. This background source and the measurement of the mistag probability is discussed in more detail in Chapter 10. *The second category* are candidates where no real signal D^0 decay is reconstructed. The following physical backgrounds are discussed within this section:

- *Reflection background* from two-body D^0 decays where the final state particles are misidentified and wrong mass hypotheses are assigned to them.
- *Multi-body D decays* from three- and more-body D decays. The D meson is either originating from the primary interaction or more likely from a B decay. These candidates do not have a sharp peak in the reconstructed mass due to at least one missed particle. The partially-reconstructed D mass might fall into the mass range chosen in the analysis.
- *Multi-body B decays* from four- and more-body B decays. The decay products of the B meson originate from the same vertex unlike the multibody D decays where two displaced vertices are present in the event. Examples are $B \to J/\psi \pi^{\pm} X$ and $B \to J/\psi K^{\pm} X$ decays where one of the muons is used as the tagging muon and the other used in the D^0 reconstruction, see also Chapter 6.3.4.
- $\Lambda_b \to \Lambda_c \mu^- \overline{\nu}_{\mu} X$ *decays* where the decay products of Λ_c decays are used to reconstruct D^0 candidates and muons from semileptonic Λ_b decays are used to tag the fake D^0 candidates.

7.1.1 Reflection background

Reflection backgrounds arise due to assignments of wrong mass hypotheses when particles are falsely identified. The dominant reflection source of reconstructed $D^0 \to K^- K^+$ and $D^0 \to \pi^- \pi^+$ decays are Cabibbo-favoured $D^0 \to K^- \pi^+$ decays. The misidentification probability of kaons as pions is on the per cent level in the relevant momentum range and for the selection cut applied, see Figure 4.8 and Table 6.4. The $D^0 \to K^- \pi^+$ branching fraction is $(3.88 \pm 0.05)\,\%$, whereas the branching fraction of $D^0 \to K^- K^+$ is and $D^0 \to \pi^- \pi^+$ decays is $(0.396 \pm 0.008)\,\%$ and $(0.1401 \pm 0.0027)\%$, respectively. Thus, a significant amount of true $D^0 \to K^- \pi^+$ decays will pass the $D^0 \to K^- K^+$ and $D^0 \to \pi^- \pi^+$ selection.

The shape of this type of reflection is seen in Figure 7.1. A sample of simulated $D^0 \to K^- \pi^+$ events where the D^0 originated from a B meson is reconstructed with all three mass hypotheses. The particle identification cuts used in the selection are applied for the given mass hypothesis. The reflection of $D^0 \to K^- \pi^+$ decays in the reconstructed $D^0 \to \pi^- \pi^+$ sample is to the left of the signal peak and for $D^0 \to K^- K^+$ decays to the right of the peak. In both cases there is only a very small leakage into the signal region. Here and in the distributions obtained in data, see Figure 6.6, the amount of reflection background is higher for $D^0 \to \pi^- \pi^+$ candidates than for $D^0 \to K^- K^+$ candidates. Additionally, the mass resolution of $D^0 \to \pi^- \pi^+$ decays is worse compared to the mass

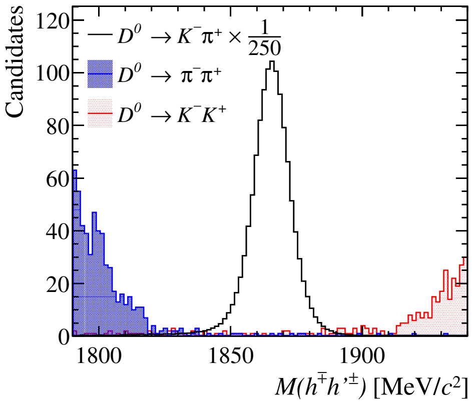

Figure 7.1: The invariant D^0 mass distributions of reconstructed $D^0 \to K^-\pi^+$, $D^0 \to K^-K^+$ and $D^0 \to \pi^-\pi^+$ candidates using simulated $\overline{B} \to D^0\mu^-X$, $D^0 \to K^-\pi^+$ decays. The reconstructed D^0 candidates are associated to simulated $D^0 \to K^-\pi^+$ decays. The number of $D^0 \to K^-\pi^+$ candidates per bin is scaled by 1/250.

resolution of $D^0 \to K^-K^+$ decays as the momentum uncertainty has a larger effect due to a higher Q value. Hence, the reflection background in reconstructed $D^0 \to \pi^-\pi^+$ decays is taken into account in the fit model. The mass fit range of $D^0 \to K^-K^+$ candidates is restricted to be smaller than 1920 MeV/c^2 and no reflection background is considered in the fit to the invariant mass distribution.

7.1.2 Multi-body B decays

The trigger selection is optimised to reconstruct inclusively all possible b-hadron decays. The off-line selection then tries to discriminate $\overline{B} \to D^0\mu^-X$ decays from other multi-body B decays. The distinct signature is a displaced muon and two displaced vertices in the event. However, there is only a loose requirement that the D^0 decay vertex is separated from the $D^0\mu^-$ vertex by requiring that the reconstructed D^0 decay time is larger than zero, cf. Chapter 6.3.3.

Hadronic three-body B decays like the decay $B^+ \to \overline{D}^0\pi^+$ where the pion is misidentified as a muon are rejected by requiring that the reconstructed B mass is smaller than 5 GeV/c^2. The mass of a fully reconstructed B decay is larger than this threshold even when wrong mass hypotheses are assigned to the decay products.

As shown before in Chapter 6.3.4, the selection is susceptible to $B \to J/\psi\,\pi^\pm X$ or $B \to J/\psi\,K^\pm X$ decays. This is expected from the measured branching fractions. The B decays involving a J/ψ meson with the largest branching fraction are $B^+ \to J/\psi\,K^+$ and $B^0 \to J/\psi\,K^+\pi^-$ decays, the branching fractions are $(1.016 \pm 0.033) \times 10^{-3}$ and $(1.2 \pm 0.6) \times 10^{-3}$, respectively. The $J/\psi \to \mu^+\mu^-$ branching fraction is $(5.93 \pm 0.06)\,\%$. Therefore, $\mu^+\mu^-X$ final states have a relative abundance of more than (0.6×10^{-5}) which is comparable to the relative abundance of $D^0 \to K^-K^+$ and $D^0 \to \pi^-\pi^+$ decays originating from a semileptonic B decay.[2] A significant contribution to the background

---

[2] As a reminder, the semileptonic branching fraction is roughly 10 %, the branching fraction of $D^0 \to K^-K^+$ decays is $(3.96 \pm 0.08) \times 10^{-3}$ and the branching fraction of $D^0 \to \pi^-\pi^+$ decays is

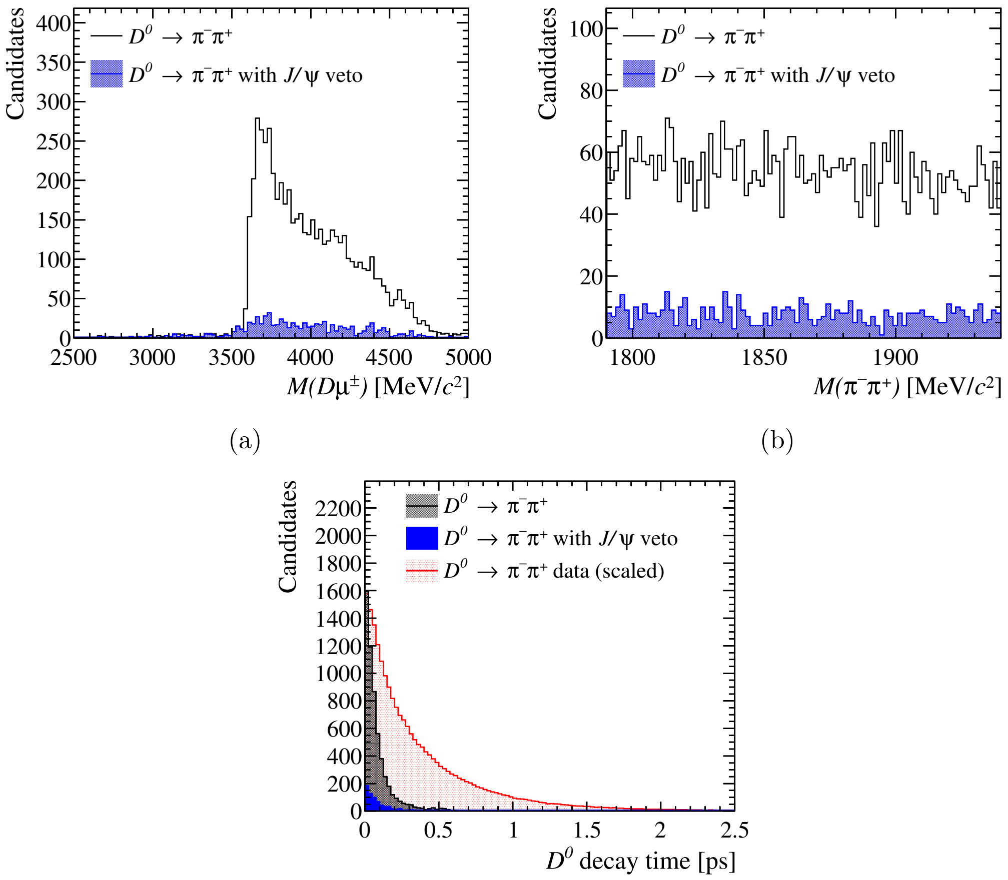

(a) (b)

(c)

Figure 7.2: The invariant (a) B and (b) D^0 mass distribution of reconstructed $D^0 \to \pi^-\pi^+$ candidates in a simulated $B \to J/\psi X$ sample. (c) The reconstructed D^0 decay time. The distribution obtained in data is overlaid as reference.

is expected and also observed from this class of B decays. In such a background event one muon from the J/ψ decay is used to tag the decay. The oppositely charged muon is combined with another B decay product to form a fake D^0 candidate.

The invariant D^0 mass distribution of this type of events is studied with a a sample of simulated $B \to J/\psi X$ decays. The simulated events are reconstructed with the selection of muon-tagged $D^0 \to \pi^-\pi^+$ decays. The invariant B mass and D^0 mass distributions are shown in Figure 7.2 with and without the J/ψ veto, cf. Chapter 6.3.4. As in many cases at least one particle is not reconstructed, the reconstructed $D^0\mu^-$ mass is below 5 GeV/c^2. Fully reconstructed decays like $B^+ \to J/\psi K^+$ have already been rejected by the selection as explained above. A peaking structure above the J/ψ mass threshold is seen in the $D^0\mu^-$ mass distribution without the J/ψ veto. This peak has been observed in data but is not visible in the distributions in Figure 6.7 as the J/ψ veto has already been applied. As seen in Figure 7.2b, the distribution of the reconstructed

---

$(1.402 \pm 0.026) \times 10^{-3}$.

D^0 mass is flat with and without the J/ψ veto. In Figure 7.2c it is shown that this type of background has low reconstructed D^0 decay times. Therefore, about half of the remaining background contribution is rejected by requiring a decay time larger than zero.

Multi-body hadronic B decays involving D^0 or D^+ mesons are a subset of the peaking backgrounds covered in Chapter 10 and the multi-body D decays discussed in the next section. Charmless hadronic B decays are Cabibbo-suppressed and disfavoured by the selection as there is no muon in the final state. They likely contribute to the combinatorial background.

7.1.3 Multi-body *D* decays

Prompt D decays are effectively rejected by the trigger and off-line selection which requires all reconstructed final state particles to be displaced from the primary vertex. Additionally, the cut on the invariant B mass is a discriminator against prompt decays like D^* resonances with a mass smaller than $2.5\,\mathrm{GeV}/c^2$ which decay into D mesons and one or more light hadrons. Consequently, if a pion from the D^* decay is misidentified as a muon, the fake B candidate is rejected due to the invariant mass cut. However, it is possible to combine a real prompt D^0 meson with a random muon candidate or a true muon from the other c-hadron decay in the event. In the latter case the tag due to the muon charge is correct and the event is accepted as a signal candidate.

The rejection of prompt D^0 decays is tested with a sample of one million simulated $D^* \to D^0\pi^+$ decays where the D^0 decays to $\pi^-\pi^+$. The muon-tagged D^0 candidate is reconstructed with the full trigger and off-line selection. The simulated D^* originates either from a $c\bar{c}$ or $b\bar{b}$ pair according to the measured relative production cross sections. In the end 181 reconstructed D^0 candidates are associated to simulated $D^0 \to \pi^-\pi^+$ decays. It is found that all candidates come from simulated B decays. Thus, it is assumed that most of the reconstructed D^0 candidates originate from B decays, even if the D mesons are not fully reconstructed.

The only two-body decays with exactly two charged particles in the final state are the decays $D^0 \to K^-K^+$, $D^0 \to \pi^-\pi^+$, $D^0 \to K^-\pi^+$ and $D^0 \to K^+\pi^-$. All other reconstructed c hadrons are partially reconstructed. Possible background sources are listed in the following:

- **Neutral *D* decays**: The most likely backgrounds are
  - $D^0 \to K^-\pi^+X$ decays.
  - $D^0 \to K^-K^+X$ decays.
  - $D^0 \to \pi^-\pi^+X$ decays.

  In most cases X is a π^0 meson. The branching ratio of $D^0 \to \pi^-\pi^+\pi^0$ decays, $(1.43 \pm 0.06)\,\%$, is about ten times higher than for $D^0 \to \pi^-\pi^+$ decays. The branching ratio of $D^0 \to K^-K^+\pi^0$ decays, $(0.328 \pm 0.14)\,\%$), is similar to that of $D^0 \to K^-K^+$ decays. Consequently, this background source is expected mainly in the reconstructed $D^0 \to \pi^-\pi^+$ sample. In both reconstructed decay modes the invariant mass is shifted away from the signal peak due the missing π^0 meson. The very small hump on the left side of the $D^0 \to K^-K^+$ mass range in Figure 6.6a

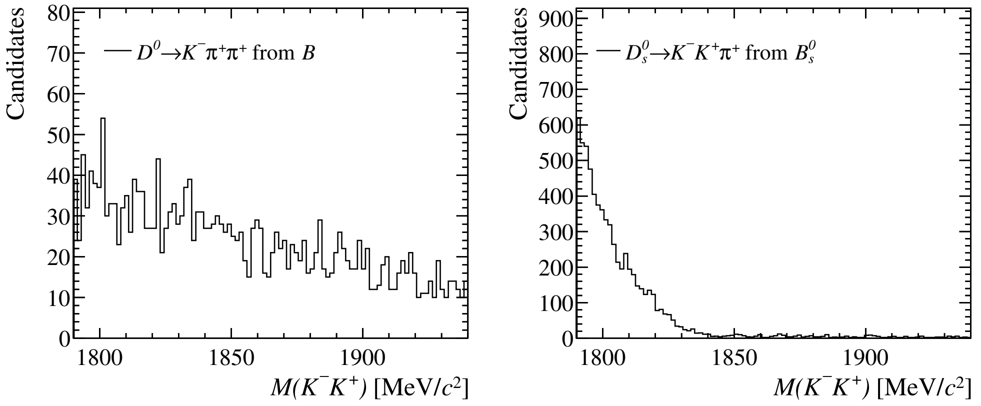

(a) (b)

Figure 7.3: (a) The invariant K^-K^+ mass distribution of reconstructed $D^0 \to K^-K^+$ candidates obtained from simulated $\overline{B} \to D^+\mu^-X$, $D^+ \to K^-\pi^+\pi^+$ events. The D^0 candidates are associated to true D^+ decays. (b) The invariant K^-K^+ mass distribution of reconstructed $D^0 \to K^-K^+$ candidates obtained from simulated $B_s^0 \to D_s^+\mu X$, $D_s^+ \to K^-K^+\pi^+$ decays. The D^0 candidates are associated to true D_s^+ decays.

is likely coming from this type of background. For $D^0 \to \pi^-\pi^+$ candidates it appears below the reflection peak. Therefore, the mass range of reconstructed $D^0 \to K^-K^+$ decays is restricted to values larger than 1810 MeV/c^2.

The branching fraction of $D^0 \to K^-\pi^+\pi^0$ decays is large, $(13.9 \pm 0.5)\,\%$. It cannot leak into the $D^0 \to \pi^-\pi^+$ mass range due to the missing mass. But if a pion is misidentified as a kaon candidate, the wrong mass hypothesis is assigned to the kaon candidate. As this increases the reconstructed mass by roughly 400 MeV/c^2, misreconstructed events will appear in the $D^0 \to K^-K^+$ mass range. The shape of the reconstructed $D^0 \to K^-K^+$ mass distribution is expected to be similar to that of a misreconstructed three-body $D^+ \to K^-\pi^+\pi^+$ decay which is shown in Figure 7.3a. The shape of the distribution does not peak anywhere in the mass range and can be modelled with an exponential function or a polynomial.

- **D^+ decays**: The majority of this background type comes from:
  - $D^+ \to K^-\pi^+\pi^+$, $\Gamma_i/\Gamma = (9.13 \pm 0.19)\,\%$. This is a possible background source in the $D^0 \to K^-K^+$ sample when one of the pions is misidentified as a kaon candidate. The shape of the invariant K^-K^+ mass distribution is shown in Figure 7.3a. The same statement as for $D^0 \to K^-\pi^+\pi^0$ decays holds.
  - $D^+ \to K^-K^+\pi^+$, $\Gamma_i/\Gamma = (0.954 \pm 0.026)\,\%$. If this decay is reconstructed as a $D^0 \to \pi^-\pi^+$ decay, the reconstructed D^0 mass is at least 500 MeV/c^2 away from the real D^0 mass. Reconstructed as a $D^0 \to K^-K^+$ decay, the tails of the distribution might be visible at the lower edge of the mass window.
  - $D^+ \to \pi^-\pi^+\pi^+$ decays, $\Gamma_i/\Gamma = (0.318 \pm 0.018)\,\%$, are a possible background source in the $D^0 \to \pi^-\pi^+$ sample. Only the lower edge of the mass window

can be affected due to the missing mass.

- **D_s^+ decays**: This type of background is similar to that of misreconstructed D^+ decays. The main contributions come from:
    - $D_s^+ \to K^+K^-\pi^+$ decays, $\Gamma_i/\Gamma = (5.49 \pm 0.27)\,\%$, are a source of background in the $D^0 \to K^-K^+$ sample. The higher D_s^+ mass partially compensates the missing particle. In Figure 7.3b it can be seen that this affects the low end of the mass spectrum.
    - $D_s^+ \to \pi^+\pi^-\pi^+$ decays, $\Gamma_i/\Gamma = (1.10 \pm 0.06)\,\%$, are a source of background in the $D^0 \to \pi^-\pi^+$ sample. Due to the higher D_s^+ mass, this background might appear in the lower mass range similar to the previous one.
- **Semileptonic D decays**: Most likely background sources come from:
    - $D^0 \to K^-\mu^+\nu_\mu$ decays, $\Gamma_i/\Gamma = (3.3 \pm 0.13)\,\%$.
    - $D^0 \to \pi^-\mu^+\nu_\mu$ decays, $\Gamma_i/\Gamma = (0.237 \pm 0.024)\,\%$.
    - $D^+ \to K^-\pi^+l^+\nu_l$ decays with $l = \mu, e$, $\Gamma_i/\Gamma \approx 7.8\%$.

  While the branching ratio is higher for the first decay, the probability to identify a muon as a kaon is smaller than to identify it as a pion. Therefore, the first two decays are expected to contribute each to reconstructed $D^0 \to K^-K^+$ and $D^0 \to \pi^-\pi^+$ decays. The latter decay can only be a potential background in the $D^0 \to K^-K^+$ sample. These background sources are not expected to peak anywhere because two particles are not reconstructed and one wrong mass is assigned.

7.1.4 $\Lambda_b \to \Lambda_c\,\mu^-\,\overline{\nu}_\mu X$ decays

The semileptonic decay of a Λ_b baryon, $\Lambda_b \to \Lambda_c\,\mu^-\,\overline{\nu}_\mu X$, has a similar signature as a semileptonic B decay. The trigger and off-line criteria also select this decay. The Λ_c decay with the highest branching fraction, $\Gamma_i/\Gamma = (5.0 \pm 1.3)\%$, is $\Lambda_c \to pK^-\pi^+$. When reconstructing this decay as a $D^0 \to h^-h^+$ decay, always one particle is missed and one particle is assigned a wrong mass hypothesis. In the $D^0 \to K^-K^+$ sample this background appears as the difference of $m_{\Lambda_c} \approx 2.29\,\mathrm{GeV}/c^2$ and $m_{D^0} \approx 1.87\,\mathrm{GeV}/c^2$ is similar to the wrong mass hypothesis when a proton is misidentified as a kaon. This decay is not a background source for $D^0 \to \pi^-\pi^+$ candidates as the reconstructed invariant mass is always outside of the mass range. The $D^0 \to K^-K^+$ mass distribution of this type of background can be seen in Figure 7.4. The distribution has the shape of a first order polynomial or an exponential function and it affects the whole mass range.

7.1.5 Conclusion

The previous discussion shows that none of the physical multi-body backgrounds, which significantly contribute, shows a peaking structure inside the signal region. The shapes are similar to what is expected from a purely combinatorial background. The only physical background in the mass range which has does not follow this shape is the

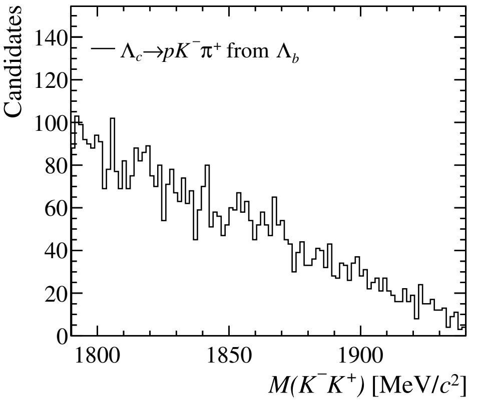

Figure 7.4: The invariant D^0 mass distribution of reconstructed $D^0 \to K^-K^+$ candidates in a simulated $\Lambda_b \to \Lambda_c \mu X$, $\Lambda_c \to pK^-\pi^+$ sample is shown. The D^0 candidates are associated to true Λ_c decays.

reflection background. The background models used in the fit to the invariant mass distributions are explained in Chapter 7.3.

7.2 Dependence of raw asymmetries versus reconstructed mass

The raw asymmetries are extracted from simultaneous fits to the invariant mass distributions of positively- and negatively-tagged events. In this section the raw asymmetry is studied as a function of the reconstructed mass to develop fit models. In order to analyse reconstruction effects, this is done separately for each decay channel, both data taking periods and the two magnet polarities.

The raw asymmetry in bins of the reconstructed D^0 mass is shown in Figures 7.5 and 7.6 for $D^0 \to K^-K^+$ and $D^0 \to \pi^-\pi^+$ candidates, respectively. The raw asymmetry per bin is calculated by counting the number of candidates per tag. The raw asymmetries per bin in the magnet up and the magnet down samples are averaged arithmetically to cancel asymmetries induced by a left–right asymmetric LHCb detector.

First of all, no asymmetries larger than 3 % are present. This justifies the assumption of small asymmetries which is used in Chapter 5 to develop the analysis strategy of measuring ΔA_{CP}. There is a difference between the two polarities in both channels, especially in the background region. The up–down asymmetry is less pronounced in 2012. In general the raw asymmetry is quite flat over the whole mass range. There might be a small trend in the background asymmetry when going from small to large reconstructed masses. This is reflected in the fit model discussed in the next section by using independent functions for each tag with different slope parameters to describe the background contributions.

The raw asymmetry of $D^0 \to K^-\pi^+$ candidates is shown in Figure 7.7. The sample has only a very small background contribution. Even the regions left and right of the peak are likely dominated by the tails of the signal peak. The signal peak has a larger

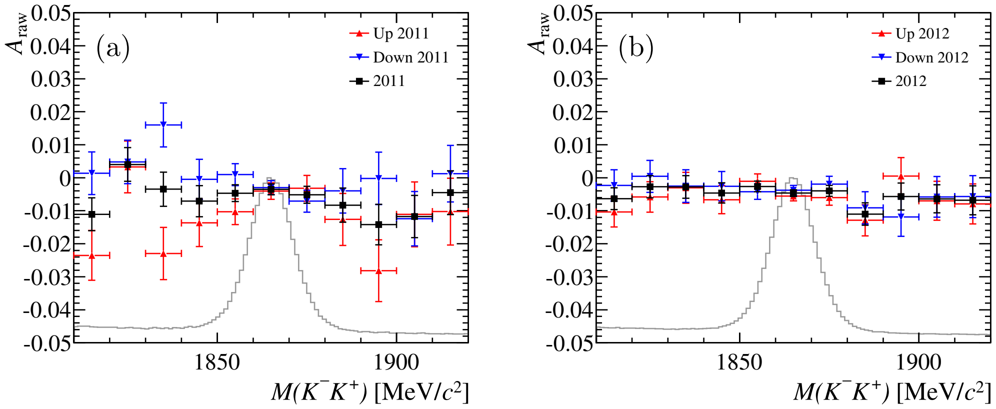

Figure 7.5: The raw asymmetry in bins of the K^-K^+ invariant mass for (a) 2011 and (b) 2012 data. The asymmetry is calculated by counting the numbers of $D^0 \to K^-K^+$ candidates per tag in each bin. The black distributions are the arithmetic mean of the raw symmetries per bin in the magnet up and down samples.

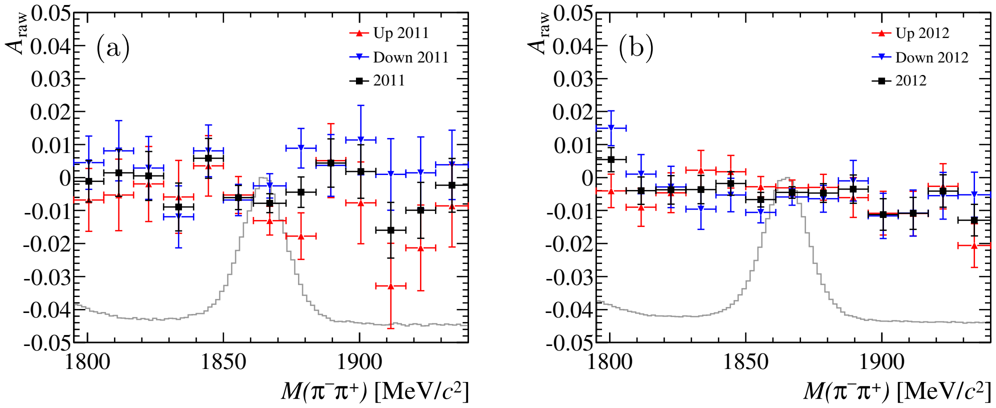

Figure 7.6: The raw asymmetry in bins of the $\pi^-\pi^+$ invariant mass for (a) 2011 and (b) 2012 data. The asymmetry is calculated by counting the numbers of $D^0 \to \pi^-\pi^+$ candidates per tag in each bin increase range. The black distributions are the arithmetic mean of the raw symmetries per bin in the magnet up and down samples.

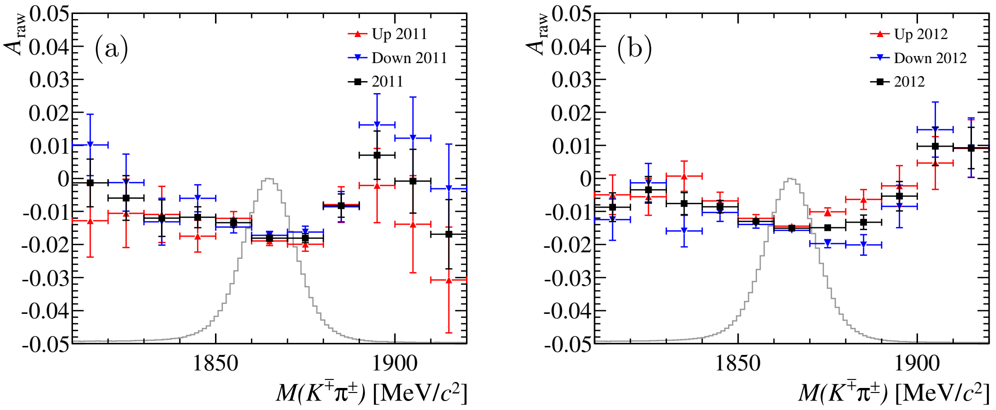

Figure 7.7: The raw asymmetry in bins of the $K^{\mp}\pi^{\pm}$ invariant mass for (a) 2011 and (b) 2012 data. The asymmetry is calculated by counting the numbers of $D^0 \to K^-\pi^+$ candidates per tag in each bin. The black distributions are the arithmetic mean of the raw symmetries per bin in the magnet up and down samples.

tail to the left. The tail is a consequence of final state radiation which leads to a smaller reconstructed mass. The asymmetry is larger in the signal region because of the kaon detection asymmetry which does not necessarily affect the combinatorial background. There is a small downward trend in the signal region. This is due to small differences ($\lesssim 0.01\,\mathrm{MeV}/c^2$) of the reconstructed masses of $K^-\pi^+$ and $K^+\pi^-$ combinations which separates slightly the two signal peaks. This shift induces a raw asymmetry in a specific mass bin. The effect is more pronounced in the prompt D^+ decay modes. It cannot appear in decays to CP eigenstates as the final state of D^0 and $\overline{D}^0$ is exactly the same.

The raw asymmetries per mass bin are shown for $D^+ \to K^-\pi^+\pi^+$ and $D^+ \to \overline{K}^0\pi^+$ candidates in Figure 7.8 and 7.9, respectively. Only the long-reconstructed $D^+ \to \overline{K}^0\pi^+$ sample is considered as the downstream-reconstructed sample is not used in the $A_{CP}(K^-K^+)$ measurement. The raw asymmetries shown here do not exceed 3 %. Hence, the assumption of small asymmetries is also valid for the prompt modes which is important for the $A_{CP}(K^-K^+)$ measurement. There, the raw asymmetries of the two prompt decay modes are used to correct $A_{\rm raw}(K^-\pi^+)$ for $A_D(K^-\pi^+)$. In both figures a clear pattern is visible in the signal region. The pattern arises due to a small shift in the invariant mass distribution between D^+ and D^- candidates. The shift is induced by different biases in the measured momentum of positive and charged particles. The reasons are misalignments of the tracking detectors and a slightly wrong magnetic field map. Therefore, the momentum measurement has to be calibrated to make precise mass measurements as discussed in Chapter 6.3.2. Unfortunately, the applied calibration is less precise than needed here. The fit models of the invariant mass distributions account for this effect by using different mean masses for positively- and negatively-tagged samples when fitting non-CP eigenstates. This shift is more pronounced in the D^+ decay modes than in $D^0 \to K^-\pi^+$ decays as the final state has a net charge. In $D^0 \to K^-\pi^+$ decays this effect can only appear due to different momenta of $K^{\mp}$ and $\pi^{\pm}$ candidates.

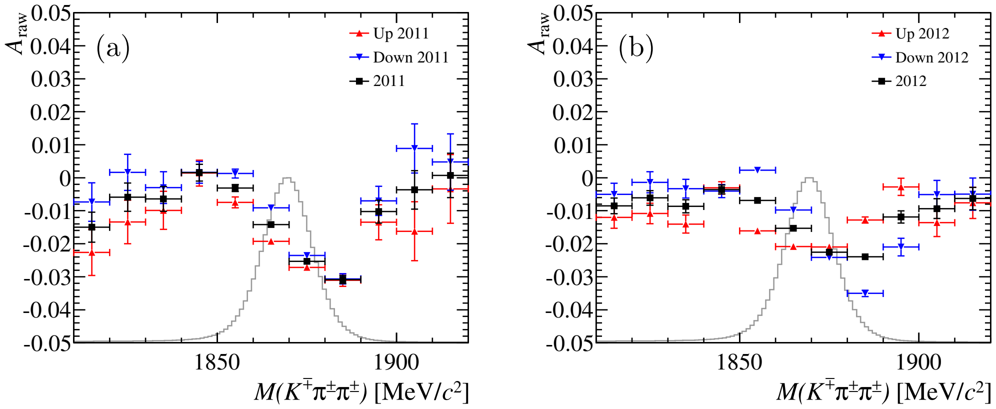

Figure 7.8: The raw asymmetry in bins of the $K^{\mp}\pi^{\pm}\pi^{\pm}$ invariant mass for (a) 2011 and (b) 2012 data. The asymmetry is calculated by counting the numbers of $D^+ \to K^-\pi^+\pi^+$ candidates per tag in each bin. The black distributions are the arithmetic mean of the raw symmetries per bin in the magnet up and down samples.

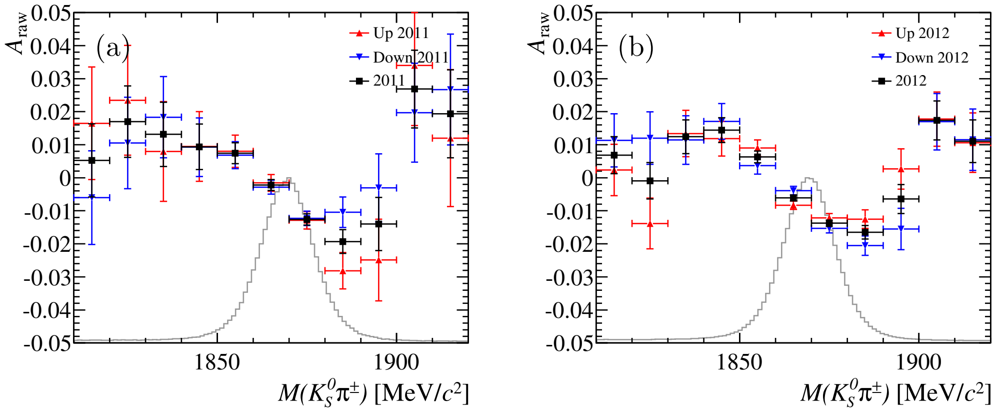

Figure 7.9: The raw asymmetry in bins of the $K^0_{\rm S}\pi^{\pm}$ invariant mass for (a) 2011 and (b) 2012 data. The asymmetry is calculated by counting the numbers of $D^+ \to \overline{K}^0\pi^+$ candidates per tag in each bin. The black distributions are the arithmetic mean of the raw symmetries per bin in the magnet up and down samples.

7.3 Extracting raw asymmetries and fit model

The raw asymmetries are determined by extended maximum-likelihood fits to the binned D^0 and D^+ mass distributions. The same probability density function (PDF) with different parameters is used for all decay modes. The PDF has two dimensions: the reconstructed D^0 mass and the muon charge for muon-tagged D^0 decays or the reconstructed $D^\pm$ mass and the charge of the candidate for the prompt D^+ decay modes. The fit is performed simultaneously in both tags. The advantage of one simultaneous PDF instead of a separate PDF for each tag is that the raw asymmetry is a parameter of the fit. Additionally, signal parameters can be easily shared between the two samples – for example for $D^0 \to K^-K^+$ and $D^0 \to \pi^-\pi^+$ candidates the signal shape does not depend on the tag and, therefore, can be chosen to be the same. In order to not use two different notations for D^0 and D^+ decay modes here, the notation follows the charge of the muon candidate. The explicit asymmetries for all channels are given later.

The PDF has two components, the signal part and the background part. The background has two components, the combinatorial background and the reflection background. The reflection part is only used in the the fit of the $D^0 \to \pi^-\pi^+$ sample. The total PDF of positively- and negatively-tagged events is then given by

$$\mathrm{PDF}_\pm = N^\pm_{\mathrm{sig}}\,\mathrm{PDF}^\pm_{\mathrm{sig}} + N^\pm_{\mathrm{bkg}}\,\mathrm{PDF}^\pm_{\mathrm{bkg}} + N^\pm_{\mathrm{ref}}\,\mathrm{PDF}^\pm_{\mathrm{ref}} \ , \tag{7.1}$$

where $N^\pm_{\mathrm{sig}}$, $N^\pm_{\mathrm{bkg}}$ and $N^\pm_{\mathrm{ref}}$ are the yields of the signal, combinatorial background and reflection background contributions, respectively. $\mathrm{PDF}^\pm_{\mathrm{sig}}$, $\mathrm{PDF}^\pm_{\mathrm{bkg}}$ and $\mathrm{PDF}^\pm_{\mathrm{ref}}$ are the PDFs of each component. They are defined in the following.

The individual signal yields for each tag, $N^\pm_{\mathrm{sig}}$, are parameterised as follows:

$$N^\pm_{\mathrm{sig}} = \frac{N_{\mathrm{sig}}(1 \mp A_{\mathrm{raw}})}{2} \ , \tag{7.2}$$

where the two fit parameters are N_{sig}, the total yield of reconstructed signal events, and A_{raw}, the measured raw asymmetry. The signal shape is described by a sum of a Crystal-Ball function (CB) and a Gaussian. The Crystal-Ball function is an empirical description of a mass distribution with a Gaussian core and an asymmetric tail on one side due to final state radiation [75]. It is defined as

$$\mathrm{CB}(m;\mu,\sigma,\alpha,n) = \frac{1}{\mathcal{N}_{\mathrm{CB}}} \begin{cases} e^{-\frac{(m-\mu)^2}{2\sigma^2}}, & \text{for } \frac{m-\mu}{\sigma} > -\alpha \\ \left(\frac{n}{|\alpha|}\right)^n e^{-\frac{|\alpha|^2}{2}} \left(\frac{n}{\alpha} - \alpha - \frac{m-\mu}{\sigma}\right)^{-n} & \text{for } \frac{m-\mu}{\sigma} \le -\alpha \end{cases} \tag{7.3}$$

where $\mathcal{N}_{\mathrm{CB}}$ is a normalisation factor[3], μ and σ are the parameters of the Gaussian core, α and n describe the asymmetric tail. The signal PDF is the following:

$$\begin{aligned} \mathrm{PDF}_{\mathrm{sig},-} &= f_1\mathrm{CB}(m;\mu,\sigma_1,\alpha,n) + (1-f_1)\mathrm{Gauss}(m;\mu,s\,\sigma_1) \ , \\ \mathrm{PDF}_{\mathrm{sig},+} &= f_1\mathrm{CB}(m;\mu+\Delta\mu,s_p\,\sigma_1,\alpha,n) + (1-f_1)\mathrm{Gauss}(m;\mu+\Delta\mu,s_p\,s\,\sigma_1) \ , \end{aligned} \tag{7.4}$$

where $\mathrm{PDF}_{\mathrm{sig},+}$ is the PDF of positively-tagged events and $\mathrm{PDF}_{\mathrm{sig},-}$ of negatively-tagged events, f_1 is the fraction of the Crystal-Ball function, μ the mean of the signal peak, σ_1

---

[3] A proper normalisation of all PDF components is implied.

the width of the Crystal-Ball, α and n are the tail parameters. The Gaussian has the same mean value μ as the Crystal-Ball function but the width is given by $s\,\sigma_1$. The fraction is defined by $(1-f_1)$. The shift between the mean mass of D and $\overline{D}$ candidates described in the previous section is reflected by the parameter $\Delta\mu$. Additionally, the resolution of one category can be scaled by the factor s_p to accommodate for potential resolution differences of tracks of positive and negative particles. In the decay channels $D^0 \to K^-K^+$ and $D^0 \to \pi^-\pi^+$ $\Delta\mu$ and s_p are fixed to 0 and 1, respectively.

The background yields, $N^{\pm}_{\text{bkg}}$, are parameterised similarly as the signal yields:

$$N^{\pm}_{\text{bkg}} = \frac{N_{\text{bkg}}(1 \mp A_{\text{bkg}})}{2} \quad , \tag{7.5}$$

where N_{bkg} is the total yield of reconstructed background events and A_{bkg} the measured asymmetry of the background events. The combinatorial background shape is described by an exponential function:

$$\begin{aligned} \text{PDF}_{\text{bkg},+} &= \frac{1}{\mathcal{N}_{\text{bkg},+}}\, e^{-a_+\, m} \quad , \\ \text{PDF}_{\text{bkg},-} &= \frac{1}{\mathcal{N}_{\text{bkg},-}}\, e^{-a_-\, m} \quad , \end{aligned} \tag{7.6}$$

where a_+ and a_- are the slope parameters of positively- and negatively-tagged events. The $D^0 \to \pi^-\pi^+$ sample is fitted in the range $[1795, 1940]\,\text{MeV}/c^2$. The reflection contribution, $N^{\pm}_{\text{ref}}$, from $D^0 \to K^-\pi^+$ events at the lower boundary is modelled with a single Gaussian with the same shape parameters, μ_{ref} and σ_{ref}, for both tags and an additional asymmetry parameter, A_{ref}:

$$\begin{aligned} \text{PDF}_{\text{ref},-} &= \text{Gauss}(m; \mu_{\text{ref}}, \sigma_{\text{ref}}) \quad , \\ \text{PDF}_{\text{ref},+} &= \text{Gauss}(m; \mu_{\text{ref}}, \sigma_{\text{ref}}) \quad , \\ N^{\pm}_{\text{ref}} &= \frac{N_{\text{ref}}(1 \mp A_{\text{ref}})}{2} \quad . \end{aligned} \tag{7.7}$$

For the $D^0 \to K^-K^+$ decay mode, the mass range is restricted to $[1810, 1920]\,\text{MeV}/c^2$ in the fit. Hence, the contamination of mis- and partially-reconstructed decays is negligible. The fit ranges of all other decay modes are the same as for the fit to the $D^0 \to K^-K^+$ sample.

7.3.1 Example fits

The fits are performed independently for each decay channel, magnet polarity and year of data taking. Furthermore, the raw asymmetries are determined in several subsets of the data samples later. Therefore, here only one representative fit of each decay channel is discussed in detail. The measured raw asymmetries of each decay mode for every sample are discussed later in Chapter 7.4.

The examples are taken from the raw asymmetry fits to the 2012 magnet up samples. Later, a complete list of fit projections and results of the final *CP* asymmetry determination is found in Chapter 11. The fit to the invariant mass distribution of the $D^0 \to K^-K^+$ sample is discussed in detail in the following. For the other modes the important points are mentioned.

7.3.2 $D^0 \to K^-K^+$

The raw asymmetry of the $D^0 \to K^-K^+$ decay mode is defined as

$$A_{\text{raw}}(K^-K^+) = \frac{N_{\text{sig}}(K^-K^+,\mu^-) - N_{\text{sig}}(K^-K^+,\mu^+)}{N_{\text{sig}}(K^-K^+,\mu^-) + N_{\text{sig}}(K^-K^+,\mu^+)} \ , \tag{7.8}$$

where μ^+ and μ^- indicate the tag. The raw asymmetry is obtained from a fit to the invariant mass distribution in the range $[1810, 1920]\,\text{MeV}/c^2$. Figure 7.10 shows the results of the fit to the 2012 magnet up sample, split into positively- and negatively-tagged events. The ΔA_{CP} trigger line selection is used, cf. Chapter 6.2.4. The figures indicate the fitted yield for each tag as well as the fitted signal asymmetry. The quality of the fit can be judged by the *pull* distribution. The pull in each mass bin is defined as

$$\text{pull}_i = \frac{x_i - \text{PDF}_i}{\sigma_i} \ , \tag{7.9}$$

where x_i is the number of entries in bin i, σ_i the statistical uncertainty of this bin and PDF_i the value of the PDF at the centre of bin i. The distribution is given in the lower part of each figure. A measure of the goodness of a binned maximum-likelihood fit is

$$\chi^2/\text{ndf} = \frac{1}{\text{ndf}} \sum_{i=1}^{N_{\text{bins}}} \text{pull}_i^2 \ , \tag{7.10}$$

where N_{bins} is the number of bins. The number of degrees of freedom (ndf) is given by the number of bins minus the number of non-constrained fit parameters. As each mass distribution has 100 bins per tag, N_{bins} is 200. The number of floating fit parameters is between 10 and 14 depending on the decay channel. The χ^2/ndf of the simultaneous fit in both tag categories is given in the figure of the positive tag. The third figure shows the asymmetry per mass bin overlaid with the projected asymmetry per bin of the fitted PDF. The χ^2 of the fit projection is calculated from the observed asymmetry per mass bin and the fit projection. The number of degrees of freedom of the asymmetry is given by 100 minus the number of fit parameters plus 1 as the total yield is not a degree of freedom of the asymmetry projection. Assuming a χ^2 distribution, the observed χ^2 and the numbers of degrees of freedom correspond to a probability that the selected model describes the data. The probability is given by $P(\chi^2, \mathrm{ndf})$ which is also called p-value.

The χ^2/ndf of the fit shown in Figure 7.10 is 1.07 which corresponds to a p-value of 0.25. The fit to the $D^0 \to K^- K^+$ mass distribution has ten free fit parameters. A mismodelling of the mass distribution has a small effect on the asymmetry determination as a scaling factor which is common to the yields of both tagging categories cancels in the asymmetry determination. Thus, the asymmetry projection has a larger p-value, 0.54. It is more apparent when looking at the Cabibbo-favoured modes.

The fit results of each parameter and their correlation with the fitted raw asymmetry A_{raw} are given in Table 7.2. The raw asymmetry is determined to be $A_{\mathrm{raw}} = (-0.449 \pm 0.12)\,\%$. The background asymmetry A_{bkg} is $(-0.671 \pm 0.19)\,\%$. The fitted mean value of the mass $\mu = (1864.8806 \pm 0.0087)\,\mathrm{MeV}/c^2$ is close to the PDG value ($m_{\mathrm{PDG}} = (1864.86 \pm 0.13)\,\mathrm{MeV}/c^2$ [16]), the averaged width of the signal peak, $\sigma_{\mathrm{av}} \equiv \sigma_1 \sqrt{f_1 + (1 - f_1)s^2}$, is about $6.8\,\mathrm{MeV}/c^2$. The tail parameters of the Crystal-Ball function, α and n, are constrained in the fits to improve the fit stability. Their choice is motivated by a proper description of the asymmetric tail. The values of α and n are given in Table 7.2. The two decay constants of the background PDF, a_+ and a_-, are consistent with each other. Therefore, the background contribution has the same asymmetry over the whole mass range.

The fitted signal asymmetry is uncorrelated to the shape parameters of the signal which are μ, σ_1 and s. The largest correlation coefficient is that of A_{raw} and A_{bkg} with a value (-0.247). The only other significant correlations of A_{raw} are the shape parameters of the combinatorial background distribution, at the low per cent level.

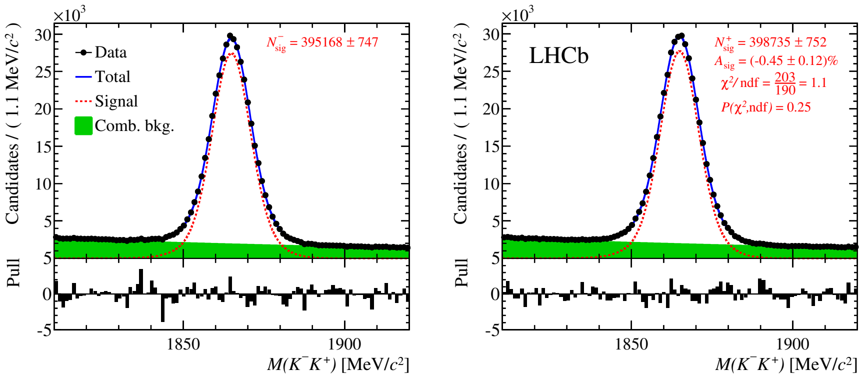

(a) μ^--tagged (b) μ^+-tagged

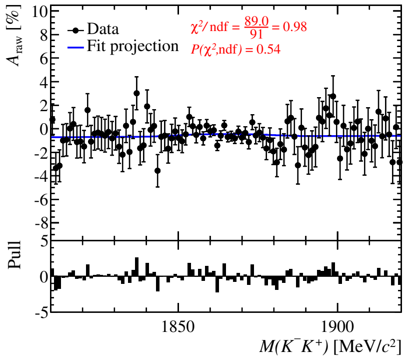

(c) Asymmetry

Figure 7.10: Invariant mass distributions of (a) μ^--tagged and (b) μ^+-tagged $D^0 \to K^-K^+$ candidates. (c) The raw asymmetry as function of the invariant mass. The projection from the fit is overlaid. The 2012 magnet up sample is used.

Table 7.2: The fit parameters and correlation coefficients with A_{raw} corresponding to Figure 7.10.

Parameter	**Fit result**	**Correlation with A_{raw}**
A_{raw} [%]	-0.449 ± 0.12	1.00
A_{bkg} [%]	-0.671 ± 0.19	-0.247
μ [MeV/c^2]	1864.8806 ± 0.0087	-0.001
σ_1 [MeV/c^2]	5.491 ± 0.030	0.00
a_+ $[(100\,\text{MeV}/c^2)^{-1}]$	-0.58039 ± 0.0072	0.03
a_- $[(100\,\text{MeV}/c^2)^{-1}]$	-0.57816 ± 0.0073	-0.031
f_1	0.670 ± 0.014	-0.000
N_{bkg}	408850 ± 939	0.00
N_{sig}	793904 ± 1126	-0.002
s	1.631 ± 0.014	-0.002
$\Delta\mu$ [MeV/c^2]	0.0	-
α	2.70	-
n	1.50	-
s_p	1.00	-

7.3.3 $D^0 \to \pi^-\pi^+$

The raw asymmetry of the $D^0 \to \pi^-\pi^+$ decay mode is defined as

$$A_{\mathrm{raw}}(\pi^-\pi^+) = \frac{N_{\mathrm{sig}}(\pi^+\pi^-, \mu^-) - N_{\mathrm{sig}}(\pi^+\pi^-, \mu^+)}{N_{\mathrm{sig}}(\pi^+\pi^-, \mu^-) + N_{\mathrm{sig}}(\pi^+\pi^-, \mu^+)} \ , \tag{7.11}$$

Figure 7.11 shows the fitted mass distributions of $D^0 \to \pi^-\pi^+$ candidates of the 2012 magnet up sample. The fit range is $[1795, 1940]\,\mathrm{MeV}/c^2$. Each mass distribution has 100 bins per tag. The fit to the $D^0 \to \pi^-\pi^+$ mass distribution has 14 free fit parameters. Three parameters are needed to model the reflection background. Similarly to the $D^0 \to K^-K^+$ fit, the tail parameters of the Crystal-Ball function, α and n, are constrained to improve the fit stability. The invariant mass distribution is well described by the chosen model. The χ^2/ndf of the shown mass fit is 0.94 which corresponds to a p-value of 0.71. The p-value of the asymmetry projection is 0.78.

Table 7.4 shows the fit results of each parameter and their correlation with the fitted signal asymmetry. As in the $D^0 \to K^-K^+$ sample, the fitted mean value of the mass $\mu = 1864.664 \pm 0.022\,\mathrm{MeV}/c^2$ is close to the PDG value, the averaged width of the signal peak, $\sigma_1\sqrt{f_1 + (1-f_1)s^2}$, is around $8.7\,\mathrm{MeV}/c^2$. The mass resolution is worse compared to $D^0 \to K^-K^+$ candidates because the Q value of the decay is larger. Thus, the momentum uncertainty of the decay products contributes more to the invariant mass measurement. The two decay constants of the background model are consistent with each other at the 2σ level.

As for the $D^0 \to K^-K^+$ sample, the fitted signal asymmetry is not correlated to the shape parameters of the signal. The correlations of A_{raw} with A_{bkg} and A_{ref} are (-0.349) and $(+0.16)$, respectively. The shape parameters of the combinatorial background distribution, a_+ and a_-, have a correlation with A_{raw} of (-0.076) and $(+0.06)$, respectively.

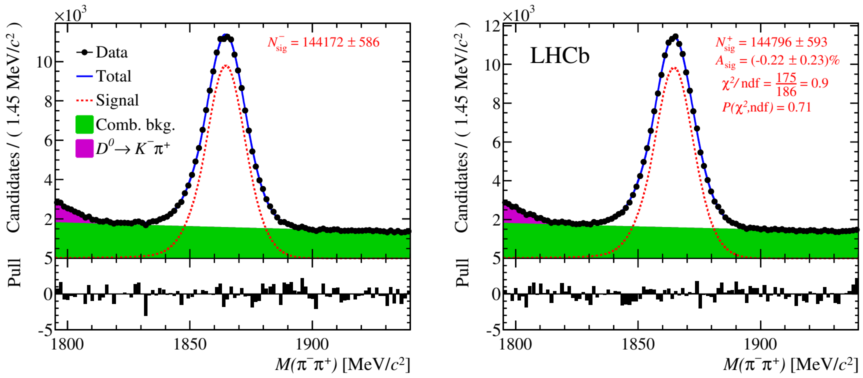

(a) μ^--tagged (b) μ^+-tagged

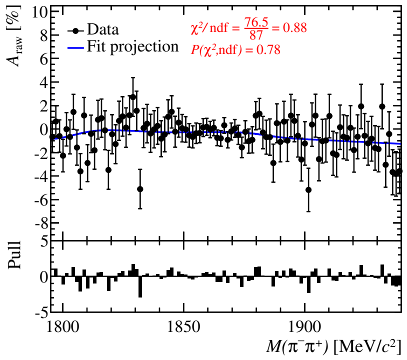

(c) Asymmetry

Figure 7.11: Invariant mass distributions of (a) μ^--tagged and (b) μ^+-tagged $D^0 \to \pi^-\pi^+$ candidates. (c) The raw asymmetry as function of the invariant mass. The projection from the fit is overlaid. The 2012 magnet up sample is used.

Table 7.4: The fit parameters and correlation coefficients with A_{raw} corresponding to Figure 7.11.

Parameter	**Fit result**	**Correlation with A_{raw}**
A_{raw} [%]	-0.216 ± 0.23	1.00
A_{bkg} [%]	-0.507 ± 0.24	-0.349
A_{ref} [%]	-2.77 ± 2.2	0.16
μ_{ref} [MeV/c^2]	1792.8 ± 1.1	0.01
μ [MeV/c^2]	1864.664 ± 0.022 [MeV/c^2]	-0.001
σ_1 [MeV/c^2]	6.425 ± 0.071	-0.005
σ_{ref} [MeV/c^2]	9.60 ± 0.60	-0.012
a_+ $\left[\left(100\,\text{MeV}/c^2\right)^{-1}\right]$	-0.19144 ± 0.0097	-0.076
a_- $\left[\left(100\,\text{MeV}/c^2\right)^{-1}\right]$	-0.21135 ± 0.0094	0.06
f_1	0.350 ± 0.018	-0.008
f_{ref}	0.0477 ± 0.0017	-0.016
N_{bkg}	317985 ± 1343	0.01
N_{sig}	288969 ± 978	-0.010
s	1.508 ± 0.017	-0.001
$\Delta\mu$ [MeV/c^2]	0.00	-
α	1.50	-
n	2.00	-
s_p	1.00	-

7.3.4 $D^0 \to K^-\pi^+$

The third semileptonic mode is the $D^0 \to K^-\pi^+$ decay channel. The raw asymmetry is defined as

$$A_{\mathrm{raw}}(K^-\pi^+) = \frac{N_{\mathrm{sig}}(K^-\pi^+ \text{ or } K^+\pi^-, \mu^-) - N_{\mathrm{sig}}(K^+\pi^- \text{ or } K^-\pi^+, \mu^+)}{N_{\mathrm{sig}}(K^-\pi^+ \text{ or } K^+\pi^-, \mu^-) + N_{\mathrm{sig}}(K^+\pi^- \text{ or } K^-\pi^+, \mu^+)} \quad . \tag{7.12}$$

The tag of a candidate is given exclusively by the charge of the muon candidate. The Cabibbo-favoured $D^0 \to K^-\pi^+$ and the doubly Cabibbo-suppressed $D^0 \to K^+\pi^-$ decays are included in the μ^--tagged events. The charge-conjugate decays are tagged by a μ^+ candidate. The raw asymmetry is obtained from a fit to the invariant mass distribution in the range $[1810, 1920]\,\mathrm{MeV}/c^2$. One tail parameter of the Crystal-Ball function is constrained, similarly to the fits to invariant mass distributions of $D^0 \to K^-K^+$ and $D^0 \to \pi^-\pi^+$ decays.

The fit results are given in Figure 7.12 and Table 7.6. The selected mass model is obviously not sufficient to fully describe the mass distribution. The choice of the fit model has been driven by the decision to have a simple and uniform model across all decay channels. This simplifies the analysis procedure, especially when fitting in a large number of sub-samples where event yields are low. In this case, clear patterns are visible in the pull distributions. Additionally, the p-value of the mass fit is zero. The pull distribution of the asymmetry projection is normal as the patterns are similar for the positively- and negatively-tagged sample. The asymmetry projection has a p-value of 0.2. The systematic uncertainties due to the fit model are discussed in Chapter 13.1.1 where different parameterisation of the background and the signal shape are tested.

The shift of the mean mass $\Delta\mu$ and the resolution scaling factor s_p between the D^0 and $\overline{D}^0$ tagged events are floating parameters in the minimisation procedure as the $K^\mp\pi^\pm$ final state is no *CP* eigenstate. The results are $\Delta\mu = (-0.0091 \pm 0.0090)\,\mathrm{MeV}/c^2$ and $s_p = 0.9960 \pm 0.0011$. For some samples the fit favours a small shift in the mean mass, e.g., in the fit to 2012 down sample $\Delta\mu$ equals $(0.0435 \pm 0.0093)\,\mathrm{MeV}/c^2$, cf. Table C.7.

As in the other modes, A_{raw} has the largest correlation with A_{bkg}, (-0.225). Additionally, the resolution scaling factor s_p is correlated to A_{raw} by (-0.124) as the scaling directly affects the measured yields of negatively- and positively-tagged events. The other correlations are small.

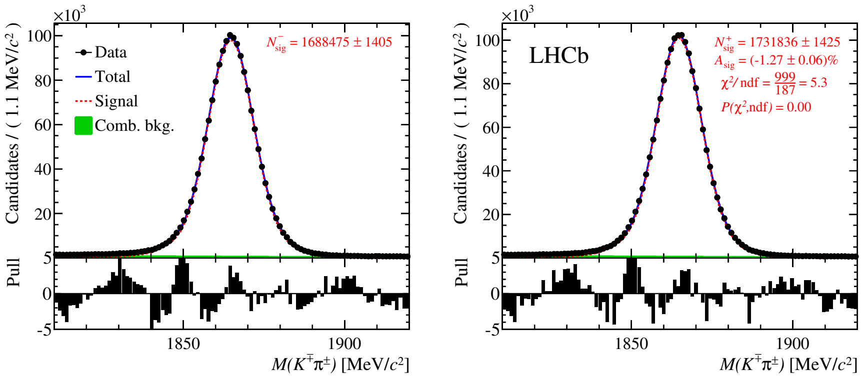

(a) μ^--tagged (b) μ^+-tagged

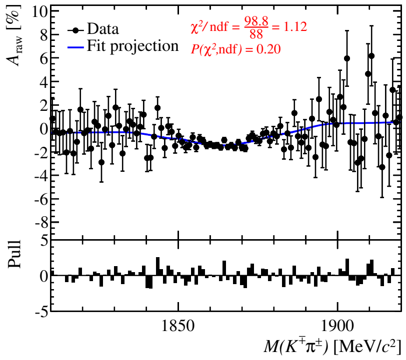

(c) Asymmetry

Figure 7.12: Invariant mass distributions of (a) μ^--tagged and (b) μ^+-tagged $D^0 \to K^-\pi^+$ candidates. (c) The raw asymmetry as function of the invariant mass. The projection from the fit is overlaid. The 2012 magnet up sample is used.

Table 7.6: The fit parameters and correlation coefficients with A_{raw} corresponding to Figure 7.12.

Parameter	**Fit result**	**Correlation with A_{raw}**
A_{raw} [%]	-1.2678 ± 0.056	1.00
A_{bkg} [%]	0.07 ± 0.35	-0.225
$\Delta\mu$ [MeV/c^2]	-0.00910 ± 0.0090	0.01
α	2.2674 ± 0.0065	0.00
μ [MeV/c^2]	1864.7058 ± 0.0065	-0.007
σ_1 [MeV/c^2]	6.547 ± 0.014	0.03
a_+ $[(100\,\text{MeV}/c^2)^{-1}]$	-0.5964 ± 0.013	0.00
a_- $[(100\,\text{MeV}/c^2)^{-1}]$	-0.5815 ± 0.013	-0.003
f_1	0.6944 ± 0.0042	-0.003
N_{bkg}	208491 ± 1033	0.00
N_{sig}	3420313 ± 2069	-0.001
s	1.6682 ± 0.0045	-0.001
s_p	0.9960 ± 0.0011	-0.124
n	1.50	-

7.3.5 $D^+ \to K^-\pi^+\pi^+$

The sample with the highest event yield is the $D^+ \to K^-\pi^+\pi^+$ sample. The raw asymmetry is defined as

$$A_{\text{raw}}(K^-\pi^+\pi^+) = \frac{N_{\text{sig}}(D^+ \to K^-\pi^+\pi^+) - N_{\text{sig}}(D^- \to K^+\pi^-\pi^-)}{N_{\text{sig}}(D^+ \to K^-\pi^+\pi^+) + N_{\text{sig}}(D^- \to K^+\pi^-\pi^-)} \ . \tag{7.13}$$

The fitted mass distributions of the 2012 magnet up sample are shown in Figure 7.13 and the fit results are given in Table 7.8. The fit range is $[1810, 1920]\,\text{MeV}/c^2$. Non of the parameters is constrained in the minimisation procedure. From the residuals it is obvious that the signal description is insufficient to describe the signal peak. As the fitted asymmetry is largely uncorrelated to the signal parameters, the asymmetry is still well described over the whole mass range. The p-value is only 0.06. Therefore, it is important that different fit models are investigated in the systematic studies, c.f. Section 13.1.1.

The background contributes only 4 % to the total event yield in the full mass range. The fitted mean value of the mass, $\mu = (1869.3885 \pm 0.0028)\,\text{MeV}/c^2$, is close to the PDG value of $1869.62 \pm 0.15\,\text{MeV}/c^2$ [16]. In this sample the mean mass shift $\Delta\mu$ between D^+ and D^- candidates is not significant. This is rather a coincidence as in the other three samples significant shifts of up to $(0.1738 \pm 0.0056)\,\text{MeV}/c^2$ are observed, cf. Table C.9. Additionally, the fit result suggests a significant resolution difference of D^+ and D^- candidates as the scaling of the width s_P is fitted to 0.99392 ± 0.00047. The two decay constants of the background are consistent with each other.

Most parameters are largely uncorrelated to the fitted asymmetry. The asymmetry of the background has a correlation of (-0.206) and the scaling of the width between D^+ and D^- has a correlation of (-0.091) with the fitted signal asymmetry A_{raw}.

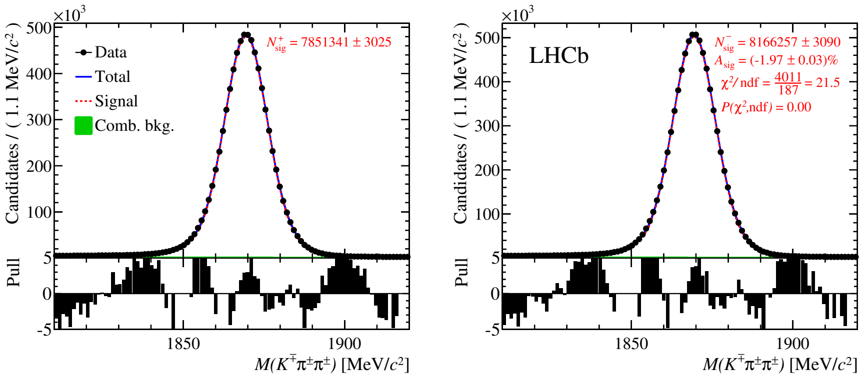

(a) D^+-tagged (b) D^--tagged

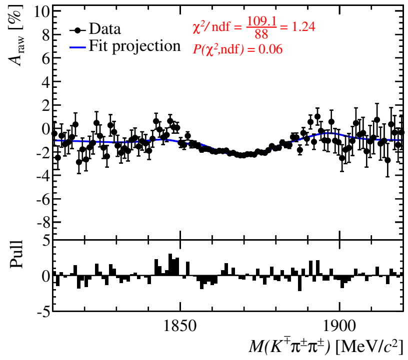

(c) Asymmetry

Figure 7.13: Invariant mass distributions of reconstructed (a) $D^+ \to K^-\pi^+\pi^+$ and (b) $D^- \to K^+\pi^-\pi^-$ candidates. (c) The raw asymmetry as function of the invariant mass. The projection from the fit is overlaid. The 2012 magnet up sample is used.

Table 7.8: The fit parameters and correlation coefficients with $A_{\rm raw}$ corresponding to Figure 7.13.

Parameter	**Fit result**	**Correlation with $A_{\rm raw}$**
$A_{\rm raw}$ [%]	-1.9661 ± 0.026	1.00
$A_{\rm bkg}$ [%]	-0.803 ± 0.21	-0.206
$\Delta\mu$ [MeV/c^2]	-0.00073 ± 0.0039	0.01
α	2.3249 ± 0.0025	0.00
μ [MeV/c^2]	1869.3885 ± 0.0028	-0.004
σ_1 [MeV/c^2]	6.0909 ± 0.0059	0.02
a_+ $[(100\,{\rm MeV}/c^2)^{-1}]$	-0.26843 ± 0.0089	-0.014
a_- $[(100\,{\rm MeV}/c^2)^{-1}]$	-0.27539 ± 0.0089	0.01
f_1	0.6382 ± 0.0020	0.00
$N_{\rm bkg}$	619107 ± 2203	-0.000
$N_{\rm sig}$	16017599 ± 4500	0.00
s	1.5908 ± 0.0017	0.00
s_p	0.99392 ± 0.00047	-0.091
n	0.90	-

7.3.6 $D^+ \to \overline{K}^0 \pi^+$

The raw asymmetry of the $D^+ \to \overline{K}^0 \pi^+$ decay channel is defined as

$$A_{\mathrm{raw}}(\overline{K}^0 \pi^+) = \frac{N_{\mathrm{sig}}(D^+ \to \overline{K}^0 \pi^+) - N_{\mathrm{sig}}(D^- \to K^0 \pi^-)}{N_{\mathrm{sig}}(D^+ \to \overline{K}^0 \pi^+) + N_{\mathrm{sig}}(D^- \to K^0 \pi^-)} \quad . \tag{7.14}$$

Figure 7.14 and Table 7.10 show the fit result of an asymmetry fit to the $D^+ \to \overline{K}^0 \pi^+$ sample. The raw asymmetry is fitted in the mass range $[1810, 1920]\,\mathrm{MeV}/c^2$. Similarly to the other Cabibbo-favoured modes, the $D^+ \to \overline{K}^0 \pi^+$ (LL) sample has a high event yield and a small background contribution. The rather simple mass model does not describe well the mass distribution. In contrast, the raw asymmetry per mass bin is modelled. The parameters constrained in the fit are the tail parameters of the Crystal-Ball function. A proper description of the radiative tail on the left side of the signal peak motivates their values. The estimated uncertainty on the raw asymmetry of the fit is not affected by this constraint as A_{raw} is largely uncorrelated to the shape of the signal model. The mass resolution is slightly worse compared to the $D^+ \to K^- \pi^+ \pi^+$ sample due to the larger Q value of the decay. The correlation of A_{raw} with the background asymmetry is (-0.257) and with s_p (-0.165).

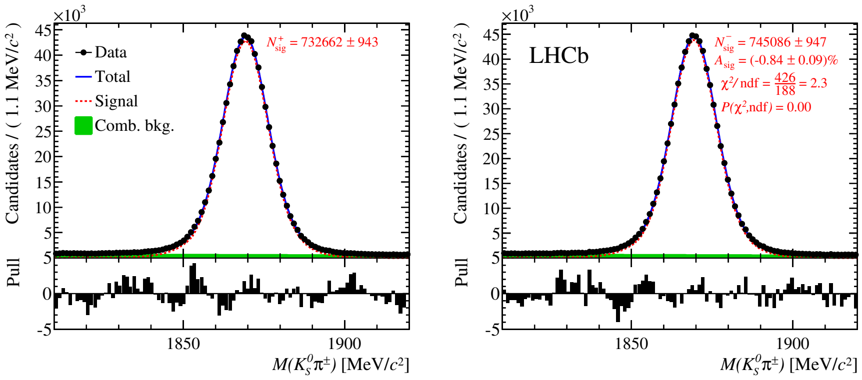

(a) D^+-tagged (b) D^--tagged

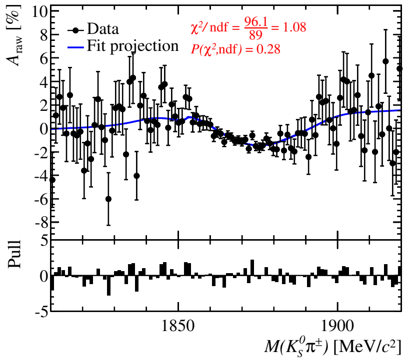

(c) Asymmetry

Figure 7.14: Invariant mass distributions of reconstructed (a) $D^+ \to \overline{K}^0\pi^+$ and (b) $D^- \to K^0\pi^-$ candidates. (c) The raw asymmetry as function of the invariant mass. The projection from the fit is overlaid. The 2012 magnet up sample is used.

Table 7.10: The fit parameters and correlation coefficients with A_{raw} corresponding to Figure 7.14.

Parameter	**Fit result**	**Correlation with A_{raw}**
A_{raw} [%]	-0.8407 ± 0.088	1.00
A_{bkg} [%]	0.71 ± 0.38	-0.257
$\Delta\mu$ [MeV/c^2]	0.097 ± 0.014	-0.001
μ [MeV/c^2]	1869.2538 ± 0.0099	-0.000
σ_1	6.491 ± 0.022	0.05
a_+ $[(100\,\mathrm{MeV}/c^2)^{-1}]$	-0.2519 ± 0.013	0.04
a_- $[(100\,\mathrm{MeV}/c^2)^{-1}]$	-0.2228 ± 0.012	-0.039
f_1	0.6906 ± 0.0069	0.00
N_{bkg}	158108 ± 762	-0.008
N_{sig}	1477749 ± 1379	0.00
s	1.7203 ± 0.0079	0.01
s_p	0.9931 ± 0.0017	-0.165
α	2.50	-
n	1.50	-

7.4 Measured raw asymmetries of each channel

The raw asymmetries are determined for every channel following the prescription introduced in the previous section. First, the measured raw asymmetries are given for 2011 and 2012, split up by magnet polarity. The averaging procedure to obtain the final result of the whole data set is again shortly summarised as well as the explicit definition of the raw asymmetry for each considered decay mode. Second, each individual raw asymmetry is discussed in detail. The discussion includes measurements of the dependence of the raw asymmetries on selected kinematic variables. The variables are p, p_{T}, η and ϕ of the D candidates and their reconstructed decay products. The purpose of this study is to illustrate that there are variations which are induced by the kinematic dependencies of detection and production asymmetries. Thus, a restricted selection is sufficient here.[4] Necessary corrections to extract the *CP* asymmetries ΔA_{CP} and $A_{CP}(K^-K^+)$ are discussed in the following chapters.

7.4.1 Summary: Raw asymmetries

The determination of the raw asymmetries is performed independently for both data taking periods and the two magnet polarities. The combined raw asymmetry of the magnet up and the magnet down sample is the arithmetic mean of both measurements:

$$A_{\mathrm{raw}}(\mathrm{year}) = \frac{A_{\mathrm{raw}}(\mathrm{year})^{\uparrow} + A_{\mathrm{raw}}(\mathrm{year})^{\downarrow}}{2} \quad . \tag{7.15}$$

The statistical uncertainty on the raw asymmetry for each year is given by

$$\sigma_{\mathrm{year}} = \frac{\sqrt{\sigma_{\mathrm{year}}^{\uparrow,2} + \sigma_{\mathrm{year}}^{\downarrow,2}}}{2} \quad . \tag{7.16}$$

The statistical power of each year is not optimally used as the two 2011 data sets are not equal in size. About 40% of the data were taken with up polarity and 60% with down polarity. In 2012 the almost equal amounts of data were recorded with both polarities. This approach averages out detection asymmetries which change sign when changing the magnet polarity. However, the analysis is in principle designed to work on each sample independently, cf. Chapter 5. The final result of the full data set corresponding to an integrated luminosity of $3\,\mathrm{fb}^{-1}$ is the weighted mean of the 2011 and 2012 result:

$$A_{\mathrm{raw}} = \frac{1}{\frac{1}{\sigma_{2011}^2} + \frac{1}{\sigma_{2012}^2}} \left(\frac{1}{\sigma_{2011}^2} A_{\mathrm{raw}}(2011) + \frac{1}{\sigma_{2012}^2} A_{\mathrm{raw}}(2012) \right) \quad . \tag{7.17}$$

with an uncertainty of

$$\sigma = \sqrt{\frac{1}{\frac{1}{\sigma_{2011}^2} + \frac{1}{\sigma_{2012}^2}}} \quad . \tag{7.18}$$

The weighted averages of the raw asymmetries, after corrections have been applied, are used to extract the final results of $A_{CP}(K^-K^+)$ and ΔA_{CP}. If raw asymmetries for the

---

[4] The full set of plots for the muon-tagged D^0 sample is given in Appendix D.1. For the prompt D^+ samples they are found in Reference [5].

Table 7.11: The measured raw asymmetry (in %) for different decay channels, magnet polarities and years. The result for a year is the arithmetic mean of the two magnet polarities. The 2011+2012 are the weighted averages of the values obtained in 2011 and 2012. If needed, the trigger line selection of the ΔA_{CP} or the $A_{CP}(K^-K^+)$ measurement is denoted.

2011	**Magnet up**	**Magnet down**	**Mean**
$A_{\text{raw}}(K^-K^+)_{(\Delta A_{CP})}$	-0.365 ± 0.217	-0.374 ± 0.186	-0.369 ± 0.143
$A_{\text{raw}}(\pi^-\pi^+)$	-1.167 ± 0.399	-0.373 ± 0.341	-0.770 ± 0.262
$A_{\text{raw}}(K^-K^+)_{(A_{CP}(K^-K^+))}$	-0.245 ± 0.242	-0.463 ± 0.207	-0.354 ± 0.159
$A_{\text{raw}}(K^-\pi^+)$	-1.704 ± 0.103	-1.6375 ± 0.0877	-1.6706 ± 0.0675
$A_{\text{raw}}(K^-\pi^+\pi^+)$	-2.1955 ± 0.0515	-1.5518 ± 0.0436	-1.8737 ± 0.0337
$A_{\text{raw}}(\overline{K}^0\pi^+)$	-0.827 ± 0.172	-0.687 ± 0.145	-0.757 ± 0.113

2012	**Magnet up**	**Magnet down**	**Mean**
$A_{\text{raw}}(K^-K^+)_{(\Delta A_{CP})}$	-0.449 ± 0.125	-0.360 ± 0.129	-0.4044 ± 0.0897
$A_{\text{raw}}(\pi^-\pi^+)$	-0.216 ± 0.229	-0.791 ± 0.235	-0.503 ± 0.164
$A_{\text{raw}}(K^-K^+)_{(A_{CP}(K^-K^+))}$	-0.515 ± 0.134	-0.389 ± 0.138	-0.4520 ± 0.0964
$A_{\text{raw}}(K^-\pi^+)$	-1.2678 ± 0.0565	-1.6614 ± 0.0583	-1.4646 ± 0.0406
$A_{\text{raw}}(K^-\pi^+\pi^+)$	-1.9661 ± 0.0258	-1.6233 ± 0.0265	-1.7947 ± 0.0185
$A_{\text{raw}}(\overline{K}^0\pi^+)$	-0.8407 ± 0.0876	-0.9640 ± 0.0906	-0.9024 ± 0.0630

2011+2012	**Magnet up**	**Magnet down**	**Mean**
$A_{\text{raw}}(K^-K^+)_{(\Delta A_{CP})}$	-0.428 ± 0.108	-0.364 ± 0.106	-0.3945 ± 0.0760
$A_{\text{raw}}(\pi^-\pi^+)$	-0.451 ± 0.198	-0.657 ± 0.193	-0.578 ± 0.139
$A_{\text{raw}}(K^-K^+)_{(A_{CP}(K^-K^+))}$	-0.452 ± 0.117	-0.412 ± 0.115	-0.4258 ± 0.0825
$A_{\text{raw}}(K^-\pi^+)$	-1.3692 ± 0.0495	-1.6541 ± 0.0485	-1.5193 ± 0.0348
$A_{\text{raw}}(K^-\pi^+\pi^+)$	-2.0123 ± 0.0231	-1.6039 ± 0.0227	-1.8130 ± 0.0162
$A_{\text{raw}}(\overline{K}^0\pi^+)$	-0.8379 ± 0.0781	-0.8865 ± 0.0769	-0.8677 ± 0.0550

combined 2011 and 2012 magnet up or magnet down samples are quoted, they are the weighted mean of the results obtained in each year for the given polarity.

The definition of all raw asymmetries is explicitly given as a summary:

$$A_{\text{raw}}(K^-K^+) = \frac{N_{\text{sig}}(K^-K^+,\mu^-) - N_{\text{sig}}(K^-K^+,\mu^+)}{N_{\text{sig}}(K^-K^+,\mu^-) + N_{\text{sig}}(K^-K^+,\mu^+)}\ , \tag{7.19}$$

$$A_{\text{raw}}(\pi^-\pi^+) = \frac{N_{\text{sig}}(\pi^+\pi^-,\mu^-) - N_{\text{sig}}(\pi^+\pi^-,\mu^+)}{N_{\text{sig}}(\pi^+\pi^-,\mu^-) + N_{\text{sig}}(\pi^+\pi^-,\mu^+)}\ , \tag{7.20}$$

$$A_{\text{raw}}(K^-\pi^+) = \frac{N_{\text{sig}}(K^-\pi^+ \text{ or } K^+\pi^-,\mu^-) - N_{\text{sig}}(K^+\pi^- \text{ or } K^-\pi^+,\mu^+)}{N_{\text{sig}}(K^-\pi^+ \text{ or } K^+\pi^-,\mu^-) + N_{\text{sig}}(K^+\pi^- \text{ or } K^-\pi^+,\mu^+)}, \tag{7.21}$$

$$A_{\text{raw}}(K^-\pi^+\pi^+) = \frac{N_{\text{sig}}(D^+\to K^-\pi^+\pi^+) - N_{\text{sig}}(D^-\to K^+\pi^-\pi^-)}{N_{\text{sig}}(D^+\to K^-\pi^+\pi^+) + N_{\text{sig}}(D^-\to K^+\pi^-\pi^-)}\ , \tag{7.22}$$

$$A_{\text{raw}}(\overline{K}^0\pi^+) = \frac{N_{\text{sig}}(D^+\to \overline{K}^0\pi^+) - N_{\text{sig}}(D^-\to K^0\pi^-)}{N_{\text{sig}}(D^+\to \overline{K}^0\pi^+) + N_{\text{sig}}(D^-\to K^0\pi^-)}\ , \tag{7.23}$$

All measured raw asymmetries are shown in Table 7.11. A discussion of the individual asymmetries follows in the next section.

Table 7.12: The measured raw asymmetries (in %) for the $D^+ \to K^-\pi^+\pi^+$ decay channel.

	Magnet up	**Magnet down**	**Mean**
2011	-2.1955 ± 0.0515	-1.5518 ± 0.0436	-1.8737 ± 0.0337
2012	-1.9661 ± 0.0258	-1.6233 ± 0.0265	-1.7947 ± 0.0185
2011+2012	-2.0123 ± 0.0231	-1.6039 ± 0.0227	-1.8130 ± 0.0162

7.4.2 $D^+ \to K^-\pi^+\pi^+$

First the $D^+ \to K^-\pi^+\pi^+$ sample is discussed in more detail than the other samples as it is most sensitive to variations which depend on kinematics due to the large signal yield, see Table 6.7. The raw asymmetry of $D^+ \to K^-\pi^+\pi^+$ decays consists of the D^+ production asymmetry, the $K^-\pi^+$ detection asymmetry and the detection asymmetry of the Trigger pion (Equation 5.19):

$$A_{\text{raw}}(K^-\pi^+\pi^+) = A_P(D^+) + A_D(K^-\pi^+) + A_D(\pi^+) \ .$$

The production asymmetry of D^+ mesons at 7 TeV has been measured by the LHCb experiment[5] to be $(-0.96 \pm 0.26\,(\text{stat}) \pm 0.18\,(\text{syst}))\,\%$ [39]. The polarity averaged pion detection asymmetry is measured to be consistent with zero with a sensitivity of 0.18 % [61]. Taking these two measurements into account, the measured $A_{\text{raw}}(K^-\pi^+\pi^+)$ of $(-1.813 \pm 0.016)\,\%$ is consistent with an expected kaon detection asymmetry of around $(-1\,\%)$, cf. Chapter 2.5.2.

The measured raw asymmetries of the four disjoint samples are shown in Table 7.12. For the 2011 and 2012 data taking period $A_{\text{raw}}(K^-\pi^+\pi^+)$ is significantly lower in the magnet up than in the magnet down sample. This shows that there are variations between different data taking periods. The difference between the magnet up and the magnet down value is likely induced by an asymmetry which changes sign as the polarity averaged values of both years are similar.

The mean values of 2011 and 2012 are about 2σ apart. Parts of the detector were moved or repaired during the data taking of 2011 and 2012, the trigger reconstruction slightly changed between the two years, see Table 6.1, and the centre-of-mass energy increased from 7 TeV to 8 TeV. Therefore, the small difference between the two raw asymmetries could be a different detection asymmetry or it could be a slightly different production asymmetry.

The strength of the method used in this analysis is that the individual production and detection asymmetries of every involved particle do not need to be determined. The analysis takes advantage of the fact that they are the same for different decay modes and, consequently, cancel in the difference of raw asymmetries. Nevertheless, dependencies of the raw asymmetries are systematically studied here and later in Chapter 12.5 for the determined *CP* asymmetries.

In Figure 7.15 the measured $A_{\text{raw}}(K^-\pi^+\pi^+)$ is shown for different ranges of the kaon candidate's momentum. In all of the four samples clear patterns are observed. There is a trend that the asymmetry is increasing with higher momentum in the two

---

[5] The quoted result uses a sample which is not statistically independent of the $D^+ \to \overline{K}^0\pi^+$ sample used in this analysis.

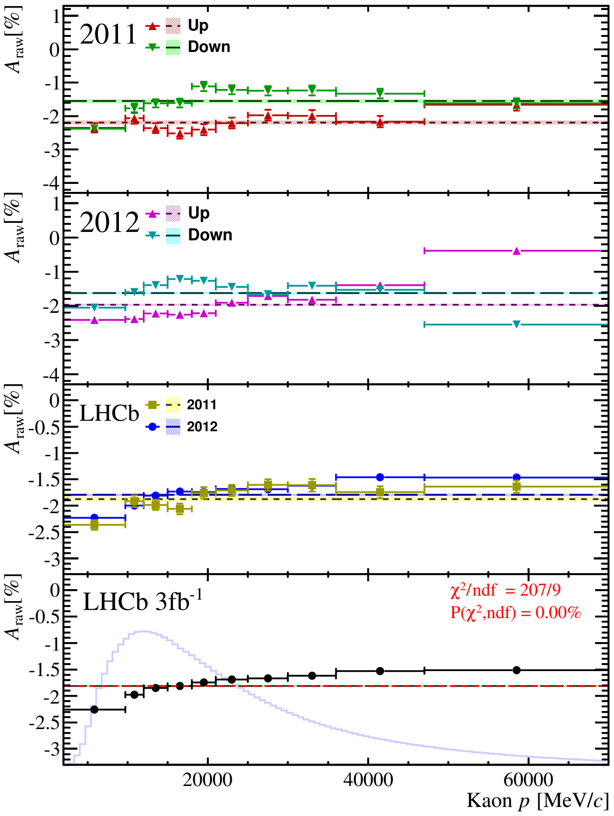

Figure 7.15: The raw asymmetry of $D^+ \to K^-\pi^+\pi^+$ candidates in bins of the K^+ candidate momentum. First, the asymmetry is fitted independently for each of the four samples (dashed lines). Then, each sample is divided into ranges of the kaon momentum and a raw asymmetry fit is performed in each subset. The signal shape is constraint to the parameters of the total fit. The averaging of polarities is done by taking the arithmetic mean. The average of both years is the weighted mean. A χ^2-fit to a constant (red line) is done for the $3\,\mathrm{fb}^{-1}$ result. The obtained χ^2 and the degrees of freedom are given together with the corresponding χ^2-probability (p-value). A low p-value is expected. The light blue line shows the momentum distribution of the kaon candidates, the background contribution is statistically subtracted.

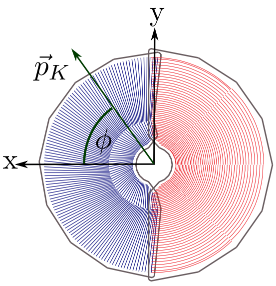

Figure 7.16: The azimuthal angle ϕ in the LHCb coordinate system. The z-axis is pointing into the drawing plane (in direction of the muon stations). The direction of the kaon's momentum is indicated.

magnet up samples, but going into opposite direction with increasing momentum in the magnet down samples. This asymmetry dependence is induced by the particle identification reconstruction and almost cancels when averaging over the samples with different magnet polarities, see Figure 4.10. Both polarity averaged asymmetries of 2011 and 2012 show the expected behaviour that the absolute value of the kaon detection asymmetry decreases with increasing momentum, cf. Chapter 2.5.2. The dependence is even more apparent when combining the two data sets. This is also reflected in the quoted p-value for the hypothesis of no dependence which is zero.

The angle ϕ of the kaon candidate is depicted in Figure 7.16 and the raw asymmetry is shown in bins of ϕ in Figure 7.17a. Large variations which change sign with the magnet polarity are seen. The source of the effect is purely geometric. Depending on the angle ϕ, the magnet polarity and the charge more or less particles with a given charge are bent out of the detector by the magnetic field. Therefore, the effect is largest for particles which have an angle of 0 or π and smallest for particles with an angle of $\pm{}^{\pi}/_{2}$. The effect vanishes when averaging over the two polarities. More over, an interesting observation is that the final result shows a slightly more negative asymmetry for $\phi = \pm{}^{\pi}/_{2}$. There the kaon candidates pass through the overlap regions of the VELO, see Figure 7.16, where the material budget is slightly higher and a larger absorption expected. The same effect is seen in the $D^0 \to K^-\pi^+$ sample.

In Figure 7.17b the raw asymmetry is presented in bins of the momentum p of the Trigger pion. Significant variations are observed in the given momentum range. They could be either induced by a small tracking asymmetry for low momentum particles or by a larger D^+ production asymmetry at small D^+ momentum. The up–down differences observed at large momenta are induced by the particle identification, see Figure 4.10, and are of opposite sign compared to the effect observed in bins of the kaon candidate's momentum.

The raw asymmetry is shown in bins of the of the D^+ candidate's p_{T} in Figure 7.17c. The momentum of the kaon and the momentum of the D^+ meson are correlated. This explains the momentum-dependent up–down differences as they are introduced by the particle identification of the final state particles. The absolute value of the polarity averaged asymmetry decreases with increasing momentum. This is likely connected to the kaon detection asymmetry. Or, the effect could also have its origin in the D^+ production asymmetry as this is expected to decrease with increasing momentum, see Figure 2.16.

The large negative asymmetry in the highest η bin of the D^+ candidate in Figure 7.17d could have its origin in the production asymmetry as it is seen in the $D^+ \to \overline{K}{}^0\pi^+$ sample as well.

As mentioned before, the purpose of these studies is not to measure the individual components of the raw asymmetries and their dependencies. This requires further methods that are out of the scope of this analysis. Nevertheless, it is important to have a qualitative understanding of the involved dynamics. In contrast, a dependence of *CP* asymmetries on the kinematics would be clear sign of not understood systematic uncertainties.

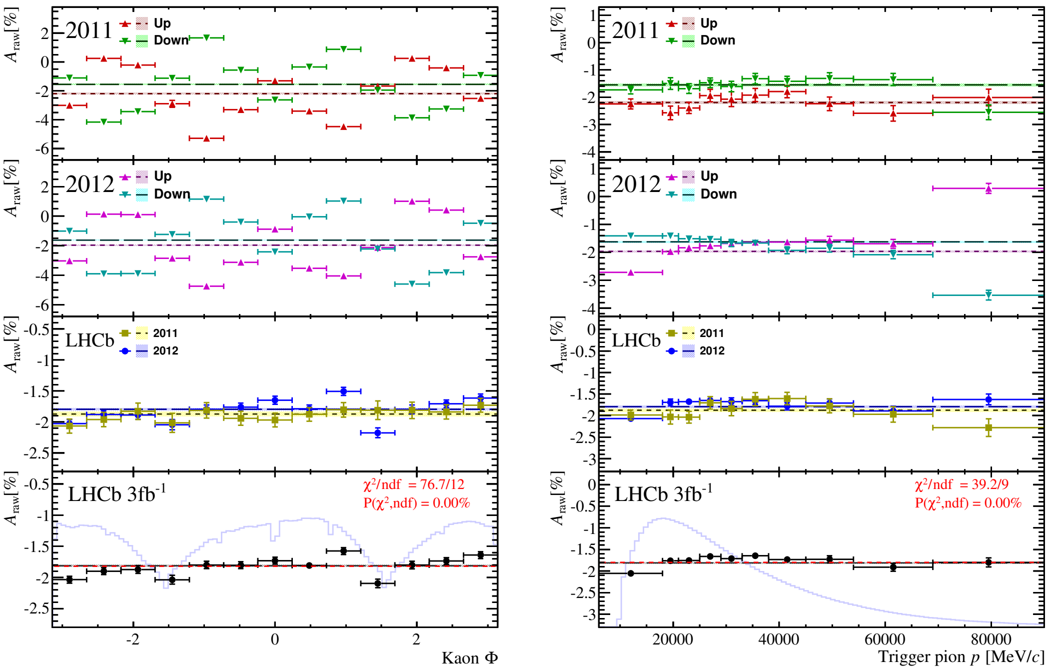

(a) Kaon ϕ (b) Trigger pion p

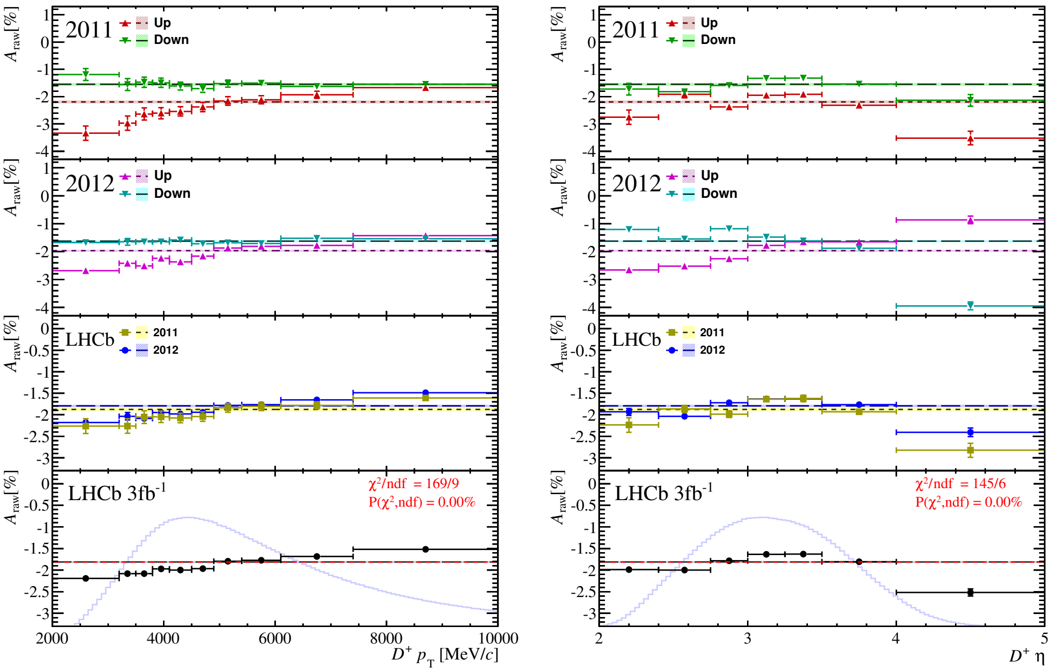

(c) D^+ p_{T} (d) D^+ η

Figure 7.17: The raw asymmetry of $D^+ \to K^-\pi^+\pi^+$ candidates in bins of kinematic variables. Low p-values are expected.

Table 7.13: The measured raw asymmetries (in %) for the $D^+ \to \overline{K}^0\pi^+$ decay channel.

	Magnet up	**Magnet down**	**Mean**
2011	-0.827 ± 0.172	-0.687 ± 0.145	-0.757 ± 0.113
2012	-0.8407 ± 0.0876	-0.9640 ± 0.0906	-0.9024 ± 0.0630
2011+2012	-0.8379 ± 0.0781	-0.8865 ± 0.0769	-0.8677 ± 0.0550

7.4.3 $D^+ \to \overline{K}^0\pi^+$

The raw asymmetry in $D^+ \to \overline{K}^0\pi^+$ consists of the D^+ production asymmetry, the detection asymmetry of the Trigger pion and the combined detection and *CP* asymmetry of neutral kaons (Equation 5.20):

$$A_{\text{raw}}(\overline{K}^0\pi^+) = A_P(D^+) + A_D(\pi^+) + A_D(\overline{K}^0) \ .$$

The measured value is $(-0.868 \pm 0.055)\,\%$. It is shown in Chapter 9 that for K^0 mesons reconstructed with long tracks the latter asymmetry is quite small, $A_D(\overline{K}^0) \approx -0.08\%$. The main contribution is likely coming from the production asymmetry. The effects from a tracking induced pion detection asymmetry, cf. Chapter 4.3.1, and potential asymmetries from the trigger selection are expected to be small in the polarity averaged values.

The measured raw asymmetries are given in Table 7.13. There is an agreement at the 1.2σ level for each magnet polarity and each year. However, the sensitivity is much smaller than in the $D^+ \to K^-\pi^+\pi^+$ mode.

The raw asymmetry in bins of four selected quantities is shown in Figure 7.18. With the sensitivity of the sample, no dependence on the transverse momentum of the D^+ candidates is seen. The largest bin in η of the D^+ candidate shows a similar behaviour as observed in the $D^+ \to K^-\pi^+\pi^+$ channel. However, this could also be connected to a pion detection asymmetry for large η as it is observed as well in Figure 7.18d. The up–down differences are induced by a detection asymmetry induced by the particle identification. The asymmetry in bins of p_{T} of the Trigger pion is relatively flat. A similar behaviour in 2011 and 2012 is observed.

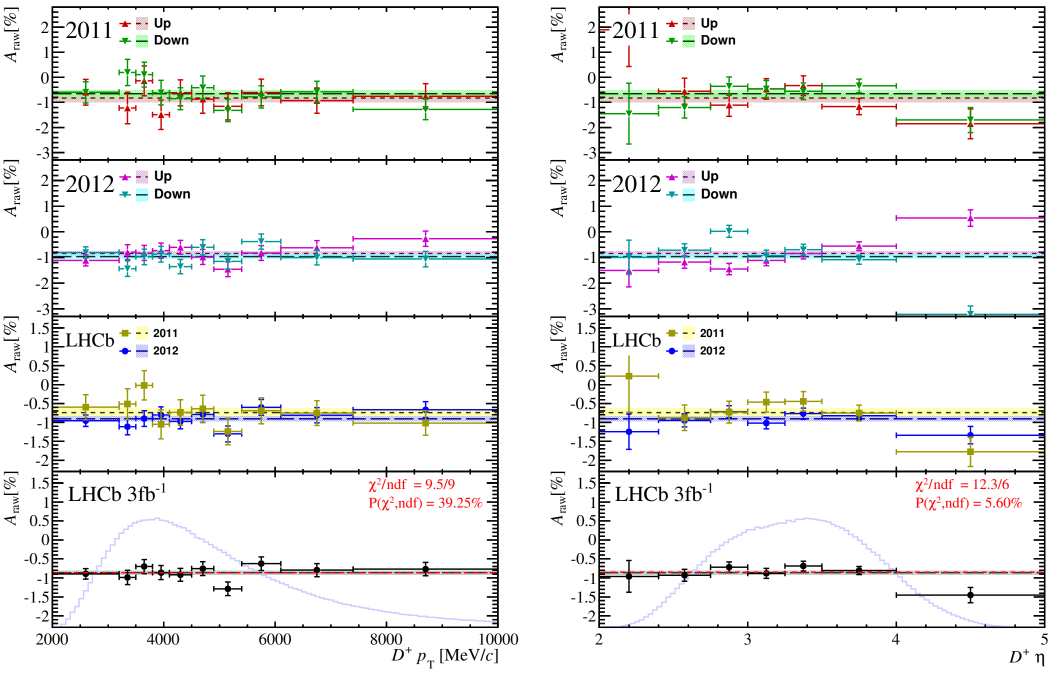

(a) D^+ p_{T}

(b) D^+ η

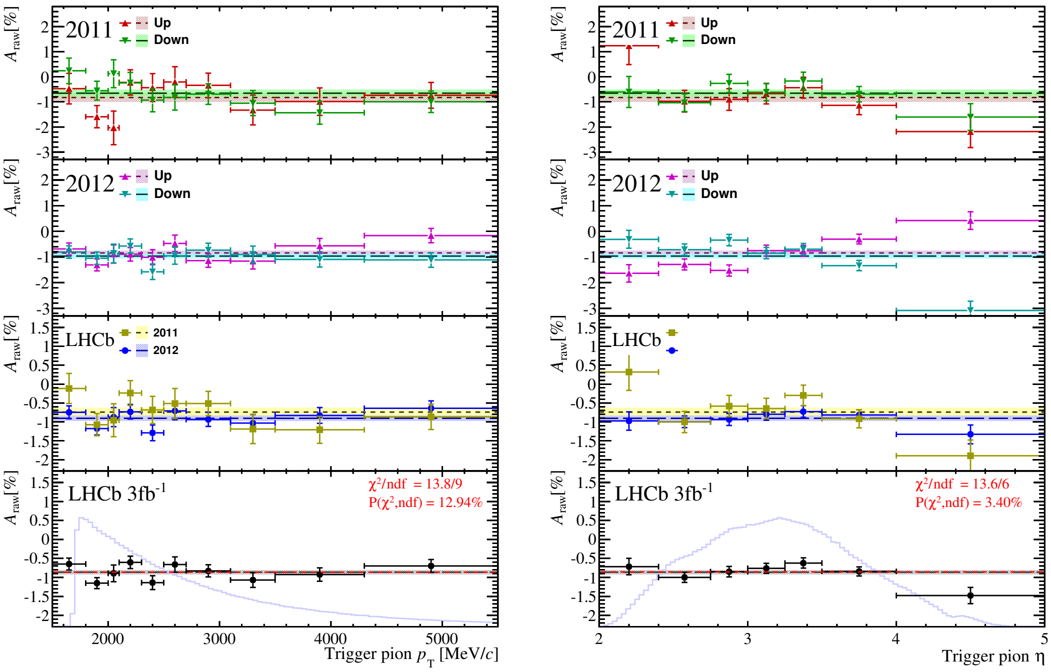

(c) Trigger pion p_{T}

(d) Trigger pion η

Figure 7.18: The raw asymmetry of $D^+ \to \overline{K}^0\pi^+$ candidates in bins of kinematic variables. Low p-values are expected.

Table 7.14: The measured raw asymmetries (in %) for the $D^0 \to K^-\pi^+$ decay channel.

	Magnet up	**Magnet down**	**Mean**
2011	-1.704 ± 0.103	-1.6375 ± 0.0877	-1.6706 ± 0.0675
2012	-1.2678 ± 0.0565	-1.6614 ± 0.0583	-1.4646 ± 0.0406
2011+2012	-1.3692 ± 0.0495	-1.6541 ± 0.0485	-1.5193 ± 0.0348

7.4.4 $D^0 \to K^-\pi^+$

The raw asymmetry of muon-tagged $D^0 \to K^-\pi^+$ decays has contributions from the muon detection asymmetry, the B production asymmetry and the $K^-\pi^+$ detection asymmetry (Equation 5.16):

$$A_{\mathrm{raw}}(K^-\pi^+) = A_D(\mu^-) + A_P(\overline{B}) + A_D(K^-\pi^+) \ .$$

The measured raw asymmetry of the full data set is $(-1.519 \pm 0.035)\,\%$. The largest contribution is likely coming from the kaon detection asymmetry. There is not yet a precise measurement of the B production asymmetry in pp collision at LHC energies. In the adapted convention it is expected to be negative with an absolute value not exceeding the per cent level, cf. Chapter 2.6.2. The contribution from the muon detection asymmetry is expected to be small after averaging the magnet up and down samples, cf. Chapter 4.5.

The values for the $(2011, 2012)\times$(magnet up, magnet down) samples are given in Table 7.14. There is a very good agreement between the values measured for magnet up and magnet down in 2011 as the `L0Muon` asymmetry, described in Chapter 4.1.3, is corrected. In 2012 there is an up–down difference of $(-0.394 \pm 0.082)\%$ which is due to a non-perfect calibration of the `L0Muon` p_{T} estimate. Still, the agreement is much better than it is in the 2011 sample without correcting for the effect. The up–down difference could also include effects from the particle identification. The absolute value of the measured asymmetry in 2012 is significantly smaller than in 2011.

In Figure 7.19 the raw asymmetry is shown as a function of four selected kinematic variables. The raw asymmetry as a function of p_{T} of the muon candidate is given in Figure 7.19a. Due to the calibrated `L0Muon` p_{T} the asymmetry in 2011 is flatter than in 2012 for each polarity. The values of the full data set have little differences below a p_{T} of $7\,\mathrm{GeV}/c$. The last bin has an asymmetry which is significantly closer to zero.

The raw asymmetry follows a similar trend as a function of the kaon candidate's momentum as seen in the $D^+ \to K^-\pi^+\pi^+$ decay channel, see Figure 7.19b. The asymmetry is more negative for small momenta and less negative for large momenta. Furthermore, in Figure 7.19c the same structure in the ϕ of the kaon candidate is observed at $\pm\pi/2$. The absolute value of the raw asymmetry is strongly decreasing with the transverse momentum of the D^0 candidate. As there is less variation observed in the kaon momentum spectrum, the effect seen in Figure 7.19d might be due to the B production asymmetry. Both contributions to the asymmetry are hard to disentangle here.

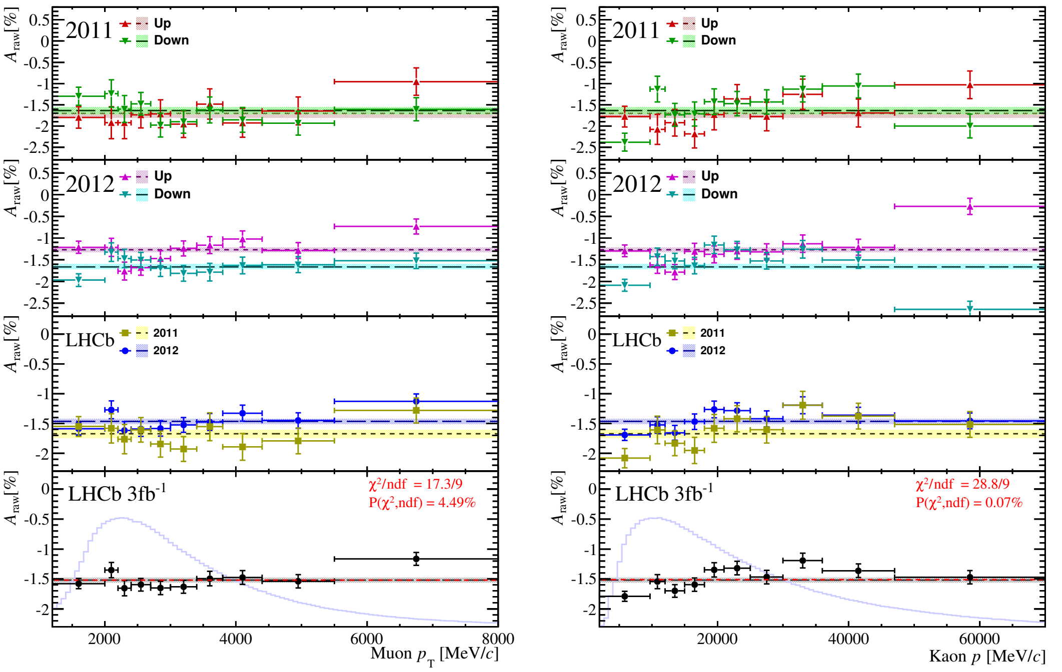

(a) Muon $p_{\rm T}$ (b) Kaon p

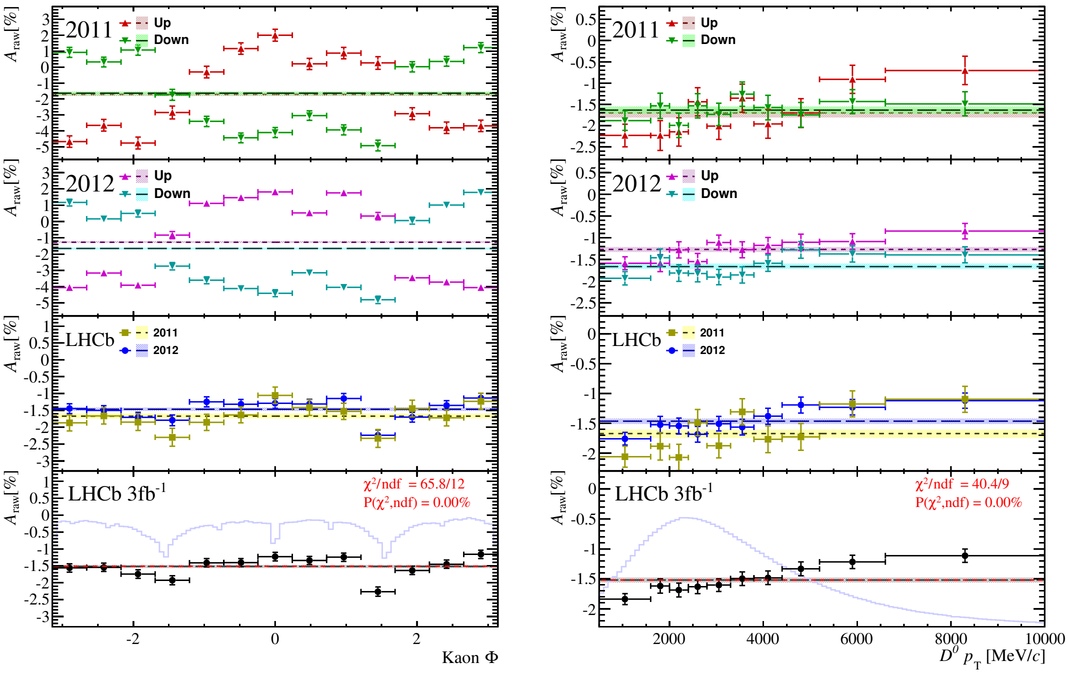

(c) Kaon ϕ (d) D^0 $p_{\rm T}$

Figure 7.19: The raw asymmetry of $D^0 \to K^-\pi^+$ candidates in bins of kinematic variables. Low p-values are expected.

Table 7.15: The measured raw asymmetries (in %) for the $D^0 \to K^-K^+$ decay channel. The raw asymmetries with the ΔA_{CP} and $A_{CP}(K^-K^+)$ trigger selection are given.

ΔA_{CP}	**Magnet up**	**Magnet down**	**Mean**
2011	-0.365 ± 0.217	-0.374 ± 0.186	-0.369 ± 0.143
2012	-0.449 ± 0.125	-0.360 ± 0.129	-0.4044 ± 0.0897
2011+2012	-0.428 ± 0.108	-0.364 ± 0.106	-0.3945 ± 0.0760

$A_{CP}(K^-K^+)$	**Magnet up**	**Magnet down**	**Mean**
2011	-0.245 ± 0.242	-0.463 ± 0.207	-0.354 ± 0.159
2012	-0.515 ± 0.134	-0.389 ± 0.138	-0.4520 ± 0.0964
2011+2012	-0.452 ± 0.117	-0.412 ± 0.115	-0.4258 ± 0.0825

7.4.5 $D^0 \to K^-K^+$

The raw asymmetry in $D^0 \to K^-K^+$ consists of a potential *CP* asymmetry, the detection asymmetry of muons and the B production asymmetry (Equation 5.12):

$$A_{\text{raw}} = A_{CP}(K^-K^+) + A_D(\mu^-) + A_P(\overline{B}) \ .$$

The measured value of the full data set is $(-0.395 \pm 0.076)\,\%$ with the ΔA_{CP} trigger line selection and $(-0.426 \pm 0.083)\,\%$ with the $A_{CP}(K^-K^+)$ trigger line selection. Both values are consistent, given the fact, that the $A_{CP}(K^-K^+)$ selection removes approximately 20 % of the events. There is a remarkable agreement between all disjoint samples, see Table 7.15.

Given the sensitivity, the raw asymmetry shows no significant variations in the muon p_{T}, D^0 p_{T} and D^0 η spectrum, see Figure 7.20. The raw asymmetry as a function of the angle ϕ of the muon candidate is shown in Figure 7.20b. In some bins asymmetries of approximately 10 % are induced by the acceptance of the LHCb forward geometry with the dipole magnet. The effect is larger for muon candidates compared to hadron candidates as the muon stations are located farther away from the magnet than the T-stations. The effect mostly vanishes when averaging over the magnet up and down samples. The same effect is also observed in the muon-tagged $D^0 \to K^-\pi^+$ and $D^0 \to \pi^-\pi^+$ samples.

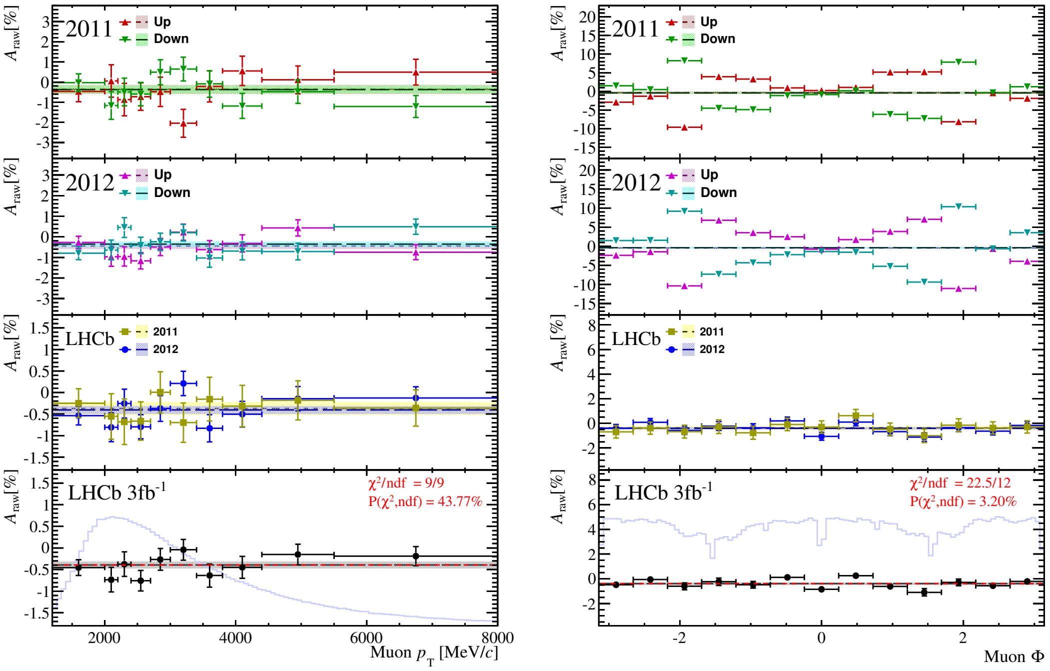

(a) Muon $p_{\rm T}$

(b) Muon ϕ

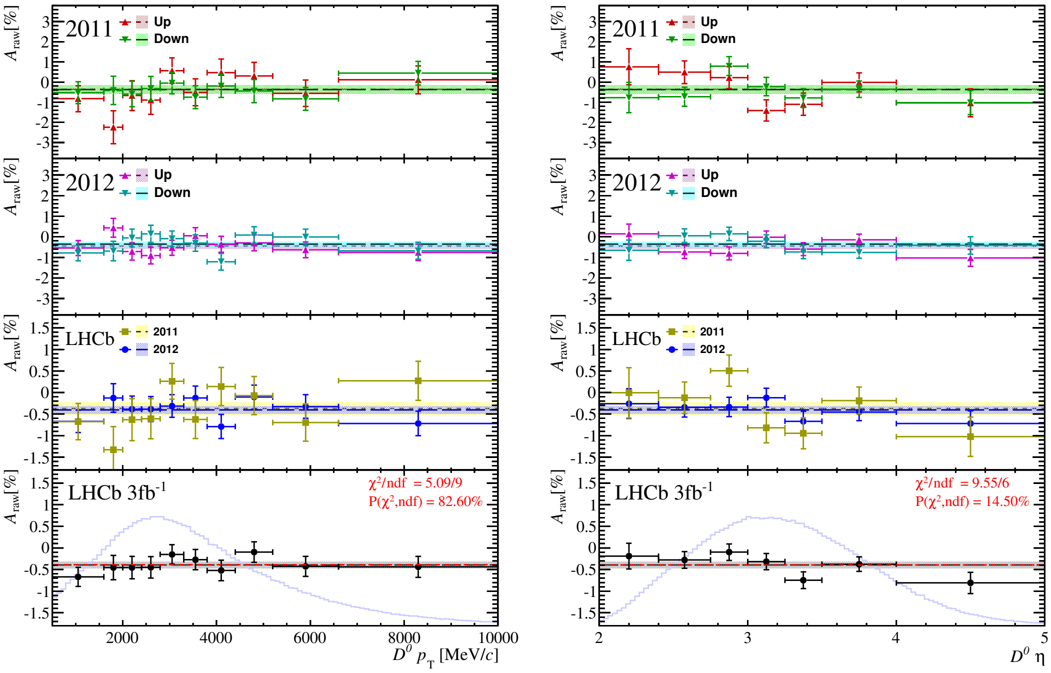

(c) D^0 $p_{\rm T}$

(d) D^0 η

Figure 7.20: The raw asymmetry of $D^0 \to K^- K^+$ candidates in bins of kinematic variables. The ΔA_{CP} trigger line selection is used. Low p-values are expected.

Table 7.16: The measured raw asymmetries (in %) for the $D^0 \to \pi^-\pi^+$ decay channel.

	Magnet up	**Magnet down**	**Mean**
2011	-1.167 ± 0.399	-0.373 ± 0.341	-0.770 ± 0.262
2012	-0.216 ± 0.229	-0.791 ± 0.235	-0.503 ± 0.164
2011+2012	-0.451 ± 0.198	-0.657 ± 0.193	-0.578 ± 0.139

7.4.6 $D^0 \to \pi^-\pi^+$

The raw asymmetry in $D^0 \to \pi^-\pi^+$ consists of a potential *CP* asymmetry, the muon detection asymmetry and the B production asymmetry (Equation 5.13):

$$A_{\text{raw}}(\pi^-\pi^+) = A_{CP}(\pi^-\pi^+) + A_D(\mu^-) + A_P(\overline{B}) \ .$$

The measured value of the full data set is $(-0.58 \pm 0.14)\,\%$. The up–down difference in 2011 is 1.5σ, in 2012 it is -1.8σ. The polarity averaged values for both years agree very well. Parts of the difference in 2012 can be attributed to the muon detection asymmetry as there is a similar difference to the same direction in the $D^0 \to K^-\pi^+$ sample.

The $D^0 \to \pi^-\pi^+$ sample has the lowest signal yield of all decay modes considered in this work. Thus, the sensitivity to variations is small. The raw asymmetry is given as a function of the same variable as are shown for the $D^0 \to K^-K^+$ decay mode in Figure 7.21. The same qualitative conclusions as for $D^0 \to K^-K^+$ decays can be drawn.

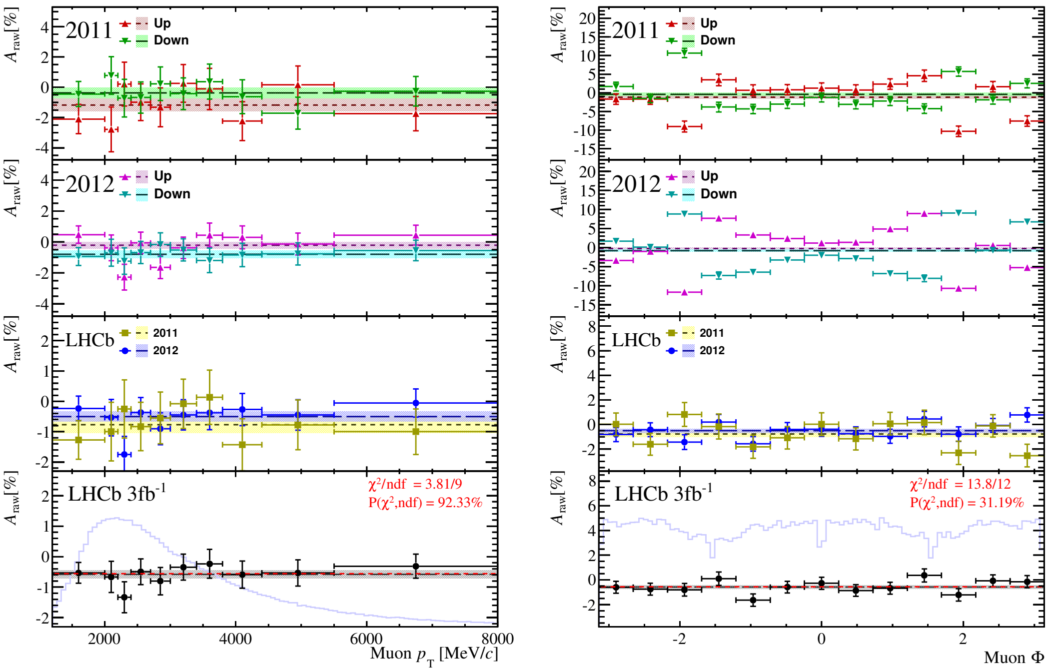

(a) Muon p_T (b) Muon ϕ

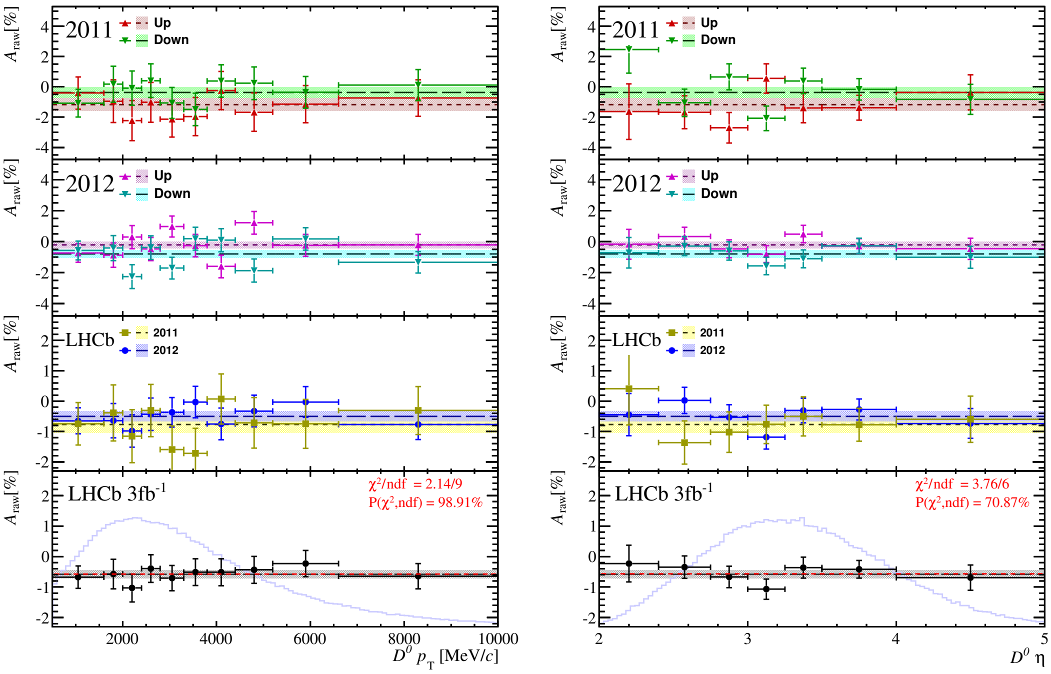

(c) D^0 p_T (d) D^0 η

Figure 7.21: The raw asymmetry of $D^0 \to K^- K^+$ candidates in bins of kinematic variables. The ΔA_{CP} trigger line selection is used. Low p-values are expected.

Table 7.17: The measured raw asymmetry (in %) for different decay channels and magnet polarities. The results are obtained from independent fits to the magnet up and down samples of 2011 and 2012. The averaging procedure is described in Chapter 7.4.1. If needed, the trigger line selection of the ΔA_{CP} or the $A_{CP}(K^-K^+)$ measurement is denoted.

2011+2012	**Magnet up**	**Magnet down**	**Mean**
$A_{\text{raw}}(K^-K^+)_{(\Delta A_{CP})}$	-0.428 ± 0.108	-0.364 ± 0.106	-0.3945 ± 0.0760
$A_{\text{raw}}(\pi^-\pi^+)$	-0.451 ± 0.198	-0.657 ± 0.193	-0.578 ± 0.139
$A_{\text{raw}}(K^-K^+)_{(A_{CP}(K^-K^+))}$	-0.452 ± 0.117	-0.412 ± 0.115	-0.4258 ± 0.0825
$A_{\text{raw}}(K^-\pi^+)$	-1.3692 ± 0.0495	-1.6541 ± 0.0485	-1.5193 ± 0.0348
$A_{\text{raw}}(K^-\pi^+\pi^+)$	-2.0123 ± 0.0231	-1.6039 ± 0.0227	-1.8130 ± 0.0162
$A_{\text{raw}}(\overline{K}^0\pi^+)$	-0.8379 ± 0.0781	-0.8865 ± 0.0769	-0.8677 ± 0.0550

7.5 Summary

The raw asymmetry of each sample is determined by a binned maximum-likelihood fit to the invariant D mass distribution. The fits are performed simultaneously in the samples of both tags. For $D^0 \to K^-K^+$ and $D^0 \to \pi^-\pi^+$ decays the signal shape for both tags is constrained to be the same. For $D^0 \to K^-\pi^+$, $D^+ \to K^-\pi^+\pi^+$ and $D^+ \to \overline{K}^0\pi^+$ decays a shift of the mean mass and a difference in the resolution are allowed. The background parameters are independent for both tags. The fit model is motivated by studies with simulated background decays and by the observed raw asymmetries per mass bin.

The measurements are performed independently for the magnet up and magnet down samples of 2011 and 2012. Differences between the samples are observed in the decay channels with large signal yields. The mean values of 2011 and 2012 are shown in Table 7.17. The largest asymmetries are $A_{\text{raw}}(K^-\pi^+)$ and $A_{\text{raw}}(K^-\pi^+\pi^+)$ as both are affected by the charged kaon asymmetry. The magnitude of all other asymmetries is smaller than 1 %. Furthermore, the raw asymmetries vary significantly when measured in bins of kinematic variables like the kaon candidate's momentum in $D^+ \to K^-\pi^+\pi^+$ decays or the transverse momentum of D^0 candidates in the muon-tagged $D^0 \to K^-\pi^+$ sample.

Chapter 8

Event weighting

The analysis method requires that production and detection asymmetries cancel in the difference of two raw asymmetries, as detailed in the previous chapters. These asymmetries depend on the kinematic distributions of the involved particles. In this chapter a method to adjust the kinematic distributions of all decay channels is presented such that the aforementioned assumption is fulfilled. The kinematic distributions of all channels are studied and it is explained how weights are assigned to each event in order to obtain a better agreement in the kinematic distributions of different decay channels. In the last part the method is validated using pseudo-experiments.

8.1 Weighting procedures of ΔA_{CP} and $A_{CP}(K^-K^+)$ measurements

First, the weighting strategy for the ΔA_{CP} measurement is discussed in detail as it is the simpler case than the $A_{CP}(K^-K^+)$ measurement. The developed weighting method can be transferred to the $A_{CP}(K^-K^+)$ measurement which is discussed thereafter.

8.1.1 Effect of kinematic differences

The raw asymmetries used in the presentation of the analysis strategy in Chapter 5 are implicitly integrated over the kinematic distributions of all involved particles. To be more explicit, the measured raw asymmetry for $D^0 \to K^-K^+$ and $D^0 \to \pi^-\pi^+$ decays coming from a semileptonic B decay can be written as a function of the kinematic variables of the B meson and the tagging muon:

$$a_{\text{raw}}({p_{\text{T}}}^{\mu}, \eta^{\mu}, \phi^{\mu}, {p_{\text{T}}}^{B}, \eta^{B}) = A_{CP} + a_D^{\mu}({p_{\text{T}}}^{\mu}, \eta^{\mu}, \phi^{\mu}) + a_P^{B}({p_{\text{T}}}^{B}, \eta^{B}) \ . \tag{8.1}$$

The *CP* asymmetry has no kinematic dependency,[1] the production asymmetry depends on p_{T} and η of the B meson, cf. Chapter 2.6.2 and the detection asymmetry depends on p_{T}, η and ϕ of the muon, cf. Chapter 7. The final state of the D^0 meson is a *CP* eigenstate and, hence, does not have a detection asymmetry. Therefore, the integrated

---

[1] There might be a small effect from indirect *CP* violation if the decay-time acceptance has a strong dependency on the kinematic distributions. The decay-time acceptance of all semileptonic decay channels has been studied and is found to be similar [5]. Thus, this effect can be safely neglected in the ΔA_{CP} and the $A_{CP}(K^-K^+)$ measurements.

measured raw asymmetry depends on the observed B spectrum, $\rho({p_\mathrm{T}}^B, \eta^B)$, and muon spectrum, $\rho({p_\mathrm{T}}^\mu, \eta^\mu, \phi^\mu)$:

$$A_\mathrm{raw} = A_{CP} + \int \rho({p_\mathrm{T}}^\mu, \eta^\mu, \phi^\mu)\, a_D^\mu({p_\mathrm{T}}^\mu, \eta^\mu, \phi^\mu)\, dp^\mu + \int \rho({p_\mathrm{T}}^B, \eta^B)\, a_P^B({p_\mathrm{T}}^B, \eta^B)\, dp^B \ , \tag{8.2}$$

with normalised distributions ρ,

$$1 = \int \rho({p_\mathrm{T}}^\mu, \eta^\mu, \phi^\mu)\, dp^\mu = \int \rho({p_\mathrm{T}}^B, \eta^B)\, dp^B \ . \tag{8.3}$$

A difference of the kinematic distributions of $D^0 \to K^-K^+$ and $D^0 \to \pi^-\pi^+$ candidates,

$$\Delta\rho(p) \equiv \rho^{D^0\to K^-K^+}(p) - \rho^{D^0\to\pi^-\pi^+}(p) \ , \tag{8.4}$$

leads to the residual asymmetry, ΔA, in the ΔA_{CP} determination

$$\Delta A_{CP} = A_{CP}(K^-K^+) - A_{CP}(\pi^-\pi^+) + \Delta A \ . \tag{8.5}$$

The residual asymmetry is given by

$$\Delta A = \int \Delta\rho({p_\mathrm{T}}^\mu, \eta^\mu, \phi^\mu)\, a_D^\mu({p_\mathrm{T}}^\mu, \eta^\mu, \phi^\mu)\, dp^\mu + \int \Delta\rho({p_\mathrm{T}}^B, \eta^B)\, a_P^B({p_\mathrm{T}}^B, \eta^B)\, dp^B \ , \tag{8.6}$$

In the case the distributions are equal, ΔA vanishes. Furthermore, no residual asymmetry is left if detection or production asymmetries do not depend on the kinematics of the involved particles, by construction $\int \Delta\rho(p)dp = 0$. The residual asymmetry depends on the size of the asymmetry variations and the differences of the kinematic distributions. The procedure described in the following is dedicated to that. As the involved asymmetries and their variations are small, the correction ΔA is expected to be small as long as the kinematic distributions are similar.

8.1.2 Weighting procedure for ΔA_{CP} measurement

Production and detection asymmetries are the same for $D^0 \to K^-K^+$ and $D^0 \to \pi^-\pi^+$ signal events but not necessarily for background events. Therefore, the kinematic distributions of genuine $D^0 \to K^-K^+$ and $D^0 \to \pi^-\pi^+$ decays have to be extracted from all events. A pure background sample can be obtained from events that have a reconstructed D^0 mass which is much smaller or much larger than the real D^0 mass. In each phase space bin the number of background events is estimated from the so-called *mass sidebands*. The mass sidebands are defined symmetrically around the D^0 mass as

$$\begin{aligned} &[m_{D^0,\mathrm{PDG}} - 60\,\mathrm{MeV}/c^2, m_{D^0,\mathrm{PDG}} - 30\,\mathrm{MeV}/c^2] \\ &\text{and } [m_{D^0,\mathrm{PDG}} + 30\,\mathrm{MeV}/c^2, m_{D^0,\mathrm{PDG}} + 60\,\mathrm{MeV}/c^2] \ . \end{aligned} \tag{8.7}$$

The signal region is chosen to have the same width, $|m_{D^0} - m_{D^0,\mathrm{PDG}}| < 30\,\mathrm{MeV}/c^2$. Thus, when subtracting the kinematic distribution of the background region from the kinematic distribution of the signal region, the number of background events is subtracted in each phase space bin (*sideband subtraction*). This method assumes a

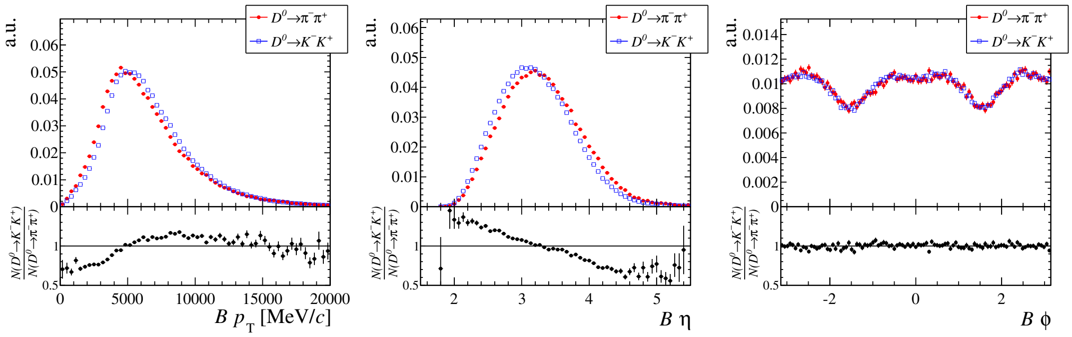

(a) B candidates

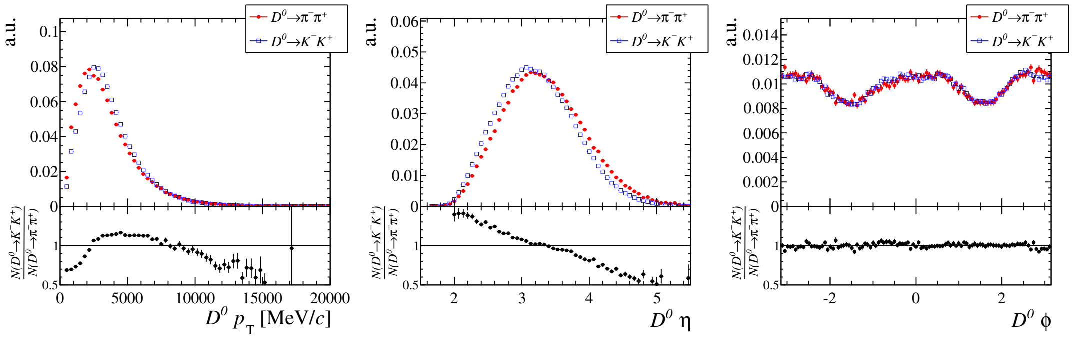

(b) D^0 candidates

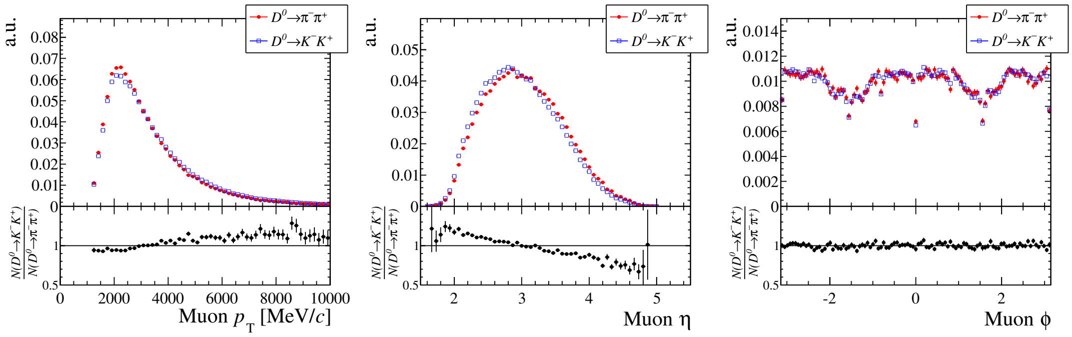

(c) Muon candidates

Figure 8.1: The kinematic distributions of reconstructed $D^0 \to \pi^-\pi^+$ and $D^0 \to K^-K^+$ decays before weighting. The 2012 data sample with magnet up polarity is used.

linear background distribution and that the background contribution in the signal region has the same kinematic distributions as in the background region. As this is only approximately true for $D^0 \to K^-K^+$ and $D^0 \to \pi^-\pi^+$ candidates, variations of this procedure are discussed within the systematic uncertainties.

The distributions of signal events are shown in Figure 8.1 for B, D^0 and muon candidates. The method described here is independently applied to each of the four samples. The 2012 magnet up distributions are studied as an example. The distributions are very similar in the other samples.[2] The ratio of $D^0 \to K^-K^+$ and $D^0 \to \pi^-\pi^+$ decays in each bin is shown as well, a clear but not large difference between the two decay modes can be seen.

The selection of muon, D^0 and B candidates is the same for all semileptonic decay modes, see Table 6.4. However, differences in the momentum distributions can occur due to selection cuts on the decay products of the D^0 candidates. The Q values of the two decays are significantly different as kaons have an about four times larger mass than pions. Applying the same momentum requirement on the D^0 decay products, therefore introduces a different D^0 momentum distribution. Differences in the momentum distributions also arise due to different requirements on the particle identification as these are implicit cuts on the momenta.

In order to get a more similar distribution for the B and muon kinematics, $D^0 \to K^-K^+$ and $D^0 \to \pi^-\pi^+$ events are first grouped in bins of p_T and η of the D^0 candidate. The bin boundaries in η are equidistantly distributed in the range $[1.5, 5.5]$. The distribution of the transverse momentum p_T has a core with a large number of events and a large tail with very few events. To have more even populated bins, p_T is transformed by the function, $g(p_\mathrm{T})$, which is defined as

$$g(p_\mathrm{T}) \equiv 2/\pi \arctan\left((p_\mathrm{T}(\,\mathrm{MeV}/c) - 450\,\mathrm{MeV}/c)/(4500\,\mathrm{MeV}/c)\right) \quad . \tag{8.8}$$

The transformation g maps p_T to the range $[0, 1]$. It allows for an equidistant binning in $g(p_\mathrm{T})$ where higher bins span a larger p_T range. The default weighting procedure uses 20 bins per dimension. This makes 400 bins in total which allows for a proper description of the kinematic distributions. The D^0 η and $g(p_\mathrm{T})$ distributions used in the weighting are shown in Figure 8.2. Variations of the bin number are discussed within the context of systematic studies. The $D^0 \to K^-K^+$ and $D^0 \to \pi^-\pi^+$ distributions are normalised to one as only the shapes of the distributions matter and not a difference in the total yields. Then, a *kinematic* weight is assigned to each $D^0 \to K^-K^+$ event, according to

$$w({p_\mathrm{T}}^{D^0}, \eta^{D^0}) = \frac{N_{\mathrm{tot},K^-K^+}}{N_{\mathrm{tot},\pi^-\pi^+}} \, \frac{n_{\pi^-\pi^+}({p_\mathrm{T}}^{D^0}, \eta^{D^0})}{n_{K^-K^+}({p_\mathrm{T}}^{D^0}, \eta^{D^0})} \quad , \tag{8.9}$$

where $n_{h^-h^+}({p_\mathrm{T}}^{D^0}, \eta^{D^0})$ denotes the measured signal yield in the given kinematic bin and N_{tot,h^-h^+} is the total signal yield of the $D^0 \to K^-K^+$ or $D^0 \to \pi^-\pi^+$ sample. The weights assigned to the $D^0 \to K^-K^+$ sample are shown in Figure 8.3. The meanings of N, N_eff, w_eff and renormalised weights is explained later in Chapter 8.1.3. The kinematic weights are distributed around one as the kinematic distributions of $D^0 \to K^-K^+$ and $D^0 \to \pi^-\pi^+$ events are also similar in two dimensions.

---

[2] A full list of all distributions is given in Reference [5].

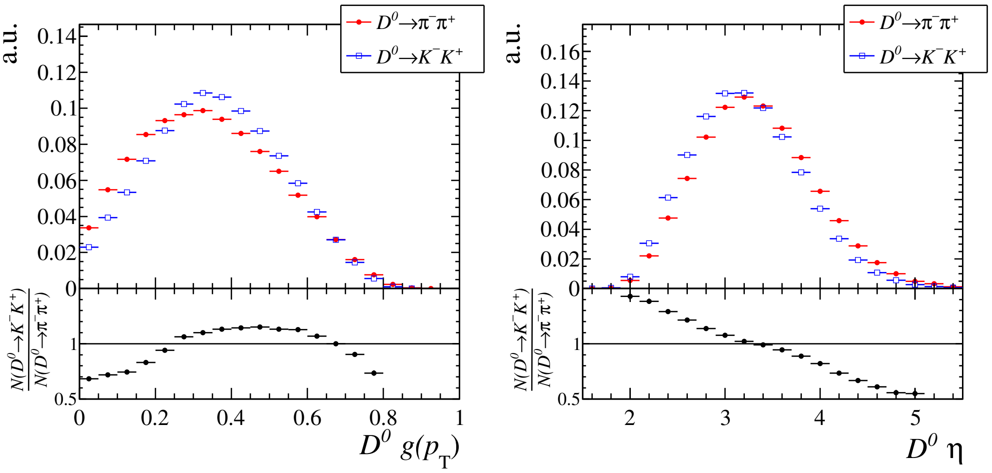

(a) $g(p_{\mathrm{T}})$ distribution of D^0 candidate (b) η distribution of D^0 candidate

Figure 8.2: The distribution of D^0 candidates used in the weighting with $g(p_{\mathrm{T}}) = 2/\pi \arctan((p_{\mathrm{T}}(\,\mathrm{MeV}/c) - 450\,\mathrm{MeV}/c)/(4500\,\mathrm{MeV}/c))$. The Up 2012 data sample is used.

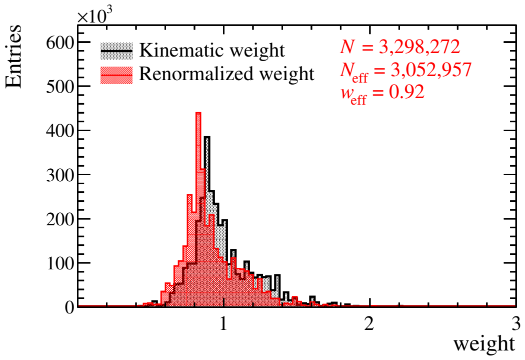

Figure 8.3: The weights assigned to the $D^0 \to K^-K^+$ samples. All data are used. The definitions of N, N_{eff}, w_{eff} and renormalised weight can be found in Chapter 8.1.3.

The result of the weighting procedure is shown in Figure 8.4. It should be noted that the bin size and number of bins in the displayed histograms are different to those used in the weighting procedure. Thus, small variations are seen in the D^0 distributions, although these distributions are used in the weighting. The kinematic distributions of the B meson and muon agree well after the weighting. This is expected as their kinematics are correlated to the D^0 meson's kinematics and, therefore, the kinematic distributions of B meson and muon are changed as well. The impact of the residual differences in B and muon kinematics is evaluated in systematic studies later together with effects due to a finite binning in the D^0 candidates' kinematics. The effects are expected to be small as the distributions agree well and the variations of detection and productions asymmetries are small.

8.1.3 Effective yields

The statistical uncertainty on small asymmetries, neglecting background contributions, is approximately $1/\sqrt{N}$, where N is the total signal yield. In the following discussion background contributions are omitted for simplicity. The obtained signal yield after the weighting procedure is

$$N^* = \sum_{i=1}^{N} w_i \ , \tag{8.10}$$

where w_i has been defined in Equation 8.9. As the kinematic weights are not limited, N^* could become larger than N. Applying different weights to each event can increase the statistical contribution of a single event but cannot increase the total statistical power of the full sample. The lower limit of the uncertainty on the asymmetry of the weighted sample is given by $1/\sqrt{N}$. This is reflected by renormalising every event with the normalisation factor, w_{eff}, which is defined as

$$w_{\text{eff}} = \frac{\sum_{i=1}^{N} w_i}{\sum_{i=1}^{N} w_i^2} \ . \tag{8.11}$$

The effective sample size, N_{eff}, is then given by

$$N_{\text{eff}} = w_{\text{eff}} \sum_{i=1}^{N} w_i \ . \tag{8.12}$$

The factor w_{eff} ensures that N_{eff} is equal to N in case of equal weights for each event. If the individual event weights are different, the effective sample size N_{eff} is smaller than N as[3]

$$\sum_{i=1}^{N} w_i \quad \leq \quad \sqrt{N \sum_{i=1}^{N} w_i^2} \tag{8.13}$$

$$\implies \quad N_{\text{eff}} = \frac{\sum_{i=1}^{N} w_i}{\sum_{i=1}^{N} w_i^2} \sum_{i=1}^{N} w_i \leq N \ . \tag{8.14}$$

---

[3] The inequality can be proven by mathematical induction.

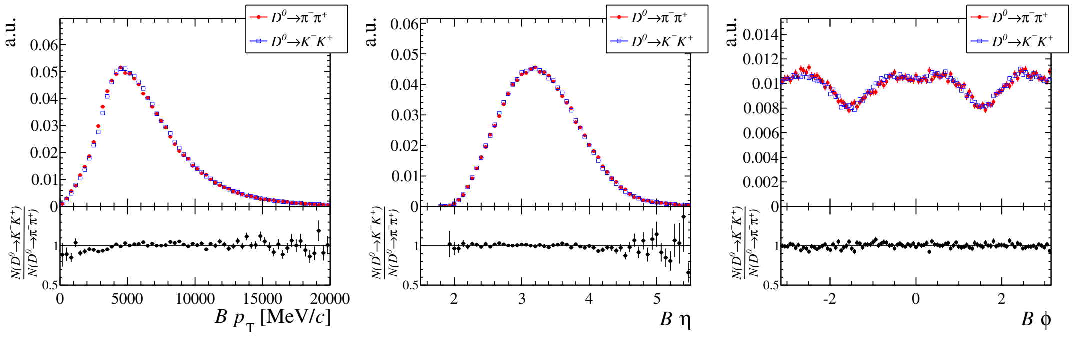

(a) B candidates

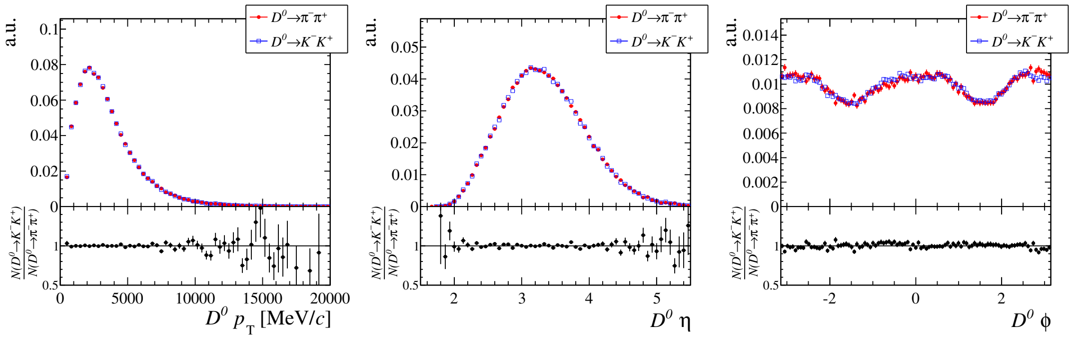

(b) D^0 candidates

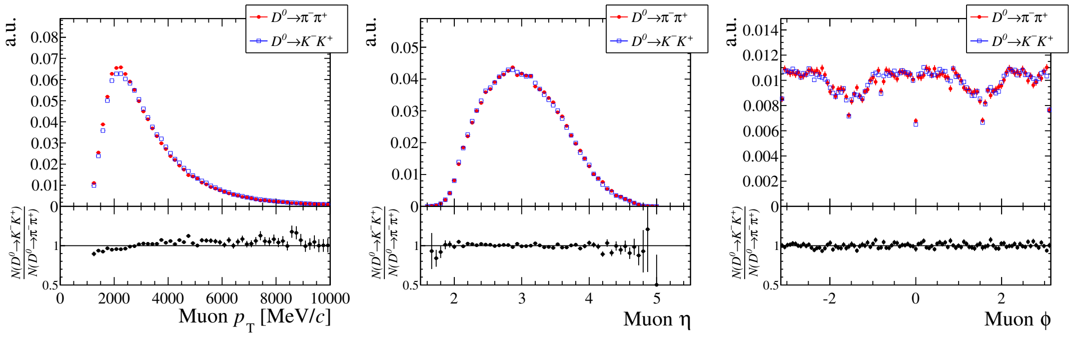

(c) Muon candidates

Figure 8.4: The kinematic distributions of reconstructed $D^0 \to \pi^-\pi^+$ and $D^0 \to K^-K^+$ decays after weighting. The 2012 data sample with magnet up polarity is used.

Consequently, the statistical power of the weighted sample decreases. The uncertainty on the asymmetry measurement is then given by $1/\sqrt{N_{\text{eff}}}$. The reduction of the statistical power depends on the spread of the weights. If the weights are distributed with a small spread around the average weight, the loss in sensitivity is small. Events with a weight much larger than the average weight lead to a large reduction of the statistical power of the sample.

The previous discussion also explains why the sample with the higher signal yield, the $D^0 \to K^-K^+$ sample, is weighted in the ΔA_{CP} measurement. The uncertainty of ΔA_{CP} is dominated by the statistical uncertainty of the measured raw asymmetry in the $D^0 \to \pi^-\pi^+$ sample as the signal yield in the $D^0 \to K^-K^+$ sample is about three times higher. The distribution of the renormalized weights is shown in Figure 8.3 for the ΔA_{CP} measurement. The effective sample size decreases only slightly as the kinematics of $D^0 \to K^-K^+$ and $D^0 \to \pi^-\pi^+$ decays are similar already before the weighting. Therefore, the loss in statistical power is only $N_{\text{eff}}/N \approx 0.93$. In the next section the weighting procedure for the $A_{CP}(K^-K^+)$ measurement is explained. There, the kinematic differences are much larger between the various samples.

The treatment of weights in binned-likelihood fits to the invariant mass distributions where also background contributions are present is discussed in Chapter 8.2.1 and the correct uncertainty coverage is tested in Chapter 8.2.2.

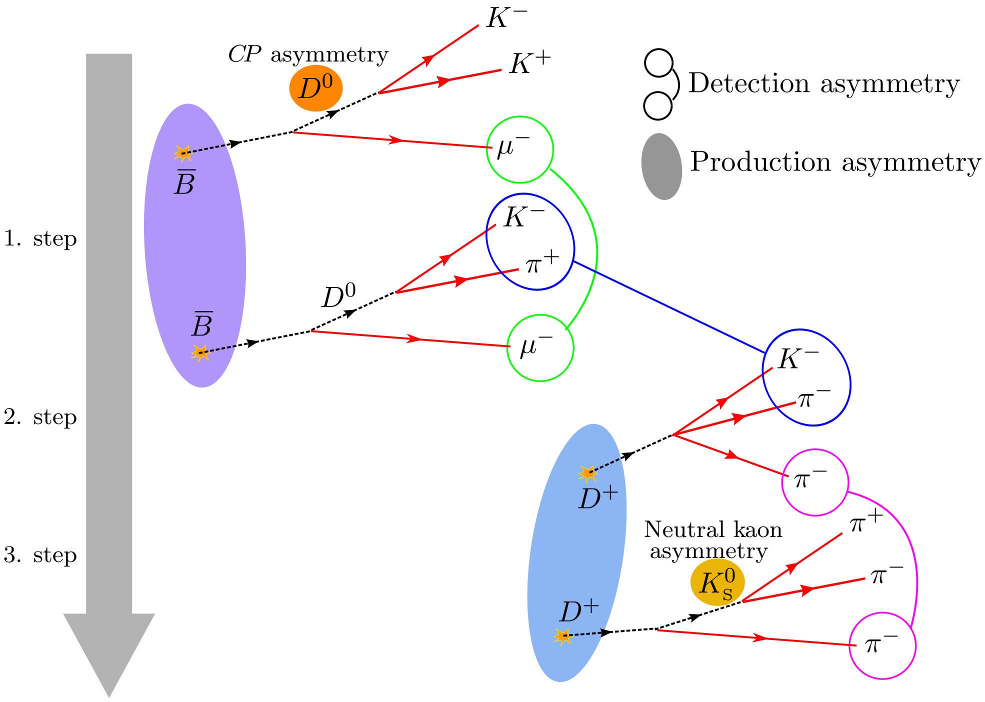

Figure 8.5: A sketch of the weighting strategy. Particles that are connected are used to cancel nuisance asymmetries. The weighting procedure starts from the top such that all calibration channels are weighted with respect to the $D^0 \to K^-K^+$ sample. It is explained in more detail in the text.

8.1.4 Weighting procedure for $A_{CP}(K^-K^+)$ measurement

The weighting procedure for the $A_{CP}(K^-K^+)$ measurement is more complex than that of the ΔA_{CP} measurement as it involves several decay channels, cf. Chapter 5. The strategy to weight events is depicted in Figure 8.5 and explained in the following. The basic idea is: First, the $D^0 \to K^-\pi^+$ sample is weighted such that it agrees with the $D^0 \to K^-K^+$ sample. Second, the weighted $D^0 \to K^-\pi^+$ sample is used to weight the $D^+ \to K^-\pi^+\pi^+$ sample. Third, the $D^+ \to \overline{K}^0\pi^+$ sample is weighted to the $D^+ \to K^-\pi^+\pi^+$ sample. The principle of each step is similar to the weighting procedure in the ΔA_{CP} measurement. However, there are some differences as discussed in detail in the following.

First step: $D^0 \to K^-K^+$ to $D^0 \to K^-\pi^+$ weighting

The first step is almost equivalent to the weighting of the ΔA_{CP} measurement explained in Chapter 8.1.2. The difference is that muon-tagged $D^0 \to K^-\pi^+$ events are used to determine the B production asymmetry $A_P(\overline{B})$ and the muon detection asymmetry $A_D(\mu^-)$.

The distribution of B, D^0 and muon signal candidates of muon-tagged $D^0 \to K^-K^+$ and $D^0 \to K^-\pi^+$ decays are compared in Figure 8.6. For example, the distributions of the 2012 magnet up sample are shown, the distributions of all other samples are found

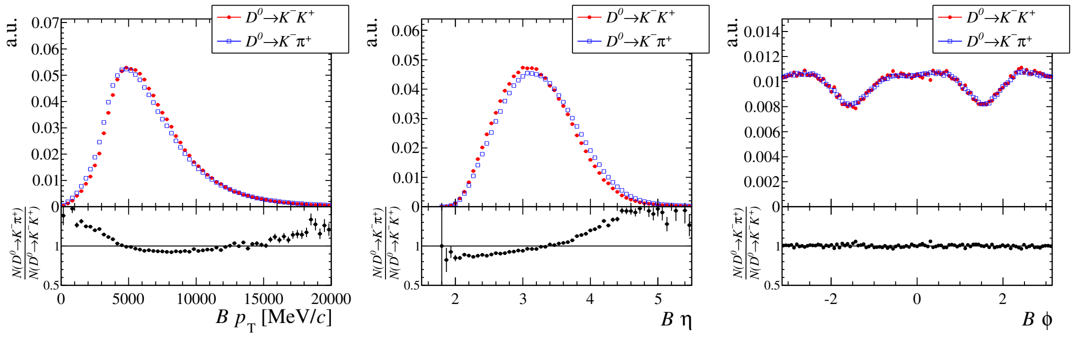

(a) B candidates

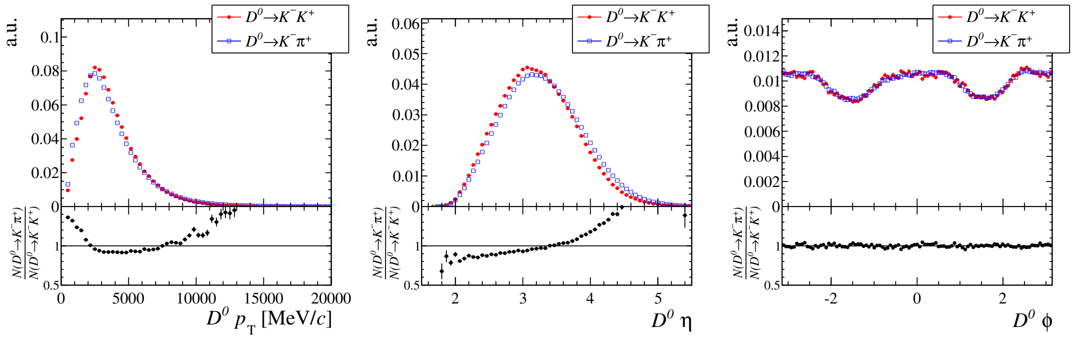

(b) D^0 candidates

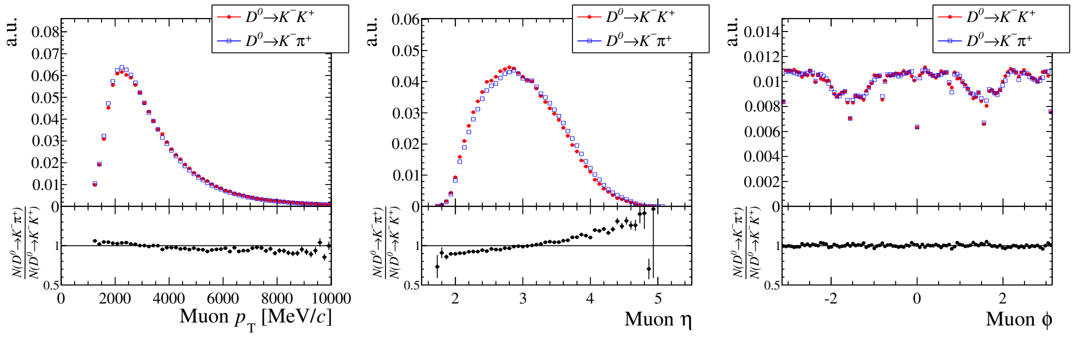

(c) Muon candidates

Figure 8.6: The kinematic distributions of reconstructed $D^0 \to K^- K^+$ and $D^0 \to K^- \pi^+$ decays before weighting. The 2012 data sample with magnet up polarity is used.

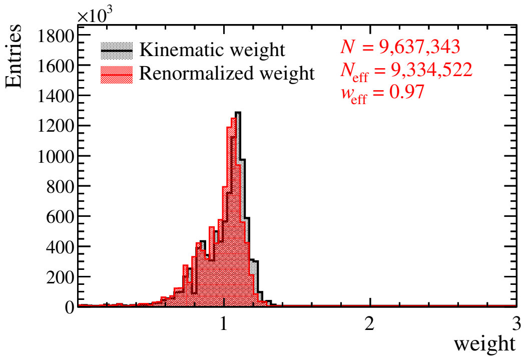

Figure 8.7: The weights assigned to the $D^0 \to K^-\pi^+$ samples. All data are used. The definitions of N, N_{eff}, w_{eff} and renormalized weight can be found in Chapter 8.1.3.

to be similar.[4] The background contribution is determined by a sideband subtraction equivalent to that used in the ΔA_{CP} measurement, cf. Chapter 8.1.2. The agreement of the kinematic distributions is similar to the agreement of $D^0 \to K^-K^+$ and $D^0 \to \pi^-\pi^+$ decays. A similar procedure is used to weight the events. The only difference is that the $D^0 \to K^-\pi^+$ sample is weighted and not the $D^0 \to K^-K^+$ sample.

The $D^0 \to K^-\pi^+$ events are assigned the weight

$$w(p_{\text{T}D^0}, \eta_{D^0}) = \frac{N_{\text{tot},K^-\pi^+}}{N_{\text{tot},K^-K^+}} \frac{n_{K^-K^+}(p_{\text{T}}{}^{D^0}, \eta^{D^0})}{n_{K^-\pi^+}(p_{\text{T}}{}^{D^0}, \eta^{D^0})} \quad , \tag{8.15}$$

where $n_{h^-h'^+}(p_{\text{T}}{}^{D^0}, \eta^{D^0})$ denotes the measured signal yield in the given bin, $N_{\text{tot},h^-h'^+}$ is the total signal yield of the $D^0 \to K^-K^+$ or $D^0 \to K^-\pi^+$ sample. The assigned weights are shown in Figure 8.7. The distribution is centred around one with little spread as differences in the kinematic distributions are small. The effective yield of the $D^0 \to K^-\pi^+$ sample is about 5 % smaller than the original sample size. The result of the weighting is shown in Figure 8.8. Weighting the D^0 kinematics largely corrects the disagreement in the B and muon distributions. As there is no full correlation between the D^0 kinematics and the muon and B kinematics, some residual differences are left. This affects mainly the kinematic distributions of muons. An additional weighting according to the muon kinematics is considered as a systematic study. The effect of an imperfect weighting is additionally studied with pseudo-experiments in Chapter 8.2.4.

---

[4] As for the ΔA_{CP} measurement, a full list of all distributions is given in Reference [5]

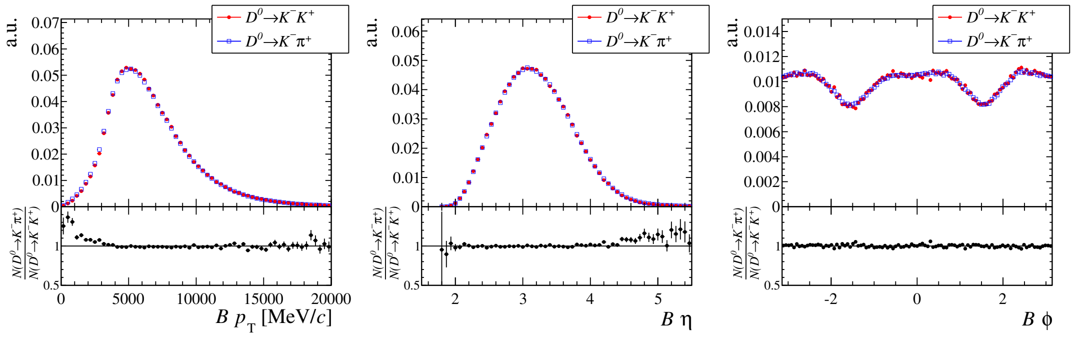

(a) B candidates

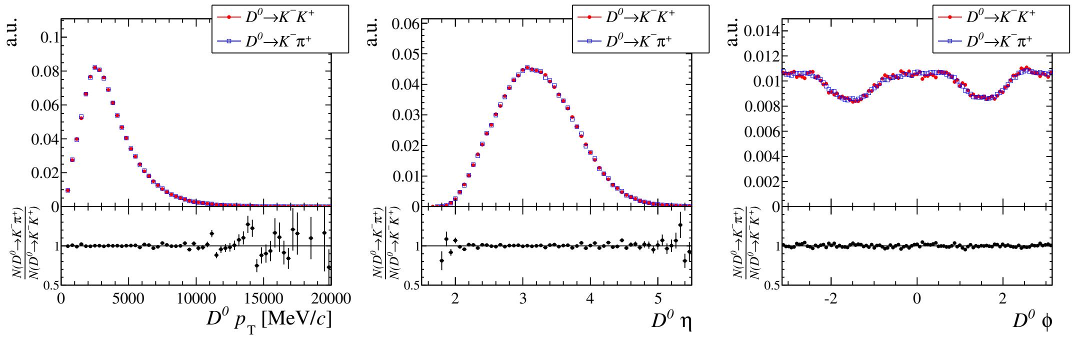

(b) D^0 candidates

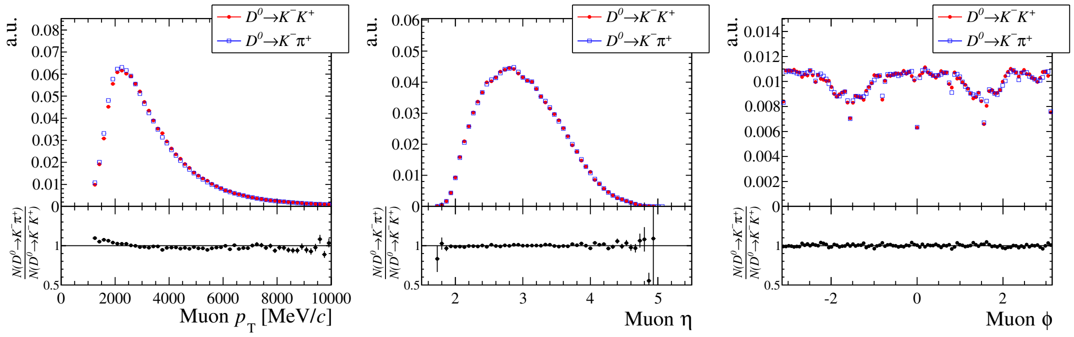

(c) Muon candidates

Figure 8.8: The kinematic distributions of reconstructed $D^0 \to K^- K^+$ and $D^0 \to K^- \pi^+$ candidates after weighting. The 2012 data sample with magnet up polarity is used.

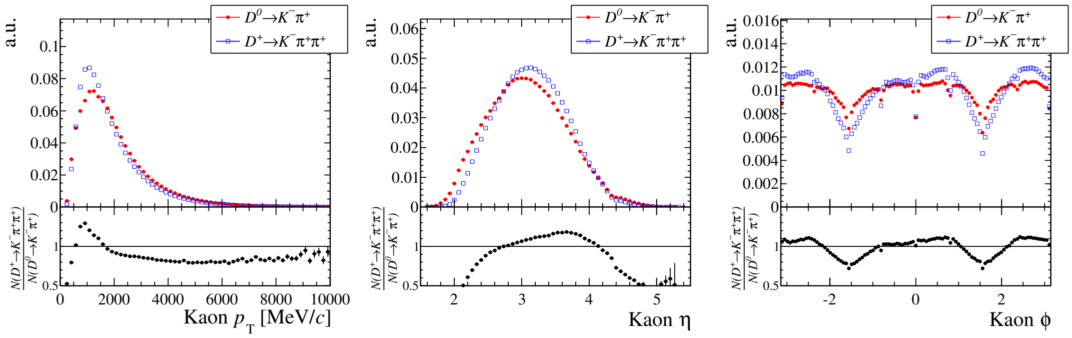

(a) Kaon candidates

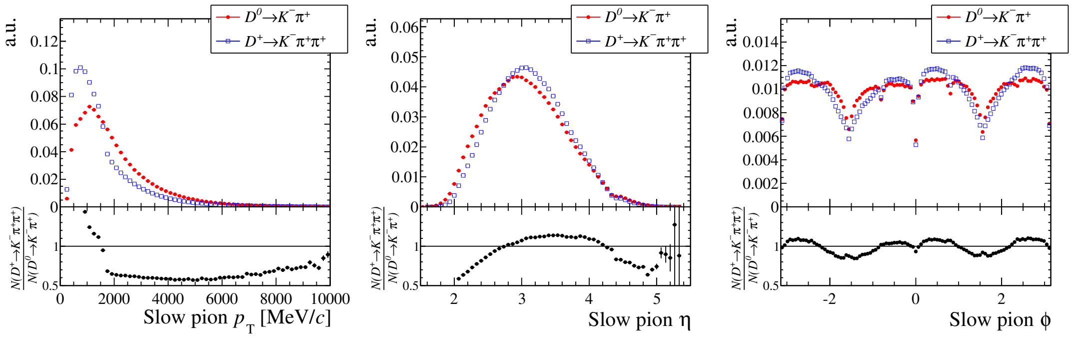

(b) Slow pions

Figure 8.9: The kinematic distributions of reconstructed $D^0 \to K^-\pi^+$ and $D^+ \to K^-\pi^+\pi^+$ decays after weighting. The 2012 data sample with magnet up polarity is used.

Second step: $D^0 \to K^-\pi^+$ to $D^+ \to K^-\pi^+\pi^+$ weighting

The second step is to assign weights to each $D^+ \to K^-\pi^+\pi^+$ candidate. This weighting step ensures that the raw asymmetries $A_{\text{raw}}(K^-\pi^+)$ and $A_{\text{raw}}(K^-\pi^+\pi^+)$ have the same contribution from the detection asymmetry $A_D(K^-\pi^+)$. The weighting of the $D^0 \to K^-\pi^+$ sample from the previous step is taken into account.

The kinematics of the pion and the kaon candidates of the $D^+ \to K^-\pi^+\pi^+$ sample have to match the muon-tagged $D^0 \to K^-\pi^+$ sample. The pion candidates of the $D^0 \to K^-\pi^+$ sample are not used in the trigger selection. Thus, the pion candidates of reconstructed $D^+ \to K^-\pi^+\pi^+$ decays are distinguished in Slow and Trigger pion, see also Chapter 6.2.4 and Figure 6.4 The pion which is used to create a positive decision of the `Hlt1TrackAllL0` line is defined as the Trigger pion, the other one is called Slow pion. In case both pions triggered, the Trigger pion is chosen randomly.

The kinematic distribution of Slow pions and kaons are shown in Figure 8.9. In both modes a sideband subtraction is done to extract the signal distribution. The signal and background region of D^+ candidates are similarly defined as for D^0 candidates. The mass sidebands are $[m_{D^+,\text{PDG}} - 60\,\text{MeV}/c^2, m_{D^+,\text{PDG}} - 30\,\text{MeV}/c^2]$ and $[m_{D^+,\text{PDG}} + 30\,\text{MeV}/c^2, m_{D^+,\text{PDG}} + 60\,\text{MeV}/c^2]$. The signal region is defined as $|m_{D^+} - m_{D^+,\text{PDG}}| < 30\,\text{MeV}/c^2$. The agreement of the distributions of $D^0 \to K^-\pi^+$

and $D^+ \to K^-\pi^+\pi^+$ decays is worse than in previous step. This is expected as two very different decays are compared. The $D^0 \to K^-\pi^+$ sample is from semileptonic B decays where the D^0 meson has two decay productes whereas the $D^+ \to K^-\pi^+\pi^+$ sample is from prompt produced D^+ mesons which has three decay products. Thus, it is not possible to weight according to the kinematics of one final state particle and obtain agreement in the other particle as well.

In principle an agreement in all six dimensions shown in Figure 8.9 is necessary to fully cancel all spurious asymmetries. However, it is not possible to weight in six dimensions as the overlap of the two samples in a large phase space is almost zero. Therefore, the number of dimensions has to be reduced. It is shown in Chapter 7.4 that the variations of the raw asymmetries in bins of the azimuthal angle ϕ of the kaon candidates are small when looking at the polarity averaged results, see Figures 7.17 and 7.19. Furthermore, dependencies on ϕ can be partly tested when changing the magnet polarity as this changes the direction in which particles with a given charge are bent. This is not possible for dependencies on p, p_{T} and η. Hence, the procedure does not include a weighting in the azimuthal angles of final state particles. As variations are seen in the raw asymmetries when looking at bins of ϕ, a weighting according to the ϕ distributions of pions and kaons is considered as a systematic study in Chapter 13. But the default method is chosen to be as simple as possible.

This leaves four dimensions. To further reduce the number, the weighting is performed in two steps. First, the p_{T} and η of the Slow pions together with the p_{T} of the kaons are used to determine the weights assigned to the $D^+ \to K^-\pi^+\pi^+$ sample. The combination of kinematic variables of the two final state particles is needed to be sensitive to the correlation between the kinematics of both particles. The bin boundaries in η are equidistantly distributed in the range $[1.5, 5.5]$. Similarly to the previous weighting step, the p_{T} of the kaon and the pion candidates are transformed by the function

$$g(p_{\mathrm{T}}) = \frac{2}{\pi} \arctan\left(\frac{p_{\mathrm{T}}(\,\mathrm{MeV}/c) - a}{b}\right) \quad , \tag{8.16}$$

where the parameter a is chosen close to the minimum p_{T}, $a = 250\,\mathrm{MeV}/c$, and the parameter b close to the average of the p_{T} distribution, $b = 2000\,\mathrm{MeV}/c$. Again 20 bins per dimension are used which results in 8000 bins in total. The weights, $w^{(1)}$, are then calculated as

$$w^{(1)}(p_{\mathrm{T}\pi^+}, \eta^{\pi^+}, p_{\mathrm{T}}{}^{K^-}) = \frac{N_{\mathrm{tot},K^-\pi^+\pi^+}}{N_{\mathrm{tot},K^-\pi^+}} \, \frac{n_{K^-\pi^+}(p_{\mathrm{T}}{}^{\pi^+}, \eta^{\pi^+}, p_{\mathrm{T}}{}^{K^-})}{n_{K^-\pi^+\pi^+}(p_{\mathrm{T}}{}^{\pi^+}, \eta^{\pi^+}, p_{\mathrm{T}}{}^{K^-})} \quad , \tag{8.17}$$

where $N_{\mathrm{tot},K^-\pi^+}$ and $n_{K^-\pi^+}(p_{\mathrm{T}}{}^{\pi^+}, \eta^{\pi^+}, p_{\mathrm{T}}{}^{K^-})$ take the weighting of the first step according to the $D^0 \to K^-K^+$ kinematics into account. The weighted event yield, $n^{(1)}_{K^-\pi^+\pi^+}$, in a kinematic bin of the $D^+ \to K^-\pi^+\pi^+$ sample is given by

$$\begin{aligned} &n^{(1)}_{K^-\pi^+\pi^+}(p_{\mathrm{T}}{}^{\pi^+}, \eta^{\pi^+}, p_{\mathrm{T}}{}^{K^-}, \eta^{\pi^+}) = \\ &n_{K^-\pi^+\pi^+}(p_{\mathrm{T}}{}^{\pi^+}, \eta^{\pi^+}, p_{\mathrm{T}}{}^{K^-}, \eta^{\pi^+}) \times w^{(1)}(p_{\mathrm{T}}{}^{\pi^+}, \eta^{\pi^+}, p_{\mathrm{T}}{}^{K^-}) \quad . \end{aligned} \tag{8.18}$$

The result of the weighting procedure is shown in Figure 8.10. By design a good agreement in p_{T} and η of the Slow pions and p_{T} of the kaons is achieved. The non-perfect agreement in the distributions is due to the finer binning in these plots than

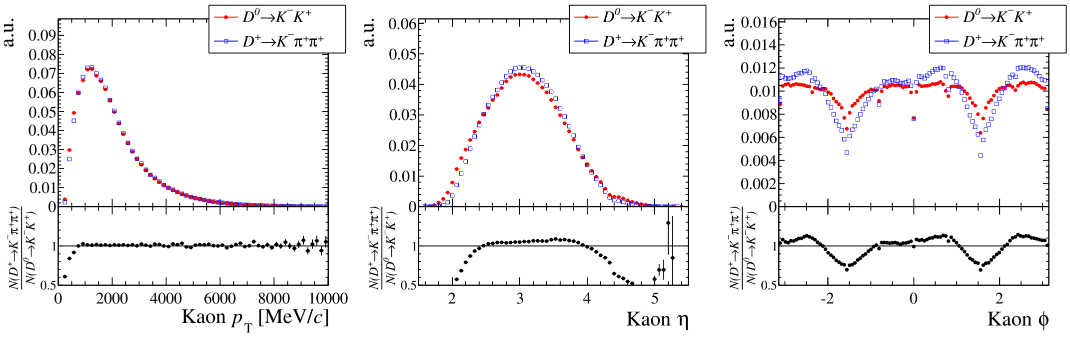

(a) Kaon candidates

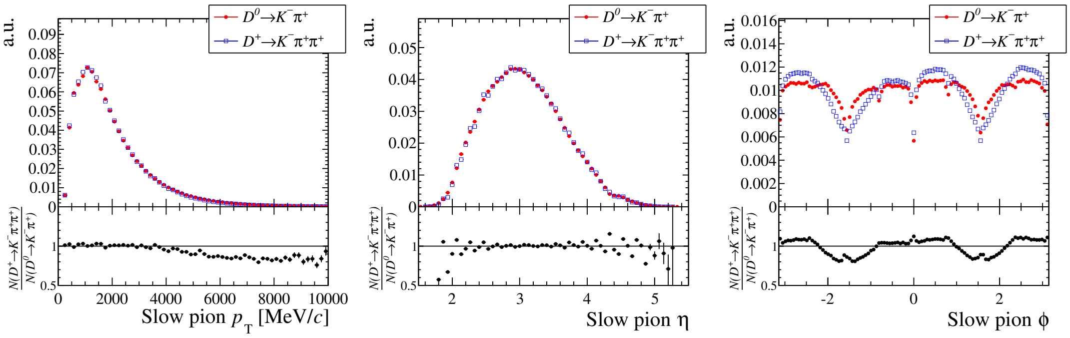

(b) Slow pions

Figure 8.10: The kinematic distributions of reconstructed $D^0 \to K^-\pi^+$ and $D^+ \to K^-\pi^+\pi^+$ candidates after the first weighting step. The 2012 data sample with magnet up polarity is used.

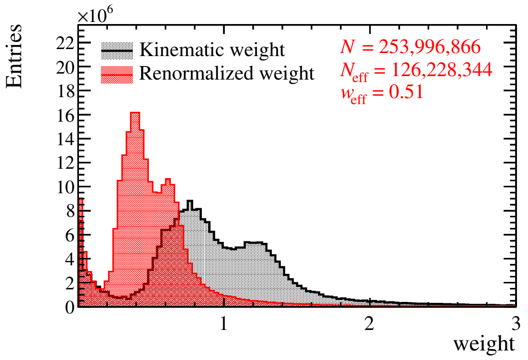

Figure 8.11: The weights assigned to the $D^+ \to K^-\pi^+\pi^+$ sample are shown for all data. The definitions of N, N_{eff} and w_{eff} can be found in Chapter 8.1.3.

the binning used for the weighting. The remaining differences in the η distribution of the kaons are decreased in a second step which takes the weights of Equation 8.17 into account. The p_{T} and η of the kaon signal candidates together with the p_{T} of the pion signal candidates are used to determine a second set of weights, $w^{(2)}$, which is assigned to the $D^+ \to K^-\pi^+\pi^+$ sample:

$$w^{(2)}(p_{\text{T}}{}^{K^-}, \eta^{K^-}, p_{\text{T}}{}^{\pi^+}) = \frac{N^{(1)}_{\text{tot},K^-\pi^+\pi^+}}{N_{\text{tot},K^-\pi^+}} \; \frac{n_{K^-\pi^+}(p_{\text{T}}{}^{K^-}, \eta^{K^-}, p_{\text{T}}{}^{\pi^+})}{n^{(1)}_{K^-\pi^+\pi^+}(p_{\text{T}}{}^{K^-}, \eta^{K^-}, p_{\text{T}}{}^{\pi^+})} \quad , \tag{8.19}$$

The 20 bins per dimension are equidistantly distributed in η and the transformed p_{T} of kaon and pion candidates. The final kinematic weight is the multiplication of both weights from Equations 8.17 and 8.19. Each weight is normalised with the factor w_{eff} defined in Equation 8.11 with $w_i = w_i^{(1)} \times w_i^{(2)}$. Thus, the renormalized weights are given as

$$w = w_{\text{eff}} \times w^{(1)} \times w^{(2)} \quad , \tag{8.20}$$

The distribution of the weights is given in Figure 8.11 and the kinematic distributions after the weighting can be seen in Figure 8.12. There is a good agreement in all dimensions which are used in the weighting procedure. The agreement in the ϕ distributions gets slightly worse. This is due to small correlations between (p_{T}, η) and ϕ due to the detector acceptance. As mentioned before, an additional weighting in ϕ is considered as a systematic study. The assigned weights have a larger spread than the weights assigned to the $D^0 \to K^-\pi^+$ sample. The statistical power of the $D^+ \to K^-\pi^+\pi^+$ sample is reduced by about a factor of two. As the $D^+ \to K^-\pi^+\pi^+$ signal yield is much larger than the signal yields of any other channel, the sensitivity of the analysis is not affected.

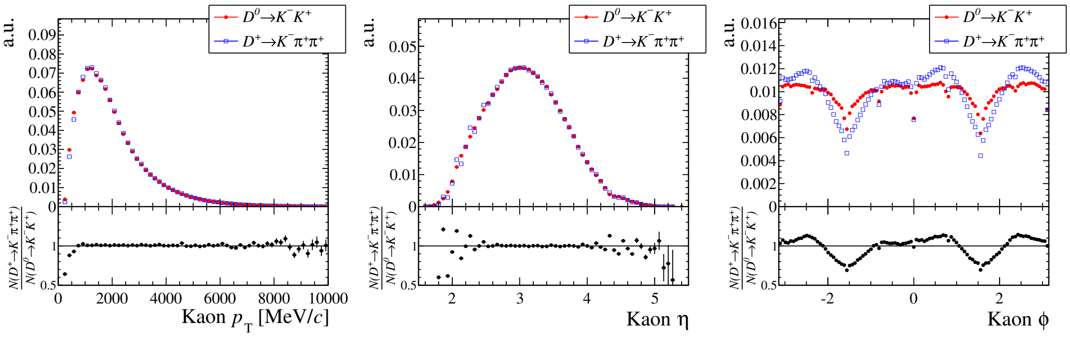

(a) Kaon candidates

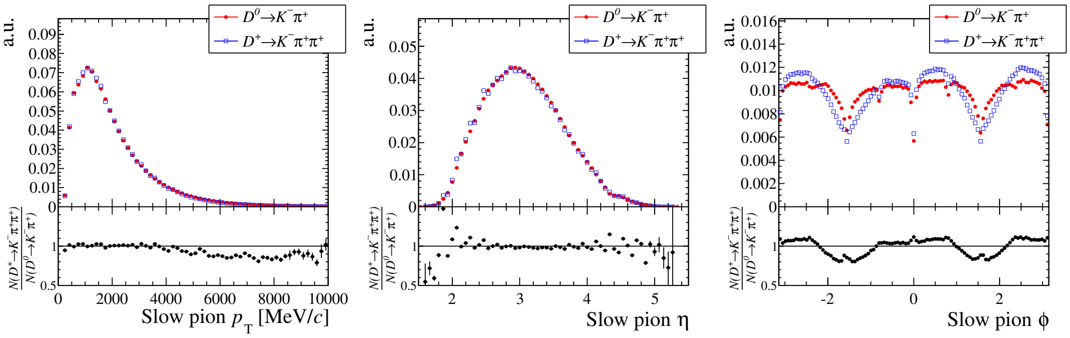

(b) Slow pions

Figure 8.12: The kinematic distributions of reconstructed $D^0 \to K^-\pi^+$ and $D^+ \to K^-\pi^+\pi^+$ candidates after weighting. The 2012 data sample with magnet up polarity is used.

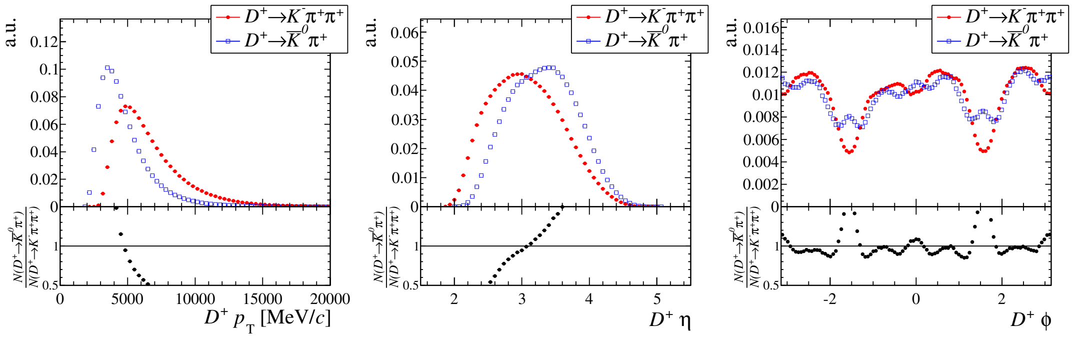

(a) D^+ candidates

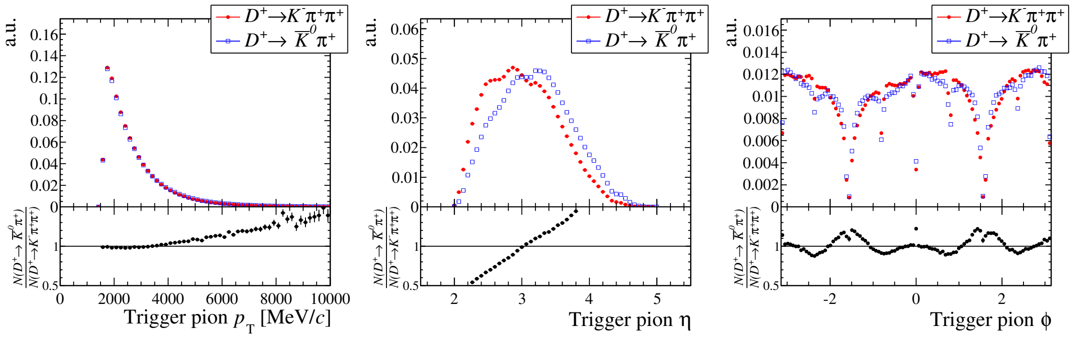

(b) Trigger pions

Figure 8.13: The kinematic distributions of reconstructed $D^+ \to K^- \pi^+ \pi^+$ and $D^+ \to \overline{K}^0 \pi^+$ decays before weighting. The 2012 data sample with magnet up polarity is used.

Third step: $D^+ \to K^- \pi^+ \pi^+$ to $D^+ \to \overline{K}^0 \pi^+$ weighting

The raw asymmetry of reconstructed $D^+ \to \overline{K}^0 \pi^+$ is used to determine the Trigger pion detection asymmetry and the D^+ production asymmetry. Both are needed to measure $A_D(K^- \pi^+)$ with the $D^+ \to K^- \pi^+ \pi^+$ sample. Therefore, the last and most complicated step is to match the D^+ and Trigger pion kinematics between the $D^+ \to K^- \pi^+ \pi^+$ sample and the $D^+ \to \overline{K}^0 \pi^+$ sample.

The kinematic distributions of D^+ and Trigger pion signal candidates[5] are shown for the $D^+ \to K^- \pi^+ \pi^+$ and $D^+ \to \overline{K}^0 \pi^+$ sample in Figure 8.13. The $D^+ \to K^- \pi^+ \pi^+$ distributions take the weighting from the previous step into account. The p_T distributions of the Trigger pions agree well as in both samples they are used in the `Hlt1TrackAllL0` line and, therefore, have passed the same thresholds. This leads to a very different D^+ momentum spectrum as one decay is a two-body and the other a three-body decay.

Similarly to the weighting of $D^+ \to K^- \pi^+ \pi^+$ and $D^0 \to K^- \pi^+$ candidates, a stepwise procedure is used to obtain a good agreement in the p_T and η distributions of Trigger pions and D^+ mesons. The azimuthal angles are not considered. This is not necessary for D^+ mesons, as production asymmetries do not depend on ϕ. The ϕ distributions of the Trigger pions are adjusted as a systematic study in Chapter 13.

---

[5] The same sideband subtraction as in the previous steps is used to extract the signal distributions.

The first step assigns weights according to the p_{T} and η of D^+ candidates and p_{T} of Trigger pions. The $D^+ \to \overline{K}^0\pi^+$ sample is weighted against the $D^+ \to K^-\pi^+\pi^+$ sample. The p_{T} distributions are again transformed with the known function $g(p_{\mathrm{T}})$, see Equation 8.16. The parameters a are 1800 MeV/c for the D^+ candidates and 1500 MeV/c for the Trigger pions. Parameters b are 5500 MeV/c and 1000 MeV/c, respectively. Equivalent to the other weightings 20 bins per dimension are used. *The first weights* assigned to the $D^+ \to \overline{K}^0\pi^+$ sample are determined by

$$w^{(1)}({p_{\mathrm{T}}}^{D^+}, \eta^{D^+}, {p_{\mathrm{T}}}^{\mathrm{Tr}\,\pi^+}) = \frac{N_{\mathrm{tot},K^-\pi^+\pi^+}}{N_{\mathrm{tot},\overline{K}^0\pi^+}} \; \frac{n_{\overline{K}^0\pi^+}({p_{\mathrm{T}}}^{D^+}, \eta^{D^+}, {p_{\mathrm{T}}}^{\mathrm{Tr}\,\pi^+})}{n_{K^-\pi^+\pi^+}({p_{\mathrm{T}}}^{D^+}, \eta^{D^+}, {p_{\mathrm{T}}}^{\mathrm{Tr}\,\pi^+})} \quad . \tag{8.21}$$

The weighted event yield, $n^{(1)}_{\overline{K}^0\pi^+}$, in a kinematic bin of the $D^+ \to \overline{K}^0\pi^+$ sample is given by

$$\begin{aligned} &n^{(1)}_{\overline{K}^0\pi^+}({p_{\mathrm{T}}}^{D^+}, \eta^{D^+}, {p_{\mathrm{T}}}^{\mathrm{Tr}\,\pi^+}, \eta^{\mathrm{Tr}\,\pi^+}) = \\ &n_{\overline{K}^0\pi^+}({p_{\mathrm{T}}}^{D^+}, \eta^{D^+}, {p_{\mathrm{T}}}^{\mathrm{Tr}\,\pi^+}, \eta^{\mathrm{Tr}\,\pi^+}) \times w^{(1)}({p_{\mathrm{T}}}^{D^+}, \eta^{D^+}, {p_{\mathrm{T}}}^{\mathrm{Tr}\,\pi^+}) \quad . \end{aligned} \tag{8.22}$$

A second step is performed to get a better agreement in the η distributions of Trigger pions. The p_{T} and η of the Trigger pions and p_{T} of the D^+ candidates are used to assign weights according to

$$w^{(2)}({p_{\mathrm{T}}}^{\mathrm{Tr}\,\pi^+}, \eta^{\mathrm{Tr}\,\pi^+}, {p_{\mathrm{T}}}^{D^+}) = \frac{N_{\mathrm{tot},K^-\pi^+\pi^+}}{N^{(1)}_{\mathrm{tot},\overline{K}^0\pi^+}} \; \frac{n^{(1)}_{\overline{K}^0\pi^+}({p_{\mathrm{T}}}^{\mathrm{Tr}\,\pi^+}, \eta^{\mathrm{Tr}\,\pi^+}, {p_{\mathrm{T}}}^{D^+})}{n_{K^-\pi^+\pi^+}({p_{\mathrm{T}}}^{\mathrm{Tr}\,\pi^+}, \eta^{\mathrm{Tr}\,\pi^+}, {p_{\mathrm{T}}}^{D^+})} \quad , \tag{8.23}$$

where the weights of the first step are taken into account. The second step changes the η distribution of the D^+ candidates. Therefore, the first step is repeated in a *third step* with the weights,

$$w^{(3)}({p_{\mathrm{T}}}^{D^+}, \eta^{D^+}, {p_{\mathrm{T}}}^{\mathrm{Tr}\,\pi^+}) = \frac{N_{\mathrm{tot},K^-\pi^+\pi^+}}{N^{(2)}_{\mathrm{tot},\overline{K}^0\pi^+}} \; \frac{n^{(2)}_{\overline{K}^0\pi^+}({p_{\mathrm{T}}}^{D^+}, \eta^{D^+}, {p_{\mathrm{T}}}^{\mathrm{Tr}\,\pi^+})}{n_{K^-\pi^+\pi^+}({p_{\mathrm{T}}}^{D^+}, \eta^{D^+}, {p_{\mathrm{T}}}^{\mathrm{Tr}\,\pi^+})} \quad . \tag{8.24}$$

where again the weights of the second step are taken into account.

After these three steps a good agreement in the four dimensions is achieved. The final normalised kinematic weight is then

$$w = w_{\mathrm{eff}} \times w^{(1)} \times w^{(2)} \times w^{(3)} \quad , \tag{8.25}$$

where w_{eff} is defined in Equation 8.11. The distribution of the weights is shown in Figure 8.14 and the result of the weighting procedure is given in Figure 8.15. The deviations in the D^+ and Trigger pion momentum spectra are largely reduced by the weighting procedure. The differences in the ϕ distributions of Trigger pions are discussed in the systematic studies. Many events of the $D^+ \to \overline{K}^0\pi^+$ sample get a weight of zero due to non-overlapping phase space regions. Additionally, the spread of the weights is large. The spread is mainly introduced by the first weighting step. The distribution of these kinematic weights looks similar to the one of the final weight shown in Figure 8.14. The kinematic weights of the other two steps are centred around one with a root mean

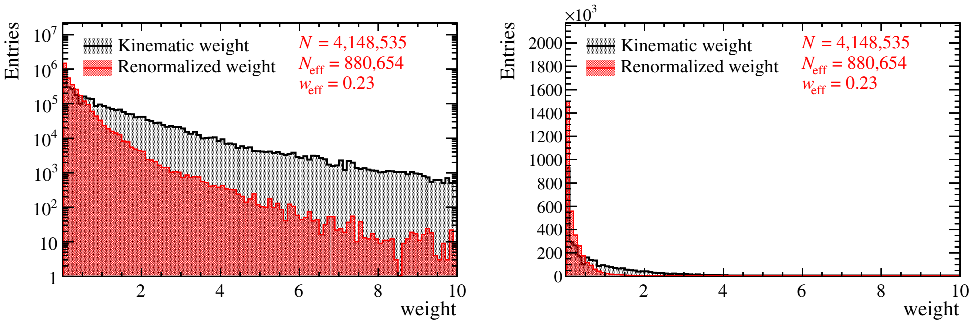

(a) Log scale

(b) Linear scale

Figure 8.14: The weights assigned to the $D^+ \to \overline{K}^0\pi^+$ (LL) sample are shown for all data. The definitions of N, N_{eff} and w_{eff} can be found in Chapter 8.1.3.

square of 0.25 and 0.4. The statistical power of the sample is reduced by almost a factor of five due to the weighting. The dominating statistical uncertainty of the $A_{CP}(K^-K^+)$ measurement is the statistical uncertainty of the weighted $A_{\text{raw}}(\overline{K}^0\pi^+)$ measurement.

The treatment of the kinematic weights in the binned maximum-likelihood fit to extract the raw asymmetries is discussed in the following.

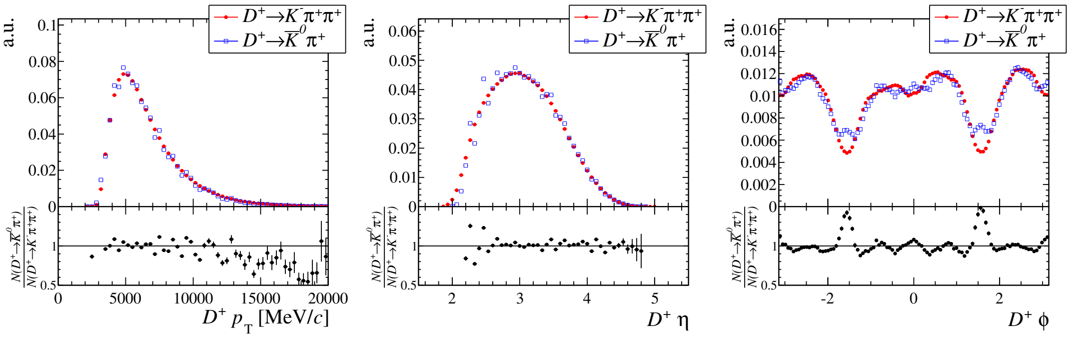

(a) D^+ candidates

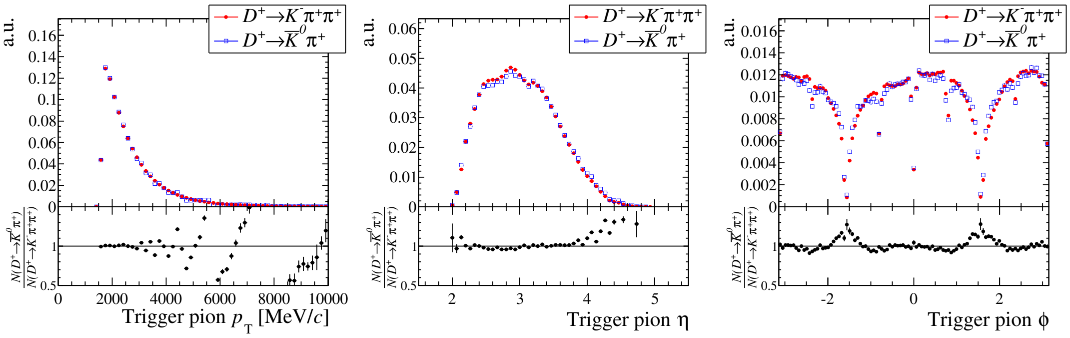

(b) Trigger pions

Figure 8.15: The kinematic distributions of reconstructed $D^+ \to \overline{K}^0\pi^+$ and $D^+ \to K^-\pi^+\pi^+$ decays before weighting. The 2012 data sample with magnet up polarity is used.

8.2 Validation of the asymmetry extraction procedure

In this section the fit procedure is validated with pseudo-experiments. First, it is checked that the fit has a correct uncertainty coverage and does not produce any biases in the raw asymmetry determination. Second, the correlation of a weighted sample and the original sample are discussed. Third, the effect of momentum-dependent asymmetries and the effect of the weighting is studied with pseudo-experiments.

8.2.1 Weighted likelihood fits

The weight of an event has to be taken into account in the binned maximum-likelihood fit otherwise the uncertainty estimate is wrong. However, the application of the renormalisation procedure discussed in Chapter 8.1.3 already gives the correct uncertainty coverage. For completeness, the formulas are repeated for the case of a binned likelihood-fit with weighted events. As previously described, after the kinematic weighting the weights are normalised with the factor

$$w_{\mathrm{eff}} = \frac{\sum_{i=1}^{N} w_i}{\sum_{i=1}^{N} w_i^2} \quad , \tag{8.26}$$

where the sum includes all events in the mass range of the fit. It should be pointed out that a second normalisation according to this formula leads to $w_{\mathrm{eff}} = 1$. The final weight is then used in the binned-likelihood fit. The effective population in a bin j, is given by

$$N_{j,\mathrm{eff}} = \sum_{i=1}^{N_j} w_i \quad . \tag{8.27}$$

where the sum runs over all events in the range of bin j. In the asymmetry fit the tag decision is also taken into account. The uncertainty of each bin is given by the sum of the weights squared:

$$\sigma_{N_{j,\mathrm{eff}}} = \sqrt{\sum_{i=1}^{N_j} w_i^2} \quad . \tag{8.28}$$

The correct uncertainty coverage of this procedure is studied in the next Section 8.2.2. The effective sample size after the weighting procedure is given by

$$N_{\mathrm{eff}} = w_{\mathrm{eff}} \sum_{i=1}^{N} w_i \quad . \tag{8.29}$$

which is always equal to or smaller than N. In the special case where all weights w_i are the same the renormalisation with w_{eff} leads to $N_{\mathrm{eff}} = N$ and there is no loss in statistical power due to the weighting. In the case where not all weights are equal, the statistical power is reduced.

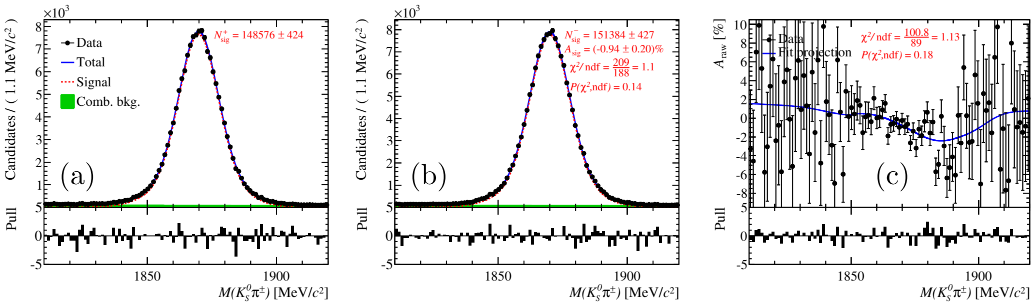

Figure 8.16: Invariant mass distributions of generated (a) $D^+ \to \overline{K}^0\pi^+$ and (b) $D^- \to K^0\pi^-$ decays, and (c) the raw asymmetry as function of the invariant mass. The fit results are overlaid. The kinematic weights and the event yield correspond to the 2012 magnet up sample.

8.2.2 Uncertainty coverage of binned maximum-likelihood fit with weighted events

A correct uncertainty coverage of the fit is necessary to determine the right uncertainty on the $A_{CP}(K^-K^+)$ and ΔA_{CP} measurement. Especially the weighting of the $D^+ \to \overline{K}^0\pi^+$ candidates reduces the statistical power of the sample drastically. The $D^+ \to \overline{K}^0\pi^+$ sample and its kinematic weights in the $A_{CP}(K^-K^+)$ measurement are used as basis for pseudo-experiments to test the uncertainty coverage.

In each pseudo-experiment events are generated with the fit model used for the asymmetry fits on data, which is discussed in Chapter 7.3. The model parameters are chosen such that they resemble the parameters of the fits to the $D^+ \to \overline{K}^0\pi^+$ sample, cf. Chapter 7.3.6. The generated asymmetry is $(-1\,\%)$ which corresponds to the observed raw asymmetries. The number of generated events is equal to the number of events of the four disjoint $D^+ \to \overline{K}^0\pi^+$ samples. A kinematic weight taken from the kinematic weights observed in data is assigned to each event. Thus, each pseudo-experiment has exactly the same distribution of kinematic weights as in the $A_{CP}(K^-K^+)$ measurement. The distribution of the weights is shown in Figure 8.14. The procedure is repeated 1200 times for the magnet up and down samples of 2011 and 2012. An example of a weighted fit is shown in Figure 8.16. It resembles the shape and the number of events of the 2012 magnet up sample. The effective signal yield is the same as observed in the $A_{CP}(K^-K^+)$ measurement, cf. Chapter 11.2.

The pull of a pseudo-experiment is defined as

$$\text{pull} = \frac{A_{\text{fit}} - A_{\text{gen}}}{\sigma_{A_{\text{fit}}}} \quad , \tag{8.30}$$

where A_{gen} is the generated value, A_{fit} is the fitted value in one pseudo-experiment and σ_A is the uncertainty estimate of the maximum-likelihood fit. Ideally the pulls are distributed as a Gaussian with a mean of zero and a width of one. In that case the fit is not biased and the uncertainty estimate is correct.

For example, the results of the pseudo-experiments corresponding to the 2012 magnet up sample are shown in Figure 8.17. The following statements hold as well for the other three samples. The distribution of the fitted asymmetries of the weighted and unweighted samples are centred around the generated value of $(-1\,\%)$. Both pull

Table 8.1: The uncertainty of the unweighted and the weighted fits and their quadratic difference. The last columns lists the width of the distribution shown Figure 8.17b.

Sample	σ_A [%]	$\sigma_{A,w}$ [%]	$\sqrt{\sigma^2_{A,w} - \sigma^2_A}$ [%]	$\sigma(A_{\text{fit,w}} - A_{\text{fit}})$ [%]
2011 up	0.17	0.35	0.30	0.27 ± 0.01
2011 down	0.15	0.27	0.23	0.22 ± 0.01
2012 up	0.09	0.19	0.17	0.17 ± 0.00
2012 down	0.09	0.20	0.18	0.17 ± 0.00

distributions show a Gaussian behaviour. The mean is centred around zero and the width is compatible with one. Neither the unweighted nor the weighted fit introduce a bias or have a wrong uncertainty coverage.

Additionally, it can be seen that the statistical uncertainty of the weighted fit is about twice the statistical uncertainty of the unweighted fit. Figure 8.17b shows the distribution of the difference of the fitted asymmetries of the weighted and unweighted sample, $A_{\text{fit},w} - A_{\text{fit}}$. The fitted width of this distribution is compared with the uncertainty of the fit with and without weighting and the *quadratic difference*, $\sqrt{\sigma^2_{A,w} - \sigma^2_A}$, in Table 8.1. As the simulated weights do not depend on any kinematic variables, the result shows that statistical variations can be expected due to the weighting. The quadratic difference is a good estimator of the expected size of these statistical fluctuations.

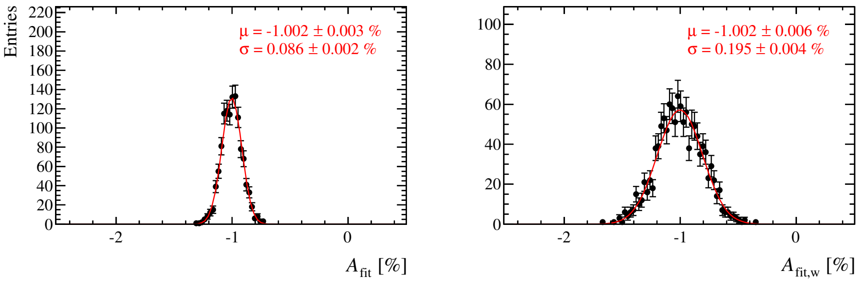

(a) Fitted asymmetries

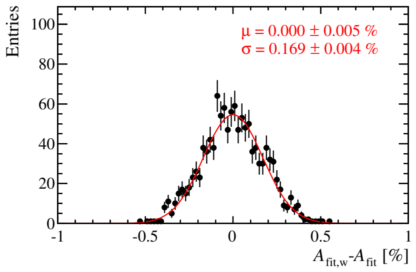

(b) Differences

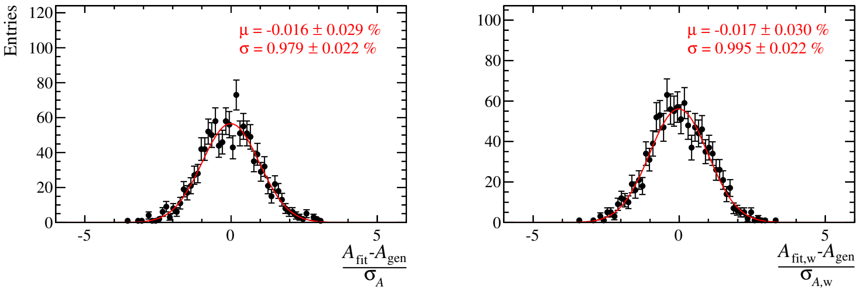

(c) Pull distributions

Figure 8.17: The results of the pseudo-experiments. The top row shows the distribution of the fitted asymmetry of the (a, left) unweighted and (a, right) weighted samples. (b) The distribution of the difference. (c) The bottom row shows the corresponding pull distributions. The event numbers and weights are taken from the 2012 magnet down sample. 1200 toys were generated for each sample.

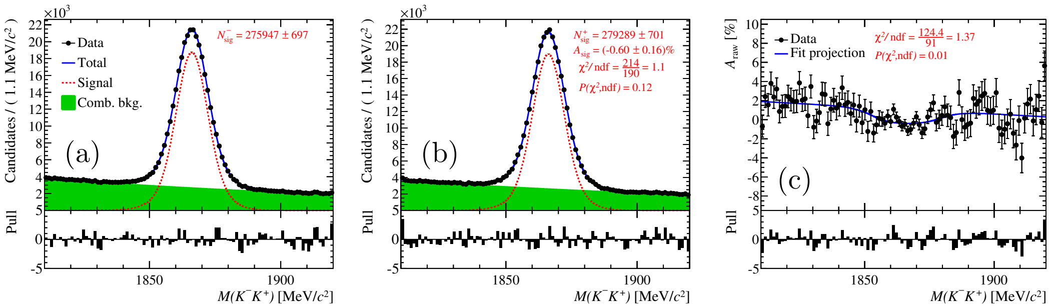

Figure 8.18: Invariant mass distributions of generated (a) $D^0 \to K^-K^+$ and (b) $\overline{D}^0 \to K^-K^+$ decays and (c) the raw asymmetry as function of the invariant mass. The fit results are overlaid. The event yield corresponds to the 2012 magnet up sample.

8.2.3 Correlation of the different $D^0 \to K^-K^+$ samples

The $A_{CP}(K^-K^+)$ and the ΔA_{CP} measurements use a common sample of $D^0 \to K^-K^+$ events. However, the $A_{CP}(K^-K^+)$ measurement uses a subset of the sample as a tighter trigger line selection is applied, see Chapter 6.2.4, and the ΔA_{CP} measurement uses weighted $D^0 \to K^-K^+$ candidates to obtain a better agreement in the kinematic distributions of $D^0 \to K^-K^+$ and $D^0 \to \pi^-\pi^+$ decays.

The correlation of a raw asymmetry determined on a sample A , A^A_{raw}, and one determined on a sample B, A^B_{raw}, is studied. The samples A and B can have a large overlap and the per-event weight of a given event is allowed to be different for samples A and B. The correlation factor of the raw asymmetries is calculated from the per-event weights by

$$\rho = \sqrt{\frac{\left(\sum_{A\cap B} w^A\, w^B\right)^2}{\sum_A \left(w^A\right)^2 \sum_B \left(w^B\right)^2}} \quad , \tag{8.31}$$

where w^A is the per-event weight of sample A and w^B the per-event weight of sample B. The two extreme cases where A and B have no overlap and where A and B are identical are obviously respected by the formula. If the samples A and B are not weighted, ρ would be given by $\sqrt{\frac{N_{A\cap B}}{N_A}\frac{N_{A\cap B}}{N_B}}$, which scales with the fractional overlap of the two samples. The effect of two different weights for one event is considered by multiplying them. Therefore, an event with large weights contributes more to the correlation than an event with small weights.

The validity of Equation 8.31 is tested with pseudo-experiments. The same number of candidates as obeserved in one $D^0 \to K^-K^+$ sample (2012 magnet up) is generated. The parameters of the mass model are taken similar to the fitted values on data. The simulated signal asymmetry is $(-0.4\ \%)$ which is representative for the raw asymmetries observed in data, cf. Tables 7.11. An example is shown in Figure 8.18. The asymmetry is fitted twice. First, the raw asymmetry is determined in an unweighted sample where roughly 16 % of the events are randomly thrown away (sample A). The fraction of 16 % corresponds to the loss of events due to the tighter selection requirements, cf. Table 6.7. Second, the events are weighted equivalently to the weighting performed in the ΔA_{CP} measurement (sample B). The weights are drawn from the distribution of

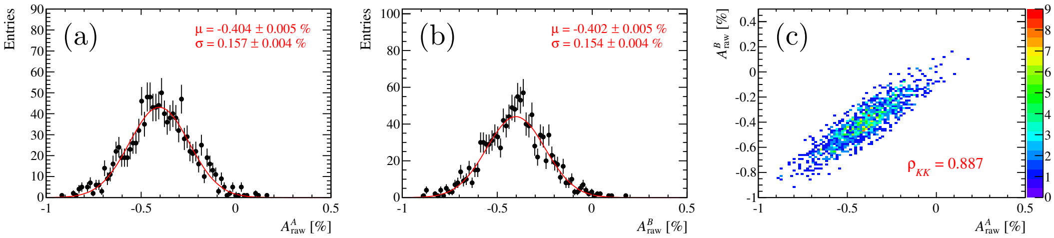

Figure 8.19: The projected distributions of (a) A^A_{raw} and (b) A^B_{raw} of 1200 pseudo-experiments. A fit with a Gaussian is overlaid. (c) The two-dimensional distribution of A^A_{raw} and A^B_{raw}. The correlation factor of the histogram is given. The generated asymmetry is (-0.4 %).

the observed weights, see Figure 8.3. The procedure is repeated 1200 times. The fitted asymmetries A^A_{raw} and A^B_{raw} of each pseudo-experiment are filled into a two-dimensional histogram. The projections on each dimension and the two-dimensional histogram are shown in Figure 8.19. Both measurements are unbiased. The correlation factor of the two-dimensional histogram is 0.887. The calculated correlation of 2012 magnet up sample according to Equation 8.32 is 0.874 which is in good agreement with the result of the pseudo-experiments. Therefore, Equation 8.31 is used to calculate correlations of raw asymmetries.

The $A_{CP}(K^-K^+)$ and ΔA_{CP} measurements are correlated due to the common $D^0 \to K^-K^+$ candidates. In terms of the two $D^0 \to K^-K^+$ samples, Equation 8.31 is written as

$$\rho_{KK} = \sqrt{\frac{\left(\sum_{i=1}^{N} w_{KK,i}^{A_{CP}(K^-K^+)}\; w_{KK,i}^{\Delta A_{CP}}\right)^2}{\sum_{i=1}^{N}\left(w_{KK,i}^{A_{CP}(K^-K^+)}\right)^2 \sum_{i=1}^{N}\left(w_{KK,i}^{\Delta A_{CP}}\right)^2}}\ , \tag{8.32}$$

where N is the total number of $D^0 \to K^-K^+$ events, $w_{KK,i}^{\Delta A_{CP}}$ is the weight of each $D^0 \to K^-K^+$ candidate in the ΔA_{CP} measurement and $w_{KK,i}^{A_{CP}(K^-K^+)}$ is the weight of each $D^0 \to K^-K^+$ candidate in the $A_{CP}(K^-K^+)$ measurement. The weight $w_{KK,i}^{A_{CP}(K^-K^+)}$ is one if the event passed the $A_{CP}(K^-K^+)$ trigger line selection and zero if not.

Using Equations 5.23 and 5.14, the covariance of the $A_{CP}(K^-K^+)$ and ΔA_{CP} measurements is derived to

$$\begin{aligned}\mathrm{Cov}(A_{CP}(K^-K^+), \Delta A_{CP}) &= \mathrm{Cov}(A_{\mathrm{raw}}(K^-K^+)^{A_{CP}(K^-K^+)}, A_{\mathrm{raw}}(K^-K^+)^{\Delta A_{CP}}) \\ &= \rho_{KK}\, \sigma_{A\mathrm{raw}}^{A_{CP}(K^-K^+)}\; \sigma_{A\mathrm{raw}}^{\Delta A_{CP}}\end{aligned} \tag{8.33}$$

where ρ_{KK} is the correlation factor of the two $D^0 \to K^-K^+$ samples according to Equation 8.32, $\sigma_{A\mathrm{raw}}^{A_{CP}(K^-K^+)}$ is the statistical uncertainty on $A_{\mathrm{raw}}(K^-K^+)$ in the ΔA_{CP} measurement and $\sigma_{A\mathrm{raw}}^{\Delta A_{CP}}$ in the $A_{CP}(K^-K^+)$ measurement. Following Equation 8.33, the correlation coefficient, ρ_{stat}, between the measurements of $A_{CP}(K^-K^+)$ and ΔA_{CP} is given by

$$\rho_{\mathrm{stat}} = \rho_{KK} \frac{\sigma_{A\mathrm{raw}}^{A_{CP}(K^-K^+)}\; \sigma_{A\mathrm{raw}}^{\Delta A_{CP}}}{\sigma_{\mathrm{stat}}^{\Delta A_{CP}}\; \sigma_{\mathrm{stat}}^{A_{CP}(K^-K^+)}}\ , \tag{8.34}$$

where $\sigma_{\text{stat}}^{\Delta A_{CP}}$ and $\sigma_{\text{stat}}^{A_{CP}(K^-K^+)}$ are the statistical uncertainties of the ΔA_{CP} and the $A_{CP}(K^-K^+)$ measurements, respectively. The former includes the statistical uncertainty of the $D^0 \to \pi^-\pi^+$ sample, the latter the statistical uncertainties of the detection asymmetry $A_D(K^-\pi^+)$ and the raw asymmetry $A_{\text{raw}}(K^-\pi^+)$. The correlation has to be determined if both results are used in a fit to extract other physics parameters, e.g., when calculating $A_{CP}(\pi^-\pi^+)$ from the difference of ΔA_{CP} and $A_{CP}(K^-K^+)$.

8.2.4 Validation of the kinematic weighting

The weighting method presented in Chapter 8.1 adjusts the kinematic distributions of all decay channels such that momentum-dependent nuisance asymmetries cancel in the difference of two raw asymmetries. The weights are taken from distributions with a limited number of dimensions and a finite number of bins. Therefore, the systematic effect of this imperfect weighting is studied with pseudo-experiments.

The effect of the weighting can only be tested when the same kinematic correlations as in data are generated. Thus, the correlations are taken directly from data. For each individual pseudo-experiment the data samples are taken and the same weighting procedure as in the $A_{CP}(K^-K^+)$ measurement is applied. The same reconstructed D mass is used as well. The tags of D candidates, this means if they are a D^0 or $\overline{D}^0$ candidate and a D^+ or D^- candidate, is randomised. The randomisation is performed according to artificial asymmetries which emulate production and detection asymmetries. Therefore, the artificial asymmetries depend on the kinematics of all involved particles. The simulated asymmetries mimic the observed behaviour of the raw asymmetries that are shown in Chapter 7.4. They are listed in Table 8.2. The pseudo-experiments assume that production and detection asymmetries sum up.

As an example $D^+ \to K^-\pi^+\pi^+$ decays are discussed. For each event the asymmetry is calculated according to

$$\begin{aligned} &A_{\text{raw}}(K^-\pi^+\pi^+)(p_{\text{T}}(D^\pm), p(K^\mp), p_{\text{T}}(\pi^\pm)) = \\ &\qquad A_P(D^+)(p_{\text{T}}(D^\pm)) + A_D(K^-\pi^+)(p(K^\mp)) + A_D(\pi^+)(p_{\text{T}}(\pi^\pm)) \ , \end{aligned}$$

where the kinematics are taken from that particular event and the functional behaviour is given in Table 8.2. A random number between zero and one is drawn. If the number is larger than $\frac{1}{2}(1 - A_{\text{raw}}(K^-\pi^+\pi^+)(p_{\text{T}}(D^\pm), p(K^\mp), p_{\text{T}}(\pi^\pm)))$, the event is tagged as a

Table 8.2: The functions of the simulated asymmetries in the pseudo-experiments.

Asymmetry	**Function**
$A_{CP}(K^-K^+)$	$-0.5\ \%$
$A_P(D^+)$	$(-2.2\, e^{\frac{-p_{\text{T}}(D^\pm)}{2500\,\text{MeV}/c}} - 0.2)\ \%$
$A_P(B)$	$(-1.7\, e^{\frac{-p_{\text{T}}(B)}{5000\,\text{MeV}/c}} + 0.0)\ \%$
$A_D(\pi^+)$	$(-0.9\, e^{\frac{-p_{\text{T}}(\pi^\pm)}{5000\,\text{MeV}/c}} + 0)\ \%$
$A_D(K^-\pi^+)$	$(-3.5\, e^{\frac{-p(K^\pm)}{8500\,\text{MeV}/c}} - 0.4)\ \%$
$A_D(\mu)$	$(-0.6\, e^{\frac{-p_{\text{T}}(\mu^\pm)}{400\,\text{MeV}/c}} + 0.0)\ \%$

D^+ candidate. If the number is smaller, the event is tagged as a D^- candidate. The other decay modes are equivalently treated according to the contributions of their raw asymmetries, cf. Chapter 5. It should be pointed out that this method assumes that the involved asymmetries are small and, thus, higher order corrections are negligible. Given the observed asymmetries, this assumption is very well justified.

In the following the 2012 magnet up sample is used as input to the pseudo-experiments. Only one sample is considered as this study is computationally intensive. The raw asymmetries are fitted with the default procedure. The results for each raw asymmetry and the measured *CP* asymmetry are shown in Figure 8.20 before and after the weighting. As expected, the sensitivity decreases due to the weighting, but there is a systematic shift between the weighted and the unweighted fit result. The central values of the raw asymmetries are approximately compatible with the raw asymmetries shown in Table 7.11. Also the difference between the weighted and the unweighted result is similar to what is obtained in data. This is shown later in Table 12.2 in Chapter 12.1 when the results of the $A_{CP}(K^-K^+)$ measurement are presented. The largest systematic shift is observed in the $D^+ \to \overline{K}^0\pi^+$ sample. This is expected as the weighting procedure removes a large part of this sample at low p_{T} of the D^+ candidates. The weighting of the semileptonic modes has negligible effect as there are little differences in the kinematic distributions and only a small muon detection asymmetry is simulated. This is also taken as a confirmation that the ΔA_{CP} weighting procedure is sufficient. It is important to point out that the unweighted $A_{CP}(K^-K^+)$ result is shifted by 0.14%, while the weighted one is shifted by only 0.03%.

The residual bias of 0.03 % is taken as systematic uncertainty due to the imperfect weighting. Further systematic studies regarding the weighting procedure are discussed in Chapter 13.2.4. There, the strategy is varied on data and deviations from the default procedure are used to extract additional systematic uncertainties.

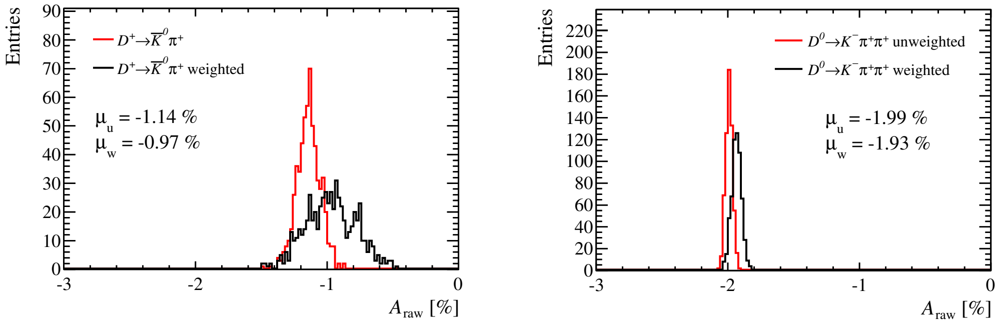

(a) $A_{\text{raw}}(\overline{K}^0\pi^+)$ (b) $A_{\text{raw}}(K^-\pi^+\pi^+)$

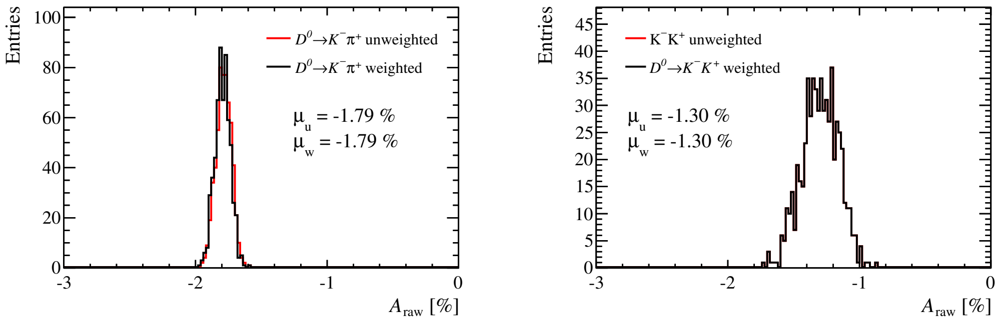

(c) $A_{\text{raw}}(K^-\pi^+)$ (d) $A_{\text{raw}}(K^-K^+)$

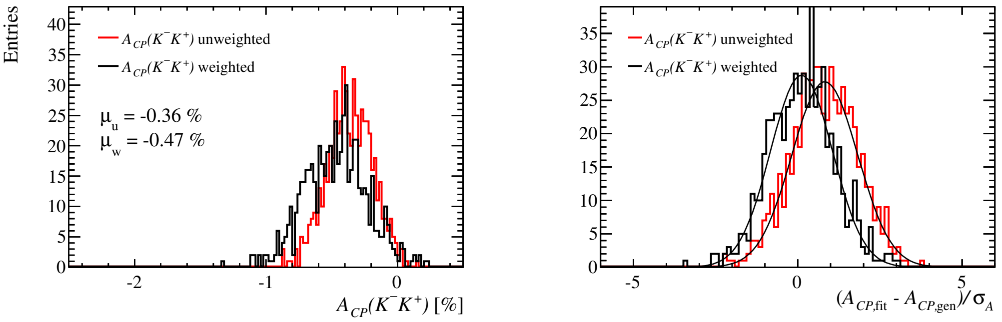

(e) $A_{CP}(K^-K^+)$ (f) Pull distribution of $A_{CP}(K^-K^+)$

Figure 8.20: The results of the pseudo-experiments dedicated to the weighting procedure. The fitted asymmetries for each raw asymmetry measurement are shown in (a),(b),(c) and (d). (e) shows the result of $A_{CP}(K^-K^+)$. (f) the according pull distribution. In total 600 pseudo-experiments are generated. The kinematic weights of the 2012 magnet up sample are used. In Figure 8.20d both distributions overlap as no weighting is applied.

8.3 Summary

The effect of momentum-dependent production and detection asymmetries is considered by the presented kinematic weighting procedure.

The kinematic weighting reduces the statistical power of a sample. The effect on the statistical uncertainty is accounted for by renormalising every weight with a global renormalisation factor which depends on the weights:

$$w_{\text{eff}} = \frac{\sum_{i=1}^{N} w_i}{\sum_{i=1}^{N} w_i^2} \quad .$$

In the ΔA_{CP} measurement the kinematic weighting adjusts the kinematic distributions of $D^0 \to K^-K^+$ candidates such that they match the distributions of $D^0 \to \pi^-\pi^+$ candidates. Then, detection and production asymmetries cancel in the difference of the two raw asymmetries. The statistical power of the $D^0 \to K^-K^+$ sample is reduced by 8 %.

The weighting procedure of the $A_{CP}(K^-K^+)$ measurement is more involved as the kinematic distributions of four channels have to be harmonised:

- First, the $D^0 \to K^-\pi^+$ sample is weighted with respect to the $D^0 \to K^-K^+$ sample to match the kinematic distributions of muon and B candidates. Due to the good agreement even before the kinematic weighting, the statistical power of the $D^0 \to K^-\pi^+$ sample is reduced by only 3 %.

- Second, the $D^+ \to K^-\pi^+\pi^+$ sample is weighted such that the distributions of kaons and Slow pions of $D^0 \to K^-\pi^+$ and $D^+ \to K^-\pi^+\pi^+$ decays are in agreement. The statistical power of the $D^+ \to K^-\pi^+\pi^+$ sample is reduced by 50 %. The final precision on $A_{CP}(K^-K^+)$ is almost unchanged due to the large abundance of $D^+ \to K^-\pi^+\pi^+$ candidates.

- Third, the $D^+ \to \overline{K}^0\pi^+$ sample is weighted to cancel the Trigger pion and the D^+ production asymmetry in the difference of $A_{\text{raw}}(K^-\pi^+\pi^+)$ and $A_{\text{raw}}(\overline{K}^0\pi^+)$. In this step the overlap of the unweighted $D^+ \to K^-\pi^+\pi^+$ and $D^+ \to \overline{K}^0\pi^+$ samples is small. Therefore, the effective yield is reduced by 78 %. This has a large effect on the final uncertainty on $A_{CP}(K^-K^+)$.

Each step takes the kinematic weights of the previous into account.

The correct uncertainty coverage of the binned maximum-likelihood fits with kinematic weights is tested with pseudo-experiments. Pseudo-experiments are performed to determine the correlation of a weighted and an unweighted sample. The cancellation of the production and detection asymmetries after the kinematic weighting is studied with pseudo-experiments. There, momentum-dependent asymmetries which are motivated by the observed asymmetries in data are simulated. A small residual asymmetry, 0.03 %, is found for the $A_{CP}(K^-K^+)$ measurement.

Chapter 9

Neutral kaon asymmetry

The initial flavour of a neutral kaon is defined in the Cabibbo-favoured $D^+ \to \overline{K}^0\pi^+$ and $D^- \to K^0\pi^-$ decays. The D^+ meson decay involves a $c \to s$ transition and the D^- meson decay a $\overline{c} \to \overline{s}$ transition. However, the mass eigenstates of the neutral kaon system are the K^0_S and K^0_L states, cf. Chapter 2.3.1. This leads to a mixing of the K^0 and $\overline{K}^0$ states. The neutral kaon candidates are reconstructed in the *CP* eigenstate $\pi^+\pi^-$. As the mass eigenstate K^0_S is not a *CP* eigenstate, the decay $K^0_\mathrm{S} \to \pi^+\pi^-$ is *CP* violating Additionally, K^0 and $\overline{K}^0$ mesons have different absorption rates in the detector material, equivalently to charged kaons. The effects of mixing, *CP* violation and absorption interfere due to coherent forward scattering. Thus, the time evolution of neutral kaons while traversing the LHCb detector is modelled and the contribution of the neutral kaon asymmetry $A_D(\overline{K}^0)$ to the raw asymmetry $A_\mathrm{raw}(\overline{K}^0\pi^+)$ is determined.

First, the experimental aspects of K^0_S reconstruction are introduced. Second, the formalism of neutral meson mixing in matter is discussed. Third, the expected asymmetry is calculated with the developed model. Fourth, the expectation is compared with the measured asymmetry. The last section gives the correction needed for the $A_{CP}(K^-K^+)$ measurement.

9.1 Reconstructed K^0_S decays

Despite their name K^0_S mesons have a rather large lifetime on the LHCb scale. Only a third of the reconstructed decays occur inside the VELO. These K^0_S decays can be reconstructed with two long tracks. Those which decay between VELO and TT are reconstructed with two downstream tracks.[1] Only the decay to the symmetric final state $\pi^+\pi^-$ is considered as it has the highest branching fraction, about 70 %, and does not introduce a detection asymmetry. K^0_L mesons have a much larger lifetime and very few decay before the TT.

The decay-position distribution and the amount of traversed material is shown for both categories in Figure 9.1. The thickness of the traversed material is quoted in terms of the nuclear collision length, cf. Chapter 2.5.1. About 25% of the long-reconstructed K^0_S candidates decay in the LHC vacuum before they reach the RF foil, without passing any material. The RF foil and the VELO material contribute to the amount of material seen by the other 75 % long-reconstructed K^0_S candidates. The

---

[1] As a reminder, the combination of two long tracks is referred to as long-reconstructed, the combination of two downstream tracks as downstream-reconstructed. The different track types are defined in Chapter 4.3.

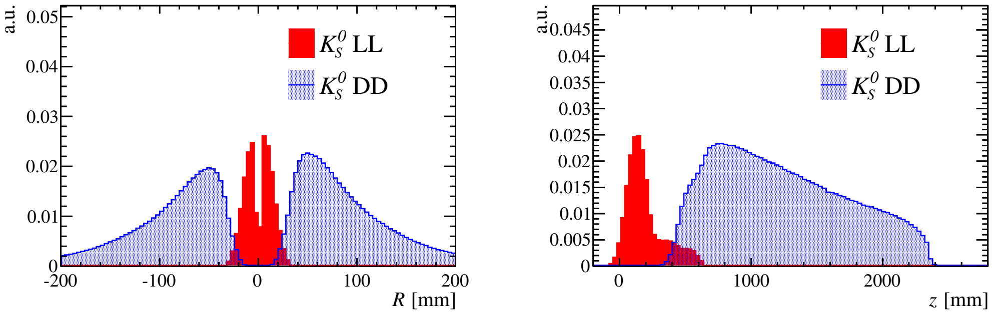

(a) Radial distance R

(b) Coordinate z

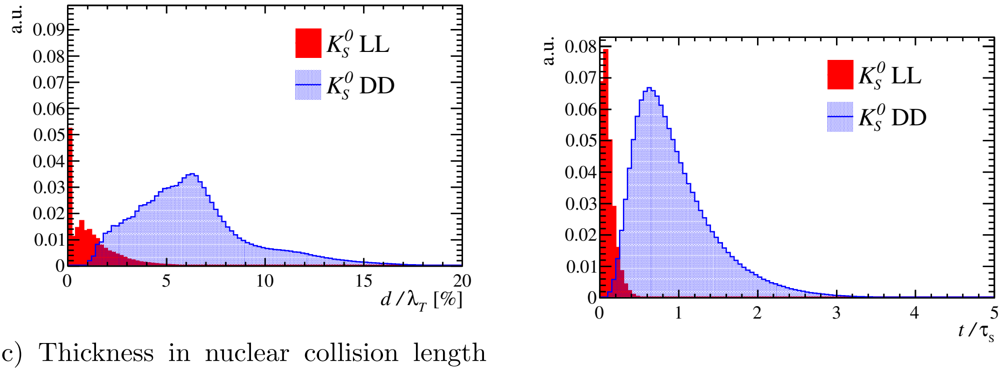

(c) Thickness in nuclear collision length d/λ_T

(d) Decay time t/τ_S

Figure 9.1: The reconstructed K^0_S decay vertex position, R and Z, the thickness in nuclear collision length d/λ_T and the decay time distributions, separately for long-reconstructed (LL) and downstream-reconstructed (DD) candidates. The RF foil is located at $R = 8\,\mathrm{mm}$, the VELO ends at $z \approx 1\,\mathrm{m}$, the TT starts at $2.2\,\mathrm{m}$. RICH1 is situated between VELO and TT. The decay time is given in terms of the K^0_S lifetime τ_S.

downstream-reconstructed K^0_S candidates traverse additionally the material of RICH1. The reconstructed decay time of long-reconstructed K^0_S candidates is significantly smaller than one K^0_S lifetime, while that of downstream-reconstructed candidates goes up to three lifetimes.

9.2 Asymmetry formalism

The phenomenology of mixing and *CP* violation in a neutral meson system is given in Chapter 2.3. Here, the formulas are adapted to the common notation in the neutral kaon system. The effective Schroedinger equation of neutral kaon mixing in vacuum can be written as[2]

$$i\frac{\mathrm{d}}{\mathrm{d}t}\begin{pmatrix}|K^0(t)\rangle\\ |\overline{K}^0(t)\rangle\end{pmatrix}_\mathrm{vac} = \left(\boldsymbol{M} - \frac{i}{2}\boldsymbol{\Gamma}\right)\begin{pmatrix}|K^0(t)\rangle\\ |\overline{K}^0(t)\rangle\end{pmatrix}_\mathrm{vac} \tag{9.1}$$

---

[2] The convention $\hbar = c = 1$ is used here to simplify the formulas.

where $\boldsymbol{M}$ and $\boldsymbol{\Gamma}$ are hermitian matrices describing mixing and decay of K^0 and $\overline{K}^0$ mesons. The eigenstates of $\left(\boldsymbol{M} - \frac{i}{2}\boldsymbol{\Gamma}\right)$ are the known K^0_S and K^0_L states. They are given as

$$\begin{aligned} \left|K^0_\mathrm{S}\right\rangle &= \frac{1}{\sqrt{2(1+|\epsilon|^2)}}\left[(1+\epsilon)\left|K^0\right\rangle + (1-\epsilon)\left|\overline{K}^0\right\rangle\right] \ , \\ \left|K^0_\mathrm{L}\right\rangle &= \frac{1}{\sqrt{2(1+|\epsilon|^2)}}\left[(1+\epsilon)\left|K^0\right\rangle - (1-\epsilon)\left|\overline{K}^0\right\rangle\right] \ , \end{aligned} \tag{9.2}$$

where ϵ is the parameter describing *CP* violation in kaon mixing. The lifetime of neutral kaons is large enough that they can traverse significant amounts of material before they decay. The interaction of K^0 and $\overline{K}^0$ mesons with matter can be written as a differential equation:

$$i\frac{\mathrm{d}}{\mathrm{d}t}\begin{pmatrix}\left|K^0(t)\right\rangle \\ \left|\overline{K}^0(t)\right\rangle\end{pmatrix}_\mathrm{nuc} = \begin{pmatrix}\chi & 0 \\ 0 & \overline{\chi}\end{pmatrix}\begin{pmatrix}\left|K^0(t)\right\rangle \\ \left|\overline{K}^0(t)\right\rangle\end{pmatrix}_\mathrm{nuc} \equiv \boldsymbol{\chi}\begin{pmatrix}\left|K^0(t)\right\rangle \\ \left|\overline{K}^0(t)\right\rangle\end{pmatrix}_\mathrm{nuc} \ , \tag{9.3}$$

where the complex numbers χ and $\overline{\chi}$ are related to the interaction of K^0 and $\overline{K}^0$ mesons with matter. The real part of χ describes phase shifts (dispersion) and the imaginary part absorption in the material. Equation 9.1 and 9.3 are combined to account coherently for the effects of mixing, *CP* violation and absorption. The full equation of the time evolution of neutral kaons in matter is given by

$$i\frac{\mathrm{d}}{\mathrm{d}t}\begin{pmatrix}\left|K^0(t)\right\rangle \\ \left|\overline{K}^0(t)\right\rangle\end{pmatrix} = \left(\boldsymbol{M} - \frac{i}{2}\boldsymbol{\Gamma} + \boldsymbol{\chi}\right)\begin{pmatrix}\left|K^0(t)\right\rangle \\ \left|\overline{K}^0(t)\right\rangle\end{pmatrix} \ . \tag{9.4}$$

The problem of Equation 9.4 is neither diagonal in the K^0 and $\overline{K}^0$ basis nor in the K^0_S and K^0_L basis. Therefore, K^0_S and K^0_L states are no longer mass eigenstates and transitions between the two states are possible. This effect has been known as *regeneration* since 1955 [76]. It is used in neutral kaon experiments as it allows to *regenerate* K^0_S mesons from a pure K^0_L beam by sending the beam through a material. In the context of this analysis it is a nuisance.

The time evolution of an arbitrary neutral kaon state, $\widetilde{\Psi}$, in matter in the K^0_L and K^0_S basis is then given by the following equations [77, 78]:

$$\left|\widetilde{\Psi}(t)\right\rangle = \alpha_\mathrm{L}(t)\left|K^0_\mathrm{L}\right\rangle + \alpha_\mathrm{S}(t)\left|K^0_\mathrm{S}\right\rangle \quad \text{with} \tag{9.5}$$

$$\alpha_\mathrm{L}(t) = \mathrm{e}^{-i\Sigma\cdot t}\left[\alpha_\mathrm{L}(0)\cos(\Omega t) - i\frac{\alpha_\mathrm{L}(0)\,\Delta\lambda + \alpha_\mathrm{S}(0)\,\Delta\chi}{2\Omega}\sin(\Omega t)\right], \tag{9.6}$$

$$\alpha_\mathrm{S}(t) = \mathrm{e}^{-i\Sigma\cdot t}\left[\alpha_\mathrm{S}(0)\cos(\Omega t) + i\frac{\alpha_\mathrm{S}(0)\,\Delta\lambda - \alpha_\mathrm{L}(0)\,\Delta\chi}{2\Omega}\sin(\Omega t)\right], \tag{9.7}$$

where the complex constants $\Omega \equiv \frac{1}{2}\sqrt{\Delta\lambda^2 + \Delta\chi^2}$ and $\Sigma \equiv \frac{1}{2}(\lambda_\mathrm{L} + \lambda_\mathrm{S} + \chi + \bar{\chi})$ describe mixing and absorption. They are given by the masses, $m_\mathrm{L,S}$, decay widths, $\Gamma_\mathrm{L,S}$, of the K^0_L and K^0_S states and the absorption coefficient χ ($\bar{\chi}$) of K^0 ($\overline{K}^0$) states by means of

$$\Delta\lambda = \lambda_\mathrm{L} - \lambda_\mathrm{S} = \Delta m - \frac{i}{2}\Delta\Gamma = (m_\mathrm{L} - m_\mathrm{S}) - \frac{i}{2}(\Gamma_\mathrm{L} - \Gamma_\mathrm{S}) \ , \tag{9.8}$$

$$\Delta\chi = \chi - \bar{\chi} = -\frac{2\pi\mathcal{N}}{m}\Delta f = -\frac{2\pi\mathcal{N}}{m}(f - \bar{f}) \ , \tag{9.9}$$

where N is the scattering density of the material, m the kaon mass, and f and $\bar{f}$ are the forward scattering amplitudes.

The imaginary part of Δf is related to the total cross section via the optical theorem:

$$\sigma_{\text{tot}} = \frac{4\pi}{p} \operatorname{Im} f \quad , \tag{9.10}$$

where p is the momentum of the neutral kaon. Similar to charged kaons, the K^0 and $\overline{K}^0$ interaction cross section depends on the momentum, p, of neutral kaons and on the number of nucleons, A, in the target. It is taken from Reference [79] as

$$\Delta\sigma(\overline{K}^0 N) = \sigma(\overline{K}^0 N) - \sigma(K^0 N) = \frac{23.2\, A^{0.758\pm0.003}}{[p(\text{ GeV}/c)]^{0.614}} \text{ mb} \quad . \tag{9.11}$$

The real and the imaginary part of Δf need to be known. The phase of Δf has been determined in References [79, 80] to be $\arg \Delta f = (-124.7 \pm 0.8)^\circ$.

The formalism of Equations 9.5 to 9.11 includes two effects. First, the incoherent absorption and elastic scattering of K^0 and $\overline{K}^0$ states is given by $\operatorname{Im}(\Delta f)$. This effect is equivalent to the case of charged kaons. Second, the term $\operatorname{Re}(\Delta f)$ describes a dispersion (relative phase shift) of K^0 and $\overline{K}^0$ states. Both effects lead to a mixing of K^0_{L} and K^0_{S} states.

At production, the flavour of the K^0 meson is defined. A $\overline{K}^0$ state is produced in the decay of a D^+ meson and a K^0 state in the decay of a D^- meson. The two pure states at production are given in the K^0_{L} and K^0_{S} basis as

$$\begin{aligned} |K^0\rangle &= \frac{\sqrt{1+|\epsilon|^2}}{2} \frac{1}{1+\epsilon} \Big[|K^0_{\text{L}}\rangle + |K^0_{\text{S}}\rangle \Big] \quad , \\ |\overline{K}^0\rangle &= \frac{\sqrt{1+|\epsilon|^2}}{2} \frac{1}{1-\epsilon} \Big[|K^0_{\text{L}}\rangle - |K^0_{\text{S}}\rangle \Big] \quad , \end{aligned} \tag{9.12}$$

which defines the initial amplitudes $\alpha_{\text{L,S}}(0)$ at $t = 0$ for the initial K^0 and $\overline{K}^0$ states.

The considered final state $\pi^+\pi^-$ is a *CP*-even eigenstate, $CP\,|\pi^+\pi^-\rangle = |\pi^+\pi^-\rangle$. The mass eigenstates K^0_{L} and K^0_{S} are no pure *CP* eigenstates. They can be written in terms of the *CP*-even eigenstate, K^0_1, and the *CP*-odd eigenstate, K^0_2, as

$$\begin{aligned} |K^0_{\text{L}}\rangle &= \frac{1}{\sqrt{1+|\epsilon|^2}} \left(|K^0_2\rangle + \epsilon\, |K^0_1\rangle \right) \quad , \\ |K^0_{\text{S}}\rangle &= \frac{1}{\sqrt{1+|\epsilon|^2}} \left(|K^0_1\rangle + \epsilon\, |K^0_2\rangle \right) \quad . \end{aligned} \tag{9.13}$$

Using Equation 9.13 yields that the decay rate of an arbitrary state $\widetilde{\Psi}$, defined in Equation 9.5, to a *CP*-even final state is proportional to

$$|\alpha_{\text{S}}(t) + \epsilon\, \alpha_{\text{L}}(t)|^2 \tag{9.14}$$

at a given time t. The time-dependent asymmetry[3] is then defined as

$$a(t) = \frac{\Gamma(\overline{K}^0_{t=0} \to \pi^+\pi^-)(t) - \Gamma(K^0_{t=0} \to \pi^+\pi^-)(t)}{\Gamma(\overline{K}^0_{t=0} \to \pi^+\pi^-)(t) + \Gamma(K^0_{t=0} \to \pi^+\pi^-)(t)} \quad , \tag{9.15}$$

---

[3] The definition has the opposite sign to the usual convention in order to be in agreement with the charged kaon asymmetry.

Table 9.1: Values of the parameters used to calculate the neutral kaon asymmetry [16, 79, 80].

Parameter	**Value**
Δm	$(0.5293 \pm 0.0009) \times 10^{10} \hbar\,\mathrm{s}^{-1}$
$\tau_{\mathrm{S}} \equiv 1/\Gamma_{\mathrm{S}}$	$(0.8954 \pm 0.0004) \times 10^{-10}\,\mathrm{s}$
$\tau_{\mathrm{L}} \equiv 1/\Gamma_{\mathrm{L}}$	$(5.116 \pm 0.021) \times 10^{-8}\,\mathrm{s}$
m	$(497.614 \pm 0.024)\,\mathrm{MeV}/c^2$
$\arg(\Delta f)$	$(-124.7 \pm 0.8)^{\circ}$
$\lvert\epsilon\rvert$	$(2.228 \pm 0.011) \times 10^{-3}$
$\phi_{+-} \equiv \arg \epsilon$	$(43.51 \pm 0.05)^{\circ}$
$\Delta\sigma(\overline{K}^0 N)$	$23.2\,A^{0.758 \pm 0.003}\,[p(\,\mathrm{GeV}/c)]^{-0.614}$ mb

where $\Gamma(\overline{K}^0_{t=0} \to \pi^+\pi^-)(t)$ is the time-dependent decay rate of an initial $\overline{K}^0$ state and $\Gamma(K^0_{t=0} \to \pi^+\pi^-)(t)$ the time-dependent decay rate of an initial K^0 state. The time-integrated asymmetry is given by

$$A = \frac{\int_0^\infty \varepsilon(t)\left[\Gamma(\overline{K}^0_{t=0} \to \pi^+\pi^-)(t) - \Gamma(K^0_{t=0} \to \pi^+\pi^-)(t)\right] \mathrm{d}t}{\int_0^\infty \varepsilon(t)\left[\Gamma(\overline{K}^0_{t=0} \to \pi^+\pi^-)(t) + \Gamma(K^0_{t=0} \to \pi^+\pi^-)(t)\right] \mathrm{d}t}\,, \qquad (9.16)$$

where $\varepsilon(t)$ is the decay-time acceptance of K^0_{S} mesons. All parameters used in the calculation are given in Table 9.1. The decay-time acceptance is treated separately as it depends on the selected K^0_{S} sample in data.

The different parts of the time-dependent asymmetry are shown in Figure 9.2. A simplified model is used in these figures, the LHCb detector is modelled by a constant material distribution with a density corresponding to 2% of that of aluminium and an average K^0_{S} meson momentum of 30 GeV/c is assumed. Later, the full detector geometry is used to get quantitative results. Two different decay-time ranges are given. The range of $0 - 25\,\tau_{\mathrm{S}}$ is only shown for illustrative purposes as K^0_{S} decays which are reconstructed by the LHCb detector rarely exceed $4\,\tau_{\mathrm{S}}$. At small decay times the asymmetries due to absorption and *CP* violation increase linearly with time. Both are of the same order and have the same sign. The interference term has little effect below $2\,\tau_{\mathrm{S}}$. After that it significantly affects the asymmetry and cannot be neglected.

Figure 9.3 shows the time-integrated asymmetry for the same simplified detector model. Here, the decay-time acceptance is modelled by a step function which starts at 0 and ends at t_{max}. As shown in Figure 9.1, K^0_{S} mesons reconstructed with two long tracks probe decay times between 0 and $0.5\,\tau_{\mathrm{S}}$, while downstream-reconstructed candidates go up to $4\,\tau_{\mathrm{S}}$. Thus, the expected time-integrated K^0 asymmetry is around 0.5 % for downstream-reconstructed candidates and smaller than 0.1 % for long-reconstructed candidates. The application of the method to the reconstructed $D^+ \to \overline{K}^0\pi^+$ samples is discussed in the next section.

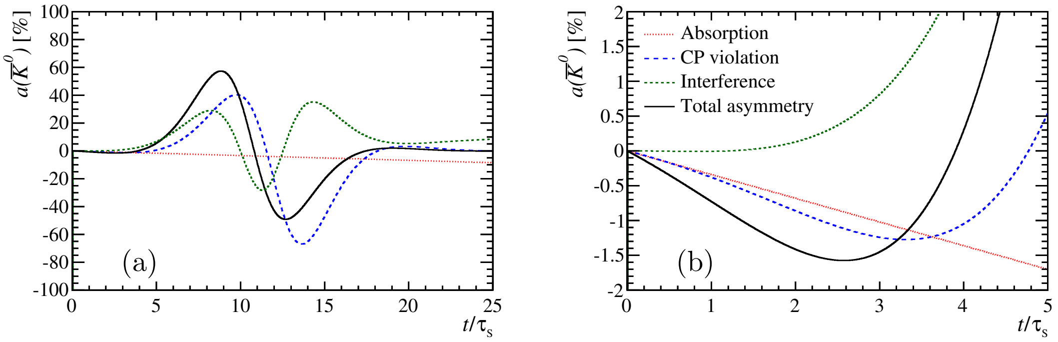

Figure 9.2: The time-dependent neutral kaon asymmetry for (a) large and (b) small K_S^0 decay times. The underlying model assumes an average K_S^0 momentum of 30 GeV/c and a constant material distribution.

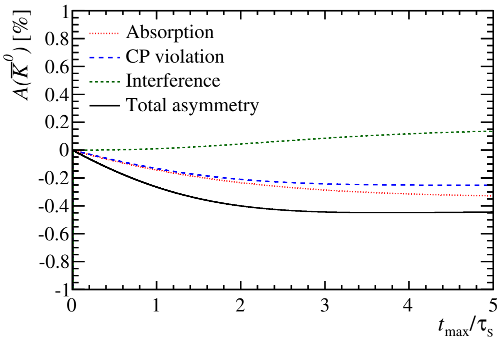

Figure 9.3: The time-integrated neutral kaon asymmetry. The integration is performed from 0 to $t_{\max}$. The underlying model assumes an average K_S^0 momentum of 30 GeV/c and a constant material distribution.

9.3 Calculated asymmetry for data samples

The material in the VELO and the RICH is not homogeneously distributed. There are several detection layers with different materials and vacuum or air in between. Therefore, the flight path of a particle is divided into sections, see Figure 9.4. The detector geometry as it is implemented in the event simulation and reconstruction is used. The amplitudes $\alpha_{L,S}(t_n)$ are calculated for a time difference $t_n - t_{n-1}$ with the start values $\alpha_{L,S}(t_{n-1}) = \alpha_{L,S}(0)$ according to Equation 9.5:

$$\alpha_S(t_n) = \alpha_S(t_n - t_{n-1}) \text{ with } \alpha_{L,S}(0) = \alpha_{L,S}(t_{n-1}) \ , \tag{9.17}$$

$$\alpha_L(t_n) = \alpha_L(t_n - t_{n-1}) \text{ with } \alpha_{L,S}(0) = \alpha_{L,S}(t_{n-1}) \ . \tag{9.18}$$

The iterative calculation of α_S and α_L is performed with initial K^0 and $\overline{K}^0$ states for the flight path of every K_S^0 candidate in the $D^+ \to \overline{K}^0\pi^+$ samples recorded by the LHCb experiment. The usage of K_S^0 candidates selected in data takes automatically the decay-time acceptance of reconstructed K_S^0 decays into account. The expected

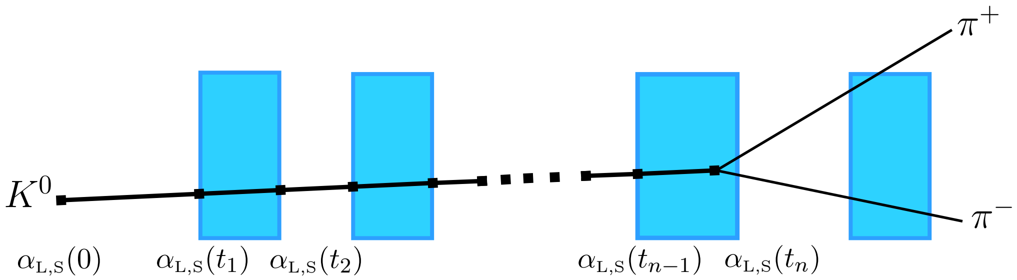

Figure 9.4: The flight path of a neutral kaon through detector material. The iterative procedure to obtain the amplitudes $\alpha_{\mathrm{L,S}}$ is depicted. In this simplified picture the blue boxes have a different number of nucleons A than the space in between.

Table 9.2: The calculated asymmetry $A_D(\overline{K}^0)$ including systematic uncertainty due to the uncertainty on the material budget. Weighted means that the long-reconstructed sample is kinematically weighted in the D^+ kinematics to match the downstream-reconstructed sample, see Chapter 9.4 for more explanation.

Sample	$\boldsymbol{A_D(\overline{K}^0)}$ [%]	**Systematic** [%]
Long 2011	-0.0796 ± 0.0001	± 0.005
Downstream 2011	–	-
Long 2012	-0.0822 ± 0.0001	± 0.005
Downstream 2012	-0.6191 ± 0.0007	± 0.027
Weighted Long 2012	-0.0732 ± 0.0001	± 0.005
Difference Down–Long 2012	-0.5459 ± 0.0007	± 0.027

time-integrated asymmetry of a K^0_{S} sample is then given as

$$A_D(\overline{K}^0) = \frac{1}{N}\sum_{j=1}^{N} a_j(t_j) \ , \tag{9.19}$$

where N is the number of K^0_{S} candidates in the sample and $a_j(t_j)$ is the expected asymmetry of candidate j with decay time t_j according to Equation 9.15.

In Table 9.2 the calculated asymmetries are shown. There was no dedicated trigger line for downstream-reconstructed $D^+ \to \overline{K}^0\pi^+$ decays in 2011. Therefore, the calculation is split up for the samples of 2011 and 2012. It is also checked that magnet up and magnet down samples give consistent results. The calculated asymmetry is about (-0.08 %) for long-reconstructed K^0_{S} decays. The asymmetry of 2012 is a bit larger than that of 2011. This is due to slightly looser trigger requirements in 2012 which shift the K^0_{S} momentum distribution to lower values. The calculated asymmetry of the downstream-reconstructed sample is (-0.61 %). The difference between the downstream- and the long-reconstructed samples is about (-0.5 %) due to the larger average decay time and the traversed material of the downstream-reconstructed sample.

The quoted systematic uncertainty of this calculation is coming from the knowledge of the material budget in front of the TT. This is known to an accuracy of about 10 % [81]. The uncertainties on the other input values are negligible in comparison,

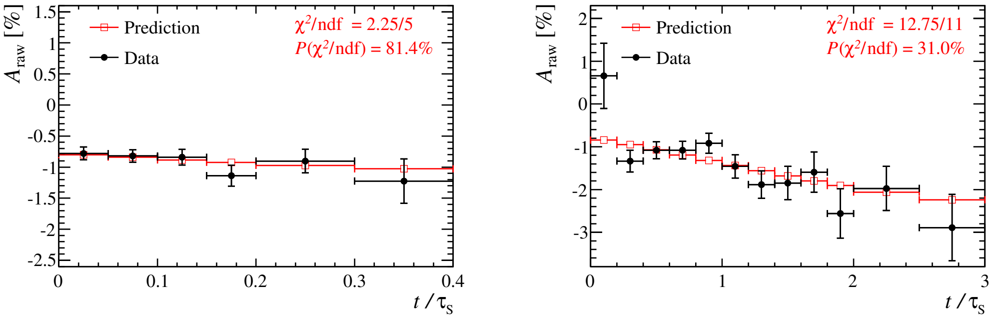

(a) Long-reconstructed (b) Downstream-reconstructed

Figure 9.5: The raw asymmetry of $D^+ \to \overline{K}^0\pi^+$ candidates and the predicted $A_D(\overline{K}^0)$ as function of the K^0_S decay times for long- and downstream-reconstructed samples. The full data set is used for the long-reconstructed sample, while a downstream-reconstructed sample is only available in the 2012 data. The predicted asymmetry is shifted by the average difference of measured and predicted asymmetry, to account for spurious detection and production asymmetries. The p-value for the hypothesis that predicted and observed asymmetry have the same slope is given.

see Table 9.1. Hence, the relative systematic uncertainty is about 5 % as the effects of *CP* violation and absorption contribute in almost equal amounts to the neutral kaon asymmetry $A_D(\overline{K}^0)$.

As the neutral kaon asymmetry is a large contribution to the raw asymmetry in the downstream-reconstructed $D^+ \to \overline{K}^0\pi^+$ sample, this sample is not used in the $A_{CP}(K^-K^+)$ measurement. However, in order to not rely on the on the quoted material budget uncertainty, the downstream-reconstructed K^0_S sample is used to study the systematic uncertainty of the correction applied to the long-reconstructed $D^+ \to \overline{K}^0\pi^+$ sample. This is discussed in the next section.

9.4 Comparison of observed and expected asymmetries

The neutral kaon asymmetry depends on the reconstructed decay times and the amount of traversed material of the K^0_S candidates, as discussed in the previous section. In order to test the described model, the raw asymmetry is determined in bins of both quantities for the long- and the downstream-reconstructed sample and compared with the predicted asymmetry in a given bin.

The raw and the predicted asymmetries are shown as function of the K^0_S decay time in Figure 9.5 for long- and downstream-reconstructed samples. The raw asymmetries have contributions from the D^+ production and the pion detection asymmetry, while the neutral kaon asymmetry vanishes for zero decay time. This overall offset is taken into account by shifting the prediction by the averaged difference of raw and predicted asymmetry. Only differences in the shape are of interest here. The shift is approximately consistent with the measured D^+ production asymmetry of $(-0.96 \pm 0.26\,(\text{stat}) \pm 0.18\,\%)$ [39], assuming a negligible pion detection asymmetry [61], cf. Chapters 2.6.2 and 4.3.1. The raw asymmetry follows the predicted downward trend in both samples. The effect

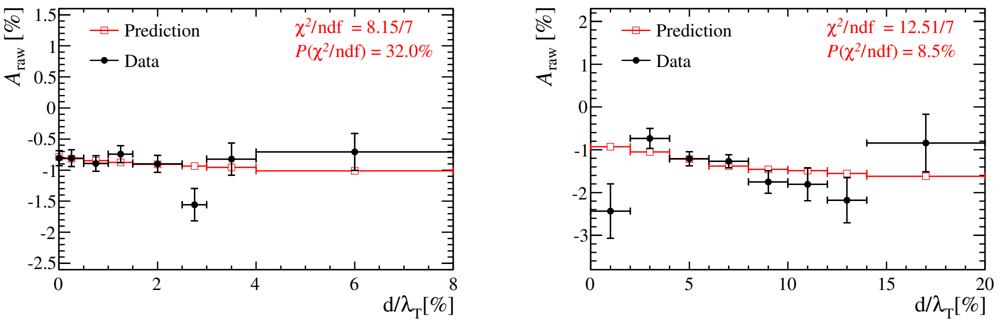

(a) Long-reconstructed

(b) Downstream-reconstructed

Figure 9.6: The raw asymmetry of $D^+ \to \overline{K}^0\pi^+$ candidates and the predicted $A_D(\overline{K}^0)$ as function of the amount of traversed material in nuclear collision lengths for long- and downstream-reconstructed samples. The full data set is used for the long-reconstructed sample, while a downstream-reconstructed sample is only available in the 2012 data. The predicted asymmetry is shifted by the average difference of measured and predicted asymmetry, to account for other detection and production asymmetries. The p-value for the hypothesis that predicted and raw asymmetry have the same slope is given.

is particularly visible in the downstream-reconstructed K^0_S sample. The p-values which are 0.81 and 0.31 for long- and downstream-reconstructed K^0_S candidates, respectively, show that the predicted asymmetries agree well with the data.

The projection into bins of the amount of traversed material is shown in Figure 9.6. The same trends are visible as decay time and flight distance of a K^0_S candidate are correlated. In the projection into bins of the K^0_S decay time material effects are smeared out. Thus, the difference of observed and expected asymmetry in bins of the thickness is more sensitive to a mismodelling of the detector geometry. The detector geometry is less precisely known than the parameters of CP violation in the neutral kaon system. Nevertheless, the agreement is quite good which gives confidence in the predicted asymmetry. The p-values for long- and downstream-reconstructed K^0_S candidates are 0.32 and 0.09, respectively.

The uncertainty on the model for $A_D(\overline{K}^0)$ has to be quantified. Therefore, the raw asymmetries of the 2012 samples are determined, see Table 9.3. The long-reconstructed $D^+ \to \overline{K}^0\pi^+$ sample is weighted to match the kinematic distributions of the down-reconstructed sample in order to cancel the D^+ production and the pion detection asymmetry in the difference of both raw asymmetries. The kinematic weighting is similar to the one discussed in Chapter 8. The measured difference between both samples is $(-0.486 \pm 0.118)\,\%$. This is in very good agreement with the expected difference of $(-0.546 \pm 0.027)\,\%$ from the previous section. The expected difference takes the kinematic weighting into account and the uncertainty is given exclusively by the material-budget uncertainty. The ratio of the expected and measured difference is (1.12 ± 0.28). The relative uncertainty of 25 % is assigned as a systematic uncertainty of the K^0_S asymmetry model.

Table 9.3: The measured raw asymmetries of long- and downstream-reconstructed $D^+ \to \overline{K}^0\pi^+$ candidates in the 2012 data set. The long-reconstructed sample is weighted to match the kinematics of the downstream-reconstructed sample.

Sample	$\boldsymbol{A_{\mathrm{raw}}(\overline{K}^0\pi^+)}$ [%]
Long 2012	-0.8189 ± 0.0779
Downstream 2012	-1.3051 ± 0.0889
Difference	-0.486 ± 0.118

9.5 Correction applied to the $A_{CP}(K^-K^+)$ measurement

The correction due to the neutral kaon asymmetry depends on the K_S^0 kinematics of the $D^+ \to \overline{K}^0\pi^+$ sample which is used in the $A_{CP}(K^-K^+)$ measurement. This changes with respect to the sample used in this chapter due to the kinematic weighting procedure described in Chapter 8.1.4. Thus, the kinematic weights of the $A_{CP}(K^-K^+)$ measurement are taken into account in the calculation of $A_D(\overline{K}^0)$, cf. Chapter 9.3. The corrected detection asymmetry $A_D(\overline{K}^0)$ is found to be

$$A_D(\overline{K}^0) = (-0.054 \pm 0.014\,(\mathrm{syst}))\,\% \ ,$$

where the systematic uncertainty is due to the difference between data and prediction, cf. Chapter 9.4. It has been checked that the calculated values of the 2011 and 2012 data samples are in agreement.

Chapter 10

Wrong flavour tags

The flavour tag of the D^0 candidate by the muon charge is not unambiguous. The combinations of real D^0 mesons with muons that do not originate from the same $b \to c\,\ell^-\,\overline{\nu}_\ell$ transitions lead to a background contribution. This contribution peaks in the D^0 mass, but can give the wrong flavour tag. Possible background sources are prompt D^0 mesons where the other D meson decays semileptonically or secondary D^0 mesons where the muon is from the decaying other b hadron in the event. Prompt D mesons have a large production cross section but are effectively suppressed by the selection, cf. Chapter 6. The wrong combination of a secondary muon and a secondary D^0 meson is mainly suppressed by the constraint to form a common B vertex. Impact parameter cuts are less effective in that case as the trajectories of D^0 and muon candidates are displaced from the primary vertex. Any residual contribution with wrong flavour tags damps the observed *CP* asymmetry. Therefore, the probability to assign a wrong flavour tag is measured, the so-called *mistag probability*.

First, the effect of wrong flavour tags on the *CP* asymmetry measurement is discussed. Second, two methods to determine the mistag probability are introduced. Third, the results of the mistag probabilities are given for the ΔA_{CP} and $A_{CP}(K^-K^+)$ measurements.

10.1 Formalism

The probabilities to wrongly tag a D^0 or $\overline{D}^0$ meson with a positively- or negatively-charged muon are defined with respect to the reconstructed semileptonic B candidates as

$$\begin{aligned} \omega_{D^0} &= \mathcal{P}\left(\mu^+\text{–tag}|D^0_{\text{true}} \wedge (B \to D\mu)_{\text{rec}}\right) \ , && (10.1)\\ \omega_{\overline{D}^0} &= \mathcal{P}\left(\mu^-\text{–tag}|\overline{D}^0_{\text{true}} \wedge (B \to D\mu)_{\text{rec}}\right) \ . && (10.2)\end{aligned}$$

Hence, a $\overline{B} \to D^0\mu^-$ or a $B \to \overline{D}^0\mu^+$ candidate is reconstructed but the real flavour of the neutral charm meson is the *CP*-conjugate of the tagged flavour. The observed yields, $N(f,\mu^-)$ and $N(f,\mu^+)$, of muon-tagged $D^0 \to K^-K^+$ and $D^0 \to \pi^-\pi^+$ decays from Equation 5.8 are modified to

$$\begin{aligned} N(f,\mu^-) &\propto (1-\omega_{D^0})\,\Gamma(D^0 \to f)\,\mathcal{P}(\overline{B})\,\varepsilon(\mu^-) + \omega_{\overline{D}^0}\,\Gamma(\overline{D}^0 \to f)\,\mathcal{P}(B)\,\varepsilon(\mu^-) \ , \\ N(f,\mu^+) &\propto (1-\omega_{\overline{D}^0})\,\Gamma(\overline{D}^0 \to f)\,\mathcal{P}(B)\,\varepsilon(\mu^+) + \omega_{D^0}\,\Gamma(D^0 \to f)\,\mathcal{P}(\overline{B})\,\varepsilon(\mu^+) \ , \end{aligned} \qquad (10.3)$$

in the presence of the mistag probabilities ω_{D^0} and $\omega_{\overline{D}^0}$. With the following definitions of the average mistag probability, ω, and mistag difference, $\Delta\omega$,

$$\omega = \frac{\omega_{D^0} + \omega_{\overline{D}^0}}{2} \ , \tag{10.4}$$

$$\Delta\omega = \omega_{D^0} - \omega_{\overline{D}^0} \ , \tag{10.5}$$

and neglecting terms of third-order in the asymmetries, the raw asymmetry of $D^0 \to K^-K^+$ and $D^0 \to \pi^-\pi^+$ samples can be written as

$$A_{\text{raw}} = (1-2\omega)\left[A_{CP} + A_P(\overline{B})\right] + A_D(\mu^-) - \Delta\omega \ , \tag{10.6}$$

where A_{CP} is defined in Equation 5.1, $A_P(\overline{B})$ in Equation 5.4 and $A_D(\mu^-)$ in Equation 5.6.

Wrong flavour tags have two consequences. First, the average mistag probability ω reduces the sensitivity to *CP* and production asymmetries. The muon detection asymmetry is not affected as the charge of the muon is unambiguous.[1] Second, any difference in the mistag probability for D^0 and $\overline{D}^0$ mesons gives rise to a systematic shift of the raw asymmetry. Both effects are expected to be independent of the D^0 final state as they are connected to the reconstruction of the muon in the final state or background contributions from the rest of the event. For example, the mistag difference $\Delta\omega$ can be a consequence of background sources affected by a muon detection or D^0 production asymmetry. Therefore, $\Delta\omega$ is expected to largely cancel in the difference of two raw asymmetries. The formula to obtain ΔA_{CP} is then modified as follows

$$\Delta A_{CP} = \frac{A_{\text{raw}}(K^-K^+) - A_{\text{raw}}(\pi^-\pi^+)}{1-2\omega} \ . \tag{10.7}$$

The $A_{CP}(K^-K^+)$ measurement uses the muon-tagged $D^0 \to K^-\pi^+$ sample to cancel $A_P(\overline{B})$ and $A_D(\mu^-)$ in the difference of $A_{\text{raw}}(K^-K^+)$ and $A_{\text{raw}}(K^-\pi^+)$. Also in the $D^0 \to K^-\pi^+$ sample the tag is given exclusively by the muon charge, equivalently to muon-tagged $D^0 \to K^-K^+$ and $D^0 \to \pi^-\pi^+$ candidates. The charges of the final state, $K^-\pi^+$ or $K^+\pi^-$, are not considered. Still, the final state $K^\pm\pi^\mp$ contains information on the initial state as about 99.7 % of the decays are Cabibbo-favoured $D^0 \to K^-\pi^+$ and $\overline{D}^0 \to K^+\pi^-$ decays. However, using the charges of the final state would break the assumption of universal mistag probabilities among the muon-tagged D^0 decays. Neglecting third-order terms in the asymmetries, the raw asymmetry of the $D^0 \to K^-\pi^+$ decay mode is given by

$$A_{\text{raw}}(K^-\pi^+) = (1-2\omega)A_P(\overline{B}) + (1-2(\omega+R))A_D(K^-\pi^+) + A_D(\mu^-) + \Delta\omega \ , \tag{10.8}$$

where R is the ratio of branching fractions of *right-sign* $D^0 \to K^-\pi^+$ over *wrong-sign* $D^0 \to K^+\pi^-$ decays. The ratio R contains the fraction of doubly Cabibbo-suppressed $D^0 \to K^+\pi^-$ decays and a time-dependent contribution from mixing. The sum of wrong-sign decays and mistagged candidates leads to a damping of the detection asymmetry $A_D(K^-\pi^+)$. The *CP* asymmetry $A_{CP}(K^-K^+)$ is then obtained as

$$A_{CP}(K^-K^+) = \frac{A_{\text{raw}}(K^-K^+) - A_{\text{raw}}(K^-\pi^+)}{1-2\omega} + \frac{1-2(\omega+R)}{1-2\omega}A_D(K^-\pi^+) \ . \tag{10.9}$$

---

[1] The effect of wrongly measured charges can be neglected here. It affects only very high momentum muons, e.g. from $W^\pm$ or Z^0 decays.

It should be pointed out here that the measured raw asymmetries are all at the per cent level or smaller, see Chapter 7.4.1. In the following section the mistag probability is determined to be approximately 1 %. Therefore, the mistag probability leads to very small corrections. Neglecting third-order terms in the asymmetries and the mistag probability, Equation 10.7 and 10.9 can be written as

$$\Delta A_{CP} = (1+2\omega)\left[A_{\mathrm{raw}}(K^-K^+) - A_{\mathrm{raw}}(\pi^-\pi^+)\right] \ , \tag{10.10}$$

$$A_{CP}(K^-K^+) = (1+2\omega)\left[A_{\mathrm{raw}}(K^-K^+) - A_{\mathrm{raw}}(K^-\pi^+)\right] + (1-2R)A_D(K^-\pi^+) \ . \tag{10.11}$$

10.2 Methods to determine mistag probability

The mistag probability is measured directly in data with the $D^0 \to K^-\pi^+$ sample and transferred to the other channels. This assumes a universal mistag probability for muon-tagged decays. Two methods are exploited to measure the mistag probability. Both are based on using a different method to unambiguously tag the candidate. One has the advantage that it uses the full $D^0 \to K^-\pi^+$ sample and, thus, is very precise. The other is less precise but can be applied to all muon-tagged D^0 samples.

Wrong-sign method

The first and default method uses the final state of the D^0 decay. A D^0 meson mainly decays to $K^-\pi^+$ as this is the Cabibbo-favoured decay. These events are called right-sign events. A small fraction of D^0 mesons decays doubly Cabbibo-suppressed to $K^+\pi^-$ or mixes and then decays. The time-dependent ratio of wrong-sign decays is well known and has been measured separately for D^0 and $\overline{D}^0$ mesons by the LHCb collaboration in Reference [82]. The mistag probability can be measured by determining how often the tag by the muon charge labels the decay as wrong- or right-sign. In order to distinguish between first, real right- and wrong-sign decays and second, reconstructed right- and wrong-sign decays, the combinations of $K^\mp\ \pi^\pm$ and $\mu^\mp$ are called *muon-right-sign*, the combinations $K^\pm\ \pi^\mp$ and $\mu^\pm$ are called *muon-wrong-sign*. The mistag probabilities $\omega_{\overline{D}^0}$ and ω_{D^0} are then given by

$$\omega_{D^0} = \frac{N(K^-\pi^+ \text{ and } \mu^+)}{N(K^-\pi^+ \text{ and } (\mu^+ \text{ or } \mu^-))} - R^+ \ , \tag{10.12}$$

$$\omega_{\overline{D}^0} = \frac{N(K^+\pi^- \text{ and } \mu^-)}{N(K^+\pi^- \text{ and } (\mu^+ \text{ or } \mu^-))} - R^- \ , \tag{10.13}$$

where the first term describes the muon-wrong-sign ratio. The parameters R^+ and R^- are the wrong-sign ratios of D^0 and $\overline{D}^0$ decays, respectively. The measurement of the yields N is discussed in Chapter 10.3. Different wrong-sign ratios R^+ and R^- are used to get a better estimate of the mistag difference $\Delta\omega$. For the measurement of the average mistag rate ω this is not important.

In the limit of small mixing parameters x and y the time-dependent ratio $R^\pm(t)$ is given by [82]

$$R^\pm(t) \approx R_D^\pm + \sqrt{R_D^\pm}\, y'^\pm\, \frac{t}{\tau} + \frac{x'^{2\pm} + y'^{2\pm}}{4}\left(\frac{t}{\tau}\right)^2 \ , \tag{10.14}$$

Table 10.1: The D^0 mixing parameters as measured in Reference [82]. Reported uncertainties and correlation coefficients include both statistical and systematic sources.

Direct and indirect *CP* violation

Results		Correlations					
Parameter	Fit value	R_D^+	y'^+	x'^{2+}	R_D^-	y'^-	x'^{2-}
R_D^+ $[10^{-3}]$	3.545 ± 0.095	1.000	−0.942	0.862	−0.016	−0.007	0.006
y'^+ $[10^{-3}]$	5.1 ± 1.4		1.000	−0.968	−0.007	0.007	−0.007
x'^{2+} $[10^{-5}]$	4.9 ± 7.0			1.000	0.005	−0.007	0.008
R_D^- $[10^{-3}]$	3.591 ± 0.094				1.000	−0.941	0.858
y'^- $[10^{-3}]$	4.5 ± 1.4					1.000	−0.966
x'^{2-} $[10^{-5}]$	6.0 ± 7.0						1.000

No *CP* violation

Results		Correlations		
Parameter	Fit value	R_D	y'	x'^2
R_D $[10^{-3}]$	3.568 ± 0.066	1.000	−0.953	0.869
y' $[10^{-3}]$	4.8 ± 1.0		1.000	−0.967
x'^2 $[10^{-5}]$	5.5 ± 4.9			1.000

where t is the decay time, τ the average D^0 lifetime and R_D the ratio of suppressed-to-favoured decay rates. The parameters x' and y' are linear combinations of the mixing parameters x and y introduced in Chapter 2.3.1. Further information is given in Reference [82]. The measured parameters and their correlations are given in Table 10.1. Assuming no decay-time acceptance,[2] the average values, $R^\pm \equiv \langle R^\pm(t) \rangle$, are given by

$$R^\pm = R_D^\pm + \sqrt{R_D^\pm}\, y' + \frac{x'^{2\pm} + y'^{2\pm}}{2} \quad . \tag{10.15}$$

Using the values from Table 10.1, R^+ is calculated to be $(0.3886 \pm 0.0047)\,\%$ and R^- is $(0.3901 \pm 0.0046)\,\%$. The value of R assuming no *CP* violation is $(0.3894 \pm 0.0030)\,\%$. A better treatment of the decay-time acceptance leads to negligible corrections, as the measured mistag probability and the asymmetries are around 1%.

$D^{*\pm}$ method

Many $\overline{B} \to D^0 X$ decays proceed via the $D^{*\pm}$ resonance and a large fraction of prompt D^0 mesons originates from this resonance as well. The $D^{*\pm}$ resonance has a branching fraction to $D^0\pi^+$ of $(67.7 \pm 0.5)\,\%$ [16]. The decay topology of such reconstructed B candidates is shown in Figure 10.1. In the following the pion from the $D^{*\pm}$ resonance is called *Slow pion*. The reconstruction of the Slow pion provides an independent tag of the D^0 flavour. As the $D^{*\pm}$ resonance is fully reconstructed with a D^0 and a pion candidate, this tag is unambiguous. The second and independent method to

---

[2] It has been checked that muon-tagged D^0 decay times have an almost flat decay-time acceptance. This can also be deduced from Figure 7.2c.

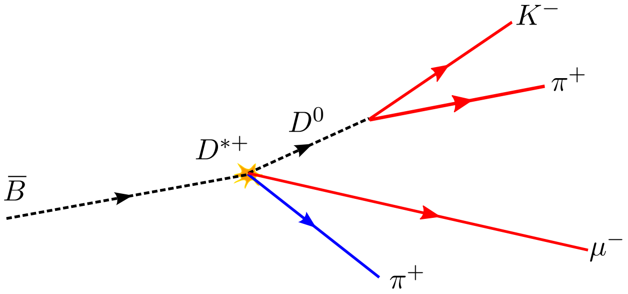

Figure 10.1: The decay topology of a $\overline{B} \to D^{*+}\mu^- X$ decay. The charges of the $K\pi$ pair and the charge of the Slow pion provide a second tag of the D^0 flavour.

determine the mistag probability compares the charge of the muon candidate with the Slow pion charge. If both have opposite sign the flavour is tagged correctly. The mistag probabilities are then given as

$$\omega_{D^0} = \frac{N(D^{*+} \text{ and } \mu^+)}{N(D^{*+} \text{ and } (\mu^+ \text{ or } \mu^-))} \quad , \tag{10.16}$$

$$\omega_{\overline{D}^0} = \frac{N(D^{*-} \text{ and } \mu^-)}{N(D^{*-} \text{ and } (\mu^+ \text{ or } \mu^-))} \quad , \tag{10.17}$$

where N denotes the observed signal yield. The sub-sample where a Slow pion and a muon candidate are reconstructed is referred to as *doubly-tagged*.

The advantage of the $D^{*\pm}$ method is that it can be applied to the muon-tagged $D^0 \to K^-K^+$, $D^0 \to \pi^-\pi^+$ and $D^0 \to K^-\pi^+$ samples. This is crucial as it has to be verified that all channels have consistent mistag probabilities. Otherwise, the effects of the mistag probability would not cancel in the difference of raw asymmetries.

The disadvantage of this method is that it probes primarily the B^0 decays in the sample and not so much the B^+ decays. The semileptonic decay of a B^0 meson to a D^0 meson needs at least one additional particle to conserve the electric charge while this is not the case for the decay of B^0 mesons. Thus, it is more likely that a B^0 meson decay proceeds via the charged $D^{*\pm}$ resonance than a B^+ decay. About 90 % of the doubly-tagged candidates come from B^0 decays and only 10 % from B^+ decays. The event yield is further reduced by the Slow pion reconstruction efficiency. In the end about 10 % of the sample have an additional Slow pion tag. The doubly-tagged subsample has slightly different kinematic distributions of the muon and D^0 candidates, cf. Appendix B.2. Mainly the η distributions are affected. This could lead to a different mistag rate in the doubly-tagged sample. It is shown in the next section that both the wrong-sign and the $D^{*\pm}$ method yield very consistent results.

The selection of the doubly-tagged sample is explained in the following. First of all, the doubly-tagged samples are strict sub-samples of the muon-tagged samples. The selection cuts are given in Table 10.2. No impact parameter cuts are applied to the Slow pion candidate as these would reject a possible contribution from prompt D^0 decays. Loose momentum and track quality requirements reject mainly ghost tracks and very low momentum background contributions. The decay tree of each D^{*+} candidate is fitted with the DTF, cf. Chapter 6.3.1. It is required that $\chi^2_{\text{vertex}}/\text{ndf}(D^{*+}) < 10$.

Table 10.2: The selection of D^{*+} candidates is given.

Variable	**Cut value**
$p_{\mathrm{T}}(\pi^{+})$	$> 150\,\mathrm{MeV}/c$
$\chi^2_{\mathrm{track}}/\mathrm{ndf}$	< 3
$P_{\mathrm{track}}(\mathrm{ghost})$	< 0.5
$\chi^2/\mathrm{ndf}(D^{*+})$	$[0, 16]$
DTF $\chi^2_{\mathrm{vertex}}/\mathrm{ndf}(D^{*+})$	$[0, 10]$
$m(D^{*+})$	$[1890, 2130]\,\mathrm{MeV}/c^2$
Δm	$[139.5, 160]\,\mathrm{MeV}/c^2$

The $D^{*\pm}$ resonance has a mass of $(2010.28 \pm 0.13)\,\mathrm{MeV}/c^2$. Only candidates with a reconstructed mass between $[1890, 2130]\,\mathrm{MeV}/c^2$ are accepted. As the $D^{*\pm}$ mass is only $6\,\mathrm{MeV}/c^2$ above the mass threshold of the $D^0\pi^+$ pair, the Q value of the decay is very small. Therefore, the mass difference, $\Delta m \equiv m(D^{*+}) - m(D^0)$, has a very sharp peak. Only candidates with a reconstructed Δm in the range $[139.5, 160]\,\mathrm{MeV}/c^2$ are used. Furthermore, the distribution of Δm is used to extract the signal yields. Due to the large abundance of pions in *pp* collisions, there are often several Slow pion candidates for each D^0 candidate. As only one Slow pion in an event can originate from the $D^{*\pm}$ decay, the $D^{*\pm}$ candidate with the best DTF $\chi^2_{\mathrm{vertex}}/\mathrm{ndf}(D^{*+})$ is selected.

10.3 Measurement of mistag probabilities

The measurement of the mistag probabilities with the two introduced methods is presented.

Wrong-sign method

The muon-wrong-sign ratio is extracted from fits to the invariant mass distributions of $D \to K\pi$ candidates. Almost the same fit model as for the asymmetry measurement which is described in Chapter 7.3 is used. The muon-right- and muon-wrong-sign events share the same signal shape, including the mean of the mass distribution. The background parameters are independent. The only change between the raw asymmetry fit and the muon-wrong-sign ratio fit is that the muon-wrong-sign ratio instead of the raw asymmetry is used as a parameter in the PDF:

$$N_{\mathrm{sig,right}} = N_{\mathrm{sig}}\,(1 - (\omega + R))\ , \tag{10.18}$$

$$N_{\mathrm{sig,wrong}} = N_{\mathrm{sig}}\,(\omega + R)\ , \tag{10.19}$$

where $\omega + R$ is the total muon-wrong-sign ratio, including wrongly-tagged and wrong-sign candidates, N_{sig} is the total number of signal candidates, $N_{\mathrm{sig,right}}$ and $N_{\mathrm{sig,wrong}}$ are the corresponding yields of rightly- and wrongly-tagged candidates. The ratio $\omega_{D^0} + R^+$ is measured by a fit to $D \to K^-\pi^+$ candidates, $\omega_{\overline{D}{}^0} + R^-$ by fitting the invariant mass distribution of $D \to K^+\pi^-$ candidates. The average muon-wrong-sign ratio $\omega + R$ is extracted from a fit to the combined sample. An example fit is shown in Figure 10.2.

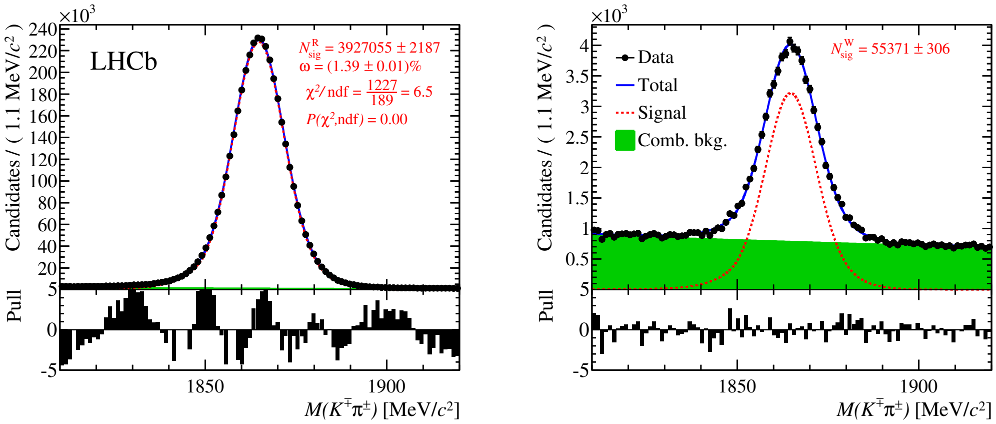

(a) Muon-right-sign (b) Muon-wrong-sign

Figure 10.2: The invariant mass distribution of (a) muon-right-sign and (b) muon-wrong-sign $D \to K\pi$ candidates. The data are taken from the 2012 magnet up sample. The ΔA_{CP} trigger selection is used.

Table 10.3: The measured muon-wrong-sign ratios and the derived mistag probabilities in the $D \to K\pi$ sample of the full data set. The results for the ΔA_{CP} and the $A_{CP}(K^-K^+)$ trigger selections are shown.

Selection	$\omega_{D^0} + R^+$ [%]	$\omega_{\overline{D}^0} + R^-$ [%]	$\Delta\omega$ [%]	$\omega + R$ [%]
ΔA_{CP}	1.3898 ± 0.0066	1.3634 ± 0.0065	0.0263 ± 0.0093	1.3765 ± 0.0046
$A_{CP}(K^-K^+)$	1.1923 ± 0.0066	1.1679 ± 0.0065	0.0253 ± 0.0093	1.1803 ± 0.0047

Selection	ω_{D^0} [%]	$\omega_{\overline{D}^0}$ [%]	$\Delta\omega$ [%]	ω [%]
ΔA_{CP}	1.0012 ± 0.0081	0.9733 ± 0.0079	0.028 ± 0.011	0.9875 ± 0.0055
$A_{CP}(K^-K^+)$	0.8037 ± 0.0081	0.7778 ± 0.0080	0.027 ± 0.011	0.7913 ± 0.0056

The mistag probabilities are determined independently for each of the 2011, 2012, magnet up and magnet down samples. Equivalently to the raw asymmetry measurement, cf. Chapter 7.4.1, the results of the fits to the magnet up and magnet down samples are arithmetically averaged. The final result is the weighted average of both years. The measurement is performed separately for the ΔA_{CP} and the $A_{CP}(K^-K^+)$ trigger selections.

The final results of the muon-wrong-sign ratios and the deduced mistag probabilities are given in Table 10.3. The mistag probabilities of the ΔA_{CP} and $A_{CP}(K^-K^+)$ measurements are $(0.9875 \pm 0.0055)\,\%$ and $(0.7913 \pm 0.0056),\%$, respectively. The $A_{CP}(K^-K^+)$ trigger selection requires the muon candidate to have a positive decision in HLT1, cf. Chapter 6.2.4. This requirement reduces the mistag probability. The measured $\Delta\omega$ is only consistent with zero at the 3σ level. Although $\Delta\omega$ is expected to cancel in the difference of raw asymmetries, it is considered in the systematic uncertainties. A table with all fitted mistag probabilities in all sub-samples is found in Appendix B.1. The values for each year and each polarity are consistent.

It should be pointed out that the mistag probability of $1\,\%$ leads to corrections

Table 10.4: The measured mistag probabilities with the $D^{*\pm}$ method for $D^0 \to \pi^-\pi^+$, $D^0 \to K^-K^+$ and $D^0 \to K^-\pi^+$ samples of the full data set. The results for the ΔA_{CP} and the $A_{CP}(K^-K^+)$ trigger selections are shown.

ΔA_{CP} selection

Sample	ω_{D^0} [%]	$\omega_{\overline{D}^0}$ [%]	$\Delta\omega$ [%]	ω [%]
$D^0 \to \pi^-\pi^+$	1.22 ± 0.12	1.01 ± 0.12	0.21 ± 0.17	1.104 ± 0.085
$D^0 \to K^-K^+$	1.037 ± 0.067	0.914 ± 0.065	0.123 ± 0.093	0.972 ± 0.046
$D^0 \to K^-\pi^+$	0.960 ± 0.028	1.004 ± 0.027	-0.043 ± 0.039	0.982 ± 0.019

$A_{CP}(K^-K^+)$ selection

Sample	ω_{D^0} [%]	$\omega_{\overline{D}^0}$ [%]	$\Delta\omega$ [%]	ω [%]
$D^0 \to K^-K^+$	0.859 ± 0.070	0.749 ± 0.068	0.111 ± 0.098	0.801 ± 0.049
$D^0 \to K^-\pi^+$	0.766 ± 0.030	0.830 ± 0.028	-0.064 ± 0.041	0.803 ± 0.021

of the *CP* asymmetries of the order 0.02% which is small compared to the statistical precision of the *CP* asymmetry measurements. Nevertheless, it is tested if the mistag probability is similar across the muon-tagged decays.

$D^{*\pm}$ method

The $\Delta m = m(D^{*+}) - m(D^0)$ distribution of doubly-tagged candidates is fitted to determine the mistag probability. Similarly to the wrong-sign method, a binned maximum-likelihood fit is performed. Rightly- and wrongly-tagged candidates are fitted simultaneously. The yields $N_{\text{sig,right}}$ and $N_{\text{sig,wrong}}$ are parameterised as

$$N_{\text{sig,right}} = N_{\text{sig}}\ (1-\omega)\ , \tag{10.20}$$

$$N_{\text{sig,wrong}} = N_{\text{sig}}\ \omega\ , \tag{10.21}$$

where N_{sig} is the total signal yield and ω is the mistag probability. This procedure allows to easily determine the signal shape with the rightly-tagged candidates and to simultaneously apply this shape to the less abundant wrongly-tagged candidates. Example fits of the doubly-tagged $D^0 \to K^-\pi^+$, $D^0 \to K^-K^+$ and $D^0 \to \pi^-\pi^+$ samples are shown in Figures 10.3a, 10.3b and 10.3c, respectively. The fit model is described in detail in Appendix B.3.

The mistag probability ω^+ is measured by a fit to D^{*+} candidates, $\omega_{\overline{D}^0}$ by fitting the Δm distribution of D^{*-} candidates. The average mistag probability ω is extracted from a fit to the combined sample. The mistag probabilities are determined independently for each of the 2011, 2012, magnet up and magnet down samples, equivalently to the wrong-sign method. The final results are given in Table 10.4. The mistag probabilities ω and mistag differences $\Delta\omega$ are consistent at the 2σ level for all three channels when using the ΔA_{CP} and $A_{CP}(K^-K^+)$ selections. A table with all fitted mistag probabilities in all sub-samples is found in Appendix B.1. The values for each year and each polarity are consistent.

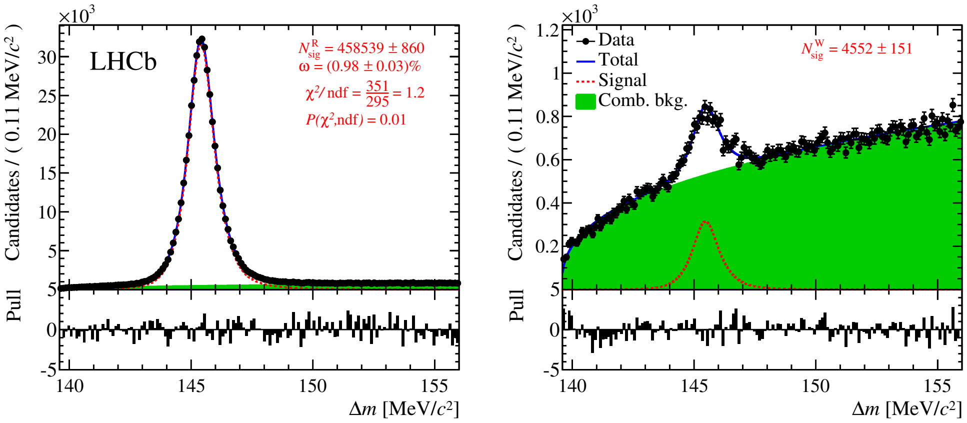

(a) Doubly-tagged $D^0 \to K^-\pi^+$ candidates

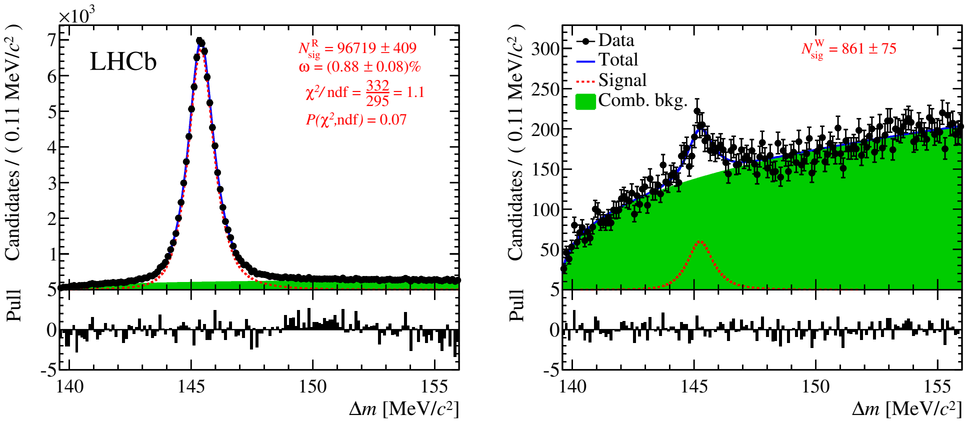

(b) Doubly-tagged $D^0 \to K^-K^+$ candidates

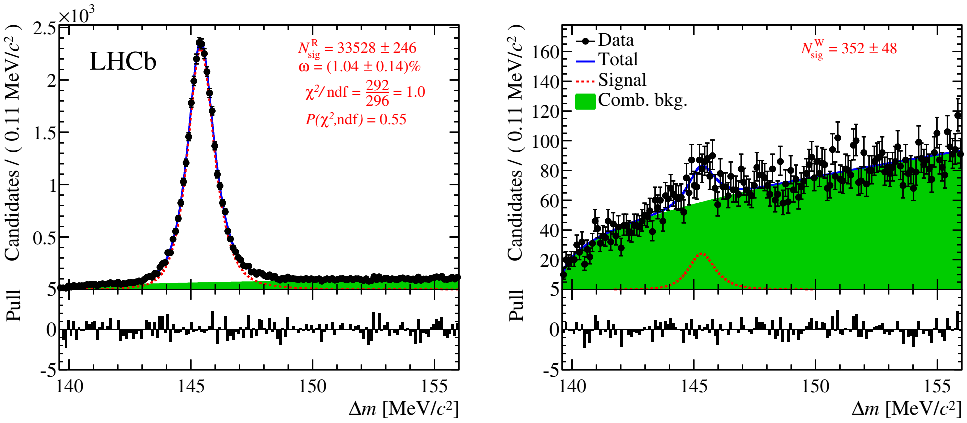

(c) Doubly-tagged $D^0 \to \pi^-\pi^+$ candidates

Figure 10.3: The Δm distribution of doubly-tagged (a) $D^0 \to K^-\pi^+$, (b) $D^0 \to K^-K^+$ and (c) $D^0 \to \pi^-\pi^+$ candidates. The left plots show the rightly-tagged candidates, the right plots the wrongly-tagged candidates. The data are taken from the 2012 magnet up sample. The ΔA_{CP} trigger selection is used.

Table 10.5: Comparison of the measured mistag probabilities of the $D^{*\pm}$ and wrong-sign method. The results for the ΔA_{CP} and the $A_{CP}(K^-K^+)$ trigger selections are shown.

ΔA_{CP} selection

Method	ω_{D^0} [%]	$\omega_{\overline{D}^0}$ [%]	$\Delta\omega$ [%]	ω [%]
wrong-sign	1.0012 ± 0.0081	0.9733 ± 0.0079	0.028 ± 0.011	0.9875 ± 0.0055
$D^{*\pm}$	0.960 ± 0.028	1.004 ± 0.027	-0.043 ± 0.039	0.982 ± 0.019

$A_{CP}(K^-K^+)$ selection

Method	ω_{D^0} [%]	$\omega_{\overline{D}^0}$ [%]	$\Delta\omega$ [%]	ω [%]
wrong-sign	0.8037 ± 0.0081	0.7778 ± 0.0080	0.027 ± 0.011	0.7913 ± 0.0056
$D^{*\pm}$	0.766 ± 0.030	0.830 ± 0.028	-0.064 ± 0.041	0.803 ± 0.021

Comparison of both methods and systematic uncertainties

Both methods are compared in Table 10.5. A very good agreement is seen in the average mistag probability ω. The mistag difference $\Delta\omega$ agrees within 2σ. It should be noted that all given uncertainties are only of statistical nature. Both methods are likely to be affected by systematic uncertainties due to the mistag probability extraction procedure. However, given the very good agreement between both methods and that the corrections due to the mistag probability of less than 1 % are very small, further systematic studies are not necessary.

The residual difference of both methods and the statistical uncertainty of the wrong-sign method are propagated as systematic uncertainties. The mistag difference $\Delta\omega$ is expected to largely cancel in the $A_{CP}(K^-K^+)$ and ΔA_{CP} measurement as its contributions do not originate from the signal decay. However, there might be small differences between the various channels. These differences should not exceed $\Delta\omega$ itself. Conservatively, the full mistag differences $\Delta\omega$ of 0.028 % and 0.027 % are assigned as systematic uncertainties to the ΔA_{CP} and $A_{CP}(K^-K^+)$ measurement, respectively.

10.4 Summary

The mistag probability of muon-tagged D^0 decays is consistently determined with two independent methods. Both methods use the $D^0 \to K^-\pi^+$ sample which has the largest signal yield. The mistag probabilities ω of muon-tagged D^0 decays are measured to be (0.9875 ± 0.0055) % and (0.7913 ± 0.0056) % for the ΔA_{CP} and $A_{CP}(K^-K^+)$ measurements, respectively. This leads to very small corrections of both measurements. The mistag differences $\Delta\omega$ which lead to shifts of the raw asymmetries but cancel in the *CP* measurements are determined to be (0.028 ± 0.011) % and (0.027 ± 0.011) % with the ΔA_{CP} and $A_{CP}(K^-K^+)$ trigger selections, respectively. The values of $\Delta\omega$ are conservatively taken as systematic uncertainties for both measurements.

Chapter 11

CP asymmetry measurements

In this chapter the methods and results of the previous chapters are combined to extract *CP* asymmetries. First, the results of the ΔA_{CP} measurement are presented. Second, the determined value of $A_{CP}(K^-K^+)$ is given. Third, the correlation of both measurements is discussed. Fourth, both measurements are combined to calculate $A_{CP}(\pi^-\pi^+)$.

11.1 Measurement of ΔA_{CP}

The method to extract ΔA_{CP} from the LHCb data is presented in Chapter 5. The formula to obtain ΔA_{CP} from the measured raw asymmetries and the measured mistag probability is according to Equation 10.10

$$\Delta A_{CP} = (1+2\omega)\left[A_{\text{raw}}(K^-K^+) - A_{\text{raw}}(\pi^-\pi^+)\right] \quad . \tag{11.1}$$

The determination of the mistag probability ω is presented in Chapter 10. Production and detection asymmetries depend on the kinematic distributions of reconstructed $D^0 \to K^-K^+$ and $D^0 \to \pi^-\pi^+$ decays. For the ΔA_{CP} measurement the $D^0 \to K^-K^+$ sample is weighted such that the kinematic distributions agree, cf. Chapter 8.1.2. The raw asymmetries of the weighted samples are obtained from binned maximum-likelihood fits to the invariant D^0 mass distributions. The fit model is described in Chapter 7.3. The additional uncertainty due to the kinematic weighting is taken into account in the fitting procedure, see Chapter 8.2.1.

The analysis is performed independently in the magnet up and down samples to test the cancellation of detection asymmetries. The arithmetic mean of the obtained raw asymmetries is taken in order to cancel residual detection asymmetries:

$$A_{\text{raw}}(\text{year}) = \frac{A_{\text{raw}}(\text{year})^{\uparrow} + A_{\text{raw}}(\text{year})^{\downarrow}}{2} \quad . \tag{11.2}$$

As production and detection asymmetries change due to different operational conditions, raw asymmetries are determined independently for each year. The final values of the raw asymmetries are the weighted means of both data taking periods:

$$A_{\text{raw}} = \frac{1}{\frac{1}{\sigma^2_{2011}} + \frac{1}{\sigma^2_{2012}}} \left(\frac{1}{\sigma^2_{2011}} A_{\text{raw}}(2011) + \frac{1}{\sigma^2_{2012}} A_{\text{raw}}(2012)\right) \quad . \tag{11.3}$$

Additionally, the weighted means of the raw asymmetries obtained in 2011 and 2012 are separately quoted for magnet up and magnet down polarity.

Table 11.1: The measured raw asymmetries for $D^0 \to K^-K^+$ and $D^0 \to \pi^-\pi^+$ decays, and the derived ΔA_{CP} (in %). The $D^0 \to K^-K^+$ samples are weighted. The results of each year are obtained by taking the arithmetic mean of both magnet polarities. The values of 2011+2012 for *magnet up*, *magnet down* and *mean* are the weighted means of both years. Note: The correction due to the mistag probability is not applied.

2011	**Magnet up**	**Magnet down**	**Mean**
$A_{\text{raw}}(K^-K^+)$	-0.480 ± 0.228	-0.404 ± 0.194	-0.442 ± 0.150
$A_{\text{raw}}(\pi^-\pi^+)$	-1.167 ± 0.399	-0.373 ± 0.341	-0.770 ± 0.262
ΔA_{CP}	$+0.687 \pm 0.460$	-0.031 ± 0.392	$+0.328 \pm 0.302$
2012	**Magnet up**	**Magnet down**	**Mean**
$A_{\text{raw}}(K^-K^+)$	-0.448 ± 0.131	-0.436 ± 0.135	-0.4417 ± 0.0939
$A_{\text{raw}}(\pi^-\pi^+)$	-0.216 ± 0.229	-0.791 ± 0.235	-0.503 ± 0.164
ΔA_{CP}	-0.232 ± 0.263	$+0.355 \pm 0.271$	$+0.062 \pm 0.189$
2011+2012	**Magnet up**	**Magnet down**	**Mean**
$A_{\text{raw}}(K^-K^+)$	-0.456 ± 0.113	-0.425 ± 0.111	-0.4418 ± 0.0795
$A_{\text{raw}}(\pi^-\pi^+)$	-0.451 ± 0.198	-0.657 ± 0.193	-0.578 ± 0.139
ΔA_{CP}	-0.005 ± 0.229	$+0.231 \pm 0.223$	$+0.137 \pm 0.160$

The measured raw asymmetries of the $D^0 \to \pi^-\pi^+$ samples and the weighted $D^0 \to K^-K^+$ samples are given in Table 11.1. The corresponding invariant mass distributions, including fit projections, are shown in Figure 11.1 and 11.2. The full list of fit parameters including correlations with the fitted signal asymmetry can be found in Appendix C.1.1. The ΔA_{CP} values obtained from the 2011 and 2012 data set are consistent within 1σ. The up–down differences are 1.2σ and -1.6σ in the 2011 and 2012 data set, respectively. These are mainly driven by the up–down differences of the $A_{\text{raw}}(\pi^-\pi^+)$ values. The difference has opposite sign in the 2011 and 2012 data set. Thus, the results of the combined data sets are very consistent between magnet up and magnet down polarity. The fit model used for $D^0 \to K^-K^+$ and $D^0 \to \pi^-\pi^+$ candidates fits well in both cases. A more detailed discussion of the fit model is found in Chapter 7.4 where the extraction of raw asymmetries is explained. The effect of the weighting procedure on the raw asymmetries is discussed in Chapter 12.1. Systematic studies related to the fit model are described in Chapter 13.1.

Combining the final raw asymmetries with the measured mistag probability ω of $(0.9875 \pm 0.0055)\%$ yields the result:

$$\Delta A_{CP} = (+0.14 \pm 0.16\,(\text{stat}) \pm 0.08\,(\text{syst}))\,\% \quad . \tag{11.4}$$

The quoted systematic uncertainty is discussed in Chapter 13. It includes studies related to the mistag probability, the weighting procedure and the extraction of raw asymmetries. The stability of the measured ΔA_{CP} in different regions of phase space and different data taking periods is tested in Chapter 12.

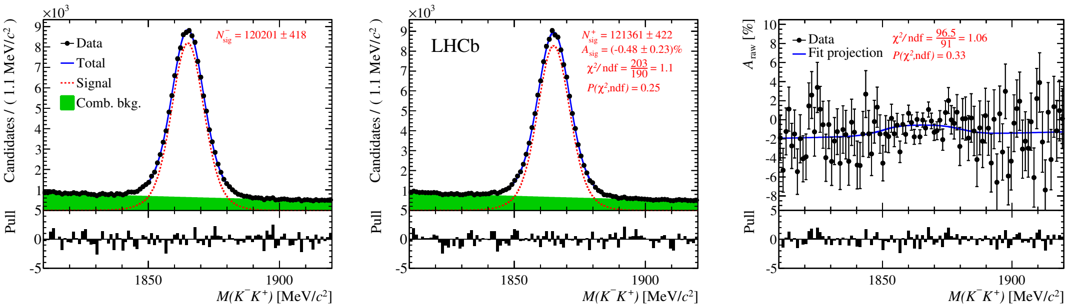

(a) Magnet up 2011

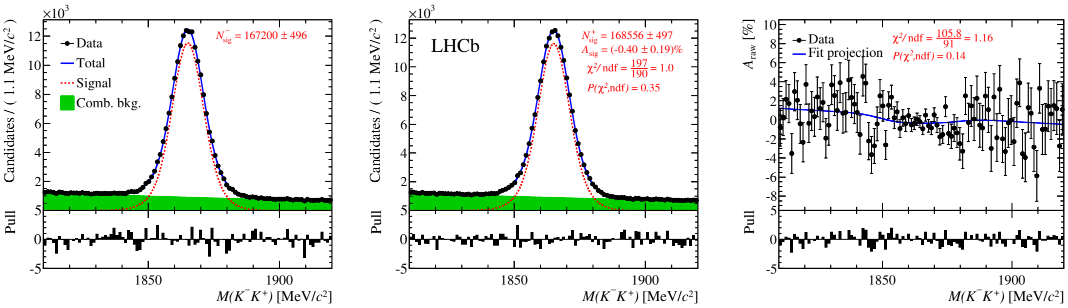

(b) Magnet down 2011

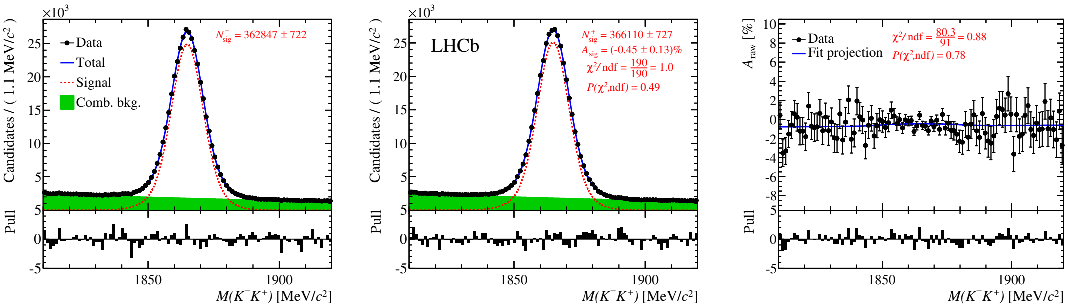

(c) Magnet up 2012

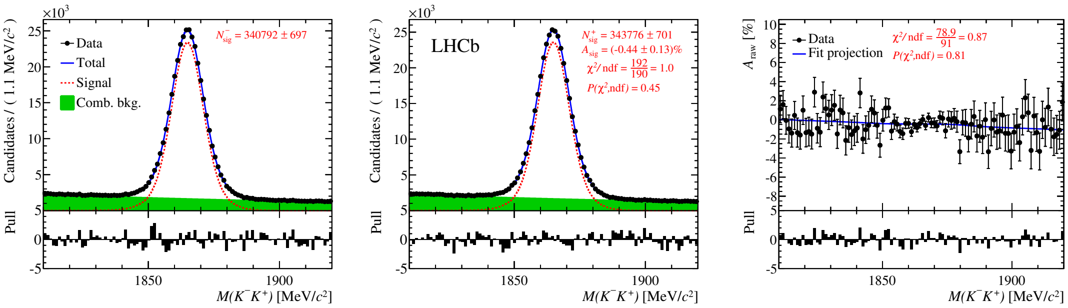

(d) Magnet down 2012

Figure 11.1: The invariant mass distribution of $D^0 \to K^-K^+$ candidates. The fit results are overlaid. The left and middle plots show negatively- and positively-tagged candidates, respectively. The right plots show the observed and fitted asymmetry in each invariant mass bin.

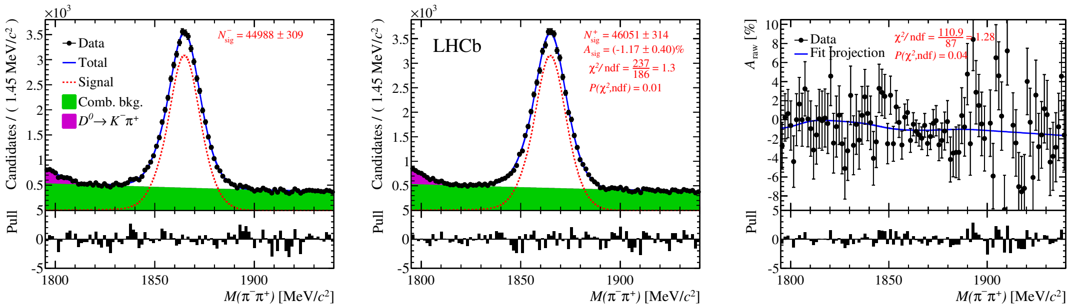

(a) Magnet up 2011

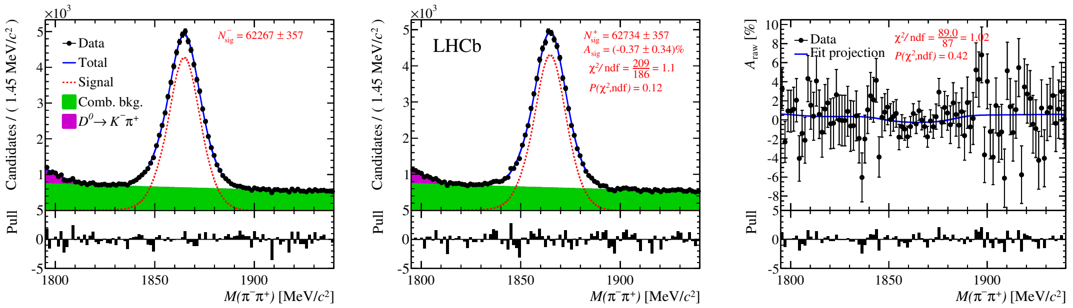

(b) Magnet down 2011

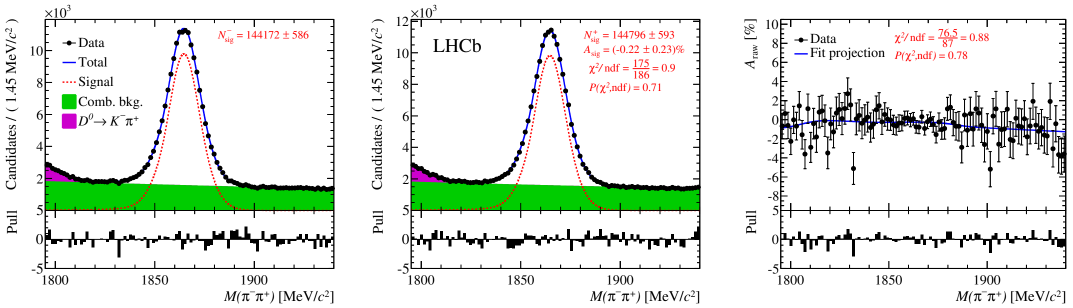

(c) Magnet up 2012

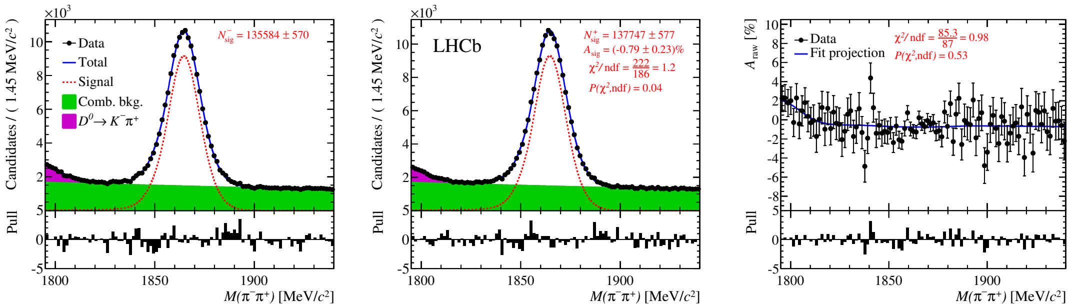

(d) Down 2012

Figure 11.2: The invariant mass distribution of $D^0 \to \pi^-\pi^+$ candidates. The fit results are overlaid. The left and middle plots show negatively- and positively-tagged candidates, respectively. The right plots show the observed and fitted asymmetry in each invariant mass bin.

11.2 Measurement of $A_{CP}(K^-K^+)$

The analysis strategy to measure $A_{CP}(K^-K^+)$ is presented in Chapter 5. Following Equations 10.11 and 5.22, the *CP* asymmetry $A_{CP}(K^-K^+)$ is determined by:

$$A_{CP}(K^-K^+) = (1+2\omega)\left[A_{\text{raw}}(K^-K^+) - A_{\text{raw}}(K^-\pi^+)\right] + (1-2R)A_D(K^-\pi^+)\,, \quad (11.5)$$

where

$$A_D(K^-\pi^+) = A_{\text{raw}}(K^-\pi^+\pi^+) - A_{\text{raw}}(\overline{K}^0\pi^+) + A_D(\overline{K}^0) \quad . \quad (11.6)$$

The cancellation of detection and production asymmetries requires a kinematic weighting of muon-tagged $D^0 \to K^-\pi^+$, and prompt $D^+ \to K^-\pi^+\pi^+$ and $D^+ \to \overline{K}^0\pi^+$ decays. The weighting procedure is described in Chapter 8.1.4. The small correction due to the mistag probability and wrong-sign events is discussed in Chapter 10.3. The determination of $A_D(\overline{K}^0)$ is performed in Chapter 9. The asymmetries of the kinematically weighted samples are extracted from binned maximum-likelihood fits to the invariant mass distributions, see Chapter 7.3 and 8.2.1. Equivalently to the ΔA_{CP} measurement, the arithmetic mean of the raw asymmetries obtained from the magnet up and magnet down samples is taken to determine the value of the measured raw asymmetry for each year:

$$A_{\text{raw}}(\text{year}) = \frac{A_{\text{raw}}(\text{year})^{\uparrow} + A_{\text{raw}}(\text{year})^{\downarrow}}{2} \quad . \quad (11.7)$$

The final result is the weighted mean of both years:

$$A_{\text{raw}} = \frac{1}{\frac{1}{\sigma^2_{2011}} + \frac{1}{\sigma^2_{2012}}} \left(\frac{1}{\sigma^2_{2011}} A_{\text{raw}}(2011) + \frac{1}{\sigma^2_{2012}} A_{\text{raw}}(2012)\right) \quad . \quad (11.8)$$

Additionally, the weighted means of the raw asymmetries obtained in 2011 and 2012 and the resulting *CP* asymmetries are separately quoted for magnet up and magnet down polarity.

The raw asymmetries to determine the value of $A_{CP}(K^-K^+)$ are shown in Table 11.2 for the 2011 and 2012 data sets. The corresponding mass plots and the asymmetry projections are shown in Figure 11.3, 11.4, 11.5 and 11.6. The full list of fit parameters can be found in Appendix C.1.2. The four independent measurements of $A_{CP}(K^-K^+)$ agree within 1σ. The selected fit model is not sufficient to describe the invariant mass distributions of the Cabibbo-favoured modes $D^0 \to K^-\pi^+$, $D^+ \to K^-\pi^+\pi^+$ and $D^+ \to \overline{K}^0\pi^+$, as seen in Figures 11.4, 11.5 and 11.6. However, the asymmetry in each invariant mass bin is well described for all decay modes. A detailed discussion of the fit model and the peculiarities of the invariant mass distributions can be found in Chapter 7.4. Systematic studies related to the fit model are described in Chapter 13.1. The weighting significantly increases the statistical uncertainties for the raw asymmetries. This is discussed later in Chapter 12.1. The largest contribution to the statistical uncertainty originates from the determination of $A_{\text{raw}}(\overline{K}^0\pi^+)$.

Table 11.2: The measured raw asymmetries for $D^0 \to K^-K^+$, $D^0 \to K^-\pi^+$, $D^+ \to K^-\pi^+\pi^+$ and $D^+ \to \overline{K}^0\pi^+$ (in %) for the 2011 and 2012 data set. The $D^0 \to K^-\pi^+$, $D^+ \to K^-\pi^+\pi^+$ and $D^+ \to \overline{K}^0\pi^+$ samples are kinematically weighted. These numbers are used to calculate $A_{CP}(K^-K^+)$. The corrections due to $A_D(\overline{K}^0)$, ω and R are taken into account. The result of each year is obtained by taking the arithmetic mean of both magnet polarities. The uncertainties for R and $A_D(\overline{K}^0)$ are fully correlated.

2011	**Magnet up**	**Magnet down**	**Mean**
$A_D(\overline{K}^0)$	-0.0540 ± 0.0140	-0.0540 ± 0.0140	-0.0540 ± 0.0140
$A_{\text{raw}}(\overline{K}^0\pi^+)$	-0.710 ± 0.345	-0.600 ± 0.269	-0.655 ± 0.219
$A_{\text{raw}}(K^-\pi^+\pi^+)$	-2.1870 ± 0.0764	-1.6194 ± 0.0627	-1.9032 ± 0.0494
$A_D(K^-\pi^+)$	-1.531 ± 0.354	-1.073 ± 0.277	-1.302 ± 0.225
$A_{\text{raw}}(K^-\pi^+)$	-1.710 ± 0.104	-1.6219 ± 0.0888	-1.6658 ± 0.0684
$A_{\text{raw}}(K^-K^+)$	-0.245 ± 0.242	-0.463 ± 0.207	-0.354 ± 0.159
ω	0.740 ± 0.014	0.742 ± 0.012	0.7409 ± 0.0091
R	0.3894 ± 0.0030	0.3894 ± 0.0030	0.3894 ± 0.0030
$A_{CP}(K^-K^+)$	-0.033 ± 0.442	$+0.111 \pm 0.357$	$+0.039 \pm 0.284$

2012	**Magnet up**	**Magnet down**	**Mean**
$A_D(\overline{K}^0)$	-0.0540 ± 0.0140	-0.0540 ± 0.0140	-0.0540 ± 0.0140
$A_{\text{raw}}(\overline{K}^0\pi^+)$	-1.016 ± 0.192	-0.457 ± 0.198	-0.736 ± 0.138
$A_{\text{raw}}(K^-\pi^+\pi^+)$	-1.9200 ± 0.0363	-1.6915 ± 0.0376	-1.8058 ± 0.0261
$A_D(K^-\pi^+)$	-0.958 ± 0.196	-1.289 ± 0.202	-1.123 ± 0.141
$A_{\text{raw}}(K^-\pi^+)$	-1.3253 ± 0.0573	-1.5816 ± 0.0590	-1.4535 ± 0.0411
$A_{\text{raw}}(K^-K^+)$	-0.515 ± 0.134	-0.389 ± 0.138	-0.4520 ± 0.0964
ω	0.8124 ± 0.0082	0.8084 ± 0.0084	0.8104 ± 0.0063
R	0.3894 ± 0.0030	0.3894 ± 0.0030	0.3894 ± 0.0030
$A_{CP}(K^-K^+)$	-0.127 ± 0.245	-0.067 ± 0.252	-0.097 ± 0.176

Table 11.3: The raw asymmetries for $D^0 \to K^-K^+$, $D^0 \to K^-\pi^+$, $D^+ \to K^-\pi^+\pi^+$ and $D^+ \to \overline{K}^0\pi^+$ (in %) after combining the 2011 and 2012 results. The values of 2011+2012 for *magnet up*, *magnet down* and *mean* are the weighted means of the values given in Table 11.2. The values for $A_{CP}(K^-K^+)$ are calculated from the raw asymmetries, corrections due to $A_D(\overline{K}^0)$, ω and R are taken into account. The uncertainties for R and $A_D(\overline{K}^0)$ are fully correlated. Note: The mean is neither the arithmetic nor the weighted average of the magnet up and magnet down values.

2011+2012	**Magnet up**	**Magnet down**	**Mean**
$A_D(\overline{K}^0)$	-0.0540 ± 0.0140	-0.0540 ± 0.0140	-0.0540 ± 0.0140
$A_{\text{raw}}(\overline{K}^0\pi^+)$	-0.944 ± 0.168	-0.507 ± 0.160	-0.713 ± 0.117
$A_{\text{raw}}(K^-\pi^+\pi^+)$	-1.9691 ± 0.0327	-1.6724 ± 0.0323	-1.8270 ± 0.0231
$A_D(K^-\pi^+)$	-1.079 ± 0.172	-1.219 ± 0.163	-1.168 ± 0.120
$A_{\text{raw}}(K^-\pi^+)$	-1.4146 ± 0.0502	-1.5940 ± 0.0492	-1.5098 ± 0.0352
$A_{\text{raw}}(K^-K^+)$	-0.452 ± 0.117	-0.412 ± 0.115	-0.4258 ± 0.0825
ω	0.7939 ± 0.0071	0.7866 ± 0.0069	0.7913 ± 0.0056
R	0.3894 ± 0.0030	0.3894 ± 0.0030	0.3894 ± 0.0030
$A_{CP}(K^-K^+)$	-0.093 ± 0.214	-0.009 ± 0.206	-0.057 ± 0.150

The combined values including the result of $A_{CP}(K^-K^+)$ for the full data set are given in Table 11.3. The final result for $A_{CP}(K^-K^+)$ is

$$A_{CP}(K^-K^+) = (-0.06 \pm 0.15\,(\text{stat}) \pm 0.10\,(\text{syst}))\,\% \quad ,$$

where the first uncertainty is statistical and the second is systematic. The two independent values for the full magnet up and down samples agree very well. Systematic uncertainties due to the cancellation of spurious asymmetries and the raw asymmetry extraction are discussed in Chapter 13. This includes systematic studies of the weighting procedure, the asymmetry extraction and the corrections due to wrong flavour tags and the neutral kaon asymmetry. The measurements of $A_{CP}(K^-K^+)$ and ΔA_{CP} are correlated due to the overlapping $D^0 \to K^-K^+$ samples. The correlation is discussed in the following section.

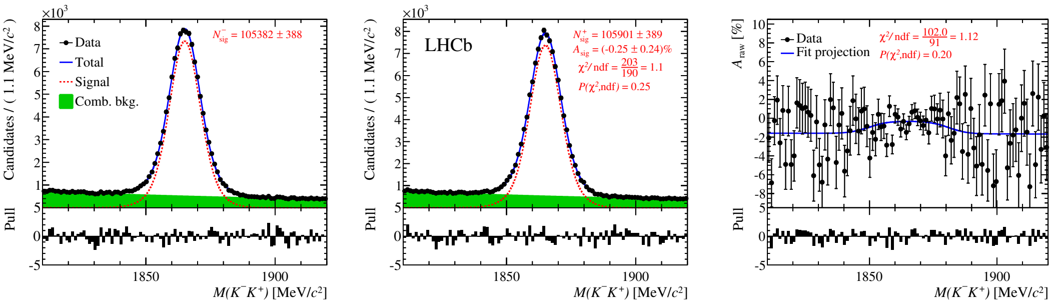

(a) Magnet up 2011

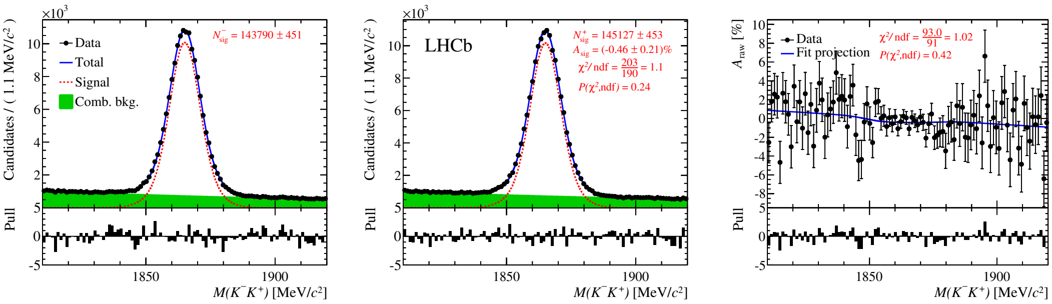

(b) Magnet down 2011

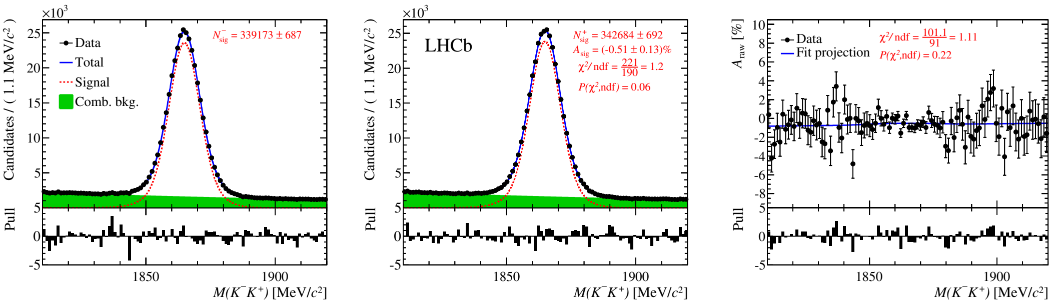

(c) Magnet up 2012

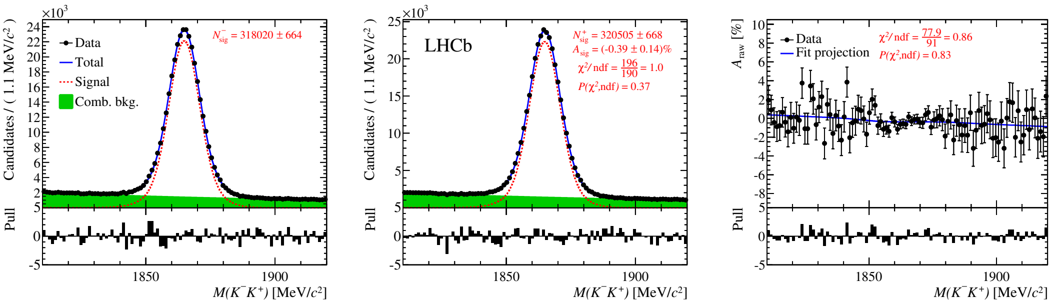

(d) Magnet down 2012

Figure 11.3: The invariant mass distribution of $D^0 \to K^-K^+$ candidates. The fit results are overlaid. The left and middle plots show negatively- and positively-tagged candidates, respectively. The right plots show the observed and fitted asymmetry in each invariant mass bin.

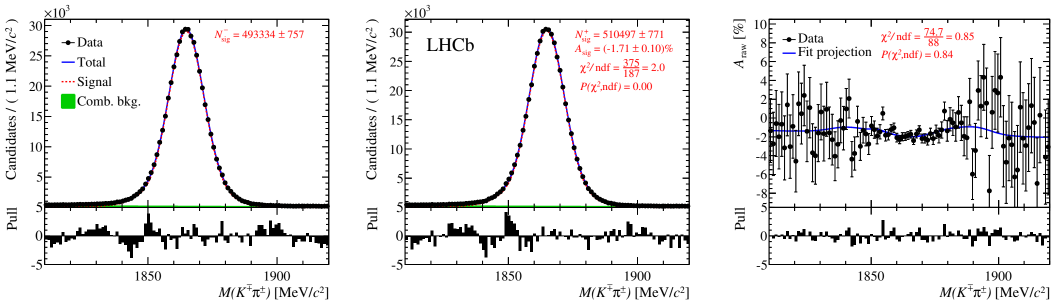

(a) Magnet up 2011

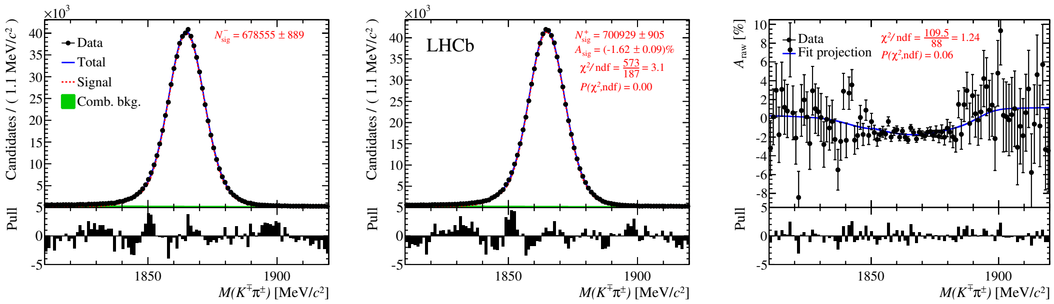

(b) Magnet down 2011

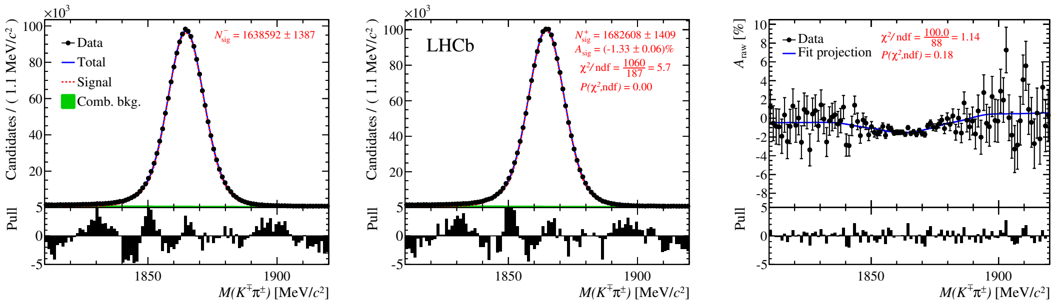

(c) Magnet up 2012

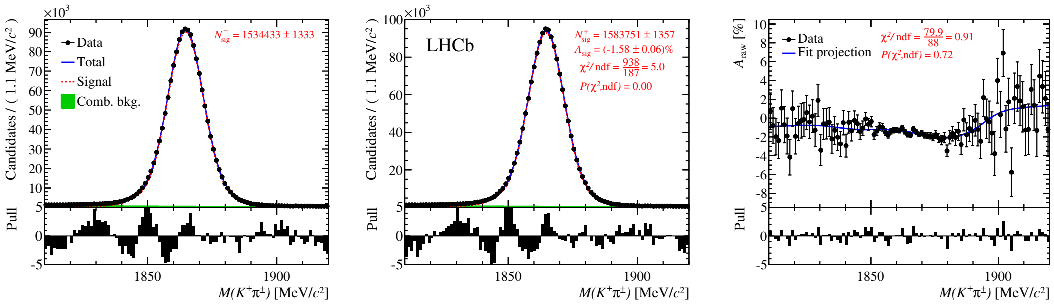

(d) Magnet down 2012

Figure 11.4: The invariant mass distribution of $D^0 \rightarrow K^-\pi^+$ candidates. The fit results are overlaid. The left and middle plots show negatively- and positively-tagged candidates, respectively. The right plots show the observed and fitted asymmetry in each invariant mass bin.

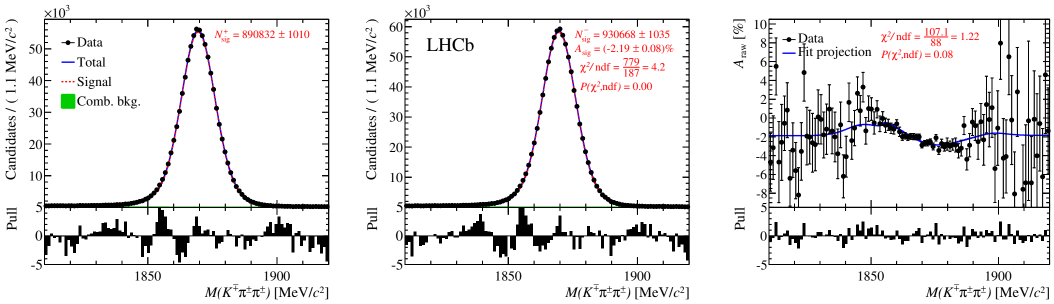

(a) Magnet up 2011

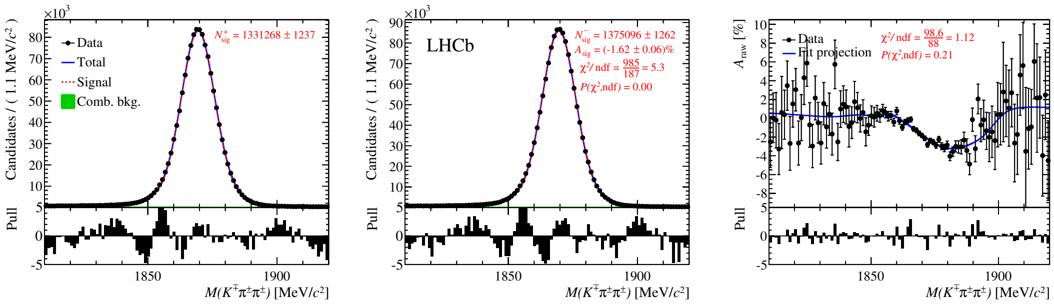

(b) Magnet down 2011

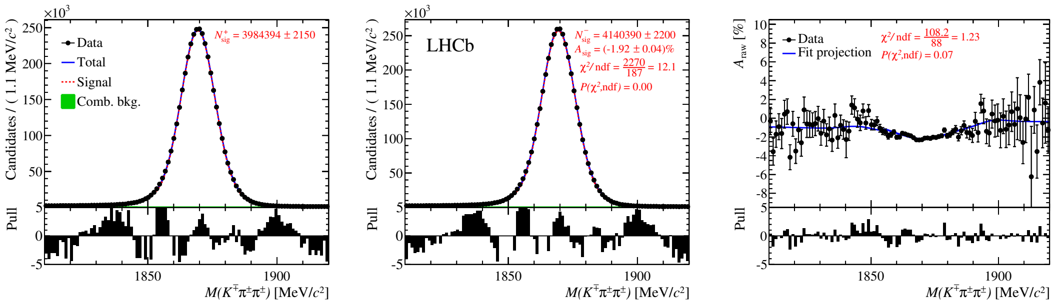

(c) Magnet up 2012

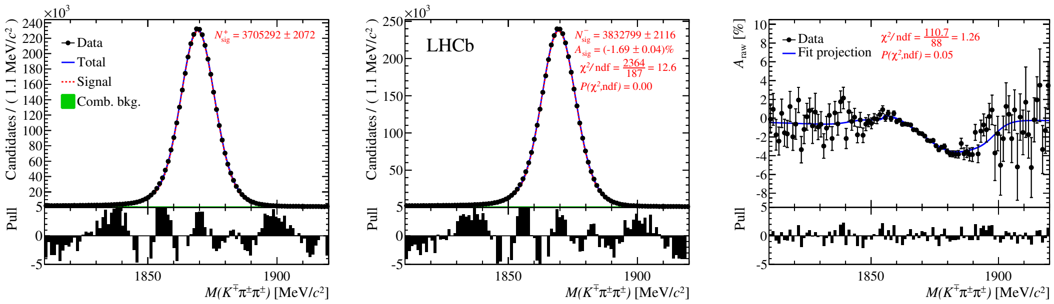

(d) Magnet down 2012

Figure 11.5: The invariant mass distribution of $D^+ \to K^-\pi^+\pi^+$ candidates. The fit results are overlaid. The left and middle plots show D^+ and D^- candidates, respectively. The right plots show the observed and fitted asymmetry in each invariant mass bin.

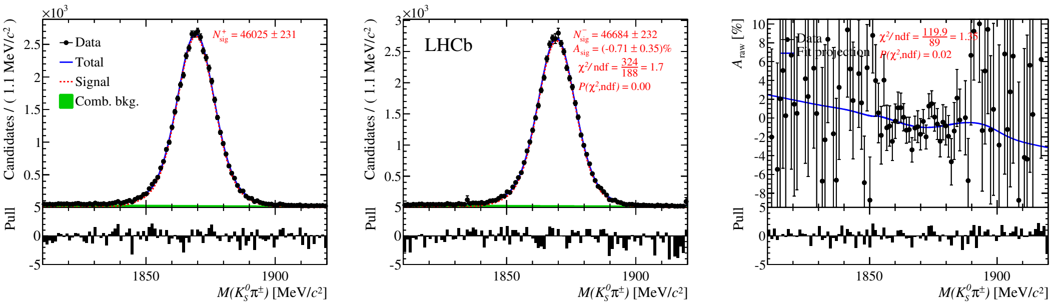

(a) Magnet up 2011

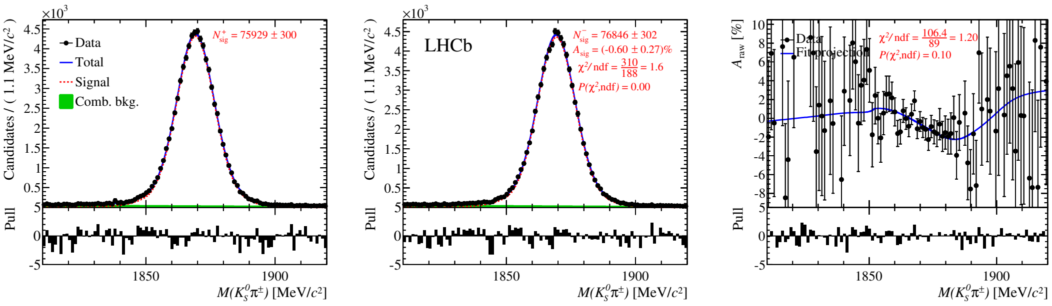

(b) Magnet down 2011

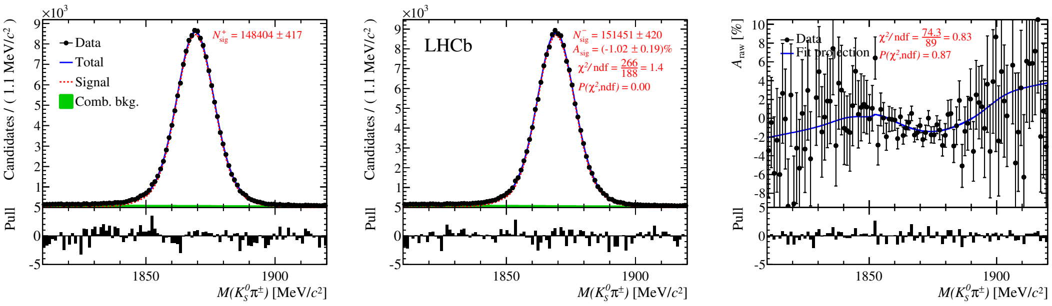

(c) Magnet up 2012

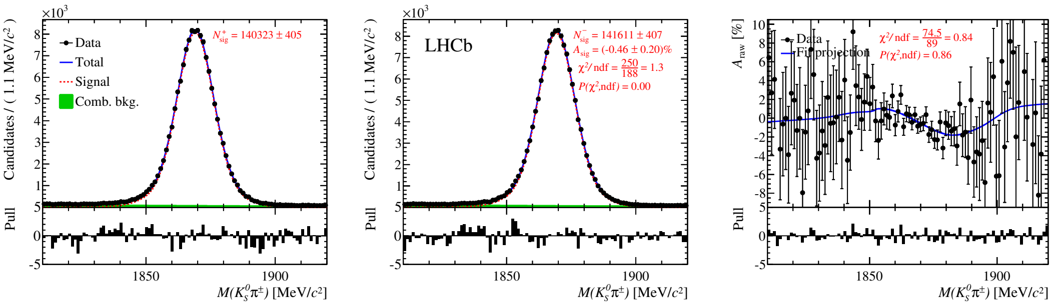

(d) Magnet down 2012

Figure 11.6: The invariant mass distribution of $D^+ \to \overline{K}^0\pi^+$ candidates. The fit results are overlaid. The left and middle plots show D^+ and D^- candidates, respectively. The right plots show the observed and fitted asymmetry in each invariant mass bin.

11.3 Correlation between ΔA_{CP} and $A_{CP}(K^-K^+)$

The measurements of $A_{CP}(K^-K^+)$ and ΔA_{CP} use a common sample to determine the raw asymmetry $A_{\text{raw}}(K^-K^+)$. However, not all candidates of the ΔA_{CP} measurement are included in the $A_{CP}(K^-K^+)$ measurement due to a tighter trigger selection, cf. Chapter 6.2.4. Furthermore, the $D^0 \to K^-K^+$ candidates are kinematically weighted in the ΔA_{CP} determination such that the kinematic distributions of the $D^0 \to K^-K^+$ and $D^0 \to \pi^-\pi^+$ samples agree, cf. Chapter 8.1.2. The correlation factor ρ_{KK} between the two samples is given in Chapter 8.2.3, see Equation 8.32:

$$\rho_{KK} = \sqrt{\frac{\left(\sum_{i=1}^{N} w_{KK,i}^{A_{CP}(K^-K^+)}\, w_{KK,i}^{\Delta A_{CP}}\right)^2}{\sum_{i=1}^{N}\left(w_{KK,i}^{A_{CP}(K^-K^+)}\right)^2 \sum_{i=1}^{N}\left(w_{KK,i}^{\Delta A_{CP}}\right)^2}} \quad , \tag{11.9}$$

where N is the total number of $D^0 \to K^-K^+$ candidates, $w_{KK,i}^{\Delta A_{CP}}$ is the kinematic weight of each $D^0 \to K^-K^+$ candidate in the ΔA_{CP} measurement and $w_{KK,i}^{A_{CP}(K^-K^+)}$ is the weight of each $D^0 \to K^-K^+$ candidate in the $A_{CP}(K^-K^+)$ measurement (0 or 1).

Using the formulas to obtain ΔA_{CP} and $A_{CP}(K^-K^+)$ and following the derivation in Chapter 8.2.3, the covariance of the two measurements is calculated to be

$$\text{Cov}(\Delta A_{CP}, A_{CP}(K^-K^+)) = \rho_{KK}\, \sigma_{A_{\text{raw}}}^{A_{CP}(K^-K^+)}\, \sigma_{A_{\text{raw}}}^{\Delta A_{CP}} \quad , \tag{11.10}$$

where $\sigma_{A_{\text{raw}}}^{\Delta A_{CP}}$ is the statistical uncertainty for $A_{\text{raw}}(K^-K^+)$ in the ΔA_{CP} measurement and $\sigma_{A_{\text{raw}}}^{\Delta A_{CP}}$ in the $A_{CP}(K^-K^+)$ measurement. The statistical correlation of the ΔA_{CP} and $A_{CP}(K^-K^+)$ measurements is given by

$$\rho_{\text{stat}} = \rho_{KK} \frac{\sigma_{A_{\text{raw}}}^{A_{CP}(K^-K^+)}\, \sigma_{A_{\text{raw}}}^{\Delta A_{CP}}}{\sigma_{\text{stat}}^{\Delta A_{CP}}\, \sigma_{\text{stat}}^{A_{CP}(K^-K^+)}} \quad , \tag{11.11}$$

see Equation 8.34, where $\sigma_{\text{stat}}^{\Delta A_{CP}}$ is the statistical uncertainty for ΔA_{CP} and $\sigma_{\text{stat}}^{A_{CP}(K^-K^+)}$ for $A_{CP}(K^-K^+)$.

The correlation factor ρ_{KK} is determined to be

$$\rho_{KK} = 0.863 \quad .$$

Using the uncertainties given in Table 11.1 and 11.3, the statistical correlation of both measurements is

$$\rho_{\text{stat}} = 0.23 \quad .$$

The correlation of systematic uncertainties is given in Chapter 13.5 after sources of systematic uncertainties have been discussed.

11.4 Determination of $A_{CP}(\pi^-\pi^+)$

The *CP* asymmetry $A_{CP}(\pi^-\pi^+)$ is obtained by taking the difference of ΔA_{CP} and $A_{CP}(K^-K^+)$:

$$A_{CP}(\pi^-\pi^+) = A_{CP}(K^-K^+) - \Delta A_{CP} \ . \tag{11.12}$$

The statistical uncertainty for $A_{CP}(\pi^-\pi^+)$ is given by

$$\left(\sigma_{\text{stat}}^{A_{CP}(\pi^-\pi^+)}\right)^2 = \left(\sigma_{\text{stat}}^{\Delta A_{CP}}\right)^2 + \left(\sigma_{\text{stat}}^{A_{CP}(K^-K^+)}\right)^2 - 2\,\rho_{\text{stat}}\,\sigma_{\text{stat}}^{\Delta A_{CP}}\,\sigma_{\text{stat}}^{A_{CP}(K^-K^+)} \ , \tag{11.13}$$

where $\sigma_{\text{stat}}^{\Delta A_{CP}}$ and $\sigma_{\text{stat}}^{A_{CP}(K^-K^+)}$ are the statistical uncertainties for ΔA_{CP} and $A_{CP}(K^-K^+)$, respectively, ρ_{stat} is the statistical correlation of both measurements.

The *CP* asymmetry $A_{CP}(\pi^-\pi^+)$ is calculated to be

$$A_{CP}(\pi^-\pi^+) = (-0.20 \pm 0.19\,(\text{stat}) \pm 0.10\,(\text{syst}))\,\% \ ,$$

using the results of Chapter 11.1, 11.2 and 11.3. The systematic uncertainty is the same as in the $A_{CP}(K^-K^+)$ measurement, for further discussion see Chapter 13.5.

Chapter 12

Consistency checks

An important part of the analysis is to perform consistency checks of the *CP* asymmetries determined in the previous chapter. This is extensively done in this chapter. The consistency checks are separated from the systematic studies which test the methods themselves in Chapter 13. First, the effect of the kinematic weighting on the raw asymmetries is discussed. Second, the derived detection and production asymmetries are compared to the expectation. Third, the measurement is independently performed for different data taking periods to test the stability against varying detection asymmetries. Fourth, the raw asymmetries of all decay modes are studied as function of the number of particles per event. Fifth, several cross-checks are performed to test the stability of ΔA_{CP} against kinematic and selection variables.

12.1 Change of raw asymmetries due to weighting

The kinematic weighting procedure is applied to correct for residual asymmetries induced by differences in kinematic distributions. However, the weighting procedure changes the statistical power of a sample. The loss in statistical precision is reflected by the signal yields obtained from the extended maximum-likelihood fits. The signal yields before and after the kinematic weighting are given in Table 12.1. While the weighted $D^0 \to K^-K^+$ and $D^0 \to K^-\pi^+$ samples have only small losses in the signal yields, the $D^+ \to K^-\pi^+\pi^+$ sample is effectively reduced by 50 % and the $D^+ \to \overline{K}^0\pi^+$ sample by 78 %. The latter has a large impact on the statistical uncertainty for the $A_{CP}(K^-K^+)$ measurement as the weighted $D^+ \to \overline{K}^0\pi^+$ sample is the sample with the smallest effective signal yield.

Table 12.1: The fitted signal yields before and after kinematic weighting. The full data set is used.

Decay sample	N_{sig}	$N_{\text{sig,w}}$	**Ratio**
$D^+ \to \overline{K}^0\pi^+$	$3,765,640 \pm 2,191$	$827,276 \pm 1,013$	0.220
$D^+ \to K^-\pi^+\pi^+$	$40,816,225 \pm 7,169$	$20,190,743 \pm 5,037$	0.495
$D^0 \to K^-\pi^+$	$9,089,861 \pm 3,374$	$8,822,702 \pm 3,322$	0.971
$D^0 \to K^-K^+ (A_{CP}(K^-K^+))$	$1,820,586 \pm 1,694$	-	-
$D^0 \to K^-K^+ (\Delta A_{CP})$	$2,164,948 \pm 1,874$	$1,990,846 \pm 1,809$	0.920
$D^0 \to \pi^-\pi^+$	$778,344 \pm 1,565$	-	-

Table 12.2: The measured raw asymmetries before and after kinematic weighting. The combined values of the 2011 and 2012 data set are given. Note: The results in the last two columns are calculated with higher precision than is given in the first two columns.

Decay sample	$\boldsymbol{A}_{\mathbf{raw}}$ [%]	$\boldsymbol{A}_{\mathbf{raw,w}}$ [%]	**Change** [%]	$\sqrt{\boldsymbol{\sigma}_{\boldsymbol{w}}^{\mathbf{2}}-\boldsymbol{\sigma}^{\mathbf{2}}}$ [%]
$D^+ \to \overline{K}^0\pi^+$	-0.868 ± 0.055	-0.71 ± 0.12	-0.15	0.10
$D^+ \to K^-\pi^+\pi^+$	-1.813 ± 0.016	-1.827 ± 0.023	0.014	0.016
$D^0 \to K^-\pi^+$	-1.519 ± 0.035	-1.510 ± 0.035	-0.009	0.006
$D^0 \to K^-K^+$	-0.394 ± 0.076	-0.442 ± 0.080	0.047	0.023

The fitted raw asymmetries before and after the kinematic weighting are given in Table 12.2. The largest shift, $-0.15\,\%$, is observed for the the raw asymmetry of the $D^+ \to \overline{K}^0\pi^+$ sample. The differences can be induced by systematic shifts due to kinematically dependent asymmetries or they might be statistical fluctuations. The size of possible statistical fluctuations is quantified by the number

$$\sqrt{\sigma_w^2 - \sigma^2}\ , \tag{12.1}$$

where σ_w is the uncertainty of the fit to the weighted sample and σ the uncertainty of the fit to the unweighted sample, cf. Chapter 8.2.2. Three out of four raw asymmetries change by more than $1\sqrt{\sigma_w^2 - \sigma^2}$, but no change exceeds $2.1\sqrt{\sigma_w^2 - \sigma^2}$.

To summarise, the ΔA_{CP} value before and after weighting changes by approximately 0.05 % which is one third of the statistical uncertainty of ΔA_{CP}. Half of this change is expected due to statistical fluctuations. The $A_{CP}(K^-K^+)$ value shifts by about 0.15 % due to the kinematic weights.[1] About 0.1 % can be attributed to the loss in statistical power. The statistical uncertainty of $A_{CP}(K^-K^+)$ is 0.15 %. Given the current statistical precisions of the ΔA_{CP} and $A_{CP}(K^-K^+)$ measurements, it cannot be disentangled if the observed shifts are primarily coming from statistical fluctuations or from corrections induced by momentum-dependent asymmetries. Still, the weighting procedure is applied to correct for these residual asymmetries. Systematic uncertainties of the weighting procedure are studied in Chapter 13.2.

---

[1] The neutral kaon asymmetry also changes by ($-0.027\,\%$) when including kinematic weights, cf. Chapter 9.5.

12.2 Detection and production asymmetries

The analysis method does not require to explicitly measure detection and production asymmetries. Nevertheless, it is checked if the kaon detection asymmetry follows the predicted trend and if muon detection and B production asymmetries have the expected order of magnitude.

12.2.1 Charged kaon detection asymmetry

The largest correction in the $A_{CP}(K^-K^+)$ measurement is the detection asymmetry $A_D(K^-\pi^+)$. It is determined to be[2]

$$A_D(K^-\pi^+) = (-1.17 \pm 0.12\,(\mathrm{stat}))\% \ ,$$

cf. Chapter 11.2. The asymmetry is dominated by the different interaction cross sections of K^- and K^+ mesons in material, cf. Chapter 2.5.2. The kaon interaction asymmetry depends on the momentum of the kaons and the amount of material in front of the last tracking station. Equivalently to the determination of $A_D(\overline{K}^0)$, cf. Chapter 9.3, the amount of traversed material of each kaon candidate can be estimated from the known material model of the LHCb detector. The momentum dependence of the cross section has been measured and is given in Chapter 2.5.2. It is assumed that the material model is known with 10 % accuracy. This has been verified for the VELO but less precise for other detectors. Using the kinematic distributions of the $D^0 \to K^-\pi^+$ sample, the estimated value of the charged kaon detection asymmetry is

$$A_D^{\mathrm{PDG}}(K^-) = (-0.89 \pm 0.09\,(\mathrm{syst}))\,\% \ .$$

The difference between the observed and the predicted value is $(0.28 \pm 0.15)\,\%$. This offset can have several reasons. The predicted value does not include a possible but small pion interaction asymmetry and no tracking or particle identification asymmetries are accounted for. Furthermore, it is not unlikely that the material budget is underestimated.

In order to compare the expected momentum behaviour with the observed, $A_D(K^-\pi^+)$ is determined in bins of the momentum for kaon candidates of the $D^+ \to K^-\pi^+\pi^+$ sample. The D^+ production and the pion detection asymmetry is determined for each bin with the $D^+ \to \overline{K}^0\pi^+$ sample. The method is the same as is used in the $A_{CP}(K^-K^+)$ measurement. The kinematics of D^+ and pion candidates of the full $D^+ \to \overline{K}^0\pi^+$ sample are weighted to the kinematic distributions of the $D^+ \to K^-\pi^+\pi^+$ decays in each kaon momentum bin. Therefore, the extracted values for $A_P(D^+) + A_D(\pi^+)$ are correlated due to the overlap between the $D^+ \to \overline{K}^0\pi^+$ samples used for each bin. The observed and expected asymmetries are shown in Figure 12.1. The observed $A_D(K^-\pi^+)$ is clearly following the predicted trend of a decreasing asymmetry with kaon momentum.

12.2.2 Muon detection asymmetry and *B* production asymmetry

The raw asymmetry of muon-tagged $D^0 \to K^-\pi^+$ candidates is given by

$$A_{\mathrm{raw}}(K^-\pi^+) = A_P(\overline{B}) + A_D(\mu) + A_D(K^-\pi^+) \ ,$$

---

[2] Systematic uncertainties for the $A_{CP}(K^-K^+)$ measurement are evaluated in Chapter 13. No individual systematic uncertainty for the detection asymmetry $A_D(K^-\pi^+)$ is quoted.

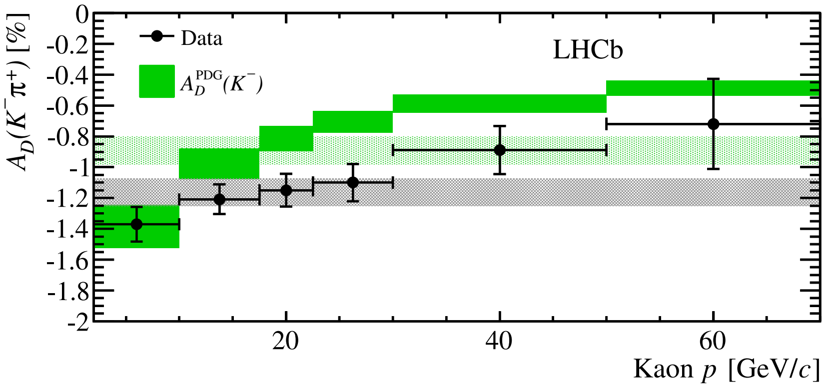

Figure 12.1: Measured $K^-\pi^+$ detection and predicted K^- asymmetry as a function of the kaon momentum. The shaded band indicates the average asymmetry integrated over the bins. There is a correlation between the data points due to the overlap between the $D^+ \to \overline{K}^0\pi^+$ samples used for each bin.

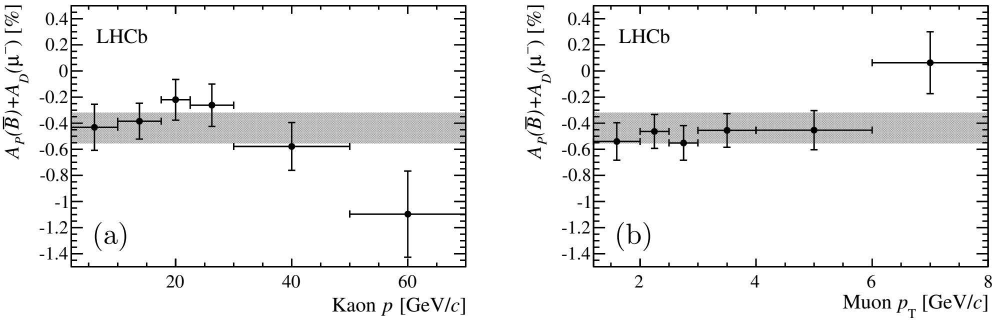

Figure 12.2: The measured $A_P(\overline{B}) + A_D(\mu)$ as function of (a) muon p_T and (b) kaon p. The shaded lines indicate the result of the full data sample. There is a correlation between the data points due to the overlap between the $D^+ \to K^-\pi^+\pi^+$ and $D^+ \to \overline{K}^0\pi^+$ samples used for each bin.

according to Equation 5.16. The dependence on several kinematic variables is studied in Chapter 7.4. In Figure 7.19b it is seen that the absolute value of the raw asymmetry decreases with the momentum of the kaon candidate. This is expected due to the kaon detection asymmetry. This effect should be reduced when correcting for $A_D(K^-\pi^+)$. Therefore, the $D^0 \to K^-\pi^+$ sample is divided into bins of the kaon candidates' momentum. Then, $A_D(K^-\pi^+)$ is determined for each bin with the full $D^+ \to K^-\pi^+\pi^+$ and $D^+ \to \overline{K}^0\pi^+$ samples. The weighting procedure is equivalent to that of the $A_{CP}(K^-K^+)$ measurement. The result is seen in Figure 12.2a. Compared to Figure 7.19b the dependence for small kaon momenta is reduced. For large kaon momenta the asymmetry becomes more negative. However, this bin has a small signal yield.

The corrected $A_{\text{raw}}(K^-\pi^+)$ has contributions from the B production and muon detection asymmetry. In order to study the muon detection asymmetry, the $D^0 \to K^-\pi^+$ sample is divided into bins of the transverse momentum of the muon candidates. Then, $A_D(K^-\pi^+)$ is determined for each bin. The combined muon detection and B production asymmetry is shown in Figure 12.2b, as function of the muon transverse momentum. As no large momentum-dependent muon detection asymmetry is expected, cf. Chapters 4.1.3 and 4.5, the distribution is very flat except for the last bin.

Assuming a small muon detection asymmetry, the B production asymmetry is estimated from the results of the $A_{CP}(K^-K^+)$ measurement, see Table 11.3, to be approximately $(-0.34\,\%)$. This is in agreement with the expectation of a negative asymmetry of the order $(-0.1$ to $-1\,\%)$, cf. Chapter 2.6.2. A precise measurement has not yet been performed at the LHCb experiment. The measured value of the B^+ production asymmetry is $A_P(B^+) = (-0.3 \pm 0.9)\,\%$ [38].

12.3 Data taking periods

The LHC is not running all the time. There are periods without data taking, see Figure 12.3. These periods are used for maintenance of the LHCb detector as many systems are easily accessible and can be moved away from the beam pipe. The maintenance might affect the efficiency of some detector parts and movements change the alignment. Furthermore, some data taking stops are used to change and improve the reconstruction in the software trigger stage or to change calibration constants. This could induce time-varying detection asymmetries. The production asymmetries have also changed between 2011 and 2012 due to the increased centre-of-mass energy although this effect is expected to be below the current sensitivity.

The measurements of $A_{CP}(K^-K^+)$ and ΔA_{CP} are designed to be insensitive to such variations as detection asymmetries are calibrated with control samples collected in the same data taking period. Nevertheless, a residual detection asymmetry which is not cancelled in the difference of raw asymmetries can appear as a variation in time of the measured CP asymmetries. To test this, the 2011 data are divided into four periods

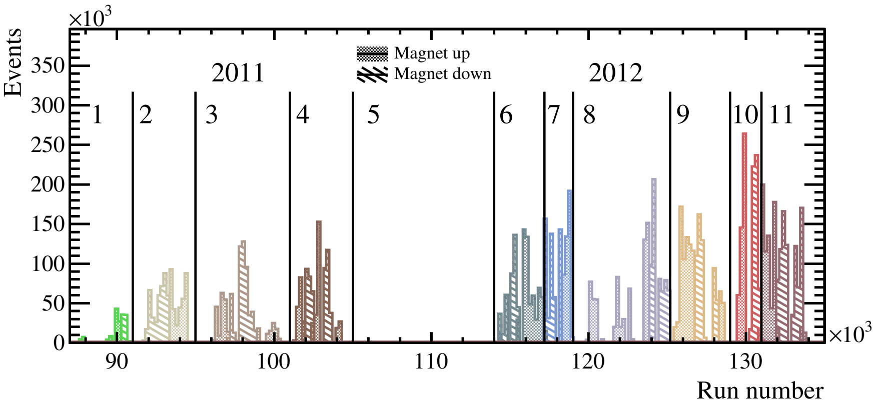

Figure 12.3: The run number distribution of reconstructed and selected events. The *run number* identifies a short period of data taking. It is always counted upwards. No single run is longer than one hour. Holes in the distribution indicate stops of the data taking as the run number increases but no events are recorded. The beginnings and ends of the 11 data taking periods are defined as $[87, 91, 95, 101, 105, 114, 117.2, 119, 152.2, 129, 131, 135] \times 10^3$. The recorded events in the range $[110, 114] \times 10^3$ are excluded due to the missing `L0Muon` calibration.

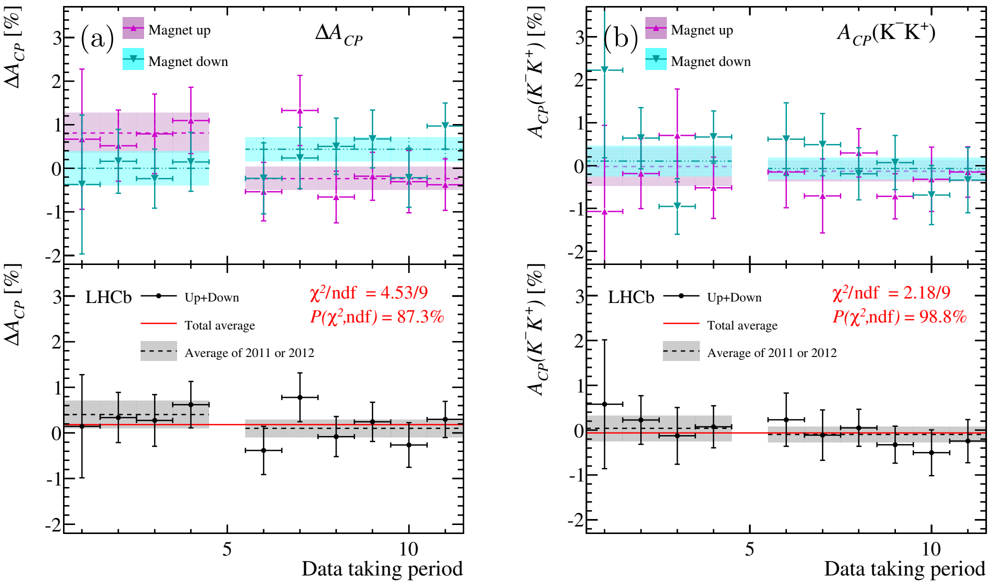

Figure 12.4: (a) ΔA_{CP} and (b) $A_{CP}(K^-K^+)$ as a function of the data taking period. The 2011 data are divided into four periods and the 2012 data into six periods. The error bars indicate the statistical uncertainty, the shaded bands show the averages for 2011 and 2012, and the (red) line shows the overall *CP* asymmetry.

and the 2012 data into six periods. Each period is given by the time between two interruptions in data taking. Furthermore, the individual data samples have to be large enough to be sensitive to variations and the magnet polarity has to be reversed at least once. The defined periods are given in Figure 12.3. The analysis is then independently performed in each data taking period. Only some parameters of the signal model are constrained from the overall fit to increase the fit stability. Figure 12.4 shows the observed ΔA_{CP} and $A_{CP}(K^-K^+)$ as function of the data taking period. The results are presented separately for the magnet up, magnet down samples and the combined value. The p-value for being consistent is quoted. No dependence of the obtained *CP* asymmetries on the data taking period is observed.

The raw asymmetries of the $A_{CP}(K^-K^+)$ and the ΔA_{CP} measurements are shown in Figure 12.5 and Figure 12.6, respectively. The raw asymmetries themselves might vary between different data taking periods, but it is reassuring if they are constant. The Cabibbo-favoured $D^0 \to K^-\pi^+$ and $D^+ \to K^-\pi^+\pi^+$ decay modes have a large signal yield. Thus, they are sensitive to small variations in the data acquisition. In the $D^+ \to K^-\pi^+\pi^+$ sample there are significant variations between data taking periods for a given magnet polarity. These variation are highly reduced after taking the average of the raw asymmetry of the magnet up and magnet down sample. In the $D^0 \to K^-\pi^+$ sample a constant shift between the magnet up and the magnet down sample is seen in 2012. The polarity averaged values of 2011 and 2012 are also slightly different. No exceptional outliers are observed in the $D^+ \to \overline{K}^0\pi^+$, the $D^0 \to K^-K^+$ and the $D^0 \to \pi^-\pi^+$ samples, due to their lower statistics.

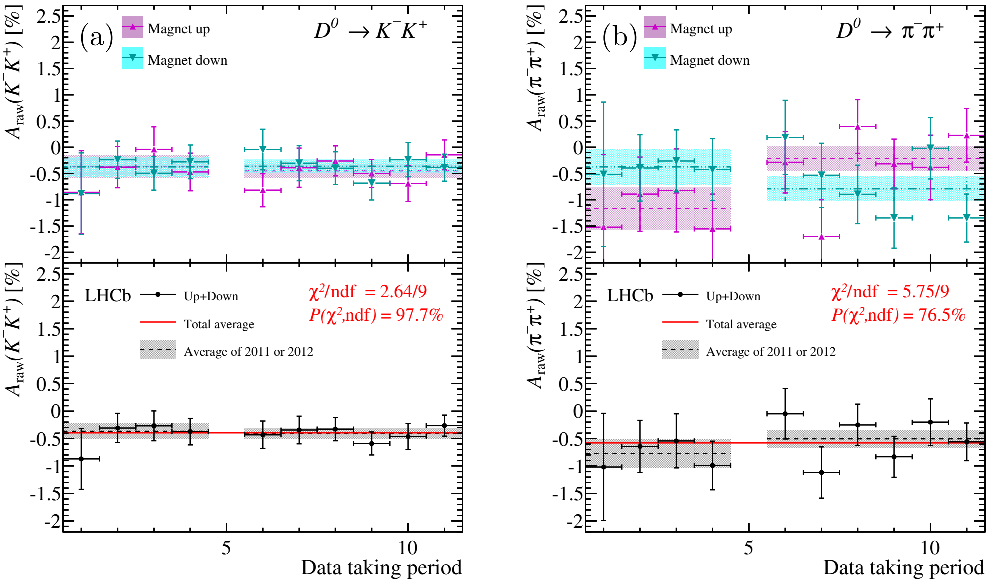

Figure 12.5: (a) $A_{\rm raw}(K^-K^+)$ and (b) $A_{\rm raw}(\pi^-\pi^+)$ of the ΔA_{CP} measurement as a function of the data taking period. The 2011 data are divided into four periods and the 2012 data into six periods. The error bars indicate the statistical uncertainty, the shaded bands show the averages for 2011 and 2012, and the (red) line shows the overall raw asymmetry.

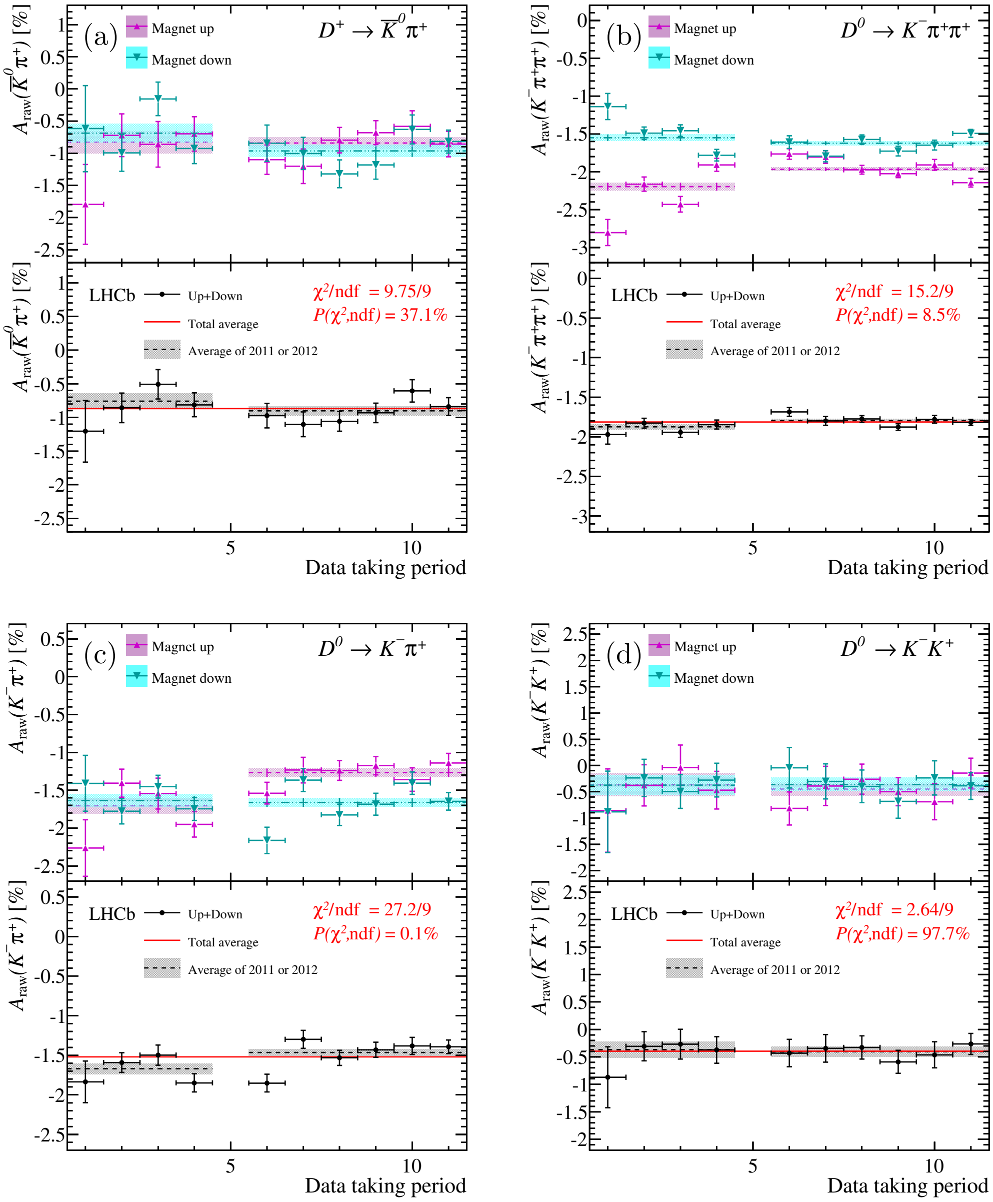

Figure 12.6: (a) $A_{\rm raw}(\overline{K}^0\pi^+)$, (b) $A_{\rm raw}(K^-\pi^+\pi^+)$, (c) $A_{\rm raw}(K^-\pi^+)$ and (d) $A_{\rm raw}(K^-K^+)$ of the $A_{CP}(K^-K^+)$ measurement as a function of the data taking period. The 2011 data are divided into four periods and the 2012 data into six periods. The error bars indicate the statistical uncertainty, the shaded bands show the averages for 2011 and 2012, and the (red) line shows the overall raw asymmetry.

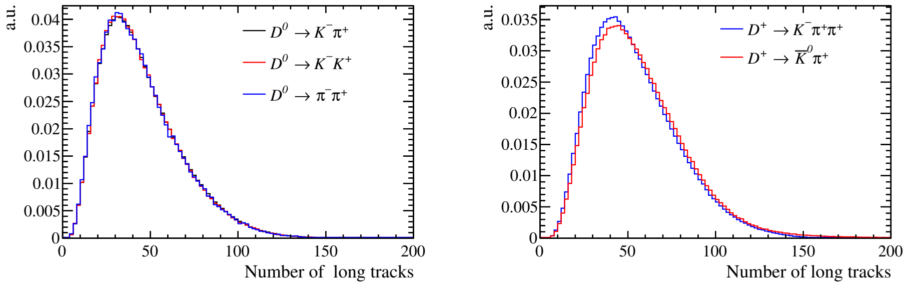

(a) Muon-tagged D^0 samples (b) Prompt D^+ samples

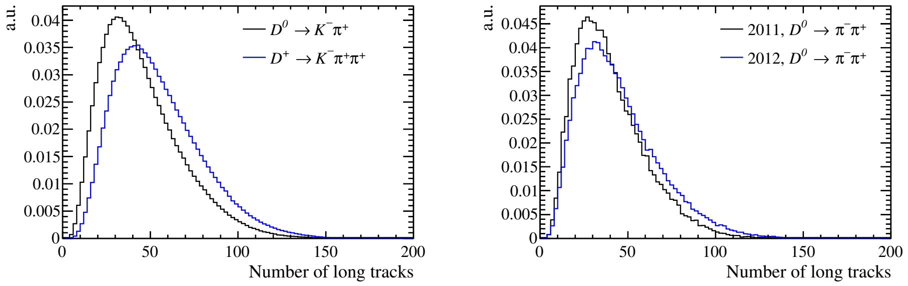

(c) Comparison of prompt and muon-tagged decays. (d) Comparison of 2011 and 2012 data.

Figure 12.7: The long track multiplicity distributions of the 2012 data set.

12.4 Track multiplicities

Tracking and particle identification efficiencies depend on the number of charged particles in an event (track multiplicity). This is shown in Figure 4.9 for the particle identification efficiency and given in Reference [55] for the track reconstruction efficiency. Generally, both efficiencies decrease with an increasing number of charged particles as events become more complex. As this change in efficiency might affect detection asymmetries, it is checked if the observed asymmetries depend on the track multiplicity.

Figure 12.7 shows the distribution of the number of reconstructed long tracks, cf. Chapter 4.3, for several decay channels. The samples of muon-tagged $D^0 \to K^-\pi^+$, $D^0 \to K^-K^+$ and $D^0 \to \pi^-\pi^+$ candidates have the same track multiplicity. The same holds for the two prompt decay modes $D^+ \to \overline{K}^0\pi^+$ and $D^+ \to K^-\pi^+\pi^+$. However, the track multiplicities of prompt D^+ and muon-tagged D^0 samples differ. The reasons are tighter cuts on the momentum in the selections of the prompt modes which select events where the initial partons have a higher energy. Additionally, the track multiplicity increased from 2011 to 2012 due to the higher centre-of-mass energy.

The dependence of the raw asymmetry on the number of long tracks is shown in Figure 12.8 for the $D^+ \to K^-\pi^+\pi^+$, $D^+ \to \overline{K}^0\pi^+$ and $D^0 \to K^-\pi^+$ samples and in Figure 12.9 for the $D^0 \to K^-K^+$ and $D^0 \to \pi^-\pi^+$ samples. The p-value for being flat is quoted. As no dependencies are observed, no residual asymmetries are expected in the $A_{CP}(K^-K^+)$ or ΔA_{CP} measurements.

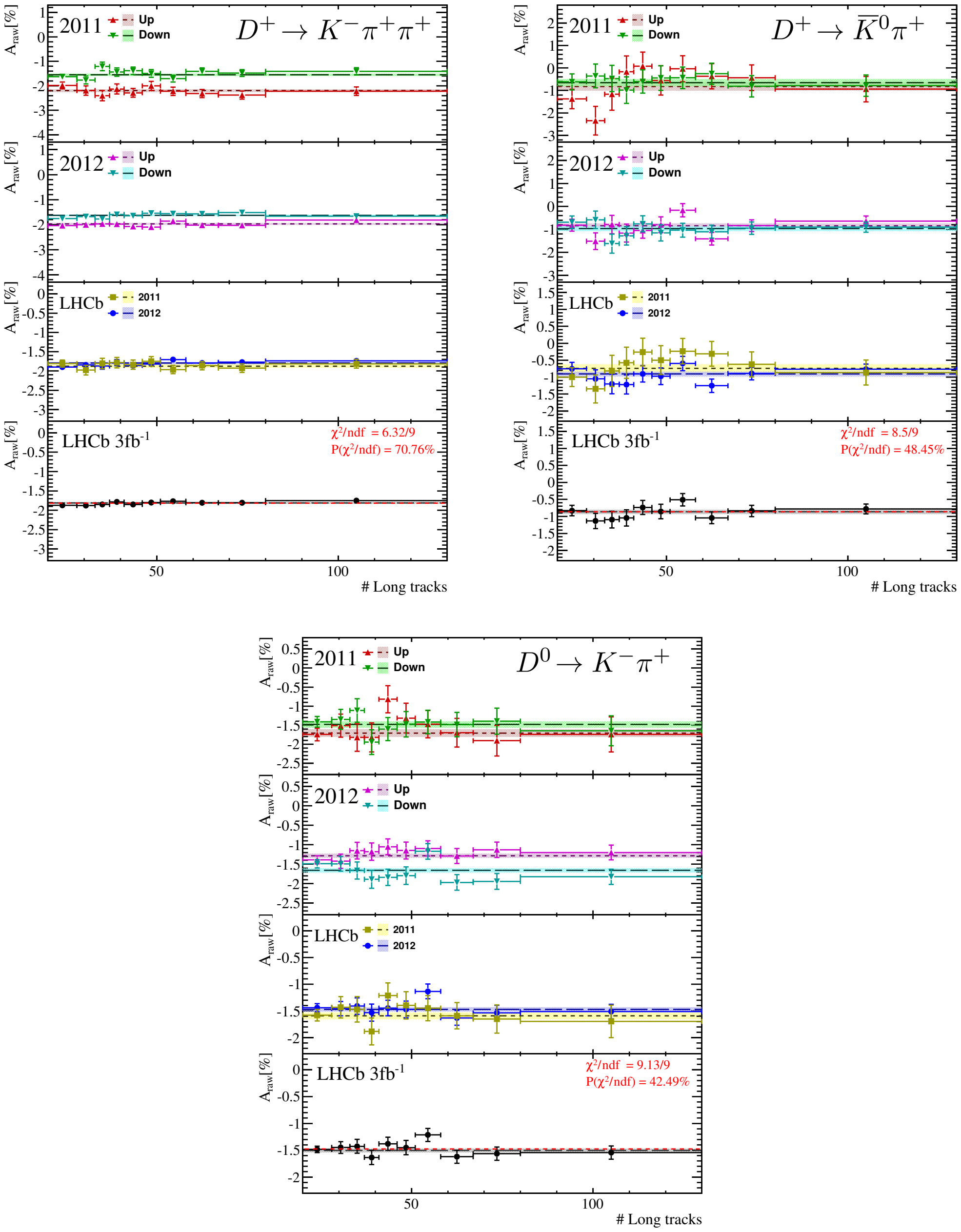

Figure 12.8: The raw asymmetry of $D^+ \to K^-\pi^+\pi^+$, $D^+ \to \overline{K}^0\pi^+$ and $D^0 \to K^-K^+$ candidates as function of the number of long tracks per event. The shaded lines indicate the result of the asymmetry fit to the total distribution. The default combination of the data sets is done.

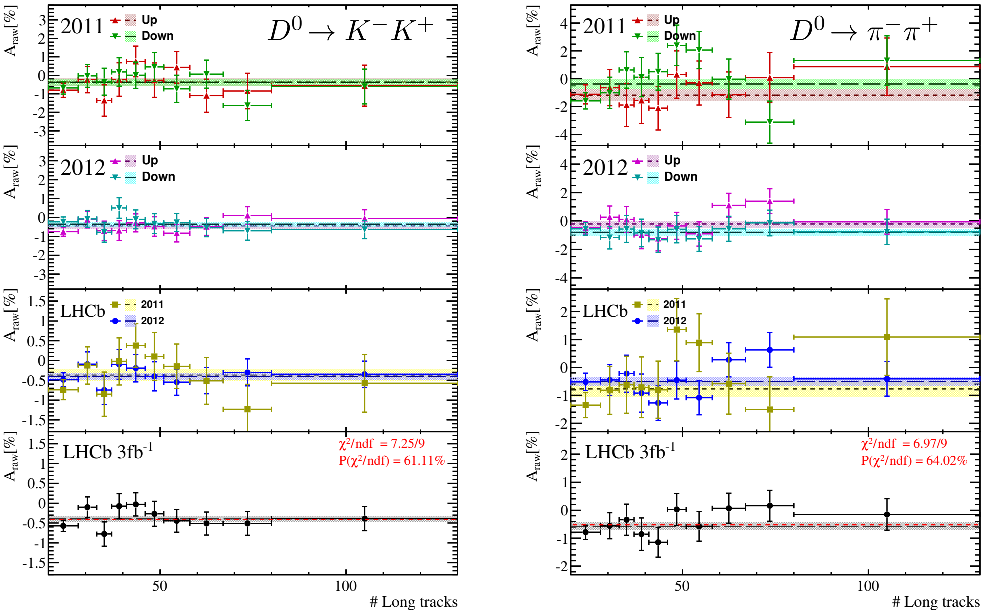

Figure 12.9: The raw asymmetry of $D^0 \to K^- K^+$ and $D^0 \to \pi^- \pi^+$ candidates as function of the number of long tracks per event. The shaded lines indicate the result of the asymmetry fit to the total distribution. The default combination of the data sets is done.

12.5 Cross-checks of ΔA_{CP}

The analysis is based on the assumption that production and detection asymmetries cancel in the difference of two raw asymmetries. As both depend on the kinematics of the involved particles, the cancellation is ensured by the kinematic weighting procedure. However, the raw asymmetries might also depend on other parameters of the reconstructed and selected events. One example has already been discussed in Chapter 12.4. There, it is checked if the asymmetry depends on the track multiplicity which affects track reconstruction and particle identification efficiencies.

In this section, the raw asymmetries of muon-tagged decays and the ΔA_{CP} measurement are tested for consistency against parameters of the selected candidates. Therefore, the raw asymmetries of the $D^0 \to K^- K^+$ and $D^0 \to \pi^- \pi^+$ samples are determined in bins of several quantities. The selected quantities are discussed shortly after. Typically ten bins with approximately equal amounts of candidates are used. The difference of $A_{\text{raw}}(K^- K^+)$ and $A_{\text{raw}}(\pi^- \pi^+)$ in each bin defines ΔA_{CP} for the given bin. The kinematic weighting has little effect on the ΔA_{CP} measurement, cf. Chapter 12.1. It is not applied here in order to not introduce additional statistical fluctuations.

The tests include, among others, the kinematic variables of D^0 and muon candidates, and selection quantities that are correlated to the kinematics, e.g. the flight distance of B candidates. Hence, the raw asymmetries might be significantly different from bin to bin. The measured ΔA_{CP} should still be the same in each bin. A possible problem with physical background sources is independent of the data taking period and magnet polarity, while detection effects could be different for both magnet polarities or data taking periods. Thus, ΔA_{CP} is measured for the 2011 and 2012 samples, separately for both magnet polarities. The default combination of the raw asymmetries and, therefore, ΔA_{CP} is used, cf. Chapter 11.1. Then, a constant is fitted to each distribution of ΔA_{CP}. The p-value of this fit is used as a measure for the hypothesis that ΔA_{CP} does not depend on the selected quantity.

In this section only the corresponding distributions of ΔA_{CP} are given. The raw asymmetry distributions of $D^0 \to K^- K^+$ and $D^0 \to \pi^- \pi^+$ decays are given in Appendix D.1. Additionally, the raw asymmetries of the $D^0 \to K^- \pi^+$ sample are presented to study the behaviour with a decay mode that has a large signal yield. The raw asymmetry of $D^0 \to K^- \pi^+$ decays has a significant contribution from the momentum-dependent charged kaon asymmetry. The tests cannot be performed so easily for the $A_{CP}(K^- K^+)$ measurement for two reasons. First, the prompt and the muon-tagged samples have different kinematic distributions which would require a full weighting procedure for each bin. Second, there is no one-to-one correspondence between prompt D^+ and muon-tagged D^0 candidates for each selection criteria.

The p-value of every presented consistency check is collected and filled into a histogram, see Figure 12.10. In the limit of infinite uncorrelated tests a flat distribution between zero and one is expected. The following consistency checks are performed:

- **Kinematics of muon and D^0 candidates**: These variables test the basic assumption that the method should be independent of the kinematic distributions. The raw asymmetries in bins of some kinematic variables of the D^0 and muon candidates have already been shown in Chapter 7.4. The observed ΔA_{CP} as function of D^0 p, p_{T}, η and ϕ is presented in Figure 12.11. The corresponding plots for the kinematics of the muon candidates are shown in Figure 12.12. None of the tests shows exceptional outliers. The p-value of the muon ϕ test is 5 %, all others are larger than 40 %.

Binning in the azimuthal angle ϕ of the muon candidate is an interesting test. As seen in Figures 7.21b and 7.20b, the raw asymmetry is larger than 10 % in some ranges if the measurement is restricted to one magnet polarity. These asymmetries are understood and induced by the detector geometry as particles with a given charge are preferentially detected in the left or the right side of the detector. Figure 12.12d shows that ΔA_{CP} is the same in every bin and for every magnet polarity. The arithmetic mean of the asymmetries of the two polarities is not needed to cancel the muon detection asymmetry.

- **Distance between muon and $\boldsymbol{D^0}$ decay products**: The independence of the reconstruction of the muon and the D^0 meson's decay products is tested with the quantity ΔR which is defined as

$$\Delta R = \min_h \left(\sqrt{(\eta_\mu - \eta_h)^2 + (\phi_\mu - \phi_h)^2} \right) \quad , \tag{12.2}$$

where the minimum of both D^0 decay products, h^+ and h^-, is taken. This quantity is a measure of the minimum distance between the muon and the two hadrons. If ΔR is small, the muon and one of the hadrons are close in phase space. Thus, their detection and track reconstruction in the VELO or the particle identification in RICH1 could interfere with each other. For large values of ΔR this cannot happen. The distribution of ΔA_{CP} as a function of ΔR is shown in Figure 12.13a. No structures are observed for small or large ΔR.

- **Reconstructed $\boldsymbol{B}$ mass**: The possibility that physical backgrounds affect the measurement is checked with a binning in the reconstructed B mass. The B mass is determined by the sum of the four-momenta of the D^0 and the muon candidate. As at least the neutrino is missing, the B mass is not fully reconstructed, see Figure 6.7. A background contribution from prompt D^0 mesons is expected at the lower edge of the spectrum, whereas B mesons or Λ_b baryons contribute to the background in the high-mass region. The determined ΔA_{CP} per bin is shown in Figure 12.13b. There are no significant variations.

- **Impact parameter of $\boldsymbol{D^0}$ and muon candidates**: The impact parameters to the primary vertex of the D^0 and the muon candidate are other selection quantities which distinguish between prompt and secondary decays. In Figure 12.13c and 12.13d ΔA_{CP} is shown as function of the impact parameter of D^0 and muon candidates, respectively. There is a hint of a trend in Figure 12.13c. However, it is not significant. Furthermore, the 2011 and 2012, magnet up and magnet down samples do not have consistent trends. Thus, it is attributed to statistical fluctuations. The corresponding plots of the raw asymmetries are given in Figure D.3. The ΔA_{CP} values in bins of the muon impact parameter show no trend at all.

- **$\boldsymbol{B}$ flight distance**: The flight distance of the B candidate is defined as the distance between the primary vertex and the reconstructed B decay vertex. Prompt background contributions are more likely to have a small distance. No anomalies are seen in Figure 12.14a.

- ***B* vertex quality**: The main handle on the genuineness of a semileptonic B decay is the quality of the fitted μ–D^0 vertex. The DTF $\chi^2_{\text{vertex}}/\text{ndf}$ is used as as quality criterion, cf. Chapter 6.3.1. A large value increases the probability of a random combination of a D^0 and muon candidate. This affects the mistag probability which has an influence on the asymmetry determination, cf. Chapter 10. The measured ΔA_{CP} values show no trend in Figure 12.14b.

- **D^0 decay time**: The reconstructed D^0 decay time is a good discriminator between multi-body B decays, like $B \to J/\psi X$ decays, and B decays with a D meson in the final state. Most of the background that is not peaking in the D^0 mass distribution is at low reconstructed decay times. Therefore, a test is performed to include events with a reconstructed decay time that is smaller than zero. The result of ΔA_{CP} changes by 0.01%. The two disjoint samples with positive and negative decay times are also fully compatible.[3]

- **Number of PVs per event**: The muon, hadron, B and D^0 candidates are selected by impact parameter cuts and pointing requirements to the primary vertex. If the number of primary vertices is larger than one, the origin vertex of the B meson can be misidentified. The larger the number of primary collisions the more likely is a wrongly-associated primary vertex. No effect on the asymmetry is expected due to this effect.[4] This hypothesis is supported by Figure 12.14c as no dependence is observed in the measured ΔA_{CP} values. The same holds for the raw asymmetries of $D^0 \to K^-\pi^+$, $D^0 \to K^-K^+$ and $D^0 \to \pi^-\pi^+$ candidates, see Figure D.6. The particle multiplicity of the total event also increases with the number of collisions. The effect of an increased particle multiplicity has already been discussed in Chapter 12.4.

- **Particle identification**: In Chapter 4.4 the basic principle of the particle identification algorithm is explained. One important aspect is that the algorithm uses the full event information. There is the potential danger that particles originating from the B decay vertex interfere with the particle identification of the D^0 decay products. The charge of the not reconstructed particles might be flavour specific and, thus, affect the raw asymmetry. For example, the charged pion of a D^{*+} resonance tags the flavour of the D^0 meson, cf. Chapter 10.2. To test this effect, the raw asymmetry of $D^0 \to K^-K^+$ and $D^0 \to \pi^-\pi^+$ candidates is determined in bins of the particle identification variable $\text{DLL}_{K\pi}$. No dependence is observed in the corresponding distributions in Figure 12.15.

---

[3] To date, no plot is shown here, as this would unblind an on-going time-dependent analysis.

[4] "There are known knowns ... But there are also unknown unknowns", Donald Rumsfeld.

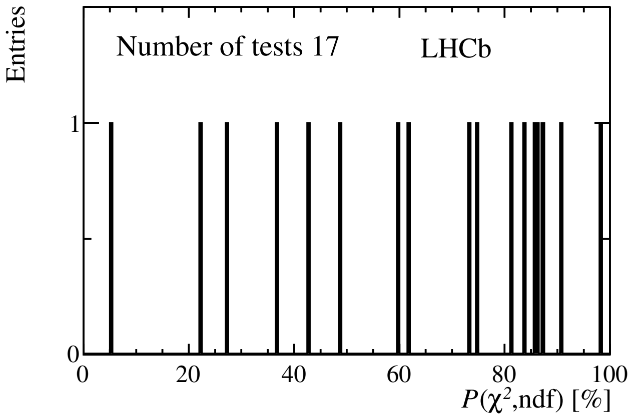

Figure 12.10: The p-value distribution of the ΔA_{CP} consistency checks. The mean of the histogram is $(63.6 \pm 6.5)\,\%$.

As mentioned before, the collected p-values are given in Figure 12.10. It should be noted that not all tests performed in this chapter are fully uncorrelated. The p-values are evenly distributed with a mean of $(62.6 \pm 6.5)\,\%$. This confirms the consistency and stability of the ΔA_{CP} measurement.

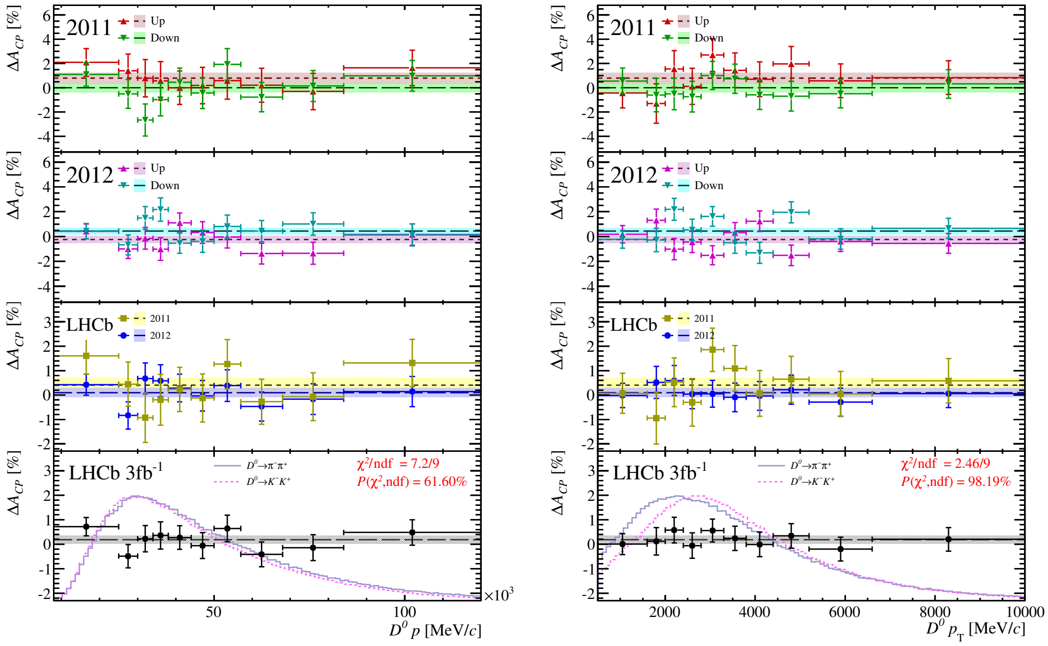

(a) D^0 p (b) D^0 p_{T}

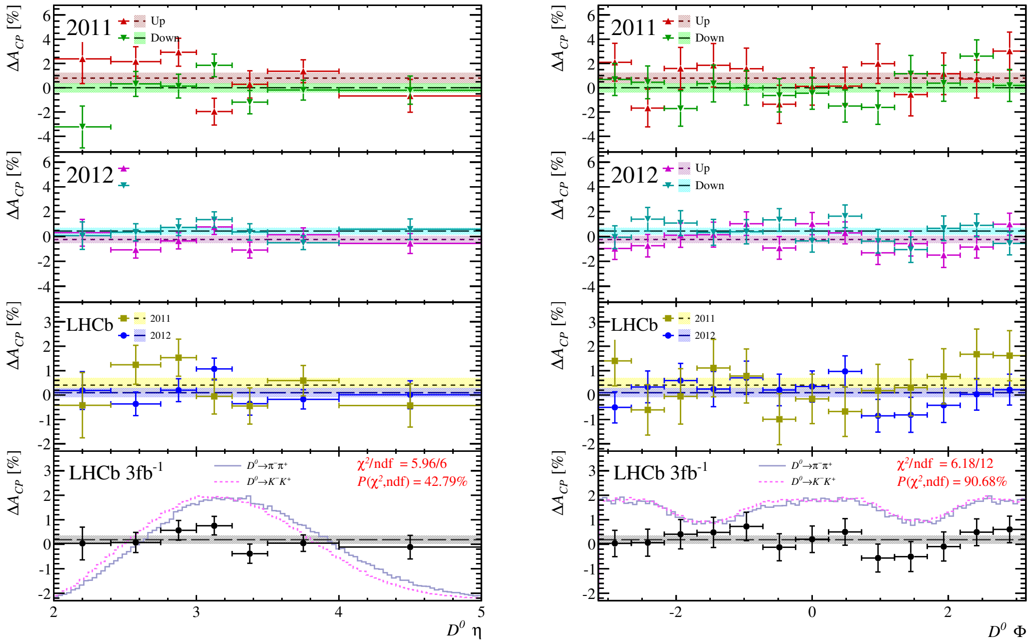

(c) D^0 η (d) D^0 ϕ

Figure 12.11: ΔA_{CP} as function of D^0 p, p_{T}, η and ϕ. The analysis is done independently for 2011 and 2012, magnet up and magnet down data sets. The default combination of the data sets is used. The p-value for the hypothesis of no dependence is quoted. The (solid) and (dashed) line in the bottom graphs show the distributions of the given quantity for $D^0 \to \pi^- \pi^+$ and $D^0 \to K^- K^+$ candidates, respectively.

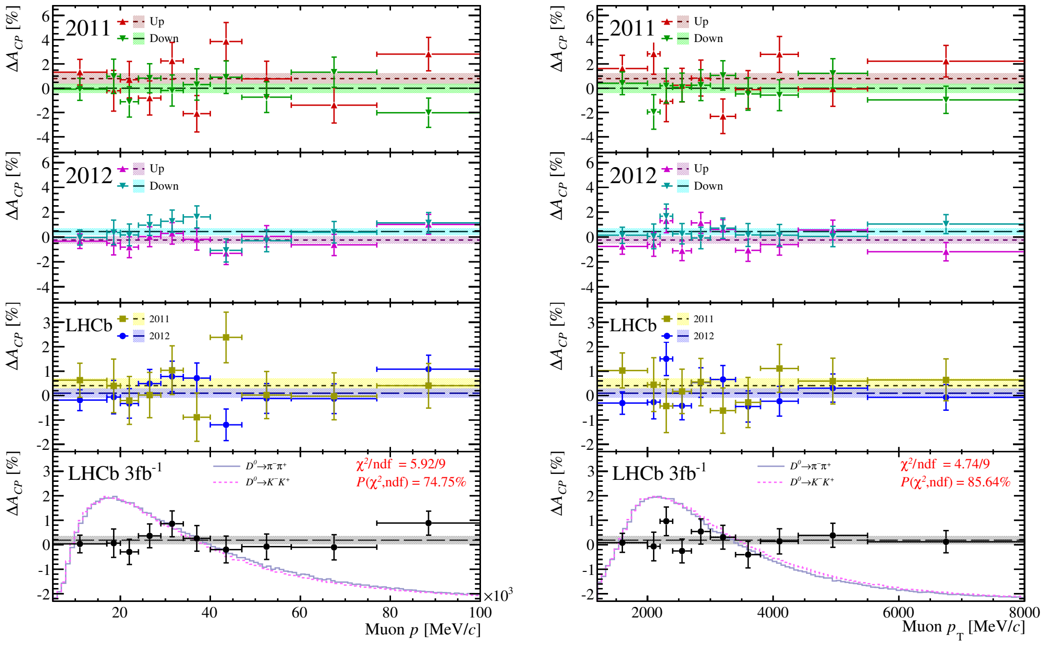

(a) D^0 p (b) D^0 p_{T}

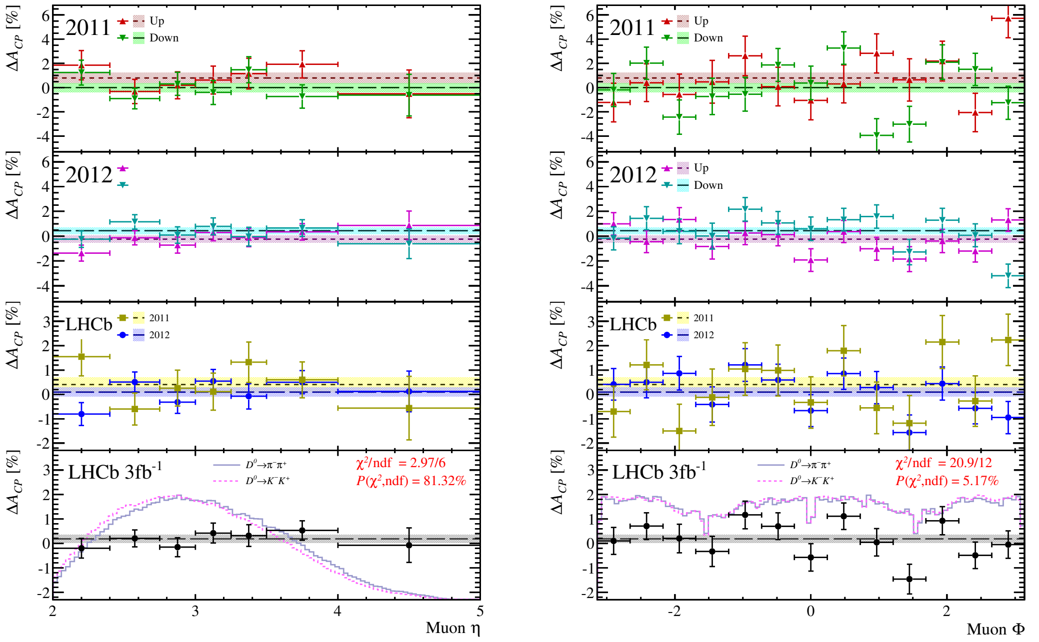

(c) D^0 η (d) D^0 ϕ

Figure 12.12: ΔA_{CP} as function of muon p, p_{T}, η and ϕ. The analysis is done independently for 2011 and 2012, magnet up and magnet down data sets. The default combination of the data sets is used. The p-value for the hypothesis of no dependence is quoted. The (solid) and (dashed) line in the bottom graphs show the distributions of the given quantity for $D^0 \to \pi^-\pi^+$ and $D^0 \to K^-K^+$ candidates, respectively.

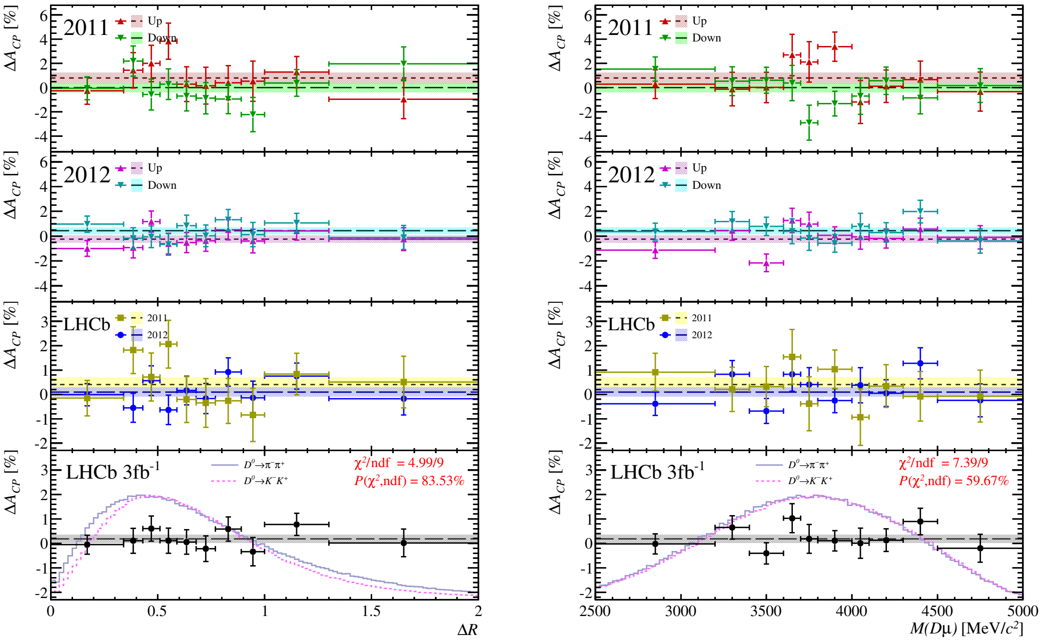

(a) ΔR (b) $M(D\mu)$

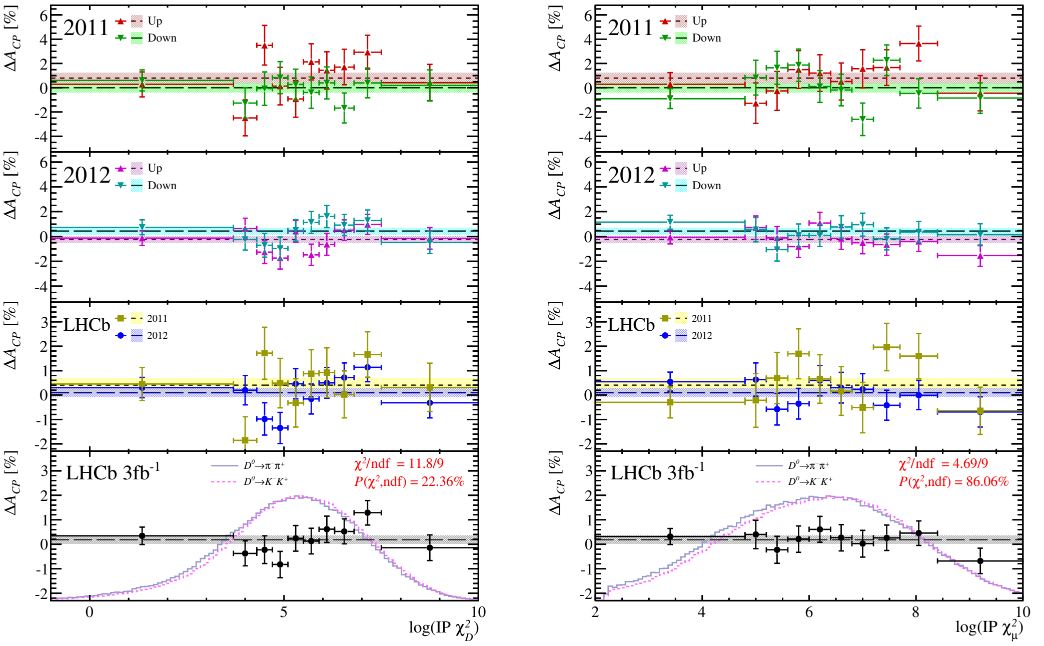

(c) D^0 χ^2(IP) (d) Muon χ^2(IP)

Figure 12.13: ΔA_{CP} as function of ΔR, $M(D\mu)$, D^0 χ^2(IP) and muon χ^2(IP). The analysis is done independently for 2011 and 2012, magnet up and magnet down data sets. The default combination of the data sets is used. The p-value for the hypothesis of no dependence is quoted. The (solid) and (dashed) line in the bottom graphs show the distributions of the given quantity for $D^0 \to \pi^-\pi^+$ and $D^0 \to K^-K^+$ candidates, respectively.

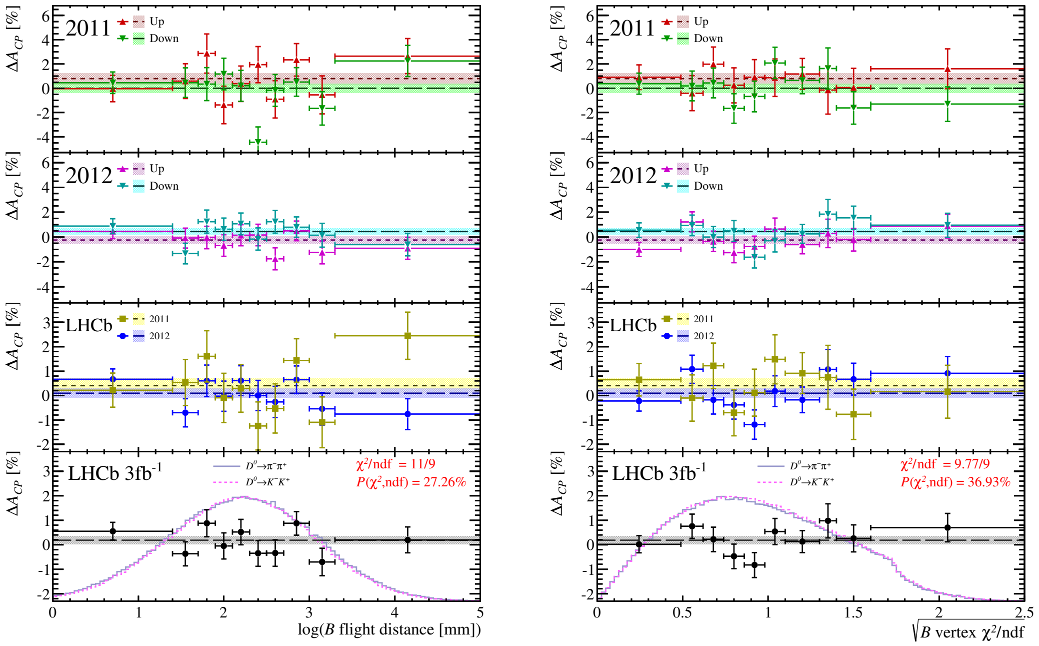

(a) B flight distance (b) B DTF χ^2_{vertex}/ndf

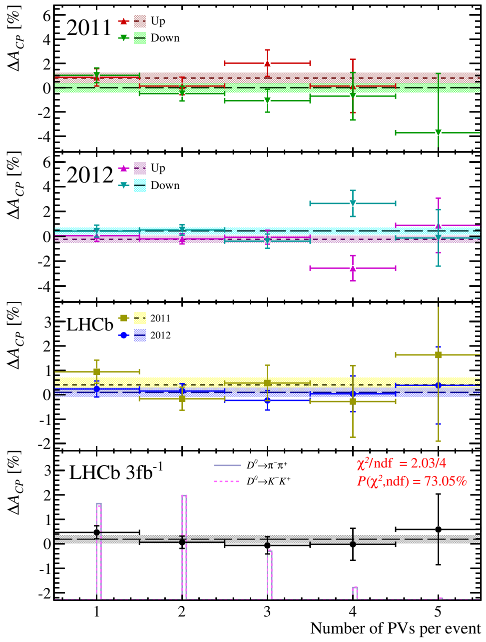

(c) Number of PVs per event

Figure 12.14: ΔA_{CP} as function of B flight distance, B DTF χ^2_{vertex}/ndf and number of PVs per event. The analysis is done independently for 2011 and 2012, magnet up and magnet down data sets. The default combination of the data sets is used. The p-value for the hypothesis of no dependence is quoted. The (solid) and (dashed) line in the bottom graphs show the distributions of the given quantity for $D^0 \to \pi^-\pi^+$ and $D^0 \to K^-K^+$ candidates, respectively.

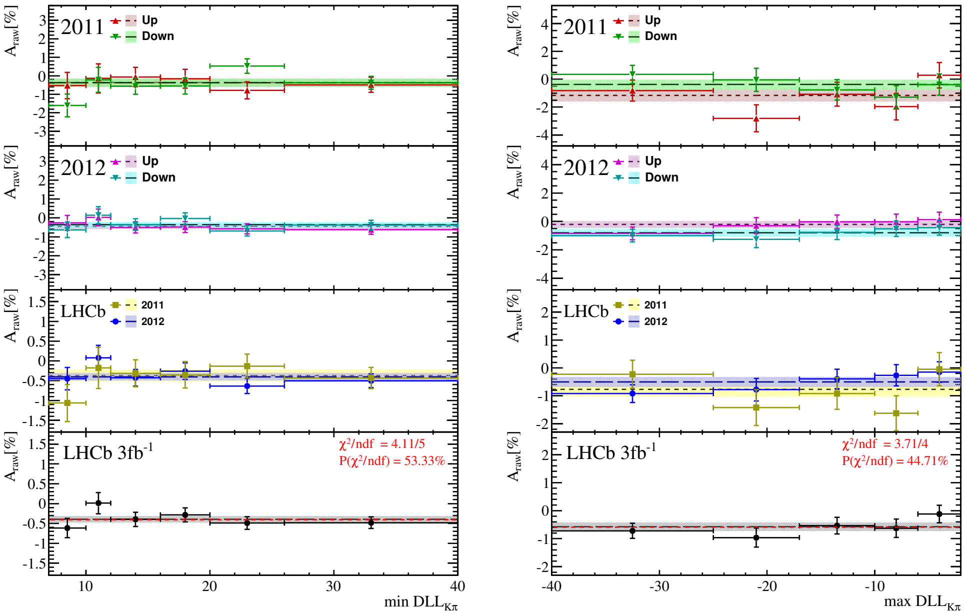

(a) $D^0 \to K^-K^+$ (b) $D^0 \to \pi^-\pi^+$

Figure 12.15: The raw asymmetry as function of the (a) minimum or (b) maximum $\mathrm{DLL}_{K\pi}$ of the D^0 decay products in $D^0 \to K^-K^+$ and $D^0 \to \pi^-\pi^+$ decays, respectively. The shaded lines indicate the result of the asymmetry fit to the total distribution. The default combination of the data sets is done.

12.6 Summary

The consistency of the $A_{CP}(K^-K^+)$ and ΔA_{CP} measurements is tested in this section:

- The kinematic weighting increases the statistical uncertainties of the raw asymmetry determinations. The applied corrections due to momentum-dependent asymmetries are of the order of the statistical uncertainty.
- The charged kaon detection asymmetry and the estimate of the B production asymmetry are within expectations.
- The measurements of $A_{CP}(K^-K^+)$ and ΔA_{CP} show no variations in different data taking periods. Furthermore, the raw asymmetries of prompt D^+ decays and muon-tagged D^0 decays are stable against event parameters like the track multiplicity.
- Several tests are performed to examine the consistency of ΔA_{CP} in bins of kinematic variables of D^0 and muon candidates, and several other selection variables. No deviations are observed.

Chapter 13

Systematic uncertainties

In this chapter the strategy to extract the *CP* asymmetries is systematically studied. First, the systematic uncertainties that are connected to the correct extraction of raw asymmetries are discussed. Second, the assumption that production and detection asymmetries cancel in the difference of raw asymmetries is investigated. This includes studies of the kinematic weighting. Third, the systematic uncertainties from the mistag probability and the neutral kaon asymmetry are shortly summarised.

In the following, systematic uncertainties below 0.005 % are considered as negligible given the statistical uncertainties of 0.15 % and 0.16 % for the $A_{CP}(K^-K^+)$ and ΔA_{CP} measurements, respectively.

13.1 Extraction of raw asymmetries

The raw asymmetries are determined with binned maximum-likelihood fits to the invariant mass distributions of D candidates. In Chapter 7.3 the fit model is introduced. This particular fit model is one possible choice[1] which has to be systematically studied. The studies consist of varying the default fit model and performing pseudo-experiments which test the background model. The correct uncertainty coverage of the binned maximum-likelihood fit has already been shown in Chapter 8.2.2.

13.1.1 Variations of fit model

The default signal models consist of a simultaneous PDF for positively- and negatively-tagged candidates which have the raw asymmetry A_{raw} as one fit parameter. The default models are the sum of a Crystal-Ball and a Gaussian function. In the Cabibbo-favoured decay modes, two additional parameters describe differences in the mean masses and resolutions of candidates with different tags. The background contributions are modelled with independent exponential functions for each tag and overall asymmetry parameters. The reflection background in the $D^0 \to \pi^-\pi^+$ sample is described by an additional Gaussian function and one asymmetry parameter.

The results of all tests are shown for the Cabibbo-suppressed and Cabibbo-favoured decay modes in Tables 13.1 and 13.2, respectively. The individual tests are discussed in the following. No kinematic weighting is applied to keep maximal statistical sensitivity.

---

[1] In this analysis it is not feasible to take the fit model from simulated events as there are no simulated samples with comparable signal and background yields. Furthermore, the simulation would need to be accurate to the sub per-mille level.

Table 13.1: Summary table of the fit model variations of the Cabibbo-suppressed decay modes. The raw asymmetry of the full data set is given (in %). No kinematic weighting is applied. The maximum difference to the default value is highlighted in red.

Test	$A_{\text{raw}}(K^-K^+)$	$A_{\text{raw}}(\pi^-\pi^+)$
Default, cf. Chapter 7.3	-0.394 ± 0.076	-0.58 ± 0.14
One Gaussian as signal PDF	-0.389 ± 0.076	-0.59 ± 0.14
Double Gaussian as signal PDF	-0.395 ± 0.076	-0.57 ± 0.14
Johnson S_U distribution plus Gaussian as signal PDF	-0.394 ± 0.076	-0.57 ± 0.14
2nd order polynomial as background description	-0.385 ± 0.082	-0.63 ± 0.15
Johnson S_U distribution plus Gaussian as signal PDF and 2nd order polynomial as background description	-0.385 ± 0.082	-0.64 ± 0.15
A_{ref} fixed to $(-1.5\,\%)$ in $D^0 \to \pi^-\pi^+$	-	-0.62 ± 0.14
Fit range decreased $(-5\,\text{MeV}/c^2)$	-0.402 ± 0.076	-0.60 ± 0.14
Fit range increased $(+5\,\text{MeV}/c^2)$	-0.408 ± 0.076	-0.59 ± 0.14
150 mass bins	-0.397 ± 0.076	-0.57 ± 0.14
Maximum difference	0.013	0.058

The largest differences to the default fits are taken as systematic uncertainties for each decay channel.

The following variations of *the signal PDFs* are used to test the stability of the extracted raw asymmetries:

- One Gaussian function to describe the signal peak is tested as an extreme case. This is the simplest possible model but it does not completely describe the invariant mass distribution.
- A symmetric double Gaussian function is used to test the influence of the asymmetric tail of the signal peak.
- An alternative description of the asymmetric tail is tested. Therefore, the sum of a Johnson S_U distribution and a Gaussian is used as signal PDF. The definition of the Johnson S_U distribution is given in Appendix B.3. It is similar to a Gaussian but has two parameters to describe asymmetric tails.

Variations that are significantly smaller than the statistical uncertainty are observed, see Tables 13.2 and 13.1. This is expected as the fitted asymmetry is largely uncorrelated to the signal shape parameters, as discussed in Chapter 7.3.1. Furthermore, the asymmetry per mass bin is well described by the default PDF, even in the decay modes with very large signal yields. It has been tested that adding further Gaussians to the signal PDF does not change the result. The fits to the invariant mass distributions improve but the projected asymmetry per mass bin has similar fit quality.

The next two tests are only performed for the Cabibbo-favoured decay modes. As the final states are no *CP* eigenstates, the signal peaks can be different for positively- and negatively-tagged candidates. As mentioned, this is accounted for in the default

Table 13.2: Summary table of the fit model variations of the Cabibbo-favoured decay modes. The raw asymmetry of the full data set is given (in %). No kinematic weighting is applied. The maximum difference to the default value is highlighted in red.

Test	$A_{\mathrm{raw}}(\overline{K}^0\pi^+)$	$A_{\mathrm{raw}}(K^-\pi^+\pi^+)$	$A_{\mathrm{raw}}(K^-\pi^+)$
Default, cf. Chapter 7.3	-0.868 ± 0.055	-1.813 ± 0.016	-1.519 ± 0.035
One Gaussian as signal PDF	-0.887 ± 0.056	-1.823 ± 0.016	-1.525 ± 0.035
Double Gaussian as signal PDF	-0.867 ± 0.055	-1.810 ± 0.016	-1.518 ± 0.035
Johnson S_U distribution plus Gaussian as signal PDF	-0.866 ± 0.055	-1.810 ± 0.016	-1.516 ± 0.035
Two independent Double Gaussians for both tags as signal PDF	-0.828 ± 0.059	-1.800 ± 0.017	-1.517 ± 0.036
No resolution difference for both tags ($s_p = 1$)	-0.884 ± 0.054	-1.827 ± 0.016	-1.532 ± 0.035
2nd order polynomial as background description	-0.915 ± 0.062	-1.836 ± 0.017	-1.537 ± 0.038
Johnson S_U distribution plus Gaussian as signal PDF and 2nd order polynomial as background description	-0.914 ± 0.063	-1.830 ± 0.018	-1.532 ± 0.039
Fit range decreased ($-5\,\mathrm{MeV}/c^2$)	-0.873 ± 0.055	-1.816 ± 0.016	-1.520 ± 0.035
Fit range increased ($+5\,\mathrm{MeV}/c^2$)	-0.871 ± 0.055	-1.811 ± 0.016	-1.522 ± 0.035
150 mass bins	-0.866 ± 0.055	-1.812 ± 0.016	-1.519 ± 0.035
Maximum difference	0.047	0.023	0.018

fit models. To test if the descriptions are sufficient, the invariant mass distributions of both tags are fitted with independent double Gaussians functions. The determined raw asymmetries in the $D^+ \to \overline{K}^0\pi^+$ and $D^+ \to K^-\pi^+\pi^+$ samples change by almost their statistical uncertainties. However, the statistical uncertainties increase as more parameters are fitted. Fixing the resolutions of both tag categories to be the same has a small effect.

The background models are varied by using second-order polynomials instead of exponential functions. This is done together with the default signal model and one different signal model. The variation of the background shape introduces the largest shifts in the fitted raw asymmetries. In the $D^+ \to K^-\pi^+\pi^+$ decay mode the change is 50 % larger than the statistical uncertainty. In $D^+ \to \overline{K}^0\pi^+$ it is 85 % of the statistical uncertainty. In the muon-tagged modes the changes are smaller although they are the largest observed for $D^0 \to K^-\pi^+$ and $D^0 \to \pi^-\pi^+$ candidates. The size of the variations is also reflected in the fact that the largest correlation of the fitted A_{raw} are with the background asymmetries.

The PDF of the $D^0 \to \pi^-\pi^+$ decay mode has an additional component due to the contribution from *reflection background*. The asymmetry of the reflection background is a free parameter in the fit. It should be similar to the observed asymmetry in the $D^0 \to K^-\pi^+$ sample. Thus, the reflection asymmetry is constrained to $(-1.5\,\%)$ in the fit. The observed variation is smaller compared to changing the combinatorial background description.

The next test varies the *mass windows* of the fitted invariant mass distributions. The fit ranges are decreased and increased by $5\,\mathrm{MeV}/c^2$ for every decay mode, except the $D^0 \to \pi^-\pi^+$ decay mode. In the $D^0 \to \pi^-\pi^+$ sample the fit range is only increased at the lower edge from $1795\,\mathrm{MeV}/c^2$ to $1790\,\mathrm{MeV}/c^2$. The selection does not allow to extend the fit range at the upper edge. When decreasing the fit range, the range is changed to $[1820\,\mathrm{MeV}/c^2, 1935\,\mathrm{MeV}/c^2]$ to exclude any contribution from reflection. In this case, the fraction of the reflection contribution is constrained to zero. All decay modes show little variations. Still, in the $D^0 \to K^-K^+$ sample the largest variation of all tests is observed. The default fit range of the $D^0 \to K^-K^+$ sample is chosen such that partially reconstructed $D \to K^-K^-X$ decays at the lower edge and the reflection contribution from misidentified $D^0 \to K^-\pi^+$ decays at the upper edge are excluded. Nevertheless, the variation is taken as a systematic uncertainty. The last test is a sanity check: The number of bins in the binned likelihood fit is increased from 100 to 150. No variations are seen.

To summarise, the largest variations are observed when changing the background model, the red numbers in Table 13.2 and 13.1 indicate this. The observed differences can be of statistical or systematic nature. The largest differences to the default fit are taken as systematic uncertainties for the extractions of raw asymmetries for each channel. Systematic uncertainties of $0.06\,\%$ are assigned to the ΔA_{CP} and $A_{CP}(K^-K^+)$ measurements, respectively, due to the selected fit model.

13.1.2 Wrong background model

It is shown in Chapter 7.1 that different physical backgrounds contribute to the invariant mass distributions of the Cabibbo-suppressed D^0 decay modes. These background contributions have different shapes and can have different asymmetries. The default background model with independent exponential functions for positively- and negatively-tagged candidates and one overall asymmetry parameter might not be sufficient. The effects of different background parameterisation in the fits have already been tested in the previous section. Here, pseudo-experiments are generated to study a possible bias of the default fit when the background is composed out of several components with different shapes and asymmetries.

From the discussion in Chapter 7.1 it is expected that background events from partially-reconstructed secondary D and Λ_c decays mostly contribute to the invariant mass distribution of reconstructed $D^0 \to K^-K^+$ decays. Only in the case of background for $D^0 \to K^-K^+$ decays the misidentification of one particle increases the reconstructed invariant mass. In the case of background for $D^0 \to \pi^-\pi^+$ decays the reconstructed invariant mass is always below the default mass window.

Three different types of backgrounds are simulated as seen in Figure 13.1: The first is to model the combinatorial background and has similar parameters as seen in data. The second is inspired by partially-reconstructed $D^+ \to K^-\pi^+\pi^+$ decays from B decays. It has an exponential shape which decays faster than the combinatorial background, see Figure 7.3 for comparison. The third has a linear shape which is prompted by the observed mass distribution of partially-reconstructed $\Lambda_c \to pK^-\pi^+$ decays from Λ_b decays, see Figure 7.4.

In each of the 1200 pseudo-experiments two million signal candidates with an

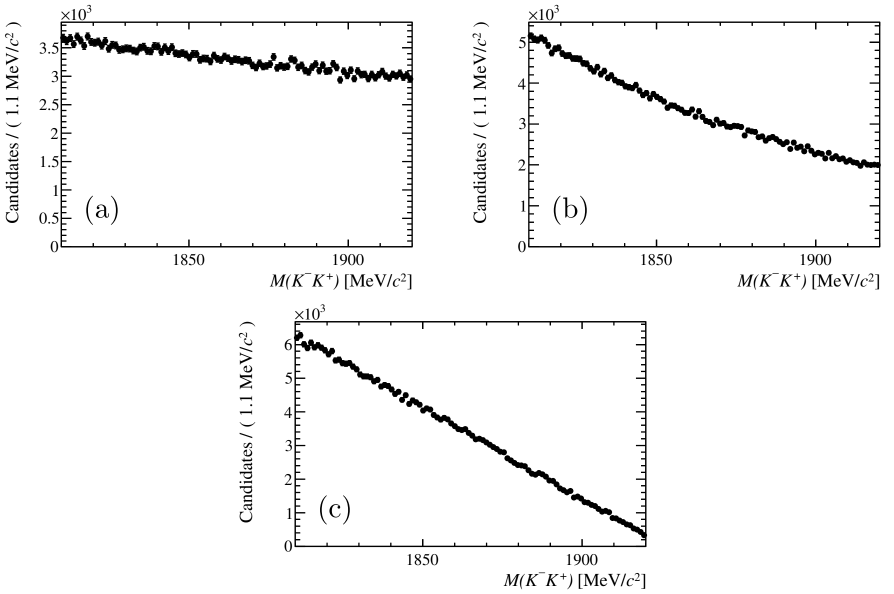

Figure 13.1: The invariant mass distribution of the generated background events. The distribution of (a) is similar to the one observed in data, (b) is inspired by partially-reconstructed $D^+ \to K^-\pi^+\pi^+$ decays and (c) is inspired by partially-reconstructed $\Lambda_c \to pK^-\pi^+$ decays.

asymmetry of ($-1\,\%$) are simulated. The signal-to-background ratio is the same as observed in the raw asymmetry fits to the $D^0 \to K^-K^+$ samples. Equal amounts of the three background contributions are generated. Different scenarios with background asymmetries of up to ($\pm 3\,\%$) are tested. This constitutes an upper limit on the magnitude of any possible effect as such large asymmetries are not observed in data and are also not expected from detection or production asymmetries.

For each pseudo experiment the generated mass distributions of negatively- and positively-tagged candidates are simultaneously fitted with the default PDF given in Chapter 7.3 to extract the raw asymmetry. The largest bias of the fitted raw asymmetries, ($0.027\,\%$), is observed when simulating an asymmetry of ($+3\,\%$) for the Λ_c-like background. One corresponding pseudo-experiment is shown in Figure 13.2. Systematic biases are present in the pull distributions of the invariant mass fits. They are not seen in the fits to data, see Figure 11.1.

Nevertheless, a systematic uncertainty of $0.03\,\%$ corresponding to the observed bias in the pseudo-experiments is assigned as systematic uncertainty to the raw asymmetry determination and is propagated to the ΔA_{CP} and $A_{CP}(K^-K^+)$ measurements. It has been checked that biases are negligible when the signal-to-background ratios of the Cabibbo-favoured D decay modes are simulated.

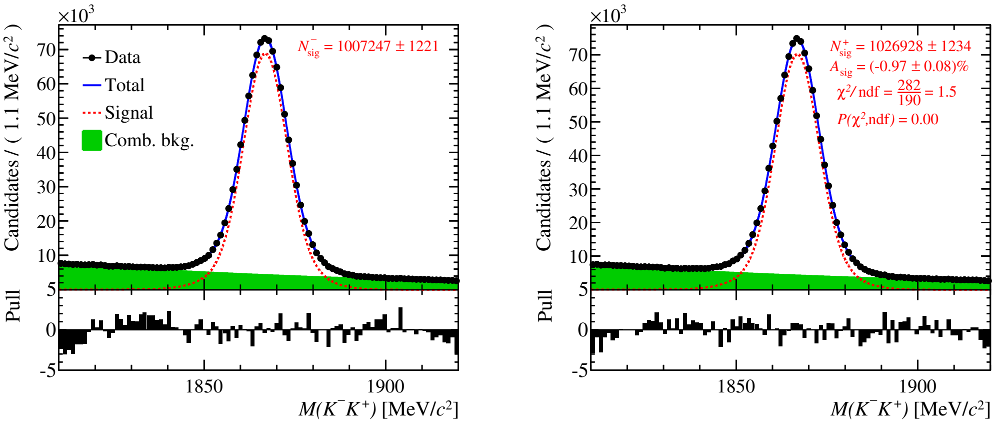

(a) Negatively-tagged candidates (b) Positively-tagged candidates

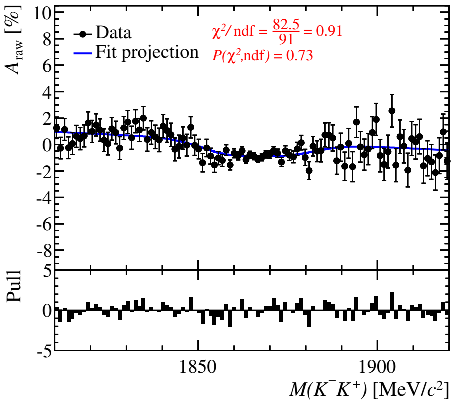

(c) Asymmetry projection

Figure 13.2: (a,b) The invariant mass distributions of one pseudo-experiment. The background shapes which are described in the text are simulated. The default PDF is used in the fit to the invariant mass distributions. The pulls at the lower and at the upper edge of both distributions deviate systematically from zero. (c) The asymmetry projection. No systematic deviations are observed in the pull distribution.

13.1.3 Multiple candidates

The trigger and off-line selection allows to select more than one candidate per event if all candidates pass the trigger and off-line requirements. All $D^+ \to \overline{K}^0\pi^+$ and $D^+ \to K^-\pi^+\pi^+$ candidates are built out of unique sets of tracks and the tag of all candidates is unambiguous. Thus, every candidate is used. In the muon-tagged decays, a D^0 candidate can be tagged twice with two different muon candidates or the same muon candidate is combined with two different D^0 candidates. Both cases create peaking backgrounds. Additionally, using the same D^0 candidate twice leads to an underestimation of the statistical uncertainty.

The fraction of multiple candidates is determined to be below 0.2 % for all muon-tagged decays. Furthermore, no asymmetry larger than 2 % is found in the events with multiple candidates. Possible biases on the raw asymmetry and the statistical uncertainty are negligible.

13.2 Cancellation of production and detection asymmetries

Systematic uncertainties due to the assumption that production and detection asymmetries cancel in the difference of two raw asymmetries are discussed.

13.2.1 Higher-order corrections

The assumption that a raw asymmetry can be written as the sum of its contribution is valid up to the third order in the asymmetries. For example, the raw asymmetry of muon-tagged $D^0 \to K^-K^+$ or $D^0 \to \pi^-\pi^+$ decays is given without approximations in Equation 5.10:

$$A_{\text{raw}}(f) = \frac{A_{CP}(f) + A_P(\overline{B}) + A_D(\mu^-) + A_{CP}(f)A_P(\overline{B})A_D(\mu^-)}{1 + A_P(\overline{B})\,A_{CP}(f) + A_P(\overline{B})\,A_D(\mu^-) + A_{CP}(f)\,A_D(\mu^-)} \ . \tag{13.1}$$

Expanding the expression to third order, yields the result

$$\begin{aligned} A_{\text{raw}}(f) =& A_{CP}(f)+A_P(\overline{B})+A_D(\mu^-)-2A_{CP}(f)\,A_P(\overline{B})\,A_D(\mu^-)-A_{CP}(f)^2\,(A_P(\overline{B})+A_D(\mu^-)) \\ & -A_P(\overline{B})^2\,(A_{CP}+A_D(\mu^-))-A_D(\mu^-)^2\,(A_{CP}(f)+A_P(\overline{B}))+\mathcal{O}(A^5) \ . \end{aligned} \tag{13.2}$$

Since all involved asymmetries are at the per-cent level or below, the correction of A^3 terms is of order 10^{-6}. Similar expressions hold for the raw asymmetries of the other decay modes.

In the ΔA_{CP} measurement two raw asymmetries are involved, in the $A_{CP}(K^-K^+)$ measurement four. The systematic uncertainties due to the higher-order corrections to the raw asymmetries are negligible in both cases.

13.2.2 Effective D^0 production asymmetry

The measurements of ΔA_{CP} and $A_{CP}(K^-K^+)$ assume the same effective production asymmetry of D^0 mesons in semileptonic B decays for the muon-tagged decay modes. The effective D^0 production asymmetry differs from the B production asymmetry due to possible *CP* violation in B decays and B^0 mixing, cf. Chapter 2.6.2. A different fraction of B^0 mesons in the muon-tagged $D^0 \to K^-K^+$, $D^0 \to \pi^-\pi^+$ and $D^0 \to K^-\pi^+$ samples leads to residual asymmetries in the ΔA_{CP} and $A_{CP}(K^-K^+)$ measurements. The fraction of B^0 mesons in semileptonic B decays is calculated to be $f(B^0) = N(B^0)/(N(B^0) + N(B^+)) = (37.5 \pm 2.9)\,\%$, cf. Chapter 2.2.2. It is found in studies with simulated events, see Reference [44], that the reconstruction efficiencies of muon-tagged D^0 decays are slightly different for B^0 and B^+ mesons, and that these relative differences are slightly different for the $D^0 \to K^-K^+$, $D^0 \to \pi^-\pi^+$ and $D^0 \to K^-\pi^+$ samples. The differences of the reconstruction efficiencies change $f(B^0)$ by up to $(0.34 \pm 0.18)\,\%$.

A conservative upper bound of this effect is estimated. According to Equation 2.49, the effective D^0 production asymmetry is given by

$$A_P(D^0 \text{ from } \overline{B}) = f(B^0)\, D\, A_P(\overline{B}^0) + (1 - f(B^0))\, A_P(B^+) \ \ .$$

A total effective D^0 production asymmetry of $(-1\,\%)$ coming only from the B^+ meson contribution is assumed, i.e., $A_P(\overline{B}^0) = 0$ and, hence, $A_P(B^+) = -1.6\,\%$. Assuming further a maximum difference in $f(B^0)$ of 1% between the muon-tagged D^0 samples, the systematic effect is estimated to be $0.016\,\% \approx 0.02\,\%$. This number is propagated as a systematic uncertainty to the $A_{CP}(K^-K^+)$ and ΔA_{CP} measurements.

13.2.3 Interference between B^0 mixing and effective D^0 production asymmetry

The effective D^0 production asymmetry from B^0 mesons is diluted by neutral meson mixing, cf. Chapter 2.6.2. According to Equation 2.48, the dilution factor is calculated to be 0.628. The calculation assumes that the reconstruction efficiency is the same for all B^0 decay times. Together with the dilution of the B^0 production asymmetry, a different decay-time acceptance of $D^0 \to K^-K^+$ and $D^0 \to \pi^-\pi^+$ candidates induces a residual asymmetry in the ΔA_{CP} measurement.

As the B^0 meson is not fully reconstructed in the muon-tagged samples, the decay time cannot be easily determined. The flight distance of the B candidates is used, see Figure 13.3, to estimate differences in the decay-time acceptance. A difference of 5% in the average flight distance of $D^0 \to K^-K^+$ and $D^0 \to \pi^-\pi^+$ candidates is found.

A possible residual asymmetry is evaluated by a simple approach where the decay-time acceptance is modelled by a step function. Using this decay-time acceptance, Equation 2.48 is modified to

$$\mathcal{P}_{\text{osc}} = \frac{\Gamma_d}{2} \int_{t_0}^{\infty} e^{-\Gamma_d t} \left(1 - \cos\left(\Delta m_d t\right)\right) \mathrm{d}t \ \ , \tag{13.3}$$

where t_0 is the minimum reconstructed decay time. From independent studies [83] it is seen that a realistic choice of t_0 is around 1 ps. Two different values are used to model

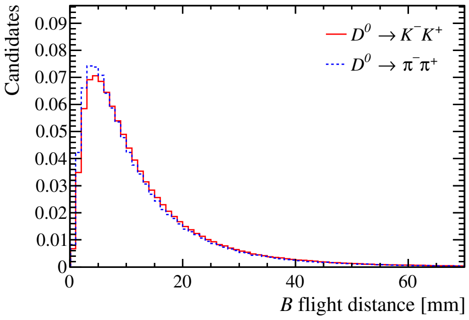

Figure 13.3: The B flight distance of $D^0 \to K^-K^+$ and $D^0 \to \pi^-\pi^+$ candidates. The average flight distances are 13.1 mm and 12.5 mm. The kinematic weights of the ΔA_{CP} measurement are taken into account.

the decay-time difference of $D^0 \to \pi^-\pi^+$ and $D^0 \to K^-K^+$ decays. The choice $t_0 = 1\,\text{ps}$ for $D^0 \to \pi^-\pi^+$ decays and $t_0 = 1.2\,\text{ps}$ for $D^0 \to K^-K^+$ decays results in a ratio of average decay-times of 1.08 which roughly corresponds to the difference observed for the B flight distances. Using Equations 13.3 and 2.49, assuming a B production asymmetry of $(-1\,\%)$ and using the calculated fraction of B^0 mesons, $f(B^0) = (37.5 \pm 2.9)\,\%$, the difference in effective D^0 production asymmetries of $D^0 \to K^-K^+$ and $D^0 \to \pi^-\pi^+$ decays is calculated to be 0.02 %. This value is stable when using different values for t_0. As the assumptions are conservative, this number constitutes an upper limit of the effect and 0.02 % is propagated as systematic uncertainty to the ΔA_{CP} and $A_{CP}(K^-K^+)$ measurements.

13.2.4 Variations of the kinematic weighting

The kinematic weighting, cf. Chapter 8.1, is applied to equalise the kinematic distributions of reconstructed particles such that momentum-dependent production and detection asymmetries cancel in the difference of two raw asymmetries. The correction induced by the weighting is 0.05 % in the ΔA_{CP} measurement and 0.15 % in the $A_{CP}(K^-K^+)$ measurement. After the weighting, residual differences remain in the kinematic distributions. The systematic studies are dedicated to quantify the effects of the residual differences and to test the extraction of the weights from the kinematic distributions. The studies are performed directly with data. There is the risk that differences are induced by statistical fluctuations as the per-event weight can fluctuate from one scenario to the other. The possible statistical fluctuations due to kinematic weights are discussed in Chapters 8.2.2 and Chapter 12.1. Still, the observed variations when changing the strategy to weight events constitute the scale of possible systematic effects.

The results of the following tests are given in Table 13.3:

- In the ΔA_{CP} and in the $A_{CP}(K^-K^+)$ measurement the weighting takes the p_{T} and η distributions of the D^0 candidates into account. Hence, differences in the kinematics of the muon candidates are visible in Figures 8.4 and 8.8. An additional weighting is performed to harmonise the p_{T}, η and ϕ distributions of

Table 13.3: The results of the systematic studies of the weighting procedure. The largest differences to the default values are highlighted in red. The tests are explained in the text.

Test	$\boldsymbol{\Delta A_{CP}}$ [%]	$\boldsymbol{A_{CP}(K^-K^+)}$ [%]
Default	$+0.137 \pm 0.160$	-0.057 ± 0.150
Additional weighting of muon p_{T},η and ϕ	$+0.146 \pm 0.160$	-0.039 ± 0.150
Additional weighting of kaon and trigger pion ϕ	-	-0.057 ± 0.150
Number of bins decreased (20 to 15)	$+0.153 \pm 0.160$	-0.007 ± 0.148
Number of bins increased (20 to 25)	$+0.138 \pm 0.160$	-0.036 ± 0.150
Different background subtraction	$+0.128 \pm 0.160$	-0.008 ± 0.151
Maximum difference	0.016	0.050

the muon candidates. The differences to the default results are below 0.02 % in both cases.

- The default weighting procedure does not include a weighting in the azimuthal angle ϕ in order to keep the procedure as simple as possible. Significant differences of the ϕ distributions are seen for example in Figure 8.10. The amount of traversed material depends on the azimuthal angle ϕ of a particle as the LHCb detector is not rotationally symmetric. Especially, the kaon detection asymmetry might change as it depends on the amount of traversed material but also other detector induced effects might play a role. Thus, the $D^+ \to K^-\pi^+\pi^+$ sample is additionally weighted to the ϕ distribution of the kaon candidates in the $D^0 \to K^-\pi^+$ sample. Furthermore, the ϕ distribution of the trigger pion in the $D^+ \to \overline{K}^0\pi^+$ sample is adjusted to the ϕ distribution of the trigger pion in the $D^+ \to K^-\pi^+\pi^+$ sample.

  No difference to the default value of $A_{CP}(K^-K^+)$ is observed. Interestingly, the raw asymmetry of the $D^+ \to K^-\pi^+\pi^+$ sample changes by 0.04 % which is more than the statistical uncertainty. This is a hint that with larger sensitivity a weighting of the ϕ distributions might be needed. In this case, the changes of the other raw asymmetries compensate the shift of $A_{\mathrm{raw}}(K^-\pi^+\pi^+)$.

- In Chapter 8.2.4 pseudo-experiments are performed to test if the kinematic weighting can correct for momentum dependencies. A second test is performed directly with the data sample to estimate the variations within the finite bins of the weighting histograms. The number of bins per dimension is decreased and increased from 20 to 15 and 25, respectively. The $A_{CP}(K^-K^+)$ result changes by 0.05 % when the bin number is decreased, the value with the increased number of bins deviates by 0.021 %. This test is likely dominated by statistical variations as the weights change. Nevertheless, it gives a scale of systematic variations. The largest difference of ΔA_{CP} is 0.016 %.

- The last study varies the procedure to subtract the background contribution from the kinematic distributions. The default procedure uses a sideband subtraction which is explained in Chapter 8.1. The background regions are defined as $[m_{D,\mathrm{PDG}} - 60\,\mathrm{MeV}/c^2, m_{D,\mathrm{PDG}} - 30\,\mathrm{MeV}/c^2]$ and $[m_{D,\mathrm{PDG}} + 30\,\mathrm{MeV}/c^2, m_{D,\mathrm{PDG}} + 60\,\mathrm{MeV}/c^2]$ and the signal regions are defined as $|m_D - m_{D,\mathrm{PDG}}| < 30\,\mathrm{MeV}/c^2$. In the prompt $D^+ \to \overline{K}^0\pi^+$ and $D^+ \to K^-\pi^+\pi^+$ samples the background regions are changed to $[m_{D,\mathrm{PDG}} - 50\,\mathrm{MeV}/c^2, m_{D,\mathrm{PDG}} - 25\,\mathrm{MeV}/c^2]\,\mathrm{MeV}/c^2$ and $[m_{D,\mathrm{PDG}} + 25\,\mathrm{MeV}/c^2, m_{D,\mathrm{PDG}} + 50\,\mathrm{MeV}/c^2]$ and the signal regions accordingly. The background contribution in the muon-tagged decays is alternatively subtracted with the *sPlot* technique[2] which uses the fitted signal and background models to assign weights to each event. The *sPlot* technique has advantages for samples with a low signal yield but the disadvantage that signal and background model have to accurately describe the data.

  The determined ΔA_{CP} and $A_{CP}(K^-K^+)$ values differ from the default values by 0.009 % and 0.049 %, respectively. The latter is likely induced by statistical fluctuations of the weights as all modes in the $A_{CP}(K^-K^+)$ measurement have a low background contribution.

The maximum shifts (rounded), 0.02 % for ΔA_{CP} and 0.05 % for $A_{CP}(K^-K^+)$, are taken as systematic uncertainties. Both numbers are about a third of the correction due to the kinematic weighting. This shows that the procedure is robust.

13.2.5 Validation of the kinematic weighting with pseudo-experiments

The cancellation of the production and detection asymmetries is tested by simulating momentum-dependent asymmetries, cf. Chapter 8.2.4. The data samples of prompt D^+ and muon-tagged D^0 candidates are used to keep the real kinematic correlations of all involved particles. The B and D^+ production asymmetries and muon, kaon and pion detection asymmetries that are generated in this way are supported by the raw asymmetries observed in Chapter 7.4. No shift is seen in the value of ΔA_{CP}, while a small bias of 0.03 % is observed in the value of $A_{CP}(K^-K^+)$. This shift is propagated as an additional systematic uncertainty of the weighting procedure.

13.3 Wrong flavour tags of muon-tagged D^0 decays

Wrong flavour tags are discussed in Chapter 10. The mistag probability ω dilutes the measured *CP* asymmetries and the contribution of doubly Cabibbo-suppressed $D^0 \to K^+\pi^-$ decays damps the kaon detection asymmetry. The formulas to obtain ΔA_{CP} and $A_{CP}(K^-K^+)$ are given by

$$\begin{aligned} \Delta A_{CP} &= (1+2\omega)\ \left[A_{\mathrm{raw}}(K^-K^+) - A_{\mathrm{raw}}(\pi^-\pi^+)\right]\ , \\ A_{CP}(K^-K^+) &= (1+2\omega)\ \left[A_{\mathrm{raw}}(K^-K^+) - A_{\mathrm{raw}}(K^-\pi^+)\right] + (1-2R)A_D(K^-\pi^+)\ . \end{aligned}$$

---

[2] A short description of the *sPlot* technique [74] is given in Appendix E.

The mistag probability is found to be $\omega = (0.9875 \pm 0.0055)\,\%$ for the ΔA_{CP} measurement and $\omega = (0.7913 \pm 0.0056)\,\%$ for the $A_{CP}(K^-K^+)$ measurement. The values are confirmed with an alternative method which finds $\omega = (0.982 \pm 0.019)\,\%$ and $\omega = (0.803 \pm 0.021)\,\%$ with the ΔA_{CP} and $A_{CP}(K^-K^+)$ trigger selections, respectively. As the observed raw asymmetries are at the per-cent level, the corrections are at the sub per-mille level. The statistical uncertainties for ω and R, and the differences of the two methods give negligible systematic uncertainties.

A small difference of $\Delta\omega = (0.028 \pm 0.011)\%$ is observed between the probabilities to wrongly tag D^0 and $\overline{D}^0$ mesons. Although any non-zero value is expected to cancel in the difference of two raw asymmetries, the full difference is conservatively taken as a systematic uncertainty. A systematic uncertainty of $0.03\,\%$ is propagated to the ΔA_{CP} and $A_{CP}(K^-K^+)$ measurements.

13.4 Neutral kaon asymmetry

The neutral kaon asymmetry is determined in Chapter 9. The asymmetry $A_D(\overline{K}^0)$ is found to be $(-0.054 \pm 0.014)\,\%$, where the uncertainty is given by the knowledge of the LHCb material budget. The uncertainty is propagated as systematic uncertainty to the $A_{CP}(K^-K^+)$ measurement.

13.5 Overall systematic uncertainty of ΔA_{CP}, $A_{CP}(K^-K^+)$ and $A_{CP}(\pi^-\pi^+)$

All systematic uncertainties of ΔA_{CP} and $A_{CP}(K^-K^+)$ are summarised in Table 13.4. They are added in quadrature to obtain the total systematic uncertainties. The total systematic uncertainty of ΔA_{CP} is

$$\sigma_{\text{syst}}^{\Delta A_{CP}} = 0.08\,\% \quad ,$$

and the total systematic uncertainty of $A_{CP}(K^-K^+)$ is

$$\sigma_{\text{syst}}^{A_{CP}(K^-K^+)} = 0.10\,\% \quad .$$

In comparison, the statistical uncertainties are $\sigma_{\text{stat}}^{\Delta A_{CP}} = 0.16\,\%$ and $\sigma_{\text{stat}}^{A_{CP}(K^-K^+)} = 0.15\,\%$. Both measurements are not systematically limited, but the systematic uncertainty of the $A_{CP}(K^-K^+)$ measurement is larger as the analysis is more complex.

Similar methods and a common $D^0 \to K^-K^+$ sample are used in both measurements. Henceforth, the systematic uncertainties are correlated. The correlation can be deduced from a potential $A_{CP}(\pi^-\pi^+)$ measurement that uses the same method and calibration samples as for $A_{CP}(K^-K^+)$. Neglecting small systematic differences due to the raw asymmetry extraction of $A_{\text{raw}}(\pi^-\pi^+)$ and $A_{\text{raw}}(K^-K^+)$, the potential $A_{CP}(\pi^-\pi^+)$ measurement and the $A_{CP}(K^-K^+)$ measurement have to have the same systematic uncertainty. Following Equation 11.13, the systematic uncertainty of $A_{CP}(\pi^-\pi^+)$ is also given by

$$\left(\sigma_{\text{syst}}^{A_{CP}(\pi^-\pi^+)}\right)^2 = \left(\sigma_{\text{syst}}^{\Delta A_{CP}}\right)^2 + \left(\sigma_{\text{syst}}^{A_{CP}(K^-K^+)}\right)^2 - 2\,\rho_{\text{syst}}\,\sigma_{\text{syst}}^{\Delta A_{CP}}\,\sigma_{\text{syst}}^{A_{CP}(K^-K^+)} \quad , \tag{13.4}$$

Table 13.4: Overview of all contributions to the systematic uncertainties of ΔA_{CP} and $A_{CP}(K^-K^+)$.

Source of uncertainty	$\boldsymbol{\Delta A_{CP}}$	$\boldsymbol{A_{CP}(K^-K^+)}$
Production asymmetry:		
Effective D^0 production asymmetry	0.02%	0.02%
Difference in B decay-time acceptance	0.02%	0.02%
Production and detector asymmetry:		
Higher-order corrections	≈ 0	≈ 0
Multiple candidates	≈ 0	≈ 0
Different weighting	0.02%	0.05%
Non cancellation	≈ 0	0.03%
Neutral kaon asymmetry	-	0.01%
Background from real $\boldsymbol{D^0}$:		
Mistag rate	≈ 0	≈ 0
Mistag asymmetry	0.03%	0.03%
Background from fake $\boldsymbol{D^0}$ mesons:		
D^0 mass fit model	0.06%	0.06%
Wrong background modelling	0.03%	0.03%
Quadratic sum	0.08%	0.10%

where $\sigma_{\text{syst}}^{A_{CP}(\pi^-\pi^+)}$, $\sigma_{\text{syst}}^{\Delta A_{CP}}$ and $\sigma_{\text{syst}}^{A_{CP}(K^-K^+)}$ are the systematic uncertainties of $A_{CP}(\pi^-\pi^+)$, ΔA_{CP} and $A_{CP}(K^-K^+)$, ρ_{syst} is the correlation factor of the systematic uncertainties of ΔA_{CP} and $A_{CP}(K^-K^+)$. Equating the systematic uncertainties of $A_{CP}(\pi^-\pi^+)$ and $A_{CP}(K^-K^+)$,

$$\sigma_{\text{syst}}^{A_{CP}(\pi^-\pi^+)} \equiv \sigma_{\text{syst}}^{A_{CP}(K^-K^+)} \quad , \tag{13.5}$$

yields the result

$$\rho_{\text{syst}} = \frac{1}{2}\frac{\sigma_{\text{syst}}^{\Delta A_{CP}}}{\sigma_{\text{syst}}^{A_{CP}(K^-K^+)}} \quad . \tag{13.6}$$

The correlation factor of the systematic uncertainties of ΔA_{CP} and $A_{CP}(K^-K^+)$ is calculated to be

$$\rho_{\text{syst}} = 0.40 \quad .$$

The total correlation coefficient, ρ_{tot}, between the ΔA_{CP} and $A_{CP}(K^-K^+)$ measurements is obtained by combining the statistical and systematic correlations

$$\rho_{\text{tot}} = \frac{\rho_{\text{stat}}\,\sigma_{\text{stat}}^{\Delta A_{CP}}\,\sigma_{\text{stat}}^{A_{CP}(K^-K^+)} + \rho_{\text{syst}}\,\sigma_{\text{syst}}^{\Delta A_{CP}}\,\sigma_{\text{syst}}^{A_{CP}(K^-K^+)}}{\sqrt{\left(\sigma_{\text{stat}}^{\Delta A_{CP}}\right)^2 + \left(\sigma_{\text{syst}}^{\Delta A_{CP}}\right)^2}\sqrt{\left(\sigma_{\text{stat}}^{A_{CP}(K^-K^+)}\right)^2 + \left(\sigma_{\text{syst}}^{A_{CP}(K^-K^+)}\right)^2}} \quad , \tag{13.7}$$

giving

$$\rho_{\text{tot}} = 0.28 \quad .$$

Chapter 14

Final results and conclusion

A measurement of direct *CP* violation in D^0 decays using semileptonic B decays, where the tag of the initial flavour is given by the accompanying muon, is performed. The full available data set of the LHCb experiment taken in 2011 and 2012 is used, corresponding to $3\,\mathrm{fb}^{-1}$ of integrated luminosity. The difference of *CP* asymmetries in $D^0 \to K^-K^+$ and $D^0 \to \pi^-\pi^+$ decays is found to be

$$\Delta A_{CP} = A_{CP}(K^-K^+) - A_{CP}(\pi^-\pi^+) = (+0.14 \pm 0.16\,(\mathrm{stat}) \pm 0.08\,(\mathrm{syst}))\,\% \quad .$$

An important part of the analysis is to study the robustness of the measurement as detection and production asymmetries are at the same level or larger than possible *CP* asymmetries. Therefore, it is extensively studied that this value is stable in different data taking periods and in different regions of the phase space of all involved particles.

The biggest challenge of this work is to disentangle the *CP* asymmetries $A_{CP}(K^-K^+)$ and $A_{CP}(\pi^-\pi^+)$. The large samples of muon-tagged Cabibbo-favoured $D^0 \to K^-\pi^+$ decays and of prompt Cabibbo-favoured $D^+ \to K^-\pi^+\pi^+$ and $D^+ \to \overline{K}^0\pi^+$ decays are used to determine momentum-dependent production and detection asymmetries. The largest detection asymmetry originates from different material interaction rates for positive and negative kaons. The measurement of the spurious asymmetries uses a weighting procedure which equalises the kinematic distributions of all involved particles. In the relevant kinematic range, the detection asymmetry $A_D(K^-\pi^+)$ is determined with high precision to be

$$A_D(K^-\pi^+) = (-1.17 \pm 0.12\,(\mathrm{stat}))\,\% \quad .$$

Furthermore, a model is developed to calculate the detection and *CP* asymmetry of neutral kaons, which leads to a small correction of $(0.054 \pm 0.014)\,\%$.

With these inputs, the *CP* asymmetry $A_{CP}(K^-K^+)$ is measured to be

$$A_{CP}(K^-K^+) = (-0.06 \pm 0.15\,(\mathrm{stat}) \pm 0.10\,(\mathrm{syst}))\,\% \quad .$$

The total correlation coefficient of ΔA_{CP} and $A_{CP}(K^-K^+)$, including statistical and systematic components, is $\rho_{\mathrm{tot}} = 0.28$. The above results are combined to determine the *CP* asymmetry in the $D^0 \to \pi^-\pi^+$ decay

$$A_{CP}(\pi^-\pi^+) = (-0.20 \pm 0.19\,(\mathrm{stat}) \pm 0.10\,(\mathrm{syst}))\,\% \quad .$$

It should be pointed out that these results are obtained assuming no *CP* violation in D^0 mixing and no direct *CP* violation in the Cabibbo-favoured $D^0 \to K^-\pi^+$, $D^+ \to K^-\pi^+\pi^+$ and $D^+ \to \overline{K}^0\pi^+$ decay modes. This work presents the most precise

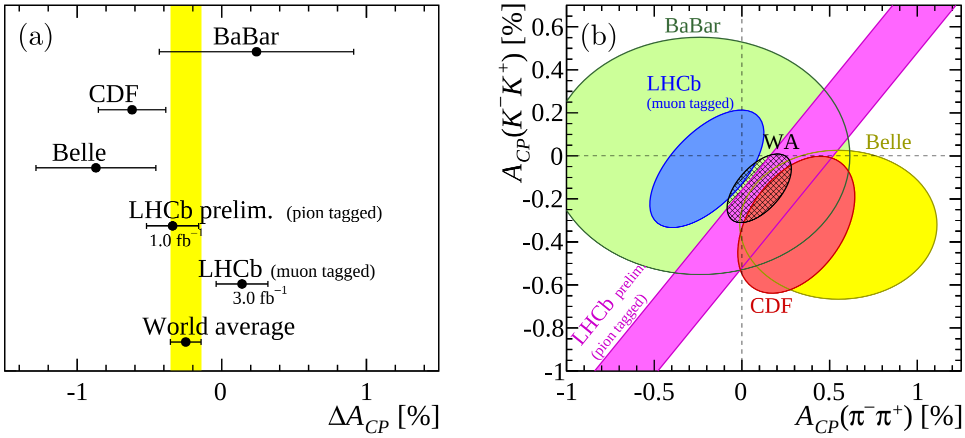

Figure 14.1: Overview of *CP* violation measurements in $D^0 \to K^-K^+$ and $D^0 \to \pi^-\pi^+$ decays showing (a) ΔA_{CP}, and (b) the $A_{CP}(K^-K^+)$ versus $A_{CP}(\pi^-\pi^+)$ plane. The 68 % confidence level contours are displayed. The results are from BaBar [25], CDF [24], Belle [26], LHCb (pion-tagged) [84] and this work. The new world average values (WA) are obtained neglecting any effect from indirect *CP* violation.

measurements of the time-integrated *CP* asymmetries $A_{CP}(K^-K^+)$ and $A_{CP}(\pi^-\pi^+)$ from a single experiment to date. They show that there is no significant *CP* violation in the singly Cabibbo-suppressed $D^0 \to K^-K^+$ and $D^0 \to \pi^-\pi^+$ decays at the level of 10^{-3}.

An overview of the current measurements of ΔA_{CP} is shown in Figure 14.1a. It includes a preliminary result of the pion-tagged analysis by the LHCb collaboration [84]. This measurement uses the full data set of 2011 in contrast to the previous measurement [1]. Due to additional data, the preliminary result of the pion-tagged analysis is $\Delta A_{CP} = (-0.34 \pm 0.15\,(\mathrm{stat}) \pm 0.10\,(\mathrm{syst}))\,\%$. This is significantly closer to zero as previously reported. Contributions from indirect *CP* violation can be safely neglected in the combination as it is measured to be small [23]. The new world average of $\Delta A_{CP} = (-0.25 \pm 0.11)\,\%$ is obtained. Figure 14.1b gives an overview of all measurements in the $A_{CP}(K^-K^+)$ versus $A_{CP}(\pi^-\pi^+)$ plane. The updated world average values are found to be $A_{CP}(K^-K^+) = (-0.15 \pm 0.11)\,\%$ and $A_{CP}(\pi^-\pi^+) = (+0.10 \pm 0.12)\,\%$ with a correlation of 0.57. The results of this work are compatible at the 2σ level with the other measurements.

More *CP* asymmetry measurements with higher precision are needed to improve our theoretical understanding of D^0 decays. They are the only meson system consisting of up-type quarks and *CP* violation in their mixing and decays still needs to be confirmed. Thus, it will be interesting to pursue these measurements in the future, but also experimentally challenging. Already now the analysis is an important benchmark of the LHCb experiment's performance as detection and production asymmetries are controlled and measured at the level of 10^{-3}. The methods and tools developed in this analysis are useful for other asymmetry measurements, especially in decays involving kaons. The analysis method has proven to be capable to improve with more statistics to the sub per-mille level.

Appendix A

Addendum to trigger and off-line selection

A.1 Trigger configurations

The analysis is restricted to a certain set of so-called *trigger configuration keys* (TCKs) to guarantee stable running conditions in the selected data sample, cf. Chapter 6.2. Every time the trigger configuration of the hard- or software trigger changes the TCK is changed. The TCKs that have been used in the 2011 data taking are listed in Table A.3. Trigger lines with a so-called *prescale* are randomly executed in a fraction of all bunch-crossings. The fraction is given by the prescale. In 2012 the number of different TCKs was higher than in 2011. However, for the decay channels of this analysis there is no difference between most TCKs. The different configurations are shown in Table A.1. Table A.2 gives a comprehensive overview of the TCKs used in the data taking of 2012. The differences are often small and contain bug-fixes for new or not working lines. ”Same as” is defined as: TCKs that have the same `L0Muon`, `L0Hadron`, `Hlt1TrackAllL0`, `Hlt1TrackMuon`, `Hlt2SingleMuon` and `Hlt2TopoMuNBodyBBDT` definition.

Table A.1: The trigger configurations used in the 2012 data taking and the relevant trigger requirements. The TCKs that are not used in the selection are indicated with a dagger (†). Each TCK represents a set of equivalent TCKs, see Table A.2. Hlt1TrackAllL0: order of cuts: $p_{\mathrm{T}} >$, $p >$ (GeV/c), χ^2_{track}/ndf $<$, ValidateWithTT: ON/OFF. `Hlt1TrackMuon`: order of cuts: $p_{\mathrm{T}} >$, $p >$ (GeV/c), χ^2_{track}/ndf $<$, ValidateWithTT: ON/OFF

TCK	`L0Muon` p_{T}	`L0Hadron` p_{T}	`Hlt1TrackAllL0`	`Hlt1TrackMuon`
0x94003d	1.76	3.62	1.7, 10.0, 1.5, OFF	1.0, 8.0, 2.5, OFF
0x95003d†	1.76	3.62	1.7, 10.0, 2.0, ON	1.0, 8.0, 2.5, ON
0x990042	1.76	3.62	1.6, 3.0, 2.0, ON	1.0, 3.0, 2.5, ON
0x9a0042†	1.76	3.62	1.7, 3.0, 1.5, ON	1.0, 3.0, 2.5, ON
0x990044	1.76	3.68	1.6, 3.0, 2.0, ON	1.0, 3.0, 2.5, ON
0x9f0045	1.76	3.74	1.6, 3.0, 2.0, ON	1.0, 3.0, 2.5, ON

Table A.2: TCKs used in 2012 for magnet down and up polarity. The fraction indicates, how many data were taken with each TCK. Same as means, that they are equivalent for the decay channels of this analysis.

Down-TCKs	**Fraction**	**Same as**
0x94003d	0.10	0x94003d
0x95003d	0.00	0x95003d
0x97003d	0.14	0x94003d
0x990042	0.23	0x990042
0x990044	0.11	0x990044
0xa30044	0.15	0x990044
0xa30046	0.01	0x9f0045
0xa90046	0.06	0x9f0045
0xab0046	0.05	0x9f0045
0xac0046	0.11	0x9f0045
0xad0046	0.00	0x9f0045

Up-TCKs	**Fraction**	**Same as**
0x94003d	0.15	0x94003d
0x95003d	0.00	0x95003d
0x97003d	0.11	0x94003d
0x990042	0.36	0x990042
0x990043	0.00	0x990042
0x9a0042	0.00	0x9a0042
0x990044	0.02	0x990044
0xa20044	0.00	0x990044
0xa30044	0.17	0x990044
0x9f0045	0.02	0x9f0045
0xa10044	0.02	0x9f0045
0xa10045	0.07	0x9f0045
0xa30046	0.01	0x9f0045
0xac0046	0.00	0x9f0045
0xad0046	0.00	0x9f0045

Table A.3: TCKs used in the 2011 data taking and the relevant trigger requirements. The TCKs that are not used in the selection are indicated with a dagger (†).

Magnet up	**Magnet down**	**Requirements**
	0x360032	`L0Hadron` threshold: $p_{\mathrm{T}} > 3.5\,\mathrm{GeV}/c$
	0x480032	`L0Muon` threshold: $p_{\mathrm{T}} > 1.48\,\mathrm{GeV}/c$
	0x6d0032	`Hlt1TrackAllL0`: $p_{\mathrm{T}} > 1.7\,\mathrm{GeV}/c$, $r_{\mathrm{PV}} < 0.5\,\mathrm{mm}$
	0x700034	`Hlt1TrackMuon`: $p_{\mathrm{T}} > 1.0\,\mathrm{GeV}/c$, $r_{\mathrm{PV}} < 0.5\,\mathrm{mm}$
	0x710035	`Hlt2SingleMuon`: $p_{\mathrm{T}} > 1.3\,\mathrm{GeV}/c$, prescale=0.5
0x5a0032	0x5a0032	
0x5b0032	0x5b0032	
0x730035	0x730035	
	0x4a0033†	`L0Hadron` threshold: $p_{\mathrm{T}} > 2.4\,\mathrm{GeV}/c$
0x5d0033†		`L0Muon` threshold: $p_{\mathrm{T}} > 0.8\,\mathrm{GeV}/c$
		`Hlt1TrackAllL0`: $p_{\mathrm{T}} > 1.7\,\mathrm{GeV}/c$, $r_{\mathrm{PV}} < 0.5\,\mathrm{mm}$
		`Hlt1TrackMuon`: $p_{\mathrm{T}} > 1.0\,\mathrm{GeV}/c$, $r_{\mathrm{PV}} < 0.5\,\mathrm{mm}$
		`Hlt2SingleMuon`: $p_{\mathrm{T}} > 1.0\,\mathrm{GeV}/c$, prescale=1.0
0x740036†		`L0Hadron` threshold: $p_{\mathrm{T}} > 4\,\mathrm{GeV}/c$
		`L0Muon` threshold: $p_{\mathrm{T}} > 1.6\,\mathrm{GeV}/c$
		`Hlt1TrackAllL0`: $p_{\mathrm{T}} > 1.7\,\mathrm{GeV}/c$, $r_{\mathrm{PV}} < 0.5\,\mathrm{mm}$
		`Hlt1TrackMuon`: $p_{\mathrm{T}} > 1.0\,\mathrm{GeV}/c$, $r_{\mathrm{PV}} < 0.5\,\mathrm{mm}$
		`Hlt2SingleMuon`: $p_{\mathrm{T}} > 1.3\,\mathrm{GeV}/c$, prescale=0.5
0x760037	0x760037	`L0Hadron` threshold: $p_{\mathrm{T}} > 3.5\,\mathrm{GeV}/c$
0x790037		`L0Muon` threshold: $p_{\mathrm{T}} > 1.48\,\mathrm{GeV}/c$
0x790038	0x790038	`Hlt1TrackAllL0`: $p_{\mathrm{T}} > 1.7\,\mathrm{GeV}/c$, $r_{\mathrm{PV}} < 0.3\,\mathrm{mm}$
		`Hlt1TrackMuon`: $p_{\mathrm{T}} > 1.0\,\mathrm{GeV}/c$, $r_{\mathrm{PV}} < 0.3\,\mathrm{mm}$
		`Hlt2SingleMuon`: $p_{\mathrm{T}} > 1.3\,\mathrm{GeV}/c$, prescale=0.5

Appendix B

Addendum to wrong flavour tags

B.1 Full tables of mistag probability results

The results of all individual mistag probability measurements with the $D^0 \to K^-\pi^+$ sample are given in Table B.1. The ΔA_{CP} trigger selection is used. The results obtained of the D^* method are given for muon-tagged $D^0 \to K^-\pi^+$, $D^0 \to K^-K^+$ and $D^0 \to \pi^-\pi^+$ decays in Table B.2. The results that are determined with the $A_{CP}(K^-K^+)$ trigger line selection are presented in Table B.3.

Table B.1: The measured muon-wrong-sign ratios and the mistag probabilities (in per cent). The ΔA_{CP} selection is used. The result for a year is obtained by taking the arithmetic mean of both magnet polarities. The final result is the weighted mean of both years.

Channel	2011	ω_{D^0} [%]	$\omega_{\overline{D}^0}$ [%]	$\Delta\omega$ [%]	ω[%]
$D^0 \to K^-\pi^+$ from D^{*+}	Up	0.940 ± 0.077	0.891 ± 0.074	0.05 ± 0.11	0.915 ± 0.054
	Down	0.983 ± 0.066	1.036 ± 0.064	-0.052 ± 0.092	1.009 ± 0.046
	Average	0.962 ± 0.051	0.963 ± 0.049	-0.002 ± 0.071	0.962 ± 0.035

Channel	2012	ω_{D^0} [%]	$\omega_{\overline{D}^0}$ [%]	$\Delta\omega$ [%]	ω[%]
$D^0 \to K^-\pi^+$ from D^{*+}	Up	0.900 ± 0.047	1.062 ± 0.045	-0.163 ± 0.065	0.984 ± 0.032
	Down	1.019 ± 0.049	0.980 ± 0.046	0.039 ± 0.067	0.999 ± 0.034
	Average	0.959 ± 0.034	1.021 ± 0.032	-0.062 ± 0.047	0.991 ± 0.023

Channel	2011	$\omega_{D^0} + R^+$ [%]	$\omega_{\overline{D}^0} + R^-$ [%]	$\Delta\omega$ [%]	$\omega + R$ [%]
$D^0 \to K^-\pi^+$ uncorrected	Up	1.370 ± 0.019	1.325 ± 0.018	0.044 ± 0.026	1.347 ± 0.013
	Down	1.381 ± 0.016	1.319 ± 0.016	0.062 ± 0.023	1.350 ± 0.011
	Average	1.375 ± 0.012	1.322 ± 0.012	0.053 ± 0.017	1.3484 ± 0.0087

Channel	2012	$\omega_{D^0} + R^+$ [%]	$\omega_{\overline{D}^0} + R^-$ [%]	$\Delta\omega$ [%]	$\omega + R$ [%]
$D^0 \to K^-\pi^+$ uncorrected	Up	1.405 ± 0.011	1.376 ± 0.011	0.029 ± 0.015	1.3904 ± 0.0076
	Down	1.386 ± 0.011	1.384 ± 0.011	0.002 ± 0.016	1.3849 ± 0.0079
	Average	1.3956 ± 0.0078	1.3800 ± 0.0077	0.016 ± 0.011	1.3877 ± 0.0055

Channel	2011	ω_{D^0} [%]	$\omega_{\overline{D}^0}$ [%]	$\Delta\omega$ [%]	ω [%]
$D^0 \to K^-\pi^+$ WS corrected	Up	0.981 ± 0.020	0.935 ± 0.019	0.046 ± 0.027	0.958 ± 0.014
	Down	0.992 ± 0.017	0.929 ± 0.016	0.064 ± 0.023	0.961 ± 0.012
	Average	0.987 ± 0.013	0.932 ± 0.013	0.055 ± 0.019	0.9594 ± 0.0092

Channel	2012	ω_{D^0} [%]	$\omega_{\overline{D}^0}$ [%]	$\Delta\omega$ [%]	ω [%]
$D^0 \to K^-\pi^+$ WS corrected	Up	1.016 ± 0.012	0.986 ± 0.012	0.030 ± 0.017	1.0014 ± 0.0082
	Down	0.997 ± 0.012	0.994 ± 0.012	0.004 ± 0.017	0.9959 ± 0.0084
	Average	1.0070 ± 0.0091	0.9899 ± 0.0089	0.017 ± 0.013	0.9987 ± 0.0062

Channel		ω_{D^0} [%]	$\omega_{\overline{D}^0}$ [%]	$\Delta\omega$ [%]	ω[%]
$D^0 \to K^-\pi^+$ from D^{*+}	2011+2012	0.960 ± 0.028	1.004 ± 0.027	-0.044 ± 0.039	0.982 ± 0.019
$D^0 \to K^-\pi^+$ uncorrected	2011+2012	1.3898 ± 0.0066	1.3634 ± 0.0065	0.0263 ± 0.0093	1.3765 ± 0.0046
$D^0 \to K^-\pi^+$ WS corrected	2011+2012	1.0012 ± 0.0081	0.9733 ± 0.0079	0.028 ± 0.011	0.9875 ± 0.0055

Table B.2: The measured mistag probabilities (in per cent) with the D^* method for $D^0 \to \pi^-\pi^+$, $D^0 \to K^-K^+$ and $D^0 \to K^-\pi^+$ decays. The ΔA_{CP} selection is used for the three channels. The result for a year is obtained by taking the arithmetic mean of both magnet polarities. The final result is the weighted mean of both years.

Channel	2011	ω_{D^0} [%]	$\omega_{\overline{D}^0}$ [%]	$\Delta\omega$ [%]	ω
$D^0 \to \pi^-\pi^+$	Up	1.39 ± 0.35	1.57 ± 0.33	-0.18 ± 0.48	1.47 ± 0.24
	Down	1.35 ± 0.29	0.80 ± 0.28	0.55 ± 0.40	1.00 ± 0.20
	Average	1.37 ± 0.23	1.18 ± 0.22	0.19 ± 0.31	1.23 ± 0.16

Channel	2011	ω_{D^0} [%]	$\omega_{\overline{D}^0}$ [%]	$\Delta\omega$ [%]	ω
$D^0 \to K^-K^+$	Up	1.17 ± 0.19	0.96 ± 0.18	0.21 ± 0.26	1.04 ± 0.13
	Down	1.06 ± 0.16	0.91 ± 0.16	0.15 ± 0.22	0.98 ± 0.11
	Average	1.11 ± 0.12	0.93 ± 0.12	0.18 ± 0.17	1.011 ± 0.085

Channel	2011	ω_{D^0} [%]	$\omega_{\overline{D}^0}$ [%]	$\Delta\omega$ [%]	ω
$D^0 \to K^-\pi^+$	Up	0.940 ± 0.077	0.892 ± 0.074	0.05 ± 0.11	0.915 ± 0.054
	Down	0.984 ± 0.066	1.036 ± 0.064	-0.052 ± 0.092	1.009 ± 0.046
	Average	0.962 ± 0.051	0.964 ± 0.049	-0.002 ± 0.071	0.962 ± 0.035

Channel	2012	ω_{D^0} [%]	$\omega_{\overline{D}^0}$ [%]	$\Delta\omega$ [%]	ω
$D^0 \to \pi^-\pi^+$	Up	1.24 ± 0.20	0.84 ± 0.20	0.40 ± 0.28	1.04 ± 0.14
	Down	1.09 ± 0.21	1.04 ± 0.20	0.05 ± 0.29	1.06 ± 0.14
	Average	1.17 ± 0.14	0.94 ± 0.14	0.23 ± 0.20	1.05 ± 0.10

Channel	2012	ω_{D^0} [%]	$\omega_{\overline{D}^0}$ [%]	$\Delta\omega$ [%]	ω
$D^0 \to K^-K^+$	Up	0.83 ± 0.11	0.93 ± 0.11	-0.10 ± 0.15	0.883 ± 0.076
	Down	1.18 ± 0.12	0.88 ± 0.11	0.29 ± 0.16	1.029 ± 0.080
	Average	1.005 ± 0.080	0.906 ± 0.077	0.10 ± 0.11	0.956 ± 0.055

Channel	2012	ω_{D^0} [%]	$\omega_{\overline{D}^0}$ [%]	$\Delta\omega$ [%]	ω
$D^0 \to K^-\pi^+$	Up	0.900 ± 0.047	1.062 ± 0.045	-0.162 ± 0.065	0.984 ± 0.032
	Down	1.019 ± 0.049	0.980 ± 0.046	0.039 ± 0.067	0.999 ± 0.034
	Average	0.959 ± 0.034	1.021 ± 0.032	-0.062 ± 0.047	0.991 ± 0.023

$D^0 \to \pi^-\pi^+$	2011+2012	1.22 ± 0.12	1.01 ± 0.12	0.21 ± 0.17	1.104 ± 0.085
$D^0 \to K^-K^+$	2011+2012	1.037 ± 0.067	0.914 ± 0.065	0.123 ± 0.093	0.972 ± 0.046
$D^0 \to K^-\pi^+$	2011+2012	0.960 ± 0.028	1.004 ± 0.027	-0.043 ± 0.039	0.982 ± 0.019

Table B.3: The measured muon-wrong-sign ratios and the mistag probabilities (in per cent) for $D^0 \to K^-\pi^+$ and $D^0 \to K^-K^+$ candidates. The $A_{CP}(K^-K^+)$ selection is used. The result for a year is obtained by taking the arithmetic mean of both magnet polarities. The final result is the weighted mean of both years.

Channel	2011	ω_{D^0} [%]	$\omega_{\overline{D}^0}$ [%]	$\Delta\omega$ [%]	ω [%]
$D^0 \to K^-\pi^+$ from D^{*+}	Up	0.678 ± 0.083	0.700 ± 0.081	-0.02 ± 0.12	0.687 ± 0.075
	Down	0.728 ± 0.072	0.887 ± 0.070	-0.16 ± 0.10	0.808 ± 0.050
	Average	0.703 ± 0.055	0.794 ± 0.053	-0.091 ± 0.077	0.748 ± 0.045

Channel	2012	ω_{D^0} [%]	$\omega_{\overline{D}^0}$ [%]	$\Delta\omega$ [%]	ω [%]
$D^0 \to K^-\pi^+$ from D^{*+}	Up	0.727 ± 0.049	0.868 ± 0.047	-0.141 ± 0.067	0.799 ± 0.034
	Down	0.855 ± 0.051	0.821 ± 0.048	0.035 ± 0.070	0.838 ± 0.035
	Average	0.791 ± 0.035	0.845 ± 0.034	-0.053 ± 0.049	0.818 ± 0.024

Channel	2011	$\omega_{D^0} + R^+$ [%]	$\omega_{\overline{D}^0} + R^-$ [%]	$\Delta\omega$ [%]	ω [%]
$D^0 \to K^-\pi^+$ uncorrected	Up	1.152 ± 0.018	1.108 ± 0.019	0.044 ± 0.026	1.129 ± 0.014
	Down	1.156 ± 0.017	1.106 ± 0.016	0.051 ± 0.023	1.131 ± 0.012
	Average	1.154 ± 0.012	1.107 ± 0.012	0.047 ± 0.017	1.1299 ± 0.0089

Channel	2012	$\omega_{D^0} + R^+$ [%]	$\omega_{\overline{D}^0} + R^-$ [%]	$\Delta\omega$ [%]	ω [%]
$D^0 \to K^-\pi^+$ uncorrected	Up	1.218 ± 0.011	1.185 ± 0.011	0.033 ± 0.015	1.2014 ± 0.0076
	Down	1.198 ± 0.011	1.197 ± 0.011	0.001 ± 0.016	1.1974 ± 0.0079
	Average	1.2078 ± 0.0078	1.1912 ± 0.0076	0.017 ± 0.011	1.1994 ± 0.0055

Channel	2011	ω_{D^0} [%]	$\omega_{\overline{D}^0}$ [%]	$\Delta\omega$ [%]	ω [%]
$D^0 \to K^-\pi^+$ WS corrected	Up	0.763 ± 0.019	0.718 ± 0.019	0.046 ± 0.027	0.740 ± 0.014
	Down	0.768 ± 0.017	0.716 ± 0.017	0.052 ± 0.024	0.742 ± 0.012
	Average	0.765 ± 0.013	0.717 ± 0.013	0.049 ± 0.019	0.7409 ± 0.0094

Channel	2012	ω_{D^0} [%]	$\omega_{\overline{D}^0}$ [%]	$\Delta\omega$ [%]	ω [%]
$D^0 \to K^-\pi^+$ WS corrected	Up	0.829 ± 0.012	0.795 ± 0.012	0.034 ± 0.017	0.8124 ± 0.0082
	Down	0.809 ± 0.012	0.807 ± 0.012	0.002 ± 0.017	0.8084 ± 0.0084
	Average	0.8192 ± 0.0091	0.8011 ± 0.0089	0.018 ± 0.013	0.8104 ± 0.0063

Channel		ω_{D^0} [%]	$\omega_{\overline{D}^0}$ [%]	$\Delta\omega$ [%]	ω [%]
$D^0 \to K^-\pi^+$ from D^{*+}	2011+2012	0.766 ± 0.030	0.830 ± 0.028	-0.064 ± 0.041	0.803 ± 0.021
$D^0 \to K^-\pi^+$ uncorrected	2011+2012	1.1923 ± 0.0066	1.1679 ± 0.0065	0.0253 ± 0.0093	1.1803 ± 0.0047
$D^0 \to K^-\pi^+$ WS corrected	2011+2012	0.8037 ± 0.0081	0.7778 ± 0.0080	0.027 ± 0.011	0.7913 ± 0.0056
$D^0 \to K^-K^+$	2011+2012	0.859 ± 0.070	0.749 ± 0.068	0.111 ± 0.098	0.801 ± 0.049

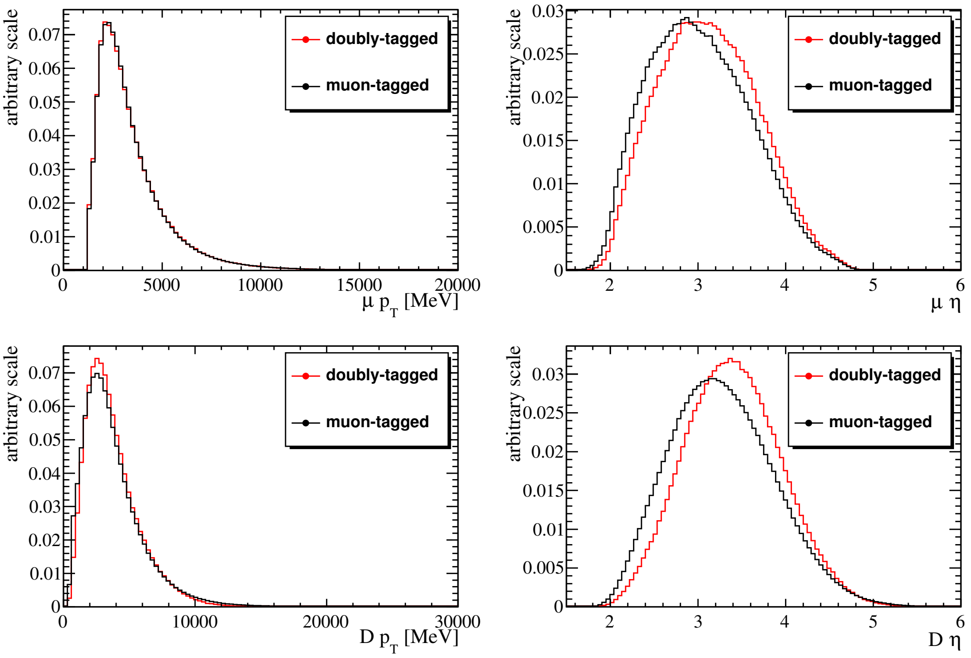

Figure B.1: The p_{T} (left) and η (right) distribution of muon (top) and D^0 (bottom) is shown for muon- and doubly-tagged $D^0 \to K^-\pi^+$ candidates.

B.2 Kinematic distributions of doubly-tagged candidates

The additional selection cuts of the D^* method change the kinematic distributions of the muon candidates, this could affect the mistag probability. In Figure B.1 the p_{T} and η distributions of the muon and the D^0 candidates are shown for all events and doubly-tagged sample. While the p_{T} spectrum is very similar, there is a clear difference in the η distribution. This is because an additional track has to be reconstructed in the LHCb acceptance. The wrong-sign method does not have this disadvantage as it uses the full sample and the same selection. However, it can only be used in the $D^0 \to K^-\pi^+$ channel and needs external input.

B.3 Fit model of Δm distribution

The $D^{*\pm}$ method reconstructs the D^* and its accompanying pion. The mistag probability is determined with a binned maximum-likelihood to the Δm distribution. The fit is performed simultaneously in the wrongly- and rightly-tagged events. Therefore, the event yields of wrongly-and rightly-tagged candidates, $N_{\mathrm{sig,right}}$ and $N_{\mathrm{sig,wrong}}$, are parameterised as

$$N_{\mathrm{sig,right}} = N_{\mathrm{sig}}\ (1-\omega)\ , \tag{B.1}$$

$$N_{\mathrm{sig,wrong}} = N_{\mathrm{sig}}\ \omega\ , \tag{B.2}$$

where N_{sig} is the total signal yield and ω the mistag probability. The signal fit model of the Δm distribution is taken from the description used in Reference [82]. It consists of two Gaussians and a Johnson S_U distribution [85] for the signal. The Johnson S_U distribution is defined as,

$$\mathcal{J}(x|\mu,\sigma,\delta,\gamma) = \frac{1}{\mathcal{N}_J} \frac{e^{-\frac{1}{2}\left[\gamma \,+\, \delta \,\sinh^{-1}\left(\frac{x-\mu}{\sigma}\right)\right]^2}}{\sqrt{1+\left(\frac{x-\mu}{\sigma}\right)^2}} \quad , \tag{B.3}$$

where δ and γ are tail parameters, μ and σ correspond to the parameters of a Gaussian. The two Gaussians have the same mean. The mean of the Johnson function can be different. Again the shape parameters are shared between rightly- and wrongly-tagged candidates. However, an offset in the mean value has to be allowed as the mean is different for wrongly-and rightly-tagged candidates, see Chapter B.4 for further information. To improve the fit stability, one of the fractions of the Gaussians is constrained in the fit. For samples with a low signal yield, additionally one width has to be fixed. The tail parameters δ and γ of the Johnson S_U distribution are constrained to 1.1 and -0.22, respectively.

The background contribution is fitted with an empirical model with the parameters Δm_0, A and C:

$$\mathrm{PDF}_{\mathrm{bkg}}(\Delta m) = \frac{1}{\mathcal{N}_{\mathrm{bkg}}} \left\{ \begin{array}{ll} 0 & \text{if } \Delta m < \Delta m_0 \\ e^{-C(\Delta m - \Delta m_0)/\Delta m_0}(\Delta m - \Delta m_0)^A & \text{if } \Delta m > \Delta m_0 \end{array} \right\} . \tag{B.4}$$

This is the same parameterisation as used in the D^0 mixing analysis [82]. The parameter Δm_0 has been fixed to 139.57 GeV/c, the parameter A was fixed for stability reasons in all channels to 0.37. Parameter C was free to float. The choice of this parameterisation is motivated by looking at combinations of D^0 candidates with pions from another event.

The parameters A and C have been fixed to 3.5 and 2.6, respectively. This is done for the description of the rightly- and wrongly-tagged candidates. The parameter B is allowed to float and is different for rightly- and wrongly-tagged candidates. In the ideal case the parameter Δm_0 should equal the pion mass of 139.57 MeV/c^2. However, the fit prefers a slightly lower value around 139.2 MeV/c^2. Thus this parameters is allowed to float as well.

B.4 Impact parameter distributions

The mean of the Δm peak of wrongly- and rightly-tagged is slightly shifted. This is because the impact parameter distribution of both samples are shifted towards each other, see Figure B.2. This leads to a bias in the Δm distribution, as the impact parameter criteria preferentially select particles which are scattered in one direction in the RF foil. This changes the opening angle between the D^0 and the pion candidate and, thus, Δm is biased.

B.5 Additional tests for mistag probability determination

The Cabibbo-favoured decay of a D^0 meson is $D^0 \to K^-\pi^+$. The muon from the semileptonic B decay is negatively-charged in the case of a D^0 meson. Thus, the

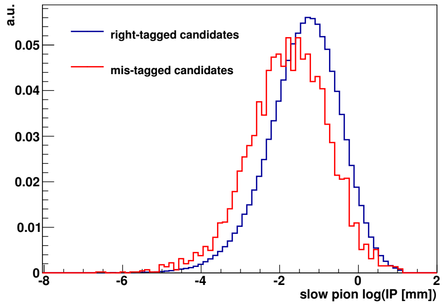

Figure B.2: The impact parameter distribution of $D^{*\pm}$ tagged $D^0 \to K^-\pi^+$ candidates.

combination of K^- π^+ and μ^- is called muon-right-sign, as well as the combination K^+ π^- and μ^+ for $\overline{D}^0$ mesons. The combinations K^+ π^- and μ^- and K^- π^+ and μ^+ are called muon-wrong-sign. A muon-wrong-sign combination can have two sources. A D^0 ($\overline{D}^0$) meson can decay doubly Cabibbo-suppressed to K^+ π^- (K^- π^+). The other source are events where a muon and a D^0 candidate are combined, although they did not originate from the same B decay. Thus, there is the possibility that the muon charge gives the wrong tag. The default method to measure the mistag probability is based on measuring the muon-wrong-sign ratio of $D^0 \to K^-\pi^+$ events. First, the ratio of muon-wrong-sign candidates is determined. Then, the known ratio of doubly Cabibbo-suppressed decays is subtracted. Therefore, muon-wrong-sign decays are included in the selection. The disadvantage of that strategy is, that it damps the kaon detection asymmetry, as a μ^- candidate is combined with K^- π^+ and K^+ π^- candidates.

The other method to measure the mistag probability is based on D^{*+} decays. It is checked, if the D^0 candidate and a charged pion in the event can be combined to D^{*+} candidate. This is possible as a B^0 meson can decay semileptonically via a D^{*+} resonance. This method has the advantage that it can be used to determine the mistag probability in $D^0 \to K^-K^+$ and $D^0 \to \pi^-\pi^+$ decays where the D^0 meson decay products contain no information about the D^0 meson flavour.

In Section 10 both methods are compared and give consistent results for the $D^0 \to K^-\pi^+$ sample. In the case of D^{*+} decays, pion-wrong-sign events can be defined. There the combination K^- π^+ and π^+ or K^+ π^- and π^- is called pion-right-sign. The other possible combinations, K^+ π^- and π^+ or K^- π^+ and π^-, are called pion-wrong-sign.

In Figure B.3 the Δm distribution of $D^0 \to K^-\pi^+$ events is shown for the default, the muon-right-sign and the pion-right-sign selection. It can be seen that a selection of muon-right-sign events leads to a very small mistag probability. While that is an advantage for the $D^0 \to K^-\pi^+$ selection, the assumption of an universal mistag probability in the semileptonic modes is broken. This is due to the fact, that additional information of the event is used. If $D^0 \to K^-\pi^+$ decays are selected, it is much more likely that also a negative muon is in the event, as a K^- π^+ pair originates in approximately 99.6 % of all events from a D^0 meson. In the case of $D^0 \to K^-K^+$ or $D^0 \to \pi^-\pi^+$ candidates this selection cannot be made.

On the other hand, the pion-right-sign sample does not have this bias as it does

Table B.4: The measured mistag probability (in per cent) for $D^0 \to K^-\pi^+$ using the ΔA_{CP} selection using the $D^{*\pm}$ method and the full data sets of 2011 and 2012.

Selection	$\boldsymbol{\omega^+}$ [%]	$\boldsymbol{\omega^-}$ [%]	$\boldsymbol{\Delta\omega}$ [%]	$\boldsymbol{\omega}$ [%]
default	0.960 ± 0.028	1.004 ± 0.027	-0.043 ± 0.039	0.982 ± 0.019
muon-right-sign	0.122 ± 0.028	0.165 ± 0.024	-0.043 ± 0.037	0.130 ± 0.017
pion-right-sign	0.879 ± 0.014	0.865 ± 0.013	0.014 ± 0.019	0.8724 ± 0.0095

not use additional information of the D^0 final state. A very clean sample of D^{*+} decays is selected by using only pion-right-sign events, see Figure B.3c. The fitted mistag probabilities with the D^* method of the default, the muon-right-sign and the pion-right-sign sample are given in Table B.4. The muon-right-sign values clearly differ from the other two due to the discussed reasons. The value of the default approach and the pion-right-sign are not compatible, but of the same order. The difference of the two could be taken as a systematic uncertainty of the Δm method to determine the mistag probability. However, the systematic uncertainty would be negligible due to the smallness of the correction.

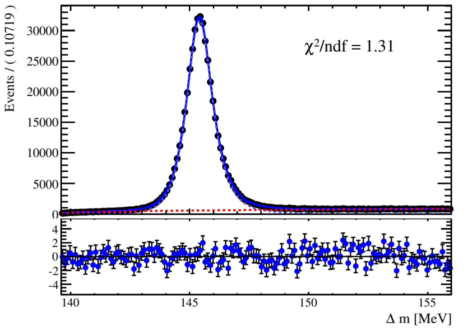

(a) Default selection

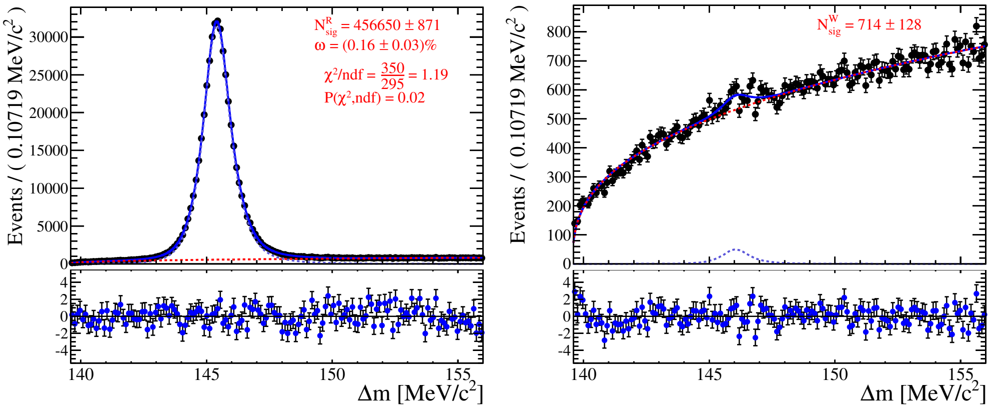

(b) Only muon-right-sign decays

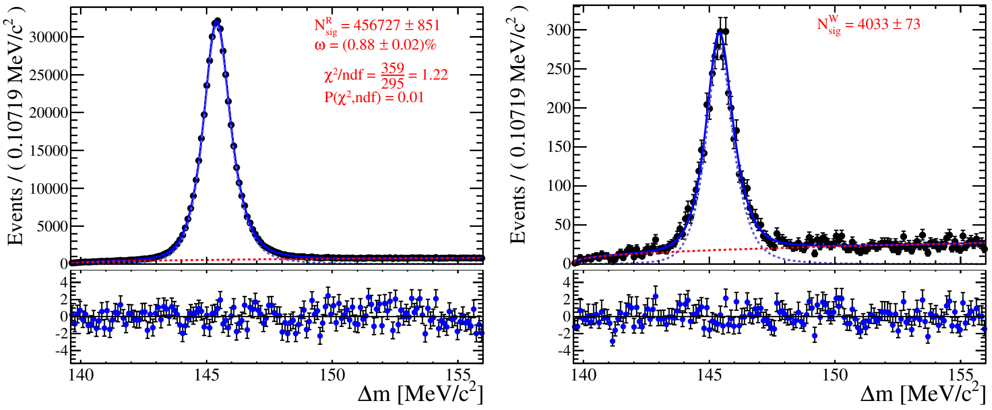

(c) Only pion-right-sign decays

Figure B.3: small The Δm distribution of doubly-tagged $D^0 \to K^-\pi^+$ decays is shown. The left plots show the right muon tagged events, the right plots the wrong muon tagged events. The blue line indicates the signal fit model, the red line the background. The 2012 Up sample is used and the merged sample of positively and negatively tagged events is used.

Appendix C

Addendum to *CP* asymmetry measurements

C.1 Fit parameters of raw asymmetry fits

C.1.1 ΔA_{CP}

All fit parameters of the ΔA_{CP} measurement are shown in Tables C.1 and C.3. The correlation with the fitted raw asymmetry are shown in Tables C.2 and C.4.

Table C.1: The fit parameters of the asymmetry fit to the $D^0 \to K^-K^+$ samples. The ΔA_{CP} trigger selection is used.

	Up 2011	Down 2011	Up 2012	Down 2012
A_{bkg}	-1.648 ± 0.33	0.45 ± 0.28	-0.699 ± 0.20	-0.449 ± 0.20
A_{raw}	-0.480 ± 0.23	-0.404 ± 0.19	-0.448 ± 0.13	-0.436 ± 0.13
μ	1865.029 ± 0.016	1865.049 ± 0.014	1864.9106 ± 0.0092	1864.9041 ± 0.0095
σ_1	5.540 ± 0.060	5.326 ± 0.073	5.523 ± 0.035	5.504 ± 0.036
$a_+ \times 100$	-0.5489 ± 0.013	-0.5234 ± 0.011	-0.56226 ± 0.0074	-0.54813 ± 0.0078
$a_- \times 100$	-0.5366 ± 0.013	-0.5542 ± 0.011	-0.55905 ± 0.0075	-0.56777 ± 0.0078
f_1	0.646 ± 0.026	0.574 ± 0.030	0.653 ± 0.015	0.646 ± 0.016
N_{bkg}	134281 ± 544	191418 ± 648	384575 ± 922	351885 ± 881
N_{sig}	241563 ± 635	335756 ± 751	728959 ± 1093	684569 ± 1053
s	1.628 ± 0.025	1.606 ± 0.016	1.630 ± 0.014	1.630 ± 0.014
$\Delta\mu$	0.00	0.00	0.00	0.00
α	2.70	2.70	2.70	2.70
n	1.50	1.50	1.50	1.50
s_p	1.00	1.00	1.00	1.00

Table C.2: The correlation with A_{raw} of the asymmetry fit to the $D^0 \to K^- K^+$ samples.

	Up 2011	Down 2011	Up 2012	Down 2012
$C[A_{\mathrm{raw}}, A_{\mathrm{bkg}}]$	-0.256	-0.254	-0.251	-0.250
$C[A_{\mathrm{raw}}, A_{\mathrm{raw}}]$	1.00	1.00	1.00	1.00
$C[A_{\mathrm{raw}}, \mu]$	0.00	-0.001	-0.001	-0.000
$C[A_{\mathrm{raw}}, \sigma_1]$	-0.001	0.00	0.00	-0.001
$C[A_{\mathrm{raw}}, a_+]$	0.03	0.03	0.03	0.03
$C[A_{\mathrm{raw}}, a_-]$	-0.032	-0.033	-0.032	-0.033
$C[A_{\mathrm{raw}}, f_1]$	-0.001	0.00	0.00	-0.001
$C[A_{\mathrm{raw}}, N_{\mathrm{bkg}}]$	0.00	-0.002	0.00	0.00
$C[A_{\mathrm{raw}}, N_{\mathrm{sig}}]$	-0.003	0.00	-0.001	-0.001
$C[A_{\mathrm{raw}}, s]$	-0.002	0.00	-0.001	-0.001

Table C.3: The fit parameters of the asymmetry fit to the $D^0 \to \pi^- \pi^+$ samples.

	Up 2011	Down 2011	Up 2012	Down 2012
A_{bkg}	-0.635 ± 0.45	0.44 ± 0.37	-0.507 ± 0.24	-0.594 ± 0.25
A_{ref}	-3.08 ± 4.2	1.2 ± 3.8	-2.77 ± 2.2	6.9 ± 2.3
A_{raw}	-1.167 ± 0.40	-0.373 ± 0.34	-0.216 ± 0.23	-0.791 ± 0.23
μ_{ref}	1793.4 ± 1.4	1791.8 ± 2.8	1792.8 ± 1.1	1791.85 ± 0.97
μ	1864.868 ± 0.039	1864.832 ± 0.033	1864.664 ± 0.022	1864.614 ± 0.023
σ_1	5.94 ± 0.19	5.76 ± 0.15	6.425 ± 0.071	6.439 ± 0.079
σ_{ref}	8.36 ± 0.76	9.1 ± 1.4	9.60 ± 0.60	10.04 ± 0.51
$a_+ \times 100$	-0.2281 ± 0.017	-0.2447 ± 0.014	-0.19144 ± 0.0097	-0.20072 ± 0.0098
$a_- \times 100$	-0.2550 ± 0.016	-0.2409 ± 0.014	-0.21135 ± 0.0094	-0.20379 ± 0.0098
f_1	0.277 ± 0.032	0.225 ± 0.023	0.350 ± 0.018	0.329 ± 0.019
f_{ref}	0.0389 ± 0.0024	0.0367 ± 0.0024	0.0477 ± 0.0017	0.0458 ± 0.0017
N_{bkg}	90643 ± 645	128439 ± 768	317985 ± 1343	298310 ± 1295
N_{sig}	91041 ± 507	125002 ± 575	288969 ± 978	273332 ± 952
s	1.612 ± 0.045	1.630 ± 0.040	1.508 ± 0.017	1.500 ± 0.018
$\Delta\mu$	0.00	0.00	0.00	0.00
α	1.50	1.50	1.50	1.50
n	2.00	2.00	2.00	2.00
s_p	1.00	1.00	1.00	1.00

Table C.4: The correlation with A_{raw} of the asymmetry fit to the $D^0 \to \pi^-\pi^+$ samples.

	Up 2011	Down 2011	Up 2012	Down 2012
$C[A_{\mathrm{raw}}, A_{\mathrm{bkg}}]$	-0.328	-0.325	-0.349	-0.349
$C[A_{\mathrm{raw}}, A_{\mathrm{ref}}]$	0.14	0.14	0.16	0.16
$C[A_{\mathrm{raw}}, A_{\mathrm{raw}}]$	1.00	1.00	1.00	1.00
$C[A_{\mathrm{raw}}, \mu_{\mathrm{ref}}]$	0.00	-0.008	0.01	-0.002
$C[A_{\mathrm{raw}}, \mu]$	-0.003	0.00	-0.001	0.00
$C[A_{\mathrm{raw}}, \sigma_1]$	-0.003	-0.001	-0.005	-0.002
$C[A_{\mathrm{raw}}, \sigma_{\mathrm{ref}}]$	-0.004	0.01	-0.012	0.01
$C[A_{\mathrm{raw}}, a_+]$	-0.055	-0.046	-0.076	-0.066
$C[A_{\mathrm{raw}}, a_-]$	0.05	0.05	0.06	0.07
$C[A_{\mathrm{raw}}, f_1]$	-0.002	-0.000	-0.008	-0.001
$C[A_{\mathrm{raw}}, f_{ref}]$	-0.005	0.00	-0.016	0.00
$C[A_{\mathrm{raw}}, N_{\mathrm{bkg}}]$	0.00	-0.005	0.01	0.00
$C[A_{\mathrm{raw}}, N_{\mathrm{sig}}]$	-0.001	0.00	-0.010	-0.000
$C[A_{\mathrm{raw}}, s]$	0.00	0.00	-0.001	0.00

C.1.2 $A_{CP}(K^-K^+)$

All fit parameters of the $A_{CP}(K^-K^+)$ measurement are shown in Tables C.5, C.7, C.9 and C.11. The correlations with the fitted are asymmetry are shown in Tables C.2, C.8, C.10 and C.12.

Table C.5: The fit parameters of the asymmetry fit to the $D^0 \to K^-K^+$ samples. The $A_{CP}(K^-K^+)$ trigger selection is used.

	Up 2011	Down 2011	Up 2012	Down 2012
A_{bkg}	-1.623 ± 0.36	0.01 ± 0.30	-0.688 ± 0.21	-0.200 ± 0.22
A_{raw}	-0.223 ± 0.24	-0.422 ± 0.20	-0.515 ± 0.13	-0.387 ± 0.14
μ	1865.021 ± 0.017	1865.011 ± 0.014	1864.8718 ± 0.0093	1864.8635 ± 0.0096
σ_1	5.310 ± 0.091	5.280 ± 0.070	5.488 ± 0.034	5.486 ± 0.034
$a_+ \times 100$	-0.5783 ± 0.014	-0.5628 ± 0.012	-0.59969 ± 0.0080	-0.58110 ± 0.0085
$a_- \times 100$	-0.5791 ± 0.014	-0.5932 ± 0.012	-0.59401 ± 0.0081	-0.60323 ± 0.0085
f_1	0.584 ± 0.039	0.582 ± 0.031	0.670 ± 0.016	0.673 ± 0.015
N_{bkg}	111363 ± 496	160711 ± 586	331495 ± 853	300484 ± 809
N_{sig}	211511 ± 589	296793 ± 693	681861 ± 1038	635643 ± 995
s	1.593 ± 0.021	1.588 ± 0.018	1.626 ± 0.015	1.635 ± 0.016
$\Delta\mu$	0.00	0.00	0.00	0.00
α	2.70	2.70	2.70	2.70
n	1.50	1.50	1.50	1.50
s_p	1.00	1.00	1.00	1.00

Table C.6: The correlation with A_{raw} of the asymmetry fit to the $D^0 \to K^-K^+$ samples. The $A_{CP}(K^-K^+)$ trigger selection is used.

	Up 2011	Down 2011	Up 2012	Down 2012
$C[A_{\mathrm{raw}}, A_{\mathrm{bkg}}]$	−0.245	−0.246	−0.243	−0.241
$C[A_{\mathrm{raw}}, A_{\mathrm{raw}}]$	1.00	1.00	1.00	1.00
$C[A_{\mathrm{raw}}, \mu]$	0.00	−0.001	−0.001	−0.000
$C[A_{\mathrm{raw}}, \sigma_1]$	0.00	0.00	0.00	−0.001
$C[A_{\mathrm{raw}}, a_+]$	0.03	0.03	0.03	0.03
$C[A_{\mathrm{raw}}, a_-]$	−0.034	−0.034	−0.032	−0.032
$C[A_{\mathrm{raw}}, f_1]$	0.00	0.00	−0.000	−0.002
$C[A_{\mathrm{raw}}, N_{\mathrm{bkg}}]$	0.00	0.00	0.00	0.00
$C[A_{\mathrm{raw}}, N_{\mathrm{sig}}]$	−0.001	−0.001	−0.002	−0.001
$C[A_{\mathrm{raw}}, s]$	0.00	−0.001	−0.002	−0.002

Table C.7: The fit parameters of the asymmetry fit to the $D^0 \to K^-\pi^+$ samples. The $A_{CP}(K^-K^+)$ trigger selection is used.

	Up 2011	Down 2011	Up 2012	Down 2012
A_{bkg}	-1.657 ± 0.67	0.76 ± 0.56	0.05 ± 0.36	0.13 ± 0.37
A_{raw}	-1.703 ± 0.10	-1.6176 ± 0.088	-1.3257 ± 0.057	-1.5784 ± 0.059
$\Delta\mu$	0.008 ± 0.016	0.014 ± 0.014	-0.01999 ± 0.0090	0.0435 ± 0.0093
α	2.187 ± 0.012	2.186 ± 0.011	2.2639 ± 0.0063	2.2717 ± 0.0066
μ	1864.834 ± 0.012	1864.843 ± 0.010	1864.6905 ± 0.0065	1864.6537 ± 0.0067
σ_1	6.390 ± 0.025	6.468 ± 0.023	6.526 ± 0.013	6.474 ± 0.014
$a_+ \times 100$	-0.5535 ± 0.025	-0.5662 ± 0.022	-0.6125 ± 0.013	-0.6335 ± 0.014
$a_- \times 100$	-0.5663 ± 0.025	-0.5576 ± 0.021	-0.5943 ± 0.013	-0.5933 ± 0.014
f_1	0.6715 ± 0.0079	0.6943 ± 0.0074	0.7081 ± 0.0042	0.6940 ± 0.0044
N_{bkg}	57237 ± 548	80753 ± 658	194821 ± 1001	181662 ± 956
N_{sig}	1004847 ± 1117	1415877 ± 1330	3320101 ± 2032	3104010 ± 1959
s	1.6450 ± 0.0076	1.6445 ± 0.0075	1.6649 ± 0.0047	1.6597 ± 0.0046
s_p	0.9944 ± 0.0020	0.9970 ± 0.0017	0.9961 ± 0.0011	1.0017 ± 0.0011
n	1.50	1.50	1.50	1.50

Table C.8: The correlation with A_{raw} of the asymmetry fit to the $D^0 \to K^-\pi^+$ samples. The $A_{CP}(K^-K^+)$ trigger selection is used.

	Up 2011	Down 2011	Up 2012	Down 2012
$C[A_{\text{raw}}, A_{\text{bkg}}]$	−0.221	−0.223	−0.220	−0.219
$C[A_{\text{raw}}, A_{\text{raw}}]$	1.00	1.00	1.00	1.00
$C[A_{\text{raw}}, \Delta\mu]$	0.01	0.01	0.01	0.01
$C[A_{\text{raw}}, \alpha]$	0.00	0.01	0.00	0.00
$C[A_{\text{raw}}, \mu]$	−0.008	−0.009	−0.007	−0.007
$C[A_{\text{raw}}, \sigma_1]$	0.03	0.03	0.03	0.03
$C[A_{\text{raw}}, a_+]$	−0.006	−0.009	−0.001	0.00
$C[A_{\text{raw}}, a_-]$	−0.000	0.00	−0.002	−0.003
$C[A_{\text{raw}}, f_1]$	−0.000	−0.002	−0.003	−0.004
$C[A_{\text{raw}}, N_{\text{bkg}}]$	0.00	0.00	0.00	0.00
$C[A_{\text{raw}}, N_{\text{sig}}]$	−0.001	−0.000	−0.001	−0.001
$C[A_{\text{raw}}, s]$	0.00	0.00	−0.001	−0.002
$C[A_{\text{raw}}, s_p]$	−0.119	−0.119	−0.119	−0.118

Table C.9: The fit parameters of the asymmetry fit to the $D^+ \to K^-\pi^+\pi^+$ samples. The $A_{CP}(K^-K^+)$ trigger selection is used.

	Up 2011	Down 2011	Up 2012	Down 2012
A_{bkg}	-1.811 ± 0.70	1.32 ± 0.58	-0.414 ± 0.32	-0.066 ± 0.33
A_{raw}	-2.1871 ± 0.076	-1.6014 ± 0.063	-1.9200 ± 0.036	-1.6918 ± 0.038
$\Delta\mu$	0.093 ± 0.011	0.1640 ± 0.0093	0.0094 ± 0.0054	0.1738 ± 0.0056
α	2.3587 ± 0.0072	2.3503 ± 0.0058	2.3357 ± 0.0034	2.3361 ± 0.0036
μ	1869.4601 ± 0.0082	1869.4163 ± 0.0067	1869.3790 ± 0.0039	1869.2926 ± 0.0040
σ_1	6.020 ± 0.016	5.994 ± 0.013	6.0312 ± 0.0078	6.0168 ± 0.0082
$a_+ \times 100$	-0.2447 ± 0.029	-0.2276 ± 0.025	-0.2350 ± 0.013	-0.2499 ± 0.014
$a_- \times 100$	-0.2462 ± 0.029	-0.2453 ± 0.024	-0.2330 ± 0.013	-0.2553 ± 0.014
f_1	0.6562 ± 0.0054	0.6548 ± 0.0043	0.6458 ± 0.0026	0.6433 ± 0.0027
N_{bkg}	59348 ± 699	87077 ± 860	292021 ± 1553	271083 ± 1494
N_{sig}	1821028 ± 1500	2672258 ± 1824	8124785 ± 3201	7537526 ± 3083
s	1.6198 ± 0.0049	1.6236 ± 0.0040	1.6148 ± 0.0023	1.6144 ± 0.0024
s_p	0.9940 ± 0.0014	0.9987 ± 0.0012	0.99457 ± 0.00066	1.00043 ± 0.00069
n	0.90	0.90	0.90	0.90

Table C.10: The correlation with A_{raw} of the asymmetry fit to the $D^+ \to K^-\pi^+\pi^+$ samples. The $A_{CP}(K^-K^+)$ trigger selection is used.

	Up 2011	Down 2011	Up 2012	Down 2012
$C[A_{\mathrm{raw}}, A_{\mathrm{bkg}}]$	-0.198	-0.199	-0.204	-0.204
$C[A_{\mathrm{raw}}, A_{\mathrm{raw}}]$	1.00	1.00	1.00	1.00
$C[A_{\mathrm{raw}}, \Delta\mu]$	0.00	0.01	0.01	0.01
$C[A_{\mathrm{raw}}, \alpha]$	0.00	0.01	0.01	0.01
$C[A_{\mathrm{raw}}, \mu]$	-0.004	-0.004	-0.005	-0.005
$C[A_{\mathrm{raw}}, \sigma_1]$	0.02	0.02	0.02	0.02
$C[A_{\mathrm{raw}}, a_+]$	-0.019	-0.024	-0.022	-0.021
$C[A_{\mathrm{raw}}, a_-]$	0.01	0.01	0.01	0.01
$C[A_{\mathrm{raw}}, f_1]$	-0.000	-0.003	-0.004	-0.003
$C[A_{\mathrm{raw}}, N_{\mathrm{bkg}}]$	0.00	0.00	0.00	0.01
$C[A_{\mathrm{raw}}, N_{\mathrm{sig}}]$	-0.001	-0.002	-0.002	-0.003
$C[A_{\mathrm{raw}}, s]$	0.00	0.00	0.00	0.00
$C[A_{\mathrm{raw}}, s_p]$	-0.083	-0.083	-0.087	-0.087

Table C.11: The fit parameters of the asymmetry fit to the $D^+ \to \overline{K}^0\pi^+$ samples. The $A_{CP}(K^-K^+)$ trigger selection is used.

	Up 2011	Down 2011	Up 2012	Down 2012
A_{bkg}	0.0 ± 1.8	1.8 ± 1.5	0.52 ± 0.99	0.5 ± 1.0
A_{raw}	-0.711 ± 0.35	-0.551 ± 0.27	-1.016 ± 0.19	-0.457 ± 0.20
$\Delta\mu$	0.032 ± 0.056	0.155 ± 0.044	0.063 ± 0.031	0.147 ± 0.032
μ	1869.238 ± 0.040	1869.164 ± 0.031	1869.111 ± 0.022	1869.055 ± 0.023
σ_1	6.55 ± 0.12	6.935 ± 0.067	6.796 ± 0.046	6.557 ± 0.066
$a_+ \times 100$	-0.5160 ± 0.059	-0.6353 ± 0.052	-0.5903 ± 0.034	-0.5811 ± 0.034
$a_- \times 100$	-0.6207 ± 0.060	-0.5718 ± 0.050	-0.4828 ± 0.033	-0.5459 ± 0.034
f_1	0.628 ± 0.036	0.772 ± 0.020	0.729 ± 0.015	0.667 ± 0.020
N_{bkg}	7511 ± 166	11181 ± 237	24078 ± 309	22751 ± 299
N_{sig}	92678 ± 336	152246 ± 444	299855 ± 609	281954 ± 590
s	1.627 ± 0.023	1.748 ± 0.038	1.689 ± 0.020	1.674 ± 0.015
s_p	0.9951 ± 0.0066	1.0013 ± 0.0052	0.9943 ± 0.0036	1.0002 ± 0.0038
α	2.50	2.50	2.50	2.50
n	1.50	1.50	1.50	1.50

Table C.12: The correlation with A_{raw} of the asymmetry fit to the $D^+ \to \overline{K}^0\pi^+$ samples. The $A_{CP}(K^-K^+)$ trigger selection is used.

	Up 2011	Down 2011	Up 2012	Down 2012
$C[A_{\text{raw}}, A_{\text{bkg}}]$	−0.233	−0.242	−0.239	−0.237
$C[A_{\text{raw}}, A_{\text{raw}}]$	1.00	1.00	1.00	1.00
$C[A_{\text{raw}}, \Delta\mu]$	0.01	0.01	0.00	0.01
$C[A_{\text{raw}}, \mu]$	−0.005	−0.005	−0.003	−0.005
$C[A_{\text{raw}}, \sigma_1]$	0.03	0.04	0.04	0.03
$C[A_{\text{raw}}, a_+]$	0.05	0.06	0.05	0.05
$C[A_{\text{raw}}, a_-]$	−0.058	−0.051	−0.047	−0.050
$C[A_{\text{raw}}, f_1]$	0.00	0.00	0.00	0.00
$C[A_{\text{raw}}, N_{\text{bkg}}]$	−0.006	−0.004	−0.008	−0.002
$C[A_{\text{raw}}, N_{\text{sig}}]$	0.00	0.00	0.00	0.00
$C[A_{\text{raw}}, s]$	0.01	0.00	0.01	0.00
$C[A_{\text{raw}}, s_p]$	−0.143	−0.143	−0.143	−0.146

Appendix D

Addendum to consistency checks

D.1 Cross-checks in the semileptonic *B* decay modes

The corresponding plots of the ΔA_{CP} cross-checks presented in Chapter 12.5 are shown in Figures D.1 to D.15. It should be noted that individual asymmetries are affected by production and detection asymmetries. Especially, the raw asymmetry of muon-tagged $D^0 \rightarrow K^-\pi^+$ candidates has large contributions from the momentum-dependent kaon detection asymmetry.

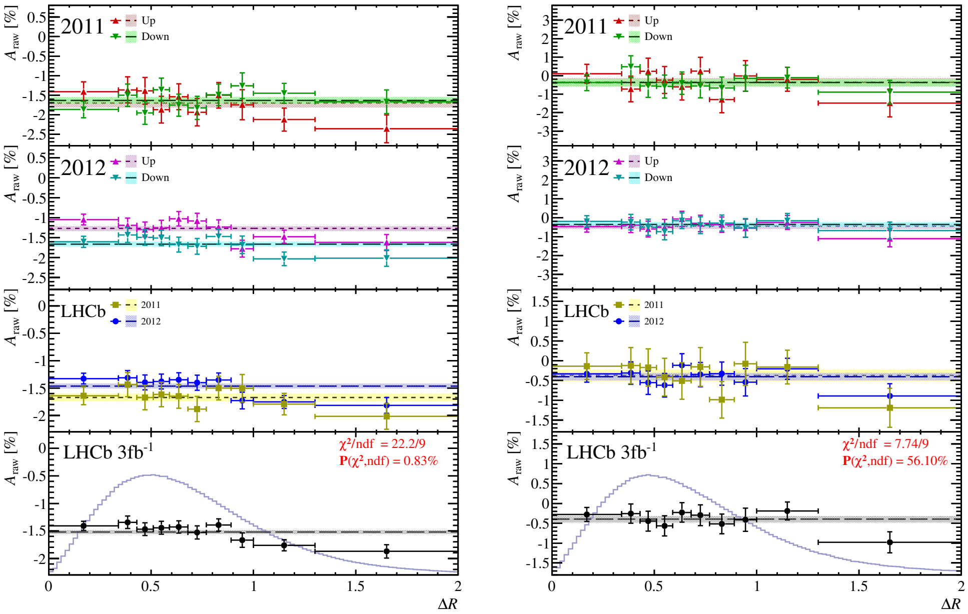

(a) $D^0 \rightarrow K^-\pi^+$ (b) $D^0 \rightarrow K^-K^+$

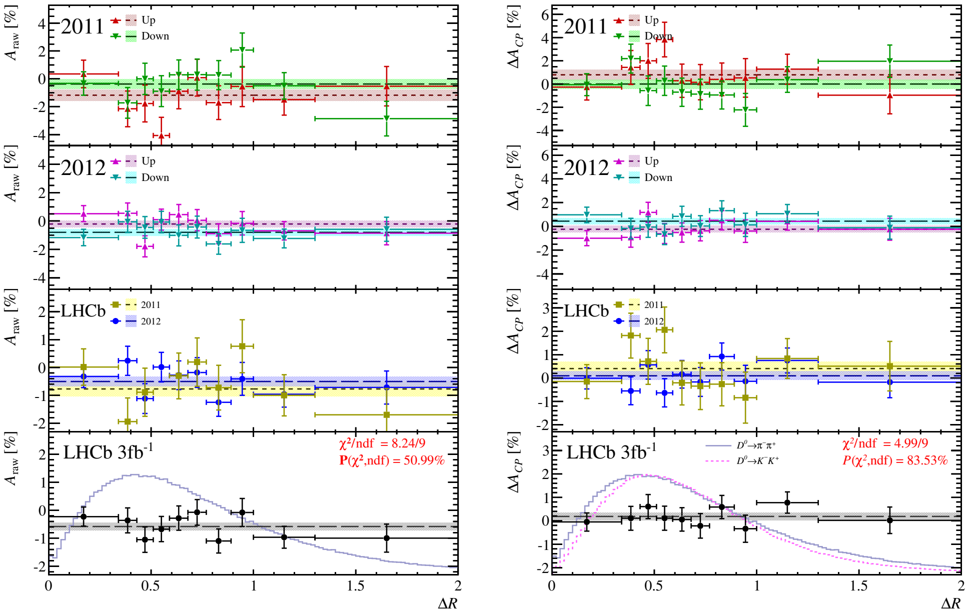

(c) $D^0 \rightarrow \pi^-\pi^+$ (d) ΔA_{CP}

Figure D.1: The raw asymmetry and ΔA_{CP} is shown as function of min(ΔR). The shaded lines indicate the result of the asymmetry fit to the total distribution. The default combination of the data sets is done.

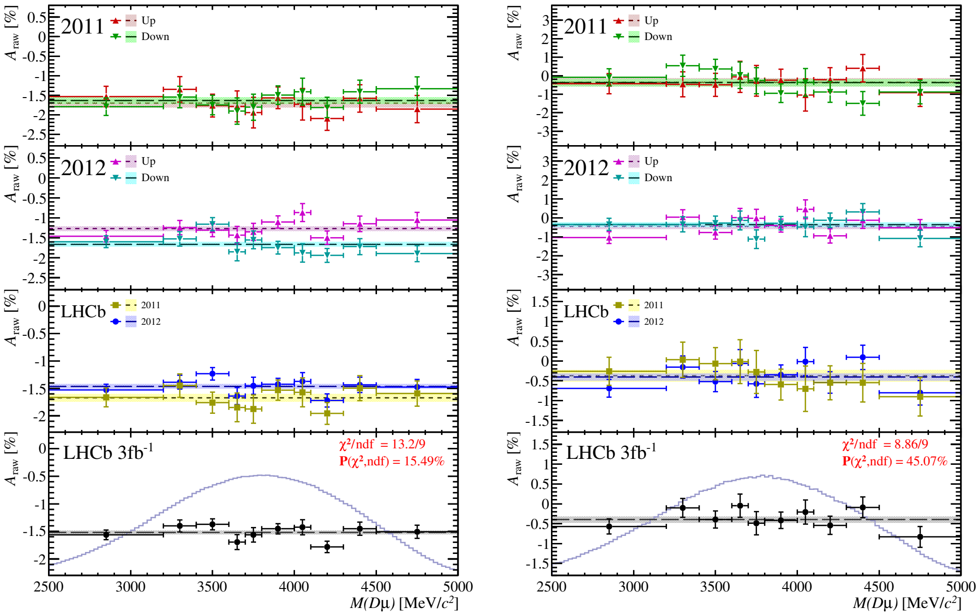

(a) $D^0 \to K^-\pi^+$ (b) $D^0 \to K^-K^+$

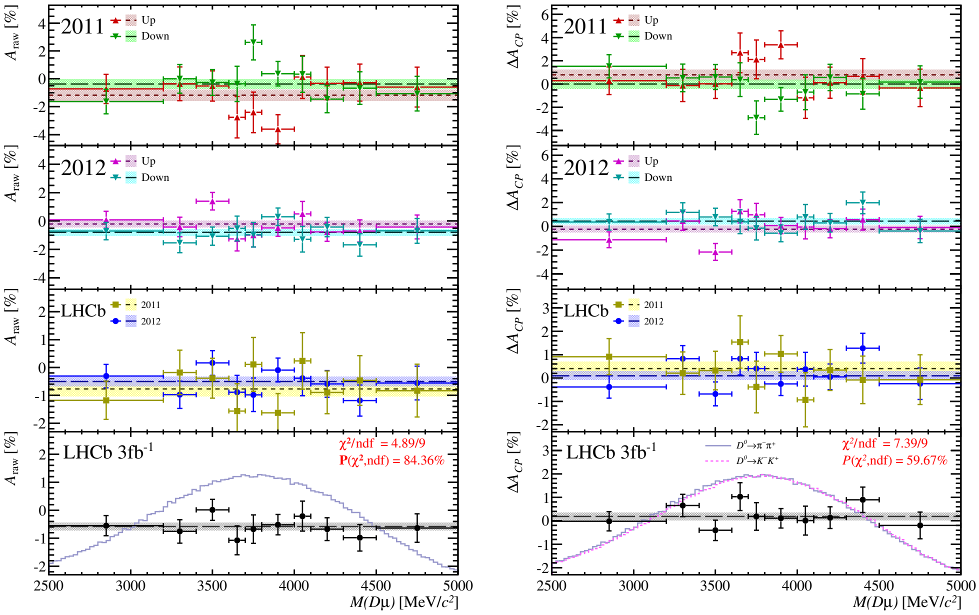

(c) $D^0 \to \pi^-\pi^+$ (d) ΔA_{CP}

Figure D.2: The raw asymmetry and ΔA_{CP} is shown as function of $m_{D^0\mu}$. The shaded lines indicate the result of the asymmetry fit to the total distribution. The default combination of the data sets is done.

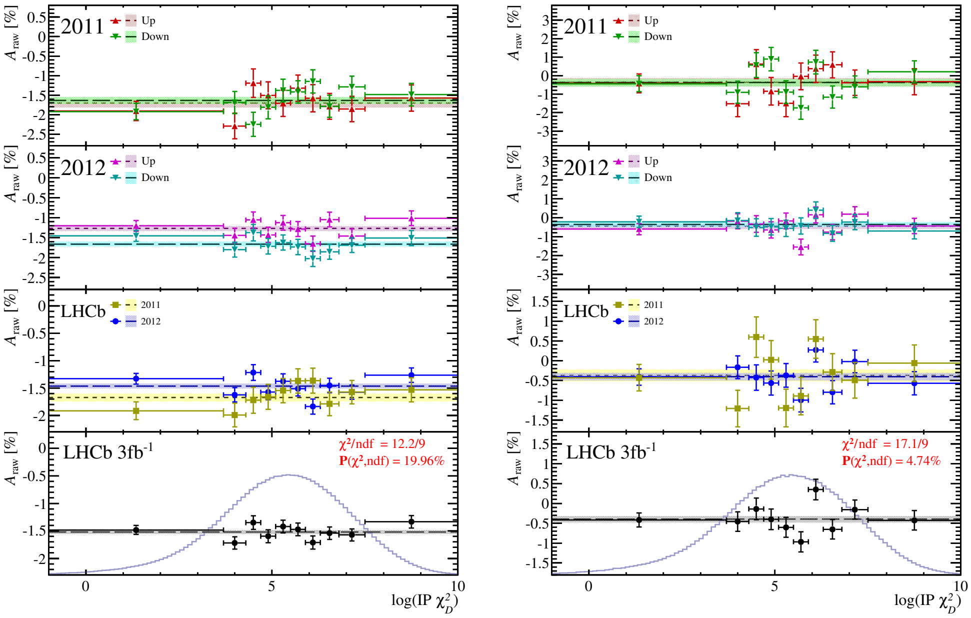

(a) $D^0 \to K^-\pi^+$ (b) $D^0 \to K^-K^+$

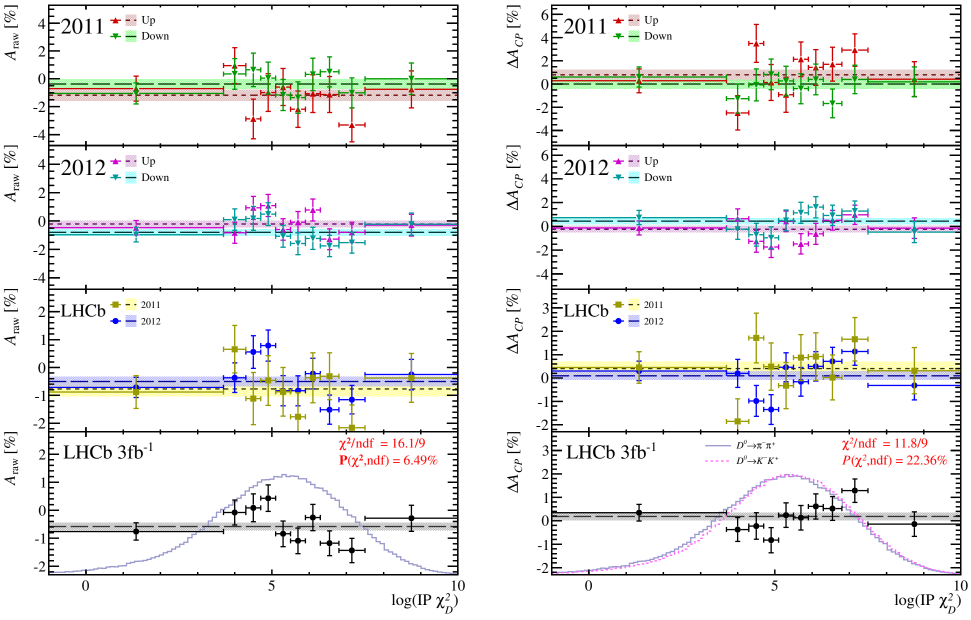

(c) $D^0 \to \pi^-\pi^+$ (d) ΔA_{CP}

Figure D.3: The raw asymmetry and ΔA_{CP} is shown as function of IP$\chi^2_{D^0}$. The shaded lines indicate the result of the asymmetry fit to the total distribution. The default combination of the data sets is done.

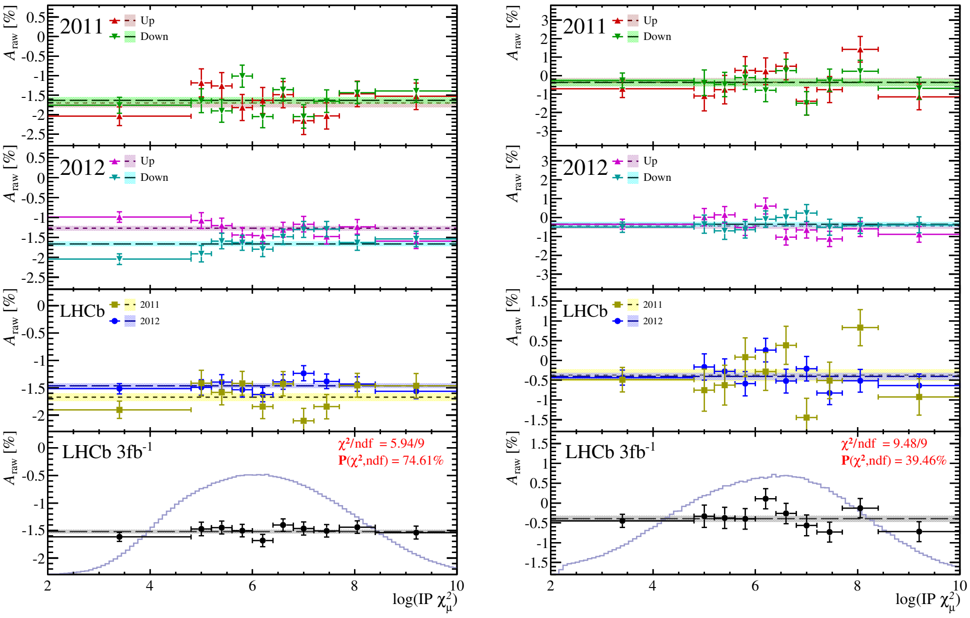

(a) $D^0 \to K^-\pi^+$ (b) $D^0 \to K^-K^+$

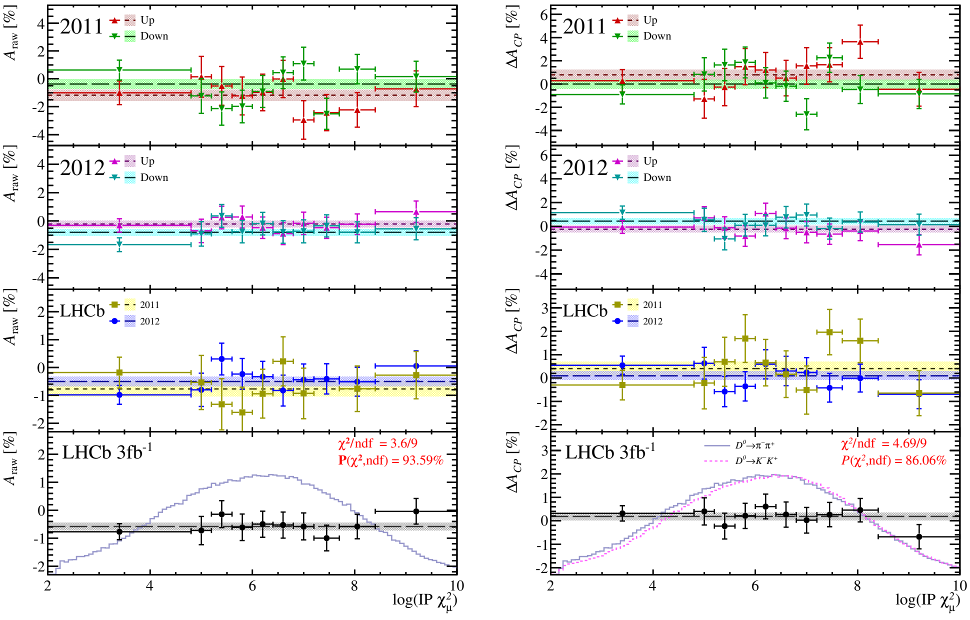

(c) $D^0 \to \pi^-\pi^+$ (d) ΔA_{CP}

Figure D.4: The raw asymmetry and ΔA_{CP} is shown as function of IPχ^2_μ. The shaded lines indicate the result of the asymmetry fit to the total distribution. The default combination of the data sets is done.

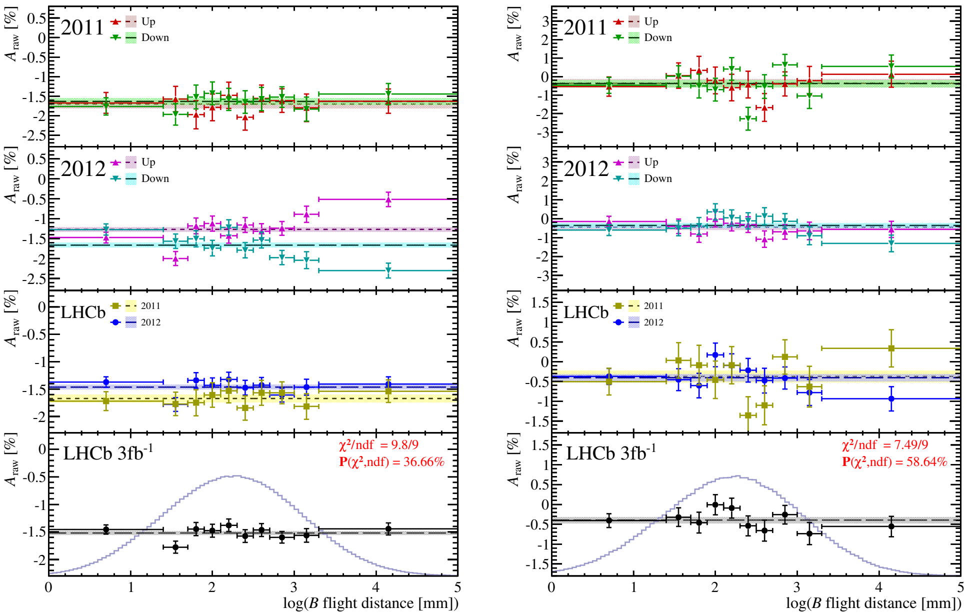

(a) $D^0 \to K^-\pi^+$ (b) $D^0 \to K^-K^+$

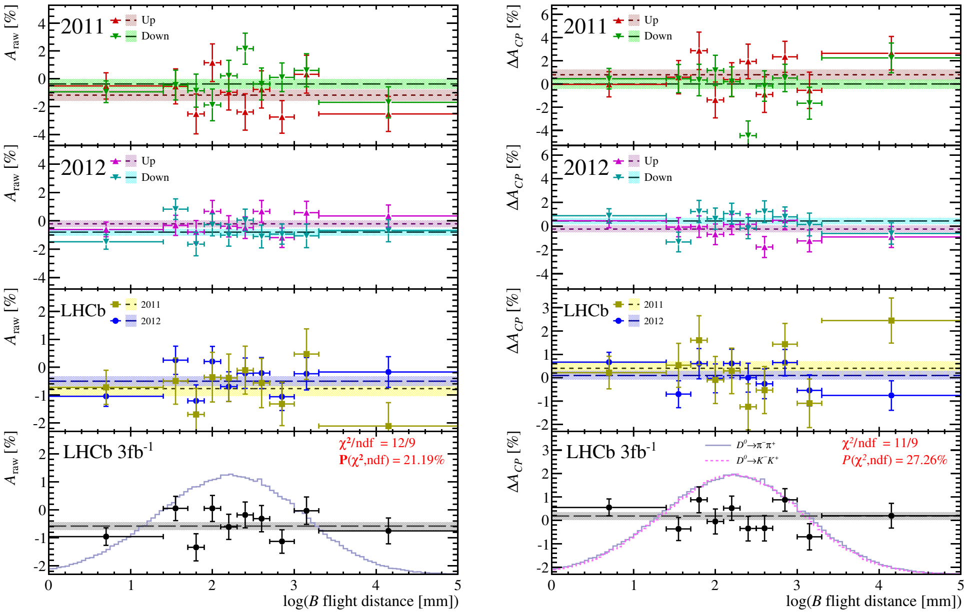

(c) $D^0 \to \pi^-\pi^+$ (d) ΔA_{CP}

Figure D.5: The raw asymmetry and ΔA_{CP} is shown as function of B flight distance. The shaded lines indicate the result of the asymmetry fit to the total distribution. The default combination of the data sets is done.

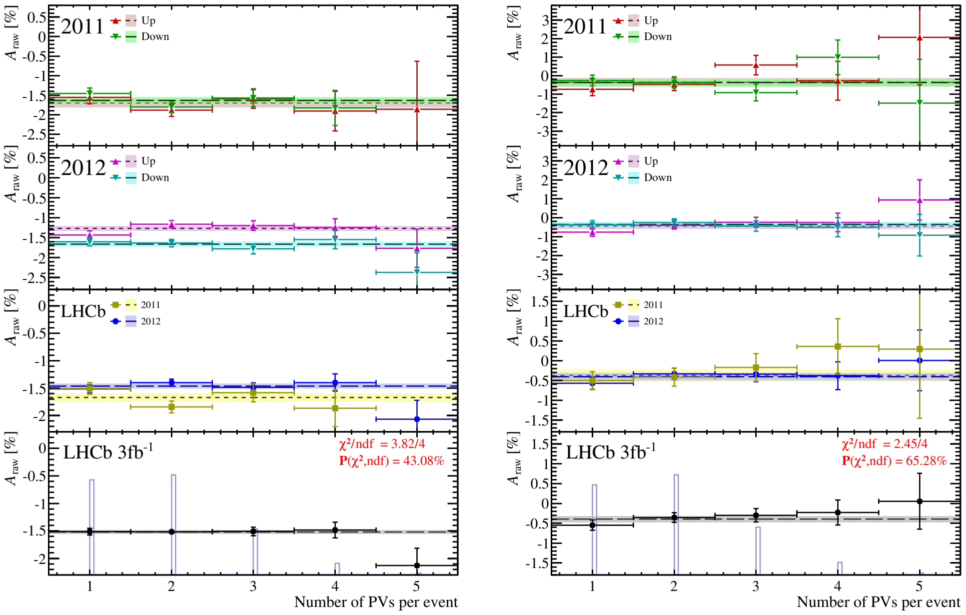

(a) $D^0 \to K^-\pi^+$ (b) $D^0 \to K^-K^+$

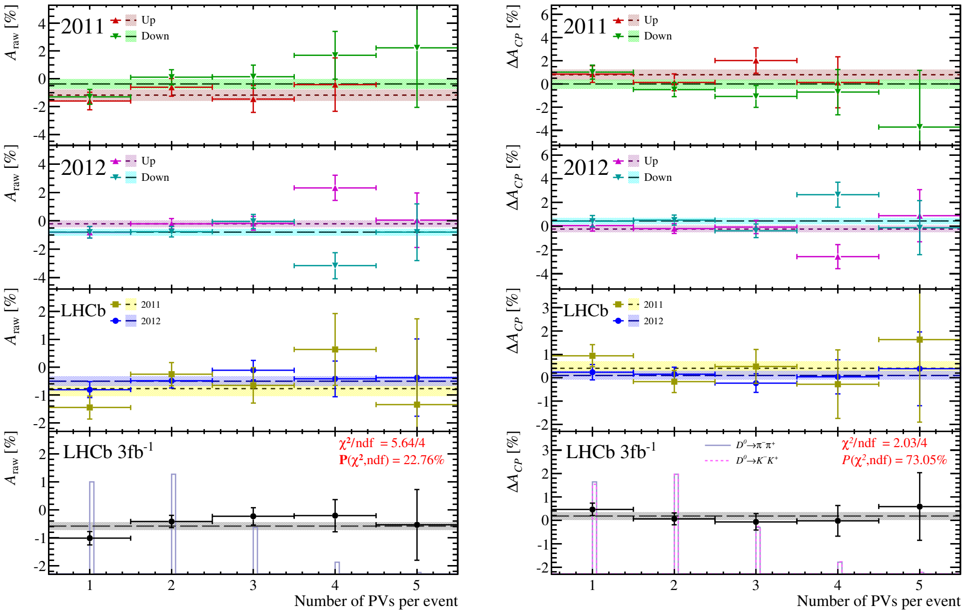

(c) $D^0 \to \pi^-\pi^+$ (d) ΔA_{CP}

Figure D.6: The raw asymmetry and ΔA_{CP} is shown as function of number of PVs per event. The shaded lines indicate the result of the asymmetry fit to the total distribution. The default combination of the data sets is done.

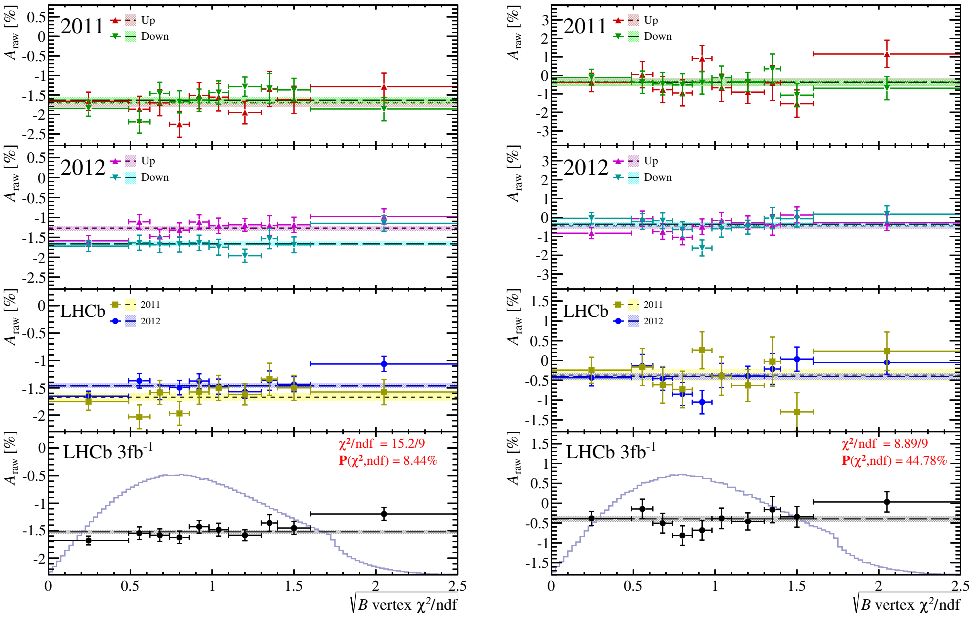

(a) $D^0 \to K^-\pi^+$ (b) $D^0 \to K^-K^+$

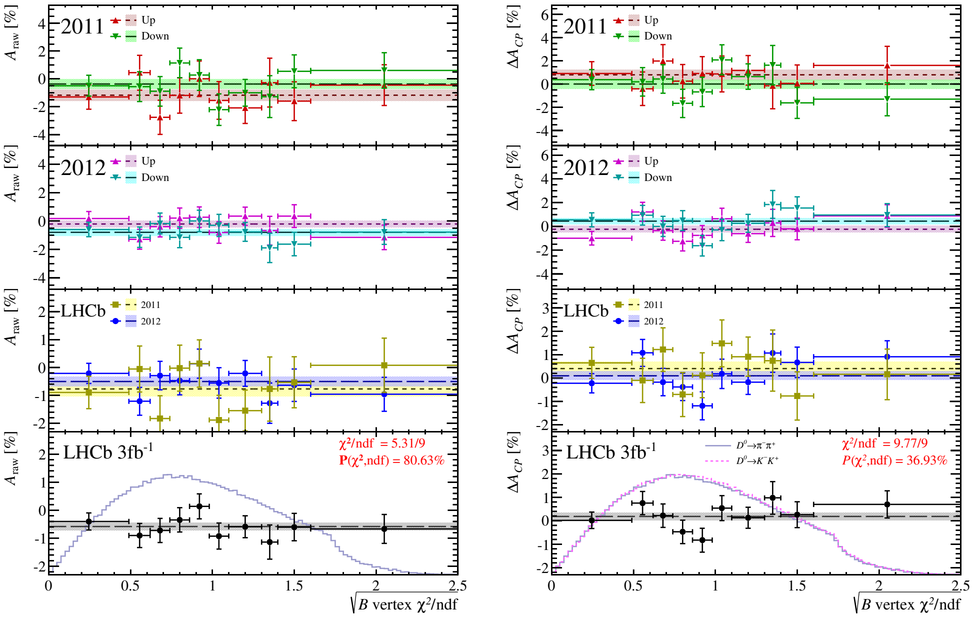

(c) $D^0 \to \pi^-\pi^+$ (d) ΔA_{CP}

Figure D.7: The raw asymmetry and ΔA_{CP} is shown as function of $\sqrt{\chi^2/\text{ndf}}$ of the fitted B vertex. The shaded lines indicate the result of the asymmetry fit to the total distribution. The default combination of the data sets is done.

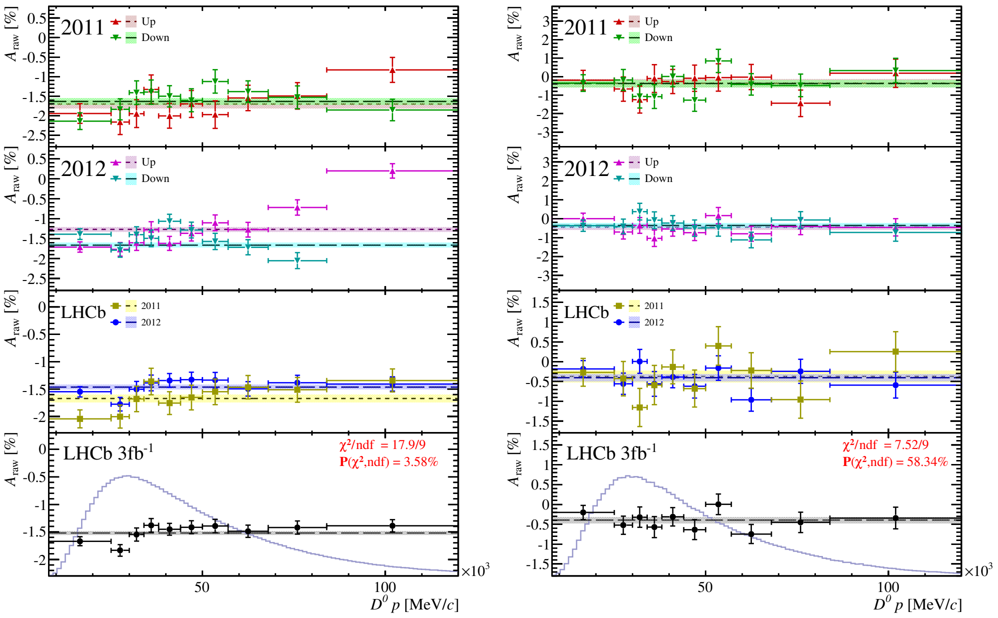

(a) $D^0 \to K^-\pi^+$ (b) $D^0 \to K^-K^+$

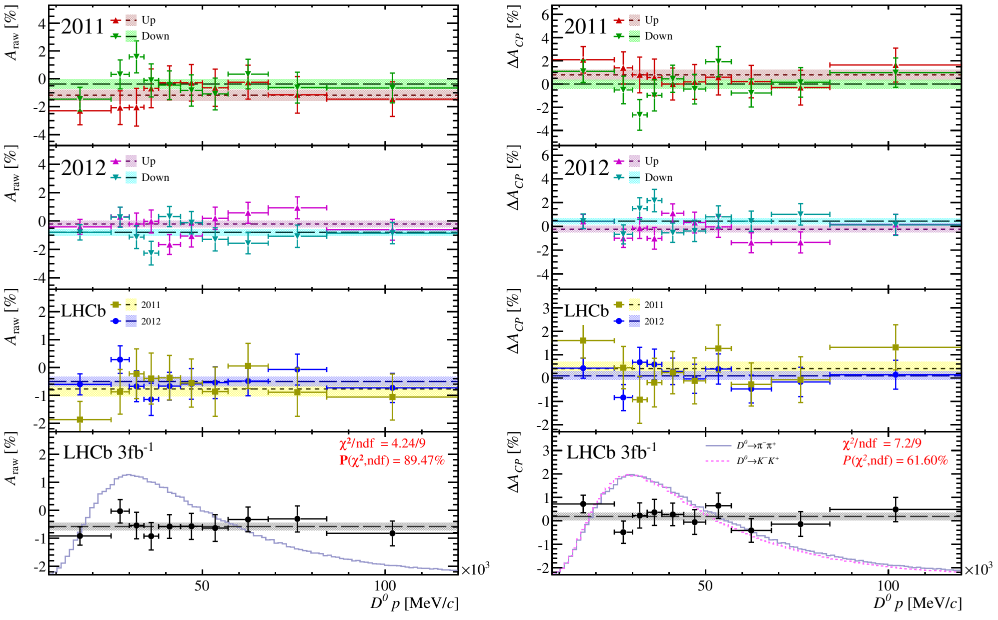

(c) $D^0 \to \pi^-\pi^+$ (d) ΔA_{CP}

Figure D.8: The ΔA_{CP} is shown as function of the D^0 kinematics. The shaded lines indicate the result of the asymmetry fit to the total distribution. The default combination of the data sets is done.

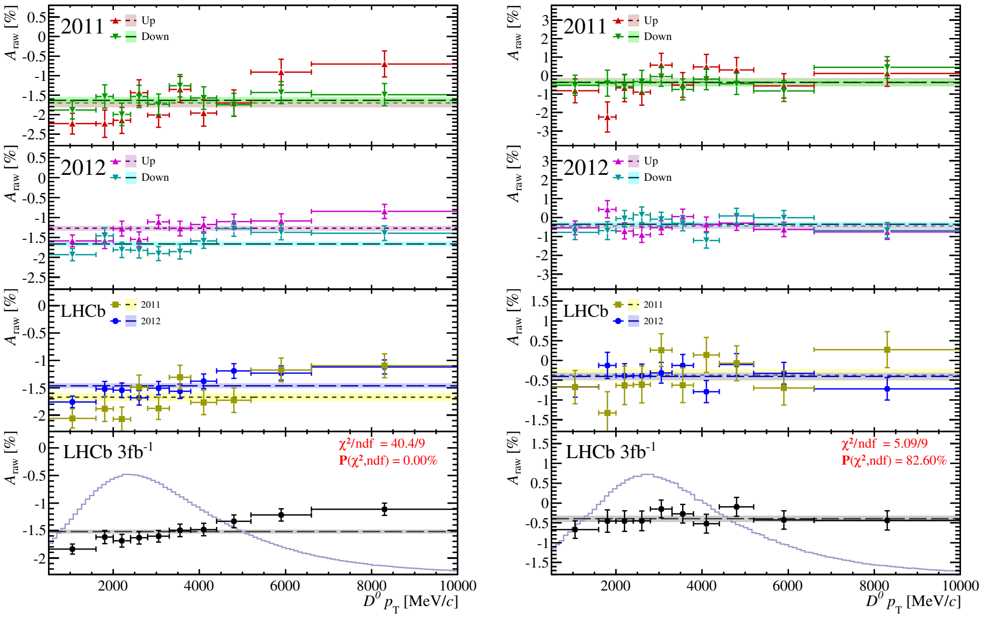

(a) $D^0 \to K^-\pi^+$ (b) $D^0 \to K^-K^+$

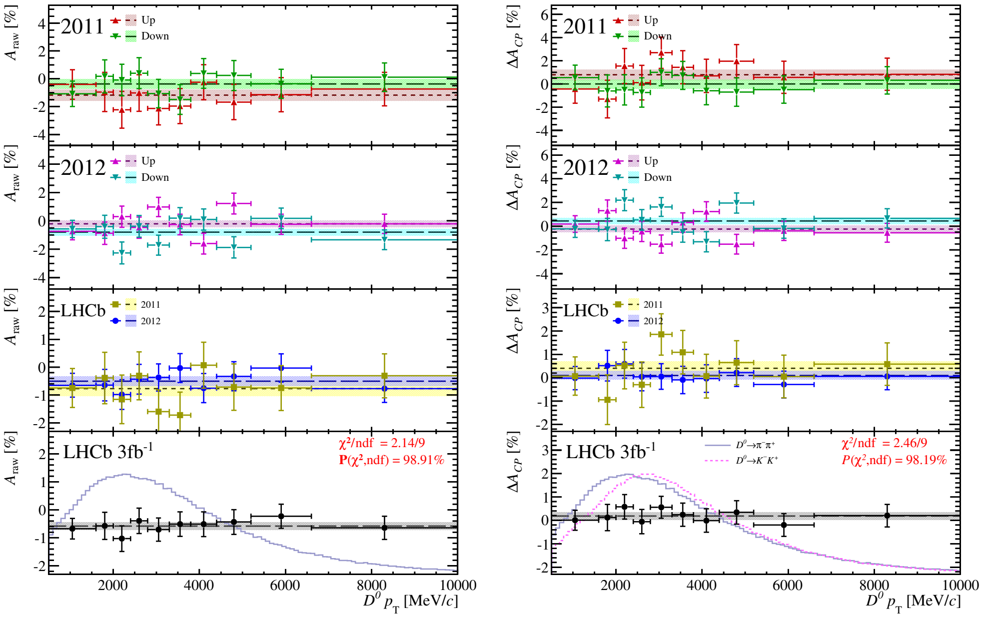

(c) $D^0 \to \pi^-\pi^+$ (d) ΔA_{CP}

Figure D.9: The ΔA_{CP} is shown as function of the D^0 kinematics. The shaded lines indicate the result of the asymmetry fit to the total distribution. The default combination of the data sets is done.

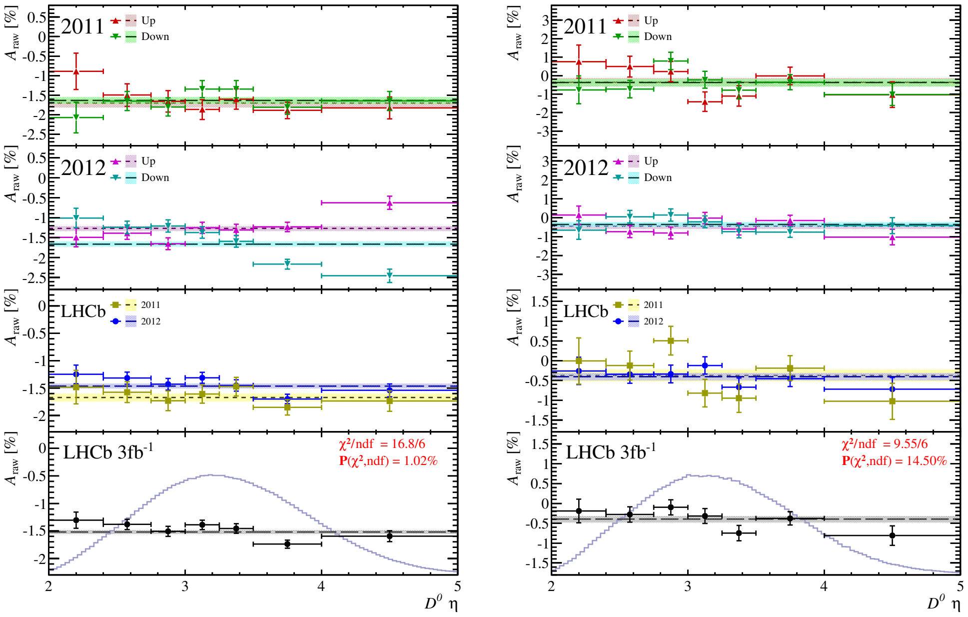

(a) $D^0 \to K^-\pi^+$ (b) $D^0 \to K^-K^+$

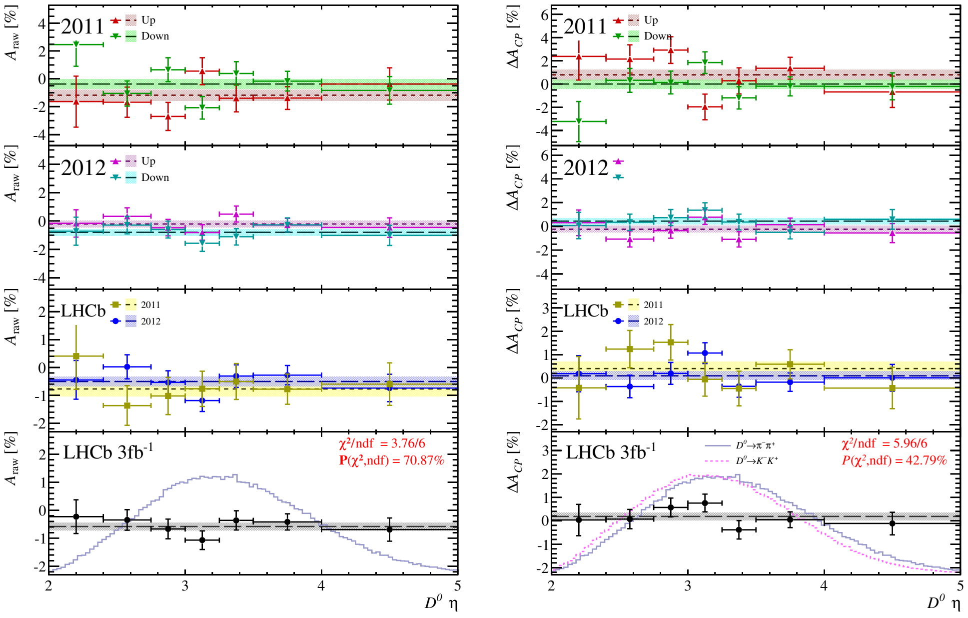

(c) $D^0 \to \pi^-\pi^+$ (d) ΔA_{CP}

Figure D.10: The ΔA_{CP} is shown as function of the D^0 kinematics. The shaded lines indicate the result of the asymmetry fit to the total distribution. The default combination of the data sets is done.

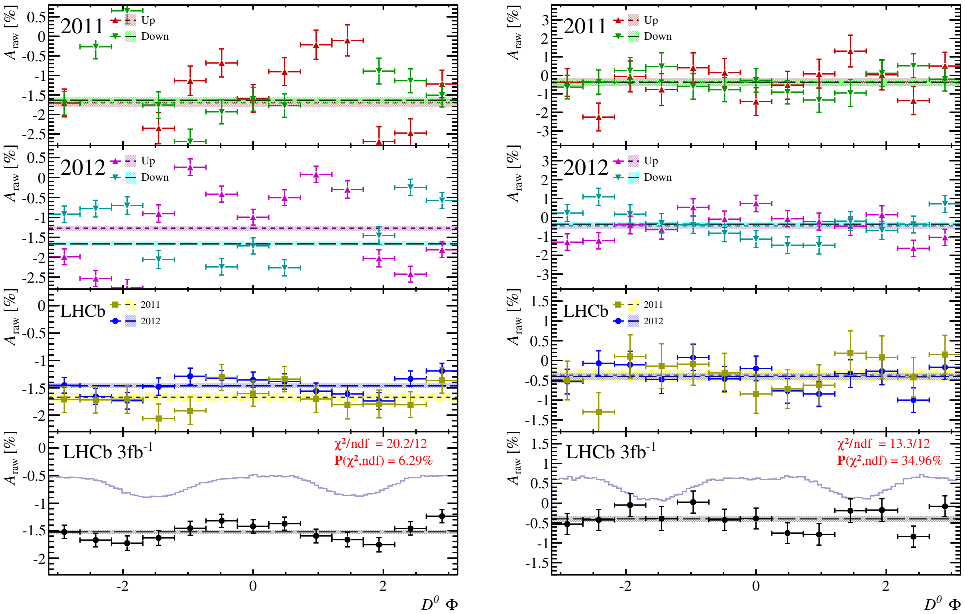

(a) $D^0 \to K^-\pi^+$ (b) $D^0 \to K^-K^+$

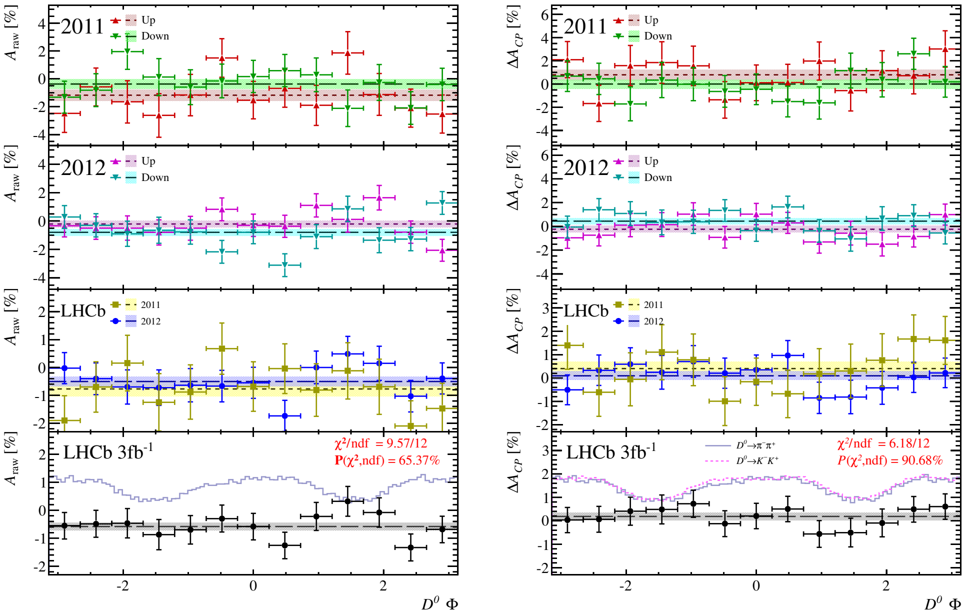

(c) $D^0 \to \pi^-\pi^+$ (d) ΔA_{CP}

Figure D.11: The ΔA_{CP} is shown as function of the D^0 kinematics. The shaded lines indicate the result of the asymmetry fit to the total distribution. The default combination of the data sets is done.

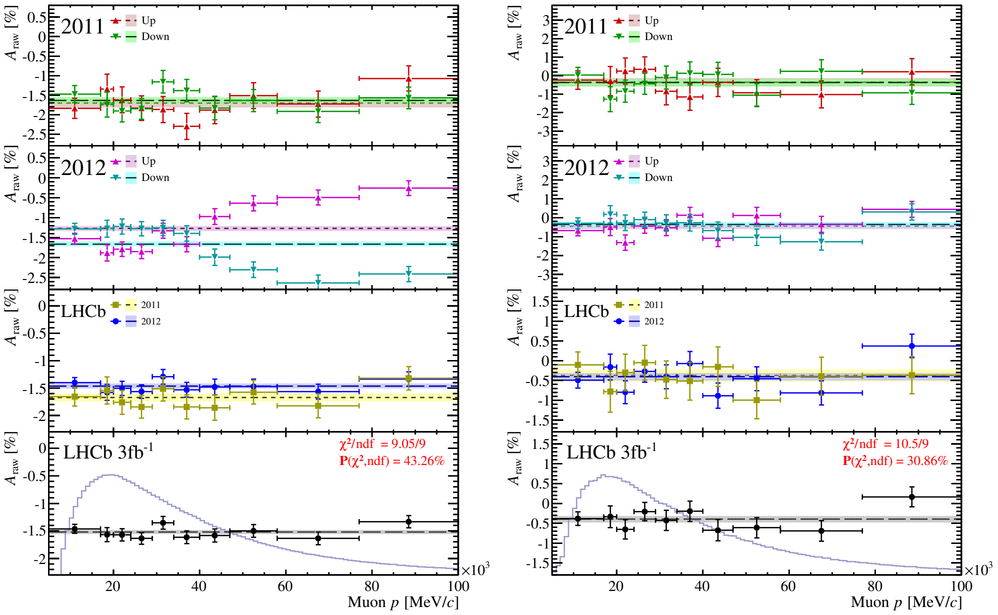

(a) $D^0 \rightarrow K^-\pi^+$ (b) $D^0 \rightarrow K^-K^+$

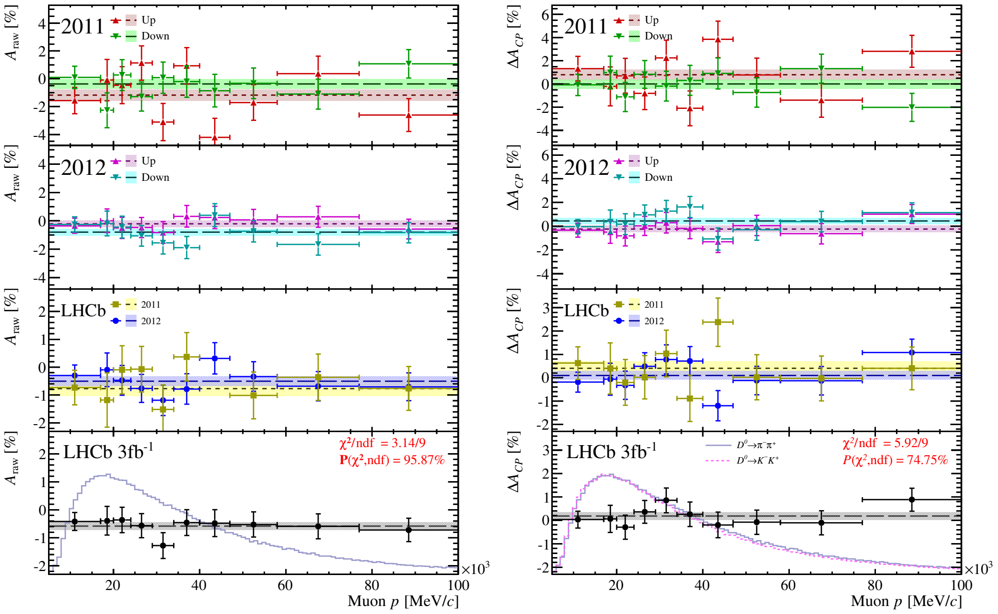

(c) $D^0 \rightarrow \pi^-\pi^+$ (d) ΔA_{CP}

Figure D.12: The ΔA_{CP} is shown as function of the D^0 kinematics. The shaded lines indicate the result of the asymmetry fit to the total distribution. The default combination of the data sets is done.

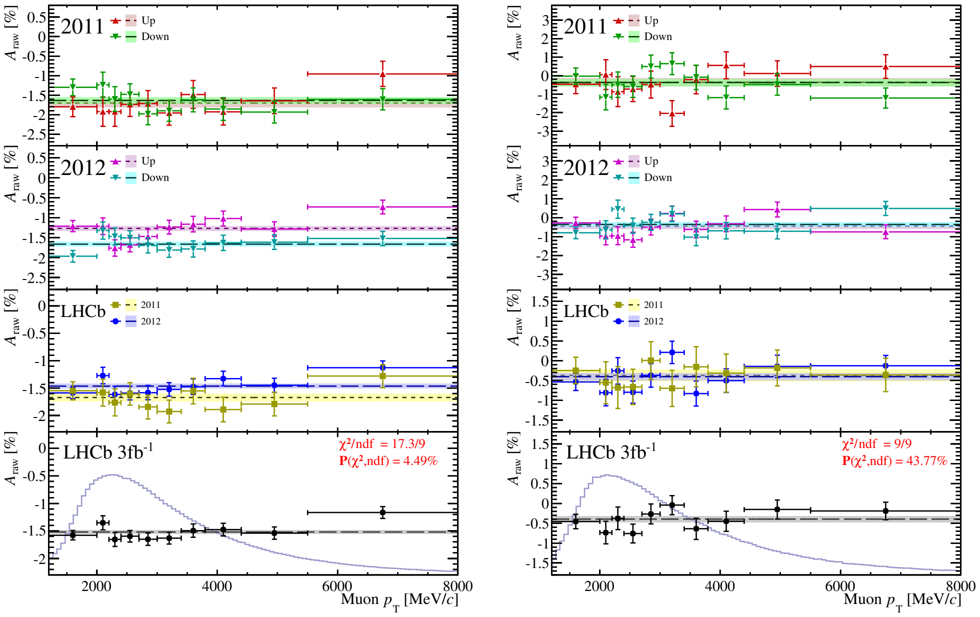

(a) $D^0 \to K^-\pi^+$ (b) $D^0 \to K^-K^+$

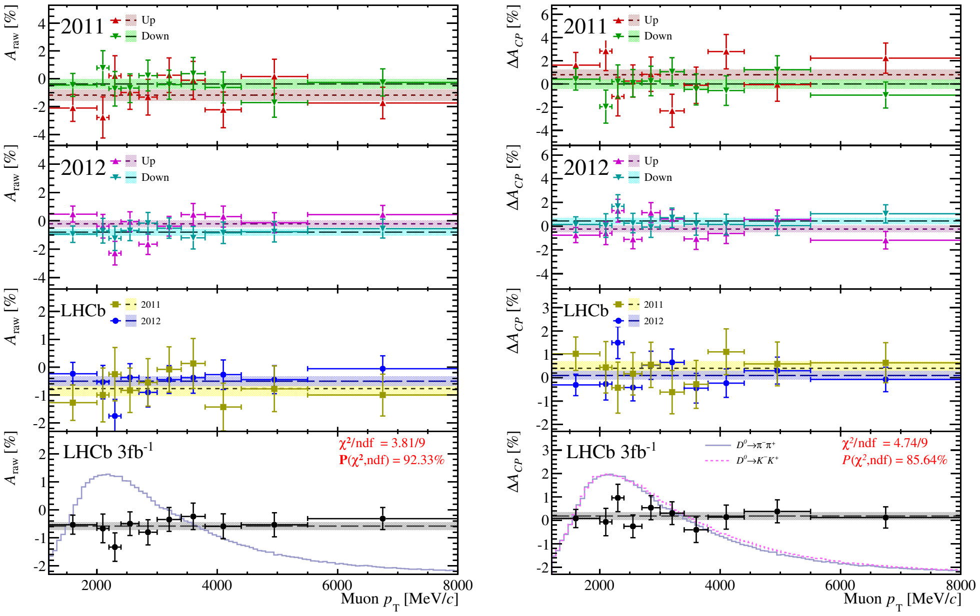

(c) $D^0 \to \pi^-\pi^+$ (d) ΔA_{CP}

Figure D.13: The ΔA_{CP} is shown as function of the D^0 kinematics. The shaded lines indicate the result of the asymmetry fit to the total distribution. The default combination of the data sets is done.

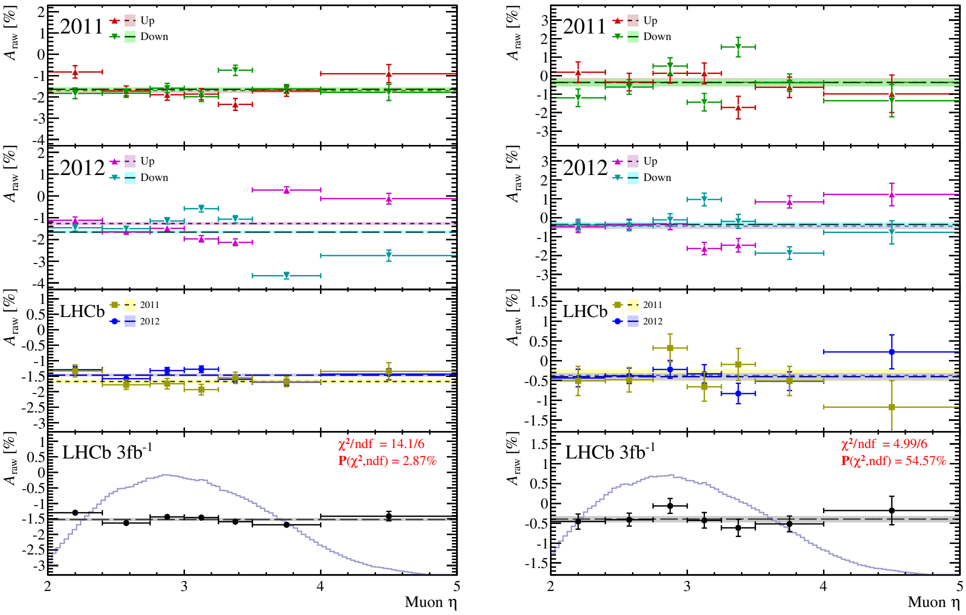

(a) $D^0 \to K^-\pi^+$ (b) $D^0 \to K^-K^+$

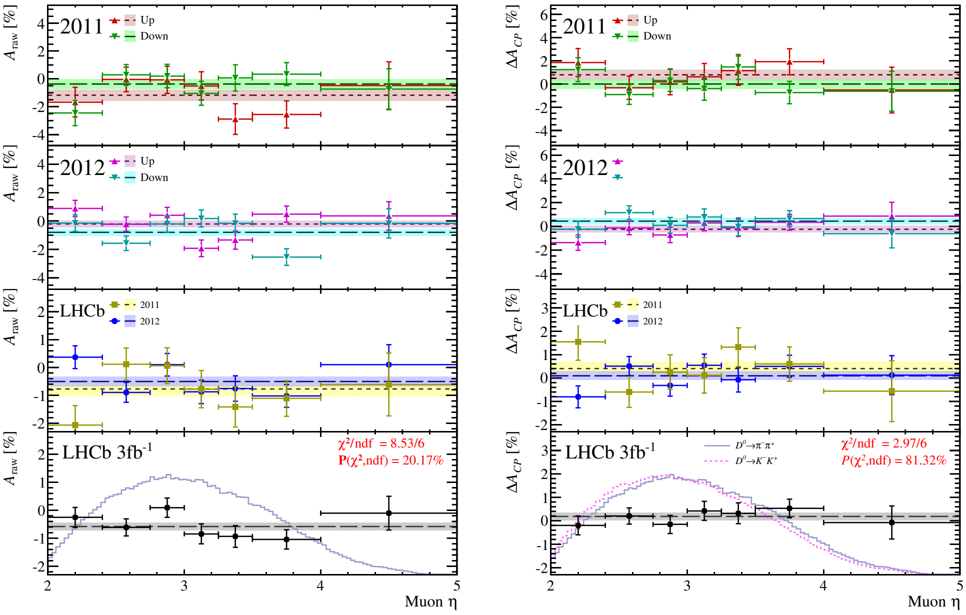

(c) $D^0 \to \pi^-\pi^+$ (d) ΔA_{CP}

Figure D.14: The ΔA_{CP} is shown as function of the D^0 kinematics. The shaded lines indicate the result of the asymmetry fit to the total distribution. The default combination of the data sets is done.

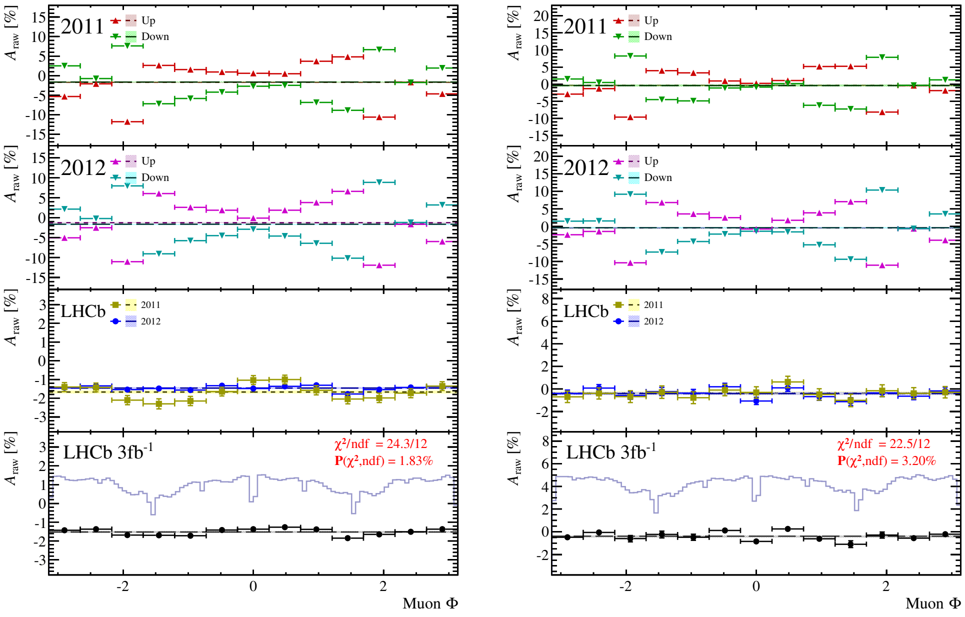

(a) $D^0 \to K^-\pi^+$ (b) $D^0 \to K^-K^+$

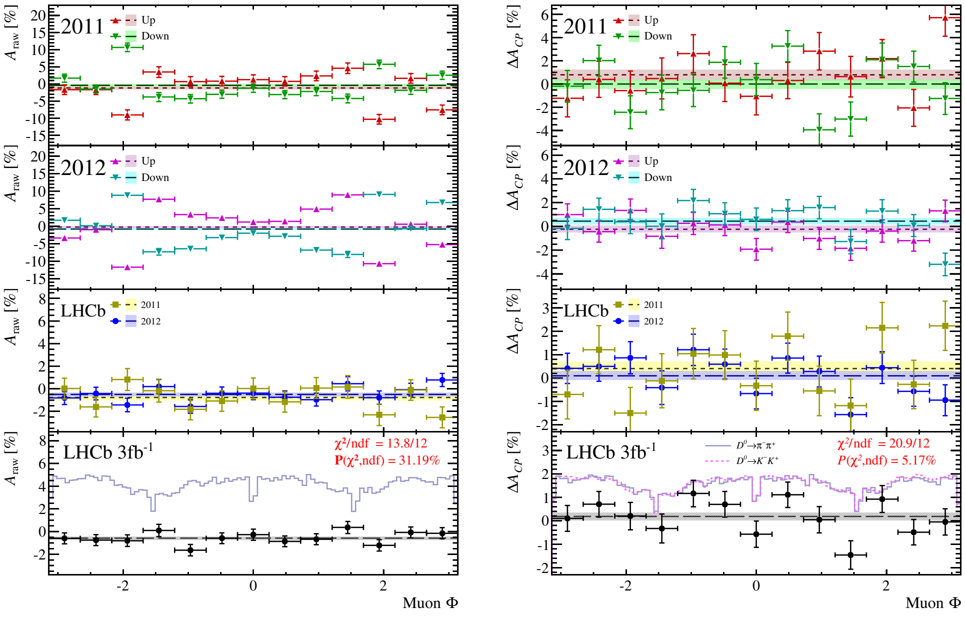

(c) $D^0 \to \pi^-\pi^+$ (d) ΔA_{CP}

Figure D.15: The ΔA_{CP} is shown as function of the D^0 kinematics. The shaded lines indicate the result of the asymmetry fit to the total distribution. The default combination of the data sets is done.

APPENDIX E

The *sPlot* technique

The *sPlot* technique [74] can be used to unfold the contributions of signal and background events to the distribution of a given *control variable*, x. The *discriminant variable*, m, is usually the invariant mass of a candidate.

The density function, $f(m,x)$, can be written as

$$f(m,x) = N_\mathrm{s}\, f_\mathrm{s}(m,x) + N_\mathrm{b}\, f_\mathrm{b}(m,x) \quad , \tag{E.1}$$

where N_s and N_b are the yields of the signal and the background contribution, and $f_\mathrm{s}(m,x)$ and $f_\mathrm{b}(m,x)$ are normalized functions describing the signal and the background distributions. If $f_\mathrm{s}(m,x)$ and $f_\mathrm{b}(m,x)$ factorize as functions of m and x, Equation E.1 can be written as

$$f(m,x) = N_\mathrm{s}\, f_\mathrm{s}(m)\, f_\mathrm{s}(x) + N_\mathrm{b}\, f_\mathrm{b}(m)\, f_\mathrm{b}(x) \quad , \tag{E.2}$$

where N_s, $f_\mathrm{s}(m)$, N_b and $f_\mathrm{b}(m)$ are known. They are usually obtained from an extended maximum-likelihood fit to the distribution $f(m)$. The function $f_\mathrm{s}(x)$ is the distribution of interest. In this case, a weight function, $w_\mathrm{s}(m)$, can be defined by

$$\begin{aligned} \int w_\mathrm{s}(m) f(m,x)\,\mathrm{d}m &= \int w_\mathrm{s}(m)\left[N_\mathrm{s}\, f_\mathrm{s}(m)\, f_\mathrm{s}(x) + N_\mathrm{b}\, f_\mathrm{b}(m)\, f_\mathrm{b}(x)\right]\,\mathrm{d}m \\ &= N_\mathrm{s}\, f_\mathrm{s}(x) \quad . \end{aligned} \tag{E.3}$$

This means that the signal distribution $f_\mathrm{s}(x)$ of the control variable x can be projected out of $f(m,x)$ if the weight function $w_\mathrm{s}(m)$ is known.[1] Equation E.3 implies that

$$\int w_\mathrm{s}(m)\, f_\mathrm{s}(m)\,\mathrm{d}m = 1 \text{ and } \int w_\mathrm{s}(m)\, f_\mathrm{b}(m)\,\mathrm{d}m = 0 \quad . \tag{E.4}$$

In principle, any function $w_\mathrm{s}(m)$ which is orthogonal to $f_\mathrm{b}(m)$ but not orthogonal to $f_\mathrm{s}(m)$ can be used. One choice of $w_\mathrm{s}(m)$ are the weights defined by the sideband subtraction used in Chapter 8.1. In the *sPlot* technique the weights, often called *sWeights*, are chosen to minimise the statistical uncertainty. Therefore, the following expression must be minimised:

$$\int w_\mathrm{s}^2(m)\, f_\mathrm{s}(m)\,\mathrm{d}m\,\mathrm{d}x \quad . \tag{E.5}$$

---

[1] In the same way a weight function $w_\mathrm{b}(m)$ can be defined to extract the background contribution.

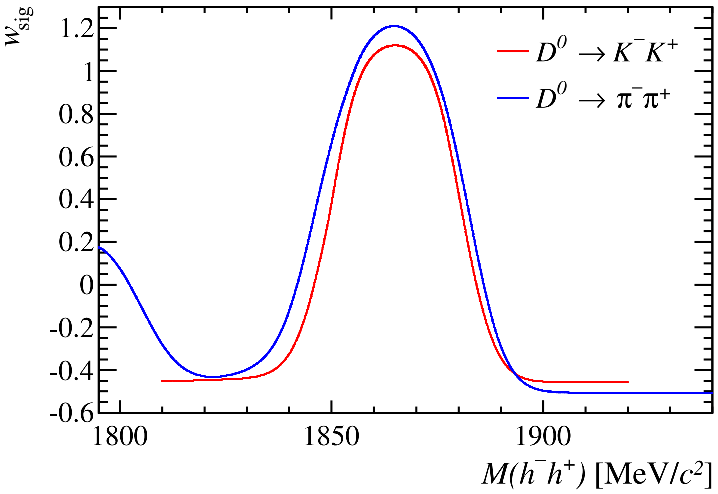

Figure E.1: The distribution of $w_{\mathrm{s}}(m)$ as a function of the invariant mass of $D^0 \to K^-K^+$ and $D^0 \to \pi^-\pi^+$ candidates. The hump of the $D^0 \to \pi^-\pi^+$ distribution in the low-mass region is due to the reflection background.

The solution of the minimisation problem is

$$w_{\mathrm{s}}(m) = \frac{V_{ss}\, f_{\mathrm{s}}(m) + V_{sb}\, f_{\mathrm{b}}(m)}{N_{\mathrm{s}} f_{\mathrm{s}}(m) + N_{\mathrm{b}} f_{\mathrm{b}}(m)} \quad , \tag{E.6}$$

where V_{ss} and V_{sb} are two real parameters. They are given by the matrix V_{ij} defined by

$$V_{ij}^{-1} = \sum_{e=1}^{N} \frac{f_{\mathrm{i}}(m_e) f_{\mathrm{j}}(m_e)}{(N_{\mathrm{s}} f_{\mathrm{s}}(m_e) + N_{\mathrm{b}} f_{\mathrm{b}}(m_e))^2} \quad . \tag{E.7}$$

Using the PDF defined in Chapter 7.3 without splitting positive and negative tags, the weights $w_{\mathrm{s}}(m)$ of $D^0 \to K^-K^+$ and $D^0 \to \pi^-\pi^+$ candidates can be obtained. The distributions are given in Figure E.1. The *sPlot* technique can be generalized for the case that the density function has more then two components. For $D^0 \to \pi^-\pi^+$ candidates, the reflection background is an additional component of the PDF.

Bibliography

[1] LHCb Collaboration, R. Aaij *et al.*, *Evidence for CP violation in time-integrated* $D \to h^- h^+$ *decay rates*, `arXiv:1112.0938`.

[2] LHCb collaboration, R. Aaij *et al.*, *Search for direct CP violation in* $D^0 \to h^- h^+$ *modes using semileptonic B decays*, Phys.Lett. **B723** (2013) 33–43, `arXiv:1303.2614`.

[3] LHCb collaboration, R. Aaij *et al.*, *Measurement of CP asymmetry in* $D^0 \to K^- K^+$ *and* $D^0 \to \pi^- \pi^+$ *decays*, `arXiv:1405.2797`.

[4] S. Stahl *et al.*, *Search for direct CP violation in* $D^0 \to K^- K^+, \pi^- \pi^+$ *using semileptonic B decays*, LHCb-ANA-2012-012; CERN-LHCb-ANA-2012-012.

[5] S. Stahl *et al.*, *Search for CP violation in* $D^0 \to K^- K^+, \pi^- \pi^+$ *using semileptonic B decays on 3 fb*$^{-}$1, LHCb-ANA-2013-055; CERN-LHCb-ANA-2013-055.

[6] LHCb collaboration, R. Aaij *et al.*, *First observation of* $\overline{B}{}^0_s \to D^{*+}_{s2} X \mu^- \overline{\nu}$ *decays*, Phys. Lett. **B698** (2011) 14, `arXiv:1102.0348`.

[7] LHCb collaboration, R. Aaij *et al.*, *Measurement of the* B^0_s*–*$\overline{B}{}^0_s$ *oscillation frequency* Δm_s *in* $B^0_s \to D^-_s(3)\pi$ *decays*, Phys. Lett. **B709** (2012) 177, `arXiv:1112.4311`.

[8] LHCb collaboration, R. Aaij *et al.*, *Prompt charm production in pp collisions at* $\sqrt{s} = 7\,\mathrm{TeV}$, Nucl. Phys. **B871** (2013) 1, `arXiv:1302.2864`.

[9] LHCb collaboration, R. Aaij *et al.*, *Measurement of the CP-violating phase* ϕ_s *in the decay* $B^0_s \to J/\psi\phi$, Phys. Rev. Lett. **108** (2012) 101803, `arXiv:1112.3183`.

[10] R. Aaij *et al.*, *The LHCb trigger and its performance in 2011*, JINST **8** (2013) P04022, `arXiv:1211.3055`.

[11] G. Altarelli, *The Standard model of particle physics*, `arXiv:hep-ph/0510281`.

[12] G. Altarelli, *The Standard electroweak theory and beyond*, `arXiv:hep-ph/0011078`.

[13] P. Langacker, *Introduction to the Standard Model and Electroweak Physics*, `arXiv:0901.0241`.

[14] ATLAS Collaboration, G. Aad *et al.*, *Observation of a new particle in the search for the Standard Model Higgs boson with the ATLAS detector at the LHC*, Phys.Lett. **B716** (2012) 1–29, `arXiv:1207.7214`.

[15] CMS Collaboration, S. Chatrchyan *et al.*, *Observation of a new boson at a mass of 125 GeV with the CMS experiment at the LHC*, Phys.Lett. **B716** (2012) 30–61, `arXiv:1207.7235`.

[16] Particle Data Group, J. Beringer *et al.*, *Review of Particle Physics (RPP)*, Phys.Rev. **D86** (2012) 010001.

[17] L. Wolfenstein, *Parametrization of the kobayashi-maskawa matrix*, Phys. Rev. Lett. **51** (Nov, 1983) 1945–1947.

[18] U. Nierste, *Three Lectures on Meson Mixing and CKM phenomenology*, `arXiv:0904.1869`.

[19] Y. Grossman, A. L. Kagan, and Y. Nir, *New physics and CP violation in singly Cabibbo suppressed D decays*, Phys.Rev. **D75** (2007) 036008, `arXiv:hep-ph/0609178`.

[20] T. Feldmann, S. Nandi, and A. Soni, *Repercussions of Flavour Symmetry Breaking on CP Violation in D-Meson Decays*, JHEP **1206** (2012) 007, `arXiv:1202.3795`.

[21] G. Hiller, M. Jung, and S. Schacht, *SU(3)-Flavor Anatomy of Non-Leptonic Charm Decays*, Phys.Rev. **D87** (2013) 014024, `arXiv:1211.3734`.

[22] A. J. Buras, *Flavor dynamics: CP violation and rare decays*, `arXiv:hep-ph/0101336`.

[23] Heavy Flavor Averaging Group, Y. Amhis *et al.*, *Averages of b-hadron, c-hadron, and tau-lepton properties as of early 2012*, `arXiv:1207.1158`.

[24] CDF Collaboration, T. Aaltonen *et al.*, *Measurement of CP–violating asymmetries in $D^0 \to \pi^+\pi^-$ and $D^0 \to K^+K^-$ decays at CDF*, Phys.Rev. **D85** (2012) 012009, `arXiv:1111.5023`; CDF collaboration, T. Aaltonen *et al.*, *Measurement of the difference of CP–violating asymmetries in $D^0 \to K^+K^-$ and $D^0 \to \pi^+\pi^-$ decays at CDF*, Phys.Rev.Lett. **109** (2012) 111801, `arXiv:1207.2158`. combined average available from `http://www-cdf.fnal.gov/physics/new/bottom/120216.blessed-CPVcharm10fb/`.

[25] BaBar Collaboration, B. Aubert *et al.*, *Search for CP violation in the decays $D^0 \to K^-K^+$ and $D^0 \to \pi^-\pi^+$*, Phys.Rev.Lett. **100** (2008) 061803, `arXiv:0709.2715`.

[26] Belle collaboration, M. Staric *et al.*, *Measurement of CP asymmetry in Cabibbo suppressed D^0 decays*, Phys.Lett. **B670** (2008) 190–195, `arXiv:0807.0148`; B. Ko, *Direct CP violation in charm at Belle*, `arXiv:1212.1975`.

[27] W. Altmannshofer, R. Primulando, C.-T. Yu, and F. Yu, *New Physics Models of Direct CP Violation in Charm Decays*, JHEP **1204** (2012) 049, `arXiv:1202.2866`.

[28] LHCb, A. Alves *et al.*, *The LHCb Detector at the LHC*, JINST **3** (2008) S08005.

[29] C. Elsasser, *Feynman Diagram Library*, `http://www.physik.uzh.ch/~che/FeynDiag/`, March, 2014. licensed under CC BY-SA.

[30] E. Norrbin and T. Sjostrand, *Production and hadronization of heavy quarks*, Eur.Phys.J. **C17** (2000) 137–161, `arXiv:hep-ph/0005110`.

[31] *The durham hepdata project*, `http://hepdata.cedar.ac.uk/`, March, 2014. group = HERAPDF, set = HERAPDF01.

[32] LHCb Collaboration, *LHCb webpage*, `http://lhcb.web.cern.ch/lhcb/speakersbureau/html/Material_for_Presentations.html`, March, 2014.

[33] Heavy Flavor Averaging Group, Y. Amhis *et al.*, *Averages of B-Hadron, C-Hadron, and tau-lepton properties as of early 2012*, `arXiv:1207.1158`.

[34] LHCb collaboration, R. Aaij *et al.*, *Prompt charm production in pp collisions at* $\sqrt{s} = 7$ *TeV*, Nucl.Phys. **B871** (2013) 1–20, `arXiv:1302.2864`.

[35] B. Andersson, G. Gustafson, G. Ingelman, and T. Sjostrand, *Parton Fragmentation and String Dynamics*, Phys.Rept. **97** (1983) 31–145.

[36] T. Sjostrand, S. Mrenna, and P. Z. Skands, *PYTHIA 6.4 Physics and Manual*, JHEP **0605** (2006) 026, `arXiv:hep-ph/0603175`.

[37] E. Norrbin, *Heavy quark production asymmetries*, `arXiv:hep-ph/9909437`.

[38] LHCb Collaboration, R. Aaij *et al.*, *Measurements of the branching fractions and CP asymmetries of B+ to J/psi pi+ and B+ to psi(2S) pi+ decays*, Phys.Rev. **D85** (2012) 091105, `arXiv:1203.3592`.

[39] LHCb Collaboration, R. Aaij *et al.*, *Measurement of the D+/- production asymmetry in 7 TeV pp collisions*, Phys.Lett. **B718** (2013) 902–909, `arXiv:1210.4112`.

[40] A. Lenz, *Theoretical update of B-Mixing and Lifetimes*, `arXiv:1205.1444`.

[41] L. Evans and P. Bryant, *LHC Machine*, JINST **3** (2008) S08001.

[42] J. Van Tilburg, *Track simulation and reconstruction in LHCb.* CERN-THESIS-2005-020, 2005.

[43] R. Aaij *et al.*, *The LHCb Trigger and its Performance in 2011*, JINST **8** (2013) P04022, `arXiv:1211.3055`.

[44] L. Darme, J. van Tilburg, and S. Stahl, *A Monte-Carlo based study of direct CP violation in* $D^0 \to K^+K^-$, $\pi^+\pi^-$ *using semileptonic B decays*, Tech. Rep. LHCb-INT-2012-026. CERN-LHCb-INT-2012-026, CERN, Geneva, Jul, 2012.

[45] LHCb Collaboration, *The Gaudi project*, `http://proj-gaudi.web.cern.ch/proj-gaudi/`.

[46] LHCb Collaboration, *The Brunel project*, `http://lhcb-release-area.web.cern.ch/LHCb-release-area/DOC/brunel/`.

[47] LHCb Collaboration, *The DaVinci project*, `http://lhcb-release-area.web.cern.ch/LHCb-release-area/DOC/davinci/`.

[48] LHCb Collaboration, *The Moore project*, `http://lhcb-release-area.web.cern.ch/LHCb-release-area/DOC/moore/`.

[49] LHCb Collaboration, *The Gauss project*, `http://lhcb-release-area.web.cern.ch/LHCb-release-area/DOC/gauss/`.

[50] D. J. Lange, *The EvtGen particle decay simulation package*, Nucl. Instrum. Meth. **A462** (2001) 152–155.

[51] Geant4 collaboration, S. Agostinelli *et al.*, *Geant4: a simulation toolkit*, Nucl. Instrum. Meth. **A506** (2003) 250; Geant4 collaboration, J. Allison *et al.*, *Geant4 developments and applications*, IEEE Trans.Nucl.Sci. **53** (2006) 270.

[52] LHCb Collaboration, *The boole project*, `http://lhcb-release-area.web.cern.ch/LHCb-release-area/DOC/boole/`.

[53] M. De Cian, U. Straumann, O. Steinkamp, and N. Serra, *Track Reconstruction Efficiency and Analysis of* $B^0 \to K^{*0}\mu^+\mu^-$ *at the LHCb Experiment.* PhD thesis, Zurich U., Sep, 2013. Presented 14 Mar 2013.

[54] O. Callot and S. Hansmann-Menzemer, *The Forward Tracking: Algorithm and Performance Studies*, Tech. Rep. LHCb-2007-015. CERN-LHCb-2007-015, CERN, Geneva, May, 2007.

[55] R. Aaij *et al.*, *Measurement of the track reconstruction efficiency at LHCb*, LHCb-DP-2013-002. in preparation.

[56] R. E. Kalman, *A new approach to linear filtering and prediction problems*, Transactions of the ASME–Journal of Basic Engineering **82** (1960), no. Series D 35–45.

[57] Frühwirth, R., *Application of Kalman Filtering to track and vertex fitting*, Nucl. Instrum. Meth. A **262** (1987) 444.

[58] R. Van der Eijk, *Track reconstruction in the LHCb experiment.* CERN-THESIS-2002-032, 2005.

[59] P. Rodríguez Pérez, *The LHCb VERTEX LOCATOR performance and VERTEX LOCATOR upgrade*, Journal of Instrumentation **7** (Dec., 2012) C2008, `arXiv:1209.4845`.

[60] LHCb collaboration, R. Aaij *et al.*, *Measurements of the* B^+*,* B^0*,* B^0_s *meson and* Λ^0_b *baryon lifetimes*, `arXiv:1402.2554`.

[61] LHCb Collaboration, R. Aaij *et al.*, *Measurement of the Ds+ - Ds- production asymmetry in 7 TeV pp collisions*, Phys.Lett. **B713** (2012) 186–195, `arXiv:1205.0897`.

[62] LHCb collaboration, R. Aaij *et al.*, *Measurement of charged particle multiplicities and densities in pp collisions at $\sqrt{s}=7$ TeV in the forward region*, `arXiv:1402.4430`.

[63] M. Adinolfi *et al.*, *Performance of the LHCb RICH detector at the LHC*, Eur. Phys. J. **C73** (2013) 2431, `arXiv:1211.6759`.

[64] F. Archilli *et al.*, *Performance of the muon identification at LHCb*, JINST **8** (2013) P10020, `arXiv:1306.0249`.

[65] LHCb collaboration, R. Aaij *et al.*, *Measurement of the flavour-specific CP-violating asymmetry a^s_{sl} in B^0_s decays*, Phys.Lett. **B728** (2014) 607–615, `arXiv:1308.1048`.

[66] R. Aaij and J. Albrecht, *Muon triggers in the High Level Trigger of LHCb*, Tech. Rep. LHCb-PUB-2011-017. CERN-LHCb-PUB-2011-017, CERN, Geneva, Sep, 2011.

[67] M. Williams *et al.*, *The HLT2 Topological Lines*, Tech. Rep. LHCb-PUB-2011-002. CERN-LHCb-PUB-2011-002, CERN, Geneva, Jan, 2011.

[68] S. Tolk, J. Albrecht, F. Dettori, and A. Pellegrino, *Data-driven measurement of trigger efficiencies with the TisTos method*, Tech. Rep. LHCb-INT-2013-038. CERN-LHCb-INT-2013-038, CERN, Geneva, Jun, 2013.

[69] W. D. Hulsbergen, *Decay chain fitting with a Kalman filter*, Nucl.Instrum.Meth. **A552** (2005) 566–575, `arXiv:physics/0503191`.

[70] LHCb Collaboration, R. Aaij *et al.*, *Measurement of b-hadron masses*, Phys. Lett. B **708** (Dec, 2011) 241–248. 15 p. Comments: 9 pages (+ title page + author list), 3 figures, 4 tables, submitted to Phys. Lett. B.

[71] LHCb Collaboration, R. Aaij *et al.*, *Precision measurement of D meson mass differences*, J. High Energy Phys. **06** (Apr, 2013) 065. 18 p. Comments: 18 pages, 3 figures, 3 tables.

[72] J. Brehmer, J. Albrecht, and P. Seyfert, *Ghost probability: an efficient tool to remove background tracks*, Tech. Rep. LHCb-INT-2012-025. CERN-LHCb-INT-2012-025, CERN, Geneva, Sep, 2012.

[73] S. Kullback, *Letter to Editor: the Kullback-Leibler Distance*, The American Statistician **41** (1987) 340. The use of the Kullback-Leibler distance at LHCb is described in M. Needham, *Clone Track Identification Using the Kullback-Leibler Distance*, LHCb-2008-002.

[74] M. Pivk and F. R. Le Diberder, *Plots: A statistical tool to unfold data distributions*, Nuclear Instruments and Methods in Physics Research A **555** (Dec., 2005) 356–369, `arXiv:physics/0402083`.

[75] T. Skwarnicki, *A study of the radiative cascade transitions between the Upsilon-prime and Upsilon resonances.* PhD thesis, Institute of Nuclear Physics, Krakow, 1986. DESY-F31-86-02.

[76] A. Pais and O. Piccioni, *Note on the decay and absorption of the* θ^0, Phys.Rev. **100** (1955) 1487–1489.

[77] M. L. Good, *Relation between scattering and absorption in the Pais-Piccioni phenomenon*, Phys.Rev. **106** (1957) 591–595.

[78] W. Fetscher, P. Kokkas, P. Pavlopoulos, T. Schietinger, and T. Ruf, *Regeneration of arbitrary coherent neutral kaon states: A new method for measuring the* $K^0 - \overline{K}^0$ *forward scattering amplitude*, Z.Phys. **C72** (1996) 543–547.

[79] A. Gsponer *et al.*, *Precise coherent* K^0_S *regeneration amplitudes for C, Al, Cu, Sn and Pb nuclei from 20 to* 140 GeV/c *and their interpretation*, Phys.Rev.Lett. **42** (1979) 13.

[80] R. A. Briere and B. Winstein, *Determining the phase of a strong scattering amplitude from its momentum dependence to better than 1°: The example of kaon regeneration*, Phys.Rev.Lett. **75** (1995) 402–405.

[81] LHCb Collaboration, R. Aaij *et al.*, *Prompt* K^0_S *production in pp collisions at* $\sqrt{s} = 0.9$ TeV, Phys.Lett. **B693** (2010) 69–80, `arXiv:1008.3105`.

[82] LHCb collaboration, R. Aaij *et al.*, *Measurement of* D^0–$\overline{D}^0$ *mixing parameters and search for CP violation using* $D^0 \to K^+\pi^-$ *decays*, Phys. Rev. Lett. **111** (2013) 251801, `arXiv:1309.6534`.

[83] LHCb collaboration, R. Aaij *et al.*, *Observation of* B^0_s *mixing and measurement of mixing frequencies using semileptonic B decays*, Eur. Phys. J. **C73** (2013) 2655, `arXiv:1308.1302`.

[84] LHCb collaboration, *A search for time-integrated CP violation in* $D^0 \to K^-K^+$ *and* $D^0 \to \pi^-\pi^+$ *decays*, LHCb-CONF-2013-003.

[85] Wikipedia, *Johnson su distribution — Wikipedia, the free encyclopedia*, `http://en.wikipedia.org/wiki/Johnson_SU_distribution`, 2014. [Online; accessed 14-April-2014].